REPORT DOCUMENTATION PAGE

1. REPORT DATE (DD-MM-YYYY)	2. REPORT TYPE	3. DATES COVERED (From - To)
07-03-2005	Final	10/01/02 – 03/31/06

4. TITLE AND SUBTITLE	5a. CONTRACT NUMBER
Control of Hydrogen Environmental Embrittlement of Ultra-High Strength Steel by Coatings	N/A
	5b. GRANT NUMBER N00014-03-1-0029
	5c. PROGRAM ELEMENT NUMBER N/A

6. AUTHOR(S)	5d. PROJECT NUMBER
Gangloff, R. P.	N/A
	5e. TASK NUMBER N/A
	5f. WORK UNIT NUMBER N/A

7. PERFORMING ORGANIZATION NAME(S) AND ADDRESS(ES)	8. PERFORMING ORGANIZATION REPORT NUMBER
University of Virginia Office of Sponsored Programs P. O. Box 400195 Charlottesville, Virginia 22904-4195	117777-101-GG10492-31340

9. SPONSORING / MONITORING AGENCY NAME(S) AND ADDRESS(ES)	10. SPONSOR/MONITOR'S ACRONYM(S)
Office of Naval Research Ballston Centre Tower One 800 North Quincy Street Arlington, Virginia 22217-5660	N/A
	11. SPONSOR/MONITOR'S REPORT NUMBER(S) N/A

12. DISTRIBUTION / AVAILABILITY STATEMENT

Approved for public release, distribution unlimited.

13. SUPPLEMENTARY NOTES
N/A

14. ABSTRACT The overarching objective of this research, conducted from October of 2002 through March of 2006, was to develop the foundation & understanding necessary to mitigate hydrogen environment embrittlement (HEE) of ultra-high strength steels (UHSS) relevant to the Navy. We seek to develop the fundamental knowledge that clarifies, as a coating/UHSS/environment system, how to deploy ultra-high strength steels that resist hydrogen embrittlement when stressed in marine environments. Specific aims are to understand the electrochemical & chemical details that govern H supply to crack tip damage sites, as well as the detailed processes that govern crack tip H damage in UHSS. By controlling H supply to crack tips through control of electrochemical & chemistry factors, as well as by understanding factors such as trapping that control intrinsic HEE resistance, we seek to identify viable mitigation strategies for resistance to HEE. The class of secondary hardened martensitic steels is emphasized in an approach that centered on two tasks: (a) fracture mechanics based measurement & modeling of HEE coupled with (b) electrochemical studies of H production & uptake in occluded geometries plus H interaction with microstructural trap sites. The results of this work are detailed in this report & include experimental data on the severe transgranular HEE produced in this class of steels, the central importance of H trapping at martensite interfaces & nano-scale carbide strengthening precipitates, the strong effect of electrochemical polarization on H production/uptake & crack growth, & avenues to mitigate such cracking by electrochemical control derived from tailored coatings. This research sets the stage for next generation modeling to scontrol HEE in UHSS>.

15. SUBJECT TERMS
mitigate hydrogen, environment embrittlement, ultra-high strength steels

16. SECURITY CLASSIFICATION OF:			17. LIMITATION OF ABSTRACT	18. NUMBER OF PAGES	19a. NAME OF RESPONSIBLE PERSON
a. REPORT	**b. ABSTRACT**	**c. THIS PAGE**	UL	15	Gangloff, R. P.
Unclassified	Unclassified	Unclassified			**19b. TELEPHONE NUMBER** (include area code) 434-982-5782

Title: CONTROL OF HYDROGEN ENVIRONMENT EMBRITTLEMENT OF ULTRA-HIGH STRENGTH STEEL FOR NAVAL APPLICATION

Authors: R.P. Gangloff and J.R. Scully

Abstract:

The overarching objective of this research, conducted from September of 2002 through March of 2006, was to develop the foundation and understanding necessary to mitigate hydrogen environment embrittlement (HEE) of ultra-high strength steels (UHSS) relevant to the Navy. We seek to develop the fundamental knowledge that clarifies, as a coating/UHSS/environment system, how to deploy ultra-high strength steels that resist hydrogen embrittlement when stressed in marine environments. Specific aims are to understand the electrochemical and chemical details that govern H supply to crack tip damage sites, as well as the detailed processes that govern crack tip H damage in UHSS. By controlling H supply to crack tips through control of electrochemical and chemistry factors, as well as by understanding factors such as trapping that control intrinsic HEE resistance, we seek to identify viable mitigation strategies for resistance to HEE. The class of secondary hardened martensitic steels is emphasized in an approach that centered on two tasks: (a) fracture mechanics based measurement and modeling of HEE coupled with (b) electrochemical studies of H production and uptake in occluded geometries plus H interaction with microstructural trap sites. The results of this work are detailed in this report and include experimental data on the severe transgranular HEE produced in this class of steels, the central importance of H trapping at martensite interfaces and nano-scale carbide strengthening precipitates, the strong effect of electrochemical polarization on H production/uptake and crack growth, and avenues to mitigate such cracking by electrochemical control derived from tailored coatings. This research sets the stage for next generation modeling to control HEE in UHSS.

20060710058

Background Need

Modern alloy steels have been developed with outstanding combinations of ultra-high strength and fracture toughness, representing a major success in experimental and computational materials science over the past 20 years. However, the performance of such steels in critical applications is degraded dramatically by the persisting problems of internal hydrogen embrittlement (IHE) and hydrogen environment embrittlement (HEE). Such steels are characterized by high purity and nano-scale strengthening clusters/coherent precipitates not generally considered in hydrogen embrittlement studies. The development of an ultra-high strength steel (UHSS) that is immune to hydrogen embrittlement is of seminal importance.

This is a stiff challenge given the localized character of crack tip H damage, the interdisciplinary problem, and many variables that affect IHE and HEE. From the engineering perspective, experiments to characterize the importance of H cracking in UHSS are often incorrectly designed counter to state-of-the-art understanding, or are partially carried out and miss windows of variables where cracking is severe. From the scientific perspective, intergranular IHE and HEE of conventional steels are reasonably understood based on H-impurity induced bond decohesion. However, new H cracking mechanisms are equally serious compared to intergranular damage; these cracking modes involve martensitic interfaces and other processes within austenite grains, and must be understood. Predictive models of IHE and HEE based on mechanistic understanding of crack tip H damage are lacking; accordingly.

Long-term Research Objective

The overarching objective of this research is to develop the fundamental foundations and understandings necessary to mitigate HEE of ultra-high strength steels of relevance to the Navy. We seek to develop the fundamental knowledge that clarifies, as a coating/UHSS/environment system, how to deploy ultra-high strength steels that resist hydrogen embrittlement when stressed in environments typical of marine hull, machinery, propulsion and component applications including marine amphibious vehicles. Specific aims are to understand the electrochemical and chemical details that govern H supply to crack tip damage sites, as well as the detailed processes that govern crack tip H damage in UHSS. By controlling H supply to crack tips through control of electrochemical and chemistry factors, as well as by understanding factors such as trapping that control intrinsic HEE resistance, we seek to identify viable mitigation strategies for resistance to HEE.

S&T Objectives

Research emphasized several objectives specific to modern ultra-high strength steels:

The objective of Task I is to characterize and understand the electrochemical and strengthening precipitate conditions that mitigate HEE in modern ultra-high strength steel (UHSS); specific to electrode potential control, small crack geometry, and marine environmental exposure. The specific goals are to:

- Implement a quantitative fracture mechanics/electrochemistry method to characterize the HEE resistance of modern UHSS in uniquely controlled marine environments.

- Apply the method to establish the effect of electrode potential on HEE resistance of modern UHSS, emphasizing the range of potentials relevant to service (coated, cathodically protected, geometrically occluded) in marine environments.

- Apply the method to establish the effect of strengthening precipitate microstructure on HEE resistance of modern UHSS, selected using trap theory, and emphasizing the range of potentials where HEE is least severe in the standard microstructure.

- Apply the method to establish the effect of ionic additions to the bulk chloride solution on HEE resistance of modern UHSS, selected using trap theory, and emphasizing the range of potentials where HEE is least severe in the standard microstructure.

- Understand the mechanism of TG hydrogen embrittlement in UHSS and improve micromechanical modeling of crack tip H embrittlement centered on the concentration of diffusible H that accumulates in the crack tip FPZ.

The objectives of Task II are to characterize and understand the relationships between applied electrochemical potential, crack geometry as well as chemical conditions and the hydrogen ingress properties that control HEE of selected modern UHSS in marine environments. Specific goals of the three subtasks in Task II are to:

- Establish the causal relationships between galvanic couple potential (controlled by galvanic coupling to components, metallic coatings or sacrificial anodes), environment (composition and pH), crack geometry (short and long cracks) and immersion condition (full immersion vs. alternate or thin-layer immersion), and the resulting hydrogen ingress properties that govern hydrogen environment embrittlement of UHSS. Identify and quantify the resulting occluded site diffusible H concentration ($C_{H\text{-diff}}$) in UHSS that governs HEE. This knowledge will form the basis for understanding how existing and next-generation sacrificial anodes, metallic coatings, and alloy modifications can be manipulated to mitigate HEE susceptibility of relevant UHSS.

- Understand the contributions of local crack tip and global hydrogen uptake on HEE susceptibility of short cracks (50-500 μm length range) of a modern UHSS.

- Establish the causal relationships between chemical species, and inhibition of hydrogen environment embrittlement of a modern UHSS. Accomplish this by elucidating how inhibitors affect H electrochemistry and ingress issues that govern hydrogen production and uptake on UHSS.

These studies are based on the view that the H-diffusion barrier properties of a metallic coating are not relevant to mitigating HEE since the coating is very likely to be defected in either application or service. As such, bare steel will be exposed to an environment capable of producing locally high concentrations of potentially embrittling H. A diffusion barrier is

irrelevant to this damage scenario. Rather, we aim to identify coating polarization, as well as "healing" ion release conditions that could eliminate hydrogen embrittlement of the bared steel. Increased intrinsic resistance of the steel, achieved through metallurgical means, is a parallel and complimentary route to solving this problem.

Other goals included: (1) refine the fundamental understanding of the role of hydrogen trapping in complex steel microstructures to better explain the root cause of transgranular hydrogen embrittlement, (2) provide guidance on generic measures to control IHE after H uptake during Cd electroplating and egress during thermal baking, as governed by H trapping.

Approach

An interdisciplinary-team approach was assembled to achieve these goals following a route that has lead to substantial successes under previous ONR funding that examined HEE in high strength titanium alloys and IHE in AerMet®100. Professors Gangloff and Scully, jointly advising three graduate research assistants (GRA) and a post-doctoral research associate, integrated state-of-the art methods in electrochemistry, fracture mechanics and metallurgy to achieve the proposed-program goals.

We characterized experimentally the H production/uptake and HEE behaviors of two main material classes, including ultra-high strength Cr-containing martensitic/age hardened stainless steel such as Custom 465, and a quenched and tempered/precipitation age hardened steel containing high Co such as AerMet®100. The later ultra-high strength steels where emphasized and may require coatings or sacrificial anode cathodic protection in marine service. These steels were tested in carefully selected environmental exposure and crack geometry conditions that are relevant to fatigue and fracture critical components in marine applications. The effect(s) of galvanic coupling to other components and coatings, and/or conventional and low output sacrificial anodes, on the crack tip environment were simulated by applied potential and bulk environment chemistry modifications including addition of soluble species that could be released from coatings to protect UHSS from H uptake. The relationship between cracking threshold and crack tip H concentration was modeled to gain understanding and reduce the need for extensive-complex experimentation.

Task I, lead by Professor Gangloff, focused on the fracture micromechanics of hydrogen environment embrittlement. The characterization approach employed a small crack fracture mechanics method to characterize the threshold and kinetics for hydrogen environment enhanced subcritical cracking under slow monotonic and low frequency cyclic loading of UHSS. This unique method provided information on the electrode potential, environment composition, and galvanic coupling dependencies of HEE. The results of the proposed experiments guided Task II and provided a starting point for mechanistic experiments. In this latter regard, experiments and micromechanical analyses examined the details of crack tip damage localization due to 3 aspects of the FPZ; high H absorption from extraordinary surface reactions, high stress from length-scale dependent plasticity, and strong H trapping at martensite and strengthening precipitate interfaces. The goal is to predict quantitatively the relationship between K_{TH} and H content in the FPZ.

Task II, lead by Professor Scully, focused on the electrochemical aspects of H production. The goal was to predict quantitatively the relationship between electrochemical, chemical and geometric conditions, and H production rates as well as diffusible and trapped H content in the simulated FPZ at a crack tip. We characterized experimentally the H production/uptake behavior of two UHSS for selected environmental exposures (solution composition and potentials as well as electrolyte layer depth) and "scaled" crack geometry conditions that are relevant to fatigue and fracture critical components in marine applications. We used the novel approach involving scaled occluded sites enabled through application of crevice laws (e.g., X^2/G) to increase the occluded site area to conduct spatially resolved hydrogen measurements. We measured local hydrogen concentrations ($C_{H\text{-diff}}$ and $C_{H\text{-total}}$) using either permeation, high resolution thermal desorption spectroscopy, and/or nuclear reaction analysis. Diffusible hydrogen, high H absorption from extraordinary surface reactions at particular potentials and strong H trapping at martensite and strengthening precipitate interfaces where detected using these novel techniques. Galvanic coupling effects on the crack tip environment where simulated by controlling applied potential as well as by control of bulk environment chemistry. In the additional phase of the project, chemical inhibition of hydrogen environment embrittlement was investigated by exploring the addition of soluble species that could protect UHSS from H uptake. Task II provides the necessary information on H uptake at various crack tip aspect ratios for a variety of environment and galvanic coupling conditions to supplement Task I. The potential dependency of cracking susceptibility is explained. The desirable and undesirable attributes of galvanic coupling from the standpoint of HEE of UHSS are better understood. The functions and features of either novel next generation low-output anodes, novel next-generation coatings or favorable galvanic couples can now be better understood.

Three graduate students have worked on this project. In June of 2003, Ms. Beth Kelher began her PhD studies on this ONR program, with emphasis on the electrochemical issues outlined in Task II of the primary objective. An MS student, Mr. Yongwon Lee, joined the research team in August of 2003 and conducted the hydrogen environment embrittlement cracking experiments associated with Task I of the primary objective. A third graduate student, Mr. Sami M. Al-Ghamdi joined this research team in August of 2004. Mr. Al-Ghamdi focused on chemical inhibition of hydrogen environment assisted cracking discussed in Task II. Dr. Daoming Li, a Post-Doctoral Research Associate in the Department of Materials Science and Engineering, was supported for 50% of his effort on this research in 2003 and 2004. Messrs Hakan Dogan and Michael Switzer conducted research sponsored under a previous ONR grant, and completed their MS thesis during the first few months of the current grant.

Completed Science and Technology

The results of the research conducted in Tasks I and II are detailed in the following published papers, chapters and reports. This is an important body of literature that will provide the foundation for future predictive modeling of H cracking, necessary to more efficiently and effectively design coatings and alloy composition/processing history to control HEE.

Technology Transfer

Research in early FY2004 completed efforts to understand internal hydrogen embrittlement (IHE) in AerMet® 100. IHE can occur as a function of manufacturing and processing involving electrochemically deposited cadmium layers when atomic hydrogen is co-deposited. The bulk of this work was reported in FY2003, and the attached papers, but there is a technology transfer opportunity to note.

We established the technical basis for controlling IHE through understanding of hydrogen-microstructure interactions that govern this process. This is a more scientific approach, as opposed to the established methodology in the literature based on trial and error analysis of the effects of various thermal baking treatments on fracture toughness of plated steels. We developed a scientific understanding of which hydrogen trap states are operative in AerMet®100, particularly which control hydrogen embrittlement, coupled with the knowledge of those trap states will release hydrogen by thermal egress during remedial baking procedures. The focus of this study was dull cadmium plated AerMet®100.

To review, mitigation of IHE requires that the reservoir of damaging hydrogen, from plating and trapped at $(Fe,Cr,Mo)_2C$ precipitates and other weaker trapping states, be removed prior to service. The results of thermal desorption spectroscopy (TDS) experiments demonstrate that $190°C$ baking readily removes this detrimental hydrogen, as expected theoretically because the thermal energy of baking at $190°C$ is similar to the trap binding energy and overall trap desorption energy to enable a high probability of hydrogen release from trap sites (e.g., $kT_{190C} \approx 11.5\pm0.5$ kJ/mol). However, this H egress is unfortunately retarded by both the slow H diffusivity in AerMet® 100, as well as in the cadmium plate. Results suggested that sufficient H can be retained in trap reservoirs when dull cadmium layers are thick and less porous, and is available to affect the fracture resistance of AerMet®100, at least near the surface of thick sections even after long baking times.

Given this research, scientific control of IHE in cadmium-plated UHSS has now been clarified. Control of IHE in cadmium plated AerMet®100 requires the following;

1. The damaging source of hydrogen during IHE is those trap sites, as well as interstitial lattice sites, that permit repartitioning of internal hydrogen from these traps to the tensile stress field of a crack tip. By definition these damaging traps that serve to supply hydrogen must have a low enough binding energies such that $E_b <$ the crack tip stress field energy. Thermal baking must be performed to remove diffusible hydrogen from such trap states that energetically allow hydrogen repartitioning to the crack tip fracture process zone. This requires that the thermal energy imparted by baking approaches the desorption energy (e.g., $kT_{baking} \approx E_d$) of $(Fe,Cr,Mo)_2C$ traps that supply damaging hydrogen.

2. Sufficiently long baking time is required to avoid short term intensification of hydrogen levels in ultra-high strength steels. This phenomenon results from hydrogen ingress supplied from co-deposited hydrogen existing in cadmium layers.

This occurs during early baking periods at 190°C. In modeling this behavior, it is necessary to use a concentration and temperature dependent H diffusivity.

.3. Control of dull cadmium plated layer thickness and porosity is necessary so that thermal egress of hydrogen from weak trap states such as $(Fe,Cr,Mo)_2C$ precipitates is not hindered.

4. Microstructural control of trapping states must be optimized such that strong traps, that do not release hydrogen upon 190°C baking, cannot themselves serve as crack initiation sites, or be interconnected to provide a continuous crack propagation path.

5. Microstructural control is necessary to avoid a high density of intermediate binding energy trap states that resist thermal egress of hydrogen (e.g., $kT_{baking} \ll E_d$), but allow repartitioning of hydrogen to the stress field of extremely sharp crack tips (e.g., $E_b < \sigma_H v_H$) with associated high stress levels. It appears fortuitous that $(Fe,Cr,Mo)_2C$ traps do not fall into this category and instead satisfy the criteria listed in (1) above. However, this is not assured for all ultra-high strength steels required in all naval applications under all conditions.

The information provided by this research can be input to H diffusion models designed to optimize post-plate thermal treatment. The investigators are available to pursue this issue to confirm that changes in baking implemented for UHSS with slower-H diffusivity are consistent with this new knowledge base.

Hydrogen Assisted Cracking of High Strength Alloys

Richard P. Gangloff

HYDROGEN ASSISTED CRACKING OF HIGH STRENGTH ALLOYS

Richard P. Gangloff

6.03.1 INTRODUCTION

Two important advances over the past 40 years enable the optimization and effective management of the structural integrity of components in high performance applications. First, the solid mechanics community established linear elastic fracture mechanics as the premier framework for modeling the damage tolerance of fracture critical components (Irwin and Wells, 1997; Paris, 1998). Second, materials scientists developed metals with outstanding balances of high tensile strength and high fracture toughness (Garrison, 1990; Wells, 1993; Boyer, 1993; Starke and Staley, 1995; Olson, 1997; Kolts, 1996). An example of achievable strength-toughness properties is provided in Fig. 1, a plot of plane strain fracture toughness (K_{IC}) *vs.* tensile yield strength (σ_{YS}) for ultra-high strength steels (UHSS) and β-Ti alloys precipitation hardened with α phase (Gangloff, 2001). New nano-scale characterization and high performance computational methods provide for additional advances in the mechanical performance properties of structural metals. These modern alloys and analysis tools satisfy technological needs for optimization and management of component performance in demanding fatigue and fracture critical applications in the aerospace, marine, energy, transportation, and defense sectors.

Counter to these successes, hydrogen broadly and severely degrades the fracture resistance of high strength metallic alloys. The Mode I stress intensity factor (K) levels that produce subcritical-hydrogen cracking are low, of order 5 to 25% of K_{IC}, as indicated by the shaded areas in Fig. 1. In essence the toughness gains from decades of metallurgical research are compromised by so-called hydrogen embrittlement. In response a massive literature on H effects in metals has evolved, as represented by important archival
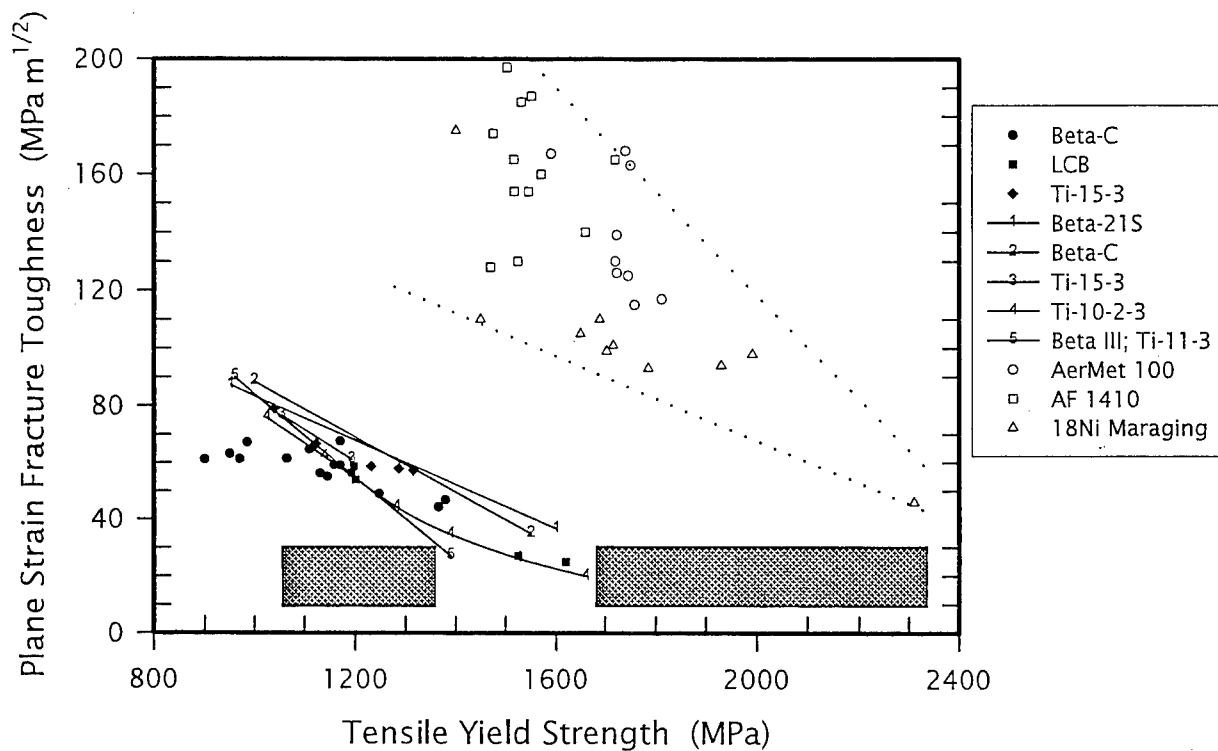
Figure 1.   The yield strength dependence of plane strain fracture toughness for high strength α-precipitation hardened β-Ti alloys and tempered martensitic alloy steels fractured in moist air at 25°C. The shaded areas generally represent the lower bound stress intensity regime for severe IHAC and HEAC.

proceedings (Scully, 1971; Raymond, 1972, 1988; Bernstein and Thompson, 1974, 1981; Swann, et al., 1977; Louthan and McNitt, 1977; Alefeld and Völkl, 1978, 1997; Staehle et al., 1977; Louthan, et al., 1981; Azou, 1982; Interrante and Pressouyre, 1982; Gangloff, 1984; Oriani et al., 1985; Jones and Gerberich, 1986; Praeger, 1989, 1994; Gangloff and Ives, 1990; Lisagor et al., 1990; Moody and Thompson, 1990a; Turnbull, 1995; Thompson and Moody, 1996; Moody and Thompson 2003) and 100s of journal papers. In spite of these efforts, hydrogen embrittlement continues to plague applications of high strength metals.

The objective of this chapter is to establish the foundation necessary to control hydrogen assisted subcritical cracking in high strength metals by quantitative structural integrity assessment. The elements of this foundation include: (a) definition of the forms of hydrogen cracking in 6.03.2, (b) the role of fracture mechanics-similitude scaling of laboratory data to enable component prediction, 6.03.3, (c) the technological importance of hydrogen cracking in 6.03.4, (d) a summary of data that describe hydrogen degradation phenomena, 6.03.5, and the effects of important variables, 6.03.6, (e) assessment of the state-of-the-art in basic mechanistic understanding, 6.03.7, (f) micromechanical and chemical modeling to predict material properties, 6.03.8, and (g) critical uncertainties that hinder life prediction, 6.03.9.

This chapter concentrates mainly on high and ultra-high strength metals with tensile yield strength/elastic modulus ratio above about 0.005 and that exhibit hydrogen assisted crack propagation in the absence of metal hydride formation. Alloy families include tempered martensitic low alloy and stainless steels, precipitation hardened aluminum alloys, precipitation hardened body-centered cubic titanium (β-Ti) alloys, and precipitation hardened austenitic superalloys. Hydride-based embrittlement of hexagonally closed packed

Ti and Zr alloys is discussed elsewhere in Volume 6. All forms of hydrogen damage, except hydride cracking, that occur in the temperature range within $\pm150°C$ of ambient are considered here. Hydrogen effects on fatigue crack propagation are reviewed elsewhere (Gangloff, 1990, 1990a, 2002). The linear elastic fracture mechanics framework provides the effective basis for each aspect of this review and only crack propagation is considered. This chapter builds on previous reviews of hydrogen embrittlement of high strength alloys (Louthan et al., 1972; Blackburn et al., 1972; Speidel and Hyatt, 1972; Speidel, 1975; Wanhill, 1975; Kerns, et al., 1977; Dautovich and Floreen, 1977; Sandoz, 1977; Oriani, 1978; Hirth, 1980; Thompson and Bernstein, 1980; Nelson, 1983; Vehoff and Rothe, 1983; Gruhl, 1984; Lynch, 1988, 2003; McIntyre, 1985; Gangloff, 1986, 2003; Moody et al., 1990; Holroyd, 1990; Marsh and Gerberich, 1992; Interrante and Raymond, 1995; Vehoff, 1997; McMahon, 2001).

6.03.2 HYDROGEN EFFECTS ON CRACK PROPAGATION

Hydrogen degradation of the crack propagation resistance of high strength alloys is categorized as either *Internal Hydrogen Assisted Cracking* (IHAC) or *Hydrogen Environment Assisted Cracking* (HEAC). These phenomena are also called *Internal Hydrogen Embrittlement* (IHE) and *Hydrogen Environment Embrittlement* (HEE), respectively. The former designations are favored since H clearly degrades crack propagation resistance by assisting the microscopic processes that constitute crack tip advance, while embrittlement restricts the perception of the precise nature of the H-damage mechanism as detailed in 6.03.7. In high strength alloys, H effects are invariably localized

to the crack tip. IHAC and HEAC are distinguished by the source of the offending H supplied to the crack tip fracture process zone (FPZ), but otherwise share common aspects. This view is summarized in Fig. 2.

6.03.2.1   Internal Hydrogen Assisted Cracking—*IHAC*

Atomic hydrogen can be introduced globally throughout the microstructure by manufacturing operations (e.g., casting, welding, surface-chemical cleaning, electrochemical machining, electroplating, and heat treatment) as well as by environmental exposure (e.g., cathodic electrochemical reactions at low temperatures and gaseous hydrogen exposure at elevated temperatures). Subcritical crack growth occurs when the hydrogen "charged" metal is subsequently stressed, as shown in the right-portion of Fig. 2. Loading causes a redistribution of dissolved hydrogen from the surrounding microstructure to the crack tip process zone to promote crack growth. Stress is not necessary during hydrogen uptake, and environmental hydrogen production at the crack tip during stressing is not significant since the loading environment is typically benign.

6.03.2.2   Hydrogen Environment Assisted Cracking--*HEAC*

HEAC involves the conjoint action of mechanical loading and chemical reaction. Atomic hydrogen is produced predominantly on clean crack surfaces localized near to the tip, followed by H uptake into the crack tip FPZ and subsequent embrittlement as shown in the left and bottom portions of Fig. 2. Mass transport of elements of the surrounding environment is unique to the occluded crack volume and supplies crack tip surface reactions,
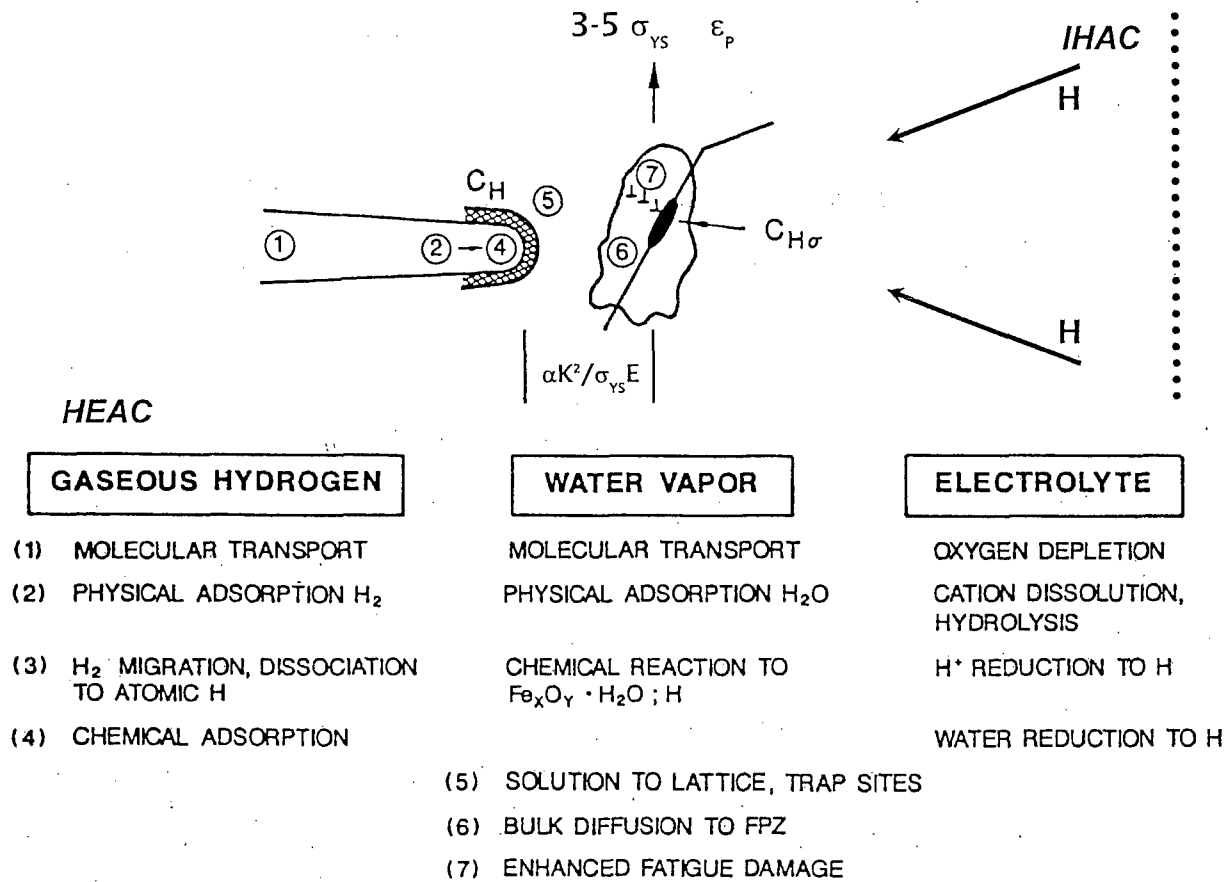
Figure 2.   The sequence of elemental processes that supply damaging H to the crack tip fracture process zone during either HEAC for gaseous hydrogen, water vapor or an electrolyte, or IHAC for a H precharged microstructure. The dotted line indicates the outer boundary of the plastic zone. Crack tip tensile stresses are maximized at some distance ahead of the tip, proportional to $K^2/\sigma_{YS}E$ (see 6.03.8.1).

as illustrated for three environments. From left to right, atomic hydrogen (H) is produced by dissociative chemical adsorption for H_2, by chemical reactions for gases such as water vapor or H_2S, or by electrochemical cathodic reactions for acidic or alkaline electrolytes. Once produced, the H diffuses ahead of the crack tip into the FPZ to affect damage. This scenario provides the hydrogen mechanism for stress corrosion cracking (SCC) and sulfide stress cracking for alloys in aqueous H_2S-bearing electrolytes. Electrochemical reactions leading to metal dissolution and passive film formation can occur at the crack tip, concurrent with H production, to affect crack growth. The extent to which hydrogen dominates damage is controversial, but the HEAC mechanism for SCC is accepted broadly for high strength metals as summarized in 6.03.7.1.

6.03.2.3   Commonalities and Differences

IHAC and HEAC share common features for high strength metals. Each damage mode occurs subcritically at stress intensity levels well below K_{IC}. IHAC and HEAC proceed by similar microscopic crack paths; typically either intergranular, interfacial, or along crystallographically defined planes through grains; in sharp contrast to the microvoid-based morphology typical of ductile fracture in high strength alloys (Shipley and Becker, 2002). Both IHAC and HEAC are affected similarly by variables such as applied K level, loading rate (dK/dt), alloy σ_{YS}, grain boundary impurity composition, temperature, and FPZ H concentration, as detailed in 6.03.6. One or more common atomistic embrittlement mechanisms are probably responsible for both IHAC and HEAC, as detailed in 6.03.7. In each case, strong gradients in H concentration and stress about the crack tip govern crack

growth, and challenge damage characterization and modeling work. Both IHAC and HEAC operate if a precharged steel is stressed in a H-producing environment,.

The differences between internal and hydrogen environment assisted cracking are associated with the kinetics of crack growth (Sandoz, 1977), and are not intrinsic (Walter et al., 1969). Each mode is time dependent, governed by mobile-H diffusion (Gangloff, 2003). The kinetics of the environmental-mass transport and H production steps illustrated in Fig. 2 may alternately control rates of HEAC depending on specific cracking conditions. The details of FPZ damage, and particularly the location of damage processes ahead of the crack tip, differ for IHAC *vs.* HEAC (Page and Gerberich, 1982). Factors that control the precise damage location include the tensile stress distribution maximized at some distance ahead of the crack tip, the plastic strain (ε_P) and associated dislocation density profile about the crack tip, the distribution of H trap sites, and the concentration of environmentally produced H on the crack tip surface, as amplified in 6.03.8 (Gangloff, 1988, 2003).

6.03.3 HAC IN DAMAGE TOLERANT STRUCTURAL INTEGRITY

6.03.3.1 Fracture Mechanics Similitude and Subcritical Crack Growth

Linear elastic fracture mechanics provides the well established basis for incorporating hydrogen cracking into structural integrity management methods (Barsom, 1987; Barsom and Rolfe, 1987). The governing role of K, as the single-parameter descriptor of loading and crack geometry effects on the rate of subcritical hydrogen crack propagation (da/dt), was established by pioneering experimental work at the Naval Research Laboratory (Brown and Beachem, 1965, 1966), and confirmed by many others over the ensuing decades (Smith

et al., 1968; Novak and Rolfe, 1969, 1970; Wei, et al., 1972; Wei and Novak, 1987). The central importance of K is cemented by micromechanical modeling of the local stresses and strains that fundamentally affect crack tip damage, as developed in 6.03.8. The high strength levels of the alloys under review minimize the need for more complex elastic-plastic analysis (Hackett, et al., 1986; Anderson, 1995).

Since hydrogen promotes subcritical crack propagation at stress intensities below K_{IC}, it is necessary for a structural integrity model to predict: (a) the threshold loading and crack size conditions below which IHAC and HEAC are not likely to occur, and/or (b) the remaining life of a component based on rates of hydrogen assisted crack propagation. Stress intensity similitude provides the foundation for such modeling; that is, da/dt depends uniquely on K for a given alloy and hydrogen exposure condition, independent of loading and crack geometry. Crack growth threshold and kinetics are measured in the laboratory with a fracture mechanics specimen. Threshold stress and crack size are predicted using the measured crack growth threshold. The functional relationship between da/dt and K is integrated in conjunction with the stress intensity solution for a cracked component, and from the initial existing to target-final crack size, to predict component propagation life. The principle of this approach has been in place for 30-40 years and parallels fatigue crack propagation life prediction (Wei et al., 1972; Barsom and Rolfe, 1987; Anderson, 1995; Hertzberg, 1996).

The K dependence of da/dt is common for a wide range of IHAC and HEAC in high strength alloys; the specific form is illustrated in Figs. 3 and 4 for an 18Ni Maraging steel cracked in low pressure H_2 as well as a quenched and tempered martensitic steel in three H-
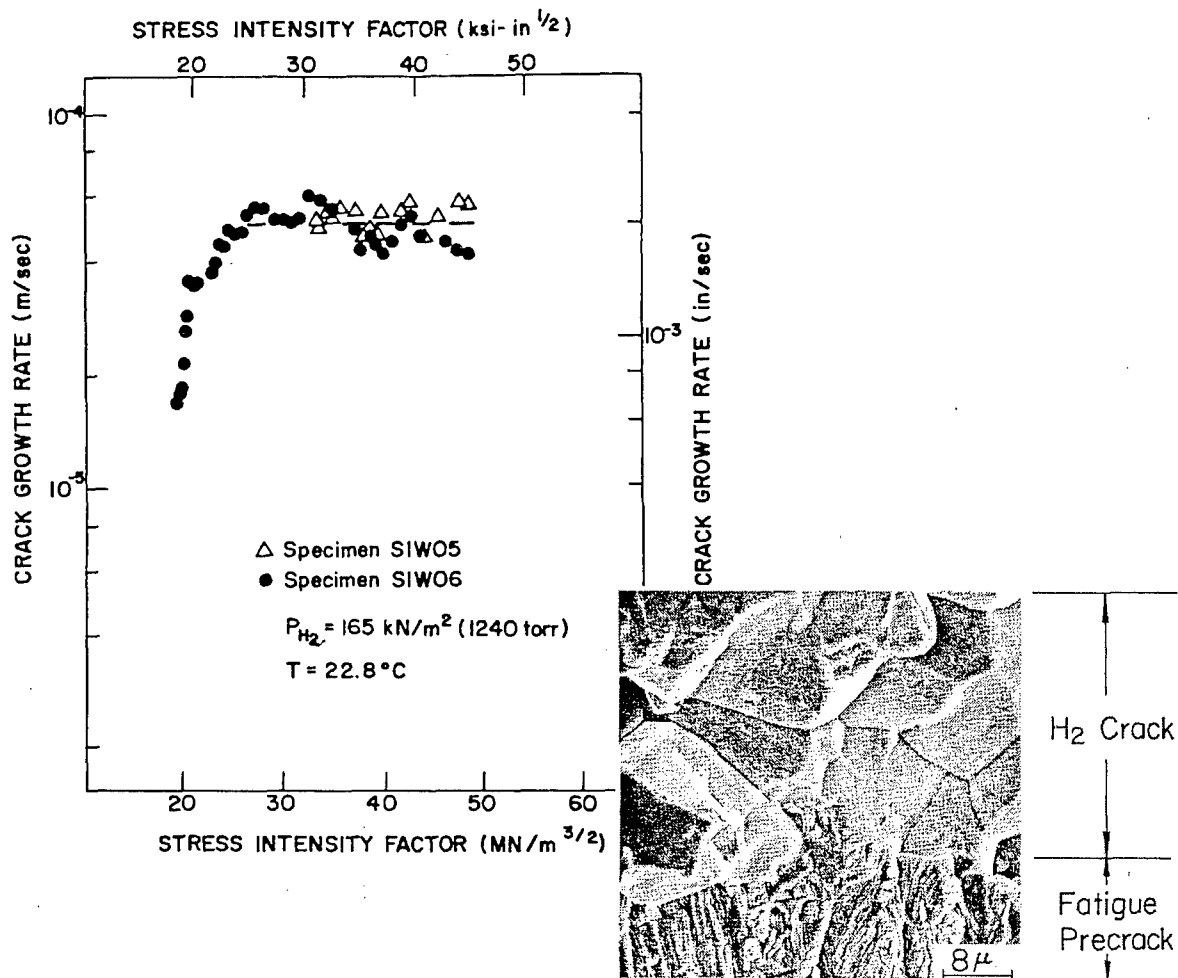
Figure 3. The stress intensity dependence of subcritical crack growth rate produced in 18Ni Maraging steel by concurrent exposure to low pressure purified hydrogen gas at 23°C and stressing at constant load. HEAC is predominantly along prior austenite grain boundaries. (Gangloff and Wei, 1977, 1978)
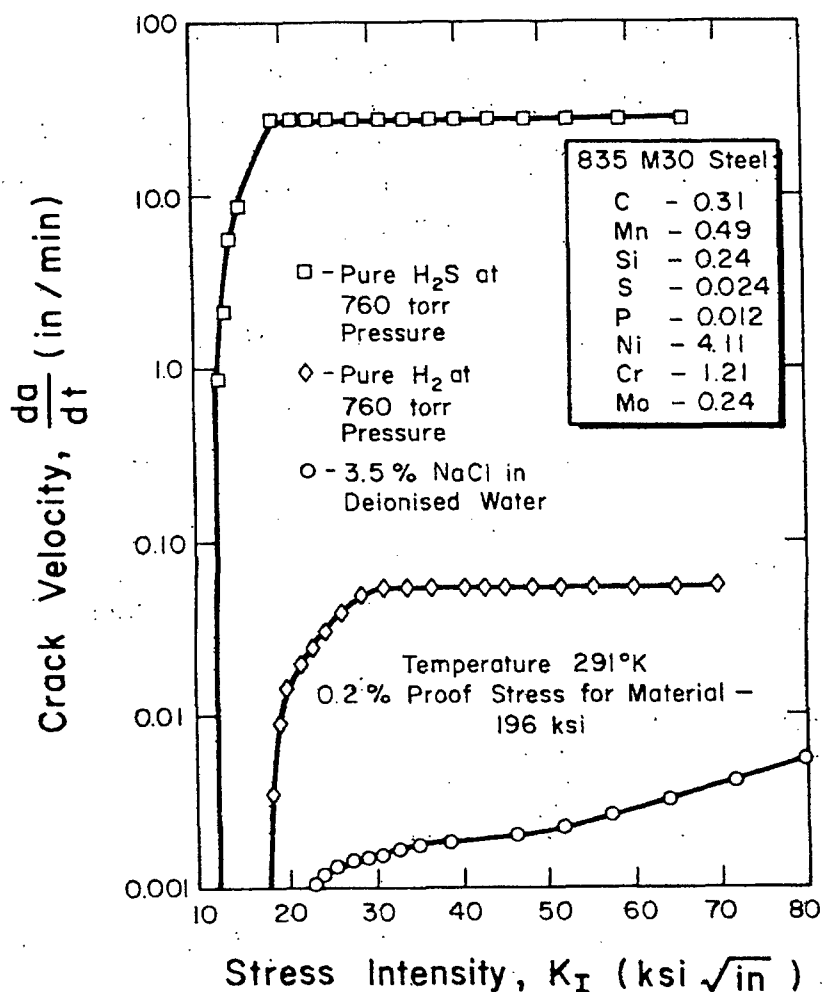
Figure 4.   The stress intensity dependence of subcritical crack growth rate produced in a tempered martensitic steel during exposure in three separate environments that produce atomic hydrogen at the crack tip during stressing under slow-rising CMOD producing dK/dt = 0.18 MPa√m/s.   (1 ksi√in = 1.098 MPa√m, 1 in/min = 0.423 mm/s, 1 ksi = 6.89 MPa, and 1 torr = 133.3 Pa.) (McIntyre and Priest, 1972; plotted by Kerns et al., 1977:   Copyright NACE International, reprinted with permission.)

producing environments, respectively. For these steels, the K_{IC} exceeds 100 MPa√m (Fig. 1), while HEAC occurs at K levels above 15 to 40 MPa√m. The crack growth behavior is defined by four features: (a) a threshold K, K_{TH} (or other terminology), below which stable crack growth is not resolved, (b) Stage I just above K_{TH} where da/dt rises sharply with increasing K due to presumed mechanical control of crack tip damage, (c) Stage II where crack growth rate (da/dt$_{II}$) is independent of K due to reaction rate/H diffusion control, and (d) Stage III where da/dt increases with rising K approaching K_{IC} due to superposition of ductile fracture damage. In some instances, Stage II crack growth rate depends on a power-law function of K, with the exponent substantially reduced compared to Stage I cracking but greater than 0 (Nelson, 1983). The precise relationship between da/dt and K depends on a wide variety of test method, environmental exposure, H concentration, temperature, alloy strength and metallurgical variables (6.03.5 and 6.03.6).

6.03.3.2   Fracture Toughness

In addition to promoting subcritical crack growth in high strength alloys, H distributed throughout the crack tip FPZ can reduce plane strain fracture toughness. This mode of H degradation has not been studied broadly for high strength alloys, but results show that it can occur. For example, the K_{IC} of ~140 MPa√m for microvoid fracture in an ultra-high strength steel (AerMet®100) was reduced to levels in the range from 50 to 90 MPa√m due to predissolved H, as shown in 6.03.5 (Thomas et al., 2003). This form of H damage is promoted by loading rates that are sufficiently rapid to preclude time dependent IHAC or HEAC, and does not involve a change in the microscopic fracture mode. Rather, one or

more aspects of the ductile fracture process is promoted by dissolved H. This H enhanced ductile fracture was studied for lower strength alloy and stainless steels (Thompson and Bernstein, 1981; Hirth, 1996; McMahon, 2001), and is not considered further in this chapter. Additionally, H has been claimed to promote cleavage cracking in low strength Cr-Mo steels and raise the ductile-to-brittle transitions temperature under impact loading (Sakai, et al., 1997). This failure mode is not typically relevant to high strength alloys.

6.03.3.3   Standard Laboratory Test Methods

Laboratory experimentation to characterize the threshold and kinetics for hydrogen assisted cracking is substantially more complex than methods dealing with fracture toughness or fatigue crack propagation. Only limited standards exist (ASTM Standard E1681-99: *Standard Test Method for Determining a Threshold Stress Intensity Factor for Environment-Assisted Cracking of Metallic Materials*; ISO Standard 7539-6: *Corrosion of Metals and Alloys-Stress Corrosion Testing with Precracked Specimens*; NACE Standard Test Method TM 0177-90: *Method for Laboratory Testing of Metals for Resistance to Sulfide Stress Cracking in H_2S Environments*). Standard E1681 is being enhanced to guide experimental measurement of K_{TH} and da/dt (Vigilante et al., 2000). Alternately, the experimentalist can follow procedures outlined in compilations (ASM International, 1985; Sedriks, 1990; Baboian, 1995) or reported in specific papers.

IHAC and HEAC experiments involve several important elements. A standard fracture mechanics specimen is fatigue precracked and stressed under either constant or programmed-rising load, constant or rising crack mouth opening displacement (CMOD), or constant K. Constant load is typically achieved using a cantilever beam and constant

weight, constant CMOD is achieved by a self-stressing bolt, and programmed-rising load/CMOD or constant K are achieved using a closed loop servo-electric or servo-hydraulic machine. Crack length, load, CMOD and time are measured typically during subcritical crack propagation to define data of the sort shown in Figs. 3 and 4. Crack length can be measured automatically with either the direct current electrical potential or elastic compliance method. For IHAC, the precracked specimen is exposed to the environment prior to loading to enable H charging by electrochemical or gaseous hydrogen reaction with bulk and crack tip surfaces. The H-precharged specimen is then loaded in ambient-moist air to produce internal hydrogen cracking. For HEAC, a chamber is affixed to the fatigue cracked area and the crack tip plus external surfaces are exposed to the H producing environment coincident with stressing. For IHAC, a calibration is required to relate environmental exposure to the hydrogen concentration. For HEAC, environment chemistry must be controlled during crack growth.

6.03.3.4 Databases and Terminology

Formal databases for IHAC and HEAC of high strength alloys are not established, but data compilations exist (Carter, not dated; Gangloff, 1986; McEvily, 1990). In the initial development of a structural integrity model, literature data on crack growth thresholds and rates should be sufficient to enable calculations of various H cracking scenarios. As the method is developed, or if the problem is sufficiently important, then published data must be augmented by experiments that incorporate the specific environment/H concentration, metallurgical, and loading variables. The resources required may be substantial.

The terminology of hydrogen cracking is diverse, particularly for threshold quantities, but common terms are emerging. The ASTM standard aims to yield a specimen-size-independent threshold K for environment assisted cracking (EAC), K_{IEAC}, using constant load or constant displacement (ASTM, 2000). This terminology is equivalent to the predecessor term, K_{ISCC}, (Brown and Beachem, 1965; Barsom and Rolfe, 1987), and is reasonably extended to K_{IHEAC} or K_{IIHAC} for situations where the damage mechanism is hydrogen based. The term, K_{TH}, describes the threshold for the onset of resolvable hydrogen cracking under rising CMOD (Gangloff, 1986; Gangloff et al., 1996). Often, K_{TH} is used to describe the threshold property for IHAC or HEAC, and either a crack arrest or crack-growth initiation experiment, provided that the context is clearly stated. The K_{IC-H} is used to designate H reduction in K_{IC} that is not associated with subcritical crack propagation.

6.03.3.5   Complications

In addition to the complexity of experiments and lack of databases, incorporating hydrogen cracking in structural integrity modeling is challenged by important complications and uncertainties (NMAB, 1982). IHAC and HEAC are affected by a number of variables that interact (6.03.6) and require a substantial number of experiments that may be of prolonged duration. Additional factors that could complicate K-similitude have not been resolved, but must be considered in structure-life modeling. The importance of loading rate and loading format are considered here. The effects of specimen size, small crack size, precrack path, mixed mode loading, interacting cracks, and statistical distribution of H cracking properties are discussed in 6.03.9.

6.03.3.5.1   Loading Rate and Format

Loading format and loading rate affect the threshold and kinetics of IHAC and HEAC. Early research employed either constant load (rising K) or fixed CMOD (falling K) experiments to define the threshold (K_{IHEAC} or K_{ISCC}) and da/dt for hydrogen assisted subcritical cracking. It is critical to load for a sufficiently long time to allow H to accumulate and stimulate damage in the FPZ. The ASTM standard focuses on the fixed CMOD method and suggests that threshold measurement requires a 1,000 h exposure for titanium alloys, 5000 h for UHSS, and 10,000 h for aluminum alloys (ASTM, 2000). In laboratory testing, it is important to avoid the complicating influence of transient-loading (Wei et al., 1972). For example, substantial incubation times and crack growth rate transients were observed immediately after a load change applied to high strength 4340 steel in distilled water (Hudak and Wei, 1981). The K_{IHEAC} for high strength steel in H_2 and NaCl solution increased monotonically with increasing level of a single prestress applied to a fatigue precracked specimen before testing at increasing low-load steps in the environment (Jonas, 1973).

A rising load or rising displacement method was advocated to accelerate determination of the kinetics of IHAC and HEAC (McIntyre and Priest, 1972; Clarke and Landes, 1976; Hirano et al., 1985; Crumly, 1988; Dietzel et al., 1989; Mayville, et al., 1989; Tyler et al., 1991; Dietzel and Ghosal, 1998; Somerday, et al., 2000; Dietzel and Mueller-Roos, 2001). For high strength alloys, this acceleration produces da/dt data (see Fig. 4) that are analogous to the K_{TH}-Stage I-Stage II response achieved by long term constant load or constant CMOD testing (Fig. 3). The rising CMOD method successfully produces lower-bound threshold

values, provided that the loading rate (best expressed as dK/dt) is sufficiently slow, as shown for a single high strength steel and purified H_2 environment in Fig. 5. Here, the critical K level for the onset of resolvable crack growth (K_{IH}) decreases with decreasing dK/dt, as expected since HEAC in this high strength steel in NaCl solution requires time for the reaction steps (Fig. 2) to produce embrittling H in the FPZ. Notably, this critical K_{IH} approaches the K_{IHEAC}; but the time for the rising load measurement, ~6 h, is up to several orders of magnitude shorter than the prolonged times typically used for the constant load or constant CMOD measurement of K_{TH}. Similar results were reported for high strength steel and aluminum alloys in chloride solutions (Hirano, et al., 1985; Crumly, 1988; Dietzel et al., 1989; Dieztel and Ghosal, 1998; Dietzel and Mueller-Roos, 2001; Thomas et al., 2003).

The loading rate necessary to achieve a lower bound threshold depends on the material and environment. Lower applied dK/dt are required to resolve a lower bound threshold as the susceptibility to IHAC or HEAC declines, for example due to reduced environmental hydrogen production. The necessary dK/dt is directly proportional to the Stage II da/dt (Dietzel and Mueller-Roos, 2001). For example, high strength β-Ti alloys exhibit very high da/dt_{II} for HEAC in chloride solution and K_{IH} values are independent of loading rate ($d\delta_m/dt$ in Fig. 6 = dCMOD/dt) for dK/dt at least as high as 30 MPa√m/s, as shown in Fig. 6 (Somerday et al., 2000). A less susceptible (lower da/dt_{II}) high strength steel required a displacement rate of 0.8 nm/s or slower to measure a lower bound K_{IH} (Dietzel and Mueller-Roos, 2001). Crack growth rate generally increases with increasing dK/dt, but understanding is limited (Mayville, et al., 1989; Dietzel and Ghosal, 1998; Somerday, et al., 2000).

The rising CMOD method is particularly important for hydrogen cracking in lower

Figure 5.   The effect of rising-K rate on the threshold stress intensity factor for the onset of resolvable HEAC in high strength steel stressed actively in purified hydrogen gas.   (1.0 ksi√in = 1.098 MPa√m, 1.0 ksi√in/min = 0.0183 MPa√m/s, 1 psig = 6.89 kPa.)   (Clark and Landes, 1976:   Copyright ASTM International, reprinted with permission.)

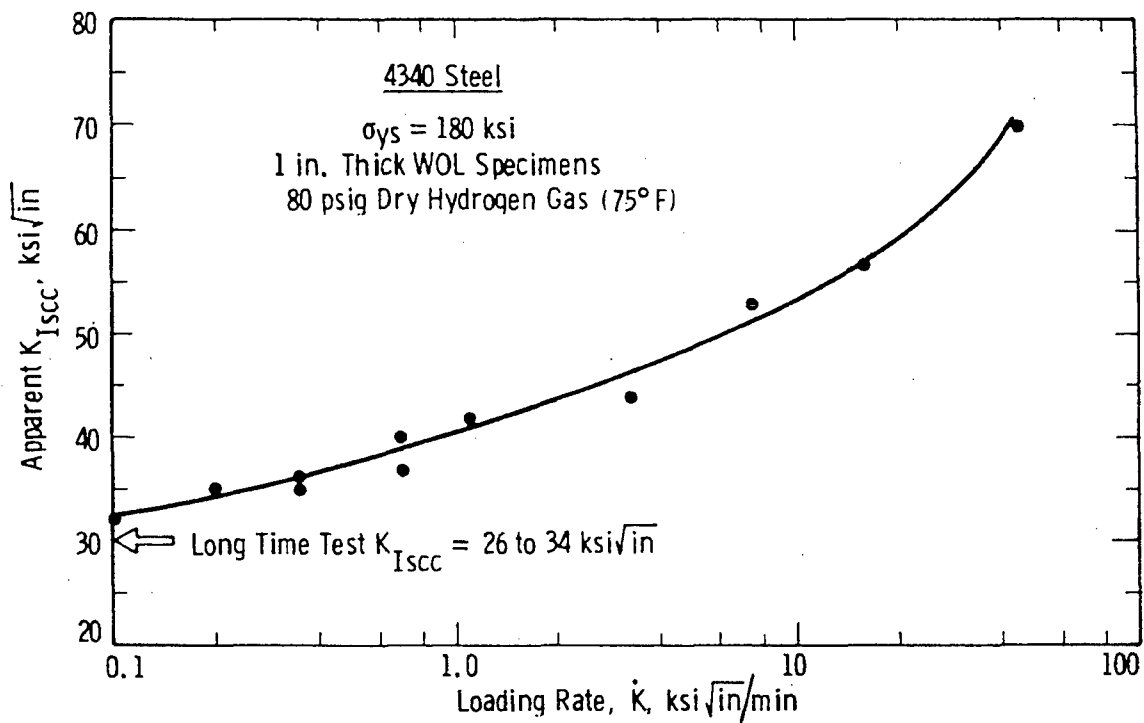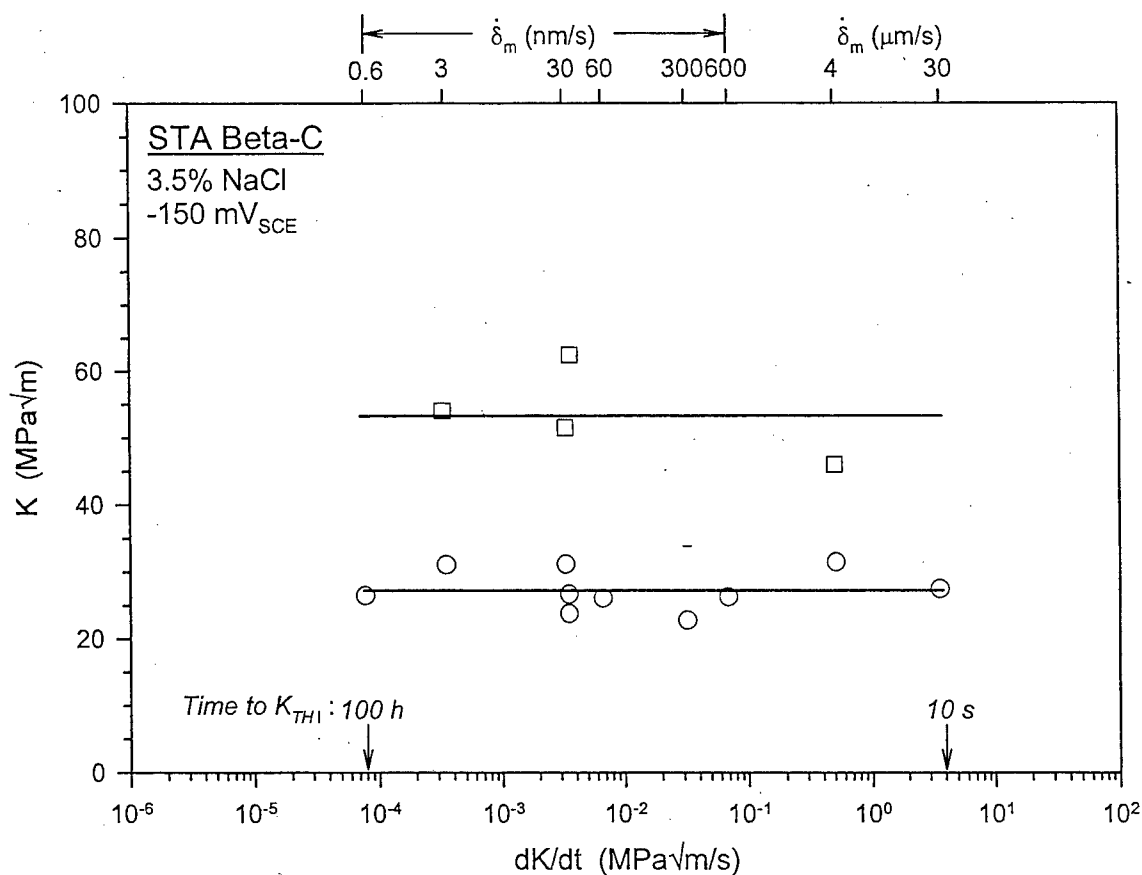**Figure 6.** The effect of rising-K rate on the threshold stress intensity factor (K_{IH}, O) for the onset of resolvable HEAC in a high strength α-precipitation hardened β-Ti alloy stressed actively in aqueous chloride solution. Plane strain initiation-fracture toughness data are shown for similar loading in moist air (K_{JIC}, 9). (Somerday et al., 2000)

strength alloys. In this case, substantial data show that K_{TH} for rising CMOD is several times less than K_{TH} defined by long term fixed CMOD experiments for IHAC in lower strength alloy steels (Gangloff, 1986). Specific data are presented in Fig. 7 for a quenched-bainitic microstructure in $2_{1/4}$ Cr-1Mo steel tempered to achieve various strengths, precharged by elevated temperature exposure to H_2, quenched to 23°C, then cracked under either rising-CMOD (□, rising K) or fixed CMOD (9, falling K) (Gangloff, et al., 1996; Gangloff, 1998). The K_{TH} for the rising CMOD case is substantially lower than K_{IHAC} defined by crack arrest under falling K, provided that the steel strength is less than about 1000 MPa. The explanation for this effect is unclear, but may involve the damaging role of active crack tip plasticity in H cracking, and/or H loss from the laboratory specimen during long term fixed CMOD testing. Fortunately, the data in Fig. 7 suggest that the difference in K_{TH} for rising *vs.* falling K conditions is small when steel yield strength exceeds about 1000 MPa. Either loading method provides reasonable values of the crack growth threshold (and perhaps kinetics) for IHAC and HEAC in the high strength alloys pertinent to this chapter.

6.03.4 TECHNOLOGICAL IMPORTANCE OF HYDROGEN CRACKING IN HIGH STRENGTH COMPONENTS

Hydrogen assisted crack propagation should be considered in a comprehensive structural integrity management methodology. First, high strength alloys based on Fe, Ni, Ti and Al are highly susceptible to hydrogen cracking. As illustrated in Fig. 1, high levels of plane strain fracture toughness that are typical of such alloys are reduced by up to an order of magnitude by hydrogen exposure. Hydrogen cracking degrades critical crack size, operating stress level, and damage tolerant life.
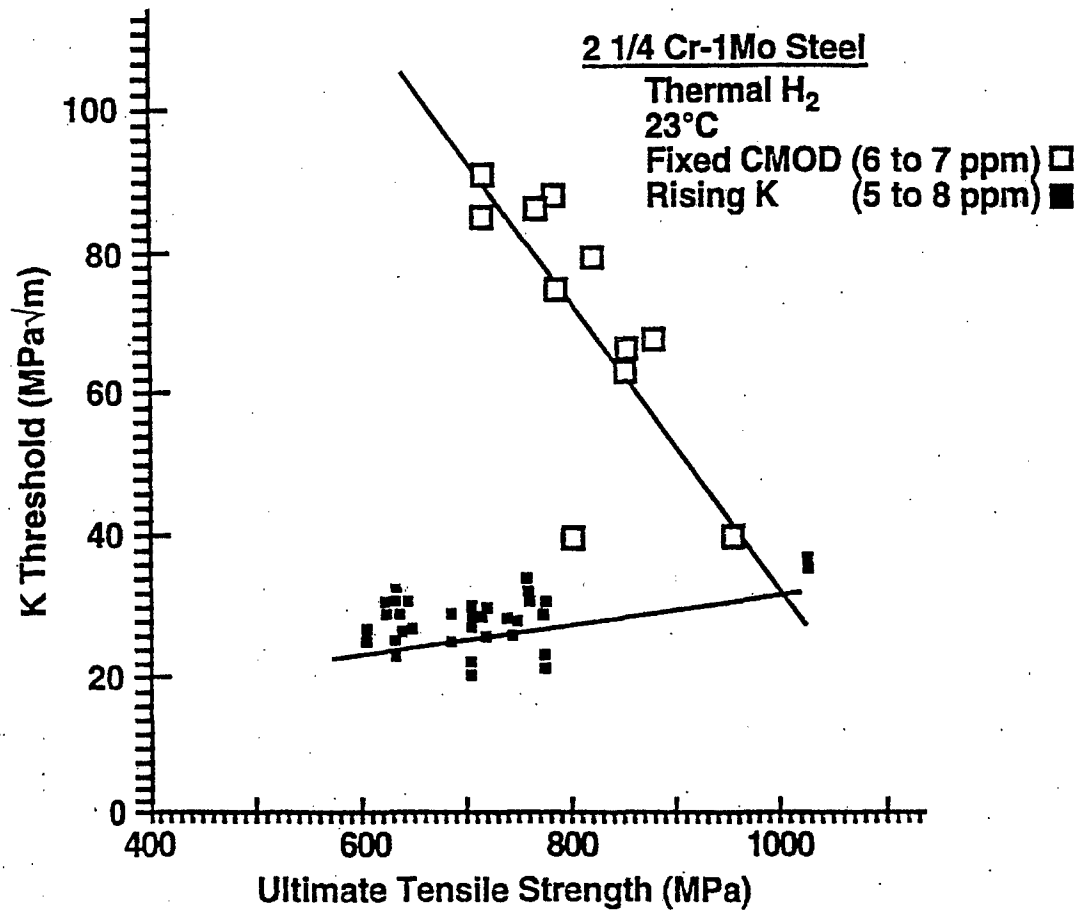
Figure 7.   The effect of loading format, including fixed CMOD yielding crack arrest under falling K (9) and rising CMOD causing crack growth initiation under rising K (□), on IHAC of a tempered bainitic alloy steel containing a claimed-constant amount of precharged H.   (Gangloff, 1998)

The breadth of the hydrogen cracking problem is significant due to the ubiquity of H. Hydrogen is readily introduced into alloys during both manufacturing and service exposure and promotes IHAC. A wide range of environments; from gases such as H_2, H_2S and C_XH_Y to aqueous electrolytes over the range of pH from 0 to 14 and applied electrode potentials above and below the free corrosion state; are capable of producing atomic H at a straining crack tip. Specific examples from failure analyses demonstrate the importance of IHAC (Baggerly, 1996; Mukhopadhyay, et al., 1999; Schmidt, et al., 2000; Reddy, et al., 2001) and HEAC (Speidel and Fourt, 1977; Whelan, 1981; Akhurst and Baker, 1981; Fritzemeier et al., 1990; Lynch, 1994; Chen et al., 1996; Vehovar, 1998; Woodtli and Kieselbach, 2000; Carter and Cornish, 2001; Troiano et al., 2002). Many other case studies are likely to exist, but are not reported in the open literature due to proprietary considerations. These examples include electroplated high strength steels for fastener and landing gear applications, pearlitic steels for concrete prestressing, precipitation hardened stainless steels and nickel based alloys for deep oil and gas well casings as well as aerospace piping and nuclear applications, forged or rolled precipitation hardened Al-Zn-Mg-Cu alloys for airframe construction, and precipitation hardened β-Ti alloys for marine and aerospace uses.

An alternate representation of the importance of IHAC and HEAC to structural integrity is provided by the results of a computer search of literature databases, Table 1. For example, the Metadex database contains almost 1000 publications since 1990 that included the four key words of hydrogen, embrittlement, high and strength. An additional 1000 papers were published between 1980 and 1990. In spite of this extensive research, the hydrogen cracking problem is not solved to the point where this failure mode can be

precluded from structural integrity management. As amplified in 6.03.5, most modern alloys based on Fe, Ni, Ti and Al continue to be susceptible to substantial hydrogen cracking. Materials scientists have not produced high strength alloys that are truly immune to H cracking. Unexpected manufacturing and service environment conditions often promote hydrogen cracking. Mechanisms of IHAC and HEAC are uncertain and controversial (6.03.7). The micromechanical/microchemical models that are necessary to augment laboratory data for life prediction are semiquantitative at best, as shown in 6.03.8

Table 1. Citations in the materials science literature since 1990 for key words relevant to IHAC and HEAC

Hydrogen Embrittlement +	Metadex	Corrosion Abstracts
Plating	159	49
Aircraft	61	25
Fastener	37	15
Landing Gear	10	3
Turbine	43	9
Concrete	54	47
High Strength	960	307
High Strength (from 1980)	2,033	479
High Strength (from 1970)	2,417	498

Hydrogen cracking in high performance components is controlled by one or more approaches, including: (1) alloy substitution, (2) metallurgical change often leading to reduced alloy strength or improved alloy purity with increased cost, (3) environment inhibition for HEAC, (4) manufacturing-environment change or improved H-outgassing treatment for IHAC, (5) reduced applied or residual stress through design and fabrication modifications, and (6) improved inspection to detect existing cracks. A comprehensive structural integrity plan should quantify and facilitate such improvements.

6.03.5 PHENOMENOLOGY OF HYDROGEN CRACKING

Laboratory data that describe the stress intensity dependencies of the subcritical rates of IHAC and HEAC, as well as microscopic crack paths, are centrally important to structural integrity modeling to control hydrogen cracking in high strength alloys. These same data provide a basis for understanding crack tip damage mechanisms (6.03.7) and micromechanical-chemical modeling of K_{TH} and da/dt (6.03.8). Extensive da/dt *vs.* K data are available in the literature. New results from experiments conducted at the University of Virginia are emphasized in this review, and demonstrate that hydrogen assisted cracking continues to degrade the most modern high strength alloys.

6.03.5.1 High Strength Steels

High and ultra-high strength alloy steels with tempered martensitic microstructure and σ_{YS} from 1200 to 2200 MPa are embrittled severely by hydrogen. (Carter, not dated; Kerns, et al., 1977; Dautovich and Floreen, 1977; Nelson, 1983; Gangloff, 1986, 2003; Moody et al., 1990; McEvily, 1990; Interrante and Raymond, 1995; McMahon, 2001).

The pioneering work of Troiano and coworkers demonstrated severe internal hydrogen assisted cracking in low alloy steels such as AISI 4340 (Johnson et al., 1958; Steigerwald et al., 1960; Troiano, 1960), and this behavior was amplified by subsequent research using fracture mechanics (Dautovich and Floreen, 1973; Gerberich et al., 1988). Here, 1-5 parts-per-million by weight (ppm) of predissolved H promoted subcritical crack growth at K levels as low as 10 MPa√m and da/dt values up to 20 μm/s for high strength steels with σ_{YS} of 1400-2000 MPa and H-free K_{IC} levels of 60-150 MPa√m.

Considering HEAC, the da/dt *vs.* K data in Figs. 3 and 4 illustrate that a wide variety of environments produce severe subcritical crack growth in tempered martensitic steels. Specific environments include gaseous H_2, H_2S, and water vapor; while electrolytes include solutions with or without chloride and spanning the range of pH from highly acidic to highly alkaline. Each is capable of producing atomic H at the crack tip through the scenario in Fig. 2. The da/dt depends on environmental variables that govern this amount of H adsorbed on the crack tip surface, and even relatively benign environments such as low pressure H_2 or H_2O, moist air, and pure-liquid water are severely embrittling (Fig. 4) (Charbonnier and Margot-Marette, 1982).

Subcritical IHAC and HEAC each occur along prior austenite grain boundaries in typical quenched and tempered martensitic steels such as AISI 4340, not processed for impurity control, as well as in higher purity maraging steels (Fig. 3) (McMahon, 2001; Eliaz et al., 2002). Such cracking can also occur along transgranular (TG) paths associated with either crystallographic planes or interfaces in the tempered martensitic structure (Gangloff and Wei, 1978; Gao and Wei, 1984; Gao, et al., 1984). The dominant morphology depends on variables such as steel purity, environment chemistry, crack tip FPZ hydrogen content, stress intensity, and temperature.

Modern ultra-high strength steels continue to be embrittled severely by predissolved or environmental hydrogen, as illustrated by the behavior of AerMet®100 steel. Here, ultra-high strength is developed through nano-scale metal carbide precipitation in unrecovered martensite, and high fracture toughness is achieved by impurity control and temper optimization (Olson, 1997). This modern steel is susceptible to severe HEAC and IHAC

that progresses largely along transgranular paths through the lath-martensite microstructure. For example, Figure 8 shows the deleterious effect of H predissolved electrochemically from $Ca(OH)_2$ solution on the threshold K for the onset of subcritical crack growth under slow-rising CMOD at various rates (Thomas, 2000; Thomas et al., 2003). For this diffusible H content (4.6 ppm), brittle subcritical cracking was produced at a K_{TH} equal to 10-15% of K_{IC} over a wide range of applied dK/dt from 0.0002 to 0.3 MPa√m/s. At higher loading rates, the threshold K rose monotonically, but never reached K_{IC} even for dK/dt levels as high as 2,000 MPa√m/s. Dissolved H affected a fracture mode transition from microvoid-based processes without H (top-right fractograph), to essentially all-brittle transgranular (TG) cracking associated with lath martensite interfaces for the low-K_{TH} plateau (bottom-left insert). A dimpled morphology correlated with the rising K_{TH} at higher loading rates for H-charged AerMet[®]100, but dimple size was substantially smaller compared to the H-free fracture surface. Reduced dimple size was reported for IHAC in high strength maraging steel (Tiwari et al., 2000), and more broadly for H-assisted ductile fracture in lower strength steels (Thompson and Brooks, 1975; Thompson and Bernstein, 1981; Hirth, 1996).

The IHAC of high strength martensitic steels is generally reversible if dissolved H is removed by outgassing at elevated temperature (Johnson et al., 1958; Barth and Steigerwald, 1970). For maraging steel, the low K_{TH}/K_{IC} of 0.3 after H charging was increased to 1.0 by baking for several hours at 150°C (Dautovich and Floreen, 1973). For AerMet[®]100, heating in moist air at 190°C for 24 h eliminated all diffusible H from the prior electrochemical charging and restored the ductile fracture resistance; K_{TH} of 16 MPa√m for a charged-diffusible H content of 4.0 wppm was increased by baking to about 140 MPa√m, equal to
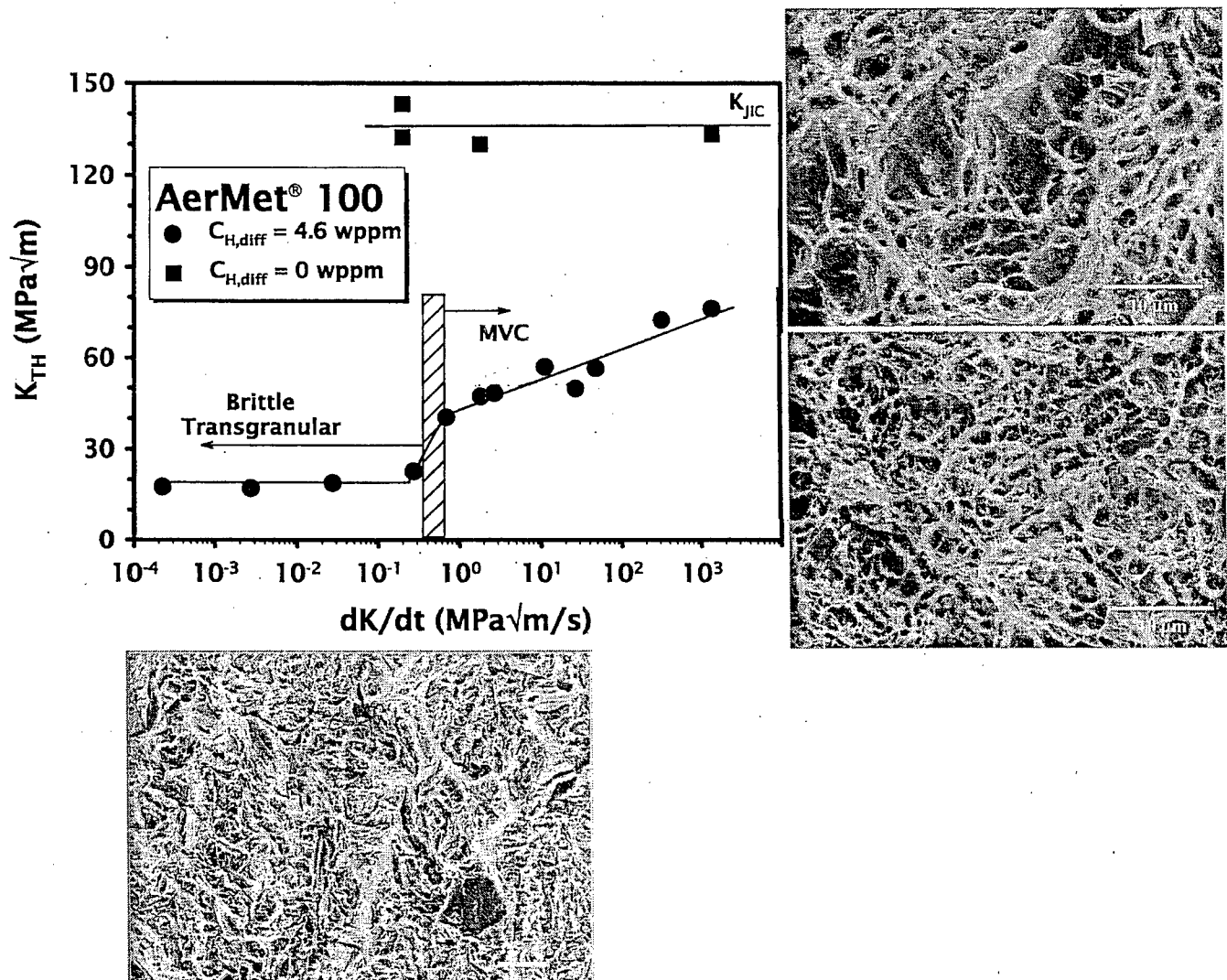
Figure 8.   Rising CMOD threshold stress intensity *vs.* applied-initial dK/dt for AerMet®100 precharged to C_{H-DIFF} = 4.6 wppm. At dK/dt less than 0.3 MPa√ms, brittle-TG fracture occurs at K_{TH} < 20 MPa√m. At dK/dt greater than 0.7 MPa√m/s, fracture occurs by MVC at K_{TH} < 60 MPa√m. The H-free plane strain elastic-plastic fracture toughness of AerMet®100 is 132-143 MPa√m.   (Thomas, 2000; Thomas et al. 2003; Gangloff and George, 2002a)

the K_{IC} of H-free steel (Thomas et al., 2003). Similarly severe transgranular HEAC was

reported for AerMet®100 stressed during exposure to several acidic environments (Buckley

et al., 1993; Buckley et al., 1994; Oehlert and Atrens, 1998; Lee et al., 2000; Vigilante et al.,

2000).

Martensitic stainless steels with 10-20% Cr, up to 10% Ni, perhaps Mo, and low C as

well as precipitation hardening elements (Al, Ti, and Cu) are susceptible to severe HEAC

even at strength levels that are less than those of ultra-high strength alloy steels such as AISI

4340 and AerMet®100. This behavior is illustrated by the threshold stress intensity data in

Fig. 9 for aged hardened PH 13-8 Mo, 17-4 PH and PH 15-5 steels, each stressed during

exposure in electrolytes with cathodic polarization (Scully, 2002). The open symbols were

reported in early studies (Carter, not dated; Fujii, 1976; various internal reports), while the

closed data are more recent (Thompson, 1978; Tyler, Levy and Raymond, 1991; Young et

al., 1995; Vigilante, et al., 1997). Cracking was either IG (Young et al., 1995) or brittle TG

(Thompson, 1978), depending on steel heat treatment and strength. Progressively less

severe HEAC was reported for these martensitic stainless steels stressed in neutral NaCl

solution or seawater as cathodic polarization was reduced towards the open circuit corrosion

condition (Tyler et al., 1991; Scully, 2002).

6.03.5.2 Superalloys

Iron and nickel-based superalloys; with a face-centered cubic austenite matrix that is

precipitation hardened by intermetallic phases based on Ti, Al, and Nb; are prone to severe

hydrogen cracking as revealed by initial studies involving high pressure H_2 exposure (Jewett
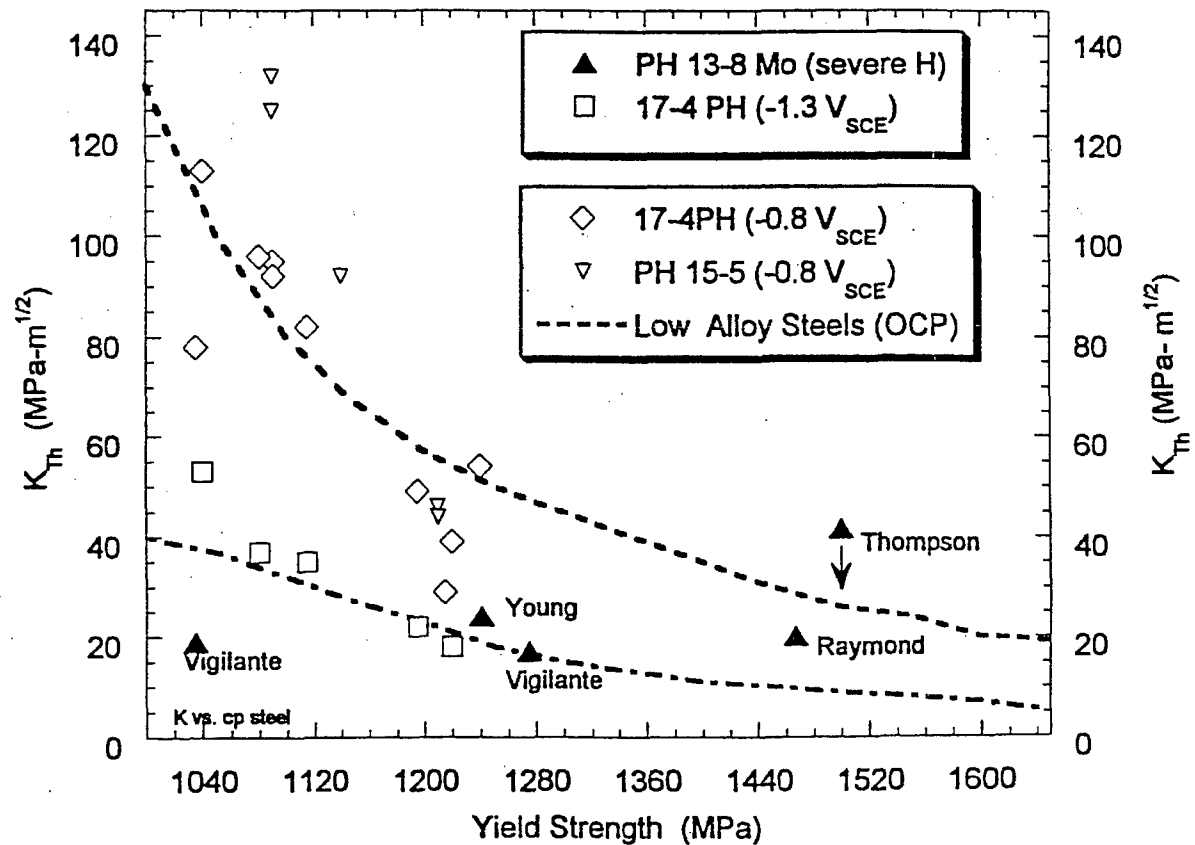
Figure 9.   The yield strength dependence of the threshold stress intensity for HEAC of precipitation hardened martensitic stainless steels stressed in neutral to acidic H-producing electrolytes with substantial-applied cathodic polarization.. (Scully, 2002)   The dashed trend lines reflect the bounds on σ_{YS} dependent K_{TH} for quenched and tempered low alloy steels tested at the open circuit potential (OCP). (Gangloff, 1986)

et al., 1973; Fritzemeier, 1990). Ensuing results have shown that iron-based alloys such as A286 and IN903 are susceptible to both IHAC and HEAC in high pressure H_2 (Perra and Stoltz, 1981; Moody et al., 1986; Moody et al., 1987; Moody et al., 1988; Moody et al., 1990; Moody et al., 1990b; Moody et al., 1991; Hicks and Altstetter, 1992; Moody et al., 2001). Other studies demonstrate that nickel-based superalloys IN718 and X-750 are prone to H-assisted cracking (Walter and Chandler, 1974, 1977; Hicks and Altstetter, 1992; Symons and Thompson, 1997; Symons, 1998, 2001; Hall and Symons, 2001). The tensile yield strengths of these materials were in the range from 800 to 1100 MPa when examined with regard to H cracking; however, yield strengths approaching 1400 MPa are possible. Hydrogen free superalloys crack by microvoid processes at high K_{IC}, but IHAC and HEAC progress by a mixture of IG separation and TG cracking associated with {111} slip planes in austenite (Moody et al., 1986; Moody et al., 1988; Moody et al., 1990b; Moody et al., 2001, Symons, 2001). The proportion of each mode depends on metallurgical variables such as grain size, as well as on H concentration, temperature, and CMOD-control mode. The IG cracking dominates for conditions that produce threshold stress intensity levels below about 50 MPa√m, while TG slip plane cracking is favored at lower H contents and higher thresholds.

As an example, H introduced to the crack tip process zone reduces substantially the stress intensity for H cracking in Fe-based alloy IN903 at 23°C, as established in Fig. 10 (Moody et al., 1988, 1990b). Considering IHAC, K_{IC} is lowered to K_{IC-H} due to predissolved H interacting with relatively rapidly rising CMOD (□), and the threshold K at crack arrest during fixed CMOD loading (K_{IHAC}, ●) is also lowered by H precharging. Considering
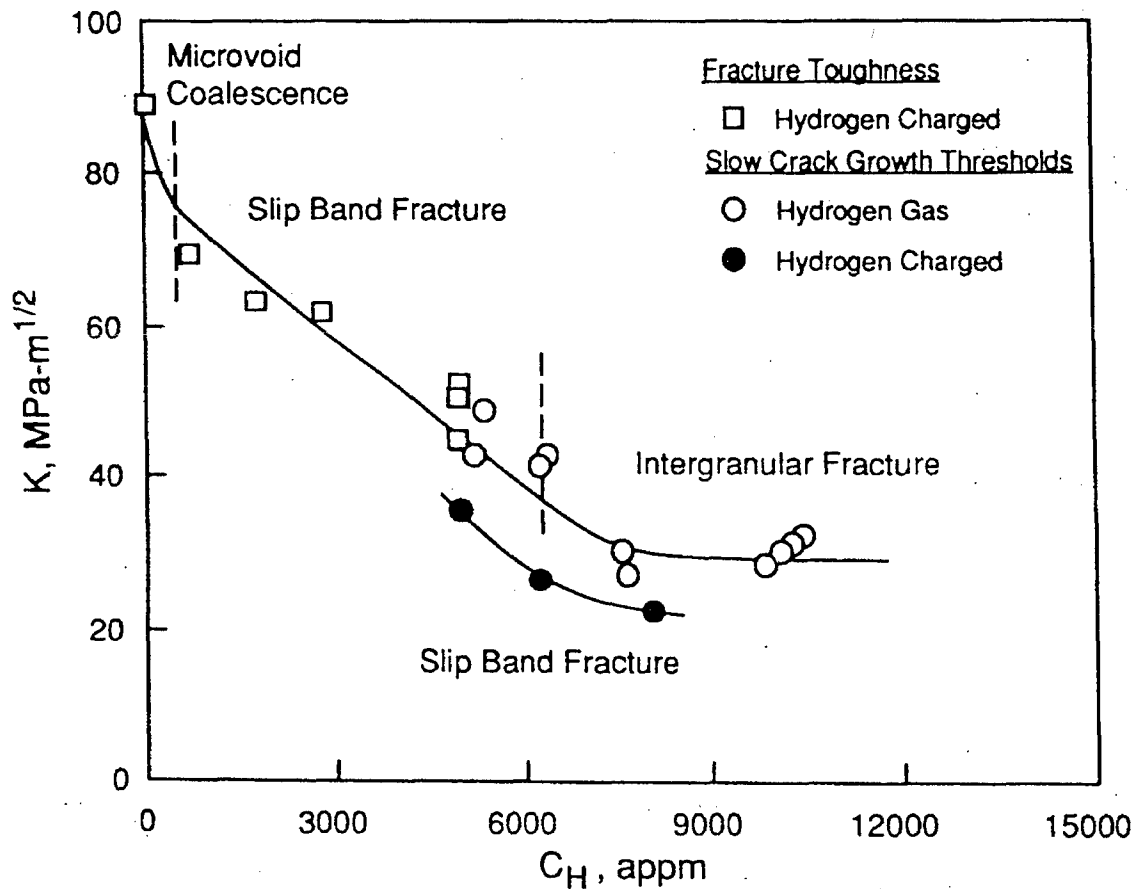
Figure 10. The crack tip total hydrogen concentration dependence of the threshold stress
intensity for H-assisted cracking in precipitation hardened IN903 (σ_{YS} = 1080
MPa): (a) stressed with precharged H in moist air for either rising CMOD (9,

K_{IC-H} at dK/dt = 0.7 MPa$\sqrt{m}$/s) or fixed CMOD ($\bullet$, K_{IIHAC}) loading
conditions, and (b) stressed at fixed CMOD (o, K_{IHEAC}) in high pressure (20.7
MPa to 207 MPa) H_2 without precharging. All experiments were conducted
at 23°C. The H concentration was calculated according to the method
described in the text and amplified in 6.03.8. (Moody, Perra and Robinson,
1988, 1990b: Copyright The Minerals, Metals and Materials Society,
reprinted with permission.)

HEAC in high pressure H_2 without H precharging, K_{IHEAC} (o) is well below K_{IC} and declines with increasing crack tip H content. In each case the concentration of atomic H at the crack tip was calculated based on experimental determination of the equilibrium H content for unstressed exposure of the superalloy in a given H_2 pressure (P_{H2}) and temperature (T) environment, coupled with enhancement due to crack tip hydrostatic stresses, as detailed in 6.03.8. The microscopic fracture path, be it microvoid cracking, slip plane cracking or IG cracking, is noted for each test condition. Symons reported identical fracture mechanics and fractographic results for IHAC and HEAC in a high strength Ni-based superalloy (X-750) (Symons, 2001).

While results are less extensive, precipitation hardened Fe and Ni-based austenitic superalloys are sensitive to HEAC when stressed during exposure to electrolytes that are capable of producing H on crack tip surfaces. Underwood and coworkers confirmed that IN718 (σ_{YS} = 1115 MPa) suffers IG subcritical cracking during fixed CMOD stressing in NaCl solution with As_2O_3 addition and cathodic polarization to stimulate H entry into the metal at 23°C; K_{IHEAC} is less than 13 MPa√m (Vigilante et al., 1997). Two other alloys, IN706 (σ_{YS} = 1110 MPa) and Fe-based A286 (σ_{YS} = 760 MPa) were not susceptible to HEAC during 2,000 h exposure in this environment.

Lillard confirmed the HEAC susceptibility of precipitation hardened superalloys, particularly IN718, stressed under slow-rising CMOD in aqueous-acidified chloride solution at 23°C (Lillard, 1998). The results in Fig. 11 show that K_{IH} is well below the plane strain fracture toughness of each of two microstructures for a wide range of applied electrode potentials that are cathodic relative to the free corrosion potentials. The STA microstructure

(a)

(b)
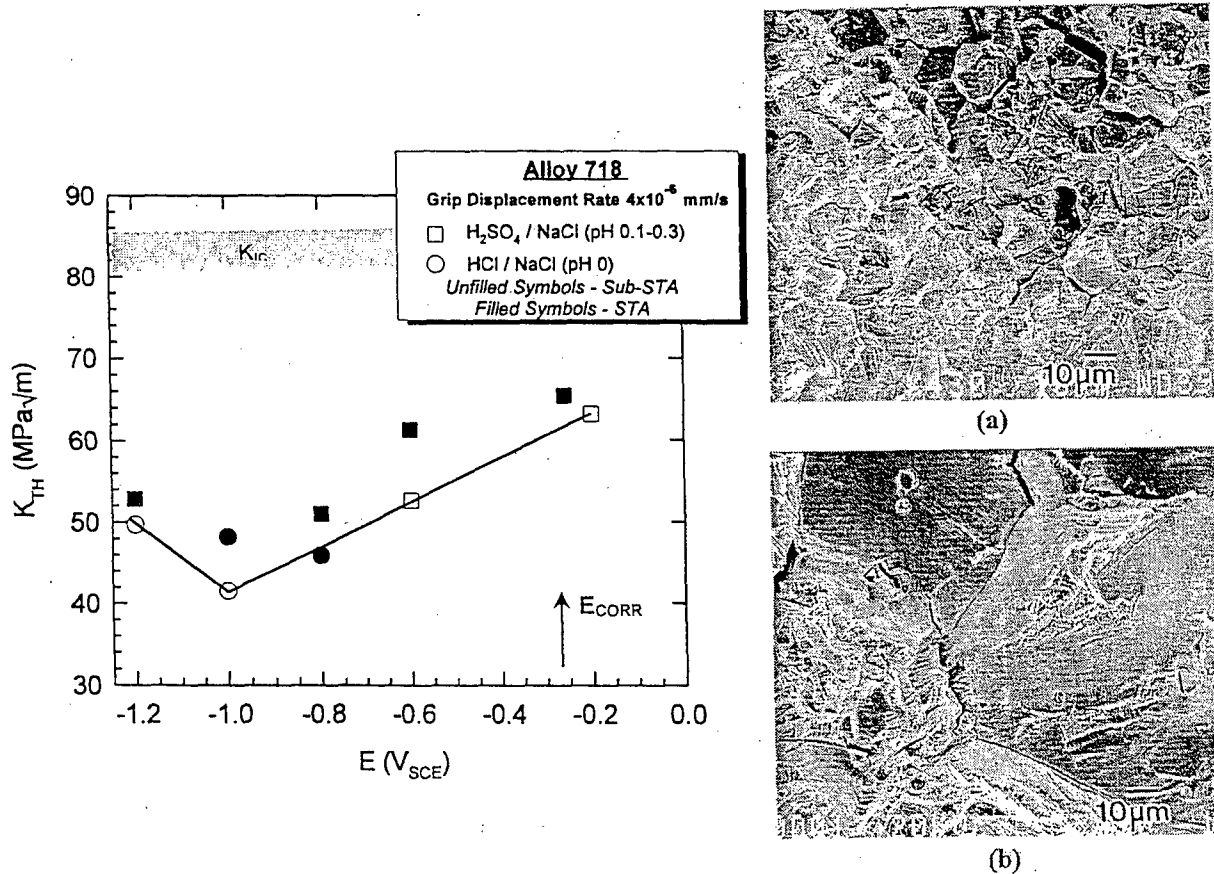
Figure 11.   Threshold stress intensity for HEAC in peak aged IN718, stressed in acidified chloride solution with varying cathodic polarization and rising CMOD at a constant grip displacement rate of 4 x 10^{-6} mm/s yielding dK/dt = 6 x 10^{-4} MPa√m/s prior to the onset of subcritical crack growth. The free corrosion potential for this alloy and solutions is between -0.25 and -0.35 V_{SCE}. HEAC produced a mixture of intergranular and transgranular slip-plane based cracking, as shown by the SEM fractographs for: (a) Sub-STA with K_{TH} = 50 MPa√m and (b) STA with K_{TH} = 53 MPa√m.   (Lillard, 1998)

was solution treated above the δ-phase solvus then aged isothermally, resulting in large grain size characterized by a yield strength of 840 MPa and K_{IC} of 85 MPa√m. The Sub-STA microstructure was solution treated below this solvus for smaller grain size and higher precipitation-hardened strength (σ_{YS} = 990 MPa and K_{IC} = 81 MPa√m). The HEAC susceptibility is similar for each of these two metallurgical conditions; however, the finer grain size microstructure is more prone to subcritical cracking at somewhat lower thresholds for each level of cathodic polarization. The IN 718 cracked by microvoid processes in air, while HEAC produced a mixture of intergranular and TG slip-plane based cracking, with the proportions dependent on H content and grain size. IG cracking dominated for K_{TH} below 55 MPa√m, as illustrated by the SEM fractographic inserts in Fig. 11.

6.03.5.3   7000 Series Aluminum Alloys

High strength aluminum alloys; particularly the 7000 series that are precipitation hardened through addition of Zn, Mg, and Cu; are susceptible to severe intergranular and transgranular subcritical cracking in moist gaseous and electrolytic environments. Internal H-assisted cracking occurs as a result of unstressed preexposure to water vapor or moist air, typically at elevated temperatures (~100°C), and followed by stressing at ambient temperature (Scamans et al., 1976; Christodoulou and Flower, 1980; Tuck, 1985). This IHAC is also produced by electrochemical precharging of H (Gest and Troiano, 1974; Albrecht et al., 1977). Alternately, 7000 series aluminum alloys crack subcritically when stressed in water vapor or aqueous solutions typically containing chloride ions (Speidel and Hyatt, 1972; Speidel, 1975; Gruhl, 1984; Holroyd, 1990; Young and Scully, 2002).

Typical subcritical crack growth kinetics are presented in Fig. 12 for two peak aged 7000 series Al alloys (σ_{YS} ~ 500 MPa) stressed in either distilled water or aqueous chloride solution at the free corrosion potential and 23°C. This figure shows the variability in crack growth rate data for multiple-replicate experiments. The 7079 composition exhibits the fastest environment-assisted crack growth kinetics of all aluminum alloys examined to date. For both alloys, the stress intensity dependence of da/dt includes an apparent K_{IHEAC} between 3 and 7 MPa$\sqrt{m}$, strongly K-dependent Stage I cracking, and K-independent Stage II growth. The fracture toughness is likely above 25 MPa$\sqrt{m}$ for these alloys and crack orientation, and Stage III HEAC is not observed in Fig. 12.

A central feature of 7000 series aluminum alloys is that HEAC is mitigated and perhaps eliminated by overaging, provided that the alloy contains Cu (Sarkar et al., 1981; Holroyd, 1990). This behavior is illustrated for aluminum alloy (AA) 7050 in Fig. 13, where the extent of isothermal aging is indicated by electrical conductivity (Young, 1999; Young and Gangloff, 2001). (Specimens were solution treated, water quenched, and aged at 154°C or 163°C for times between 1 h and 30 h. The conductivity, as %IACS, increases monotonically with the evolution of precipitate nucleation and growth as solute is removed progressively from the aluminum lattice.) The crack orientation in Fig. 13 is the susceptible SL case, the solution is acidified chloride with chromate inhibitor at a fixed electrode potential, and the da/dt levels are typical of fixed-CMOD loading at Stage II K levels between 12 and 18 MPa$\sqrt{m}$. For commercial unrecrystallized AA7050, the da/dt decreases by over 5 orders of magnitude due to increased isothermal aging from the under to peak to overaged conditions. No crack growth was resolved for the overaged condition in the S
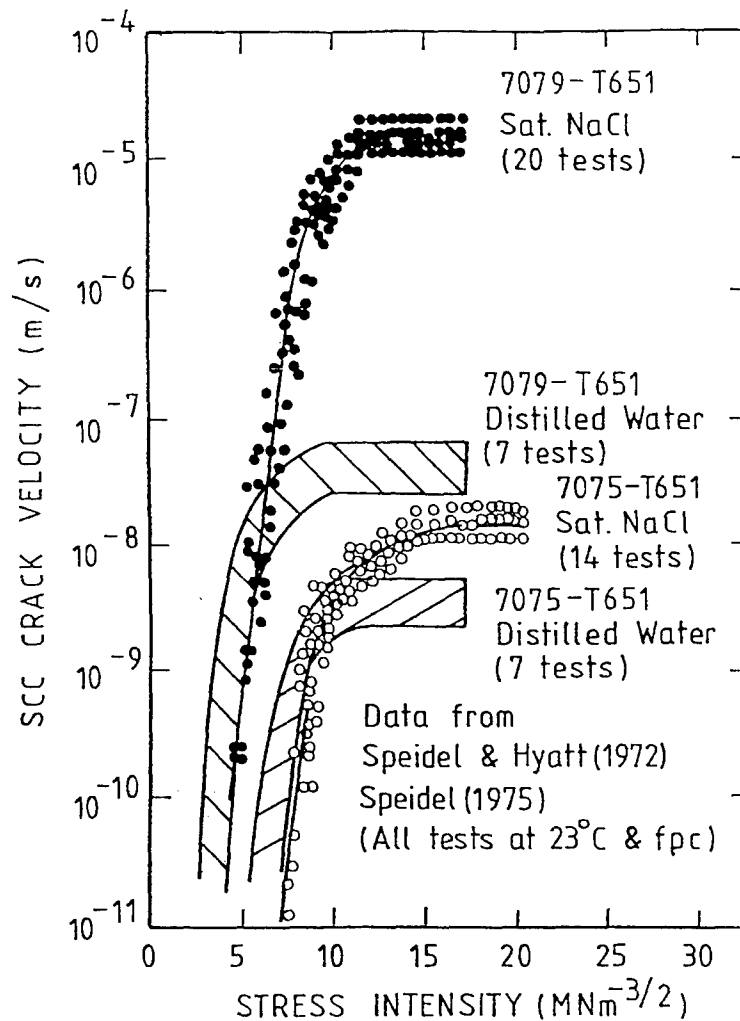
Figure 12. The stress intensity dependence of subcritical crack growth rate for two peak aged 7000 series aluminum alloys stressed in either distilled water or aqueous chloride solution at the free corrosion potential and 23°C. The crack orientation is TL (stress parallel to the transverse (T) direction and crack growth in the longitudinal or rolling (L) direction). (Holroyd, 1990; reproduced from Speidel and Hyatt, 1972; Speidel, 1975: Copyright NACE International, reprinted with permission.)
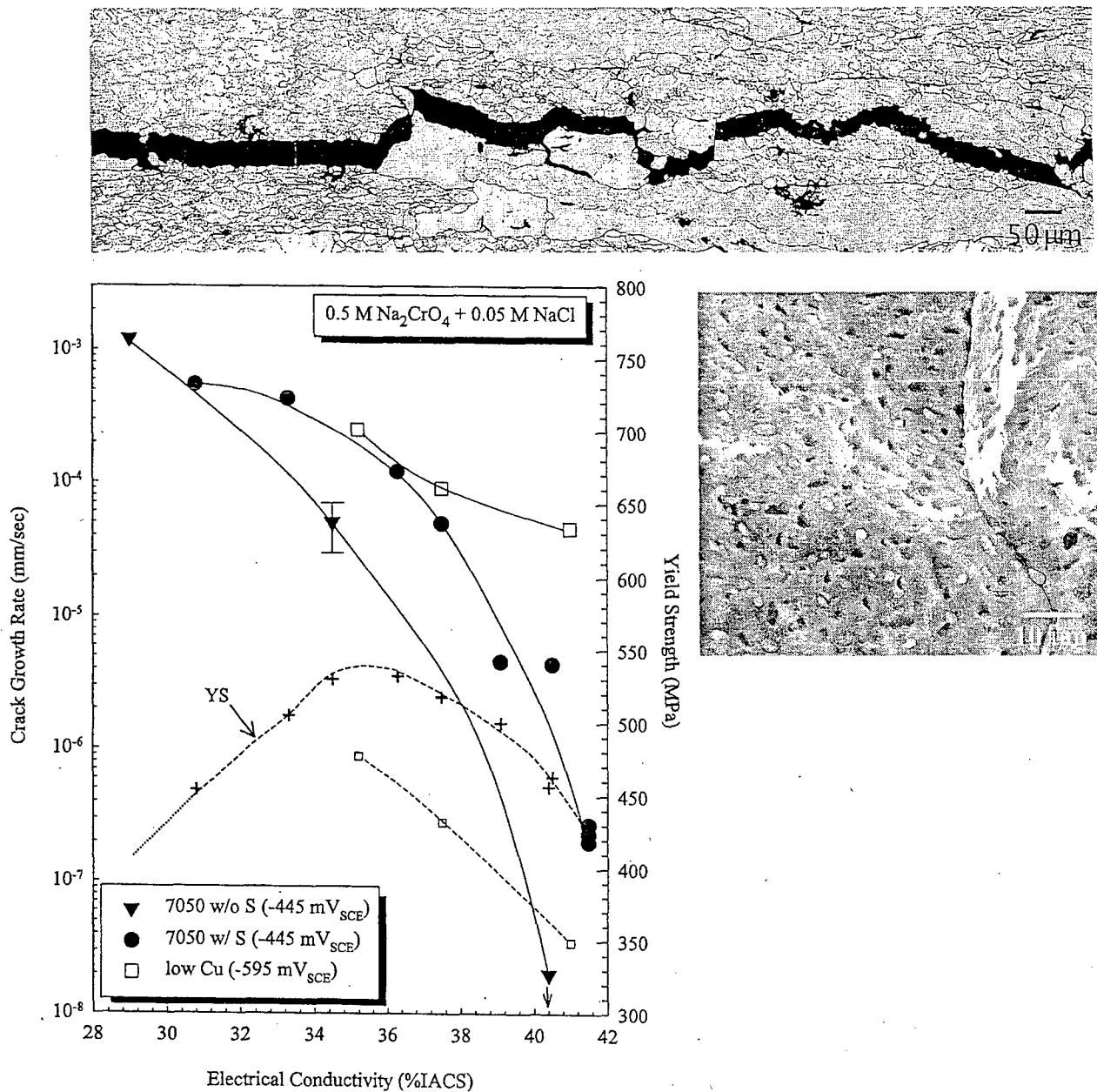
Figure 13. The effect of temper on steady state HEAC rate at fixed CMOD ($20 > K >$
10 MPa$\sqrt{m}$) and electrochemical conditions for S-free ($\square$) and S-bearing ($\bullet$) AA7050, as
well as for low-Cu ($\square$) AA7050. The aging dependence of yield strength is presented for
S-bearing ($+$) AA7050 and low-Cu AA;7050 ($\square$). The crack orientation is SL (stress
parallel to the short transverse (S) direction and crack growth in the longitudinal or rolling
(L) direction). The metallographic section (S-direction is vertical and L direction is
horizontal) and fractograph show intergranular cracking in the T6 temper of S-bearing
AA7050. (Young, 1999; Young and Gangloff, 2001)

phase (Al₂CuMg) free microstructure stressed in the environment for 30 days. The presence of S reduced the amount of Cu available to enable the beneficial effect of aging in AA7050. The severe HEAC produced in a Cu-free model composition is apparent, even for the overaged microstructure.

6.03.5.4 Beta Titanium Alloys

Body-centered cubic β-titanium alloys, hardened by fine precipitates of the hexagonally-close packed α phase, exhibit high strength-to-weight and corrosion resistance, but are susceptible to severe hydrogen assisted cracking (Feeney and Blackburn, 1970; Wanhill, 1975; Young et al., 1995). This cracking differs from the behavior of α and α + β titanium alloys discussed elsewhere in this volume (Chapter 6.3b) because the solubility of H in β is large and the brittle hydride phase is almost certain not to form or participate in H cracking (Gaudett and Scully, 2000; Teter et al., 2001). Two factors are necessary requisites for subcritical hydrogen cracking to occur in β/α-Ti alloys; a fatigue precrack, as well as a threshold amount of aging and/or the associated α must be present in the β matrix.

The occurrence of transgranular IHAC in a H-precharged peak aged β-Ti alloy is illustrated in Fig. 14 (Hayes, 2000; Gangloff, 2001). Fracture mechanics specimens of Ti-15V-3Cr-3Al-3Sn (weight pct) were solution treated and aged isothermally to produce increasing amounts of α precipitation and increased tensile strength. Specimens were then fatigue precracked, H charged to a level of 1300 ppm by an electrochemical method, and cracked under slow-rising CMOD in moist air. Surface oxide precluded significant H loss from the specimen during this testing. The critical stress intensity for the onset of stable
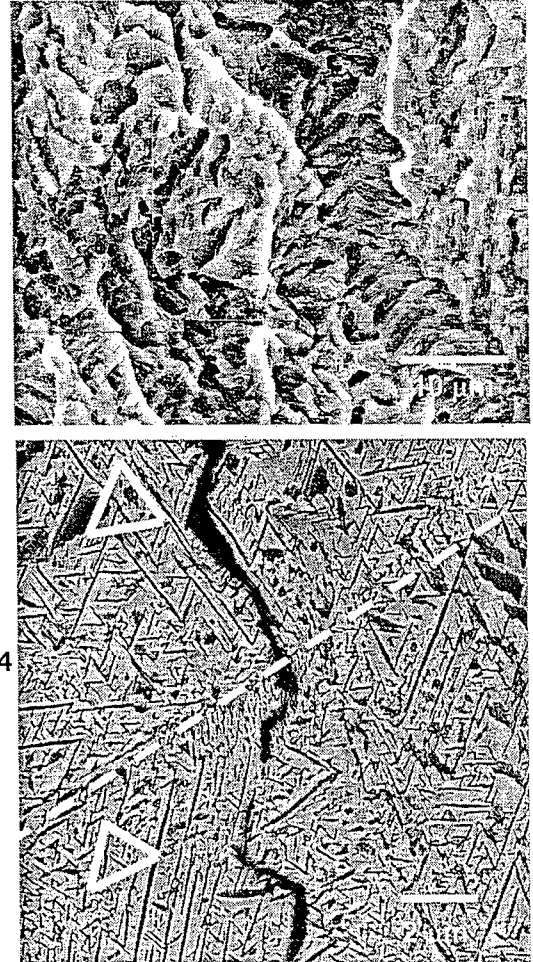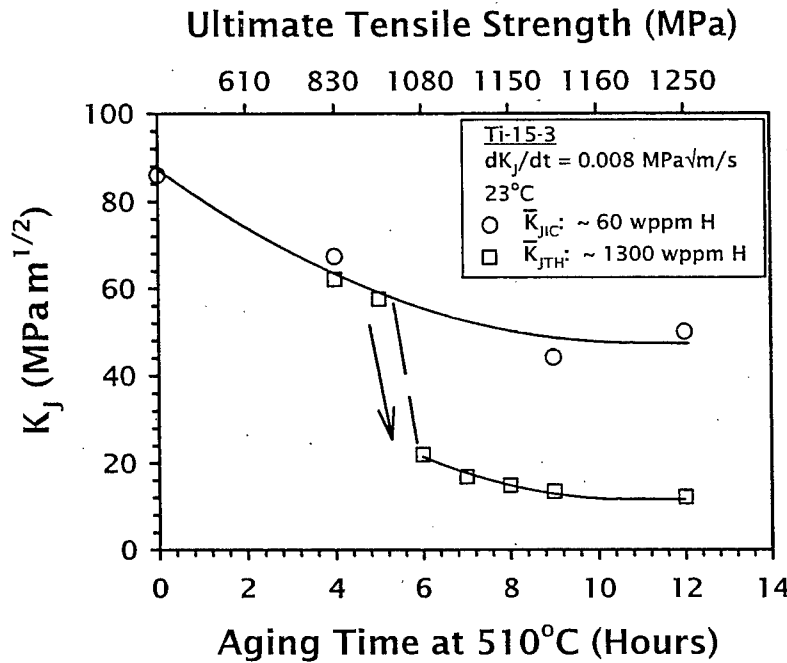
Figure 14. The isothermal-aging time and yield strength dependencies of plane strain fracture toughness at the as-processed H content of 60 ppm and threshold stress intensity for IHAC in H-precharged (C_{H-TOT} = 1300 ppm) Ti-15V-3Al-3Sn stressed in moist air at 25°C. The SEM fractograph shows the morphology of transgranular IHAC for the 12 h age case and the metallographic cross-section shows that H-cracking progresses along β/α interfaces, with the α needles (dark phase) present in three variants shown by the triangles on either side of a high angle grain boundary (dashed line). The subscript, J, denotes elastic K calculated from the elastic-plastic J-integral, and the bar indicates the average of 1st initiation and blunting-line offset definitions of crack growth. (Hayes, 2000; Gangloff, 2001)

cracking in the H-charged microstructures equals the H-free fracture toughness, but only for aging times less than about 4 h. Specimens aged for longer times exhibit substantial IHAC. The short-term aged specimens that were immune to H cracking failed by microvoid processes, while a brittle TG morphology was produced where K_{IIHAC} was less than K_{IC}, as illustrated by the fractographic insert. This H cracking progressed along β/α interfaces, as shown in the metallographic section where the α needles (dark phase) are present in 3 variants shown by the white triangles on either side of a high angle grain boundary (dashed line). Similarly severe IHAC was reported for other β/α-Ti alloys, including Ti-3Al-8V-6Cr-4Mo-4Zr (Beta-C) and Ti-15Mo-3Nb-3Al (Gaudett and Scully, 1999, 2000; Young and Scully, 1994).

The HEAC behavior of aged β-Ti alloys is both similar and strikingly different from IHAC. Figure 15 shows that the all-β-phase microstructure of Beta-C, produced by solution treatment without aging, is immune to HEAC during rising-CMOD loading in neutral chloride solution. This immunity persists for the initial stage of α-precipitation hardening (Somerday, 1998b; Gangloff, 2001; Somerday et al., 2003). Continued aging and increased amount of α precipitation results in severe environment assisted cracking with K_{IHEAC} substantially less than K_{IC}. In contrast to IHAC of these alloys, subcritical cracking in chloride solution is essentially fully intergranular, as shown by the fractographic insert in Fig. 15. Similarly severe cracking was reported for the α-precipitation hardened β-Ti alloy, Beta-21S (Young et al., 1995).

The HEAC in β/α-Ti alloys stressed in neutral-aqueous chloride solution is notable in that the kinetics are rapid. The results in Fig. 6 show that the rising-CMOD K_{IH} is low for
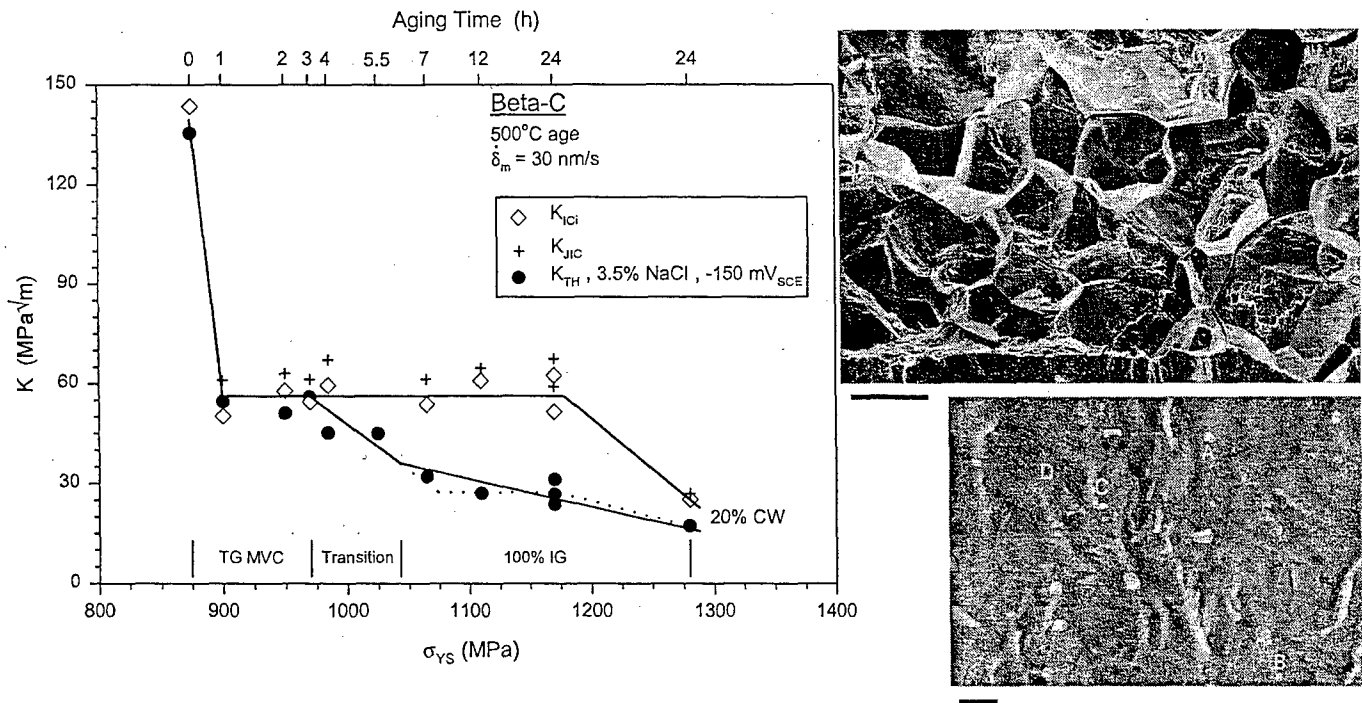
Figure 15.   The strength and isothermal-aging time dependencies of fracture toughness and threshold K for the onset of HEAC in solution treated Beta-C (Ti-3Al-8V-6Cr-4Mo-4Zr) stressed under slow-rising CMOD (or δ_m) loading in moist air and aqueous-chloride solution at constant applied electrode potential of −150 mV$_{SCE}$ and 25°C.   The highest strength and lowest cracking resistances were achieved by 20% cold work (CW) prior to aging to stimulate fine-α precipitation.   SEM fractographs show the morphology of 100% intergranular HEAC for the 6 to 24 h age cases (top, 100 μm bar) and the high magnification view of an IG facet surface in these STA microstructures (bottom, 250 nm bar), as amplified in Fig. 43.   (Somerday, 1998; Somerday et al., 2002)

24h aged Beta-C and independent of loading rate for applied dK/dt between 0.0001 and 4 MPa√m/s; severe IG cracking can propagate under loading that rises over a period of less than 10 s (Somerday et al., 2000). Paralleling this behavior, subcritical rates of HEAC in these alloys are very fast, on the order of 10 to 40 μm/s, and independent of applied K as shown in Fig. 16.

6.03.6 IMPORTANT VARIABLES AFFECTING HYDROGEN CRACKING

The rate of subcritical H cracking is governed by K, as given by threshold and da/dt *vs.* K properties. However, a large number of mechanical, metallurgical, and environment chemical variables affect the kinetics of IHAC and HEAC. The more important effects of these variables are summarized. Mechanism-based explanations and quantitative model predictions of these effects are discussed in 6.03.8. The implementation of a fracture mechanics based structural integrity model requires that the variables relevant to the application be incorporated into the basic materials properties that define crack propagation threshold and rates.

6.03.6.1 Fracture Mechanics Variables

The mechanical variables that affect threshold and growth rate properties pertinent to IHAC and HEAC include loading format (fixed CMOD, rising CMOD or constant load) and rate (dK/dt) as discussed in 6.03.3.5. Data showing the effect of applied dK/dt on the threshold for HEAC were presented in Fig. 5 for a low alloy steel in pure H_2 and in Fig. 6 for a high strength β/α-Ti alloy in aqueous NaCl solution. The effect of loading rate on the
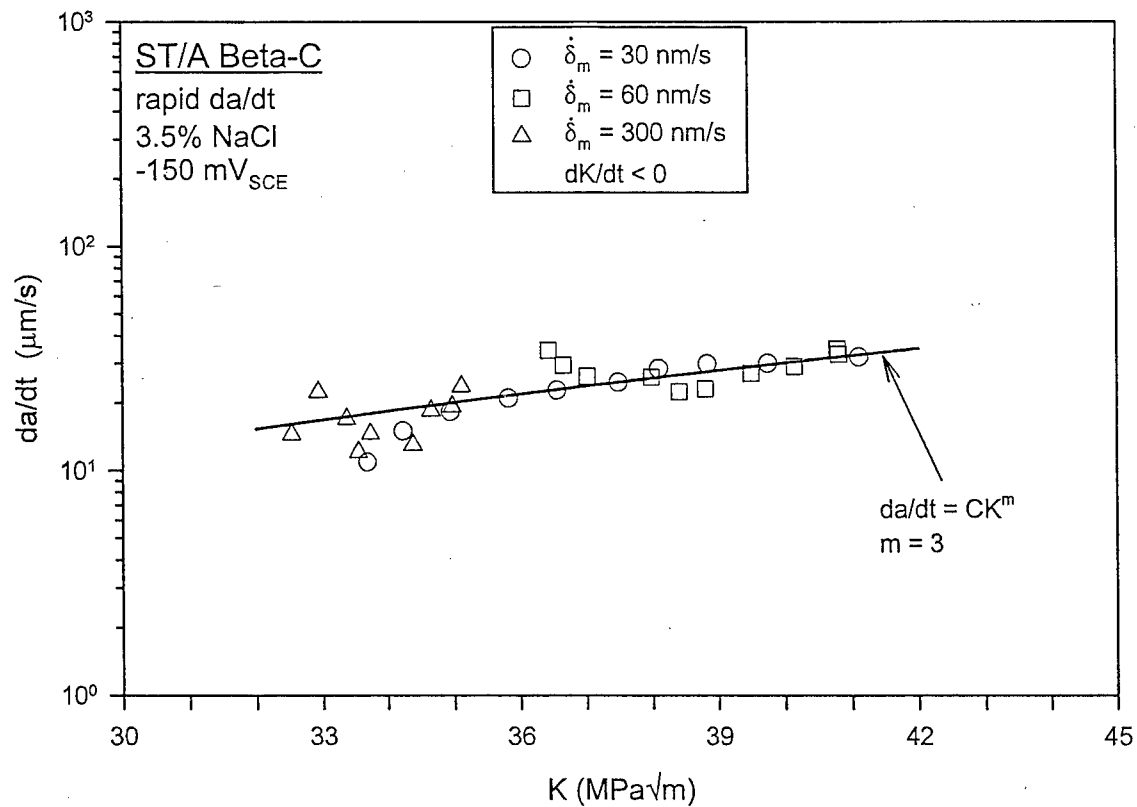
Figure 16.   The stress intensity dependence of subcritical crack growth rate for intergranular HEAC in 24 h aged Beta-C stressed under slow-rising CMOD (or δ_m) loading in aqueous-chloride solution at a constant applied electrode potential of −150 mV$_{SCE}$ and 25°C.   The crack growth rates are independent of the applied loading rate between 30 and 300 nm/s (Somerday et al., 2000).

threshold stress intensity for IHAC in ultra-high strength steel is shown in Fig. 8. Additionally, loading mode (I, II or III, as well as mixed modes), cracked body constraint, small crack size, and load transients can affect crack propagation. These variables have not been studied broadly, as discussed in 6.03.9.1 on the issues that hinder the fracture mechanics prediction of H cracking life.

Researchers at the Naval Research Laboratory contended that the threshold stress intensity for HEAC is reduced by superposition of a small-amplitude cyclic (or ripple) load on a fixed or rising K (Bayles et al., 1993). Specific data were presented to show a strong reduction in the K_{IHEAC}, due to a cyclic K range ($\Delta K = K_{IHEAC} - 0.90$ to $0.95K_{IHEAC}$) for high strength steels (Pao, et al., 1991), a β/α-Ti alloy (Yoder et al., 1990; Pao, et al., 1996) and AA7075 (Pao, Gill and Bayles, 1991a). The reduction in the K_{IHEAC} in chloride solutions was substantial for alloys that otherwise resisted environmental cracking and exhibited a relatively high K_{IHEAC} from quasi-static loading experiments, including overaged AA7075 compared to AA7075-T6 and lower strength martensitic steel compared to higher strength 4340 (Pao et al., 1991, 1991a). The results of the experiments presented to date are best interpreted as high mean stress environmental fatigue crack growth (Gangloff, 1990; Horstmann and Gregory, 1991). A material that resists quasi-static HEAC will exhibit a large ripple load effect if the alloy is susceptible to high mean stress environmental fatigue at low stress intensity amplitudes and a maximum K level that is below the static K_{IHEAC}. In this interpretation, ripple loading is not an intrinsic aspect of quasi-static load HEAC, and correlation of H-assisted quasi-static and fatigue crack propagation data on a single plot of maximum K levels *vs.* time to failure is misleading (Bayles et al., 1993). For example, a

ripple load will cause stable cracking at maximum K levels below K_{IC} for an alloy in ultra-high vacuum. The toughest alloys will show the largest effect of the ripple load. However, there is no novel environmental damage involved, but only crack tip fatigue and the problem is best viewed in this context.

·Cyclic loading at low stress intensity amplitudes and a wide range of maximum K levels should exacerbate H assisted cracking in high strength alloys (Gangloff, 1990). Whether this is claimed as a novel ripple load effect in H cracking, or environment assisted fatigue crack growth is unimportant. The key is to explain the effect of K variation on crack tip H production, uptake and damage in the context of a micromechanical-chemical model (6.03.8). No definitive results have been reported to explain a unique small-amplitude cyclic load effect on a basic element of the HEAC scenario (Fig. 2) and H damage mechanism (6.03.7). The fertile area for such study is at very low ΔK, below 0.5-1 MPa√m. For example, cracking in AA7075-T6 in chromate-chloride solution progressed at a da/dt_{II} level of 4 x 10^{-6} mm/s for a constant K of 13 MPa√m (Mason and Gangloff, 1994). This da/dt did not increase when K was cycled from 13 to 12.3 MPa√m at frequencies of 5 Hz or 30 Hz, demonstrating the lack of an effect for a system where ripple plasticity could destabilize the crack tip passive film from chromate addition. Rather, this time-based rate is consistent with the expected-small effect of cyclic loading from superposition of a corrosion fatigue growth rate and the quasi-static da/dt. Additional work is required to explore the interface between monotonic and cyclic loading effects in H cracking of high strength alloys. Ripple loading critically influences environment-sensitive crack propagation in low strength alloys through film rupture considerations (Parkins, 1990, 1991).

6.03.6.2   Metallurgical Variables

A broad literature exists describing the effects of metallurgical variables on IHAC and

HEAC, as reviewed elsewhere (Bernstein and Thompson, 1976; Thompson and Bernstein,

1980).   Fundamental interpretation and application of such results to structural integrity

modeling is compromised by three factors: (a) yield strength varies concurrently with one

or more microstructure changes to affect crack tip mechanics, (b) a metallurgical effect on H

cracking can vary in different regimes of chemical and mechanical variables, and (c)

mechanisms of H production, uptake and damage are controversial.   Examples of recent

results are reviewed to amplify the data presented in previous sections.   These findings

represent improved attempts to account for these important interactions.

6.03.6.2.1   Alloy Strength

Invariably, IHAC and HEAC are exacerbated by increased yield strength, as manifest by

decreased K_{TH} and increased da/dt. The largest body of data on the strength dependence of

H cracking exists for steels, as illustrated in Fig. 17. Lower bound trend lines represent over

400 measurements of the threshold stress intensity factors for IHAC and HEAC in C-Mn

ferrite-pearlite and martensitic alloy steels exposed to a variety of IHAC and HEAC

environmental conditions at 23°C (Gangloff, 1986, 1988). The trend lines marked "JSW"

and "Thermally Charged Hydrogen" represent the data base for IHAC in tempered bainitic

Cr-Mo steels, with a portion of these data shown previously in Fig. 7, as well as limited

results for low alloy martensitic steels at higher strengths.   The JSW line from Fig. 7

illustrates the strong effect of rising-CMOD loading on K_{TH}, mainly for lower strength steels
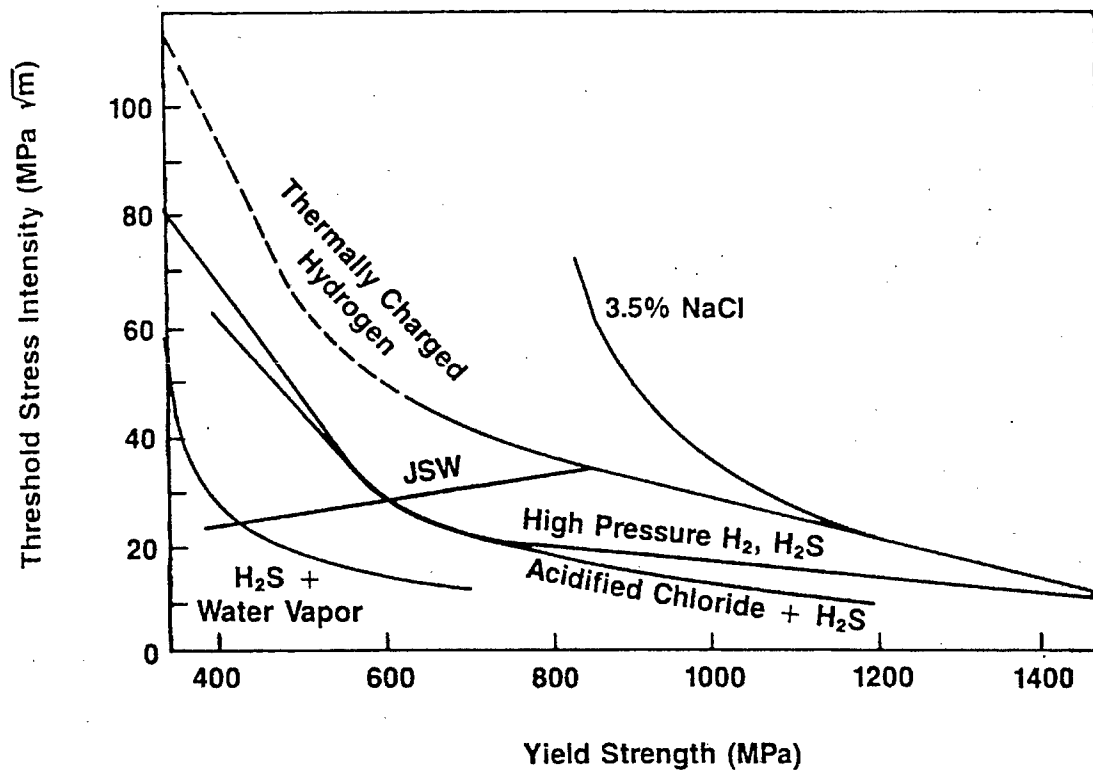
Figure 17.   Lower bound trend lines drawn to represent the results of over 400 measurements of the threshold stress intensity factor for IHAC and HEAC in C-Mn and alloys steels exposed to a variety of IHAC and HEAC environmental conditions at 23°C.   JSW refers to results reported by the Japan Steel Works in the early 1980s, specific to rising CMOD loading (see Fig. 7). Most other thresholds were measured for quasi-static loading, typically involving crack arrest.   (Gangloff, 1986, 1988).

and compared to the standard quasi-static crack arrest thresholds that was measured for the other trend lines in Fig. 17 (see 6.03.3.5.1). The remaining curves describe HEAC in several environments including 3.5% NaCl solution at free corrosion, high pressure H_2 and H_2S gases, acid-chloride solution saturated with H_2S gas, and a mixture of water vapor and H_2S.

For each environment, the strength dependence of the threshold stress intensity exhibits two regimes of behavior; K_{TH} decreases with increasing steel yield strength, sharply at the lower strengths and more gradually in the high to ultra-high strength regime. The location of this transition shifts to lower σ_{YS} as the hydrogen-producing activity of the environment increases. Specific data are presented in Fig. 18 for martensitic low alloy steels in near-neutral NaCl solution, with the mild strength dependence suggested for σ_{YS} exceeding about 1350 MPa. A similar result was reported for 4340 steel in low pressure H_2 (Moody et al, 1990). A second result is shown in Fig. 9 for martensitic stainless steels tested under HEAC conditions (Scully, 2002). The K_{TH} declines strongly with increasing strength in the lower strength regime, with a reduced dependence on strength, or perhaps a plateau, at σ_{YS} above about 1300 MPa. The data in Figs. 9, 17 and 18 establish that steel strength is particularly important for lower strength alloys and/or mildly aggressive environments where immunity to hydrogen cracking may be observed. However, aggressive H production or rising-CMOD loading promote embrittlement in the lowest strength alloys. Increasing steel strength from 1300 to 2000 MPa and above does little to exacerbate already severe embrittlement.

The influence of strength on IHAC and HEAC in Ni, Ti and Al alloy systems is not clearly defined, in part because strong and concurrent microstructure effects complicate the
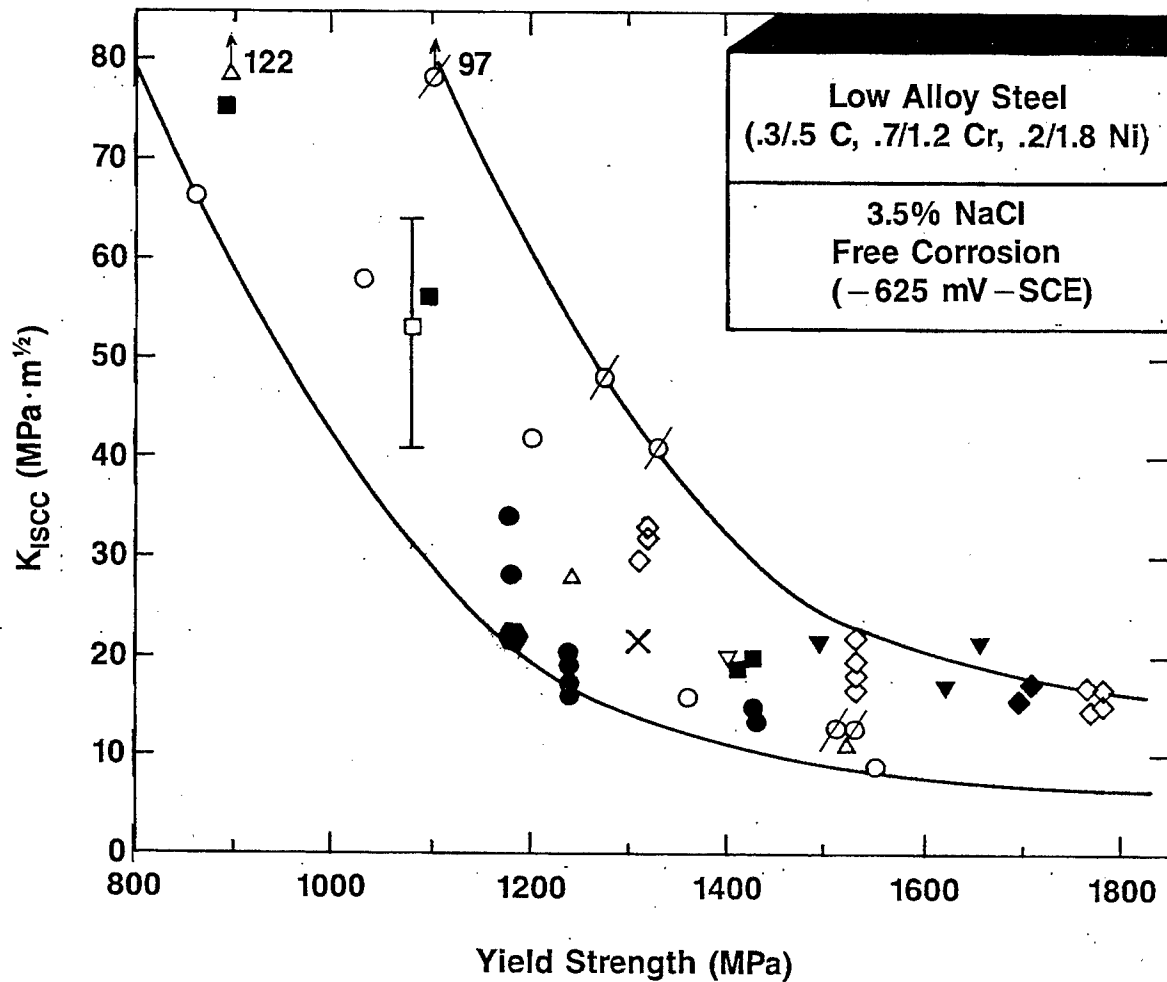
Figure 18.   The yield strength dependence of the threshold stress intensity factor for HEAC in tempered martensitic steels cracked quasi-statically during stressed exposure in near-neutral NaCl solution at free corrosion potentials and 23°C.   (Gangloff, 1986).

intrinsic strength effect.

6.03.6.2.2   Alloy Composition and Microstructure

6.03.6.2.2.1   7000-series Al alloys: Cu Content and Precipitate Condition

Alloy composition and microstructure dominate the IHAC and HEAC resistance of

precipitation hardened 7000 series aluminum alloys (Holroyd, 1990; Burleigh, 1991; Starke

and Staley, 1995). Examples include the effect of aging on HEAC in Cu-bearing AA7050

stressed in either chromate-chloride solution, Fig. 13 (Young, 1999; Young and Gangloff,

2001), or water vapor saturated air, Fig. 19 (Young and Scully, 2002). For all cases in Figs.

13 and 19, the H-assisted subcritical crack growth rate declines monotonically with

increasing aging time, while tensile yield strength exhibits the expected maximum at an

intermediate aging time. All cracking in Figs. 13 and 19 is intergranular for the susceptible

SL crack orientation. While strength should play a role in HEAC susceptibility (6.03.8),

changes in solute content and precipitate microstructure dominate the cracking response in

these Al alloys. This conclusion is supported by the fact that the Cu free alloy in Figs. 13

and 19 exhibits the lowest strengths but highest rates of da/dt for HEAC at each aging time.

The mechanism for the aging dependence of HEAC in 7000 series aluminum alloys is

unclear in spite of 40 years of research (Speidel, 1975; Thompson and Bernstein, 1980;

Pickens et al., 1987; Holroyd, 1990; Burleigh, 1991; Young, 1999; Young and Scully,

2002). The problem is complex since several aspects of the precipitate-matrix microstructure

likely affect one or more of the elements involved in HEAC, including crack chemistry

evolution, H production at the crack tip, H uptake into the FPZ, H transport to damage sites,
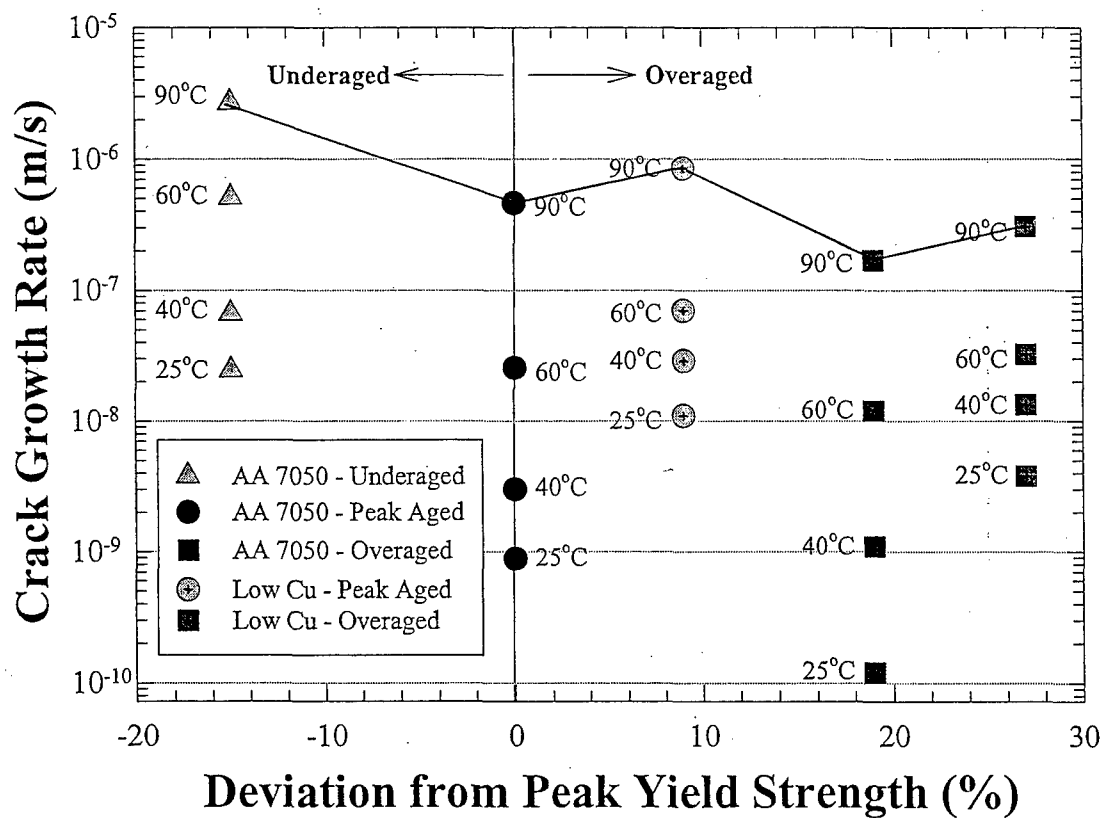
Figure 19. The yield strength, precipitate microstructure, and temperature dependencies of the subcritical HEAC growth rate in AA7050 and a low-Cu model alloy stressed in water vapor saturated moist air. (Scully and Young, 2002: Copyright The Minerals, Metals and Materials Society, reprinted with permission.)

and the H embrittlement mechanism (Fig. 2). These microstructural factors change concurrently during aging, and direct observation of such changes interacting with H damage in the crack tip FPZ is hindered by the sub-micrometer scale and highly gradated-transient character of these processes. For example, changes during under through peak to overaging aging include: (a) increasing amount and changing Al/Zn/Mg/Cu content of grain boundary precipitates that affect local electrochemical reactions and act as trap sites for H, (b) increasing thickness and changing composition of soft precipitate free zones adjacent to grain boundary precipitates that affect strain localization and electrochemical reaction kinetics, (c) increasing and/or decreasing amounts of grain boundary segregation of elements such as Zn, Mg and Cu, and (d) planar-heterogeneously localized to homogeneous slip transition due to changing interaction of dislocations with intragranular precipitates that evolve from solute zones through coherent then incoherent particles. Given these complex interactions, it is no wonder that the governing mechanisms for the aging dependence of HEAC in 7000 series alloys remain elusive.

The composition and heat treatment of modern 7000 series alloys are tailored for strength and H cracking resistance (Starke and Staley, 1995). Heat treatment focuses on controlled solution treatment temperature plus heating/cooling rates, followed by multi-step aging (Holroyd, 1990). For example, the retrogression and reaging process couples short-term high temperature aging of under or peak aged alloy to achieve HEAC resistance with a subsequent low temperature-aging step for high strength (Thompson, et al., 1987).

6.03.6.2.2   Beta-Ti Alloys: Alpha Precipitation

The opposite situation exists for the age hardened β-Ti alloys, where susceptibility to transgranular IHAC and intergranular HEAC increases with increasing isothermal aging. For the two alloys represented in Figs. 14 and 15, the thresholds for IHAC and HEAC decline monotonically with increased precipitation of fine α particles and the associated increase in yield strength (Somerday, 1998b; Hayes, 2000; Gangloff, 2001; Somerday et al., 2003). Neither strength nor H cracking susceptibility decrease for the increasing isothermal aging times examined. In this case H cracking is likely to be exacerbated by an interaction of increasing amount of the deformable α phase in the microstructure, as well as increasing macroscopic strength without overaging.

Experiments were conducted to separate these contributions to HEAC by cold working the single-β phase microstructure to various levels and thus yield strengths. The all-β microstructure of Beta-C was immune to both IHAC and HEAC for cold work levels from 0 to 80 pct, suggesting that IG cracking is promoted primarily by a metallurgical property associated with aging and not by increased yield strength or decreased work hardening (Somerday and Gangloff, 1998, 1998a; Gaudett and Scully, 2000). The precise mechanism for the effect of aging on H cracking susceptibility of β/α-Ti alloys was not established, but may involve elemental segregation to β/α interfaces during aging, as well as the micromechanics of plastic deformation in the β/α mixture where each phase is capable of plastic deformation with the possibility of microscopic constraint (Somerday et al., 2003).

6.03.6.2.2.3   Nickel Superalloys and Steels: Grain Size

Austenite grain size affects the H cracking resistance of precipitation hardened superalloys, as well as high strength martensitic steels (Bernstein and Thompson, 1976; Moody et al., 1990).   The results (•) in Fig. 20 show that the threshold stress intensity for HEAC in Fe-based IN903 stressed during exposure in high pressure (207 MPa) H_2 increases with increasing grain size, d, following a relationship of the form $K_{IHEAC} \propto \sqrt{d}$ (Moody and Robinson, 1990; Somerday and Moody, 2001).   A similar grain size effect is shown by the K_{IHEAC} data in Fig. 11 for IN718 stressed in acidic solutions (Lillard, 1998).

A compilation of data for H-cracking in high strength martensitic 4340 steels showed a similar-strong grain size effect on K_{TH} for a single study involving IHAC (o in Fig. 20) (Lessar and Gerberich, 1976), but only a mild to nil dependence on $\sqrt{d}$ for two heats of commercial 4340 steel tested in aqueous environments constituting HEAC ($\square$ and ∇ in Fig. 20) (Procter and Paxton, 1962; Carter, 1969).   Kameda showed that K_{TH} was independent of prior austenite grain size, from 40 to 500 μm, for H_2-assisted cracking in two high purity laboratory heats of Fe-3.5Ni-1.7Cr-0.3C (Kameda, 1986).   The threshold for cracking declined modestly for the largest grain size when the steel was doped with P impurity. With increasing grain size, da/dt decreased for the pure steel and increased for the impure alloy. For each grain size and purity, HEAC was severe and intergranular.

Interpreting the effect of grain size on H cracking is complicated since several microstructural factors change as grain size increases. For example, the results in Fig. 20 for IN903 reflect an intrinsic grain size dependence since σ_{YS} did not vary significantly with grain size in this precipitation hardened alloy.   In contrast, strength decreased with
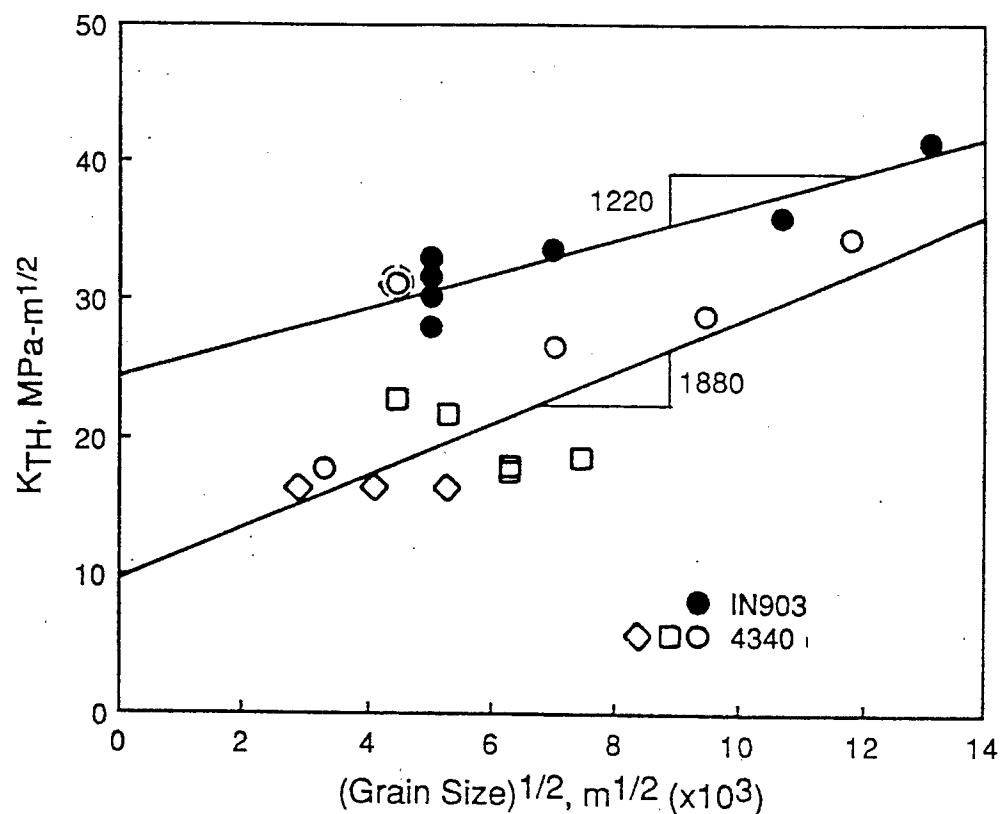
Figure 20.   The austenite grain size dependence of the threshold stress intensity
factor for subcritical HEAC in iron-based superalloy IN903 in high pressure H_2
(•), as well as for HEAC (∇ and 9) and IHAC (o) in tempered martensitic AISI
4340 steel, all at 23°C.   (Moody, Robinson and Garrison, 1990: Reprinted with
permission from Elsevier.)

increasing grain size for 4340 steel, and to some extent for the IN718 data in Fig. 11.

Additionally, the amount of impurity segregation (see 6.03.6.2.2.4) may decrease as grain

size increases for Fe and Ni-based alloys, since higher temperatures in the austenite phase

field are employed to achieve increased grain size (Kameda, 1986). These factors should

reduce susceptibility to H cracking with increasing grain size. Understanding the grain size

effect in the superalloy is further complicated by a change in H-crack path, from IG for fine

grain size to TG for large grain sizes (Somerday and Moody, 2001). This behavior was

interpreted based on a fundamental change in the governing-H cracking mechanism, from

grain size sensitive crack tip stress-based damage in fine grain size microstructures, to grain

size independent damage governed by plastic strain in the large grain size conditions.

6.03.6.2.2.4   Steels: Purity

Metalloid impurity elements affect the intergranular H cracking resistance of martensitic

steels. Elements such as P, S, Sn, As, or Sb segregate to and embrittle prior austenite grain

boundaries in martensitic microstructures in the absence of hydrogen (Briant and Banerji,

1978, 1983), and moreover, interact with H to promote intergranular IHAC and HEAC. The

literature on impurity effects on H cracking in low alloy steels is broad (McMahon, 2001)

and this issue is particularly important for moderate strength steels with $\sigma_{YS} < 1000$ MPa

(Yoshino and McMahon, 1974; Viswanathan and Hudak, 1977). Boundary segregation

effects have been considered as a factor in the H cracking of β/α-Ti alloys (Somerday et al.,

2003), 7000 series Al alloys (Pickens, et al., 1987; Holroyd, 1990) and superalloys (Moody

et al., 1990), although systematic studies are lacking for these nonferrous alloys.

Two important correlations, reproduced in Figs. 21 and 22, establish the effect of purity

on H cracking in high strength steels (Bandyopadhyay et al., 1983). Tempered martensitic

4340-type steels were processed for varying P, S, Si and Mn; tempered to vary σ_{YS} between

1200 and 1900 MPa, and cracked subcritically by stressed exposure in pure H_2 at pressures

between 30 and 200 kPa and 23°C. Considering these data *in toto*, Fig. 21 shows that

K_{IHEAC} declines from the H-free K_{IC} of about 130 MPa√m to 15-20 MPa√m, correlating with

the increase in percentage of IG cracking from 0 to 100%. The K_{IHEAC} decreases uniquely

with increasing composition parameter, Ψ, as established in Fig. 22. This parameter is the

sum of the bulk amounts of impurity (S and P), Mn and Si that promote segregation of

impurities to austenite boundaries, and the H present in the crack tip FPZ. This H content

was computed based on H solubility from H_2 (proportional to √P_{H2} at constant T) and

enhanced by crack tip hydrostatic stress (6.03.8). These correlations demonstrate that the

deleterious effects of hydrogen and impurity elements are additive since a single trend

represents the range of H contents from varying H_2 pressure, as well as different impurity

contents from steel processing. This impurity parameter, without the H contribution,

correlated the relatively low K_{IHEAC} values (15-25 MPa√m) for AISI 4340 steel stressed

during exposure to aqueous NaCl solution (Moody et al., 1990). In this view, H affects

grain boundary fracture resistance analogous to other impurity elements, consistent with the

decohesion theory summarized in 6.03.7.

The practical implication is that production of high strength martenstic steels of high

purity substantially eliminates IHAC and HEAC. For example considering high and ultra-

high strength steels, Olson speculated that IG hydrogen cracking is eliminated by rare-earth
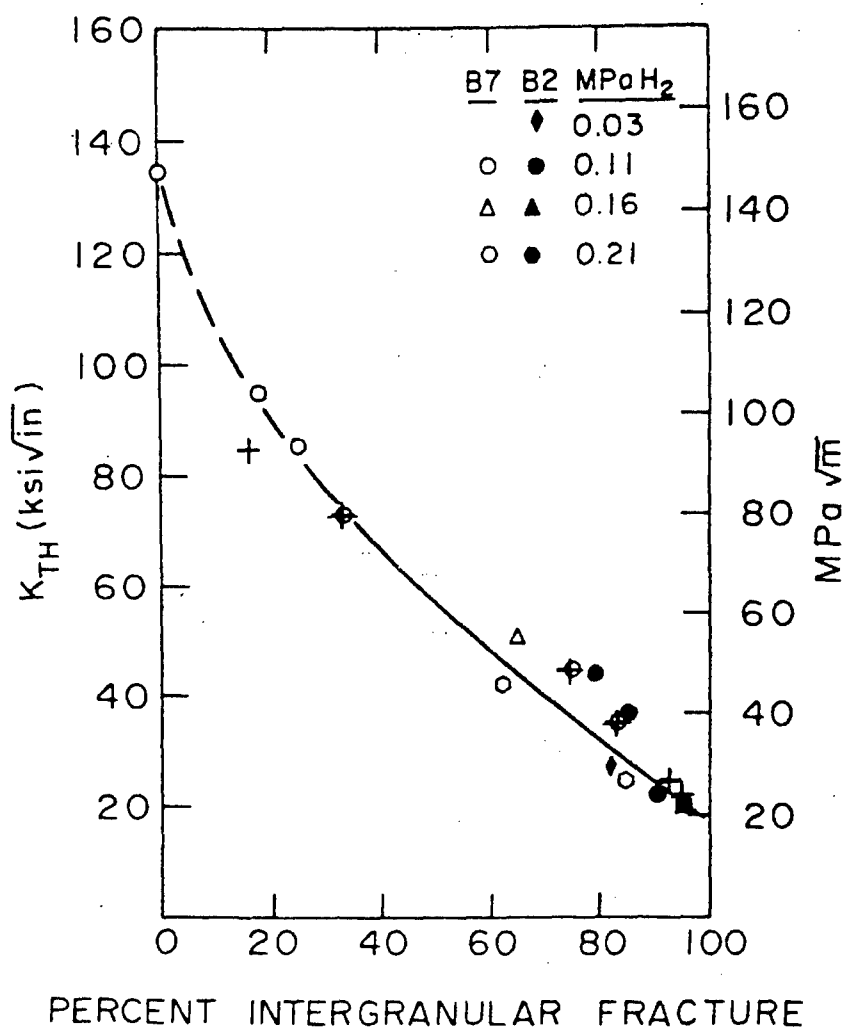
Figure 21. The correlation between the amount of IG cracking and K_{IHEAC} for tempered martensitic low alloy steels of the AISI 4340 base composition stressed during exposure in moderate pressure H_2 at 23°C. (McMahon, 2001; Bandyopadhyay et al., 1983: Reprinted with permission from Elsevier.)
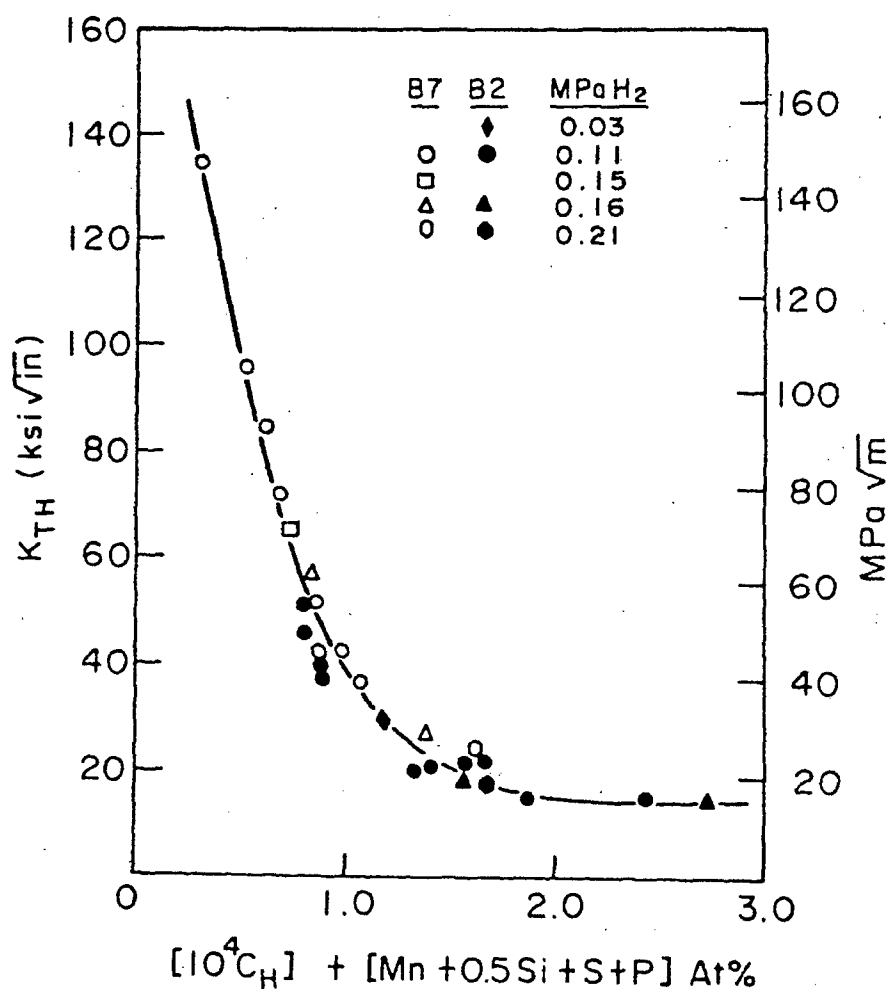
Figure 22. The H and metalloid impurity concentration dependence of the K_{IHEAC} in tempered martensitic low alloy steels of the AISI 4340 base composition stressed during exposure in moderate pressure H_2 at 23°C. (McMahon, 2001; Bandyopadhyay et al., 1983: Reprinted with permission from Elsevier.)

addition that reduces grain boundary impurity segregation (Olson, 1987, 1997). Unfortunately, severe embrittlement is encountered in modern steels that are processed for high purity and ultra-high strength. High strength 18Ni Maraging steels contain only trace levels of P, S, Si and Mn, but are susceptible to severe intergranular IHAC and HEAC as illustrated in Fig. 3 (Dautovich and Floreen, 1977). Severe embrittlement is produced in high purity martensitic stainless steels at high strength levels, Fig. 9 (Scully, 2002). AerMet®100 is produced by double-vacuum melting to yield ultra-low S and P levels, and neither Mn nor Si are added. However, this UHSS is prone to IG HEAC in acids and near-neutral chloride solutions with cathodic polarization, but less so than less pure steels (Buckley et al., 1993; Buckley et al., 1994; Oehlert and Atrens, 1998; Vigilante et al., 2000).

Approaches to produce H-cracking resistant high strength steels by improving the purity of prior austenite grain boundaries are ineffective for two reasons. First, micromechanical models of interface decohesion suggest that H trapping and very high stress at a crack tip are sufficient to promote hydrogen embrittlement without a dominant impurity contribution (6.03.8). Second, high strength steels are susceptible to severe transgranular H cracking, as illustrated by the low K_{IHAC} results for AerMet®100 steel (Fig. 8). Grain boundary composition is not therefore a primary factor in the H cracking of high strength alloys.

6.03.6.3   Chemical Variables

6.03.6.3.1   Hydrogen Concentration in IHAC

Hydrogen is trapped at various microstructural features in a complex alloy, and this behavior critically affects H solubility and diffusion, as well as IHAC and HEAC (Oriani,

1970; Kumnick and Johnson, 1970; Pressouyre and Bernstein, 1978; Pressouyre, 1979, 1983; Hirth, 1980; LeBlond and Dubois, 1983; Krom and Bakker, 2000; Scully, et al., 2000; Moody et al., 2001; Thomas, et al. 2002). High tensile strength and strong H-trapping frequently correlate because nano-scale features that strengthen an alloy often provide effective sites for H segregation. When trapping occurs, it is necessary to specify the H content in the alloy as either total H concentration (C_{H-TOT}) or diffusible H concentration (C_{H-DIFF}). The former represents the sum of: (a) H dissolved in the alloy lattice, (b) H in dynamic equilibrium with 1 or more reversible trap states, and (c) H trapped strongly in irreversible sites (Pressouyre, 1979, 1983). The C_{H-DIFF} is that H dissolved in the lattice plus trapped at reversible sites, and depends on temperature exponentially through the energies of H-lattice solution (H_S) and H-trap binding, E_B (Hirth, 1980).

The concentration of H, predissolved in a high strength alloy microstructure, affects both the threshold stress intensity and subcritical crack growth rates for IHAC. Extensive data show that K_{IHAC} decreases as C_{H-TOT} increases for low alloy steels such as 4340 and 300M, as well as precipitation hardened maraging steels (Dautovich and Floreen, 1973, 1977; Gerberich et al., 1988; Yamaguchi, et al., 1997). This behavior is typically described by a relationship of the form:

$$K_{IHAC} = \alpha (C_{H-TOT})^{-\beta} \tag{1}$$

where α and β are fitting constants determined from the experimental data (Gangloff, 1986). C_{H-TOT} is typically measured by hot vacuum or inert gas extraction of H at a sufficiently high temperature where trapping does not occur.

Yamakawa and coworkers suggested that the threshold stress intensity for H cracking

correlates with C_{H-DIFF} determined from H permeation experiments with an unstressed membrane (Yamakawa et al., 1984, 1986). Results for high strength quenched and tempered AISI 4135 steel were well described by:

$$K_{TH} \ (MPa\sqrt{m}) = 16.1 \ (C_{H-DIFF})^{-0.10} \quad (ppm) \tag{2}$$

This result is not relevant to IHAC or HEAC *per se* because the correlation was based on K_{TH} for specimens that were H precharged and stressed in the charging solution, constituting a worst-case combination of the two forms of H cracking. Experiments systematically characterized H trapping and the cracking threshold for AerMet®100 steel stressed in moist air (Thomas, 2000, Thomas et al., 2002, 2003). The K_{IIHAC} decreased with increasing diffusible and total H concentrations, according to regression-based relationships of the data in Fig 23:

$$K_{IIHAC} \ (MPa\sqrt{m}) = 40 \ C_{H-DIFF}^{-0.54} \quad (ppm)$$

$$K_{IIHAC} \ (MPa\sqrt{m}) = 100 \ C_{H-TOT}^{-0.49} \quad (ppm) \tag{3}$$

Similar H-concentration dependences were reported for other high strength alloys. Results in Fig. 10 show the deleterious effect of increased precharged-H content on K_{IIHAC} as well as K_{IC-H} for IHAC of an Fe-based precipitation hardened superalloy (Moody, Perra and Robinson, 1988, 1990b). IHAC in high strength β/α-Ti alloys is exacerbated by increasing H concentration, as illustrated by the data contained in Fig. 24, extending the findings shown in Fig. 14. The threshold stress intensity for IHAC in α-precipitation hardened Ti-15-3 sheet is plotted as a function of C_{H-TOT} for specimens that were H-charged electrochemically then stressed at constant dK/dt and 23°C in moist air (Hayes, 2000). Results suggest that the alloy is toughened somewhat by H addition up to about 400 ppm,
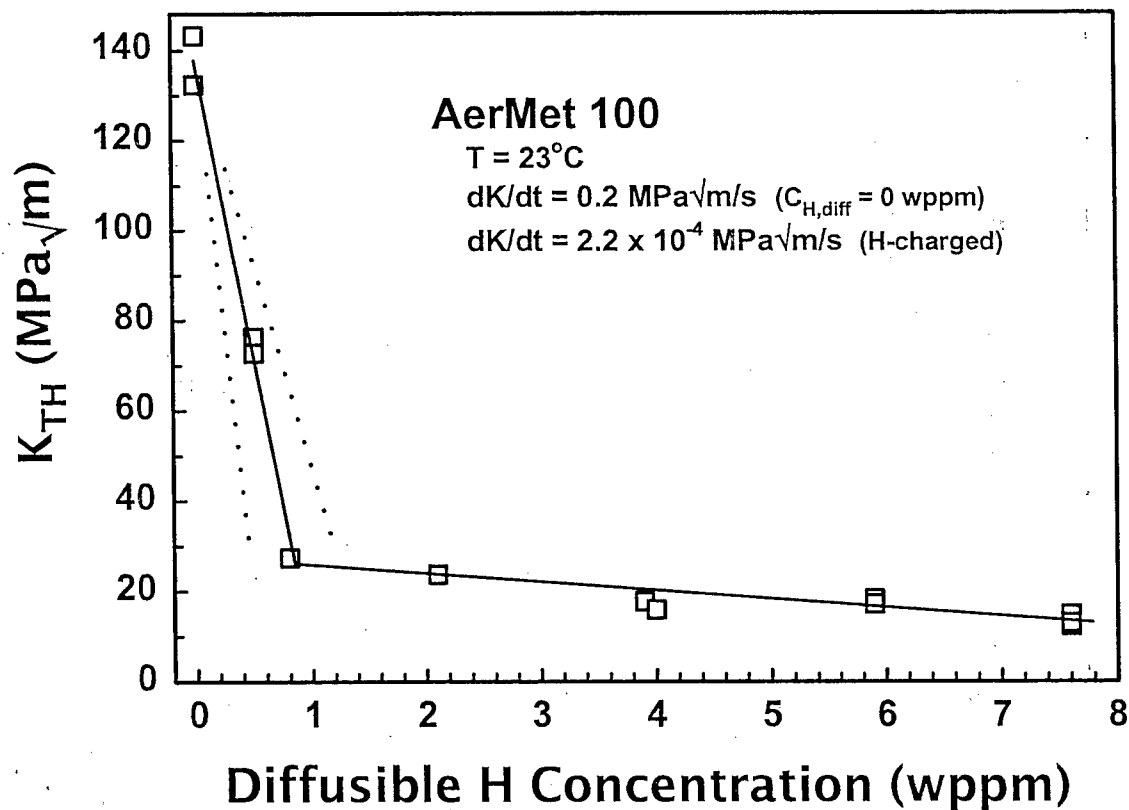
Figure 23.   Threshold stress intensity for IHAC in peak aged AerMet®100, containing varying diffusible H concentration dissolved electrochemically, and stressed at constant dK/dt of 2.2 x 10^{-4} MPa√m/s. (Thomas, 2000; Thomas et al. 2002, 2003)
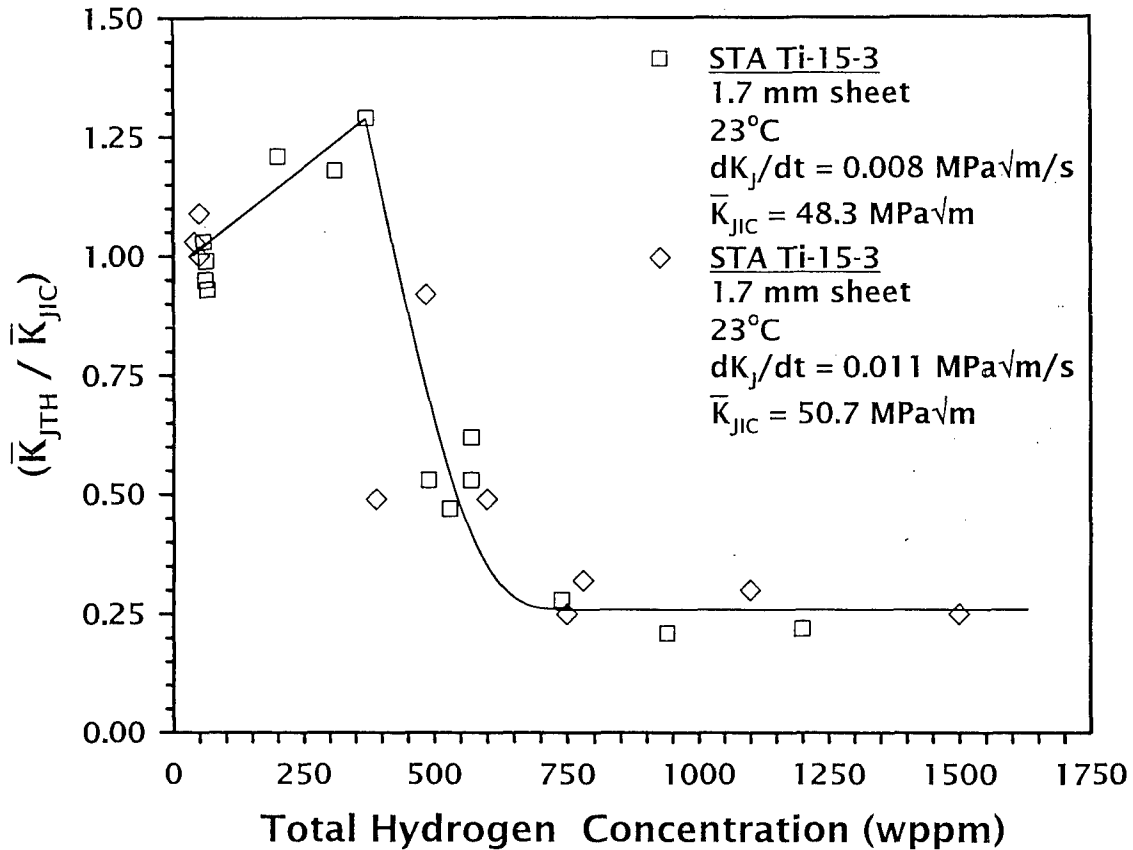
Figure 24.   Threshold stress intensity for IHAC in α-precipitation hardened Ti-15-3 sheet, containing varying total H concentration dissolved electrochemically, and stressed at constant dK/dt of either 0.011 or 0.008 MPa√m/s. The threshold K in this plot was determined by an elastic-plastic J-integral analysis and normalized by the average plane strain fracture toughness for this alloy containing 60 ppm H.   (Hayes, 2000).

followed by a precipitous decrease in K_{IH} for increasing C_{H-TOT} from 400 to 700 ppm. Additional increase in H content did not affect the low threshold for IHAC in this alloy. Analogous results were reported for a second high strength β/α-Ti alloy, Ti-7Mo-4.5Fe-1.5Al (Hayes, 2000). For both β/α-Ti alloys, IHAC progressed along a brittle transgranular crack path, (e.g., Fig. 14) for all H concentrations examined (Hayes, 2000).

Extensive H trapping can increase or decrease the hydrogen embrittlement susceptibility of an alloy (Pressouyre and Bernstein, 1979, 1981; Pressouyre, 1980; Morgan and McMahon 1985). A homogeneous distribution of strong (irreversible) traps increases resistance to cracking by preventing (or shielding) H segregation to the crack tip FPZ containing lower H-binding energy sites that are interconnected and susceptible to decohesion. This is particularly true if a finite quantity of H is available, as typical of IHAC (Coudreuse and Bocquet, 1995). Embrittlement was reduced by strong H trapping at TiC particles in HSLA steel (Stevens and Bernstein, 1985), VC in 2¼-1Mo-0.3V (Coudreuse and Bocquet, 1995) and PdAl in PH 13-8 Mo stainless steel (Scully, et al., 1991). In contrast weak (reversible) traps provide a reservoir of diffusible H to supply the crack tip fracture process zone and decrease resistance to IHAC (Thomas, et al., 2002, 2003). Both beneficial and detrimental effects of H trapping are likely in high strength alloys due to the number and variety of trap sites in such complex microstructures.

6.03.6.3.2   Environmental H-Producing Activity in HEAC

The amount of atomic hydrogen, absorbed on crack surfaces in close proximity to the tip, critically affects HEAC in high strength alloys, analogous to the influence of

predissolved H concentration in IHAC. This uptake of H is controlled by environmental variables for gases and electrolytic solutions.

6.03.6.3.2.1 Gaseous Environments

Increasing H_2 pressure promotes HEAC in high strength alloys, as manifest by decreasing K_{IHEAC} and increasing da/dt. The P_{H2} dependence of K_{IHEAC} is presented in Fig. 25 for high and ultra-high strength steels with σ_{YS} between 1350 and 1650 MPa (Gangloff, 1986). This pressure dependence is observed broadly for steels (Oriani and Josephic, 1974; Clarke, 1979; Bandyopadhyay, 1983; Moody et al., 1990) as well as Fe and Ni based superalloys (Moody et al., 1990); however, the slope of the dependence declines sharply as alloy strength increases. For example, steels with σ_{YS} < 1200 MPa exhibit an extremely strong P_{H2} dependence of K_{IHEAC}, while very high strength steels with σ_{YS} > 1700 MPa do not (Akhurst and Baker, 1981; Moody et al., 1990). The H_2 pressure dependence of K_{TH} is affected by steel impurity content (Bandyopadhyay, 1983) and temperature, but data for the latter are limited. Clarke reported that K_{IHEAC} for 4140 steel is independent of the pressure of H_2S from 100 to 2000 kPa; however, an effect is likely at lower P_{H2S} (Clarke, 1979).

The H_2 pressure dependence of subcritical crack growth rate likely reflects the dependence of the threshold. For example, the Stage II da/dt increases with increasing P_{H2} raised to a power less than 1.0 for ultra-high strength 18Ni Maraging steel. The precise power law depends on gas temperature as illustrated in Fig. 26, and determined by both equilibrium and kinetic considerations (6.03.8) (Gangloff and Wei, 1977). The pressure dependence of da/dt$_{II}$ also depends on steel strength (Nelson and Williams, 1977).
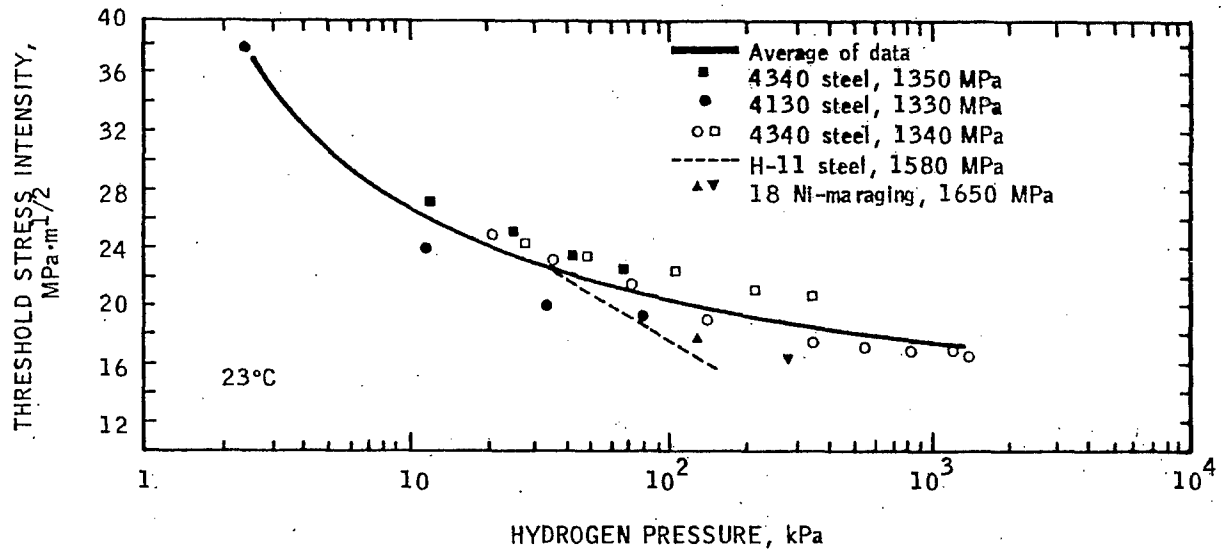
Figure 25.   The effect of H_2 pressure on the threshold stress intensity factor for HEAC of several high and ultra-high strength steels stressed in this environment at 23°C.   (Gangloff, 1986)
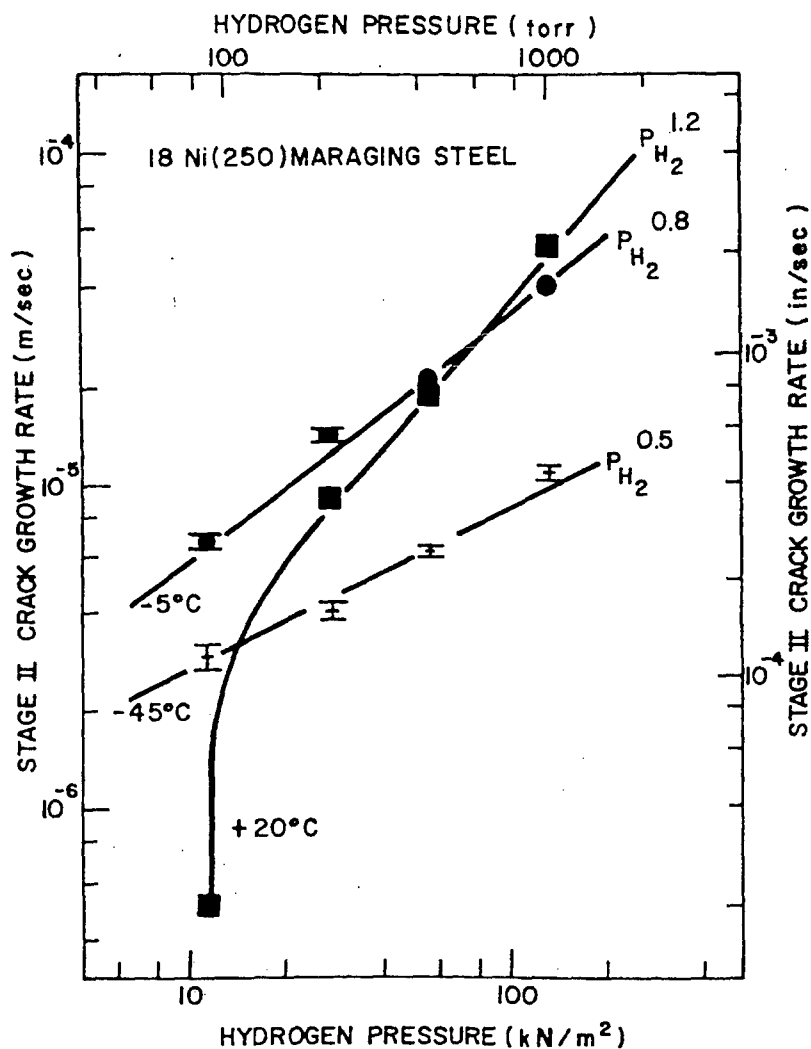
Figure 26. The effect of H_2 pressure on the HEAC growth rate for ultra-high strength 18Ni Maraging steel stressed in a highly purified hydrogen environment at three temperatures. (Gangloff and Wei, 1977)

The composition of the gas environment affects susceptibility to HEAC. Nelson and coworkers reported astonishingly fast rates of subcritical HEAC when AISI 4130 steel (σ_{YS} = 1344 MPa) was stressed in an H_2-H gas mixture produced by thermal dissociation of the hydrogen molecule (Nelson et al., 1971). High rates of subcritical HEAC were reported for ultra-high strength steel stressed during exposure to gaseous HCl, HBr and H_2S (Kerns et al., 1977; Opoku and Clark, 1980). This work also evidenced significant crack growth in Cl_2, suggesting either a residual impurity effect or a damage mechanism other than HEAC (Sieradzki and Ficalora, 1979).

Gas addition can inhibit rates of HEAC. For example, substantial subcritical crack growth that occurs in a high strength martensitic steel stressed in pure water vapor or H_2 was arrested by small addition of O_2 (Hancock and Johnson, 1966; Sawicki, 1971; Kerns et al., 1977). Hydrocarbon molecules such as ethylene (C_2H_4) and acetylene (C_2H_2) react with an iron surface to consume adsorbed H and thus inhibit HEAC when added to H_2 (Gangloff, 1988). The key is the number of unsaturated C-C bonds available to react with surface H to inhibit HEAC; C_2H_4 addition to pure H_2 reduced rates of HEAC in high strength AISI 4130 steel (σ_{YS} = 1330 MPa) but CH_4 with saturated C bonds did not. When present in pure form, hydrocarbon molecules may be catalytically dissociated to produce surface H and HEAC; however, rates of cracking are substantially less than those produced by H_2 (Kerns, et al., 1977; Opoku and Clark, 1980; Gangloff, 1988).

6.03.6.3.2.2   Aqueous Electrolytic Environments

Substantial data show the generally deleterious effects of cathodic polarization,

decreasing pH, H_2S addition, temperature, and other chemical variables on the susceptibility of high strength alloys to HEAC in electrolytes. Extensive reviews document such environmental effects on subcritical crack growth in steels (Carter, not dated; Kerns et al., 1977). Holroyd reviewed the substantial amount of data that pertain to environment chemistry effects on cracking in high strength 7000 series Al alloys (Holroyd, 1990). Those aqueous environmental conditions that promote increased H production and uptake into the crack tip FPZ reduce K_{IHEAC} and increase da/dt, analogous to the deleterious effect of increasing C_{H-DIFF} in IHAC.

Permeation-Based Correlation: A first step in correlating a range of environmental effects on HEAC employed the permeation experiment to determine the C_{H-DIFF} produced in a high strength alloy in equilibrium with a gas or electrolyte (Yamakawa et al., 1984, 1986; Gangloff, 1986). Permeation experiments have not generally included stress or occluded-crack chemistry effects; however, such issues can be incorporated by using specialized specimens or an environment that simulates the occluded crack situation (Scully and Moran, 1988; Kolman and Scully, 1997).

The permeation-based approach without considering crack chemistry is illustrated in Fig. 27 for martensitic 4340-type steels ($1300 < \sigma_{YS} < 1500$ MPa). For gaseous hydrogen, K_{IHEAC} is plotted (including data similar to those presented in Fig. 25) *vs.* C_{H-DIFF} estimated from permeation experiments and corrected to a yield strength of 1400 MPa using an elastic analysis with crack tip hydrostatic stress of $2.4\sigma_{YS}$ (6.03.8). For reference, *log H solubility* of -0.1 ppm ($C_{H-DIFF} = 0.3$ ppm) corresponds to $P_{H2} = 7$ kPa and *log H solubility* of 1.8 ($C_{H-DIFF} = 63$ ppm) corresponds to $P_{H2} = 11.4$ MPa at 23°C. The data (□) are well fit by:
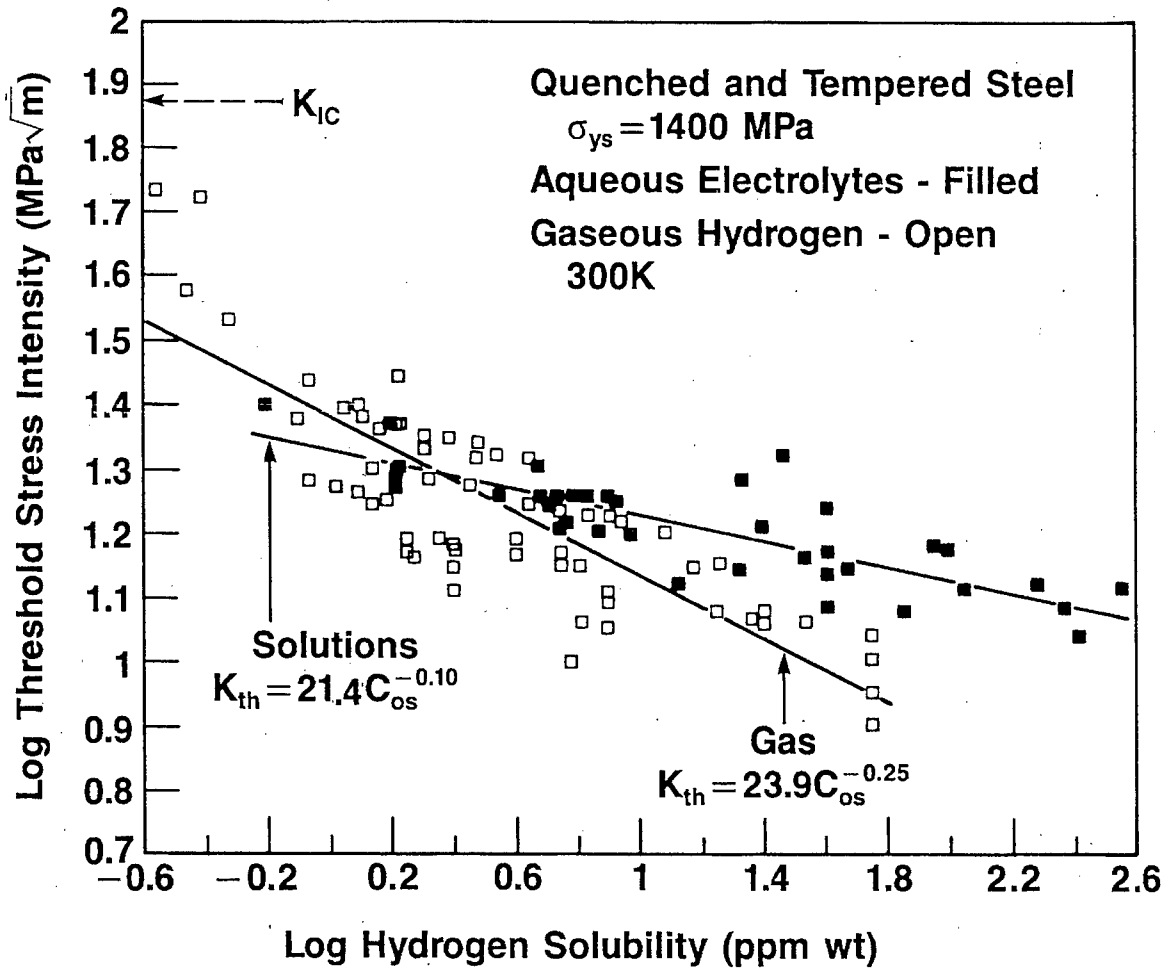
Figure 27. The correlation between crack tip H concentration and the threshold stress intensity for HEAC in tempered martensitic steels of the 4340 type (σ_{YS} = 1400 ± 100 MPa) stressed in various gaseous and electrolytic environments at 23°C. (Gangloff, 1986)

$$K_{IHEAC} \; (MPa \sqrt{m}) = 23.9 \; (C_{H\text{-}DIFF})^{-0.25} \quad (ppm) \qquad\qquad (4)$$

with a regression coefficient of 0.84 and 95% confidence interval estimate of the slope as

0.246 ± 0.040. The filled data points represent a similar analysis performed on data for

cracking of this steel class in various electrolytes. For reference, *log H solubility* of 0.2 ppm

($C_{H\text{-}DIFF}$ = 1.6 ppm) corresponds to neutral 3.5% NaCl solution at the free corrosion potential

and *log H solubility* of 2.2 ($C_{H\text{-}DIFF}$ = 160 ppm) corresponds to acidified NaCl solution

saturated with H_2S gas. The data for HEAC in these electrolytes (□) are well fit by:

$$K_{IHEAC} \; (MPa \sqrt{m}) = 21.4 \; (C_{H\text{-}DIFF})^{-0.10} \quad (ppm) \qquad\qquad (5)$$

with a regression coefficient of 0.83 and 95% confidence interval estimate of the slope as

0.100 ± 0.023. Statistically equivalent trend lines at the 95% confidence level do not fit the

populations of K_{IHEAC} data for H_2 and the electrolytes. Bulk pH, electrode potential, and

solution composition are easily matched for permeation and cracking experiments.

However, consistent with the statistically distinct trends in Fig. 27, crack solution pH and

near tip electrode potential differ from bulk conditions and govern H uptake near the crack

tip to predominantly drive cracking in high strength metals.

Effect of Applied Electrode Potential: The effect of applied electrode potential on

HEAC in high strength alloys is important from engineering and mechanistic perspectives.

Considering steel, the general view is that K_{IHEAC} is reduced with increasing cathodic

polarization, as illustrated for 17-4 PH stainless steel (Fig. 9) in chloride solution and

coupled with Mg or Zn, or polarized potentiostatically (Fujii, 1976). Increasing anodic

polarization also exacerbates HEAC in high strength steels; that is, cracking resistance can

be highest in the vicinity of the free corrosion potential, and decrease with both anodic and

cathodic polarization (Brown, 1971, 1977; Sandoz, 1977; Dautovich and Floreen, 1977;

Tyler et al., 1991; Buckley, et al., 1993; Lee et al., 2000). An example is provided by the

data in Fig. 28 for AerMet®100 where H cracking is transgranular. A similar maximum in

IG cracking susceptibility near the free corrosion potential was reported for 18Ni Maraging

steel in neutral NaCl solution (Dautovich and Floreen, 1977). The K_{IH} for the AISI 4340

steel in Fig. 28 is low and independent of cathodic or anodic polarization. A similar nil to

mild maximum in HEAC susceptibility, just anodic of the free corrosion potential, was

reported for five strengths of AISI 4340 steel ($1250 < \sigma_{YS} < 2200$ MPa) in NaCl solution

(Sandoz, 1977).

Anodic polarization exacerbates environmental cracking in 7000-series aluminum alloys

exposed to chloride solution. The da/dt increases with increasing anodic polarization at

levels above the free corrosion range and until a plateau crack growth rate is achieved near

the bold-surface pitting potential (Speidel and Hyatt, 1972; Speidel, 1975; Holroyd, 1990).

(Bold in this usage refers to a surface that is exposed to a bulk electrolyte and not occluded

compared to a crack or crevice). This electrode potential dependence is confirmed for a

modern alloy, AA7050, as shown in Fig. 29 building on the data in Fig. 13 (Young, 1999).

The rate of subcritical cracking in the susceptible peak aged microstructure increases with

increasing applied electrode potential. Notably, the cracking resistant overaged temper does

not exhibit subcritical HEAC over a wide range of applied potential. Results in Fig. 29 were

developed for steady-state cracking conditions; however, substantial and potential dependent
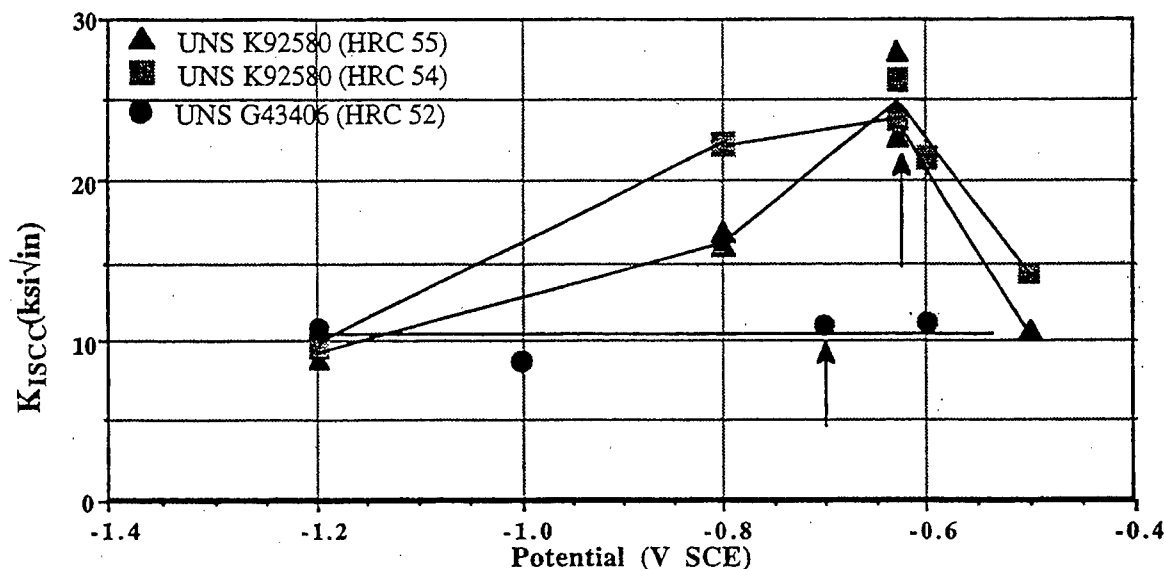
Figure 28.   The applied electrode potential dependence of the threshold stress intensity for HEAC in two ultra-high strength steels, AerMet[®]100 (UNS K92580) and ESR 4340 (UNS G43406), each stressed in neutral chloride solution under slow-rising CMOD at 23°C. The free corrosion potential for each steel is between −600 and −700 mV$_{SCE}$, as shown by the vertical arrows, and K$_{IC}$ is about 130 MPa√m for AerMet[®]100 and 80 MPa√m for ESR 4340 steel.   (Buckley et al., 1993: Publication permission requested from US Army Research Laboratory.)
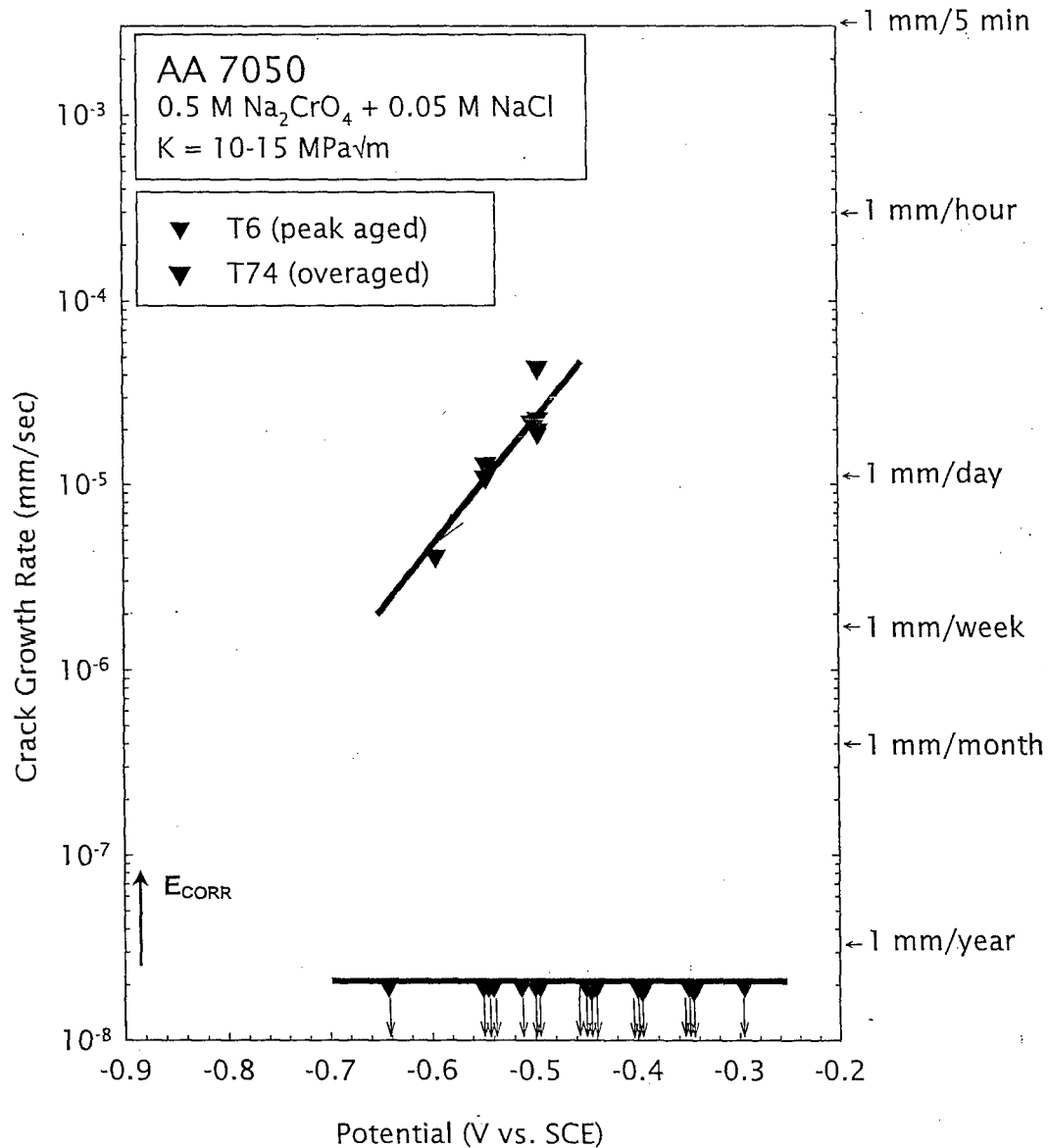
Figure 29. The effect of applied electrode potential on the steady state subcritical crack growth rate for two tempers of AA7050 stressed at fixed CMOD (20 > K > 10 MPa√m) in acidified chloride-chromate solution. The free corrosion potential was between –935 and –890 mV$_{SCE}$ during 48 h immersion in quiescent solution and the pitting potential was -230 mV$_{SCE}$. The vertical arrows indicate that environment-assisted crack growth was not observed after a 20 day exposure and hence da/dt is less than the resolution limit of the compliance-based crack length measurement system. The peak aged microstructure was tempered at 118°C for 20 h plus 154°C for 12 h. The overaged condition was produced for the same solution treatment condition, but with aging at 163°C for 27 h. The crack orientation was SL. (Young, 1999)

incubation occurred prior to this steady-state (Young, 1999). For example, the precrack was stagnant for up to several days of stressed exposure, prior to acceleration to the growth rates shown. This incubation was attributed to time-dependent crack chemistry development and was minimized by anodic polarization to affect high da/dt, followed by reduced potential to develop the data in Fig. 29.

The applied electrode potential dependence of environmental cracking in high strength Ni and β-Ti alloys introduces a new behavior; HEAC mitigation by polarization away from free corrosion. For the superalloy represented in Fig. 11, IN718 stressed in two acidic solutions, cathodic polarization from the free corrosion range reduced the threshold stress intensity for subcritical cracking for acidic solution conditions (Lillard et al., 1997; Lillard, 1998), analogous to the behavior of high strength steels in Fig. 28. However, there is the suggestion in Fig. 12 that highly cathodic polarization improves resistance to environmental cracking. The effect of anodic polarization has not been reported for this class of superalloys. The data for β/α-Ti alloys stressed in near-neutral NaCl solution, Fig. 30, amplifies the occurrence of a strong cathodic inhibition of environmental cracking and show that the threshold stress intensity also rises toward K_{IC} with increasing anodic potential.

These complex electrode potential dependencies shown in Figs. 11 and 28-30 are explained within the HEAC framework of Fig. 2 by considerations of crack tip H production and uptake resulting from local-occluded chemistry and crack tip potential changes upon bold surface polarization, as discussed in 6.03.7.1.2.
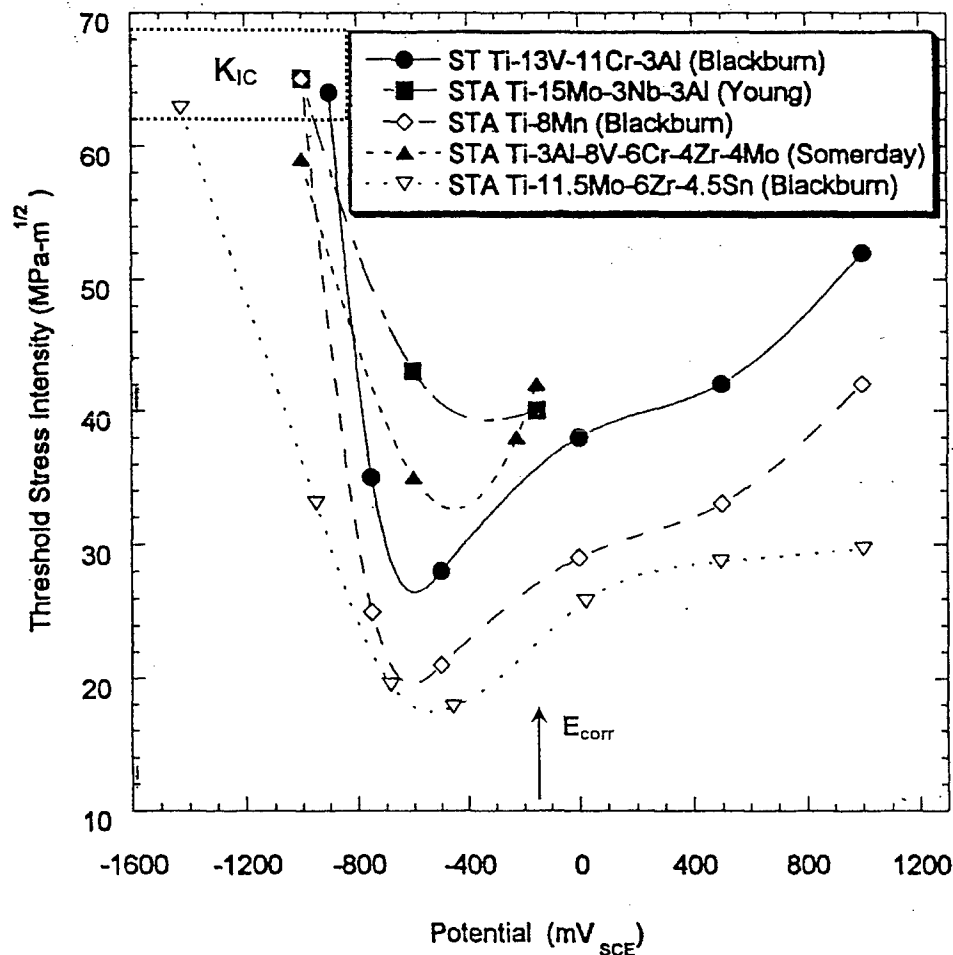
Figure 30.   The applied electrode potential dependence of the threshold stress intensity for HEAC in five α-precipitation hardened β-Ti alloys, each stressed in chloride solution under slow-rising CMOD at 23°C.   The free corrosion potential for this class of alloys and neutral chloride solution is −100 to −200 mV$_{SCE}$. The H-free plane strain fracture toughness for this strength level of β/α-Ti alloy is 60-75 MPa√m.   (Blackburn et al., 1972; Grandle et al., 1994; Young et al., 1995; as presented in Kolman and Scully, 1997: Reprinted with permission from Elsevier.)

6.03.6.3.3 Temperature

The severity of both IHAC and HEAC in high strength alloys is maximized at a temperature within $\pm$ 150°C of ambient. The precise relationship depends on H content, alloy strength, and environment chemistry. The temperature dependence of cracking is understood qualitatively by the temperature dependencies of the elemental processes shown in Fig. 2 and modeled quantitatively in 6.03.8.

6.03.6.3.3.1 Internal Hydrogen Assisted Cracking

Temperature affects both the threshold and kinetics for IHAC in high strength alloys, due to the temperature dependencies of H trapping and diffusion. The results presented in Fig. 31 show that K_{IHAC} is a minimum and da/dt is maximized near 25°C for H precharged IN903 (Moody et al., 2001). A similar trend is illustrated in Fig. 32 for Stage II da/dt measured for ultra-high strength AISI 4340 steel containing 3 ppm of predissolved H (Gerberich et al., 1988). In this case, da/dt is maximized at 50-100°C. For both alloys at temperatures below the maximum, da/dt depends on 1/T according to an Arrhenius relationship with activation energies of 69 kJ/mol and 27 kJ/mole for the superalloy and martensitic steel, respectively. For temperatures above the maximum, da/dt declines sharply for the steel and somewhat less so for the Fe-based austenitic superalloy. The loss of H from the fracture mechanics specimen, and specifically the fracture process zone, must be considered when selecting data for structural integrity modeling and mechanistic interpretation (Thomas, et al., 2003). Since the diffusivity of H in high strength alloys is low ($< 10^{-7}$ cm^2/s) below 200°C (Gangloff, 2003), this problem is often not limiting.
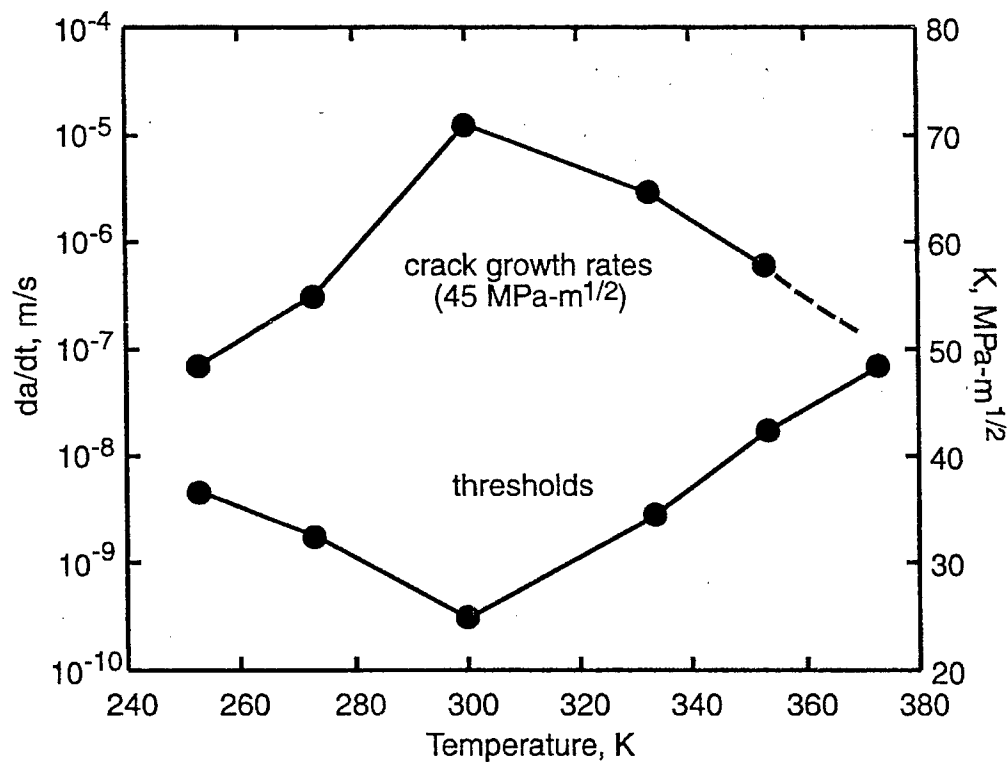
Figure 31. The temperature dependence of the threshold stress intensity and subcritical crack growth rate for IHAC in precipitation hardened IN903 (σ_{YS} = 1080 MPa and K_{IC} = 90 MPa$\sqrt{m}$), H-precharged ($C_{H\text{-}TOT}$ = 2900 ppm), and tested at fixed CMOD in moist air. (Moody, Robinson and Garrison, 1990: Reprinted with permission from Elsevier.)

INTERNAL HYDROGEN, 4340 STEEL

$H_b = 27 \ kJ/mol$
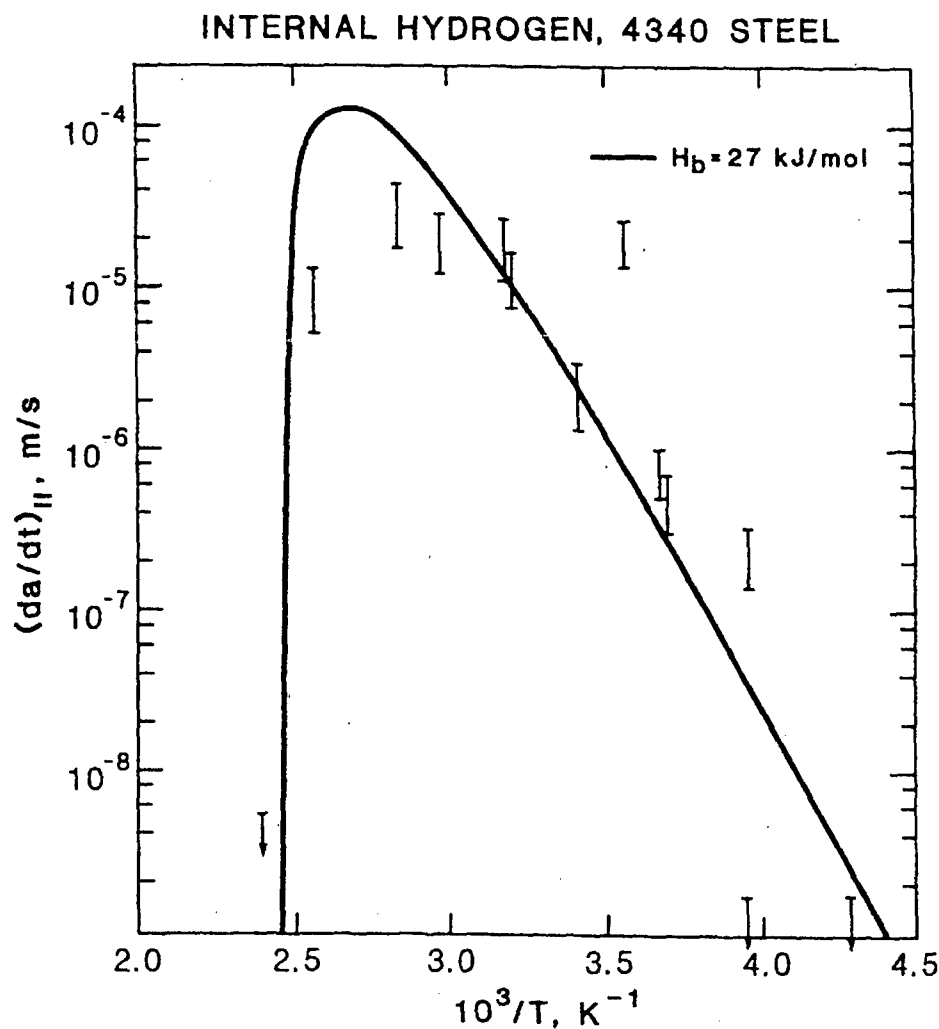
Figure 32. The temperature dependence of the Stage II K-independent subcritical crack growth rate for IHAC in tempered martensitic 4340 steel (σ_{YS} = 1660 MPa), H-precharged ($C_{H\text{-}TOT}$ = 3 ppm or more) and tested at fixed load in moist air. The bars represent experimental measurements and the solid line is the model prediction using a H-trap binding energy of H_b = E_B = 27 kJ/mol. (Gerberich et al., 1988: Reprinted with permission from Elsevier.)

Fracture mechanics based data have not been reported to define the temperature dependencies of K_{IIHAC} and da/dt for IHAC of high strength β-Ti and 7000 series aluminum alloys.

6.03.6.3.3.2   Hydrogen Environment Assisted Cracking

Temperature affects both the threshold and kinetics for HEAC in high strength alloys, with the effect complicated by the temperature dependencies of crack-environment chemistry, H production, and H uptake; as well as H trapping and diffusion (Fig. 2).

Threshold Stress Intensity: The threshold stress intensity for HEAC increases monotonically with rising temperature, as illustrated by the data in Fig. 33 for several high strength steels stressed during exposure in pure H_2 (Moody et al., 1990 as first reported by Gangloff and Wei, 1977; Nelson and Williams, 1977; Clark, 1979). This is consistent with the results for IHAC in Fig. 31. Low temperature threshold behavior must be considered with caution since slower reaction and mass transport kinetics could prolong the testing time required to achieve a true near-equilibrium condition. In this regard, the rise in K_{IIHAC} in Fig. 31, and the suggestion of such an increase for the 18Ni (200) Maraging steel in Fig. 33 may reflect artificially high threshold values from insufficient duration experiments. The intrinsic threshold for IHAC and HEAC may be temperature independent or fall mildly with decreasing temperature in the low-T regime.

Subcritical Crack Growth Rate: Substantial data describe the temperature dependence of the Stage II da/dt for HEAC in high strength alloys. The specific behavior is different for pure H_2 compared to water vapor environments, particularly in the high temperature regime.
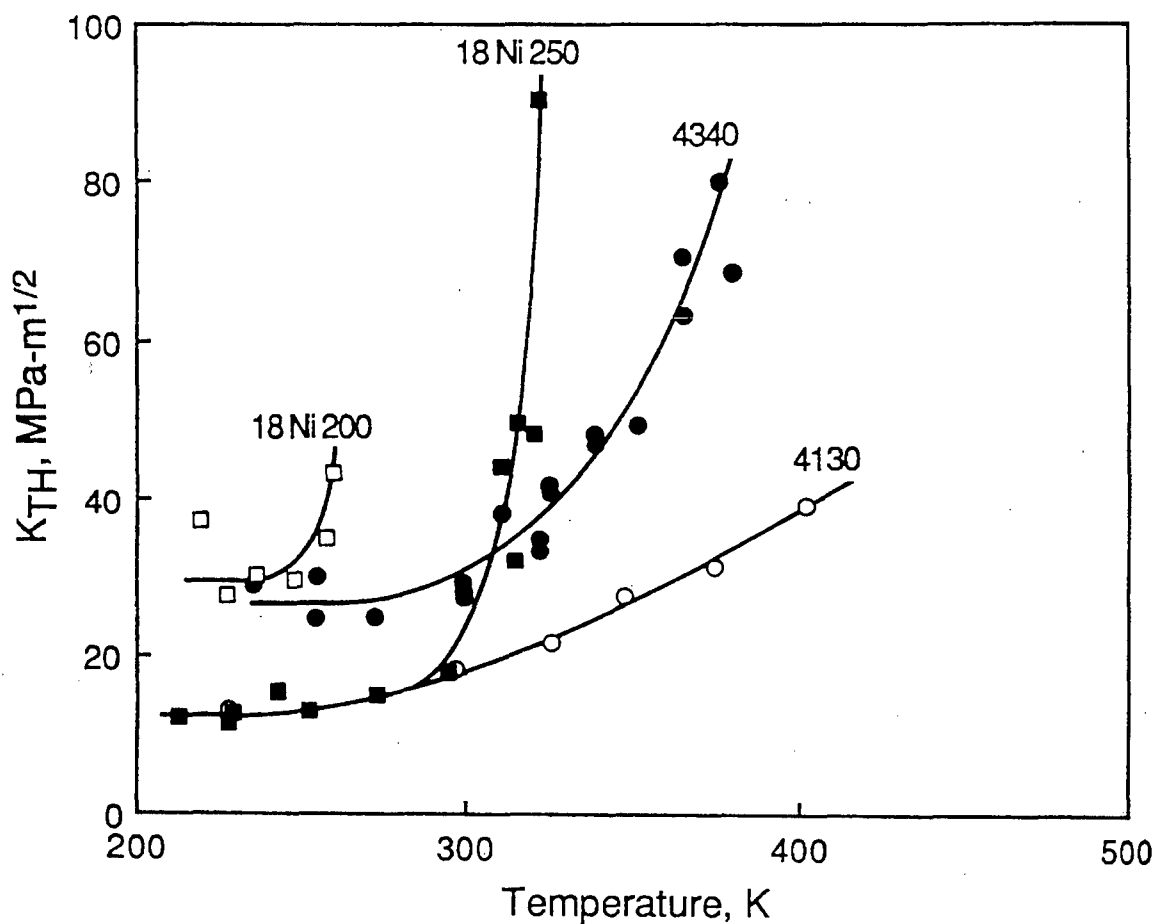
Figure 33. The temperature dependence of the threshold stress intensity for HEAC in several high and ultra-high strength martensitic steels tested in purified H_2 at either constant or rising load (Moody et al., 1990). Tensile yield strength levels are: 18 Ni (200) = 1270 MPa and 18 Ni (250) = 1650 MPa (Gangloff and Wei, 1977); 4340 = 1235 MPa (Clark, 1979); 4130 = 1330 MPa (Nelson and Williams, 1977. (Reprinted with permission from Elsevier.)

HEAC in the high strength steel/H_2 system parallels the temperature dependence of IHAC in such alloys, as illustrated by the data in Fig. 34 for ultra-high strength 18Ni (250) Maraging steel in pure H_2 at two pressures (Gangloff and Wei, 1977, 1978). Based on more extensive data, the maximum in da/dt_{II} occurs at about 25°C for the higher P_{H2} and 0°C for the lower pressure; in general, the temperature for maximum da/dt increases with increasing H_2 pressure and increasing steel strength (Gangloff and Wei, 1977). At lower temperatures, H cracking is thermally activated, with activation energy of 18 kJ/mole. At higher temperatures, da/dt declines precipitously by several orders of magnitude for a 1-3°C temperature increase. This growth rate decrease is reversed essentially immediately by a 1-3°C temperature reduction. The scanning electron fractographs in Fig. 34 show that HEAC is fully intergranular in the low temperature regime and transitions with increasing temperature to brittle TG cracking through the martensitic microstructure. Similar temperature dependent da/dt data were reported for AISI 4130 steel (σ_{YS} = 1344 MPa), with a low temperature activation energy of 16-17 kJ/mole for IG H cracking, but a less steep decline in da/dt in the high temperature regime and a transition from IG to transgranular microvoid-based cracking (Williams and Nelson, 1970, 1970a; Nelson and Williams, 1977). In novel experiments Nelson and coworkers showed that the maximum in da/dt was eliminated for the AISI 4130 steel in thermally dissociated H_2/H gas mixture; simple Arrhenius behavior was reported for –20°C < T < 40°C with an activation energy of 29 kJ/mol and HEAC appeared to occur for temperatures as high as 160°C (Nelson, et al., 1971). Older data suggested low temperature activation energy for IG H_2 cracking of ultra-high strength steels in the range from 9 to 12 kJ/mol (Sawicki, 1971; McIntyre et al., 1972a).

Figure 34. The temperature dependence of the Stage II subcritical crack growth rate for HEAC in ultra-high strength 18Ni (250) Maraging steel (σ_{YS} = 1650 MPa), stressed at fixed load in highly purified H_2. (Gangloff and Wei, 1977, 1978)

Chen and Gerberich reported thermally activated Stage II cracking in Fe-Si single crystals in 100 kPa H_2, with a low temperature activation energy of 25 kJ/mol, a maximum in crack growth rate at about 125°C, and a 100-fold decrease in da/dt between 105°C and 160°C (Chen and Gerberich, 1991). This result is notable since HEAC was by transgranular cleavage along {100} planes in the Fe-Si single crystal at all temperatures.

The composition of the environment affects the temperature dependence of HEAC. This result is illustrated by the data collected in Fig. 35 for tempered martensitic AISI 4340 steel (σ_{YS} = 1345 MPa) stressed during exposure in several environments (Wei, 1981; Wei and Gao, 1985). The temperature dependence of this steel in 133 kPa pure H_2 parallels the behavior of AISI 4340 and the 18 Ni maraging steels, particularly in terms of a low temperature activation energy of 15 kJ/mol and maximum da/dt at 80°C. Different behavior is noted for H_2S, where the low temperature activation energy is lower, equaling either 5 kJ/mol or 0 kJ/mol for higher and lower H_2S pressures, respectively. In these two cases, da/dt$_{II}$ appears to decline with increasing temperatures above 25°C. A similar result of nearly temperature independent da/dt$_{II}$ was reported for AISI 4130 steel in low pressure (0.2 kPa) H_2S (–40°C < T < 50°C) (Nelson, 1983), with a higher activation energy of 8 kJ/mol reported for the steel of Fig. 4 in 13 kPa H_2S (-75°C < T < 130°C) (McIntyre et al., 1972a).

The temperature dependence of HEAC in high strength 4130 and 4340 steels in pure-liquid water is unique. As shown in Fig. 35, da/dt$_{II}$ increases monotonically with increasing T up to 80°C for AISI 4340 steel, with higher activation energy of 34 kJ/mol. The identical result was reported for lower strength AISI 4130 steel, with a monotonic da/dt increase for 0°C < T < 90°C and activation energy of 80 kJ/mol (Nelson, 1983). The da/dt for 4130

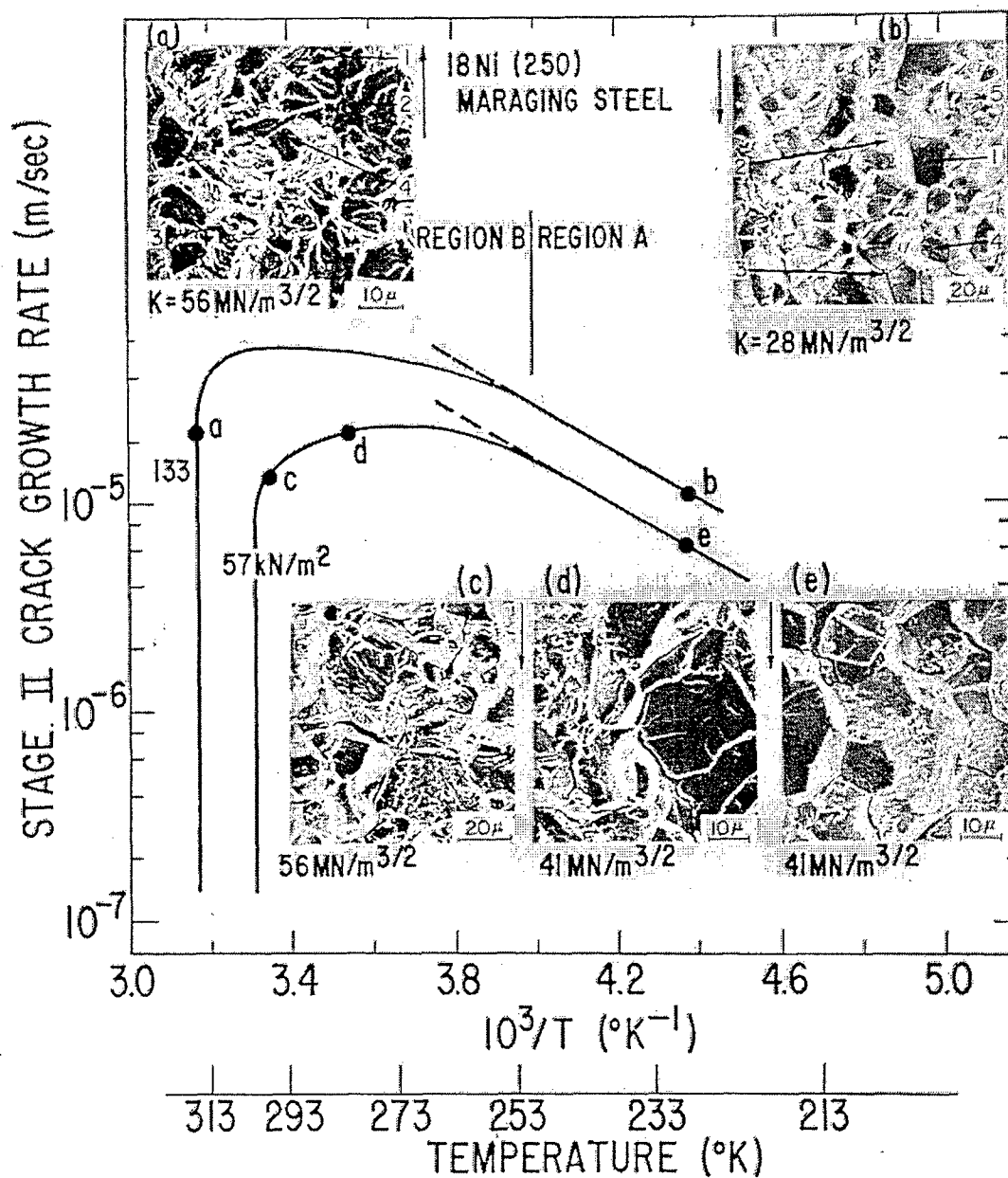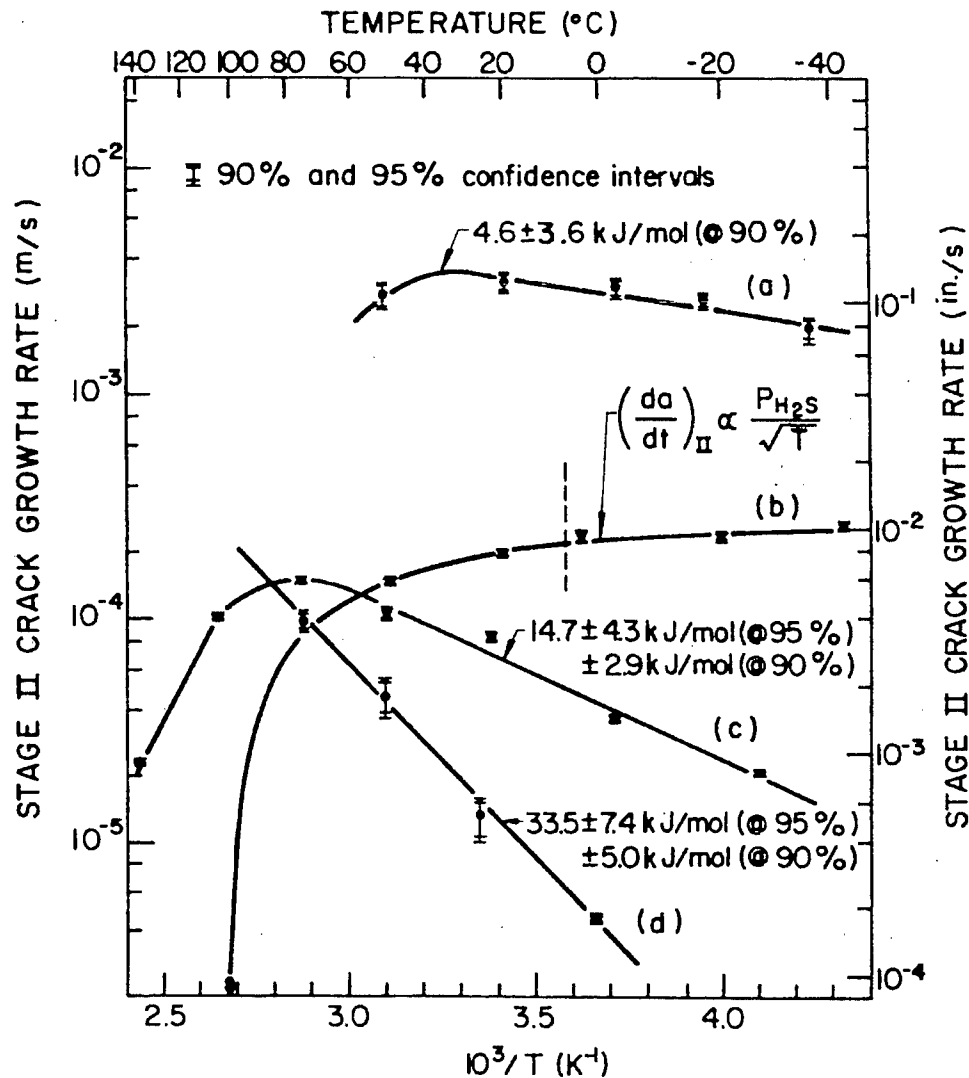**Figure 35.** The temperature dependence of the Stage II subcritical crack growth rate for HEAC in high strength 4340 steel (σ_{YS} = 1345 MPa), stressed at fixed load in several highly purified environments. (a) 2.7 kPa H_2S, (b) 0.13 kPa H_2S, (c) 133 kPa H_2, and (d) liquid water. (Wei, 1981; Wei and Gao, 1985: Copyright The Minerals, Metals and Materials Society, reprinted with permission.)

began to decline, below the Arrhenius line, suggesting a maximum growth rate at 70-80°C

or higher, but the high temperature regime was not well characterized. Older data for other

martensitic steels in distilled water are consistent with the lower activation energy of 30-40

kJ/mol for 0°C < T < 100°C (Johnson and Willner, 1965; Van der Sluys, 1969; Speidel,

1974). McIntyre and coworkers reported that the temperature dependence of HEAC in the

steel of Fig. 4, stressed in aqueous NaCl solution, was defined by a single Arrhenius

relationship with an activation energy of 36 kJ/mol (McIntyre et al., 1972a).

While data are limited, precipitation hardened Ni-based superalloys and 7000 series

aluminum alloys exhibit temperature dependent crack growth rates that parallel the behavior

of high strength steels. The temperature dependence of the subcritical crack growth rate in

Ni-based alloy X-750 (σ_{YS} = 800 to 1000 MPa, depending on precise heat treatment)

stressed in pure water is shown in Fig. 36; da/dt$_{II}$ for H cracking is a maximum at 100-

125°C and eliminated at 150°C (Mills et al., 1999; Hall and Symons, 2001). Crack growth

at lower temperatures obeys an Arrhenius relationship with activation energy of 40-48

kJ/mol from straight line approximation to the log da/dt *vs.* 1/T data. Speidel reported

simple Arrhenius behavior for lower strength Nimonic 105 (σ_{YS} = 825 MPa) for 0°C < T <

100°C (Speidel, 1974). The very high temperature crack growth behavior in Fig. 36 (Shen

and Shewmon, 1991), labeled *Creep Limited*, is not considered, as it is outside the scope of

this chapter on H cracking of high strength alloys within ±150°C of ambient.

Arrhenius behavior described the temperature dependence of da/dt$_{II}$ for 7000 series

aluminum alloys in moist environments generally below 100°C, without evidence of reduced

crack growth rate at higher temperatures. Specific activation energies are 40 kJ/mole for
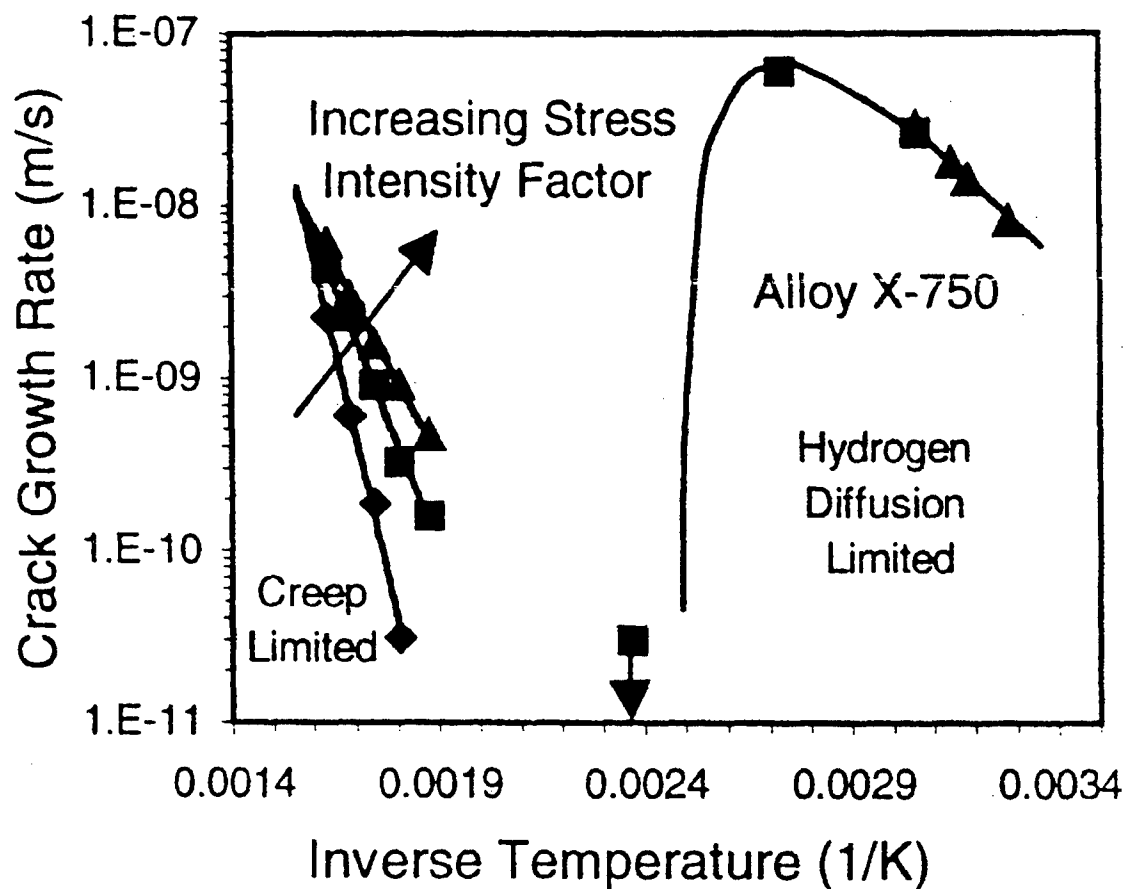
Figure 36. The temperature dependence of the Stage II K-independent subcritical crack growth rate for HEAC in precipitation hardened superalloy X-750 (σ_{YS} = 800 to 1000 MPa) stressed in high purity pressurized water. Only the low temperature regime, between 30 and 150°C, is relevant to the present review of H cracking in high strength alloys. (Hall and Symons, 2001; using low temperature data ($\square$) by Mills et al., 1999; low temperature data ($\square$) by Symons; and high temperature data ($\square$, $\square$, $\square$) at several K levels (15, 32, and 61 MPa$\sqrt{m}$) by Shen and Shewmon, 1991.) (Copyright The Minerals, Metals and Materials Society, reprinted with permission.)

AA 7039-T6 in distilled water (0°C < T < 100°C) (Speidel, 1974), 60 kJ/mol for AA7022-T6 in high purity water (0°C < T < 140°C) (Vogt and Speidel, 1998), 85 kJ/mol for AA7039-T6 in aqueous KI electrolyte (20°C < T < 110°C) (Speidel and Hyatt, 1972), and 82 kJ/mol for AA7050-T6 in water vapor (25°C < T < 90°C) (Young and Scully, 2002). The study by Vogt and Speidel is unique in suggesting a maximum da/dt_{II} in this 7000 series aluminum alloy at about 30°C, with subsequent sharp decline in da/dt, followed by a 2nd rise, as shown in Fig. 37. The mechanistic explanation for the low temperature trend and da/dt_{II} maximum followed by further increase in crack growth rate at very high temperatures approaching the aging temperature is summarized in 6.03.8.4.2. In work by Young and Scully summarized in Fig. 19, the activation energy increased from 66 to 98 kJ/mol as AA7050 was aged from under to overaged conditions, consistent with an earlier result by Lee and coworkers (Lee et al., 1991; Young and Scully, 2002). The activation energy for Cu-free AA7050 was 59 kJ/mol for peak and overaged microstructures.

The activation energy computed by curve fitting a simple Arrhenius relationship to log da/dt *vs*. 1/T data is useful for engineering algorithms that describe temperature dependent cracking in structural integrity modeling. Fundamental mechanistic interpretation is; however, complicated because each of the fast and slow steps in the HEAC scenario shown in Fig. 2 is temperature dependent. A mechanism-based model for da/dt is required to explain an observed temperature dependence by establishing the precise combination of elemental-process activation energies that constitute the overall activation energy computed from crack growth rate measurements. Modeling in this regard is presented in 6.03.8.4.
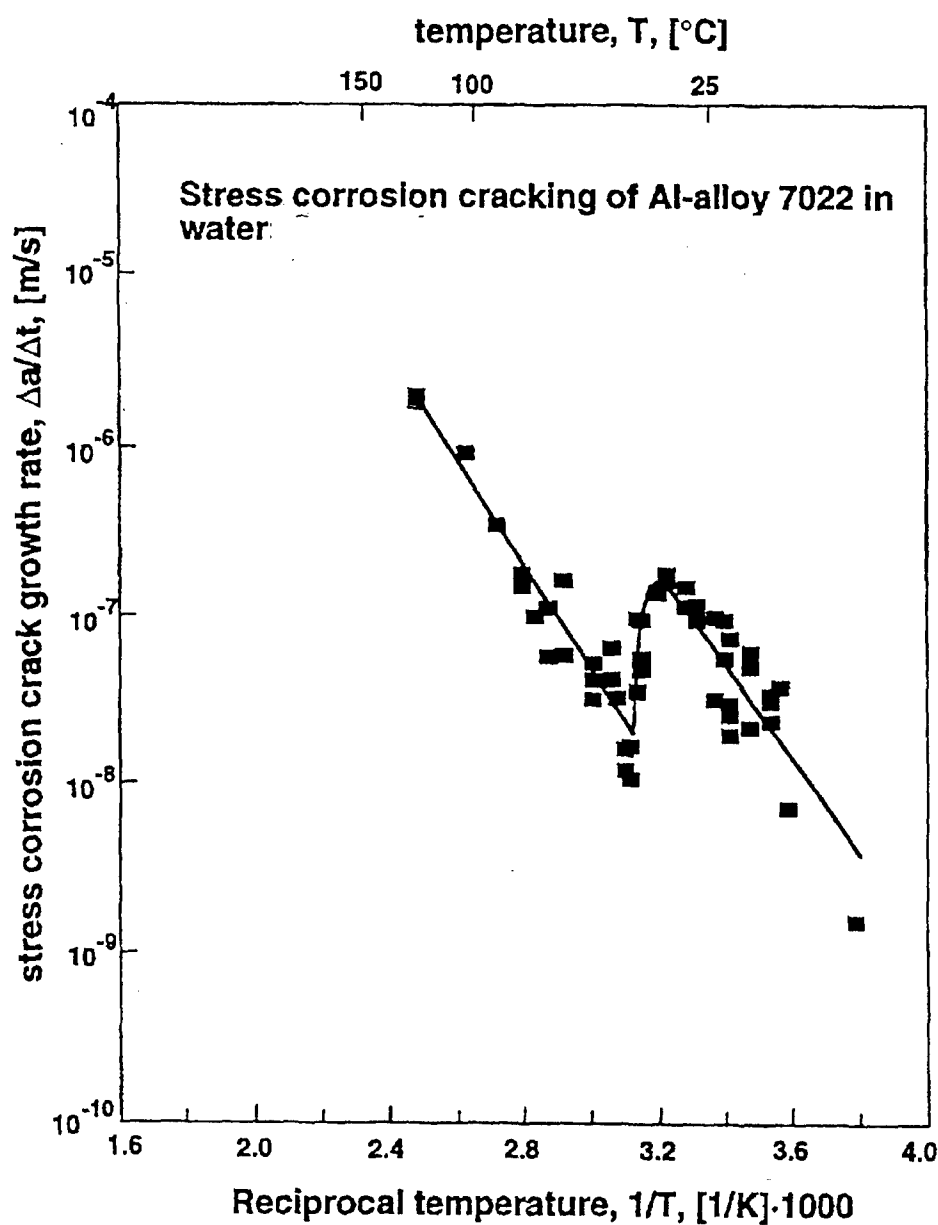
Figure 37. The temperature dependence of the Stage II crack growth rate in peak aged AA7022 (σ_{YS} = 495 MPa) stressed in high purity water. The solid line represents a crack growth rate prediction by the surface mobility model of Galvele, modified to include the effect of H from environmental reaction at the crack tip (6.03.8.4.2). (Vogt and Speidel, 1998: Publication permission requested from Elsevier Science.)

6.03.7 MECHANISTIC BASIS FOR HYDROGEN ASSISTED CRACK GROWTH

Mechanistic understanding of H cracking is essential to develop micromechanical-chemical models that predict threshold and growth rate properties for use in structural integrity modeling. Two mechanistic issues have dominated scientific discussions over the past several decades: (1) *Does the HEAC mechanism explain stress corrosion crack growth in high strength alloys in moist environments?* and (2) *What is the basic mechanism by which hydrogen causes crack tip damage leading to subcritical crack growth?*

6.03.7.1 Role of Hydrogen Assisted Damage in Stress Corrosion Cracking

Controversy has centered on the ability of the HEAC mechanism (Fig. 2) to explain subcritical crack growth in alloys stressed in environments that support concurrent crack tip dissolution, passive film formation, and atomic hydrogen production. A strong consensus has emerged that H provides the dominant damage mechanism for most high strength alloys stressed in moist environments.

6.03.7.1.1 Example of Experimental Support for HEAC: *7000-series Al Alloys*

Most reviews have concluded that hydrogen causes significant intergranular cracking in 7000-series aluminum alloys stressed in chloride solutions and moist gases (see Figs. 12 and 13) (Speidel and Hyatt, 1972; Gest and Troiano, 1974; Speidel, 1974, 1975; Thompson and Bernstein, 1980; Gruhl, 1984; Nguyen, 1987; Pickens et al., 1987; Burleigh, 1991; Lee et al., 1991;). However, supporting evidence is circumstantial (Holroyd, 1990). The nature of this experimental support is typical of that advanced to identify the HEAC mechanism for

stress corrosion cracking of other high strength alloy systems based on Fe, Ni and Ti.

The 7000 series aluminum alloys that are not susceptible to HEAC in dry gases including H_2 (Speidel and Hyatt, 1972; Speidel, 1974) do crack in H_2 that is ionized to produce atomic H, as well as in water vapor at pressures that are sufficiently low to preclude condensation and electrochemical reaction at the crack tip, but not H production through oxidation (Speidel, 1974; Koch, 1979; Wei and Gangloff, 1989). Similar IG fracture surface features were observed for cracking in atomic H and aqueous environments (Koch, 1979). The 7000-series alloys are susceptible to IG IHAC, similar to cracking in the external environment, and this IHAC is reversible when the H is removed by thermal treatment (Gest and Troiano, 1974; Montgrain and Swan, 1974; Scamans et al., 1976; Albrecht et al., 1979, 1982; Holroyd and Hardie, 1981; Tuck, 1985). Subcritical IG cracking was produced by H that was charged electrochemically during stressing, but on surfaces removed from the crack tip to separate H damage from dissolution and film formation (Ratke and Gruhl, 1980).

Environmental cracking in AA7075 in NaCl is substantial in Mode I, but greatly reduced for Mode III loading (Swanson, et al., 1981; Pickens et al., 1983), consistent with the dominant role of hydrostatic stress in HEAC (see 6.03.8.1 and 6.03.9.1.4). Atomic Mg and Zn segregate to grain boundaries in 7000 series alloys and there contribute, with H from environmental reaction, to decohesion analogous to temper embrittled steels (Pickens et al., 1983; Schmiedel and Gruhl, 1983). Subcritical crack growth in AA7075 stressed during exposure in a chloride environment was discontinuous, as evidenced by acoustic emission measurements and fracture surface crack arrest markings, consistent with repeated H accumulation within the crack tip FPZ as opposed to continuous crack advance by a

dissolution-based mechanism (Scamans, 1980; Martin et al., 1985). Discontinuous crack advance can be explained reasonably by mechanisms for environmental cracking that do not involved H (Parkins, 1990).

6.03.7.1.2   Crack Chemistry Advances

Stemming from the seminal work of Brown and coworkers (Sandoz et al., 1970; Smith et al., 1970; Brown, 1977), modern considerations of occluded crack electrochemistry more firmly establish the contributing roles of H production, dissolution and passive film formation in environment-assisted cracking (Gangloff, 1984; Turnbull, 1984; Turnbull and Ferriss, 1987). This recent work supports the HEAC mechanism as governing subcritical crack growth in high strength alloys. A critical accomplishment was a demonstration that the effects of various environmental variables on K_{TH} and da/dt (6.03.6.3.2) are described by the amount of atomic hydrogen produced locally at the straining crack tip.

6.03.7.1.2.1   Superalloys

Subcritical environment-assisted cracking in high strength superalloys is described by HEAC for gases and electrolytes, and using occluded-crack chemistry analysis for the latter situation. In separate studies the threshold for IN718 was measured to decrease with increasing P_{H2} (Moody et al., 1986; Moody et al., 1988) or decreasing electrolyte pH (Lillard, 1998), with regression analyses giving:

$$K_{IHEAC} \ (MPa \ \sqrt{m}) = 110 \ P_{H2}^{-0.25} \quad (MPa)$$

$$K_{IH} \ (MPa \ \sqrt{m}) = 46.8 \ exp(0.311 \ pH) \tag{6}$$

The microscopic cracking modes were similar for each environment and involved a mixture of IG and TG slip-plane based cracking. Figure 38 shows that these thresholds are defined by a single function of the crack tip H concentration for IN718 stressed in aqueous-acidified chloride solution (•) as well as high pressure H_2 (o) (Lillard, 1998). The K_{TH} declines with increasing crack tip H concentration, above 20 ppm and independent of the crack tip environment that produced this H. The specific regression result for these data in Fig. 38 is:

$$K_{IHEAC} \ (MPa\sqrt{m}) = 345 \ (C_{H\text{-}TOT})^{-0.53} \quad (ppm) \tag{7}$$

This single correlation for gas and aqueous environment-assisted cracking supports the HEAC mechanism.

For the H_2 results in Fig. 38, the H content of the FPZ, in equilibrium with P_{H2} that is everywhere equal, was estimated using lattice-H solubility from Sievert's law, extrapolated from elevated temperature and increased to account for trapping using results for a similar superalloy microstructure (Moody et al., 1989). For IN718 in acid, the H concentration at the crack tip was estimated considering crack chemistry change. First, crack tip pH was estimated vs. bulk solution pH. The cathodic current density at this crack tip pH was determined experimentally from current density vs. applied potential data for IN718 exposed boldly in acid at several pH levels. Local H content was related to cathodic current density by hot extraction measurements of boldly preexposed specimens. With these estimates of $C_{H\text{-}TOT}$ in Fig. 38, the resulting correlation with K_{IHEAC} is identical for the acid and gas environments. This correlation is based on two assumptions. Since the strengths of these two lots of IN 718 were equal, the H contents in Fig. 38 were not increased to reflect crack
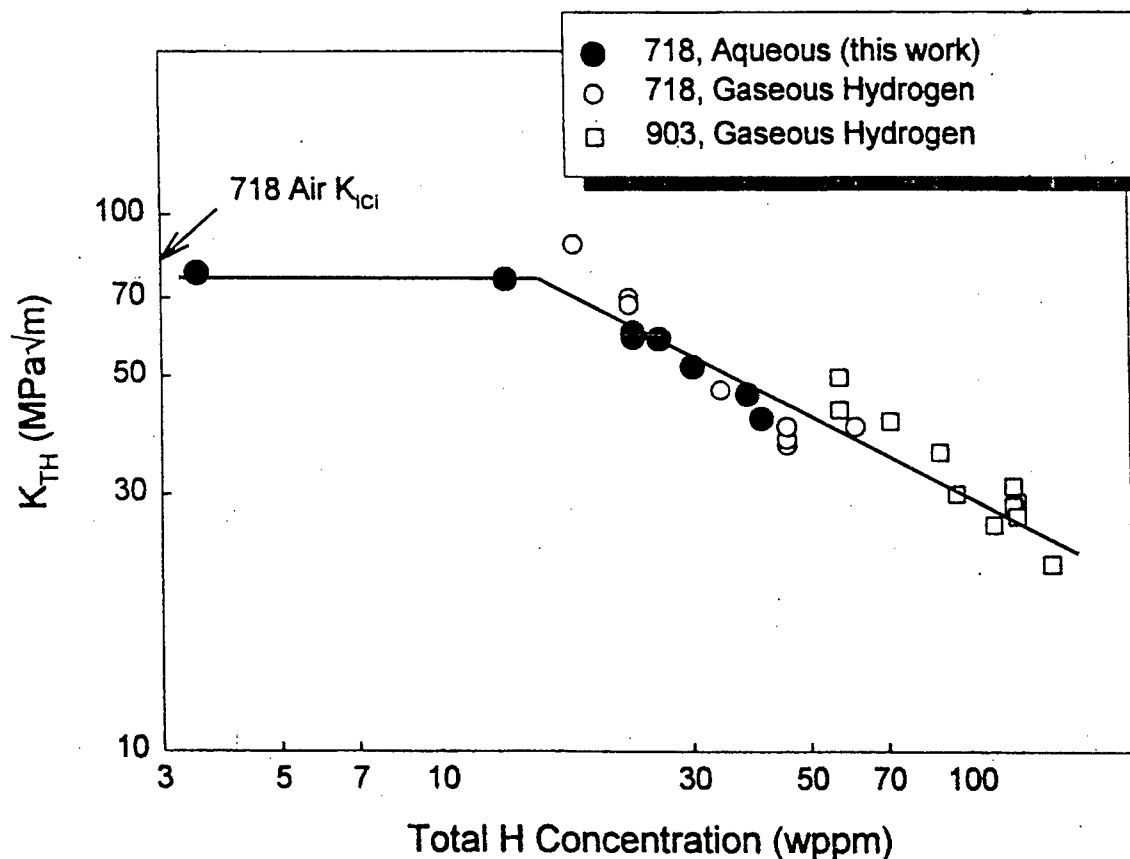
Figure 38. Threshold stress intensity for HEAC in peak aged IN718 and IN903, stressed in either high pressure H_2 (9, O), or acidified chloride solution with cathodic polarization at -1.0 V_{SCE} (•), *vs.* calculated H content produced at the crack tip. H-free superalloys cracked by microvoid processes at high K_{IC}, while HEAC in each environment produced a mixture of intergranular and transgranular slip-plane based cracking. IG cracking dominated at K_{TH} below about 50 MPa$\sqrt{m}$. (Lillard, 1998; Moody et al., 1986; Moody et al., 1988)

tip hydrostatic stress enhancement. The electrode potential gradient along the crack tip was judged to be sufficiently small so as not to affect crack tip H uptake.

6.03.7.1.2.2   Electrode Potential Dependence

Crack electrochemistry studies establish that the electrode potential dependence of environmental cracking in high strength metallic alloys is explained within the HEAC scenario. Applied potential affects both crack pH and tip electrode potential. The key parameter is the overpotential (η_H) that governs H production, equaling the difference between the pH dependent reversible potential for H production (E_H°) and crack tip potential. For fixed surface film and microstructure, H content increases as η_H becomes more negative.

Steel: The deleterious effects of both anodic and cathodic polarization on subcritical crack growth thresholds for high strength steel in neutral chloride solution (Fig. 28) are explainable by crack chemistry considerations, strengthening the HEAC argument for these alloys (Smith et al., 1970; Sandoz et al., 1970; Brown, 1977). As potential is made more anodic, crack pH decreases due to increased cation dissolution and hydrolytic acidification (e.g., $Fe^{+2} + H_2O = H^+ + FeOH^+$ and $Cr^{+3} + H_2O = H^+ + CrOH^{+2}$) and E_H° becomes more noble. Crack IR tends to depress the crack tip potential to values more negative than those applied to the external surface, near or above the free corrosion potential. The result of these two contributions from anodic polarization is that η_H becomes more negative and H concentration is intensified at the crack tip; K_{TH} decreases.

Increasing cathodic polarization promotes H uptake and lower threshold, provided that

the crack tip is polarized proportionate to the boldly exposed surface. Local polarization is required to maintain a favorable-negative overpotential for H production since E_H^o is progressively more negative as the crack pH becomes more alkaline. With this chemistry change, bold-surface H production could become the dominant supply of H to the crack tip FPZ provided there is sufficient time for H diffusion (Turnbull and deSanta Maria, 1990).

The sum of these behaviors explains the electrode potential dependence of a maximum in HEAC resistance for high strength steels (Fig. 28); however, the contributions of crack tip and bold-surface H are not defined and may vary with exposure time, specimen size and geometry, and H diffusivity. This analysis was quantified by extensive crack chemistry modeling by Turnbull and coworkers (Turnbull, 1984; Turnbull and Ferriss, 1987, 1987a; Turnbull, 2001, 2001a). Crack tip pH and electrode potential were modeled, and the amount of crack tip H was predicted. This approach is capable of predicting the effects of a wide range of environmental, crack geometry, and loading variables on crack tip H production. An example is provided by the results shown in Fig. 39, where the effect of crack depth on the threshold K_{IH} is modeled for high strength AISI 4130 steel in neutral NaCl solution and measured with short crack fracture mechanics experiments; agreement between theory and experiment is good (Gangloff and Turnbull, 1986).

7000-series Aluminum Alloys: The results in Fig.29, showing that Stage II crack growth rate increases with increasing anodic polarization for AA7050 in acidic chloride solution are consistent with HEAC. This hypothesis is confirmed directly by the data in Fig. 40, a plot of da/dt$_{II}$ for peak aged AA7050 *vs.* the concentration of H measured local to the cracking process (Young, 1999; Cooper, et al., 2000). A 1 mm-thick specimen was cut from
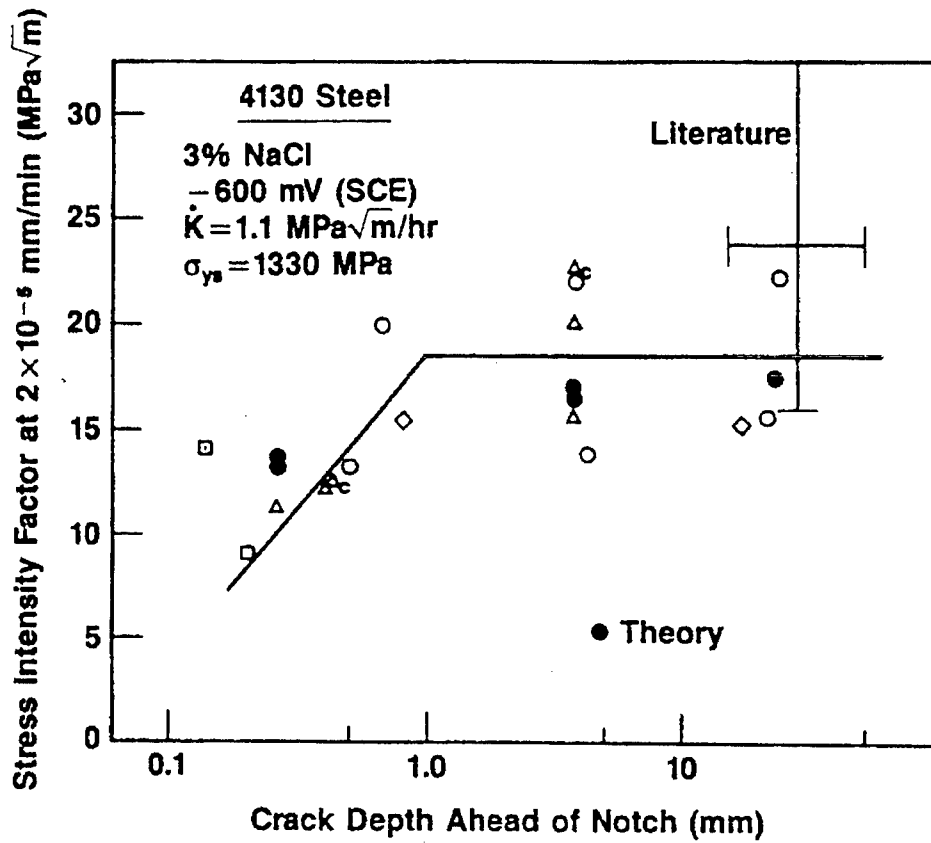
Figure 39. The model predicted (•) and measured (open symbols) crack depth dependence of the threshold stress intensity factor for subcritical crack growth in high strength AISI 4130 steel stressed under slow-rising CMOD ($dK/dt = 3 \times 10^{-4}$ MPa√m/s) in neutral NaCl solution at fixed electrode potential in the free corrosion regime.   (Gangloff and Turnbull, 1986)
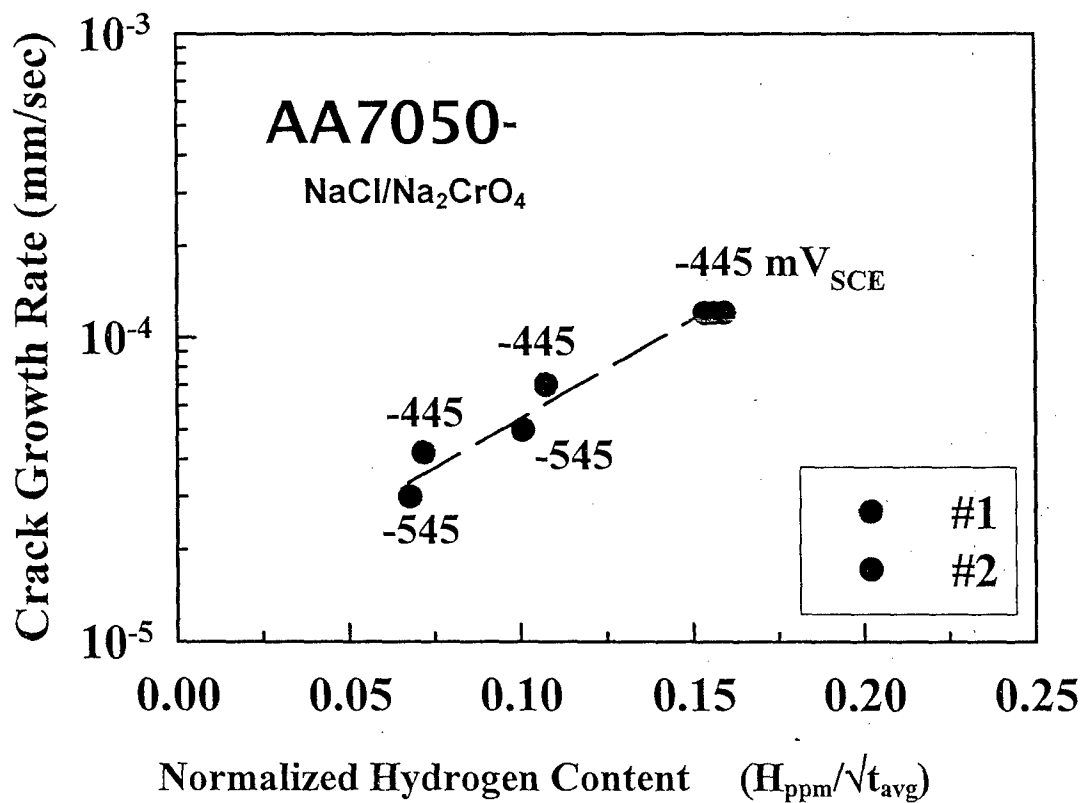
Figure 40.   The dependence of da/dt on crack wake H content measured by thermal desorption spectroscopy and normalized by the average wake exposure time for two AA7050-T651 specimens cracked in acidic chloride-chromate solution at either -445 or -545 mV$_{SCE}$, corresponding to the conditions shown in Fig. 29.   (Cooper et al., 2000:)

the wake of a crack grown in acidic chloride solution, processed to retain H, and subjected

to thermal desorption spectroscopy to yield the H content that was presumably within the

crack tip FPZ during subcritical crack growth. Crack growth rate is directly proportional to

H concentration, normalized by the square root of the average time that the crack wake was

exposed to solution. This normalization provides a speculative means to account for H

uptake during crack surface corrosion well behind the growing crack tip. The most anodic

polarization produced the highest-normalized H content and higher da/dt_{II}. Polarization to –

545 mV$_{SCE}$ produced less H and lower da/dt_{II}, while subsequent polarization to –445 mV$_{SCE}$

produced the same low H content due to a complex hysteresis effect and da/dt_{II} remained

low. These average H concentrations were confirmed by nuclear reaction analysis that

showed a very large amount of H, of order 0.01 to 0.1 atom pct, localized within the first

micrometer of the crack surface (Young, 1999; Cooper et al., 2000).

The presence of very high H in the FPZ, as well as enhanced H content due to anodic

polarization that correlates with da/dt_{II}, each support the HEAC mechanism. Enriched H

with anodic polarization is consistent with hydrolytic acidification (e.g., $Al^{+3} + H_2O = H^+ +$

$AlOH^{+2}$). Moreover for AA7050, direct measurements showed that the crack tip potential is

relatively insensitive to applied-anodic potentials in the range of Fig. 29, with the net result

that η_H becomes more negative and H content on the crack tip surfaces increases with

increasing anodic polarization (Cooper et al., 2000; Cooper and Kelly, 2001). These recent

results strengthen the older evidence for predominant HEAC in 7000 series Al alloys, as

summarized in 6.03.7.1.1.

Considering cathodic polarization, the situation is less clear and additional work is

required.   Enhanced H production under both anodic and cathodic polarization of 7000

series aluminum alloys was inferred from permeation data (Gest and Troiano, 1974). There

are; however, only limited data on crack growth rate under cathodic polarization and there is

no evidence to support increased da/dt_{II} at potentials below those shown in Fig. 29 (Speidel

and Hyatt, 1972; Holroyd, 1990). Increased growth rates are expected since the crack tip in

AA7075 is polarized in the active sense in response to applied cathodic polarization

(Edwards, 1985; Turnbull, 1984).   The Al_2O_3 passive film dissolves under alkaline

conditions and H uptake should occur in the crack with $\eta_H < 0$, as well as on bold surfaces if

transient alkalinity is present.

Superalloys: The potential dependence of cracking in this class of alloys in strong

acid solutions is consistent with the arguments developed for steels and aluminum alloys.

The reduction in K_{IH} with increasing cathodic polarization (Fig. 11) is consistent with

increasingly negative η_H because the crack tip potential parallels the applied values and E_H°

is unlikely to decrease since the solutions are highly acidic. Anodic polarization effects

have not been reported and may not be significant since enhanced crack tip acidification is

not likely in acidic-bulk solution. The data in Fig. 11 suggest that HEAC is mitigated at

high-cathodic potentials. The reason for this is considered in the next section.

β/α-**Ti:**   Extensive research established that severe intergranular environmental

cracking in β-Ti alloys in neutral chloride solution (Figs. 6, 15 and 16) was by HEAC

(Kolman and Scully, 1997, 1998, 2000). This work ruled out the formation of brittle

hydride phase, as well as crack advance due to film rupture and dissolution. Rather, the

scenario for cracking for this alloy class in the free corrosion regime in neutral chloride

solution followed that discussed previously: (1) crack tip passive film rupture from dislocation plasticity, (2) local dissolution of the exposed titanium and repassivation, (3) hydrolytic acidification of dissolved cations to lower crack tip pH, (4) H^+ reduction to form adsorbed H, and (5) H diffusion into the FPZ to nucleate damage (Kolman and Scully, 1997). Kolman and Scully performed electrochemical measurements to establish that elements (1) through (4) are valid and sufficient to enable H-assisted cracking. The passive film that forms on Ti crack and boldly exposed surfaces is stable for all chemical conditions typical of the results in Fig. 30. This behavior is unique compared to the Fe, Ni and Al-based alloy cases, and is critical to the cracking mechanism.

From this scenario, the applied potential dependence of K_{TH} (Fig. 30) is explained by H production at $\eta_H < 0$ governed by the hydrolysis reaction and crack IR in the free corrosion regime. Initial cathodic polarization exacerbates this cracking to a minimum K_{TH}, but polarization to more cathodic levels inhibits HEAC. This initial increase in cracking susceptibility should correspond to increasingly negative η_H, but this detail was not modeled. Cathodic inhibition was explained based on reduced η_H towards 0 as the crack tip electrode potential shifted in the negative sense less strongly compared to the reduction in E_H^o as the crack chemistry became increasingly alkaline. Bulk surface H production never contributed to cracking due to the stable TiO_2 passive film that blocked H uptake. The benefit of anodic polarization, shown by the data for the older alloys in Fig. 30 (Blackburn et al., 1972), was explained speculatively by anodic polarization of the crack tip to above E_H^o even with this reversible potential increased from hydrolytic acidification.

Local electrochemistry and HEAC explain two aspects of crack growth in β/α-Ti alloys.

Environmental cracking requires a preexisting crack. This is explained because crack tip acidification and IR polarization necessary for H production require a tight-occluded crack geometry (Kolman and Scully, 1997, 1998). Hydrogen production is nil on a surface that is exposed boldly to near-neutral chloride solution in the free corrosion regime. Second, the stable TiO_2 film at the crack tip must be ruptured to enable H production and uptake. Mechanical destabilization of this film was attributed to intersection of superdislocations with the crack front, followed by transients in anodic current as the Ti repassivated (Kolman and Scully, 1999). This behavior suggests that the rate of crack tip straining relative to Ti repassivation is an important variable.

An experimental study confirmed that intergranular HEAC was exacerbated by loading conditions that promoted increased crack tip strain rate ($\dot{\varepsilon}_{CT}$) to levels sufficient to destabilize the crack tip passive film and permit H entry to the FPZ(Somerday et al., 2000). $\dot{\varepsilon}_{CT}$ depends on dK/dt and da/dt, as well as crack tip creep deformation. The severe cracking susceptibility represented in Fig. 6 was produced by rising-K loading over a range of dK/dt, as well as during quasi-static loading where dK/dt $\sim$ 0 but da/dt was high. In contrast IG HEAC was mitigated at low $\dot{\varepsilon}_{CT}$, insufficient to destabilize the crack tip passive film that remains in tact and thus is capable of blocking hydrogen uptake and subsequent embrittlement. For example, a stationary crack under slow dK/dt or fixed CMOD loading, or prolonged air preexposure at fixed K to reduce the primary creep strain rate, caused low $\dot{\varepsilon}_{CT}$ and eliminated IG cracking. Crack tip strain rate formulations have not been developed sufficiently from either continuum or dislocation mechanics modeling to reconcile these results quantitatively.

6.03.7.2   Hydrogen Assisted Damage Mechanisms

The fundamental mechanisms for hydrogen-assisted damage in metals have been reviewed extensively (Troiano, 1960, 1974; Lynch, 1988, 1997, 2003; Oriani, 1978, 1987, 1990; Hirth, 1980; Nelson, 1983; Birnbaum, 1990; Gerberich et al., 1996; Birnbaum et al., 1996; McMahon, 2001). Apart from cracking due to hydride formation, discussed elsewhere in this volume, the atomistic mechanism for hydrogen embrittlement is controversial with three major candidates advanced: Hydrogen Enhanced Decohesion (HEDE), Hydrogen Enhanced Localized Plasticity (HELP), and Adsorption Induced Dislocation Emission (AIDE).   Each of these mechanisms is summarized, and the supporting theoretical and experimental evidence is noted.   An additional and controversial mechanism based on surface diffusion of corrosion-induced vacancies to the crack tip (6.03.8) has not been applied extensively to H cracking in high strength alloys (Galvele, 1987; Parkins, 1990).

6.03.7.2.1   Hydrogen Enhanced Decohesion

The HEDE mechanism was first suggested by Troiano, and developed in detail by Oriani and coworkers (Fromberg, Barnett and Troiano, 1955; Troiano, 1960, 1974; Oriani, 1972, 1977, 1987, 1990; Oriani and Josephic, 1974, 1977; Gerberich et al., 1991). In this model, H accumulates within the crack tip FPZ and there reduces the cohesive bonding strength between metal atoms. Initially, H accumulation above the unstressed-lattice solubility was driven by lattice dilation due to elastic hydrostatic stresses (Li et al., 1966), while later work recognized that trapping is a potent mechanism for H segregation (Pressouyre, 1980). McMahon and coworkers advanced the view that impurity elements segregated to grain

boundaries similarly reduced host-metal bond cohesion, adding to the embrittling effect of H (Bandyopadhyay, et al., 1983; Briant and Banerji, 1983; McMahon, 2001). The HEDE provides the basic notion that H damage occurs in the FPZ when the local crack tip opening tensile stress exceeds the maximum-local atomic cohesion strength, lowered by the presence of H (Oriani, 1972). In the HEDE scenario, H damage sites are located at a distance ahead of the crack tip surface where tensile stresses are maximized. Predictions are derived from knowledge of crack tip stress, H concentration at damage sites, and its relationship with the interatomic bonding force vs. atom displacement law.

A consensus is emerging that HEDE is the dominant mechanism for IHAC and HEAC in high strength alloys that do not form hydrides (Oriani, 1987, 1990). HEDE is likely for several reasons. First, large concentrations of H should accumulate in the FPZ due to very high crack tip stresses plus H trapping along a crack path, as suggested by Oriani (1987) and supported by modern considerations of crack tip mechanics and trapping (see 6.03.8.1 and 6.03.8.2) (Gangloff, 2003). For example, the model calculations in Fig. 41 show that substantial levels of H, approaching full interface coverage at 100 atomic pct, can in principle accumulate along grain boundaries in a Ni-based superalloy undergoing HEAC. The higher H contents shown in Fig. 41, achieved during stressing at 54°C in H_2, are particularly relevant to this discussion of HEDE. The data points for cracking at 260 and 338°C may be pertinent to a creep based damage mechanism rather than decohesion, as suggested by the crack growth rate data in Fig. 36 (Hall and Symons, 2001). Figure 36 also reflects the temperature dependence of H production from electrochemical reactions of Ni with water, while Fig. 41 relates to temperature dependent dissociative chemisorption of H_2
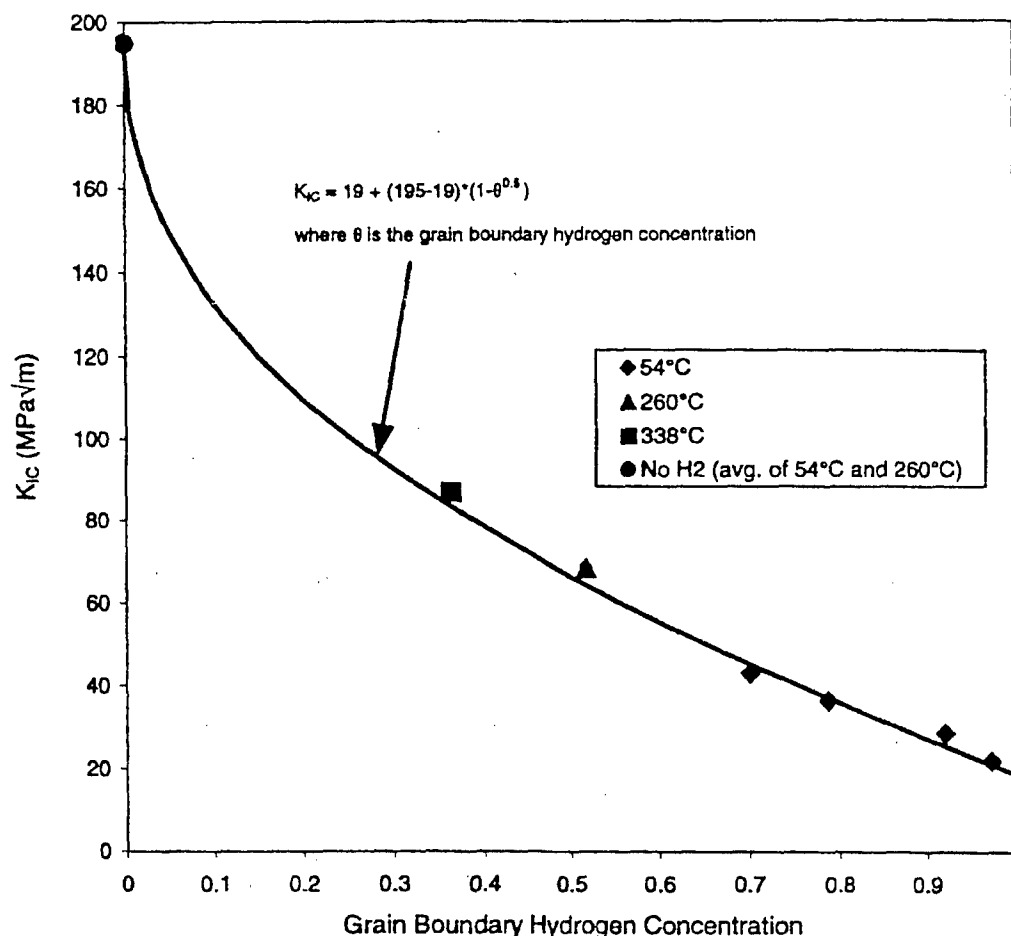
Figure 41. The localized-H concentration dependence of the threshold stress intensity for HEAC of high strength superalloy X-750 (σ_{YS} = 800 MPa) tested in H_2 at several pressures and temperatures under rising CMOD at dK/dt = 0.0012 MPa√m/s. The plotted H concentration (atom fraction of H in Ni) was calculated as localized at grain boundaries due to H trapping at boundary carbides (E_B = 26 kJ/mol) coupled with crack tip hydrostatic stress estimated from conventional plasticity theory as σ_H = 4.5σ_{YS}, see 6.03.8.1 and 6.03.8.2. Tests at 260 and 338°C were conducted in 13.8 MPa H_2, while those at 54°C were conducted at several P_{H2} levels between 0.14 and 34.5 MPa. (Symons, 2001: Reprinted with permission from Elsevier.)

to H, coupled with H trapping in both cases (6.03.8.4). Similarly high crack tip hydrogen concentrations, approaching many atomic pct, were predicted for IHAC in AerMet®100 UHSS due to very high-local tensile stress and H trapping (Thomas et al., 2003).

Second, experiments show directly that the sharpness of a crack tip in stressed Fe-3%Si single crystal increases progressively with increasing H_2 pressure and decreasing temperature; shown by decreasing crack tip angle (α) in Fig. 42 (Vehoff and Rothe, 1983; Vehoff and Neumann, 1985). In this figure, the horizontal-dashed line represents crack growth by slip only, at a crack tip opening angle, α, of 70° that equals the angle between active slip planes in the single crystal. This angle will decrease as a second mechanism of crack growth becomes increasingly important. Since the crack planes in Fe-3Si were always parallel to {100} and dimples were not resolved on these crack surfaces (see ensuing discussion of AIDE), the results in Fig. 42 were interpreted to prove that the decohesion mechanism progressively replaced crack tip slip as the advance process, as least for this case of transgranular HEAC and with increasing P_{H2}. The temperature and P_{H2} dependencies were argued to be consistent with the amount of H expected to adsorb on an Fe surface.

Third, atomistic simulations suggest that H can reduce atomic cohesion (Oriani, 1987, 1990; Gerberich, et al., 1991). Finally, a wide range of micromechanical models have been derived from the decohesion principle and effectively fit experimental values of K_{TH} and da/dt_{II} for IHAC and HEAC. These models span the range from continuum fracture mechanics to crack tip dislocation mechanics (Gerberich et al., 1991). The effects of P_{H2} and T, including rapid pressure or temperature-change experiments, as well as the effects of H concentration and σ_{YS}, have been predicted reasonably as summarized in 6.03.8.
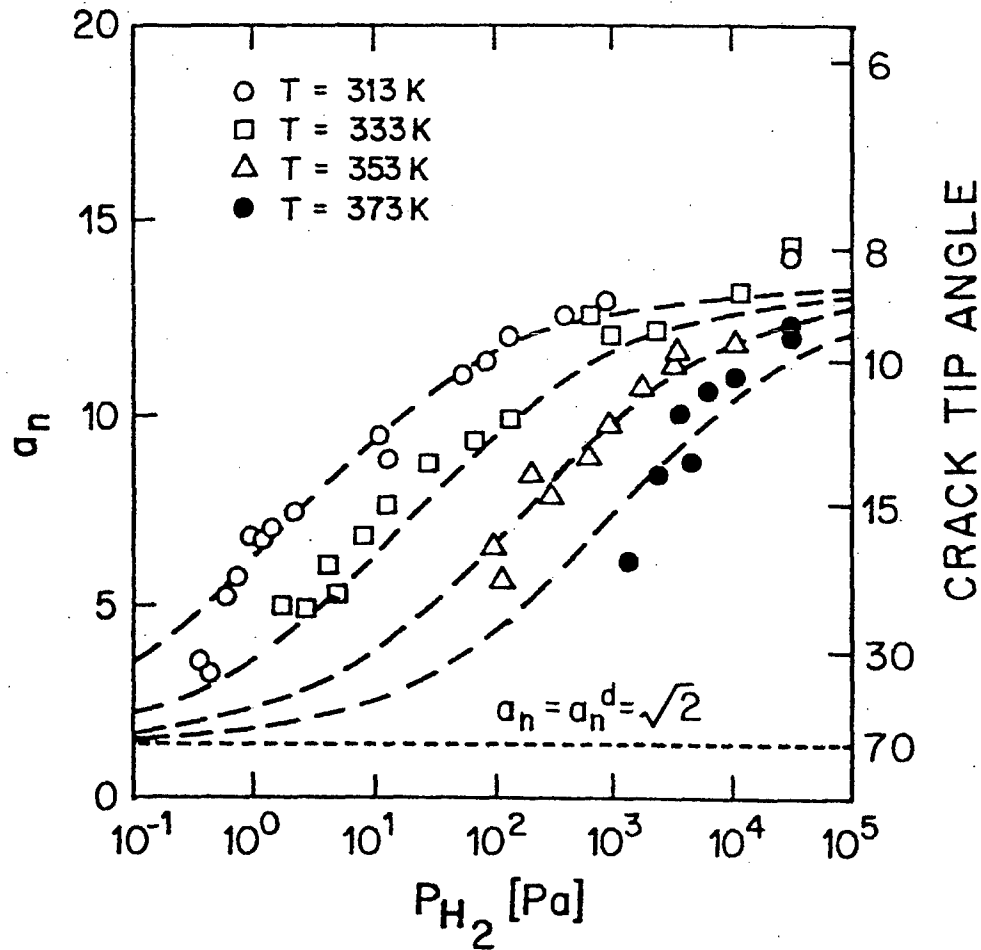
Figure 42.   The dependence of *in situ* measured crack tip opening angle, α, on H_2 pressure for Fe-3%Si single crystals stressed at several temperatures.   The parameter a_n represents the ratio of incremental crack extension to crack mouth opening; $a_n = \cot(\alpha/2)$.   The horizontal-dashed line represents crack growth exclusively by crack tip slip, with α as the angle between active slip planes in the single crystal.   As decohesion-based growth becomes increasingly important, α decreases.   (Oriani, 1990.   After data from Vehoff and Rothe, 1983 as well as Vehoff and Neumann, 1985:   Copyright NACE International, reprinted with permission.)

The HEDE mechanism is debated because of weaknesses in the supporting evidence. Foremost, there is no direct experimental demonstration that atomic H dissolved in a metal lowers the interatomic force-displacement relationship, or alters elastic properties or surface energy that are derived from such bonding. The primary problem is that the amount of H that can be dissolved in a specimen for bulk-property measurement is orders of magnitude less than that projected to accumulate locally within the crack tip FPZ. While theory suggests effects of H on metal bonding, results are limited by the capabilities of such modeling and necessary assumptions. The theoretical demonstration of H-sensitive bond strength can similarly support HEDE, HELP and AIDE (Daw and Baskes, 1987). Finally, all HEDE-based models of macroscopic K_{TH} and da/dt properties contain one or more adjustable parameters due to uncertain features of the crack tip problem, as outlined in 6.03.8. As such, good predictions of IHAC and HEAC data are tempered.

6.03.7.2.2   Hydrogen Affected Localized Plasticity

Beachem first suggested that H stimulates dislocation processes that localize plastic deformation sufficiently to result in subcritical crack growth with brittle characteristics on the macroscopic scale (Beachem, 1972). Two variations of this notion have been advanced as the AIDE and HELP mechanisms.

6.03.7.2.2.1   Adsorption Induced Dislocation Emission

Lynch argued that H-induced weakening of metal-atom bond strength results in enhanced emission of dislocations from crack tip surfaces where H is absorbed (Lynch,

1977, 1988, 1997, 2003). AIDE attributes H-enhanced crack growth as predominantly due to this focused emission of dislocations, exactly from the crack front and along intersecting planes that geometrically favor sharp-crack opening and advance rather than crack tip blunting in the absence of H. During loading, plastic deformation is also triggered within the crack tip plastic zone; and microvoid formation, with or without an assist from dissolved H, could occur. The linkup of voids adds a component to crack advance and maintains a sharp crack tip by interacting with the intense slip bands from crack tip dislocation emission.

The crack surface should reflect this advance process and contain facet-like features parallel to the plane that bisects crack tip slip planes, as well as a high density of microvoids if this latter feature occurs. Voids should occur on a size scale that is substantially less than those formed about inclusions and larger dispersoids or precipitate particles during fracture without H and AIDE. Facets may be parallel to low index planes for certain symmetric slip plane configurations, but also along higher index planes if the crack tip slip state is unbalanced. Intergranular cracking in the AIDE formulation reflects preferential adsorption of H along the line of intersection between the grain boundary plane and crack front, and perhaps a higher density of precipitates that may form preferentially along grain boundaries (Lynch, 1988). This mechanism is best suited for HEAC; however, H localization to a crack tip during IHAC could also be result in AIDE.

The main evidence for the AIDE mechanism is fractographic (Beachem, 1972; Lynch, 1977, 1988). Specifically, the geometry of transgranular cracking, largely along low index planes that intersect active slip systems intersecting a crack front in single crystals of Al alloys and Fe-Si, was claimed to support AIDE. A high density of very small dimples

populated IG facet surfaces produced by HEAC in several alloy systems and polycrystalline microstructures. Critically, these features were reported to be similar for HEAC and liquid metal embrittlement (LME). Cracking by LME is clearly restricted to a crack surface mechanism, consistent with AIDE. Since similar fracture surface features are reported for HEAC and LME, logic suggests that the AIDE mechanism is similarly operative at the crack surface only (Lynch, 1997, 2003). Third, Lynch argued that the very fast da/dt reported for HEAC in high strength alloys is only explained by surface embrittlement, as envisioned in the AIDE mechanism and counter to HEDE where H damage sites are within the crack tip FPZ. Atomistic calculations that suggest H-reduced atomic cohesion can be invoked to support AIDE as well as HEDE (Daw and Baskes, 1987).

The AIDE mechanism is debated because of weaknesses in the supporting evidence. The structure of slip about a crack tip in a hydrogen exposed metal has never been characterized sufficiently to show H stimulated dislocation emission and associated geometric crack extension. High strength polycrystalline alloys are strengthened by a complex array of finely spaced barriers to dislocation motion that should provide significant back-stress to stifle dislocation emission from a crack tip. Intergranular cracking is predominant in IHAC and HEAC, but AIDE does not provide a clear explanation of why this is prevalent, apart from enhanced fine-scale voiding. The presence of very small voids on intergranular facets from HEAC and LME is controversial. Those who favor HEDE tend to not observe an organized void-like structure on facet surfaces. The initial argument that small-shallow voids are only resolved by careful transmission electron microscopy of low-angle shadowed replicas viewed at high tilt was reasonable (Lynch, 1977), but has been diluted by modern

SEM methods. An example of a modern-SEM analysis is summarized in Fig. 43, where an

IG facet from HEAC in α precipitation hardened β-Ti was examined with a high brightness

electron source, multiple detectors to change surface topography, high magnification, and

matching surface stereographic analysis (Somerday, 1998b; Somerday et al., 2003).

Shallow microvoids as small as 0.02-0.04 μm in diameter should be resolvable with this

method; however, there was no evidence of an organized surface structure indicative of

shallow microvoiding. Rather, the features were undulations with occasional matching

ridges and protrusion-cavity pairs, each consistent with decohesion of β-Ti grain boundaries

that are impacted by α precipitates in the complex-underlying microstructure. While there is

need for systematic observations, surface features typical of AIDE have not been reported

widely. The argument that only AIDE can explain rapid rates of crack growth is refuted by

the analysis of H diffusion from the crack tip surface to damage sites in the FPZ, as

presented in 6.03.8.4.2 (Gangloff, 2003). Finally, the AIDE mechanism has not been

developed to yield semi-quantitative predictions of K_{TH} or da/dt_{II} for subcritical IHAC and

HEAC. As such, this model has not been tested and the AIDE perspective is to date not

useful for supporting structural integrity analysis.

6.03.7.2.2.2   Hydrogen Enhanced Localized Plasticity

Birnbaum and coworkers proposed that dissolved H enhances the mobility of

dislocations, resulting in extreme localization of plastic deformation sufficient to enable
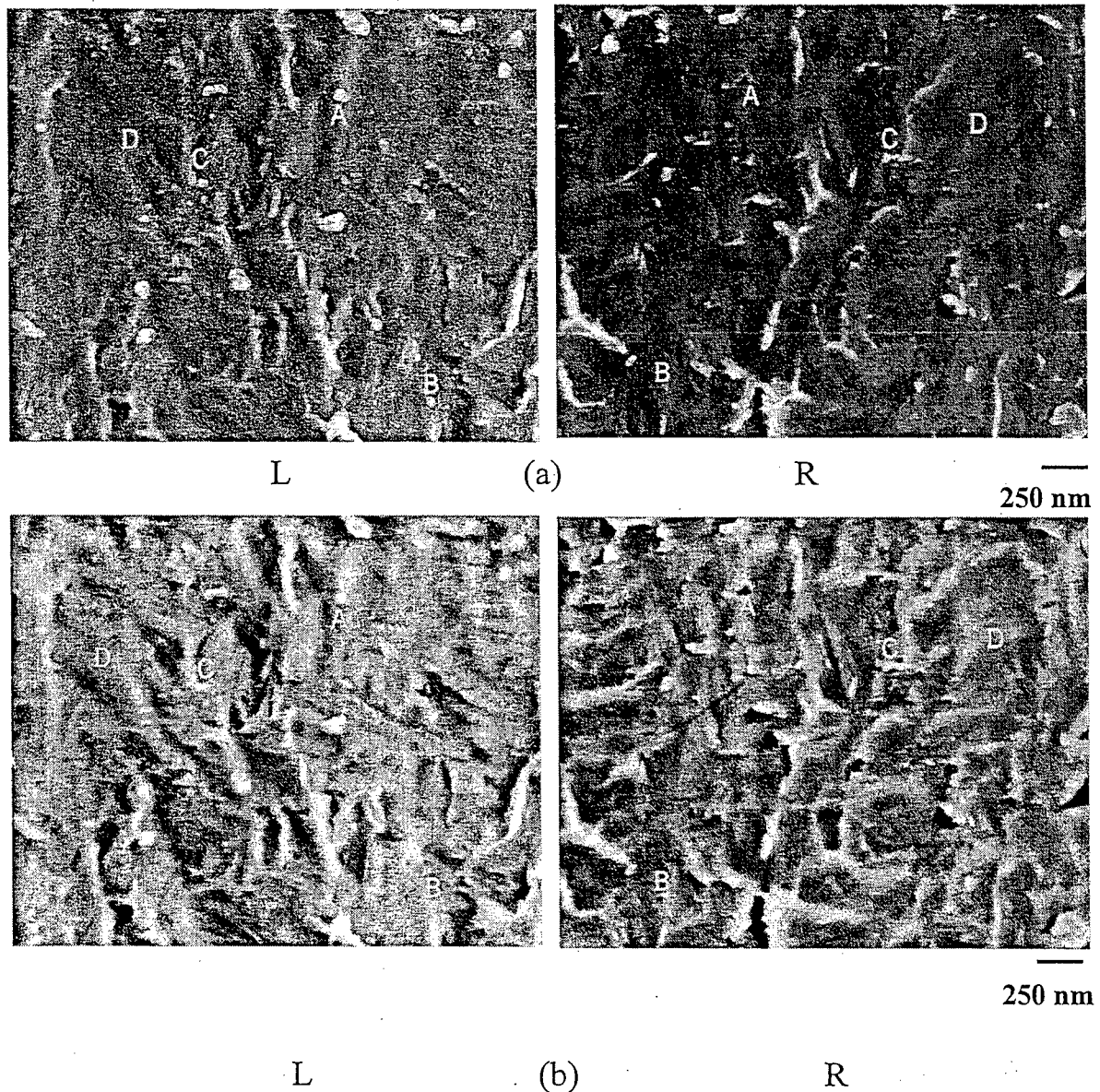
Figure 43: Matching field emission SEM images of an IG facet in α-hardened β-Ti (Beta-C) cracked in aqueous NaCl following the conditions illustrated in Fig. 15. These high magnification images were formed with the signal accumulated from: (a) the secondary electron detector immediately above the specimen, and (b) dual secondary electron detectors. The images marked "L" and "R" were obtained from the matching-opposite areas of the fracture surface. The features marked A, B, and C are matching protrusion/cavity pairs; D shows subtle undulations on the fracture surface. (Somerday, et al., 2003)

subcritical crack growth that is macroscopically brittle (Birnbaum, 1990; Birnbaum et al., 1997, Robertson, 2001). This effect was reported for high strength Al alloys (Bond et al., 1987), pure Ni (Robertson and Birnbaum, 1986), pure Fe (Tabata and Birnbaum, 1984), austenitic stainless steel (Rozenak et al., 1990), and single phase α-Ti (Shih et al., 1988). The HELP mechanism differs from AIDE in that dislocation mobility is enhanced due to H accumulation about dislocation cores, resulting in reduced elastic energies of interaction between moving dislocations and a variety of obstacles (Birnbaum and Sofronis, 1993; Robertson, 2001). Since H reduces interaction energy, the stress required for dislocation motion is decreased and plasticity is enhanced.

The primary evidence for HELP is *in situ* high voltage electron microscopy of thinned specimens subjected to plastic deformation during exposure to either vacuum or H_2 (Robertson, 2001). Such observations revealed an increased number of dislocations in a pileup, as well as initiation of dislocation motion, due to H_2 introduction to the electron microscope. Similar plastic deformation accompanies crack growth in the TEM; however, such growth occurred at lower-applied stresses in the presence of H. For example, a stationary crack formed in vacuum began to propagate after introduction of H_2 to the microscope. Such cracks propagated along a grain boundary and in the matrix volume adjacent to a boundary; with the interface mode prevalent when impurities such as S in Ni were present to augment H damage.

Studies of H effects on bulk specimens show decreased flow stress, increased stress relaxation, and altered strain rate sensitivity due to dissolved-bulk H (Robertson, 2001). However, H effects on hardening/softening are controversial, with diametrically opposed

results reported for the same alloy and debate on experimental differences or artifacts possibly responsible for each trend (Robertson, 2001; Birnbaum, 1990). While such information can confirm that H interacts with dislocations to affect plastic flow, the point is moot since the high hydrogen content, highly triaxial stress state, and gradated character of the crack tip FPZ are not represented by bulk crystal uniaxial deformation experiments.

The HELP mechanism is debated because of additional weaknesses in the supporting evidence. The TEM studies use a thin foil (< 200 nm) with at best a two-dimensional stress state and substantial possibility for surface effects on dislocation motion. Surface issues may be exacerbated by the high fugacity H, produced by H_2 dissociation in the electron beam and capable of reducing surface oxide and oxidizing hardening solute such as carbon or oxygen. These changes, rather than a core-H interaction could cause the observed plasticity and thus be unique to the thinned foil. Studies have not been extensive for complex microstructures with multiple obstacles and very short slip distances typical of high strength alloys. The geometry of localized flow in such high strength microstructures has not been developed. Modeling of dislocation mobility has not included H drag on the moving-dislocation line. Finally, the HELP mechanism has not been developed to yield semi-quantitative predictions of K_{TH} or da/dt_{II}. As such, the HELP model does not support structural integrity analysis.

6.03.8 MECHANISM-BASED MICROMECHANICAL-CHEMICAL MODELING OF HYDROGEN ASSISTED CRACKING

The goal of micromechanical-chemical modeling of IHAC and HEAC is to predict the dependencies of the threshold stress intensity and subcritical crack growth rate on

environmental, material and loading variables. This is accomplished by focusing on the

crack tip FPZ shown in Fig.2 and developing relationships that describe:

- *Crack tip stress and plastic strain distributions*

- *Crack tip H concentration localization*

- *Location of H-damage sites at a critical distance (χ_{CRIT}) into the crack tip FPZ*

- *Failure criterion involving a critical H content-local stress combination*

Modeling must include the key factors that govern IHAC and HEAC, including: (a) H

production by occluded crack electrochemistry, (b) trap-sensitive H solubility and mobility,

(c) specific microscopic crack path, (d) coupling of continuum and dislocation-based crack

mechanics over multiple length scales, and (e) the mechanism of H damage, either

decohesion or plasticity based. Models of the threshold assume an equilibrium perspective,

while da/dt formulations must include kinetics.

Three complications hinder modeling. First, it is necessary to integrate the mass

transport and reaction processes that drive crack growth. Second, these factors change

sharply over distances on the order of 0.05-10 µm in the FPZ, and finally, the location of H-

damage ahead of a crack tip is controversial. All models developed to date contain one or

more unknown parameters that are adjusted to fit experimental data. As such, the best of

models are informative but not fully predictive for use in structural integrity analysis.

6.03.8.1   Crack Tip Mechanics

Quantitative descriptions of crack tip stress and strain distributions are central to

micromechanical models of H cracking. The singularity and (distance, x)$^{-1/2}$ dependence are

central features of the elastic tensile stresses about the crack tip. The correct plasticity treatment to predict actual opening direction (σ_{YY}) and hydrostatic (σ_H) tensile stresses, as well as the tensile-plastic strain (ε_P), is critically important. Three approaches have been taken, including: (a) elastic-plastic fracture mechanics with finite element analysis, (b), strain gradient plasticity, and (c) dislocation-configuration shielding.

Rice proposed the basic elastic-plastic fracture mechanics approach that has provided the foundation for IHAC and HEAC modeling over the past two decades (Rice, 1977). The Hutchinson-Rice-Rosengren (HRR) field describes stresses and strains within the crack tip plastic zone, based on the J-integral and augmented by large strain finite element analysis by McMeeking and others (Anderson, 1995). The critical features of this formulation are illustrated schematically by the curve labeled *Conventional J_2 Plasticity* in Fig. 44. The σ_{YY} increases from near the uniaxial σ_{YS} at the crack tip surface, through a maximum at a distance ahead of the crack tip given by $x \sim J/\sigma_{flow} \sim K^2/\sigma_{flow}E$, and merges with the HRR and elastic stress distributions that decay as $1/x^{(1/1+n)}$ where n is a hardening exponent that equals 1 for elastic deformation and 10 to 20 for plasticity in high strength alloys. The hydrostatic stress distribution mirrors the σ_{YY} trend, with the maximum level of each equaling a multiple of σ_{YS} and the exact value depending on work hardening. For the high strength and low work hardening alloys relevant to this chapter, the maximum levels of σ_{YY} and σ_H are $3.5\sigma_{YS}$ and $2.5\sigma_{YS}$, respectively (Akhurst and Baker, 1981; Anderson, 1995). The crack tip is modeled to blunt in this formulation to an opening, δ_T, equaling $K^2/2\sigma_{YS}E$ where $\sigma_{YS} \sim \sigma_{flow}$ for high strength alloys, and crack tip tensile stresses are maximum at
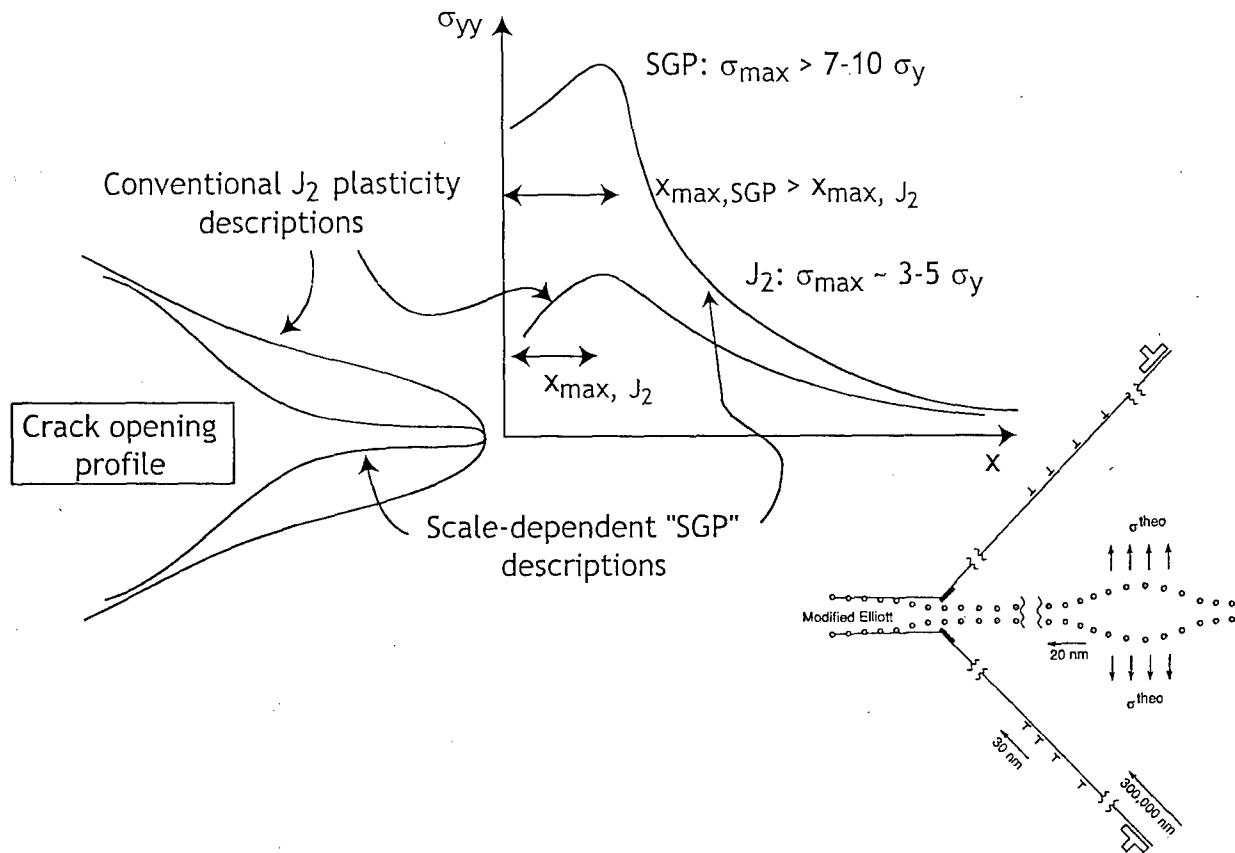
Figure 44. Schematic diagrams of: (top) the distributions of crack tip tensile stress reflecting either conventional plasticity description of elastic-plastic deformation, or a length-scale dependent hardening description of near-crack tip deformation in the presence of a strong strain gradient (Wei and Hutchinson, 1997; Jiang et al., 2001), and (bottom-right) the discrete dislocation model of crack tip mechanics from Gerberich and coworkers (Gerberich et al., 1991). SGP refers to strain gradient plasticity. (Publication permission requested from Taylor and Francis Group.)

about $2\delta_T$ ahead of the crack tip surface.   Typical distances are shown in Table 2.

Table 2.   Calculated maximum stress distances for high strength alloys at low applied K

Alloy	σ_{YS} (MPa)	Applied K ($MPa\sqrt{m}$)	$2\delta_T = K^2/\sigma_{YS}E$ (μm)
Fe-3%Si Single Crystal	300	30	20
Precipitation Hardened Austenitic Steel	850	90	48
Nickel Based Superalloy	1125	50	12
Precipitation Hardened Aluminum	500	15	6
18Ni Maraging Steel	1700	30	4
Tempered Martensitic Steel	1600	40	6
$\beta + \alpha$ Ti Alloy	1150	30	8

The blunt crack solution may not be relevant to H cracking in high strength alloys. Recent attention focused on strain gradient plasticity (SGP) as a mechanism to produce a very sharp crack tip and extraordinary stress elevation just ahead of the tip, as shown schematically by the higher trend in Fig. 44 (Hutchinson, 2000; Fleck and Hutchinson, 2001; Needleman and Sevillano, 2003).   Geometrically necessary dislocations form to accommodate a high gradient in strain, as exists at a crack tip, and provide an additional hardening source to augment work hardening. This behavior persists at a crack tip if the size of plasticity is on the order of the material length scale that defines the gradient hardening response; of order 0.5-5 μm.

IHAC and HEAC in high strength alloys at low applied K levels are within the crack tip deformation regime where gradient plasticity effects must be considered. Hutchinson and others applied this plasticity description to the crack tip problem, and predicted a factor of 3 reduction in the blunted δ_T, increases in σ_{YY} to as high as $10\sigma_{YS}$, and increased σ_H to $8\sigma_{YS}$

(Wei and Hutchinson, 1997; Jiang et al., 2001). As strain gradient based descriptions of crack tip plasticity are emerging rapidly, these results are approximate and require verification for various crack tip boundary conditions. None-the-less, the possibility for stress elevation of the sort shown in Fig. 44 must be incorporated in micromechanical models of crack tip IHAC and HEAC. To date, this had not been accomplished formally (Thomas et al., 2003). The location of the maximum stresses in an SGP affected FPZ is not clear, but is certainly no larger than the values indicated in Table 2 from J_2 plasticity theory.

As a third approach, dislocation considerations have been employed to determine an elastic-plastic crack tip stress distribution for input to H damage modeling. Thompson and latter Kameda described the stresses adjacent to the tip of an atomistically sharp intergranular crack pertinent to hydrogen embrittlement (Thomson, 1978; Kameda, 1986a). A very small dislocation-free zone between the crack tip and dislocation pileup that screened the elastic crack tip singularity guaranteed this sharpness in the Mode I opening direction. The crack opening-direction stress in the dislocation free zone was estimated to equal between 6.5 and 9 GPa for a high strength material (σ_{YS} = 1,500 MPa and 0.08 < n < 0.10) and subjected to applied K levels typical of IG hydrogen cracking thresholds (Kameda, 1986a).

Gerberich and coworkers extended this approach by modeling the interaction of elastic stress fields associated with a sharp crack tip under remote loading, as well as a distribution of discrete-shielding dislocations that dominate very-near tip stresses and a superdislocation that is removed from the tip and defines global crack tip plasticity with work hardening (Gerberich et al., 1991; Gerberich et al., 1996; Katz et al., 2001). This situation is shown

schematically in the lower portion of Fig. 44. The aim is to connect the local crack tip driving force, as stress or the crack tip stress intensity (k_{tip}) with the standard far-field stress intensity factor, K, used to correlate H cracking properties for structural integrity applications. This dislocation model, applied to understand HEAC in an Fe-Si single crystal ($\sigma_{YS} = 300$ MPa), predicted crack tip σ_H of 15 to 25 GPa, maximized 20 nm ahead of a sharp crack tip (Chen and Gerberich, 1991). These very near tip stresses are substantially higher than those associated with the continuum plasticity solution pertinent to the relatively large crack tip plastic zone. Away from the crack tip, into the plastic zone and beyond, the dislocation simulation is consistent with the HRR and elastic stresses (Huang and Gerberich, 1992). Notably, the existence of a dislocation free zone and morphology of slip about the crack tip have not been determined experimentally for high strength alloys with complex microstructures.

Plastic strain-based models have also been proposed to describe H-assisted threshold and crack growth rate properties, particularly in austenitic superalloys that exhibit a substantial amount of H-assisted transgranular cracking associated with slip bands (Moody et al., 1990b, 2001; Somerday and Moody, 2001). These models are not reviewed here as they are specific to IHAC and HEAC in lower strength alloys.

6.03.8.2   Crack Tip Hydrogen Accumulation

Hydrogen accumulates in the crack tip FPZ under the influence of two driving forces. First, it is well known that the concentration of H in interstitial lattice sites is increased proportional to an exponential dependence on hydrostatic stress that dilates the lattice (Li,

Oriani and Darken, 1966; Zhang and Hack, 1999). The exact magnitude of the crack tip σ_H is critically important to this H accumulation, be it ~$3\sigma_{YS}$ from conventional J_2 plasticity theory or ~$8\sigma_{YS}$ from strain gradient or dislocation-shielding based models.

Hydrogen also accumulates at a crack tip due to trapping associated with the high density of dislocations present from plastic deformation. This contribution was modeled and shown to be dominant provided that crack tip blunting is significant, as is typical of lower strength alloys with limited gradient plasticity enhancement of the hydrostatic stress (Krom, 1999; Taha and Sofronis, 2001). Modeling of IHAC and HEAC in high strength alloys has emphasized hydrostatic stress enhancement of H accumulation. This approach is particularly compelling if crack tip stresses are of order $8\sigma_{YS}$.

Hydrogen trapping at microstructural features within and about the FPZ is important to micromechanical-chemical modeling of K_{TH} and da/dt_{II}. The details of this behavior were summarized in 6.03.6.3.1, and H enhancement is controlled by the lattice H concentration and an exponential temperature dependence including the H-trap binding energy, E_B.

6.03.8.3   Threshold Stress Intensity Modeling

6.03.8.3.1 HEAC

The first quantitative model aimed at predicting the threshold stress intensity for HEAC was put forth by Oriani and Josephic based on the HEDE mechanism (Oriani and Josephic, 1974). Here, K_{TH} is the equilibrium threshold condition where the crack tip tensile stress is just sufficient to exceed the cohesive strength of atomic bonding, lowered by local H that accumulates in response to σ_H acting on the lattice concentration in equilibrium with the

surrounding H_2 pressure. Sievert's law related lattice H concentration to P_{H2} and T, trapping was allowed through a multiplying constant, stress-induced solute accumulation was defined by σ_H from an elastic expression, and the critical distance for H damage was avoided by relating crack tip stress to tip radius proportional to a power law function of K. These mechanics assumptions predicted high σ_H (18-26 GPa) and were judged to be inadequate in not dealing with plasticity (Rice, 1977). HEDE was modeled by assuming that H reduced the maximum cohesive force linearly. While these assumptions resulted in several unknown-adjustable parameters, the model reasonably predicted the relationship between K_{TH} and P_{H2} for high strength steel, as well as the very fast response time of changes in K_{TH} to changing H_2 pressure expected for the very-near surface location of H-damage sites dictated by the assumed stress distribution (Oriani and Josephic, 1974, 1977). This model also predicted the measured shift in the H_2 *vs.* D_2 pressure dependencies of K_{TH}.

Gerberich as well as Akhurst and Baker coupled the decohesion model with a continuum mechanics description of the crack tip stress field considering elastic-plastic behavior (Gerberich, 1974; Gerberich and Wright, 1981; Akhurst and Baker, 1981). The latter model defined the threshold as the equilibrium condition where the crack tip tensile stress exceeded the H-reduced cohesive strength over a critical distance into the FPZ, χ_{CRIT}, as dictated by the elastic-plastic fracture mechanics result that maximum σ_{YY} and σ_H are independent of K, but the breadth of the peak shown schematically in Fig. 44 increases as K rises (Rice, 1977). This χ_{CRIT} was hypothesized to be a material constant. The equation describing the H-reduced cohesive strength, σ^*, is:

$$\sigma^* = \sigma_o^* - A\sqrt{P_{H2}}\ \exp\left[V_H\left(2.6\sigma_{YY} - 1.3\sigma_{YS}\right)\middle/3RT\right]$$

(8)

where σ_o^* is the

cohesive strength of the H-free metal lattice, A is a group of adjustable constants, V_H is the

partial molar volume of H in the metal, and R is the gas constant. The crack tip stress

distribution, just beyond the peak in Fig. 44, was approximated by (Schwalbe, 1977):

$$\sigma_{YY}\middle/\sigma_{YS} = \left[0.3\middle/(X+1)\right]\left[0.04\middle/X\right]^{\frac{1}{n+1}} \qquad \text{for } 0.04 < X < 0.073 \qquad (9)$$

where n is the exponent in the constitutive relationship $\sigma \propto \varepsilon^n$ and is ~0.1 for high strength

alloys that exhibit limited work hardening, and the normalized parameter X is:

$$X = \frac{x}{\left(K\middle/\sigma_{YS}\right)^2}$$

(10)

K equals K_{TH} when x equals χ_{CRIT} and numerical solutions to Eqs. 9 and 10 predict K_{TH} as a

function of P_{H2}, T, and σ_{YS} for a microstructurally meaningful χ_{CRIT}. Such predictions are

reasonable, as illustrated by the modeled trends in Fig. 45 (Akhurst and Baker, 1981).

Similar trends were predicted for HEAC in austenitic superalloys (Stoltz, et al., 1983). This

model is extended to HEAC in electrolytes, provided that permeation or crack chemistry

based descriptions of the crack surface H concentration exist, paralleling Sievert's law

(Gangloff, 1986).

The σ_o^* and A are difficult to define and were selected to provide reasonable values of

K_{TH} for the pressures and yield strengths in Fig. 45. Alternately, Moody and coworkers

related fracture stress to values from uniaxial tensile experiments (Moody et al., 1986;

Somerday and Moody, 2001). The critical distance was selected to span the range of
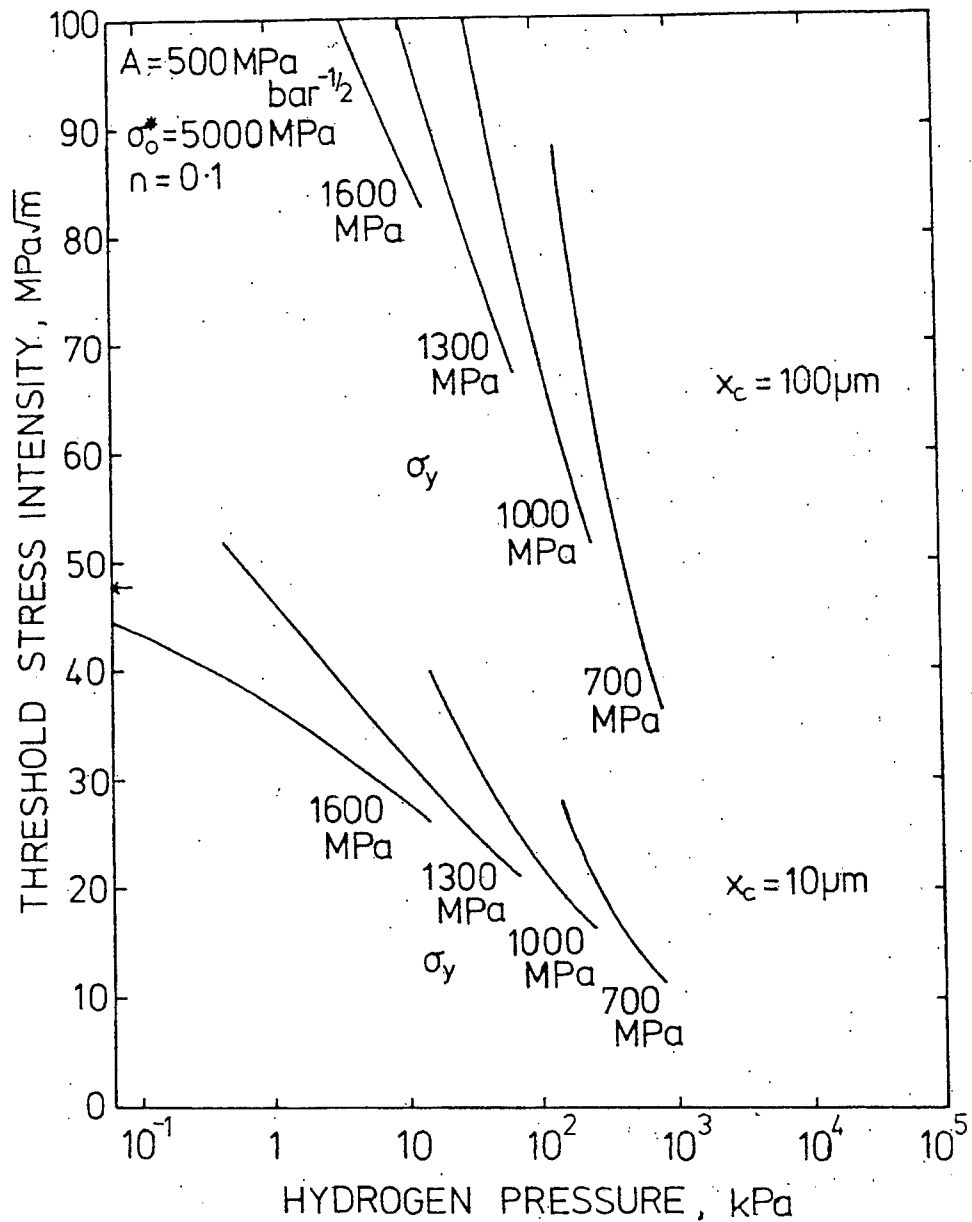
Figure 45. The model-predicted dependencies of the threshold stress intensity for HEAC on alloy yield strength and hydrogen gas pressure for two assumed values of the critical distance (x_C is referred to as χ_{CRIT} in the text). (Akhurst and Baker, 1981: Copyright The Minerals, Metals and Materials Society, reprinted with permission.)

austenite grain sizes typical of high strength steels, but there was no physical basis for this assumption. Finally, the crack tip stresses were based on conventional J_2 plasticity (Fig. 44), relevant to a blunted crack tip. The validity of critical distances in the range of 10 to 100 µm for threshold HEAC is questioned for two reasons. First, very high tensile stresses near the sharp H-crack tip (Fig. 44) could result in small χ_{CRIT}. Second, very high levels of crack tip surface H, unexpected from the simple permeation concept and Sievert's law for unstressed specimens, could override the dominant role of stress and lattice dilation in concentrating the critical H content. High levels of surface H were reported for a 7000-series aluminum alloy in NaCl solution (Cooper et al., 2000). These concepts have not been incorporated into a model of the threshold stress intensity for HEAC; however, this approach was employed recently to model da/dt_{II} for HEAC and the threshold for IHAC.

6.03.8.3.2 IHAC

The models of HEAC threshold are extendable to describe IHAC in high strength alloys. Mobile H dissolved in both the surrounding lattice and at lower binding energy trap sites feeds the crack tip FPZ due to stress enhancement, and there promotes cracking in conjunction with a critical stress and distance concept (Gerberich, 1974; van Leeuwen, 1979). The equations that describe the yield strength, temperature and bulk concentration dependencies of K_{TH} are similar to those presented for HEAC. Unknown values for σ_o^*, A and χ_{CRIT} limit the predictive capability of this modeling.

A dislocation description of crack tip mechanics (Huang and Gerberich, 1992; Katz et al., 2001) was employed to develop a new formulation of the threshold for HEAC and IHAC

(Gerberich et al., 1991). This approach was first developed to predict the temperature dependence of the macroscopic fracture toughness for cleavage, then extended to predict the yield strength, temperature and H concentration dependencies of K_{TH} (Gerberich, Marsh and Hoehn, 1996). Crack tip fracture is governed by the intrinsic Griffith toughness, k_{IG}, for cleavage fracture without H ($G_C \sim \gamma_S \sim k_{IG}^2/E$), where E is elastic modulus and γ_S is the energy required to produce unit crack surface. The local toughness is assumed to be reduced by accumulated H, yielding a Griffith-type threshold stress intensity for hydrogen embrittlement, k_{IH}, that equals ($k_{IG} - \alpha C_{H\sigma,T}$) where α is a coefficient in units of MPa$\sqrt{m}$/atom-fraction H and $C_{H\sigma,T}$ is the concentration of H localized at the embrittlement site due to the combined effects of hydrostatic stress and microstructural trapping unique to the FPZ. Local k_{IG} and k_{IH} were connected to macroscopic K_{IC} and K_{TH} for Mode I loading using the discrete dislocation simulation of the crack tip shown in Fig. 44 including emission from the crack and a standoff distance to the first dislocation. The resulting model prediction is:

$$K_{TH} = \frac{1}{\beta'} \exp\left[\frac{\left(k_{IG} - \alpha C_{H\sigma,T}\right)^2}{\alpha'' \sigma_{YS}} \right] \tag{11}$$

where β' and α'' are constants determined by computer simulation of this dislocation structure about the crack tip. While developed for TG cleavage due to H, this formulation is likely relevant to H-assisted IG cracking.

This model explains the measured hydrogen concentration dependence of K_{TH} for transgranular IHAC in ultra-high strength AerMet®100 shown in Fig. 23. In Fig. 46 these K_{TH} are plotted *vs.* the $C_{H\sigma,T}$ dependent reduction in k_{IG} (Thomas, Li, Scully and Gangloff,
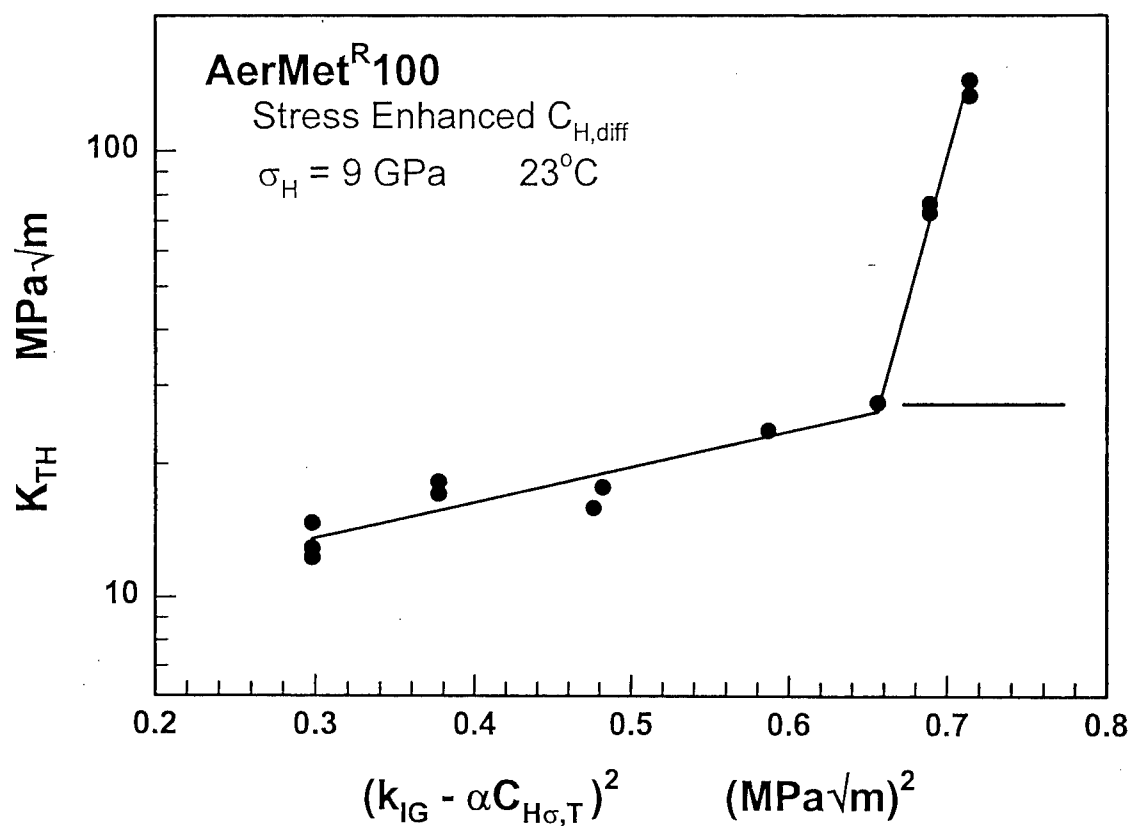
Figure 46. The measured and model-predicted effects of hydrostatic-stress enhanced H concentration, $C_{H\sigma,T}$ on the threshold for IHAC of AerMet[®]100. All measured K_{TH} values less than 30 MPa$\sqrt{m}$ relate to brittle-transgranular H cracking and the associated regression line is log $K_{TH} = 0.90 + 0.80 (k_{IG} - \alpha C_{H\sigma,T})^2$ with $r^2 = 0.85$. Cracking at higher K_{TH} involved some MVC. (Thomas et al., 2003)

2003). The $C_{H\sigma,T}$ was calculated from the measured-calibration value of precharged C_H for each K_{TH} and increased to include hydrostatic stress enhancement using a high value of $\sigma_H = 9$ GPa suggested by dislocation and strain gradient plasticity arguments. The parameters reported for Fe-Si ($k_{IG} = 0.85$ MPa√m and $\alpha = 0.5$ MPa√m/atom fraction H (Gerberich et al., 1996)) were used to calculate the concentration term in Fig. 46. The K_{TH} values less than 30 MPa√m represent H charged specimens that failed by brittle TG cracking and are well described with the regression line; the slope yields $\alpha'' = 3 \times 10^{-4}$ MPa·m and $\beta'_{IHE} = 0.13$ (MPa√m)$^{-1}$. Gerberich reported good fits between modeled and experimental measurements of K_{TH} *vs.* H_2 pressure and temperature for HEAC of a high strength steel using $\alpha'' = 2 \times 10^{-4}$ MPa·m and $\beta'_{IHE} = 0.2$ (MPa√m)$^{-1}$ (Gerberich et al., 1996). The good fit between model predictions and measurements of K_{TH} supports the argument that IHE at low K_{TH} is due to the large amount of H that localizes in the highly stressed and trap laden FPZ, and validates this new model approach.

Kameda proposed a microscopic model for K_{IIHAC} based on the notion that the growth of an atomically sharp grain boundary microcrack is induced by H segregated to both grain interface and crack surfaces (Kameda, 1986a, 1986b). Crack sharpness was maintained by a dislocation free zone, with associated high near-tip stresses (6.03.8.1 and Fig. 44). Hydrogen promoted crack growth by reducing energies associated with the grain boundary and crack surfaces in local equilibrium with segregated H. Fracture was modeled by a Griffith-type energy balance between released-stored elastic energy and the H-sensitive energies associated with crack tip plasticity and surface creation. This thermodynamic approach was first recognized by Petch and Stables (Petch and Stables, 1952; Petch, 1956);

but was criticized by Oriani as not providing a mechanistic description of H damage, as well as based on the fact that adsorbed oxygen reduces substantially the surface energy of iron, but does not promote embrittlement under quasi-static loading (Oriani, 1990). While Sieradzki argues that a surface adsorption mechanism is valid (Pasco et al., 1984), and the Kameda formulation is intriguing, the point is moot since this formulation contains unknown-adjustable parameters and does not provide a confirmed-predictive capability that in any way exceeds the models based on crack tip stress plus decohesion. None-the-less, this modeling demonstrates that substantial levels of H accumulate in a zone very near to the crack tip surface due to stress and trapping.

6.03.8.3.3 Temperature Dependence

The data in Fig. 33 show that K_{TH} for HEAC rises sharply with increasing temperature just above ambient. The models summarized in the previous two sections suggest that this effect is due to reduced H accumulation at damage sites within the FPZ. There are two contributions to this reduction in H content with increasing T. First, H accumulation due to lattice dilation from hydrostatic stress declines proportionate to $\exp[\sigma_H V_H/RT]$. Second, the amount of microstructurally trapped hydrogen decreases with increasing temperature, proportionate to $\exp[E_B/RT]$. These important and beneficial effects of temperature on HEAC and IHAC are amplified by crack growth rate modeling.

6.03.8.4 Crack Growth Rate Modeling

The subcritical crack growth rates for IHAC and HEAC have been modeled extensively,

particularly the K-independent Stage II level. This da/dt_{II} is assumed proportional to the rate of H supply to the FPZ, limited by one or more slow steps in the mass transport and reaction sequence illustrated in Fig. 2 (Wei, 1981). Existing models emphasize the temperature, electrochemical or gas environment, H trapping, and time dependencies of each step in the embrittlement sequence. Uncertainties arise since damage is not described explicitly, χ_{CRIT} is unknown, transport/reaction kinetics are complex, and processes are highly gradated about the crack tip. None-the-less, existing models provide important guidance on incorporating the effects of key variables into structural integrity modeling.

Model predictions of the important effect of temperature on da/dt_{II} are highlighted to illustrate the capability of mechanism-based modeling. Both IHAC and HEAC are eliminated above a critical temperature, as shown in Figs. 31 to 36 (but not for the 7000 series aluminum alloy in Fig. 41). The explanations for this beneficial effect are worthy of particular consideration, as this temperature dependence provides a means to shield high strength alloys from hydrogen embrittlement. Several models have been advanced, with each focused on either thermally stimulated elimination of absorbed H on the reacting crack surface in HEAC, or elimination of H trapping accumulation at microstructural features that constitute the brittle-crack path for both HEAC and IHAC.

6.03.8.4.1   IHAC

6.03.8.4.1.1   H Diffusion and Trapping Control

The kinetics of internal hydrogen assisted cracking from H predissolved prior to loading have been modeled as governed by H diffusion to the crack tip FPZ (van Leeuwen, 1974,

1979; Gerberich, 1974; Gerberich et al., 1988, 1996; Moody et al., 1996; Toribio and Kharin, 1997; Moody et al., 2001; Symon, 2001). Diffusion-based models for IHAC include three important parameters: the critical distance ahead of the crack tip surface where H damage nucleates (χ_{CRIT}), the trap-sensitive diffusivity of H in the metal (the effective H diffusivity, D_{Heff}), and the concentration of H trapped at damage sites in the FPZ.

Gerberich and coworkers developed a detailed model to predict the da/dt_{II} for IHAC in high strength tempered martensitic steels (Gerberich, Chen and St. John, 1975; Gerberich, Livne and Chen, 1986; Gerberich et al., 1988). Hydrogen was partitioned at trap and lattice sites in the steel microstructure at time zero, and attracted to the crack tip by hydrostatic stress on load application. The crack path was typically along prior austenite grain boundaries, with H trapping at these boundaries as well as adjacent lath martensite interfaces. The point of maximum H accumulation was taken to be χ_{CRIT} ahead of the crack tip governed by the J_2 plasticity result in Fig. 44. The crack tip stress field was defined consistent with a blunt crack analysis ($\sigma_H \sim 3\sigma_{YS}$), and the intrinsic fracture strength (σ_o^*) was assumed to be reduced linearly by accumulated H according to HEDE. Trap sites in close proximity to this stressed zone were occupied by this diffused H and served as the preferred path for H damage. Hydrogen diffusion into the crack tip process zone, from the surrounding microstructure to a point χ_{CRIT} from the crack tip, was modeled by a transient solution to the diffusion equation including the hydrostatic stress term and H trapping described approximately by D_{Heff}. The crack growth rate was inferred from χ_{CRIT} and the time (t_i) required accumulating a critical amount of H to affect HEDE. For $da/dt_{II} = \chi_{CRIT}/t_i$:

$$\left(\frac{da}{dt}\right)_{II} = \frac{4D_{Heff}}{\chi_{CRIT}}\left\{1 - \exp\left[\frac{\xi\left(T - T_o\right)}{R\,T\,T_o}\right]\right\}^2 \tag{12}$$

where ξ is the sum of the binding energy for the trap state that is the dominant H-damage

site plus the lattice dilation effect ($\sigma_H V_H$), and T_o is the temperature where da/dt_{II} falls to 0.

In a later version of this model, $1/\chi_{CRIT}$ was represented as the ratio of crack advance

distance ($\chi_A = \chi_{CRIT}$) to diffusion distance (χ_D)^2 (Chen and Gerberich, 1991). These two

distances are different for IHAC, but equal for HEAC since the source of H varies from the

surrounding microstructure for the former to the crack tip surface for the latter.

Moody and coworkers developed a model for H-diffusion limited da/dt_{II} pertinent to

transgranular IHAC in precipitation hardened austenitic superalloys (Moody, Robinson,

Angelo and Perra, 1996; Moody, Baskes, Robinson and Perra, 2001). Cracking nucleated as

microvoids at slip band intersections that strongly trapped H, located in the FPZ and ahead

of cracked carbide particles. The da/dt_{II} was limited by short-range diffusion of H from

normal lattice sites to these slip band interactions and equaled a critical distance, given by

the slip band spacing, over the time required for this local H diffusion. The time for H

accumulation between progressive crack nucleation events was modeled by a transient

solution to the diffusion problem that was solved to yield quantitative predictions of da/dt_{II}.

6.03.8.4.1.2   Predicted Temperature Dependence

The H diffusion/trapping models by Gerberich, Moody and coworkers reasonably

describe the temperature dependence of da/dt_{II} for IHAC. The Gerberich model fits the

experimental measurements of da/dt_{II} for intergranular IHAC in H precharged AISI 4340 steel, as shown by the solid line *vs.* data points in Fig. 32. This fit was achieved by assuming a reasonable binding energy for H trapped at martensite lath interfaces adjacent to the prior austenite grain boundary crack path, D_{Heff} of 1 x 10^{-8} cm^2/s for a trap-rich high strength steel, χ_{CRIT} of 1 μm based on both the spacing of martensite laths and the maximum stress point at $2\delta_T$ (Table 2), and T_o of 400K. Similar good agreement is obtained with other combinations of these parameters, but the values selected are reasonable and the approach of this modeling is validated. The major improvement needed is to incorporate higher levels of crack tip stress and a smaller critical distance, consistent with the dislocation and gradient plasticity perspectives in Fig. 44.

The model explanation for the temperature dependence in Fig. 32 is based on the opposing effects of thermally activated H diffusion control, dominant in the low temperature regime, and thermally stimulated H detrapping control at higher temperatures. As T rises from low temperatures, D_{Heff} increases as given by standard Arrhenius behavior with activation energy for H diffusion that is trapping dependent. The exponential term involving T_o dominates the high temperature reduction in da/dt_{II}. Physically, da/dt_{II} declines because the amount of H accumulated at sites of damage nucleation ($C_{H\text{-}FPZ\ trap}$) in the FPZ is lowered according to:

$$\left(C_{H-FPZ\ trap}\right) = C_l\ exp\left(\frac{E_B + \left(\sigma_H V_H\right)}{RT}\right)$$

(13)

For the example shown in Fig. 32, $C_{H\text{-}FPZ\ trap}$ at the experimentally defined T_o (127°C) is 25 times less than the trapped H concentration at 25°C for ($E_B + \sigma_H V_H$) of 6.7 kJ/mol for a σ_{YS}

of 1600 MPa and H trapping at martensite lath interfaces that constitute the sites of H damage. When the equilibrium amount of H partitioned at damage sites decreases, the time required achieving the critical level for embrittlement increases and da/dt_{II} falls. Decreasing H requires increased local stress at damage sites, but maximum crack tip FPZ stresses are relatively independent of K and subcritical H cracking is effectively eliminated.

The model by Moody and coworkers predicts the measured temperature dependence of da/dt_{II} for H precharged IN 903 (Fig. 31), using a measured slip length of 0.6 μm and lattice-H diffusivity from the literature. The explanation is based on partitioning of H between various microstructural sites, and how this trapping affects H diffusivity that in turn controls crack growth rate. For T < 25°C, H diffuses from lattice sites to slip band intersection traps to control da/dt_{II} that increases with increasing T and H mobility. For higher temperatures, the interdiffusion distance increases and a significant amount of dislocation-sheared γ' strengthening precipitate is encountered as well as multiple slip band intersections. These additional trap states reduce the relatively rapid lattice H diffusivity to a trap affected D_{Heff} and da/dt_{II} declines. Additionally, trap site occupancy decreases with increasing temperature, for a given lattice solubility of H, to further decrease H damage and H-enhanced crack growth rate (Pressouyre and Bernstein, 1978, 1979; Hirth, 1980; Moody et al., 2001). The decline in da/dt_{II} with increasing T for IN 903 (Fig. 31) was predicted quantitatively assuming additional H trap states with a specific volume percentage that increased with increasing temperature (diffusion distance) and constant binding energy. Several combinations of trap density and E_B fit the crack growth data.

6.03.8.4.2   HEAC

6.03.8.4.2.1   Framework

Modeling da/dt_{II} for HEAC is complicated since H production and uptake at the crack tip are each time dependent. Wei and coworkers modeled da/dt_{II} as proportional to the rate of supply of H to the FPZ; enabled by environment-mass transport, surface reaction to produce H, and H diffusion to competing fracture sites in the FPZ (Wei, 1981; Wei and Gao, 1985; Wei and Gangloff, 1989). A major aim of this work was to develop model predictions of the effects of gas pressure, electrochemical potential, solution composition, and temperature on da/dt_{II} in high strength alloys.

Model predictions were developed for each rate limiting step (Wei, 1981; Wei and Gao, 1985). When transport of a reactant in the crack environment is slow, the near-tip chemical activity is reduced and surface reaction rate is lowered, as expected for gaseous environments at low-bulk pressure and low concentration components in an electrolyte. The resulting da/dt_{II} prediction is:

$$\left(\frac{da}{dt}\right)_{II} = \frac{C_T P_O}{\sqrt{T}}$$

(14)

When mass transport to reaction sites at the crack tip is rapid, then surface reaction rate limits da/dt_{II}, as expected for high pressure gases or electrolytes:

$$\left(\frac{da}{dt}\right)_{II} = C_S P_O^m \exp\left(\frac{-E_S}{RT}\right)$$

(15)

When H production on the crack tip surface is rapid, and in equilibrium with the bulk and local environments, H diffusion in the crack tip FPZ limits da/dt according to:

$$\left(\frac{da}{dt}\right)_{II} = C_D \sqrt{P_O} \exp\left(\frac{-E_D}{2RT}\right) \tag{16}$$

In these equations P_o is bulk pressure for a gas environment or pH-electrode potential dependent H fugacity for an electrolyte, T is temperature, E_D and E_S are activation energies for diffusion and surface reaction, respectively, and the C_I constants reflect (electro)chemical kinetics and boundary conditions. The C_I can depend on temperature, pH, electrode potential and gas pressure. This constant also reflects the local failure criterion, but this aspect of the models has not been well developed. When multiple steps limit da/dt_{II}, for example in a transition temperature or pressure regime, then more complex formulations of these equations are required as illustrated by the schematic in Fig. 47 (Wei, 1981). Here, da/dt_{II} is governed by surface reaction rate for H production at lower temperatures and hydrogen fugacities, and by H diffusion in the FPZ at higher temperatures or for more active H producing environments. The transition function (a-a) is easily derived. More than one microscopic crack path may exist, depending on H partitioning to trap sites within the FPZ, and can affect da/dt_{II} (Gao and Wei, 1985).

6.03.8.4.2.2 Rate Limiting Step Identification

The majority of the work to predict da/dt_{II} has focused on HEAC in high strength steels. The rate limiting step identifications established to date are not absolute because of modeling assumptions and unknown material-environment parameters. Modeling is complicated by uncertainties in chemical reaction kinetics pertinent to the crack tip, location of H damage between surface and bulk sites, and H diffusion in the midst of trapping.
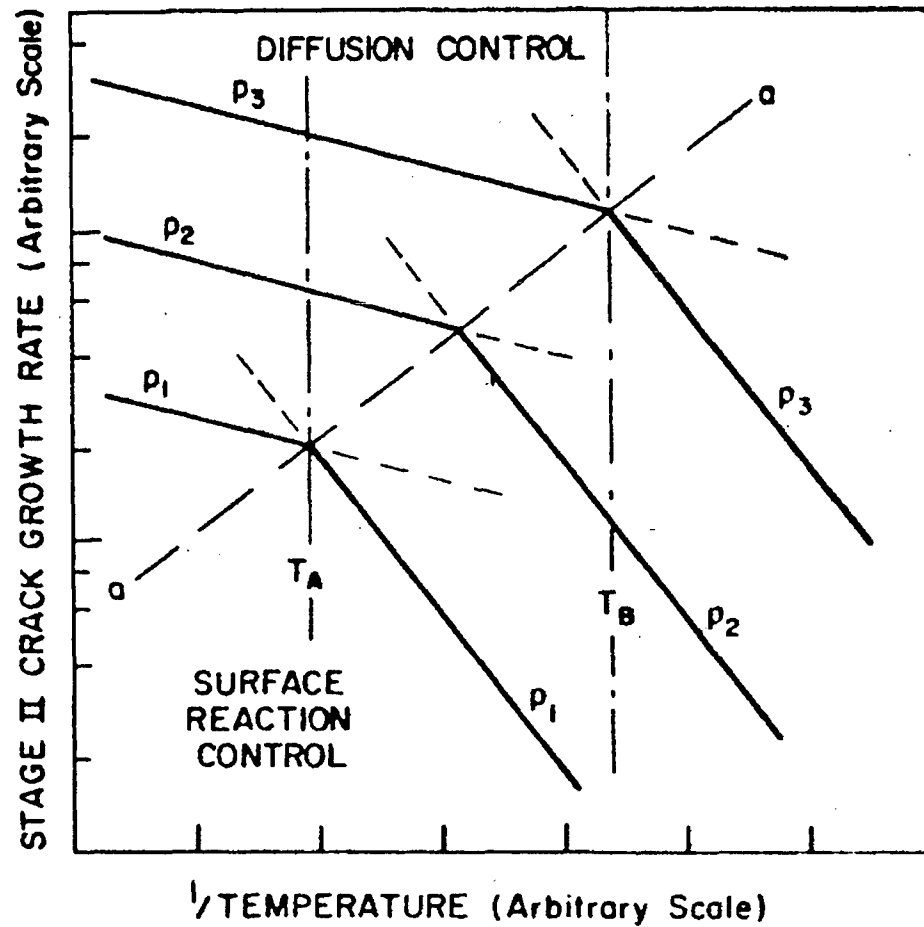
Figure 47. Schematic of the temperature and environment pressure or H fugacity dependencies of the Stage II crack growth rate for HEAC in high strength alloys, illustrating the transition from rate control by surface reaction limited H production to H diffusion in the crack tip FPZ. (Wei, 1981: Copyright The Minerals, Metals and Materials Society, reprinted with permission.)

Surface reaction has not been well integrated with H diffusion in the FPZ (Turnbull, Ferriss and Anzai, 1996). None-the-less, semiquantitative results are useful to understand variable effects and guide structural integrity analysis.

The measured temperature dependencies of da/dt_{II} in Fig. 35 and activation energies calculated from the crack growth rate data, illustrate the approach to determining the rate limiting step (Wei, 1981; Wei and Gao, 1985). These results suggest that da/dt_{II} is limited by: (a) surface reaction producing H for HEAC in distilled water, water vapor, and H_2 (curves c and d) (Simmons et al., 1978; Gao et al., 1984); (b) gas-phase transport of reactants for low pressure H_2S (curve b) (Lu et al., 1981; Gao et al., 1984), and (c) H diffusion in the FPZ for higher-pressure H_2S (curve a) (Lu et al., 1981; Gao, et al., 1984).

Substantial research focused on HEAC in H_2 and identifications of the rate limiting processes are contradictory. Several groups argue that da/dt_{II} in the thermally-activated low temperature regime is limited by surface reaction to produce H (Williams and Nelson, 1970, 1970a; Oriani et al., 1971; Nelson and Williams, 1977; Sieradzki and Ficalora, 1979a; Pasco et al., 1982, 1984; Pasco and Ficalora, 1983). Alternately, Vehoff and coworkers argue that crack tip H is in equilibrium with the surrounding H_2, with da/dt_{II} limited by short range diffusion of H from surface sites into the FPZ (Vehoff and Rothe, 1983; Vehoff and Neumann, 1985). A similar scenario was suggested to explain the low temperature behavior of 18Ni Maraging steels in Fig. 34 (Gangloff and Wei, 1977).

6.03.8.4.2.3   Surface Reaction Rate Control and Temperature Dependence

For HEAC in H_2, surface reaction and production processes for H were purported to

control da/dt$_{II}$ (Williams and Nelson, 1970, 1970a; Oriani et al., 1971; Nelson and Williams, 1977; Sieradzki and Ficalora, 1979a; Pasco and Ficalora, 1983; Pasco et al., 1982, 1984). The low temperature thermally-activated behavior of da/dt$_{II}$ was limited by dissociative chemisorption of H$_2$ to produce H on crack tip surfaces. Thermal desorption of H, as H$_2$, controlled the high temperature decline in da/dt$_{II}$; this decrease appears to be eliminated when H$_2$ was predissociated by a hot filament near the cracked specimen, supporting the importance of surface processes (Nelson, Williams and Tetelman, 1971). Pasco et al. modeled da/dt$_{II}$ as proportional to the rate of surface-H production from this reaction sequence to yield (Pasco and Ficalora, 1983):

$$\left(\frac{da}{dt}\right)_{II} = k_1 \sqrt{P_{H2}}\, exp\left[-E_E\Big/RT\right] - k_2\, exp\left[-E_D\Big/RT\right] \qquad (17)$$

where the activation energy in the first exponential term defines the kinetics of dissociation of H$_2$ to H, surface migration of H, and adsorption; while the second term defines the rate of H desorption to H$_2$. Reasonable values of constants and energies yielded predictions of both the high and low temperature HEAC kinetics for the maraging steels (e.g., Fig. 34), but not the more shallow reduction in da/dt$_{II}$ for AISI 4340 (e.g., Fig. 36) and other steels (Williams and Nelson, 1970; Nelson and Williams, 1977; Simmons et al., 1978).

An alternate explanation was put forth for elimination of HEAC in 18Ni Maraging steel (Fig. 34), where da/dt$_{II}$ decreased by orders of magnitude in response to a 2-4°C temperature increase, and increased by a like amount with the same temperature decrease (Gangloff and Wei, 1977). The P$_{H2}$ dependence of this critical temperature (T$_C$) lead to the speculation that H was adsorbed as a 2-dimensional phase that transitioned through T$_C$, and crack growth

rate followed the presence or absence of this H source (Gangloff and Wei, 1977; Chan et al., 1978). These models each suggest that the high temperature reduction in HEAC in H_2 is due to the dominance of H desorption to reduce hydrogen supply to the FPZ.

Hydrogen uptake to the FPZ should be reduced by increased H recombination at increasing temperature for HEAC in electrolytes, but the detailed kinetics are not established. The data for distilled water (Fig. 35), as well as other results discussed in 6.03.6.3.3 do not show this reduction in da/dt_{II} for temperatures up to about $100°C$ (Johnson and Willner, 1965; Van der Sluys, 1969; Speidel, 1974; McIntyre et al., 1972a), but experiments with pressurized water environments at yet higher temperatures may show this effect. An example of this behavior is shown in Fig. 36 where the Ni superalloy exhibited declining da/dt_{II} in the range from 100 to $150°C$ in pressurized-pure water (Hall and Symons, 2001). There is; however, another explanation for the decline in da/dt_{II} at these high temperatures; reduced H trapping.

6.03.8.4.2.4 Diffusion-Trapping Control and Temperature Dependence

As an alternative to surface reaction control, diffusion of H from the crack tip surface to damage sites within the FPZ has been proposed to explain temperature dependent da/dt_{II} for high strength alloys, including martensitic steels. Chen and Gerberich modeled HEAC in ferrous alloys by modifying the IHAC model described in 6.03.8.4.1.1 to include the temperature dependence of H uptake from the gas (Chen and Gerberich, 1991). The resulting expression for da/dt_{II} is:

$$\left(\frac{da}{dt}\right)_{II} = \frac{4D_{Heff}}{\chi_{CRIT}}\left\{1 - \frac{\theta_o}{\theta_T}\exp\left[\frac{\xi\,(T - T_o)}{R\,T\,T_o}\right]\right\}^2 \qquad (18)$$

The parameter, ξ, equals $(E_B + \sigma_H V_H + H_S)$ where H_S is the heat of solution for H in the lattice in equilibrium with the surrounding H_2. The term, θ_o/θ_T is the ratio of surface coverage of H at T_o and any T. This surface coverage ratio is given by a complex function of temperature involving the activation energy for desorption and H_2 pressure. This version of the model used the discrete dislocation estimate of σ_H (22 GPa for Fe-Si), while the earlier model for IHAC employed $\sigma_H \sim 2\text{-}3\sigma_{YS}$, a much lower stress (3,000 to 5,000 MPa).

Using reasonable values of the energies, Chen and Gerberich explained the two-dominant features of temperature dependent HEAC illustrated in Figs. 34 and 35. First, rising da/dt_{II} in the low temperature regime is consistent with H diffusion control and thermally activated D_{Heff}. Second, thermal detrapping of H from damage sites explains the reduction in da/dt_{II} at elevated temperatures, analogous to the temperature dependence of IHAC. This important role for thermal detrapping of H is not necessarily general as different combinations of the adsorption, solution, trapping and stress enhancement energies change the dominant term in this analysis. Clearly; however, thermal detrapping of H from damage sites is a key mechanism for elimination of both HEAC and IHAC at elevated temperatures.

Hall and Symons developed a similar model for intergranular Stage II crack growth rate in high strength austenitic superalloys stressed in high purity water (Hall and Symons, 2001). The da/dt_{II} was limited by H diffusion in the FPZ, as supplied by water oxidation of

the Ni rich crack surfaces:

$$\left(\frac{da}{dt}\right)_{II} = \frac{4D_{Heff}}{\chi_{CRIT}}\left[erf^{-1}\left(\frac{C_S - C^*(K,T)}{C_S - C_\infty}\right)\right] \approx \frac{4D_o}{\chi_{CRIT}}\left(1 - \frac{c_{gb}^*}{c_{gb}}\right)^2 \exp\left[\frac{-\Delta H_D}{RT}\right] \quad (19)$$

where $D_{Heff} = D_o \exp(-H_D/RT))$, χ_{CRIT} is the critical distance ahead of the crack tip where H damage nucleates, C_S is the amount of H produced by the oxide-metal equilibrium-H fugacity and enhanced by both σ_H and trapping, C_∞ is the H content far from the crack tip, $C^*(K,T)$ is the critical H concentration needed for grain boundary fracture, c_{gb} and c_{gb}^* are the grain boundary H contents corresponding to K levels of K_{IC} and K_{IHEAC}, respectively. The fit between measured da/dt_{II} in the low temperature regime and the predictions of this model is shown in Fig. 36. The parameters in the crack growth rate equation were taken from experimental and literature results, and the χ_{CRIT} was a fitting parameter as amplified in 6.03.8.4.2.7. The importance of H diffusivity at low temperatures and H detrapping at higher temperatures is apparent.

6.03.8.4.2.5   Rate Limitation, Trapped-H Partition and Temperature Dependence

Wei and Gao formalized the concept that, in addition to the rates of surface-H production and H diffusion in the FPZ, temperature affects H partitioning to various embrittlement (trap) sites in the microstructure (Gao and Wei, 1985). This partitioning of H is manifest by a changing crack path. In essence this model combines thermally stimulated detrapping of H with temperature dependent rate of H supply. Specifically:

$$\left(\frac{da}{dt}\right)_{II} = \left(\sum_i \alpha_i \, f_i \, \kappa_i\right)\frac{dQ}{dt} \tag{20}$$

where dQ/dt is the total rate of H supply set by the rate limiting step and supporting

chemical quantities, α_i is the constant in the assumed proportionality between H supply rate

and crack growth rate specific to the ith microscopic crack path, f_i is the area fraction of the

i[th] crack path, and κ_i gives the fraction of dQ/dt that is provided to the ith microscopic feature

as governed by H trapping at this feature. The dQ/dt follows from any of the previous

equations for a specific rate limiting processes.

This model explained the temperature dependence of da/dt$_{II}$ in high strength AISI 4340-

steel as shown in Fig. 35. For this case, the total dQ/dt partitions to three sites; prior

austenite grain boundaries, lath martensite interfaces, and the martensite lattice. However,

the amount of lath martensite H cracking was small for the data in Fig. 35. Assuming that

da/dt$_{II}$ is limited by a surface reaction for this tempered martensitic steel and low pressure H$_2$

environment:

$$\left(\frac{da}{dt}\right)_{II} = \left\{\frac{\alpha_{IG} f_{IG} \tau \delta\left(a^3/n\right) N_x \exp\left(E_B/RT\right)}{1 + \tau \delta\left(a^3/n\right) N_x \exp\left(E_B/RT\right)} + \frac{\alpha_l (1 - f_{IG})}{1 + \tau \delta\left(a^3/n\right) N_x \exp\left(E_B/RT\right)}\right\} C_S P_O^m \exp\left(-E_S/RT\right) \tag{21}$$

where δ is the volume fraction of prior austenite grain boundary, a is metal lattice parameter,

N_x is density of trap sites on austenite grain surfaces, n is number of atoms per metal-unit

cell, and τ is a parameter that describes a nonequilibrium situation in the Fermi-Dirac

description of the temperature and coverage dependence of H trap occupancy. This cracking

in AISI 4340 steel in H$_2$ was purely IG at all low temperatures where da/dt$_{II}$ increased with

increasing temperature according to an Arrhenius relationship. Here, $da/dt_{II} = \alpha_{IG}(dQ/dt)$ and the H supply rate was controlled by surface reaction (or perhaps short range H diffusion). At higher temperatures, where da/dt_{II} deviates from Arrhenius behavior and declines from a maximum, an increasing proportion of TG microvoid cracking occurs. Here, $da/dt_{II} = (\kappa_{IG}\alpha_{IG} + \kappa_{TG}\alpha_{TG})(dQ/dt)$, where κ_i gives the fraction of dQ/dt supplied to either IG or TG embrittlement sites. These H distribution coefficients are given by:

$$\kappa_{IG} = \frac{\delta C_{IG}/C_l}{1 + \delta C_{IG}/C_l} \qquad\qquad \kappa_{TG} = \frac{1}{1 + \delta C_{IG}/C_l} \qquad (22)$$

where C_{IG} is the concentration of H trapped at prior austenite grain boundaries and C_l is the concentration of H in martensite lattice sites. The equilibrium partitioning of H between austenite boundary and lattice sites is governed by the binding energy for trapping at the austenite boundary:

$$C_{IG}/C_l = \frac{\alpha_1 \exp\left(\frac{E_B}{RT}\right)}{1 + \alpha_2 \exp\left(\frac{E_B}{RT}\right)} \qquad (23)$$

where α_1 and α_2 are known constants. For a typical binding energy of H to a prior austenite grain boundary ($E_B \sim 75$ kJ/mol), C_{IG}/C_l decreases substantially with increasing temperature; κ_{TG} approaches 1 and κ_{IG} tends to 0 as C_{IG} tends to 0 due to thermal desorption. The amount of IG H cracking diminishes and TG microvoid damage is enhanced due to increasing temperature. The crack growth rate due to H embrittlement declines since the microvoid damage is presumed to be unaffected by H and α_{TG} is small to fit measured da/dt_{II}.

6.03.8.4.2.6 Vacancy-Diffusion Control and Temperature Dependence

Vogt and Speidel implemented a surface-process model of crack growth first advanced by Gavele to predict the temperature dependence of da/dt_{II} for intergranular HEAC in a 7000 series aluminum alloy stressed in aqueous chloride solution (Galvele, 1987; Vogt and Speidel, 1998). Crack advance is controlled by vacancy diffusion along the crack surface to a captured state at the tip where tension lowers the free energy of vacancy formation. Vacancies are produced by anodic corrosion and, critically for HEAC, the rate of vacancy migration is enhanced by surface-adsorbed H from cathodic reaction. The resulting prediction of growth rate is:

$$\left(\frac{da}{dt}\right)_{II} = \frac{D_S}{L}\left[\exp\frac{\left(\sigma a^3 + \alpha E_B\right)}{kT} - 1\right]$$
(24)

where D_S is surface diffusivity, L is distance between unstressed and stressed lattice, σ is the elastic stress at the crack-tip surface, a is Al atom diameter, and α is a stress dependent parameter that describes the trapping of H at vacancies with a binding energy, E_B. These parameters are uncertain for 7000 series aluminum alloys and the surface-vacancy diffusion model is generally controversial (Parkins, 1990).

The prediction of this model in Fig. 37 was fit with the experimental measurements using reasonable values for these parameters, including a crack tip stress of 500 MPa. This stress equals σ_{YS} for this alloy and is substantially lower than the elastic stress generally associated with the crack tip FPZ, but not a free surface (Fig. 44). Thermally activated D_S and increased vacancy mobility govern the general increase in da/dt_{II} with increasing temperature. The exponential term, describing the effect of stress in attracting vacancies to

the crack tip, declines as T increases. The discontinuity in the plot, and general reduction in da/dt$_{II}$ at all higher temperatures, is due to proportionately reduced H binding to vacancies between 30 and 50°C, or decreasing α, with full detrapping ($\alpha = 0$) of H from vacancies at higher temperatures.

6.03.8.4.2.7   Broad-based Growth Rate Correlation and Diffusion Control

Part of the controversy in defining the correct rate limiting step for HEAC in high strength alloys is due to the limited range of data typically examined when testing a model. A recent analysis of HEAC in a wide range of alloys stressed in electrolytes and gases provides a basis to identify the specific material and environment chemistry variables that favor H diffusion *vs.* surface reaction control of da/dt$_{II}$ (Gangloff, 2003).

The fastest rates of HEAC were obtained from recent experiments at the University of Virginia, using a common experimental method, and from literature results for high strength alloys stressed during exposure in chloride solutions. As shown in Fig. 48, these da/dt$_{II}$ are directly proportional to the best available estimate of trap affected D$_{Heff}$ based on permeation experiments. This correlation is particularly strong for the alloy steels where declining D$_{Heff}$, from 10^{-7} cm^2/s for conventional tempered martensitic steels to 10^{-8} cm^2/s for precipitation hardened AerMet®100 and 10^{-9} cm^2/s for 18Ni Maraging steels, resulted in a 2 order of magnitude reduction in da/dt$_{II}$. There are two outliers. The ASTM A723 steel (σ_{YS} = 1310 MPa) exhibits unexpectedly high da/dt$_{II}$ of 600 μm/s when stressed in pure H$_2$SO$_4$ (Troiano et al., 2002). AA7079-T6 is the only aluminum alloy that exhibits growth rates in chloride solution that exceed 0.1 μm/s, as shown in Fig. 12 (Holroyd, 1990). The causes of
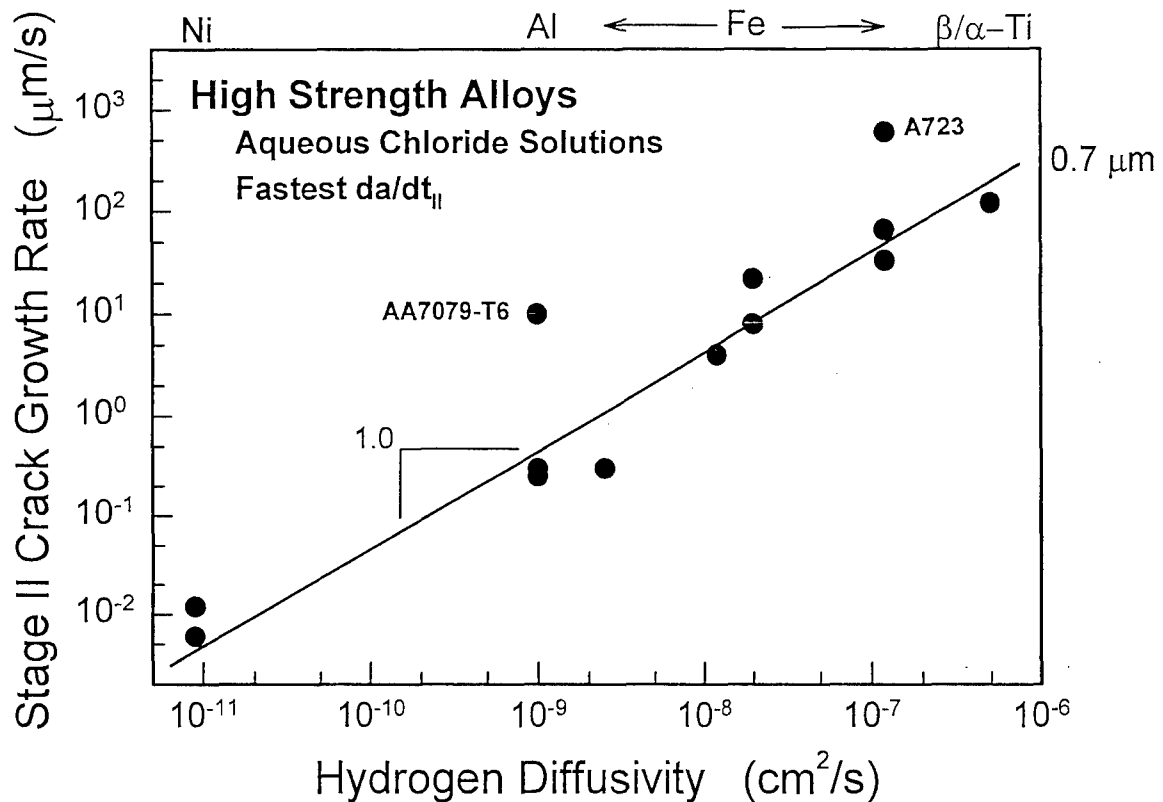
Figure 48. The dependence of the fastest-measured da/dt_{II} on effective hydrogen diffusivity, D_{Heff}, from permeation measurements for high strength alloys that exhibit HEAC in aqueous chloride solutions at 25°C. The Ni-based superalloy was cracked in NaCl that was either acidified (pH 0.3–1) or contained a H recombination poison (As_2O_3) with cathodic polarization; aluminum alloys in acidified chromate-chloride solution; steels in neutral NaCl, H_2S-bearing acidified chloride (NACE), or concentrated H_2SO_4/H_3PO_4 acid; and Ti alloys in neutral chloride solution. (Gangloff, 2003; containing references to specific data.)

these high crack growth rates are not understood.

Diffusion-based models were developed to describe da/dt_{II} for HEAC based on FPZ supply from the concentration of H on the crack tip surface and in equilibrium with the local environment (C_S) (Johnson, 1974; van Leeuwen, 1975, 1979; Doig and Jones, 1977; Chen and Gerberich, 1991; Gerberich et al., 1996; Toribio and Kharin, 1997; Krom et al., 1999; Hall and Symons, 2001; Taha and Sofronis, 2001; Yokobori et al., 2002). The da/dt_{II} is modeled as equaling the ratio of χ_{CRIT} to the time required for H to diffuse from C_S and over this distance to reach C_{CRIT}. Specific da/dt_{II} predictions from two of these models are represented by Eqs. 18 and 19 in 6.03.8.4.2.4. In general models of this type are of varying complexity depending on whether the H-diffusion field is: (a) concentration and/or stress driven, (b) transient or steady state, (c) ahead of a stationary or moving crack, (d) modeled in one or two dimensions (e) emanating from environment-sensitive C_S, (f) microstructure-trap affected, (g) plastic strain-trap affected, and (h) coupled with a H-failure criterion.

The results of diffusion modeling are of the general form:

$$\frac{da}{dt_{II}} = \frac{D_{Heff}}{\chi_{CRIT}} \left[\xi \left(\frac{C_S}{C_{CRIT}}, D_{Heff}, \chi_{CRIT}, \sigma_{YS}, t \right) \right]$$
(25)

where ξ is a function of the indicated variables and equals between 4.0 (Chen and Gerberich, 1991; Gerberich et al., 1996), 2.9 (Gerberich, 1974; Gerberich et al., 1975), 2.8 (van Leeuwen, 1979), 0.4 to 2.3 (Toribio and Kharin, 1997), and 0.01 to 0.3 (Johnson, 1974).

The observed and predicted proportionality between Stage II crack growth rate and D_{Heff} in Fig. 48 supports H-diffusion control of HEAC. An upper bound χ_{CRIT} can be determined

from these data. The highest-reasonable value of ξ is 3 and constant, provided that the

da/dt_{II} are not sensitive to C_S for the various chloride solutions and if cracking is governed

by constant C_{CRIT}/C_S of order 0.5. These assumptions result in $\chi_{CRIT} = 0.7$ μm for the trend

line in Fig. 48, independent of alloy. The smallest possible ξ is 0.03, yielding a lower bound

on χ_{CRIT} of 70 nm. The low temperature dependence of da/dt_{II} for Ni superalloy X-750

illustrated in Fig. 36 and fit with the diffusion model in Eq. 19, agrees well with the trend

line in Fig. 48, with D_H in the range from 4 x 10^{-11} to 2 x 10^{-9} cm^2/s as temperature increased

from 30 to 130°C. Equivalently, Mills and coworkers, as well as Hall and Symons noted

that the activation energy descriptive of this low temperature cracking (47.2 kJ/mol)

essentially equals the activation energy for trapping sensitive diffusion of H in X-750 (48.1

kJ/mol) (Mills et. al., 1999; Hall and Symons, 2001; Symons, 2001). This limited set of

data lead to an estimated χ_{CRIT} of 0.6 μm, and perhaps as low as 0.1 μm (Hall and Symons,

2001), consistent with the broad correlation shown in Fig. 48.

The complexity of modeling crack growth rate data for HEAC is illustrated by a

correlation of all available da/dt_{II} with D_{Heff} in Fig. 49 (Gangloff, 2003). The da/dt_{II} can be

1-3 orders of magnitude less than the upper-bound trend from Fig. 48. With $\xi = 3$, larger

apparent χ_{CRIT} (5 to 850 μm) are associated with the dashed lines for da/dt_{II} α D_{Heff}, but

these diffusion-based fits are incorrect due to three situations that reduce da/dt_{II} below the

fastest levels. These include: (1) reduced-equilibrium C_S due to environment chemistry

factors, (2) strength or metallurgy effects on C_{CRIT}, and (3) the intervention of environmental

mass transport or surface reaction rate control that reduces H concentration to below the
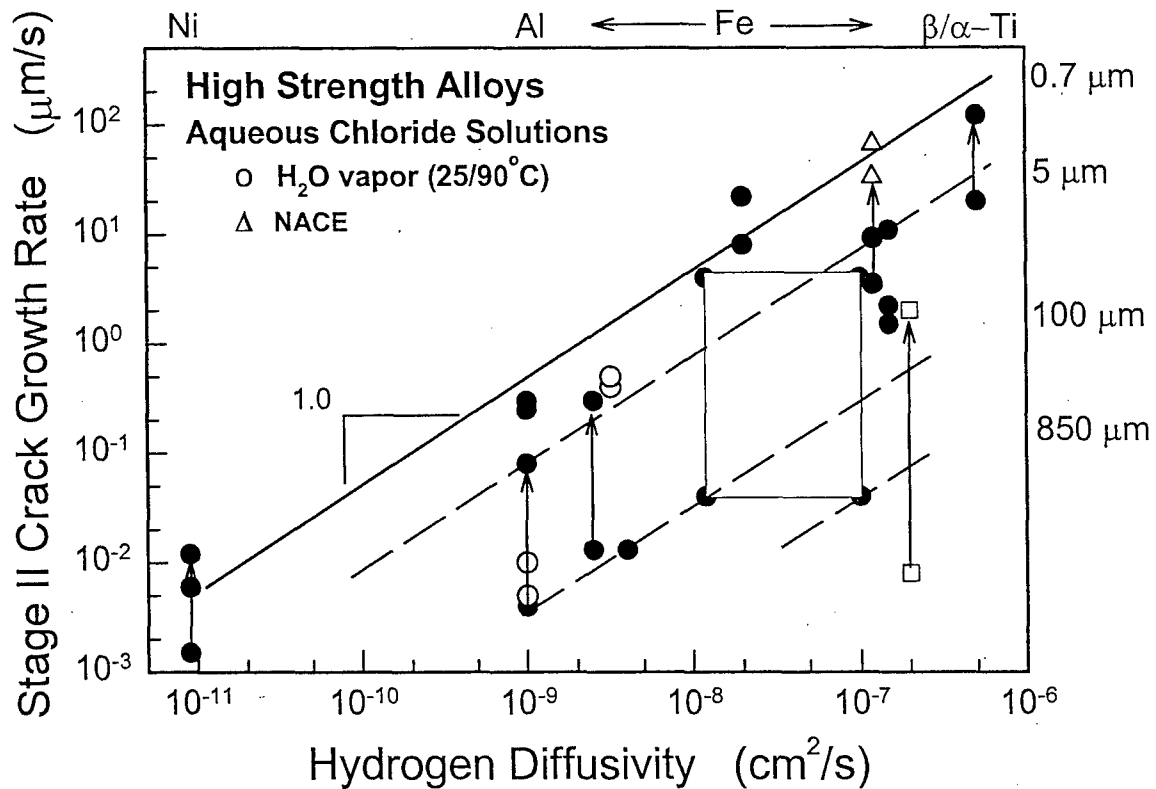
Figure 49. The dependence of da/dt$_{II}$ on D$_{Heff}$ for high strength alloys that exhibit HEAC in various chloride solutions at 25°C. The vertical arrows represent the range of growth rates reported for a given material and in response to electrochemical or metallurgical variables. The increases in da/dt$_{II}$ for IN718 (D$_{Heff}$ ~ 10^{-11} cm^2/s) and AA7050 (1-4 x 10^{-9} cm^2/s) were produced by changing-applied electrode potential; for the 18Ni Maraging steel (2-5 x 10^{-9} cm^2/s) due to steel composition and strength change from the 250 to 350 grades; for 4340-type steels (10^{-8} to 10^{-7} cm^2/s) due to chemistry and metallurgical changes (boxed area) or sulfide addition to the chloride solution (Δ), for Ni-Cr-Mo ASTM A723 steel (10^{-7} cm^2/s) due to increasing σ$_{YS}$ from 1150 to 1380 MPa (□), and for β-Ti alloys (5 x 10^{-7} cm^2/s) due to crack tip strain rate increase. (Gangloff, 2003; containing references to specific data)

equilibrium C_S. Essentially, ξ depends on C_S and C_{CRIT}, and is reduced below 3.

As an example, consider the large amount of data for steels ($10^{-8} < D_{Heff} < 10^{-7}$ cm^2/s) cracked in neutral NaCl solution at the free corrosion potential. Electrochemical conditions (e.g., cathodic polarization) that increase C_S will increase da/dt$_{II}$ toward the upper bound line. This is supported by data for high strength AISI 4340-type steel cracked in neutral NaCl solution ($\bullet$ at $D_{Heff} = 1.0$-1.2×10^{-7} cm^2/s) and H$_2$S-saturated acidified chloride (NACE solution, Δ). A second example is provided for ASTM A723 ($\square$ in Fig. 49), where the vertical arrow shows increasing da/dt$_{II}$ for σ_{YS} from 1150 to 1380 MPa and HEAC in NaCl solution. This adverse effect of strength on da/dt$_{II}$ is due to increasing crack tip stress, proportionate to σ_{YS} for a given K and achieving the H-failure condition at reduced C_{CRIT}. Reduced C_{CRIT} results in increased ξ and da/dt$_{II}$ at fixed C_S.

Hydrogen diffusion control of HEAC is further established by correlating D_{Heff} with da/dt$_{II}$ for IG cracking of high strength alloys in gaseous H$_2$ and H$_2$S environments at 23°C, Fig. 50 (Gangloff, 2003). The fastest Stage II crack growth rates in H$_2$ and H$_2$S are proportional to D_{Heff}, paralleling the correlation from Fig. 48 for chloride solutions and suggesting that H diffusion limits crack growth. The results for AISI 4340-type steels at high D_{Heff} ($\square$, 1.5×10^{-7} cm^2/s), and 18Ni Maraging steels ($\square$, 2.5×10^{-9} cm^2/s), are consistent with C_S reduced by low P_{H2} at equilibrium, or surface reaction limitation (Gangloff and Wei, 1977; Wei, 1981; Wei and Gao, 1985). The vertical arrows in Fig. 50 reflect increasing hydrogen pressure and hence C_S. While the alloy steels have not been studied in high pressure H$_2$, faster da/dt$_{II}$ were reported for HEAC in H$_2$S (Δ in Fig. 50) where surface reaction is not likely to limit da/dt$_{II}$ and efficient-H uptake leads to a high-
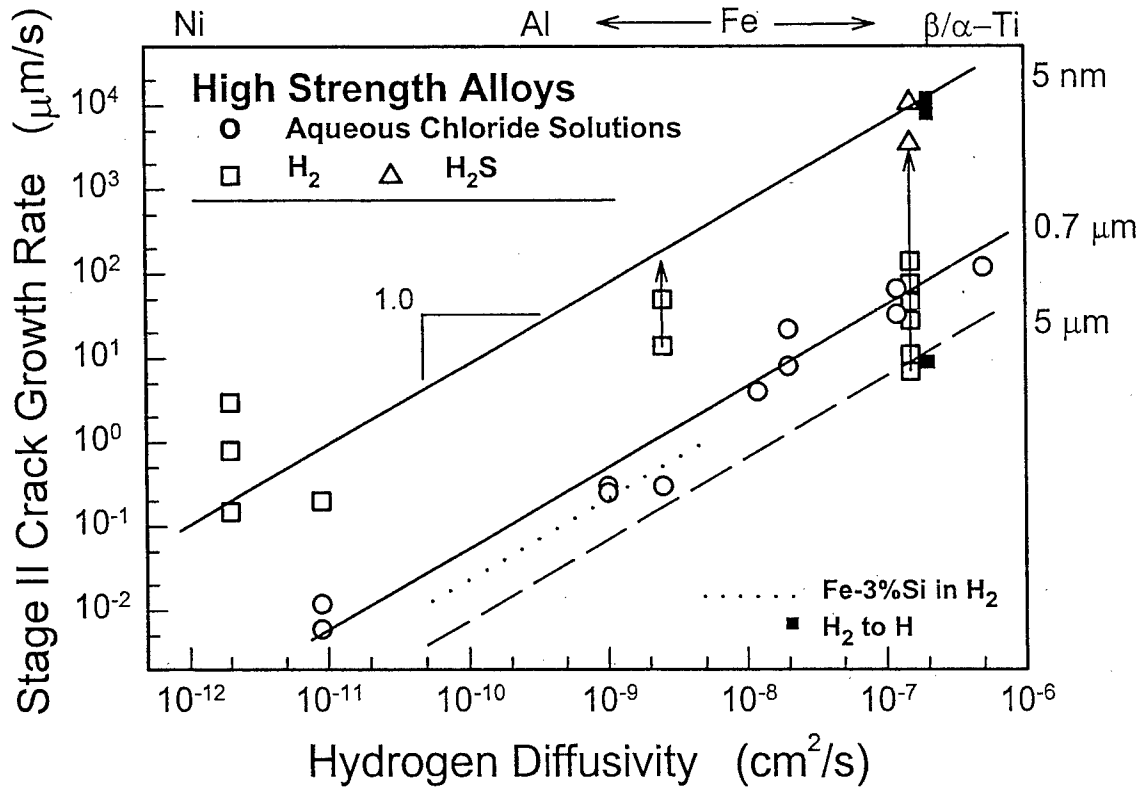
Figure 50 The dependence of da/dt_{II} on D_{Heff} for high strength alloys that exhibit HEAC in gases and electrolytes at $25^{\circ}C$. High strength austenitic stainless steel and nickel superalloys were cracked in high pressure (100–200 MPa) H_2, while maraging and tempered-martensitic steels were cracked in low pressure (~100 kPa) H_2. The dotted line represents TG cracking of Fe-3%Si single crystal in 100 kPa H_2 at $0^{\circ}C$ to $125^{\circ}C$. Filled symbols (◻) represent the transition from molecular to atomic hydrogen gas. (Gangloff, 2003; containing references to specific data)

equilibrium C_S. Support for this argument is provided by da/dt_{II} data reported for AISI 4130 steel tested in either low pressure H_2 (lowest $\square$ at $D_{Heff} = 2.0 \times 10^{-7} cm^2/s$) or thermally dissociated H (highest two values of da/dt_{II}, $\square$) (Nelson, Williams and Tetelman, 1971).

An extremely low critical distance, $\chi_{CRIT} = 5$ nm, is suggested for the H-producing gases based on the diffusion analysis of the trend line using $\xi = 3$. This distance is 150 times lower than the value calculated for the upper bound for the electrolytes, contradicting the notion that χ_{CRIT} should be independent of environment and C_S. The correlations in Fig. 50 suggest an intriguing possibility. Corrosion could produce a high concentration of vacancies localized to within a short distance of the crack-tip surface (Magnin et al., 1990; Jones et al., 1997). Highly mobile H is trapped at vacancies or vacancy clusters that are not annihilated by self-diffusion (Hirth, 1980; Pressouyre, 1980), suggesting that H transport in this near-surface layer is characterized by a reduced D_{Heff}. The correlations in Fig. 50 show that D_{Heff} must be reduced 200-fold to superpose the gas and electrolyte data.

6.03.8.4.3   Location of H Damage Sites in FPZ

A consensus is emerging that χ_{CRIT} is small for HEAC in high strength alloys. Supporting evidence includes: (1) H-diffusion correlations in Figs. 48-50 suggest χ_{CRIT} between 50 nm and 1 µm, (b) acoustic emission and crack-surface arrest markings suggest $\chi_{CRIT} < 1$ µm (Chen and Gerberich, 1991), (c) rapid changes in da/dt with changing H_2 pressure (Oriani and Josephic, 1974, 1977; Vehoff and Rothe, 1983) or temperature (Gangloff and Wei, 1977) suggest $\chi_{CRIT} < 0.1$ to 1 µm, (d) surface reaction-limiting models describe da/dt_{II} (Williams and Nelson, 1970, 1970a; Nelson, Williams and Tetelman, 1971;

Nelson and Williams, 1977; Pasco et al., 1982, 1984; Vehoff and Rothe, 1983; Pasco and Ficalora, 1983; Vehoff and Neumann, 1985), hence the process zone must be near to the crack tip to enable non-limiting H diffusion, (e) the temperature dependence of da/dt_{II} for HEAC of high strength steels cracked in H_2 is described by a H-diffusion model with χ_{CRIT} from 50 to 400 nm (Gerberich, Livne and Chen, 1986), and (f) the independence of K_{IH} on applied dK/dt is consistent with $\chi_{CRIT} < 1$ μm for X-750 in H_2 (Symons, 2001) and two β/α-Ti alloys cracked in NaCl (Fig. 6) (Somerday, Young and Gangloff, 2000).

A sub-μm process zone is consistent with three aspects of the crack tip FPZ that are only recently appreciated. First, crack chemistry considerations and direct measurements by nuclear reaction analysis and thermal desorption spectroscopy demonstrate that H is concentrated to unexpectedly high levels (0.01 to 0.1 atom pct) on the crack tip surface in contact with the occluded crack electrolyte, at least for a 7000 series aluminum alloy in chloride solution (L.M. Young, 1999; Cooper et al., 2000; Cooper and Kelly, 2001). This H accumulation may be stabilized by near-surface vacancies from dissolution and degrade the fracture resistance of the alloy in this region within 1 μm of the crack surface. Unfortunately, such measurements are complex and limited; this perspective is presently speculative.

Second, modern dislocation and strain gradient plasticity models of the crack tip demonstrate that extremely high stresses are localized within 20 nm to several micrometers of the crack tip surface (Fig. 44 and 6.03.8.1). The existence of these high stresses is consistent with experimental observations of very sharp and small-opening crack tips produced under H-embrittlement conditions, as opposed to crack blunting considerations

(Vehoff and Rothe, 1983; Vehoff and Neumann; Somerday et al., 2000). High crack tip stress exacerbates HEAC by promoting high levels of H accumulation through lattice dilation and associated H trapping (Thomas et al., 2003) and results in damage at lower C_{CRIT}. Finally, modeling shows that H is trapped by the high density of dislocations that are produced by plastic deformation immediately adjacent to the crack tip surface (Krom et al., 1999; Taha and Sofronis, 2001). If this H participates in damage and crack extension, then a small χ_{CRIT} is reasonable.

Lynch argued that fast crack growth rates can only be explained by AIDE focused on the crack surface (Lynch, 1988, 1997, 2003). HEDE-based models reasonably describe da/dt_{II} levels up to 10,000 μm/s (Fig. 50), given the evidence that χ_{CRIT} is small. Unexpectedly large levels of H accumulated in this region provide a compelling reason to accept HEDE.

6.03.9   UNCERTAINTIES AND NEEDS

Substantial successes have been recorded in developing the fracture mechanics framework, laboratory data on the properties of materials, and fundamental-mechanistic understanding necessary to quantitatively describe subcritical H-cracking in structural integrity modeling involving high strength alloys. However, substantial uncertainties exist.

6.03.9.1   Fracture Mechanics Issues
6.03.9.1.1   Specimen Constraint

Specimen size, particularly thickness for a Mode I through crack, is a variable that affects hydrogen cracking by both mechanical constraint and chemical mechanisms. Constraint results in increased crack tip opening-direction and hydrostatic stresses for a

crack tip plastic zone and FPZ governed by either conventional J_2 plasticity or length-scale dominant plasticity (Fig. 44) (Anderson, 1995; Needleman and Sevillano, 2003). This higher crack tip stress environment exacerbates H cracking, in terms of lowered K_{TH} and increased da/dt_{II}, as suggested by each of the micromechanical models summarized in 6.03.8.

Specimen size and geometry can affect crack tip H concentration, and hence K_{TH} and da/dt. For IHAC, a through-thickness gradient in H concentration from insufficient precharging exposure results in raised threshold and lowered crack growth rate (Thomas, et al., 2003). For HEAC, K_{IHEAC} decreases with decreasing thickness, counter to a constraint effect and traced to increasing amount of H distributed about the crack tip FPZ from environmental reaction (Fujii, 1976; Kobayashi and Takeshi, 1985). This effect depends on the relative amounts of H provided by reactions at boldly exposed surfaces *vs.* the crack tip, as governed by the electrochemical considerations detailed in 6.03.6.3.2 and 6.03.7.1.2 (Turnbull and Saenz de Santa Maria, 1990); generalization is not possible.

Only limited guidance is available to guarantee small-scale yielding and quantify mechanical constraint for laboratory testing that yields K_{IHEAC} and da/dt under quasi-static loading (ASTM, 2000). This standard requires that the plane strain thickness criterion determined empirically from fracture toughness experiments be satisfied so that the environmental cracking threshold is certified as a plane strain value. There are no data to support that this criterion ensures a specimen-thickness independent and lower-bound threshold for hydrogen cracking (Barsom and Rolfe, 1987). Furthermore, the geometry necessary for size independent measurement of K_{IH} under rising load is not known. Crack

tip constraint is high in laboratory specimens of high strength alloys at the low K levels that cause IHAC and HEAC. As such, size dependent chemical effects on H distribution about the crack tip are likely to be most important in structural integrity modeling.

6.03.9.1.2   Small Crack Size

Small crack size could invalidate stress intensity similitude due to mechanical or chemical mechanisms (Clark, 1976). The hypothesis that the threshold for H cracking depends on crack size was demonstrated experimentally for high strength AISI 4130 steel stressed in NaCl solution. The measured K_{TH} was constant at 20 ± 5 MPa$\sqrt{m}$ for crack depths between 1 and 20 mm, but declined to 8 MPa$\sqrt{m}$ for short cracks sized below 1 mm, as shown in Fig. 39 (Gangloff, 1985; Gangloff and Turnbull, 1986). This effect was explained based on a 10-fold increase in the H production rate at the crack tip, as crack size declined from 20 to 0.3 mm, and modeled based on the role of crack geometry in setting the occluded crack tip electrochemistry that established the level of H production. Similar effects were reported for other high strength alloys, but data and crack chemistry modeling are limited (Gangloff and Wei, 1986).

6.03.9.1.3   Precrack Path

Precrack path could affect subsequent H cracking kinetics, but data showing this behavior are limited. Conceptually, a precrack tip located apart from the H-susceptible crack path in the microstructure could exhibit a different K_{TH} and early growth kinetics compared to a starting crack located along the H-sensitive path. A recent study of HEAC in

high strength β-Ti showed that cracking during fixed-CMOD loading in chloride solution occurred when the precrack was transgranular, as produced by fatigue (Somerday, et al., 2000). Hydrogen cracking did not occur for the same solution and applied K level when the precrack was intergranular, produced by prior HEAC. This behavior was ascribed speculatively to the effect of crack tip path and morphology on crack tip strain and strain rate, that in turn influenced the stability of a crack tip passive film that blocked the uptake of H. Similar studies have not been reported for steels and aluminum alloys.

6.03.9.1.4   Mixed Mode Hydrogen Assisted Cracking

Mixed mode hydrogen cracking in high strength alloys has received substantially less attention than the Mode I case. Several studies showed that HEAC was substantial for high strength steel, aluminum and α-based titanium alloys under Mode I, but not resolved under pure Mode III loading (Hayden and Floreen, 1971; St. John et al., 1973; Swanson, et al., 1981; Pickens et al., 1983). In contrast other studies showed that H promoted subcritical crack growth for IHAC and HEAC in high strength steels under simple Mode III loading (Chu et al., 1986; Gao and Cao, 1998), as well as pure Mode II loading (McGuinn and Aballe, 1982; Gao and Cao, 1998). In these cases the threshold for H cracking was equal to the low level measured for Mode I. Results for mixed mode cracking typically show that the addition of a Mode II component to Mode I loading reduces the severity of IHAC and HEAC (Gao and Xue, 1989; Ohsaki et al., 1997; Gao and Cao, 1998). A specific example of these trends is presented in Fig. 51 for both IHAC and HEAC of martensitic steel.
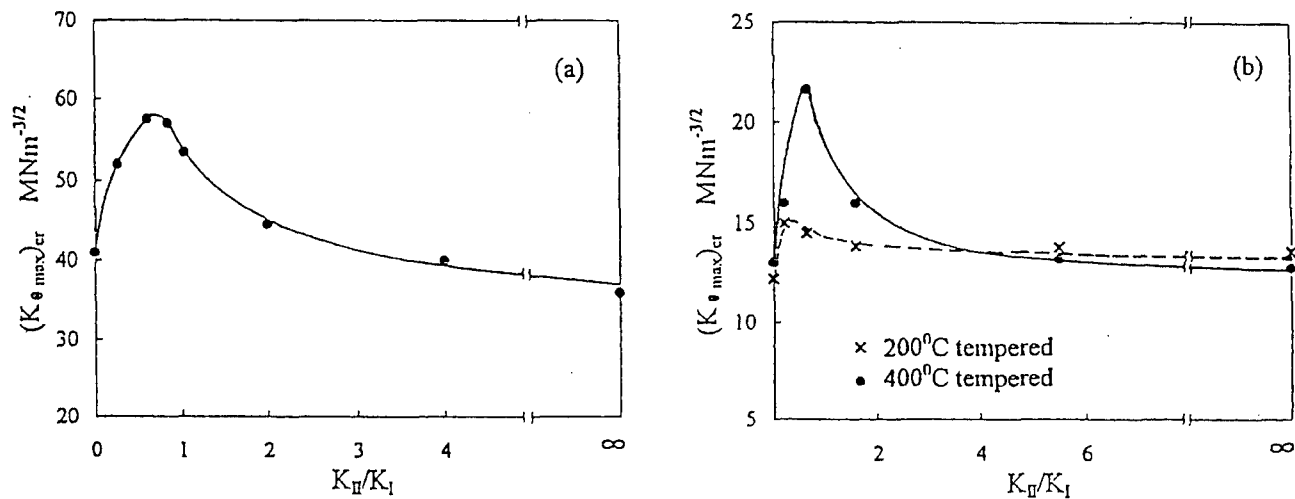
Figure 51. The effect of loading mode, represented as the ratio of applied K_{II}/K_I, on the threshold stress intensity for: (a) IHAC and (b) HEAC of high strength low alloy steel ($1300 < \sigma_{YS} < 1600$ MPa) in H_2SO_4. $K_{\theta max}$ represents a trigonometric combination of K_I and K_{II}, and H cracking was always in the plane normal to the maximum crack tip tensile stress from elastic analysis. (Gao and Cao, 1998: Copyright *Fatigue and Fracture of Engineering Materials and Structures*, reprinted with permission.)

These complex effects of loading mode are explained qualitatively by the interaction of H in the FPZ with two aspects of crack tip mechanics that depend on loading mode; hydrostatic tensile stress and plastic strain/dislocation density as summarized in 6.03.8.1. Hydrostatic stress enhanced H accumulation and damage is optimized for pure Mode I, but is none-the-less present at reduced levels for Modes II and III (Nichols, 1983; Zang and Hack, 1999; Jones et al., 2000). The detrimental plasticity effect on H accumulation increases with increasing amounts of Mode II or III loading over Mode I. Additionally, plastic flow is localized by Mode III loading and can in some instances exacerbate H damage (Kumar et al., 1993). To further complicate the situation, theory and experiment suggest that the effect of Mode II addition to Mode I depends on the loading format, be it constant load or rising CMOD (Gao and Cao, 1998). The implication to structural integrity modeling is clear; Mode I cannot be assumed to be the most damaging from the hydrogen cracking perspective and mixed-mode loading must be considered. New laboratory experimentation will be required to support such life prediction.

6.03.9.1.5   Transient Exposure

Transient mechanical and chemical effects are likely present in component service, and present a formidable challenge to structural integrity modeling. Reduced H cracking due to prestressing or overloading of a precracked specimen, as well as prolonged incubation prior to crack propagation at K levels above K_{TH}, were demonstrated for laboratory specimens as discussed in 6.03.3.5.1 (Wei et al., 1972; Jonas, 1973; Hudak and Wei, 1981). Of equal importance, alternating environmental exposure likely affects crack chemistry and the

resulting H production plus uptake. An example is atmospheric exposure involving a thin-layer electrolyte where ohmic voltage drop within the crack should be increased while occluded chemistry changes may be muted. For this case, as well as alternate immersion in an electrolyte, anodic and cathodic reactions are forced to occur largely within the crack. Lack of separation of anode and cathode sites should reduce acidification, and thus affect H uptake at the crack tip. Finally, drying could form condensed and concentrated corrosion products that rehydrate into a more aggressive state when rewet. There have been no systematic laboratory studies of these speculative effects on HEAC.

6.03.9.1.6 Interacting Cracks

A distribution of interacting cracks confounds structural integrity modeling (Parkins, 1990). Research to date on hydrogen cracking has almost exclusively examined the behavior of a single Mode I crack in high strength alloys, following the classic fracture mechanics approach. Studies in the peripheral areas of environment-sensitive fatigue in precipitation hardened aluminum alloys (Harlow and Wei, 2001, 2001a, 2002), stress corrosion cracking in low strength pipeline steels (Parkins, 1991; Leis and Parkins, 1998), and hydrogen induced stepwise cracking in low strength C-Mn steels in sour-environment service (Iino, 1979; Suarez, et al., 2000) demonstrate the challenges associated with understanding the formation and coalescence of multiple cracks. Unique crack electrochemistry effects, accurate stress intensity solutions, and reexamination of K as the proper crack tip driving force are challenging issues.

6.03.9.1.7   Distribution of Material Cracking Properties

Distribution of material properties and the associated statistical description are essential to structural integrity modeling, particularly with probabilistic analysis. Variability in the threshold and kinetics of IHAC and HEAC results from measurement errors in laboratory experiments (Wei and Novak, 1987) as well as the distribution of intrinsic variables such as grain boundary purity.

The complexity and duration of hydrogen cracking experiments has limited determinations of distributions of K_{TH} and da/dt measurements for a specific material-environment situation. The many possible variables (6.03.6) and measurement issues are too numerous to permit either precise definition of laboratory precision or intrinsic material variability (ASTM, 2000). Two interlaboratory studies indicate the magnitude of variability for two lots of high strength steel in chloride solution. The K_{IHEAC} of 34.5 MPa√m varied by ±17% for 4000 h duration experiments conducted by 8 laboratories (Wei and Novak, 1987), and the K_{IHEAC} of 28.9 MPa√m varied by ±19% based on data from 6 laboratories, all employing a similar experimental protocol (Yokobori, et al., 1988). This level of uncertainty should be viewed as typical of best effort by an experienced laboratory, with larger errors possible given the difficulty of long term chemical environment control. No study has reported on heat-to-heat threshold variability for a given alloy. Variations in crack growth rates have not been reported and are likely to be substantial, a factor of 2 to10. Figure 12 provides an example of multiple specimen variability in da/dt that likely represents the best-achievable agreement between experiments.

6.03.9.2   Research Needs

The discussions of fundamental H cracking mechanisms in 6.03.7 and micromechanical-chemical models of H cracking thresholds and kinetics in 6.03.8 demonstrate substantial uncertainties in the understanding of HEAC and IHAC. The majority of these issues are traced to the complexity and highly localized character of H production, uptake and damage about the very small crack tip process zone. Advances in each of the following four areas will improve the capability for next generation structural integrity modeling.

6.03.9.2.1   Hydrogen Damage Mechanism

While the decohesion mechanism is favored by many to explain H cracking in high strength alloys, this effect has never been demonstrated directly. The last review of HEDE by Oriani is timely, with no substantial results or approaches recorded in the interim (Oriani, 1990; McMahon, 2001; Katz et al., 2001). First principles modeling of the effect of H on bond cohesion, as well as the implications for both sequential (slip) and sympathetic (fracture) bond breaking, continues to be an obvious need. Additionally, micromechanical-chemical models of macroscopic cracking properties must be formulated, stemming from the H-enhanced plasticity mechanisms, AIDE and HELP, when operative.

6.03.9.2.2   Crack Chemistry and H Production

While the framework exists for modeling occluded-crack chemistry and electrochemistry (Wei, 1981; Wei and Gangloff, 1989; Turnbull, 2001), specific information on transport and reaction rates is lacking. For example, it is important to determine H production kinetics for

multi-component and multi-phase metal surfaces exposed to hydrogen bearing gases and aqueous electrolytes while under stress and plastic deformation (Pasco and Ficalora, 1983). The compositions of these environments must be selected carefully to simulate the actual conditions affecting crack tip reaction sites. Second, it is important to integrate recent crack mass transport and reaction models with a quantitative description of H diffusion in the crack tip FPZ (Turnbull, 1996).

To calibrate and validate crack chemistry modeling, it is necessary to measure H content local to the crack tip FPZ. While a suite of methods exists to measure H in metals (e.g., Sakurai and Pickering, 1982; Birnbaum et al., 1982; Myers et al., 1985), local H contents are elusive due to the small and gradated scale of the FPZ and mobility of H. Success with thermal desorption spectroscopy (Fig. 40) and neutron reaction analysis of crack wake specimens should be confirmed and developed (Young, 1999; Cooper, et al., 2000).

6.03.9.2.3   Crack Tip Mechanics

The discussion in 6.03.8.1 establishes substantial progress in modeling crack tip stress and strain. Conventional plasticity theory that enabled ductile fracture modeling (Anderson, 1995), must be modified to properly reflect the steep gradient and small-process zone size typical of H cracking in high strength alloys (Hutchinson, 2000; Needleman and Sevillano, 2003). The resulting constitutive description should be incorporated into a high resolution finite element analysis of the crack tip region. The characteristic-material length should be defined and explained physically for high strength microstructures). Following this work, crack tip strain rate should be better quantified, particularly for the crack surface where film

destabilization by plastic strain is a critical aspect of HEAC (Somerday, et al., 2000).

Experimental results are required to calibrate and confirm crack mechanics modeling. For example, transmission electron microscope determination of crack tip dislocation structures is limited due to the small size of the FPZ and complex microstructures typical of high strength alloys. Results are necessary to guide formulations of dislocation-based descriptions of crack tip stress (Kameda, 1986a; Gerberich et al., 1991; Gerberich et al., 1996; Katz et al., 2001), and confirm the validity of AIDE and HELP (Lynch, 2003). Measurement of crack tip strain has been limited for H cracking in high strength alloys compared to the extensive *in situ* scanning electron microscope studies of fatigue crack tips in a variety of alloys (Davidson and Lankford, 1983, 1992). Application of this method used the environmental scanning electron microscope to examine the effect of H_2 and H_2O on crack-tip opening in AISI 4340 steel (σ_{YS} = 1670 MPa) with a fine (3-5 μm) prior austenite grain size (Kinaev et al., 1999, 1999a, 1999b). Measured crack tip strains were increased by H from each environment, compared to those recorded for loading to the same remote K level (15-35 MPa$\sqrt{m}$) in vacuum. Additionally, creep at 23°C was stimulated and the plastic zone shape was altered by environment compared to vacuum. These results were interpreted to support the HELP mechanism (6.03.7.2.2). The resolution of this method was ~1 μm, sufficient to detect environment-sensitive changes in crack tip opening and plastic zone size on the specimen surface, but large compared to the sub-micrometer critical distance that likely controls HEAC in high strength alloys (6.03.8.4.3). It is important to extend this experimental approach to improve resolution and include other materials and environments.

6.03.9.2.4   Hydrogen Trapping

Hydrogen trapping is centrally important to cracking in high strength alloys (6.03.6.3.1). The need is to better determine H-binding energies for each of the trap states encountered in a high strength alloy microstructure. This identification is complex and often non-unique due to uncertainties in trap characteristics (Thomas, et al., 2002). Modeling of temperature-dependent H diffusion through a forest of multiple trap states, surrounding and included within the crack tip FPZ, is needed. Much of the work to date, including the modeling and correlations in 6.03.8.4, was based on effective-H diffusivity. A fundamental treatment employs lattice-H diffusivity coupled with Fick's laws modified to include rates of trapping and detrapping from multiple binding-energy states (Oriani, 1970; Griffiths and Turnbull, 1995; Krom et al., 1999; Taha and Sofronis, 2001; Moody et al., 2001).

6.03.10   CONCLUSIONS

➤ Hydrogen from a variety of sources substantially degrades the subcritical crack growth resistance of most advanced high strength metallic alloys at threshold stress intensity levels as low as 5 to 25% of the plane strain fracture toughness and crack growth rates as high as 10,000 μm/s. Hydrogen assisted cracking is either intergranular or transgranular, with each sufficiently distinct to enable failure analysis.

➤ While metallurgical advances have resulted in high performance materials with outstanding strength and fracture toughness, the lack of H-cracking immune alloys in the iron, nickel, titanium and aluminum classes requires that structural integrity modeling of fracture critical components consider subcritical hydrogen embrittlement.

➤ Modern fracture mechanics methods provide the framework for structural integrity modeling to combat H-assisted cracking, following the damage tolerant procedures developed broadly for fatigue crack propagation-life prediction.

➤ Effective laboratory methods exist to determine the threshold and kinetics properties for both Internal Hydrogen Assisted Cracking and Hydrogen Environment Assisted Cracking in high strength alloys. These methods are complex and often require prolonged environmental exposure, but have been employed successfully to develop substantial K_{TH} and da/dt data relevant to structural integrity modeling.

➤ A wide range of metallurgical, mechanical, and environment chemistry variables affect IHAC and HEAC in high strength alloys. Alloy strength, grain size, purity, and 2nd phase characteristics; stress intensity level and application rate, small crack size, constraint, loading mode, and load transients; predissolved hydrogen content, surrounding gas pressure, electrode potential, solution pH, environment composition, and temperature; interact to affect K_{TH} and da/dt. The effects of these variables must be considered in structural integrity modeling.

➤ IHAC and HEAC are eliminated by decreasing and increasing temperature from near-ambient levels. The temperature range where H-cracking is severe depends on alloy strength and crack tip H concentration. This temperature dependence is traced to limited H diffusion to the FPZ at low temperature and reduced H supply at elevated temperature. Regarding supply, thermally stimulated desorption of H from the adsorbed state on the crack surface is important for HEAC. Thermal detrapping of H from low-binding energy traps that constitute the embrittlement path is important for IHAC and HEAC.

➤ Important albeit circumstantial evidence establishes that HEAC provides the dominant contribution to stress corrosion cracking in high strength alloys stressed in moist gases

and aqueous electrolytes near ambient temperature. Extensive threshold and Stage II crack growth rate data are correlated with the amount of H absorbed on the crack tip surface and transported into the fracture process zone, as established semi-quantitatively by crack electrochemistry measurements and modeling.

➤ The consensus is emerging that hydrogen enhanced decohesion is the basic damage mechanism for IHAC and HEAC in high strength alloys. This view is dictated by the high accumulation of H, local to the crack tip FPZ and driven by the concentrating effects of high tensile stress coupled with H trapping at microstructural features. Between the competing H-enhanced decohesion and H-localized plasticity concepts, only decohesion has been developed into models capable of predicting macroscopic hydrogen cracking properties relevant to structural integrity modeling.

➤ Micromechanical-chemical models have been developed to predict the quasi-equilibrium threshold stress intensity, as well as Stage II subcritical crack growth rate for both IHAC and HEAC in high strength alloys. These models contain adjustable constants that hinder quantitative predictions, but are useful to guide extrapolations of limited laboratory data and explain the influences of important variables.

➤ Fundamental understanding of H cracking is limited by the highly localized and gradated nature of crack tip H production and trapping, tensile stress and plastic strain, and H damage in high strength alloys. Nano-scale atomistic processes dominate material degradation within a micrometer-scale fracture process zone, leading to millimeter-scale crack growth. Future research on IHAC and HEAC must better integrate such behavior across these length scales.

➤ Uncertainties confound implementation of the capability to manage H cracking in a comprehensive structural integrity plan. Descriptions of interacting cracks, mixed mode loading, transient load and environment exposure, and the statistics of cracking

properties are in an infant state. Mechanistic understanding and associated micromechanical models are insufficient to predict quantitative algorithms for K_{TH} and da/dt_{II}.

6.03.11 ACKNOWLEDGEMENT

6.03.12 REFERENCES

K.N. Akhurst and T.J. Baker, The threshold stress intensity for hydrogen induced crack growth. *Metall. Trans. A*, **12A**, 1981, 1059-1070.

J. Albrecht, B.J. McTiernan, I.M. Bernstein and A.W. Thompson, Hydrogen embrittlement in a high-strength Al alloy. *Scripta Metall.*, **11**, 1977, 893-897.

J. Albrecht, A.W. Thompson and I.M. Bernstein, The role of microstructure in hydrogen-assisted fracture of 7075 aluminum. *Metall. Trans. A*, **10A**, 1979, 1759-1766.

J. Albrecht, A.W. Thompson and I.M. Bernstein, Evidence for dislocation transport of hydrogen in aluminum. *Metall. Trans. A*, **13A**, 1982, 811-820.

G. Alefeld and J. Völkl. Eds., "Hydrogen in Metals," Springer-Verlag, Berlin, Germany, 1978.

G. Alefeld and J. Völkl, Eds., "Hydrogen in Metals III: Properties and Applications," Springer-Verlag, Berlin, Germany, 1997.

T.L. Anderson, "Fracture Mechanics: Fundamentals and Applications," 2nd Ed., CRC Press, Boca Raton, FL, 1995, pp. 117-181.

ASM International, "Metals Handbook Ninth Edition: Vol.8, Mechanical Testing", Materials Park, OH, 1985.

ASTM, "Standard Test Method for Determining a Threshold Stress Intensity Factor for Environment-Assisted Cracking of Metallic Materials," Designation E1681-99, *Standards on Disc*, Vol. 03.01, ASTM International, West Conshohocken, PA, 2000.

P. Azou, Ed., "Third International Congress on Hydrogen and Materials," Pergamon Press, New York, NY, 1982.

Robert Baboian, Ed., "Corrosion Tests and Standards," ASTM International, West Conshohocken, PA, 1995.

R.G. Baggerly, Hydrogen-assisted stress cracking of high-strength wheel bolts. *Engr. Fail. Anal.*, 3, 1996, 231-240.

N. Bandyopadhyay, J. Kameda, and C.J. McMahon, Jr., Hydrogen-induced cracking in 4340-type steel: Effects of composition, yield strength and hydrogen pressure. *Metall. Trans. A*, 14A, 1983, 881-888.

J.M. Barsom and S.T. Rolfe, "Fracture and Fatigue Control in Structures," 2nd Ed., Prentice-Hall, Englewood Cliffs, NJ, 1987.

J.M. Barsom, "Fracture Mechanics Retrospective: *Early Classic Papers (1913-1965)*," ASTM International, West Conshohocken, PA, 1987.

C.E. Barth and E.A. Steigerwald, Evaluation of hydrogen embrittlement mechanisms. *Metall. Trans.*, 1, 1970, 3451-3455.

B.A. Bayles, P.S. Pao, S.J. Gill and G.R. Yoder, in: "Systems Engineering Approach to Mechanical Failure Prevention," Eds., H.C. Pusey and S.C. Pusey, Vibration Institute, Willowbrook, IL, 1993, 167-176.

C.D. Beachem, A new model for hydrogen-assisted cracking (hydrogen embrittlement). *Metall. Trans.*, 3, 1972, 437-451.

I.M. Bernstein and A.W. Thompson, Eds., "Hydrogen in Metals", ASM International, Materials Park, OH, 1974.

I.M Bernstein and A.W. Thompson, Effect of metallurgical variables on environmental fracture of steels. *Intl. Metall. Rev.*, 21, 1976, 269-287.

I.M. Bernstein and A.W. Thompson, Eds., "Hydrogen Effects in Metals," The Minerals, Metals & Materials Society, Warrendale, PA, 1981.

H.K. Birnbaum, H. Fukushima and J. Baker, in: "Advanced Techniques for Characterizing Hydrogen in Metals," The Minerals, Metals & Materials Society, Warrendale, PA, 1982, pp. 149-154.

H.K. Birnbaum, in: "Environment Induced Cracking of Metals", Eds., R.P. Gangloff and M.B. Ives, NACE, Houston, TX, 1990, pp. 21-29.

H.K. Birnbaum, I.M. Robertson, P. Sofronis and D. Teter, in: "Second International Conference on Corrosion-Deformation Interactions," Ed., T. Magnin, The Institute of Materials, London, UK, 1997, pp. 172-195.

H.K. Birnbaum and P. Sofronis, Hydrogen-enhanced plasticity—a mechanism for hydrogen related fracture. *Mater. Sci. Engr.*, **A176**, 1993, 191-202.

M.J. Blackburn, J.A. Feeney and T.R. Beck, in: "Advances in Corrosion Science and Technology," Vol. 3, Eds., M.G. Fontana and R.W. Staehle, Plenum Publishing, New York, NY, 1972, pp. 67-292.

B.M. Bond, I.M. Robertson and H.K. Birnbaum, The influence of hydrogen on deformation and fracture processes in high-strength aluminum alloys. *Acta Metall.*, **35**, 1987, 2289-2296.

R.R. Boyer, in "Beta Titanium Alloys in the 1990s," eds., D. Eylon, R.R. Boyer and D.A. Koss, The Minerals, Metals & Materials Society, Warrendale, PA, 1993, 335-346.

C.L. Briant and S.K. Banerji, Intergranular failure in steel: The role of grain boundary composition. *Intl. Metall. Rev.*, **23**, 1978, 164-199.

C.L. Briant and S.K. Banerji, in: "Treatise on Materials Science and Technology: Embrittlement of Engineering Alloys," Eds., C.L. Briant and S.K. Banerji, Vol. 25, Academic Press, New York, NY, 1983, pp. 21-58.

B.F. Brown and C.D. Beachem, A study of the stress factor in corrosion cracking by use of the precracked cantilever-beam specimen. *Corros. Sci.*, **5**, 1965, 745-750.

B.F. Brown and C.D. Beachem, "Specimens for Evaluating the Susceptibility of High Strength Steels to Stress Corrosion Cracking," Naval Research Laboratory Report, Washington, DC, 1966.

B.F. Brown, in: "The Theory of Stress Corrosion Cracking," Ed., J.C. Scully, NATO Scientific Affairs Division, Brussels, Belgium, 1971, pp. 186-204.

B.F. Brown, in: "Stress Corrosion Cracking and Hydrogen Embrittlement of Iron Base Alloys," Eds., R.W. Staehle, et al., NACE, Houston, TX, 1977, pp. 747-751.

P.F. Buckley, R. Brown, G.H. Graves, E.U. Lee, C.E. Neu and J. Kozol, in: "Metallic Materials for Lightweight Applications, 40th Sagamore Army Materials Research Conference," Eds., M.G.H. Wells, E.B. Kula and J.H Beatty, US Army Laboratory Command, Watertown, MA, 1993, 377-388.

P. Buckley, B. Placzankis, J. Beatty and R. Brown, "Characterization of the Hydrogen Embrittlement Behavior of High Strength Steels for Army Applications," *Corrosion/94*, Paper No. 547, NACE, Houston, TX, 1994.

T.D. Burleigh, The postulated mechanisms for stress corrosion cracking of aluminum alloys. *Corrosion*, **47**, 1991, 89-98.

C.S. Carter, "Stress Corrosion Cracking and Corrosion Fatigue of Medium-Strength and High Strength Steels," Boeing Commercial Airplane Company report, Seattle, WA, unpublished,

C.S. Carter, The effect of silicon on the stress corrosion resistance of low alloy high strength steels. *Corrosion*, **25**, 1969, 423-431.

T.J. Carter and L.A. Cornish, Hydrogen in metals. *Engr. Fail. Anal.*, **8**, 2001, 113-121.

N.H. Chan, K. Klier and R.P. Wei, A preliminary investigation of Hart's model in hydrogen embrittlement in maraging steels. *Scripta Metall.*, **12**, 1978, 1043-1046.

J.C. Charbonnier and H. Margot-Marette, in: "Current Solutions to Hydrogen Problems in Steels," Eds., C.G. Interrante and G.M. Pressouyre, ASM International, Materials Park, OH, 1982, pp. 462-466.

P.S. Chen, B. Panda and B.N Bhat, in: "Hydrogen Effects in Materials", Eds., A.W. Thompson and N.R. Moody, The Minerals, Metals & Materials Society, Warrendale, PA, 1996, pp. 1011-1019.

X. Chen and W.W. Gerberich, The kinetics and micromechanics of hydrogen assisted cracking in Fe-3 pct Si single crystals. *Metall. Trans. A*, **22A**, 1991, 59-70.

L. Christodoulou and H.M. Flower, Hydrogen embrittlement and trapping in Al-6%Zn-3%Mg. *Acta Metall.*, **28**, 1980, 481-487.

W.Y. Chu, C.M. Hsiao and B.J. Xu, Stress corrosion cracking in high strength steel under Mode III loading. *Metall. Trans. A.*, **17A**, 1986, 711-716.

W.G. Clark, Jr. and J.D. Landes, in: "Stress Corrosion Cracking—New Approaches, ASTM STP 610", Ed., H.L. Craig, Jr., ASTM International, West Conshohocken, PA, 1976, pp. 108-127.

W.G. Clark, Jr., in: "Cracks and Fracture, ASTM STP 601," ASTM International, West Conshohocken, PA, 1976, pp. 138-153.

W.G. Clark, Jr., Effect of temperature and pressure on hydrogen cracking in high strength type 4340 steel. *J. Matls. Energy Sys.*, **1**, 1979, 33-40.

K.R. Cooper, L.M. Young, R.P. Gangloff, and R.G. Kelly, The electrode potential dependence of environment-assisted cracking of AA7050. *Matls. Sci. For.*, **331-337**, 2000, 1625-1634.

K.R. Cooper and R.G. Kelly, in: "Chemistry and Electrochemistry of Stress Corrosion Cracking: A Symposium Honoring the Contributions of R.W. Staehle," Ed., R.H. Jones, The Minerals, Metals & Materials Society, Warrendale, PA, 2001, pp. 523-542.

L. Coudreuse and P. Bocquet, in: "Hydrogen Transport and Cracking in Metals," Ed., A. Turnbull, University Press, Cambridge, UK, 1995, 227-252.

W.R. Crumly, in: "Hydrogen Embrittlement: Prevention and Control, ASTM STP 962," Ed., L. Raymond, ASTM International, West Conshohocken, PA, 1988, pp. 173-178.

D.P. Dautovich and S. Floreen, The stress intensities for slow crack growth in steels containing hydrogen. *Metall. Trans.*, **4**, 1973, 2627-2630.

D.P. Dautovich and S. Floreen, in: "Stress Corrosion Cracking and Hydrogen Embrittlement of Iron Base Alloys," Eds., R.W. Staehle, et al., NACE, Houston, TX, 1977, pp. 798-815.

D.L. Davidson and J. Lankford, Fatigue crack growth in metals and alloys: mechanisms and micromechanics. *Intl. Metall. Rev.*, **37**, 1992, 45-76.

D.L. Davidson and J. Lankford, in: "Fatigue Mechanisms: Advances in Quantitative Measurement of Physical Damage," ASTM International, West Conshohocken, PA, 1983, pp. 371-399.

M.S. Daw and M.I. Baskes, in: "Chemistry and Physics of Fracture," Eds., R.M. Latanision and R.H. Jones, Martinus Nijhoff Publishers BV, Netherlands, 1987, pp. 196-218.

W. Dietzel and K. Ghosal, Effect of displacement rates on EAC of AISI 4340 steel. *Fatg. Fract. Engr. Matls. Struct.*, **21**, 1998, 1279-1286.

W. Dietzel and J. Mueller-Roos, Experience with rising load/rising displacement stress corrosion cracking testing. *Materials Science (Russia)*, **37**, 2001, 264-271.

W. Dietzel, K.-H. Schwalbe and D. Wu, Application of fracture mechanics techniques to the environmentally assisted cracking of aluminum 2024. *Fatg. Fract. Engr. Matls. Struct.*, **12**, 1989, 495-510.

P. Doig and G.T. Jones, Model for the initiation of H embrittlement cracking at notches in gaseous H environments. *Metall. Trans. A*, **8A**, 1977, 1993-1998.

R.A.H. Edwards, in: "Predictive Capabilities in Environmentally Assisted Cracking," American Society of Mechanical Engineers, New York, NY, 1985, pp. 153-175.

N. Eliaz, A. Shachar, B. Tal and D. Eliezer, Characteristics of hydrogen embrittlement, stress corrosion cracking and tempered martensite embrittlement in high strength steels. *Engr. Fail. Anal.*, **9**, 2002, 167-184.

J. A. Feeney and M. J. Blackburn, Effect of microstructure on the strength, toughness and stress-corrosion cracking susceptibility of a metastable beta titanium alloy. *Metall. Trans*, 1, 1970, 3309-3323.

N.A. Fleck and J.W. Hutchinson, A reformulation of strain gradient plasticity. *J. Mech. Phys. Sol.*, **49**, 2001, 2245-2271.

L.G. Fritzemeier, R.J. Walter, A.P. Meisels and R.P. Jewett, in: "Hydrogen Effects on Material Behavior", Eds., N.R. Moody and A.W. Thompson, The Minerals, Metals & Materials Society, Warrendale, PA, 1990, pp. 941-954.

R.P. Frohmberg, W.J. Barnett and A.R. Troiano, Delayed failure and hydrogen embrittlement in steel. *Trans. ASM*, **47**, 1955, 892-925.

C.T. Fujii, in "Stress Corrosion-New Approaches, ASTM STP 610," Ed., H.L. Craig, Jr., ASTM International, West Conshohocken, PA, 1976, pp. 213-225.

J.R. Galvele, A stress corrosion cracking mechanism based on surface mobility. *Corros. Sci.*, **27**, 1987, 1-33.

R.P. Gangloff and R.P. Wei, Gaseous hydrogen embrittlement of high strength steels. *Metall. Trans.*, *A*, 1977, **8A**, 1043-1053.

R.P. Gangloff and R.P. Wei, in: "Fractography in Failure Analysis, ASTM STP 645," eds., B.M. Strauss and W.H. Cullen, Jr., ASTM International, West Conshohocken, PA, 1978, pp. 87-106.

R.P. Gangloff, Ed., "Embrittlement by the Localized Crack Environment," The Minerals, Metals & Materials Society, Warrendale, PA, 1984.

R.P. Gangloff, Crack size effects on the chemical driving force for aqueous corrosion fatigue. *Metall. Trans., A,* **16A**, 1985, 953-969.

R.P. Gangloff, in: "Corrosion Prevention and Control," 33rd Sagamore Army Materials Research Conference, Eds., M. Levy and S. Isserow, US Army Laboratory Command, Watertown, MA, 1986, pp. 64-111.

R.P. Gangloff and R.P. Wei, in "Small Fatigue Cracks," Eds., R.O. Ritchie and J. Lankford, The Minerals, Metals & Materials Society, Warrendale, PA, 1986, pp. 239-264.

R.P. Gangloff and A. Turnbull, in: "Modeling Environmental Effects on Crack Initiation and Propagation," Eds., R.H. Jones and W.W. Gerberich, The Minerals, Metals & Materials Society, Warrendale, PA, 1986, pp. 55-81.

R.P. Gangloff, Crack tip models of hydrogen environment embrittlement: applications to fracture mechanics life prediction. *Matls. Sci. Engr.,* **A103**, 1988, 157-166.

R.P. Gangloff, in: "Basic Questions in Fatigue, Vol. 2, ASTM STP 924," Eds., R.P. Wei and R.P. Gangloff, ASTM International, West Conshohocken, PA, 1988, pp. 230-251.

R.P. Gangloff, in: "Environment Induced Cracking of Metals", Eds., R.P. Gangloff and M.B. Ives, NACE, Houston, 1990, TX, pp. 55-109.

R.P. Gangloff and M.B. Ives, Eds., "Environment-Induced Cracking of Metals," NACE, Houston, TX, 1990.

R.P. Gangloff, in: "Advanced Earth-To-Orbit Propulsion Technology", Eds., R.J. Richmond and S.T. Wu, NASA CP 3092, Vol. III, 1990a, Washington, DC, pp. 483-510.

R.P. Gangloff, B.P. Somerday and D.L. Cooke, in: "Life Prediction of Structures Subject to Environmental Degradation," Eds., P.L. Andresen and R.N. Parkins, NACE, Houston, TX, 1996, pp. 161-175.

R.P. Gangloff, Fracture mechanics characterization of hydrogen embrittlement in Cr-Mo Steel. in: "Present Situation on Steels for Hydrogen Pressure Vessels," Creusot-Loire Industrie, Le Creusot, France, 1998.

R.P. Gangloff, Embrittlement of high strength β-Ti alloys. In: "Advances in Fracture Research, Proceedings of ICF10," Eds. K. Ravi-Chandar, et al., Paper No. ICF108920R, CD version, Elsevier Science, Oxford, UK, 2001.

R.P. Gangloff, in: "Fatigue '02", Ed., Anders Blom, Engineering Materials Advisory Services, West Midlands, UK, 2002, pp. 3401-3433.

R.P. Gangloff, Diffusion control of hydrogen environment embrittlement in high strength alloys. in "Hydrogen Effects in Materials," Eds., N.R. Moody and A.W. Thompson, The Minerals, Metals & Materials Society, Warrendale, PA, 2002, in press.

R.P. Gangloff and K. George, unpublished research, University of Virginia, Charlottesville, VA, 2002a.

H. Gao and W. Cao, Effects of stress-strain conditions on hydrogen-induced fracture. *Fatg. Fract. Engr. Matls. Struct.,* 1998, **21**, 1351-1360.

M. Gao and R.P. Wei, Quasi-cleavage and martensite habit plane. *Acta metall.,* **32**, 1984, 2115-2124.

M. Gao, M. Lu and R.P Wei. Crack paths and hydrogen-assisted crack growth response in AISI 4340 steel. *Metall. Trans. A*, **15A**, 1984, 735-746.

M. Gao and R.P. Wei, A hydrogen partitioning model for hydrogen assisted crack growth. *Metall. Trans. A*, **16A**, 1985, 2039-2050.

H. Gao and L. Xue, (I + II) mixed mode hydrogen induced cracking. *Acta Metall. Sin.*, **25**, 1989, A48-A52.

W.M. Garrison, Jr., Ultrahigh-strength steels for aerospace applications. *J. Metals*, May, 1990, 20-24.

M.A. Gaudett and J.R. Scully, The effects of pre-dissolved hydrogen on cleavage and grain boundary fracture initiation in metastable beta Ti-3Al-8V-6Cr-4Mo-4Zr. *Metall. Mater. Trans. A*, **30A**, 1999, 65-79.

M.A. Gaudett and J.R. Scully, Metallurgical factors governing the H-assisted intergranular cracking of peak-aged Ti-3Al-8V-6Cr-4Mo-4Zr (Beta-C). *Metall. Mater. Trans. A*, **31A**, 2000, 81-92.

W.W. Gerberich, in: "Hydrogen in Metals", Eds., I.M. Bernstein and A.W. Thompson, ASM International, Materials Park, OH, 1974, pp. 115-147.

W.W. Gerberich, Y.T. Chen and C. St. John, A short-time diffusion correlation for hydrogen induced crack growth kinetics. *Metall. Trans. A*, **6A**, 1975, 1485-1498.

W.W. Gerberich and A.G. Wright, in: "Environmental Degradation of Engineering Materials in Hydrogen," Eds., M.R. Louthan, R.P. McNitt and R.D. Sisson, VPI Press, Blacksburg, VA, 1981, pp. 183-205.

W.W. Gerberich, T. Livne, and X.-F. Chen, in: "Modeling Environmental Effects on Crack Initiation and Propagation," Eds., R.H. Jones and W.W. Gerberich, The Minerals, Metals & Materials Society, Warrendale, PA, 1986, pp. 243-257.

W.W. Gerberich, T. Livne, X.-F. Chen and M. Kaczorowski, Crack growth from internal hydrogen-temperature and microstructure effects in 4340 steel. *Metall. Trans. A*, **19A**, 1988, 1319-1344.

W.W. Gerberich, R.A. Oriani, M.-J. Lii, X. Chen and T. Foecke, The necessity of both plasticity and brittleness in the fracture thresholds of iron. *Phil. Mag. A*, **63**, 1991, 363-376.

W.W. Gerberich, P.G. Marsh and J.W. Hoehn, in: "Hydrogen Effects in Materials," Eds., A.W. Thompson and N.R. Moody, The Minerals, Metals & Materials Society, Warrendale, PA, 1996, pp. 539-553.

R.J. Gest and A.R. Troiano, Stress corrosion and hydrogen embrittlement in an aluminum alloy. *Corrosion*, **30**, 1974, 274-279.

J.A. Grandle, B.P. Somerday and R.P. Gangloff, in: "Proceedings of the Tri-Service Conference on Corrosion," Ed., T. Naguy, USAF Wright-Patterson Air Force Base, OH, 1994, pp. 375-392.

A.J. Griffiths and A. Turnbull, On the effective diffusivity of hydrogen in low alloys steels. *Corros. Sci.*, **37**, 1995. 1879-1881.

W. Gruhl, Stress corrosion cracking of high strength aluminum alloys. *Z. Metallkd.*, **75**, 1984, 819-826.

E.M. Hackett, P.J. Moran and J.P. Gudas, in: "Fracture Mechanics: 17th Volume, ASTM STP 905," Eds., R. Chait, et al., ASTM International, West Conshohocken, PA, 1986, pp. 512-541.

M.M. Hall, Jr. and D.M. Symons, in: "Chemistry and Electrochemistry of Stress Corrosion Cracking," Ed., R.H. Jones, The Minerals, Metals & Materials Society, Warrendale, PA, 2001, pp. 447-466.

G.G. Hancock and H.H. Johnson, Hydrogen, oxygen, and subcritical crack growth in a high-strength steel. *Trans. Met. Soc. AIME*, **236**, 1966, 513-516.

D.G. Harlow and R.P. Wei, Probability modeling and statistical analysis of damage in the lower wing skins of two retired B-707 aircraft. *Fatg. Fract. Engr. Matls. Struct.*, **24**, 2001, 523-535.

D.G. Harlow and R.P. Wei, Life prediction—the need for a mechanistically based probability approach. *Key Engineering Materials*, **200**, 2001a, 119-138.

D.G. Harlow and R.P. Wei, A critical comparision between mechanistically based probability and statistically based modeling for materials aging. *Matls. Sci. Engr. A*, **323**, 2002, 278-284.

H.W. Hayden and S. Floreen, Effects of various modes of loading on the stress corrosion cracking of a maraging steel. *Corrosion*, **27**, 1971, 429-433.

S.P. Hayes, "Internal Hydrogen Embrittlement of High-Strength Beta-Alpha Titanium Alloys," PhD Dissertation, University of Virginia, Charlottesville, VA, 2000.

R.W. Hertzberg, "Deformation and Fracture of Engineering Materials," 4th Ed., John Wiley & Sons, New York, NY, 1996.

P.D. Hicks and C.J. Altstetter, Hydrogen-enhanced cracking of superalloys. *Metall. Trans. A*, **23A**, 1992, 237-249.

K. Hirano, S. Ishizaki, H. Kobayashi and H. Nakazawa, Determination of threshold stress corrosion cracking characteristics using rising load K_{ISCC} testing based on ultrasonic method. *J. Test. Eval.*, **13**, 1985, 162-168.

J.P. Hirth, Effects of hydrogen on the properties of iron and steel. *Metall. Trans. A*, **11A**, 1980, 861-890.

J.P Hirth, in: "Hydrogen Effects in Metals," Eds., A.W. Thompson and N.R. Moody, The Minerals, Metals & Materials Society, Warrendale, PA, 1996, pp. 507-522.

N.J.H. Holroyd and D. Hardie, Strain-rate effects in the environmentally assisted fracture of a commercial high-strength aluminium alloy (7049). *Corros. Sci.*, **21**, 1981, 129-144.

N.J.H. Holroyd, in: "Environment-Induced Cracking of Metals," Eds., R.P. Gangloff and M.B. Ives, NACE, Houston, TX, 1990, pp. 311-345.

M. Horstmann and J.K. Gregory, Observations on the ripple-loading effect. *Scripta Metall. Mater.*, **25**, 1991, 2503-2506.

H. Huang and W.W. Gerberich, Crack-tip dislocation emission arrangements for equilibrium-II: Comparisons to analytical and computer simulation models. *Acta metall. mater.*, **40**, 1992, 2873-2881.

S.J. Hudak, Jr. and R.P. Wei, Consideration of nonsteady-state crack growth in materials evaluation and design. *Intl. J. Pressure Vessels*, **9**, 1981, 63-74.

J.W. Hutchinson, Plasticity at the micron scale. *Intl. J. Sol. Struc.*, **37**, 2000, 225-238.

M. Iino, Influence of sulfur content on the hydrogen-induced fracture in linepipe steels. *Metall. Trans. A*, **10A**, 1979, 1691-1698.

C.G. Interrante and G.M. Pressouyre, Eds., "Current Solutions to Hydrogen Problems in Steels," ASM International, Materials Park, OH, 1982.

C.G. Interrante and L. Raymond, in: "Corrosion Tests and Standards: Application and Interpretation," R. Baboian, Ed., ASTM International, West Conshohocken, PA, 1995, pp. 272-286.

G.R. Irwin and A.A. Wells, in: "Selected Papers on Foundations of Linear Elastic Fracture Mechanics," Vol. MS 137, SPIE Milestone Series, SEM, Bethel, CT, 1997, 215-266.

R.P. Jewett, R.J. Walter, W.T. Chandler and R.P. Fromberg, "H Environment Embrittlement of Metals," NASA CR-2163, NASA, Washington, DC, 1973.

H. Jiang, Y. Huang, Z. Zhuang and K.C. Hwang, Fracture in mechanism-based strain gradient plasticity. *J. Mech. Phys. Solids*, **49**, 2001, 979-993.

H.H. Johnson, J.G. Morlet and A.R. Troiano, Hydrogen, crack initiation, and delayed failure in steel. *Trans. AIME*, **212**, 1958, 528-535.

H.H. Johnson and A.M. Willner, Moisture and stable crack growth in a high strength steel. *App. Matls. Res.*, **4**, 1965, 34-43.

H.H. Johnson, in: "Hydrogen in Metals," Eds., I.M. Bernstein and A.W. Thompson, ASM International, Materials Park, OH, 1974, pp. 35-49.

O. Jonas, Influence of preloading on the sustained load cracking behavior of maraging steels in hydrogen. *Corrosion*, **29**, 1973, 299-304.

D.A. Jones, A.F. Jankowski and G.A. Davidson, "Diffusion of Anodically Induced Vacancies in Cu/Ag Thin-Film Couples", Paper No. 188, *Corrosion 97*, NACE International, Houston, TX, 1997.

R.H. Jones and W.W. Gerberich, Eds., "Modeling Environmental Effects on Crack Initiation and Propagation," The Minerals, Metals & Materials Society, Warrendale, PA, 1986.

R.H. Jones, H. Li, and J.P. Hirth, 2000, "Effects of Mixed Mode I/III Loading on Environment-Induced Cracking," Paper No. 00360, *Corrosion 2000*, NACE International, Houston, TX, 2000.

J. Kameda, Equilibrium and growth characteristics of hydrogen-induced intergranular cracking in phosphorus-doped and high purity steels. *Acta Metall.*, **34**, 1986, 1721-1735.

J. Kameda, A microscopic model of H-induced intergranular cracking—I. Equilibrium crack growth. *Acta Metall.*, **34**, 1986a, 867-882.

J. Kameda, A microscopic model of H-induced intergranular cracking—II. Steady state crack growth. *Acta Metall.*, **34**, 1986b, 883-889.

Y. Katz, N. Tymiak and W.W. Gerberich, Nanomechanical probes as new approaches to hydrogen/deformation interaction studies. *Engr. Frac. Mech.*, **68**, 2001, 619-646.

G.E. Kerns, M.T. Wang and R.W. Staehle, in: "Stress Corrosion Cracking and Hydrogen Embrittlement of Iron Base Alloys," Eds., R.W. Staehle, et al., NACE, Houston, TX, 1977, pp. 700-735.

N.N. Kinaev, D.R. Cousens and A. Atrens, The crack tip strain field of AISI 4340: Part I Measurement Technique. *J. Matls. Sci.*, **34**, 1999, 4909-4920.

N.N. Kinaev, D.R. Cousens and A. Atrens, The crack tip strain field of AISI 4340: Part II Experimental measurements. *J. Matls. Sci.*, **34**, 1999a, 4921-4929.

N.N. Kinaev, D.R. Cousens and A. Atrens, The crack tip strain field of AISI 4340: Part III Hydrogen Influence. *J. Matls. Sci.*, **34**, 1999b, 4931-4936.

A.S. Kobayashi and Y. Takeshi, in: "Predictive Capabilities in Environmentally Assisted Cracking," PVP-Vol. 99, ASME, New York, NY, 1985, pp. 223-234.

G.H. Koch, Hydrogen induced fracture of a high strength aluminum alloy. *Corrosion*, **35**, 1979, 73-78.

D.G. Kolman and J.R. Scully, Understanding the potential and pH dependency of high-strength beta -titanium alloy environmental crack initiation. *Metall. Mater. Trans. A*, **28A**, 1997, 2645-2656.

D.G. Kolman and J.R. Scully, in: "Effects of the Environment on the Initiation of Crack Growth, ASTM STP 1298," Eds., W.A. Van der Sluys, R.S. Piascik and R. Zawierucha, ASTM International, West Conshohocken, PA, 1998, pp. 61-73.

D.G. Kolman and J.R. Scully, Continuum mechanics characterization of plastic deformation-induced oxide film rupture. *Phil. Mag. A*, **79**, 1999, 2313-2338.

D.G. Kolman and J.R. Scully, An assessment of the crack tip potential of beta-titanium alloys during hydrogen environmentally assisted crack propagation based on crack tip and passive surface electrochemical measurements. *Corros. Sci.*, **42**, 2000, 1863-1879.

J. Kolts, in: "Corrosion Resistant Alloys in Oil and Gas Production," Vol. II, eds., J. Kolts and S.M. Corey, NACE, Houston, TX, 1996, 733-748.

A.H.M. Krom, R.W.J. Koers, and A. Bakker, Hydrogen transport near a blunting crack tip. *J. Mech. Phys. Solids*, **47**, 1999, 971-992.

A.H.M. Krom and A. Bakker, Hydrogen trapping models in steel. *Metall. Trans. B*, **31B**, 2000, 1475-1482B.

J.M. Kumar, J.P. Hirth, N.R. Moody, Jr. and J.A. Gordon, Effects of hydrogen on the mixed Mode I/III toughness of a high-purity rotor steel. *Metall. Trans. A*, **24A**, 1993, 1450-1451.

A.J. Kumnick and H.H. Johnson, Deep trapping states for hydrogen in deformed iron. *Acta Metall.*, **28**, 1980, 33-39.

J.B. Leblond and D. Dubois, A general mathematical description of hydrogen diffusion in steels---II: Numerical study of permeation and determination of trapping parameters. *Acta Metall.*, **31**, 1983, 1471-1478.

S.M. Lee, S.I. Pyun and Y.G. Chun, Critical evaluation of the stress-corrosion cracking mechanism in high-strength aluminum alloys. *Metall. Trans. A*, **22A**, 1991, 2407-2414.

E.U. Lee, H. Sanders and B. Sarkar, Stress corrosion cracking of high strength steels. CD file s08p2a.pdf, in: "Proceedings of the Tri-Service Conference on Corrosion," Eds., J.V. Kelley and B. Placzankis, US Army Research Laboratory, Aberdeen, MD, 2000.

B.N. Leis and R.N. Parkins, Mechanics and materials aspects in predicting serviceability limited by stress-corrosion cracking. *Fatg. Fract. Engr. Matls. Struct.*, **21** 1998, 583-601.

J.F. Lessar and W.W. Gerberich, Grain size effects in hydrogen-assisted cracking. *Metall. Trans. A*, **7A**, 1976, 953-960.

J.C.M. Li, R.A. Oriani and L.S Darken, The thermodynamics of stressed solids. *Z. Physik. Chem.*, **49**, 1966, 271-290.

J.A. Lillard, R.G. Kelly and R.P. Gangloff, "Effect of Electrode Potential on Stress Corrosion Cracking and Crack Chemistry of a Nickel-Base Superalloy", Paper No. 197, *Corrosion '97*, NACE, Houston, TX, 1997.

J.A. Lillard, "Environment Assisted Cracking of a Nickel-Based Superalloy in Hydrogen-Producing Solutions," PhD Dissertation, University of Virginia, Charlottesville, VA, 1998.

W.B. Lisagor, T.W. Crooker and B.N. Leis, Eds., "Environmentally Assisted Cracking: Science and Engineering, ASTM STP 1049," ASTM International, West Conshohocken, PA, 1990.

M.R. Louthan and R.P. NcNitt, Eds., "Environmental Degradation of Engineering Materials," VPI Press, Blacksburg, VA, 1977.

M.R. Louthan, Jr., G.R. Caskey, J.A. Donovan and D.E. Rawl, Jr., Hydrogen embrittlement of metals. *Matls. Sci. Engr.*, **10**, 1972, 357-368.

M.R. Louthan, R.P. McNitt and R.D. Sisson, Eds., "Environmental Degradation of Engineering Materials in Hydrogen," Eds., VPI Press, Blacksburg, VA, 1981.

M. Lu, P.S. Pao, T.W. Weir, G.W. Simmons and R.P. Wei, Rate controlling processes for crack growth in hydrogen sulfide for an AISI 4340 steel. *Metall. Trans. A*, **12A**, 1981, 805-811.

S.P. Lynch, in: "Mechanisms of Environment Sensitive Fracture of Materials," Eds., P.R. Swann, F.P. Ford, and A.R.C. Westwood, The Metals Society, London, UK, 1977, pp. 201-212.

S.P. Lynch, Environmentally assisted cracking: Overview of evidence for an adsorption-induced localized slip process. *Acta Metall.*, **36**, 1988, 2639-2661.

S.P. Lynch, Failures of structures and components by environmentally assisted cracking. *Engr. Fail. Anal.*, **1**, 1994, 77-90.

S.P. Lynch, in: "Second International Conference on Corrosion-Deformation Interactions," Ed., T. Magnin, The Institute of Materials, London, UK, 1997, pp 206-219.

S.P. Lynch, Mechanisms of hydrogen assisted cracking—A review. in "Hydrogen Effects in Materials," Eds., N.R. Moody and A.W. Thompson, The Minerals, Metals & Materials Society, Warrendale, PA, 2003, in press.

T. Magnin, R. Chieragatti, and R. Oltra, Mechanism of brittle fracture in a ductile 316 alloy during stress corrosion. *Acta Metall.*, **38**, 1990, 1313-1319.

P. Martin, J.I. Dickson and J.-P. Bailon, Stress corrosion cracking in aluminum alloy 7075-T651 by discrete crack jumps as indicated by fractography and acoustic emission. *Mater. Sci. Engr.*, **69**, 1985, L9-13.

M.E. Mason and R.P. Gangloff, in: "Advanced Structural Integrity Methods for Airframe Durability and Damage Tolerance," Ed., C.E. Harris, NASA Conference Publication 3274, Part 1, NASA-Langley Research Center, Hampton, VA, 1994, pp. 441-462.

A.J. McEvily, "Atlas of Stress-Corrosion and Corrosion Fatigue Curves," ASM International, Materials Park, OH, 1990.

K.F. McGuinn and M. Aballe, Hydrogen embrittlement in Mode II, *Brit. Corros. J.*, **17**, 1982, 18-20.

P. McIntyre and A.H. Priest, "Accelerated Test Technique for the Determination of K_{ISCC} in Steels," British Steel Corporation Report MG/31/72, London, England, 1972.

P. McIntyre, A.H. Priest and C.E. Nicholson, "Hydrogen Induced Subcritical Flaw Growth in Steels Under Static and Cyclic Loading," British Steel Corporation Report No. MG/38/72, London, UK, 1972a.

P. McIntyre, in: "Hydrogen Degradation of Ferrous Alloys," Eds., R.A. Oriani, J.P. Hirth and S. Smialowska, Noyes Publications, Park Ridge, NJ, 1985, pp. 763-798.

C.J. McMahon, Jr., Hydrogen-induced intergranular fracture of steels. *Engr. Frac. Mech.*, **68**, 2001, 773-788.

R.A. Mayville, T.J. Warren and P.D. Hilton, in "Fracture Mechanics: Perspectives and Directions, ASTM STP 1020", Eds., R.P. Wei and R.P. Gangloff, ASTM International, West Conshohocken, PA, 1989, pp. 605-614.

P.G. Marsh and W.W. Gerberich, in: "Stress Corrosion Cracking," Ed., R.H. Jones, ASM International, Materials Park, OH, 1992, pp. 63-90.

W.J. Mills, M.R. Lebo and J.J. Kearns, Hydrogen embrittlement, grain boundary segregation and stress corrosion cracking of alloy X-750 in low and high-temperature water. *Metall. and Matls. Trans. A*, **30A**, 1999, 1579-1596.

N.R. Moody, R.E. Stoltz and M.W. Perra, in: "Corrosion Cracking," Ed., V.S. Goel, ASM International, Materials Park, OH, 1986, pp. 43-53.

N.R. Moody, S.L. Robinson and M.W. Perra, The effect of hydrogen on fracture toughness of the Fe-Ni-Co superalloy IN903. *Metall. Trans. A*, **18A**, 1987, 1469-1482.

N.R. Moody, M.W. Perra and S.L. Robinson, Hydrogen pressure and crack tip stress effects on slow crack growth thresholds in an iron-based superalloy. *Scripta Metall.*, **22**, 1988, 1261-1266.

N.R. Moody, S.L. Robinson, S.M. Myers and F.A. Greulich, Deuterium concentration profiles in Fe-Ni-Co alloys electrochemically charged at room temperature. *Acta Metall.*, **37**, 1989, 281-290.

N.R. Moody, S.L. Robinson and W.M. Garrison, Jr., Hydrogen effects on the properties and fracture modes of iron-based alloys. *Res. Mech.*, **30**, 1990, 143-206.

N.R. Moody and A.W. Thompson, Eds., "Hydrogen Effects on Material Behavior," The Minerals, Metals & Materials Society, Warrendale, PA, 1990a.

N.R. Moody, M.W. Perra and S.L. Robinson, in: "Hydrogen Effects on Material Behavior," Eds., N.R. Moody and A.W. Thompson, The Minerals, Metals & Materials Society, Warrendale, PA, 1990b, pp. 625-635.

N.R. Moody, S.L. Robinson and M.W. Perra, Internal hydrogen effects on thresholds for crack growth in the iron-based superalloy IN903. *Engr. Frac. Mech.*, **39**, 1991, 941-954.

N.R. Moody, S.L. Robinson, J.E. Angelo and M.W. Perra, in: "Hydrogen Effects in Materials," Eds., A.W. Thompson and N.R. Moody, The Minerals, Metals & Materials Society, Warrendale, PA, 1996, pp. 967-977.

N.R. Moody, M.I Baskes, S.L Robinson and M.W. Perra, Temperature effects on hydrogen-induced crack growth susceptibility of iron-based superalloys. *Engr. Frac. Mech.*, **68**, 2001, 731-750.

N.R. Moody and A.W. Thompson, Eds., "Hydrogen Effects on Material Behavior," The Minerals, Metals & Materials Society, Warrendale, PA, 2003, in press.

L. Montgrain and P.R. Swann, in: "Hydrogen in Metals", Eds., I.M. Bernstein and A.W. Thompson, ASM International, Materials Park, OH, 1974, pp. 575-584.

M.J. Morgan and C.J. McMahon, Jr., in: "Hydrogen Degradation of Ferrous Alloys," Eds., R.A. Oriani, J.P. Hirth, and M. Smialowski, Noyes Publications, Park Ridge, NJ, 1985, 608-40.

N.K. Mukhopadhyay, G. Sridhar, N. Parida, S. Tarafder and V.R. Ranganath, Hydrogen embrittlement failure of hot dip galvanized high tensile wires. *Engr. Fail. Anal.*, **6**, 1999, 253-265.

S.M. Myers, W.R. Wampler, F. Besenbacher, S.L. Robinson and N.R. Moody, Ion beam studies of hydrogen in metals. *Mater. Sci. Engr.*, **69**, 1985, 397-409.

National Materials Advisory Board, "Characterization of Environmentally Assisted Cracking for Design: State of the Art," NMAB-386, Washington, DC, 1982.

A. Needleman and J.G. Sevillano, Preface to the viewpoint set on geometrically necessary dislocations and size dependent plasticity. *Scripta Mater.*, **48**, 2003, 109-111.

H.G. Nelson, D.P. Williams and A.S. Tetelman, Embrittlement of a ferrous alloy in a partially dissociated hydrogen environment. *Metall. Trans.*, **2**, 1971, 953-959.

H.G. Nelson and D.P. Williams, in: "Stress Corrosion Cracking and Hydrogen Embrittlement of Iron Base Alloys," Eds., R.W. Staehle, et al., NACE, Houston, TX, 1977, pp. 390-404.

H.G. Nelson, in: "Treatise on Materials Science and Technology: Embrittlement of Engineering Alloys," Eds., C.L. Briant and S.K. Banerji, Vol. 25, Academic Press, New York, NY, 1983, pp. 275-359.

D. Nguyen, A.W. Thompson and I.M. Bernstein, Microstructural effects on hydrogen embrittlement in a high purity 7075 aluminum alloy. *Acta. Metall.*, **35**, 1987, 2417-2425.

F.A. Nichols, 1983, Loading mode and stress corrosion cracking mechanisms. *Corrosion*, **39**, 449-451.

S.R. Novak and S.T. Rolfe, Comparison of fracture mechanics and nominal stress analysis in stress corrosion cracking. *Corrosion*, **26**, 1970, 121-130.

S.R. Novak and S.T. Rolfe, Modified WOL specimen for K_{ISCC} environmental testing. *J. Matls.*, **4**, 1969, 701-728.

A. Oehlert and A. Atrens, Stress corrosion crack propagation in AerMet[®]100. *J. Matls. Sci.*, **33**, 1998, 775-781.

S.H. Ohsaki, M. Iino and M. Utsue, SCC extension of 7075 series aluminum alloys under mixed-mode I-II loading. *J. Japan Inst. Light Metals*, **47**, 1997, 370-377.

G.B. Olson, in: "Innovations in Ultrahigh Strength Steel Technology, 34th Sagamore Army Materials Research Conference," Eds., G.B. Olson, M. Azrin, and E.S. Wright, US Army Laboratory Command, Watertown, MA, 1987, pp. 549-593.

G.B. Olson, Brains of steel: Designing metallurgists. *Advanced Matls. Proc.*, July, 1997, 72-79.

J. Opoku and W.G. Clarke, Jr., The effects of various hydrogen bearing environments on the K_{ISCC} of AISI type 4340 and 3.5%NiCrMoV steels. *Corrosion*, **36**, 1980, 251-258.

R.A. Oriani, Diffusion and trapping of hydrogen in steel. *Acta Metall.*, **18**, 1970, 147-157.

R.A. Oriani, D.P. Williams and H.G. Nelson, Discussion of evaluation of hydrogen embrittlement mechanisms. *Metall. Trans.*, **2**, 1971, 1987-1988.

R.A. Oriani, The mechanistic theory of hydrogen embrittlement of steels. *Berichte Bunsen Gesellschaft fur Physik Chem.*, **76**, 1972, 848-857.

R.A. Oriani and P.H. Josephic, Equilibrium aspects of H-induced cracking of steels. *Acta Metall.*, **22**, 1974, 1065-1074.

R.A. Oriani, in: "Stress Corrosion Cracking and Hydrogen Embrittlement of Iron Base Alloys," R.W. Staehle, et al., Eds., NACE, Houston, TX, 1977, pp. 32-50.

R.A. Oriani and P.H. Josephic, Equilibrium and kinetic studies of the H-assisted cracking of steel. *Acta Metall.*, **25**, 1977, 979-988.

R.A. Oriani, Hydrogen embrittlement of steels. *Annual Reviews in Materials Science*, 1978, **8**, 327-357.

R.A. Oriani, J.P. Hirth and S. Smialowska, Eds., "Hydrogen Degradation of Ferrous Alloys," Noyes Publications, Park Ridge, NJ, 1985.

R.A. Oriani, Hydrogen-the versatile embrittler. *Corrosion*, **43**, 1987, 390-397.

R.A. Oriani, in: "Environment Induced Cracking of Metals", Eds., R.P. Gangloff and M.B. Ives, NACE, Houston, 1990, TX, pp. 439-448.

R.A. Page and W.W. Gerberich, The effect of hydrogen source on crack initiation in 4340 steel. *Metall. Trans.* A, **13A**, 1982, 305-311.

R.N. Parkins, in: "Environment Induced Cracking of Metals," Eds., R.P. Gangloff and M.B. Ives, NACE, Houston, 1990, TX, pp. 1-119.

R.N. Parkins, in: "Life Prediction of Corrodible Structures," Vol. 1, Ed., R.N. Parkins, NACE, Houston, TX, 1991, pp. 97-119.

P.S. Pao, R.A. Bayles and G.R. Yoder, Effect of ripple load on stress corrosion cracking in structural steels. *J. Engr. Matls. Tech.*, **113**, 1991, 125-129.

P.S. Pao, S.J. Gill and R.A. Bayles, Effect of ripple loads on stress-corrosion cracking in AA7075 Al alloys. *Scripta Metall. Mater.*, **25**, 1991a, 2085-2089.

P.S. Pao, C.R. Feng, R.A. Bayles, D.A. Meyn and G.R. Yoder, in: "Titanium '95: Science and Technology," Eds., P.A. Blenkinsop, W.J. Evans and H.M.Flower, The Institute of Materials, London, UK, 1996, pp. 1219-1226.

P.C. Paris, Fracture mechanics and fatigue: A historical perspective. *Fatg. Fract. Engr. Matls. Struct.*, 1998, **21**, 535-540.

R.W. Pasco, K. Sieradzki and P.J. Ficalora, Surface chemistry kinetic model of gaseous hydrogen embrittlement. *Scripta Metall.*, **16**, 1982, 881-883.

R.W. Pasco and P.J. Ficalora, A work function-chemisorption study of hydrogen on iron-kinetics and strain effects. *Acta Metall.*, **31**, 1983, 541-558.

R.W. Pasco, K. Sieradzki and P.J. Ficalora, in: "Embrittlement by the Localized Crack Environment," Ed., R.P. Gangloff, The Minerals, Metals & Materials Society, Warrendale, PA, 1984, pp. 375-381.

M.W. Perra and R.E. Stoltz, in: "Hydrogen Effects in Metals," Eds., I.M. Bernstein and A.W. Thompson, The Minerals, Metals & Materials Society, Warrendale, PA, 1981, pp. 645-653.

N.J. Petch, Lowering of fracture stress due to surface adsorption. *Phil. Mag.*, **1**, 1956, 331-337.

N.J. Petch and P. Stables, Delayed fracture of metals under static load. *Nature*, **169**, 1952, 842-851.

J.R. Pickens, J.R. Gordon and J.A.S. Green, The effect of loading mode on the stress corrosion cracking of aluminum alloy 5083. *Metall. Trans. A*, **14A**, 1983, 925-930.

J.R. Pickens, T.J. Langan and J.A.S. Green, in: "Environment Sensitive Fracture of Metals and Alloys," eds., R.P. Wei, D.J. Duquette, T.W. Crooker, and A.J. Sedriks, Office of Naval Research, Arlington, VA, 1987, pp. 115-131.

Martin Prager, Ed., "Interaction of Steels with Hydrogen in Petroleum Industry Pressure Vessel Service," Materials Properties Council, New York, NY, 1989.

Martin Prager, Ed., "Second International Conference on Interaction of Steels with Hydrogen in Petroleum Industry Pressure Vessel and Pipeline Service," Materials Property Council, New York, NY. 1994.

G.M. Pressouyre and I.M. Bernstein, A quantitative analysis of hydrogen trapping. *Metall. Trans. A,* **9A**, 1978, 1571-1580.

G.M. Pressouyre, A classification of hydrogen traps in steel. *Metall. Trans. A,* **10A**, 1979, 1571-1573

G.M. Pressouyre and I.M. Bernstein, A kinetic trapping model for hydrogen-induced cracking. *Acta Metall.,* **27**, 1979, 89-100.

G.M. Pressouyre, Trap theory of hydrogen embrittlement. *Acta Metall.,* **28**, 1980, 895-911.

G.M. Pressouyre and I.M. Bernstein, An example of the effect of hydrogen trapping on hydrogen embrittlement. *Metall. Trans. A,* **12A**, 1981, 835-844.

G.M. Pressouyre, Hydrogen traps, repellers, and obstacles in steel: Consequences on hydrogen diffusion, solubility and embrittlement. *Metall. Trans. A.,* **14A**, 1983, 2189-2193.

R.P.M. Procter and H.W. Paxton, The effect of prior austenite grain size on the stress corrosion cracking susceptibility of AISI 4340 steel. *Trans. ASM,* **62**, 1962, 989-999.

V.L. Ratke and W. Gruhl, Model experiments concerning the mechanisms of stress corrosion cracking of Al-Zn-Mg alloys. *Werkst. Korros.,* **31**, 1980, 768-773.

L. Raymond, Ed., "Hydrogen Embrittlement Testing, ASTM STP 543," ASTM International, West Conshohocken, PA, 1972.

L. Raymond, Ed., "Hydrogen Embrittlement: Prevention and Control, ASTM STP 962," ASTM International, West Conshohocken, PA, 1988.

K.G. Reedy, A.K. Jha and V. Diwakar, Failure of cadmium plated maraging steel tension bolt. *Engr. Fail. Anal.,* **8**, 2001, 263-269.

I.M. Robertson and H.K. Birnbaum, HVEM study of hydrogen effects on the deformation of nickel. *Acta Metall.,* **34**, 1986, 353-366.

I.M. Robertson, The effect of hydrogen on dislocation dynamics. *Engr. Frac. Mech.,* **68**, 2001, 671-692.

P. Rozenak, I.M. Robertson and H.K. Birnbaum, HVEM studies of the effects of hydrogen on the deformation and fracture of AISI type 316 austenitic stainless steel. *Acta metall. Mater.,* **38**, 1990, 2031-2040.

J.R. Rice, in: "Stress Corrosion Cracking and Hydrogen Embrittlement of Iron Base Alloys," Eds., R.W. Staehle, et al., NACE, Houston, TX, 1977, pp. 11-15.

T. Sakai, T. Takahashi, M. Yamada, S. Nose and M. Katsumata, in "High Pressure Technology, PVP-Vol. 344," ASME, New York, NY, 1997, pp. 79-98.

T. Sakurai and H.W. Pickering, in: "Advanced Techniques for Characterizing Hydrogen in Metals," The Minerals, Metals & Materials Society, Warrendale, PA, 1982, pp. 171-181.

G. Sandoz, C.T. Fujii and B.F. Brown, Solution Chemistry within stress corrosion cracks in alloy steels. *Corros. Sci.*, **10**, 1970, 839-845.

G. Sandoz, in: "Second International Congress on Hydrogen and Materials," Ed., P. Azou, l'Ecole Centrale des Arts et Manufactures, Paris, FR, 1977, pp. 335-341.

B. Sarkar, M. Marek and E.A. Starke, Jr., The effect of copper content and heat treatment on the stress corrosion characteristics of Al-6Zn-2Mg-xCu alloys. *Metall. Trans. A*, **12A**, 1981, 1939-1943.

V.R. Sawicki, "Hydrogen Induced Cracking in a High Strength Steel," PhD Dissertation, Cornell University, Ithaca, NY, 1971.

G.M. Scamans, R. Alani and P.R. Swann, Pre-exposure embrittlement and stress corrosion failure in Al-Zn-Mg alloys. *Corros. Sci.*, **16**, 1976, 443-459.

G.M. Scamans, Evidence for crack arrest markings on intergranular stress corrosion cracks in Al-Zn-Mg alloys. *Metall. Trans. A.*, **11A**, 1980, 846-850.

J.H. Schmidt, R.B. Meade and L. Raymond, Process management to control risk of hydrogen embrittlement. *Plating and Surface Finishing*, **87**, 2000, 53-55.

H. Schmiedel and W. Gruhl, The influence of the zinc, magnesium and copper concentrations at the grain boundaries on the stress corrosion susceptibility of AlZnMg alloys. *Z. Metallkd.*, **74**, 1983, 777-783.

K.-H. Schwalbe, Finite element solutions of crack tip behavior in small scale yielding. *J. Engr. Matl. Tech.*, **99**, 1977, 186-188.

J.C. Scully, Ed., "The Theory of Stress Corrosion Cracking," NATO Scientific Affairs Division, Brussels, Belgium, 1971.

J.R. Scully and P.J. Moran, The influence of strain on hydrogen entry and transport in a high strength steel in sodium chloride solution. *J. Electrochem. Soc.*, **135**, 1988, 1337-1348.

J.R. Scully, J.A. Van Den Avyle, M.J. Cieslak, A.D. Romig and C.R. Hills, The influence of Pd on the hydrogen-assisted cracking resistance of PH 13-8 Mo stainless steel. *Metall. Trans. A*, **22A**, 1991, 2429-2443.

J.R. Scully, G.A. Young, Jr. and S.W. Smith, Hydrogen solubility, diffusivity and trapping in high purity aluminum and selected Al-base alloys. *Matls. Sci. Forum*, **331-337**, 2000, 1583-1600.

J.R. Scully, unpublished research, University of Virginia, Charlottesville, VA, 2002.

A.J. Sedriks, "Stress Corrosion Cracking Test Methods", NACE, Houston, TX, 1990.

Y. Shen and P.G. Shewmon, IGSCC crack growth of Alloy 600 and X-750 in steam. *Corrosion*, **47**, 1991, 712-718.

D.S. Shih, I.M. Robertson and H.K. Birnbaum, Hydrogen embrittlement of alpha titanium: in situ TEM studies. *Acta Metall.*, **36**, 1988, 111-124.

R.J. Shipley and W.T. Becker, Eds., "Failure Analysis and Prevention", *Metals Handbook*, Vol. 11, ASM International, Materials Park, OH, 2002, in press.

K. Sieradzki and P. Ficalora, The dependence of the fracture toughness of 4340 steel on an external chlorine gas environment. *Scripta Metall.*, **13**, 1979, 535-536.

K. Sieradzki and P.J. Ficalora, Kinetic aspects of slow crack growth in the gaseous hydrogen embrittlment of steels. *J. Mater. Sci.*, **14**, 1979a, 2703-2708.

G.W. Simmons, P.S. Pao, and R.P. Wei, Fracture mechanics and surface chemistry studies of subcritical crack growth in AISI 4340 steel. *Metall. Trans. A*, **9A**, 1978, 1147-1158.

H.R. Smith, D.E. Piper and F.K. Downey, A study of stress corrosion cracking by wedge-force loading. *Engr. Frac. Mech.*, **1**, 1968, 123-128.

J.A. Smith, M.H. Peterson and B.F. Brown, Electrochemical conditions at the tip of an advancing stress corrosion crack in AISI 4340 steel. *Corrosion*, **26**, 1970, 539-542.

B.P. Somerday and R.P. Gangloff, Effect of strength on environment-assisted cracking of Ti-8V-6Cr-4Mo-4Zr-3Al in aqueous chloride: age hardening *vs.* work hardening. *Matls. Sci. Engr. A*, **A254**, 1998, 166-178.

B.P. Somerday and R.P. Gangloff, Effect of strength on environment-assisted cracking of Ti-8V-6Cr-4Mo-4Zr-3Al in aqueous chloride: crack tip strain rate. *Matls. Sci. Engr. A*, **A254**, 1998a, 179-188.

B.P Somerday, "Metallurgical and Crack-Tip Mechanics Effects on Environment-Assisted Cracking of Beta-Titanium Alloys in Aqueous Chloride," PhD Dissertation, University of Virginia, Charlottesville, VA, 1998b.

B.P. Somerday, L.M. Young and R.P. Gangloff, Crack tip mechanics effects on environment-assisted cracking of beta-titanium alloys in aqueous NaCl. *Fatg. Fract. Engr. Matls. Struct.*, **23**, 2000, 39-58.

B.P. Somerday and N.R. Moody, Micromechanical modeling of hydrogen-induced fracture modes in IN903. in "Advances in Fracture Research, Proceedings of ICF10," Eds., K. Ravi-Chandar, et al., Paper No. ICF108920R, CD version, Elsevier Science, Oxford, UK, 2001.

B.P. Somerday, A.W. Wilson, J.M. Howe, and R.P. Gangloff, Microstructural cause of intergranular hydrogen environment embrittlement of aged beta-titanium alloys. *Metall. Mater. Trans., A*, in review, 2003.

M.O. Speidel and M.V. Hyatt, in: "Advances in Corrosion Science and Technology," Vol. 2, Eds., M.G. Fontana and R.W. Staehle, Plenum Press, New York, NY, 1972, pp. 115-335.

M.O. Speidel, in: "Hydrogen in Metals", Eds., I.M. Bernstein and A.W. Thompson, ASM International, Materials Park, OH, 1974, pp. 249-276.

M.O. Speidel, Stress corrosion cracking of aluminum alloys. *Metall. Trans. A*, **6A**, 1975, 631-651.

M.O. Speidel and P.M. Fourt, in: "Stress Corrosion Cracking and Hydrogen Embrittlement of Iron Base Alloys," Eds., R.W. Staehle, et al., NACE, Houston, TX, 1977, pp. 57-60.

R.W. Staehle, et al., Eds., "Stress Corrosion Cracking and Hydrogen Embrittlement of Iron Base Alloys," NACE, Houston, TX, 1977.

E.A. Starke, Jr. and J.T. Staley, Application of modern aluminum alloys to aircraft. *Prog. Aerospace Sci.*, 1995, **32**, 131-172.

C. St. John and W.W. Gerberich, The effect of loading mode on hydrogen embrittlement. *Metall. Trans.*, **4**, 1973, 589-598.

E.A. Steigerwal, F.W. Schaller and A.R. Troiano, The role of stress in hydrogen induced delayed failure. *Trans. AIME*, **218**, 1960, 832-841.

M.F. Stevens and I.M. Bernstein, The role of aging reactions in the hydrogen embrittlement susceptibility of an HSLA steel. *Metall. Trans. A*, **16A**, 1985, 1879-1886.

R.E. Stoltz N.R. Moody, and M.W. Perra, Microfracture model for hydrogen embrittlement of austenitic steels. *Metall. Trans. A*, **14A**, 1983, 1528-1531.

C. Suarez, G. Velazquez, G. Lopez and R. Robles, in "ECF 13—Fracture Mechanics: Applications and Challenges," Elsevier Science Publishing Co., New York, NY, 2000, pp. 163-181.

P.R. Swann et al., Eds., "Mechanisms of Environment Sensitive Fracture of Materials," The Metals Society, London, UK, 1977.

R.E. Swanson, A.W. Thompson, I.M. Bernstein and J.L. Maloney, in: "Hydrogen Effects in Metals", Eds., I.M. Bernstein and A.W. Thompson, The Minerals, Metals & Materials Society, Warrendale, PA, 1981, pp. 459-466.

D.M. Symons and A.W. Thompson, The effect of hydrogen on the fracture toughness of alloy X-750. *Metall. Trans. A*, **28A**, 1997, 817-824.

D.M. Symons, The effect of hydrogen on the fracture toughness of alloy X-750 at elevated temperatures. *J. Nucl. Matls.*, **265**, 1998, 225-231.

D.M. Symons, A comparison of internal hydrogen embrittlement and hydrogen environment embrittlement of X-750. *Engr. Frac. Mech.*, **68**, 2001, 751-771.

T. Tabata and H.K. Birnbaum, Direct observations of hydrogen enhanced crack propagation in iron. *Scripta Metall.*, **18**, 1984, 231-236.

A. Taha and P. Sofronis, A micromechanics approach to the study of hydrogen transport and embrittlement. *Engr. Frac. Mech.*, **68**, 2001, 803-837.

D.F. Teter, I.M. Robertson and H.K. Birnbaum, The effects of hydrogen on the deformation and fracture of beta–titanium. *Acta Mater.*, **49**, 2001, 4313-4323.

R.L.S. Thomas, "Internal Hydrogen Embrittlement of a Trap-Rich Ultrahigh-Strength Steel, AerMet®100," MS Thesis, University of Virginia, Charlottesville, VA, 2000.

R.L.S. Thomas, J.R. Scully and R.P. Gangloff, Internal hydrogen embrittlement of ultrahigh-strength AerMet®100 Steel. *Metall. Trans., A*, **34A**, 2003, 327-344.

R.L.S. Thomas, D. Li, R.P. Gangloff and J.R. Scully, Trap-governed hydrogen diffusivity and uptake capacity in ultrahigh-strength AerMet® 100 steel. *Metall. Mater. Trans. A*, **33A**, 2002, 1991-2004.

A.W. Thompson, in: "Fracture 1977, Advances in Research on the Strength and Fracture of Materials," Vol. II, Pergamon, New York, NY, 1978, pp. 237-242.

A.W. Thompson and I.M. Bernstein, in: "Advances in Corrosion Science and Technology," Eds., M.G. Fontana and R.W. Staehle, Plenum Publishing Company, New York, NY, 1980, pp. 53-175.

A.W. Thompson and I.M. Bernstein, in: "Hydrogen Effects in Metals," Eds., I.M. Bernstein and A.W. Thompson, The Minerals, Metals & Materials Society, Warrendale, PA, 1981, pp. 291-308.

A.W. Thompson and J.A. Brooks, Hydrogen performance of precipitation-strengthened stainless steels based on A-286. *Metall. Trans. A*, 6A, 1975, 1431-1442.

A.W. Thompson and N.R. Moody, Eds., "Hydrogen Effects in Metals," The Minerals, Metals & Materials Society, Warrendale, PA, 1996.

J.J. Thompson, E.S. Tankins and V.S. Agarwala, A heat treatment for reducing corrosion and stress corrosion cracking susceptibilities in 7xxx aluminum alloys. *Matls. Perf.*, 26, 1987, 45-52.

R.M. Thomson, Brittle fracture in a ductile material with application to H embrittlement. *J. Mater. Sci.*, 13, 1978, 128-142.

G.P. Tiwari, A. Bose, J.K. Chakravartty, S.L. Wadekar, M.K. Totlani, R.N. Arya and R.K. Fotedar, A study of internal hydrogen embrittlement of steels. *Matls. Sci. Engr. A*, A286, 2000, 269-281.

J. Toribio and V. Kharin, The effect of history on hydrogen assisted cracking. *Intl. J. Frac.*, 88, 1997, 233-258.

A.R. Troiano, The role of hydrogen and other interstitials in the mechanical behavior of metals. *Trans. ASM*, 52, 1960, 54-80.

A.R. Troiano, in: "Hydrogen in Metals," Eds., I.M. Bernstein and A.W. Thompson, ASM International, Materials Park, OH, 1974, pp. 3-15.

E. Troiano, G.N. Vigilante and J.H. Underwood, in: "Fatigue and Fracture Mechanics: 33rd Volume, ASTM STP 1417," Eds., W.G. Reuter and R.S. Piascik, ASTM International, West Conshohocken, PA, 2002, pp. 116-128.

C.D.S. Tuck, The embrittlement of Al-Zn-Mg and Al-Mg alloys by water vapor. *Metall. Trans. A*, 16A, 1985, 1503-1514.

A. Turnbull, in: "Embrittlement by the Localized Crack Environment," Ed., R.P. Gangloff, The Minerals, Metals & Materials Society, Warrendale, PA, 1984, pp. 3-31.

A. Turnbull and D.H. Ferriss in: "Corrosion Chemistry Within Pits, Crevices and Cracks," ed., A. Turnbull, HMSO Books, London, UK 1987, pp. 357-396.

A. Turnbull and D.H. Ferriss, Mathematical modeling of the electrochemistry in corrosion fatigue cracks in steel corroding in marine environments. *Corros. Sci.*, 27, 1987a, 1323-1350.

A. Turnbull and M.S. Saenz de Santa Maria, in "Environment-Induced Cracking of Metals," Eds., R.P. Gangloff and M.B. Ives, NACE, Houston, TX, 1990, pp. 193-196.

A. Turnbull, Ed., "Hydrogen Transport and Cracking in Metals," Institute of Materials, London, UK, 1995.

A. Turnbull, D.H. Ferriss, and H. Anzai, Modeling of the hydrogen distribution at a crack tip. *Matls. Sci. Engr.*, A206, 1996, 1-13.

A. Turnbull, Modeling of the chemistry and electrochemistry in cracks--a review. *Corrosion*, **57**, 2001, 175-189.

A. Turnbull, in: "Aging Studies and Lifetime Extension of Materials," Kluwer Academic/Plenum Publishers, New York, NY, 2001a, pp. 397-414.

P.S. Tyler, M. Levy and L. Raymond, Investigation of the conditions for crack propagation and arrest under cathodic polarization by rising step load bend testing. *Corros.*, **47**, 1991, 82-87.

W.A. Van der Sluys, Mechanisms of environment induced subcritical flaw growth in AISI 4340 steel. *Engr. Frac. Mech.*, **1**, 1969, 447-462.

H.P. van Leeuwen, The kinetics of hydrogen embrittlement: A quantitative diffusion model. *Engr. Frac. Mech.*, **6**, 1974, 141-161

H.P. van Leeuwen, Plateau velocity of high strength steel in SCC- A quantitative treatment. *Corrosion*, **31**, 1975, 42-50.

H.P. van Leeuwen, Quantitative models of hydrogen-induced cracking in high strength steels. *Review on Coatings and Corrosion*," **4**, 1979, 5-93.

H. Vehoff and W. Rothe, Gaseous hydrogen embrittlement in Fe-Si and Ni-single crystals. *Acta Metall.*, **31**, 1983, 1781-1793.

H. Vehoff and P. Neumann, in: "Hydrogen Degradation of Ferrous Alloys," Eds., R.A. Oriani, J.P. Hirth and S. Smialowska, Noyes Publications, Park Ridge, NJ, 1985, pp. 686-711.

H. Vehoff, in: "Hydrogen in Metals III: Properties and Applications," Eds., G. Alefeld and J. Völkl, Spinger-Verlag, Berlin, Germany, 1997, pp. 215-278.

L. Vehovar, Hydrogen-assisted stress corrosion of prestressing wires in a motorway viaduct. *Engr. Fail. Anal.*, **5**, 1998, 21-27.

G.N. Vigilante, J.H. Underwood, D. Crayton, S. Tauscher, T. Sage and E. Troiano, in: "Fatigue and Fracture Mechanics: 28th Volume, ASTM STP 1321," Eds., J.H. Underwood, B.D. MacDonald and M.R. Mitchell, ASTM International, West Conshohocken, PA, 1997, pp. 602-616.

G.N. Vigilante, J.H. Underwood and D. Crayton, in: "Fatigue and Fracture Mechanics: 30th Volume, ASTM STP 1390," Eds., P.C. Paris and K.L. Jerina, ASTM International, West Conshohocken, PA, 2000, pp. 377-387.

R. Viswanathan and S.J. Hudak, Jr., The effect of impurities and strength level on hydrogen induced cracking in a low alloy turbine steel. *Metall. Trans. A*, **8A,** 1977, 1633-1637.

H. Vogt and M.O. Speidel, Stress corrosion cracking of two aluminium alloys: a comparison between experimental observations and data based on modeling. *Corros. Sci.*, **40**, 1998, 251-270.

R.J. Walter, R.P. Jewett and W.T. Chandler, On the mechanism of hydrogen-environment embrittlement of iron- and nickel-based alloys. *Matls. Sci. Engr.*, **5**, 1969/70, 99-110.

R.J. Walter and W.T. Chandler, in: "Hydrogen in Metals," Eds., I.M. Bernstein and A.W. Thompson, ASM International, Materials Park, OH, 1974, pp. 515-525.

R.J. Walter and W.T. Chandler, in: "Environmental Degradation of Engineering Materials," Eds., M.R. Louthan and R.P. McNitt, VPI Press, Blacksburg, VA, 1977, pp. 513-522.

R.J.H. Wanhill, Aqueous stress corrosion in Ti alloys. *Brit. Corros. J.*, **10**, 1975, 69-78.

R.P. Wei, S.R. Novak and D.P. Williams, Some important considerations in the development of stress corrosion cracking test methods. *Matls. Res. Stds.*, **12**, 1972, 25-30.

R.P. Wei, in: "Hydrogen Effects in Metals," Eds., I.M. Bernstein and A.W. Thompson, The Minerals, Metals & Materials Society, Warrendale, PA, 1981, pp. 677-689.

R.P. Wei and M. Gao, in: "Hydrogen Degradation of Ferrous Alloys," Eds., R.A. Oriani, J.P. Hirth and S. Smialowska, Noyes Publications, Park Ridge, NJ, 1985, pp. 579-607.

R.P. Wei and S.R. Novak, Interlaboratory evaluation of K_{ISCC} and da/dt measurement procedures for high-strength steels. *J. Test. Eval.*, **15**, 1987, 38-75.

R.P. Wei and R.P. Gangloff, in: "Fracture Mechanics: Perspectives and Directions, ASTM STP 1020," Eds., R.P. Wei and R.P. Gangloff, ASTM International, West Conshohocken, PA, 1989, pp. 233-264.

Y. Wei and J.W. Hutchinson, Steady state crack growth and work of fracture for solids characterized by strain gradient plasticity. *J. Mech. Phys. Sol.*, **45**, 1997, 1253-1273.

M.G.H. Wells, Advances in steels for aerospace applications. *Key Engr. Matls.*, 1993, **77-78**, 71-80.

E.P. Whelen, in: "Hydrogen Effects in Metals," Eds., I.M. Bernstein and A.W. Thompson, The Minerals, Metals & Materials Society, Warrendale, PA, 1981, pp. 979-986.

D.P. Williams and H.G. Nelson, Embrittlement of 4130 steel by low pressure gaseous hydrogen. *Metall. Trans.*, **1**, 1970, 63-68.

D.P. Williams and H.G. Nelson, Discussion of embrittlement of 4130 steel by low-pressure gaseous hydrogen. *Metall. Trans.*, **1**, 1970a, 2346-2357.

J. Woodtli and R. Kieselbach, Damage due to hydrogen embrittlement and stress corrosion cracking. *Engr. Fail. Anal.*, **7**, 2000, 427-450.

Y. Yamaguchi, H. Nonaka and K. Yamakawa, Effect of H content on threshold stress intensity factor in carbon steel in hydrogen-assisted cracking environments. *Corrosion*, **53**, 1997, 147-155.

K. Yamakawa, S. Yonezawa and S. Yoshizawa, in: "International Congress on Metallic Corrosion," National Research Council, Toronto, Canada, 1984, pp. 254-261.

K. Yamakawa, H. Tsubakino and S. Yoshizawa, in: "Critical Issues in Reducing the Corrosion of Steels," Eds., H. Keidheiser Jr. and S. Haruyama, NACE, Houston, TX, 1986, pp. 348-358.

G.R. Yoder, P.S. Pao and R.A. Bayles, Ripple load cracking in a titanium alloy. *Scripta Metall. Mater.*, **24**, 1990, 2285-2289.

T. Yokobori, J. Watanabe, T. Aoki and T. Iwadate, in: "Fracture Mechanics, 18th Symposium, ASTM STP 945," ASTM International, West Conshohocken, PA, 1988, pp. 843-866.

A.T. Yokobori, Jr., Y. Chinda, T. Nemoto, K. Satoh and T. Yamada, The characteristics of hydrogen diffusion and concentration around a crack tip concerned with hydrogen embrittlement. *Corros. Sci.*, **44**, 2002, 407-424.

K. Yoshino and C.J. McMahon, Jr., Cooperative relation between temper embrittlement and H embrittlement in a high-strength steel. *Metall. Trans.*, **5**, 1974, 363-370.

G.A. Young, Jr. and J.R. Scully, Hydrogen embrittlement of solution treated and aged β-titanium alloys Ti-15%V-3%Cr-3%Al-3%Sn and Ti-15%Mo-3%Nb-3%Al. *Corrosion*, **50**, 1994, 919-933.

G.A. Young, Jr. and J.R. Scully, The effects of test temperature, temper and alloyed copper on the hydrogen-controlled crack growth rate of an Al-Zn-Mg-Cu alloy. *Metall. Mater. Trans.A*, **33A**, 2002, 1167-1181.

L.M. Young, M.R. Eggleston, H.D. Solomon and L.R. Kaisand, Hydrogen-assisted cracking in a precipitation-hardened stainless steel: Effects of heat treatment and displacement rate. *Matls. Sci. Engr.*, **A203**, 1995, 377-387.

L.M. Young, G.A. Young, Jr., J.R. Scully, and R.P. Gangloff, Aqueous environment enhanced crack propagation in high strength beta titanium alloys. *Metall. Mater. Trans.*, *A*, **26A**, 1995, 1257-1271.

L.M. Young, "Microstructural Dependence of Aqueous-Environment Assisted Crack Growth and Hydrogen Uptake in AA7050," PhD Dissertation, University of Virginia, Charlottesville, VA, 1999.

L.M. Young and R.P. Gangloff, in: "Advances in the Metallurgy of Aluminum Alloys," Ed., M. Tiryakioglu, ASM International, Materials Park, OH, 2001, pp. 135-140.

Tong-Yi Zhang and J.E. Hack, The equilibrium concentration of hydrogen atoms ahead of a mixed Mode I-Mode III crack tip in single crystal iron. *Metall. Mater. Trans. A*, **30A**, 1999, 155-159.

Hydrogen Trap States in Ultrahigh-Strength AERMET 100 Steel

Daoming Li, Richard P. Gangloff and John R. Scully

Hydrogen Trap States in Ultrahigh-Strength AERMET 100 Steel

DAOMING LI, RICHARD P. GANGLOFF, and JOHN R. SCULLY

Hydrogen (H) trap states and binding energies were determined for AERMET 100 (Fe-13.4Co-11Ni-3Cr-1.2Mo-0.2C), an ultrahigh-strength steel using thermal desorption methods. Three major H desorption peaks were identified in the precipitation-hardened microstructure, associated with three distinct metallurgical trap states, and apparent activation energies for desorption were determined for each. The lattice diffusivity (D_L) associated with interstitial H was measured experimentally and verified through trapping theory to yield H-trap binding energies (E_b). Solid-solution elements in AERMET 100 reduce D_L by decreasing the pre-exponential diffusion coefficient, while the activation energy for migration is similar to that of pure iron. M_2C precipitates are the major reversible trap states, with E_b of 11.4 to 11.6 kJ/mol and confirmed by heat treatment that eliminated these precipitates and the associated H-desorption peak. A strong trap state with E_b of 61.3 to 62.2 kJ/mol is likely associated with martensite interfaces, austenite grain boundaries, and mixed dislocation cores. Undissolved metal carbides and highly misoriented grain boundaries trap H with a binding energy of 89.1 to 89.9 kJ/mol. Severe transgranular hydrogen embrittlement in peak-aged AERMET 100 at a low threshold-stress intensity is due to H repartitioning from a high density of homogeneously distributed and reversible M_2C traps to the crack tip under the influence of high hydrostatic tensile stress.

I. INTRODUCTION

ULTRAHIGH-STRENGTH steel (UHSS) is used in high-performance aerospace applications that require high tensile strength and fracture toughness.[1,2] A secondary-hardening UHSS, AERMET* 100, was developed to provide plane-strain

---

*AERMET is a trademark of Carpenter Technology Corporation, Wyomissing, PA.

---

fracture toughness (K_{IC}) in excess of 120 MPa$\sqrt{m}$ doubling that of older steels such as AISI 4340 and 300M, each at a constant yield strength (σ_{YS}) of 1750 MPa.[3,4] This strength is produced by a homogeneous distribution of nanoscale coherent M_2C alloy carbides in a highly dislocated Fe-Ni lath martensite matrix.[5,6] The high K_{IC} value of AERMET 100 is achieved by advanced melting to minimize sulfur plus phosphorus and inclusion contents, austenitization to control the undissolved carbides and grain size, and aging to optimize austenite precipitates along martensite lath interfaces.[2,4,7,8]

Ultrahigh-strength steels are susceptible to severe internal hydrogen embrittlement (IHE) as well as hydrogen environment embrittlement (HEE), and AERMET 100 is no exception.[9] Several studies demonstrated subcritical HEE at apparent threshold stress-intensity levels as low as 20 to 30 MPa$\sqrt{m}$ when the microstructure, optimized for a high K_{IC} (~130 MPa$\sqrt{m}$), was stressed in neutral chloride near the free corrosion potential.[10,11,12] An UHSS is often electroplated for corrosion resistance, introducing codeposited hydrogen (H) and the potential for IHE.[13,14] Thomas and co-workers demonstrated

that optimally aged AERMET 100 is susceptible to severe IHE at threshold stress-intensity levels as low as 20 MPa$\sqrt{m}$ and is produced by diffusible H contents as low as 1 ppm by weight (wppm).[15] Both IHE and HEE in AERMET 100 are transgranular, associated with cracking of the various interfaces associated with the martensitic microstructure.[10–12,15–17] This transgranular H-cracking mode is traced to the low concentration of metalloid impurities segregated to prior-austenite grain boundaries, to minimize intergranular cracking, coupled with substantial H accumulation by trapping at transgranular sites in the crack-tip process zone.[9,15]

Understanding of hydrogen interactions and transport in UHSS microstructures is necessary to control hydrogen embrittlement. For example, thermal treatment eliminates H from electroplating and reverses IHE.[13,14] Process parameters must be selected based on knowledge of H solubility and diffusion through the complex UHSS microstructure. From the mechanistic perspective, micromechanical models of the threshold and kinetics of IHE and HEE require descriptions of H diffusion ahead of a stationary or moving crack tip and segregation at highly dilated regions of the stressed crack tip.[9,18] The microstructural features that provide the high strength and toughness of secondary-hardening martensitic steels such as AERMET 100, including dislocations, carbides, martensite lath interfaces, solute, and prior-γ grain boundaries,[5–8] are likely sites for H segregation or trapping.

Hydrogen solubility in an UHSS/environment system, as well as H diffusivity, is controlled by trapping. Generally, increasing the number density of trap sites and/or increasing the binding energy (E_b) of H to a trap state decrease the apparent H diffusivity (D_{app}) and increase the apparent solubility of H compared to pure iron.[19–24] The influences of H trapping in IHE and HEE are important but complex.[18,25–27] Reversible trap sites with low E_b values provide a reservoir of mobile H that diffuses to areas of lower H chemical potential, such as the dilated region under triaxial tensile stress

---

DAOMING LI, Research Scientist, RICHARD P. GANGLOFF, Professor and Chair, and JOHN R. SCULLY, Professor, are with the Department of Materials Science and Engineering, University of Virginia, Charlottesville, VA 22904-4745. Contact e-mail: jrs8d@virginia.edu
Manuscript submitted June 20, 2003.

ahead of a crack tip. Such traps exacerbate IHE, as illustrated by the decreasing threshold stress intensity with increasing diffusible H concentration reported for AISI 4340–type steels[28,29,30] as well as in AERMET 100.[15] A trap-affected low D_{app} value slows the crack growth rate in these situations.[9] In contrast, a homogeneous distribution of irreversible or strong-reversible traps, that do not themselves constitute fracture-initiation sites and a connected crack path, could prevent H from segregating to susceptible interfaces prone to H-enhanced crack growth and, thus, alleviate IHE.[31,32,33]

A basic understanding of the role of H trapping in solubility, diffusivity, and embrittlement requires information on the trap binding energy and trap distribution in the microstructure. This analysis is hindered by the multiple trapping states present in an UHSS microstructure. Hydrogen trapping parameters have been determined using various experimental approaches. Permeation,[26] thermal-desorption spectroscopy (TDS),[34,35] internal friction,[36] and potentiostatic-pulse[37] methods are typical approaches. However, the permeation, internal friction, and potentiostatic-pulse methods only provide an overall impression of trap strength and capacity and do not determine specific properties of multiple trap states. The TDS method is well suited to provide such detailed information, provided that validated models of the thermodynamics and kinetics of H trapping and transport are available for data analysis.

There have been significant advances in theoretical approaches to trap-affected H transport, with models by McNabb and Foster[38] and Oriani[23] effectively describing the process applicable to steels. For traps with low binding energies, termed reversible traps, it is assumed that dynamic equilibrium exists between the trapped H population and H in interstitial lattice sites.[23] The H diffusion is slowed because of this interaction. Irreversible traps are generally not in equilibrium and do not interact with lattice H after saturation. With these assumptions, Oriani's model correlated important parameters, including D_{app}, E_b, and the density of trap sites.[23] This model is utilized in the present work.

A previous study showed that H trapping plays an important role in reducing the kinetics of H transport and enhancing H uptake in AERMET 100.[39] Multiple trap states were indicated by a preliminary TDS experiment, and an approximate energy for H desorption (E_d) of 21 kJ/mol was estimated for an important-reversible state speculatively attributed to H interaction with M_2C. The objective of the present investigation is to precisely establish the binding energy associated with each H trap state in optimally aged AERMET 100. These values of E_b are determined from TDS experiments using available analytical methods and assuming a specific H detrapping model. The dominant trap state over the temperature range from 60 °C

to 200 °C is independently verified from evaluation of D_{app} using trap theory.[23] Trap binding energies are correlated with the specific microstructural features of AERMET 100, and an assessment is made of H redistribution from reversible trap sites to the stressed crack-tip process zone during IHE.

II. EXPERIMENTAL AND ANALYTICAL PROCEDURES

A. Material and Heat Treatment

The AERMET 100 was received as a forged and annealed bar, 15.2 cm in diameter and 30.5 cm in length, with the chemical composition shown in Table I. To achieve optimal strength and toughness,[5,40] specimens were solution treated in vacuum at 885 °C for 1 hour, air cooled to room temperature in 2 hours, chilled at −73 °C for 1 hour, and tempered at 482 °C for 5 hours. The mechanical properties that resulted from this treatment are shown in Table II.

This processing produced an extremely fine and complex microstructure having the following features:[5–8] (1) less than 0.1-μm-diameter incoherent carbides (i.e., $(MoCr)_7C_3$, $(FeCr)_xC_y$, TiC, and (TiCrMo)C) that provide grain refinement, (2) prior-austenite grain boundaries, (3) martensite laths on the order of 0.15-μm thick, both twinned and untwinned, with interfaces that are qualitatively high-angle and arrayed in packets, (4) dislocations in martensite and not recovered at this tempering temperature, (5) finely distributed, partly coherent M_2C (where M = 75 at. pct Cr, 13 Fe, and 12 Mo) in martensite, averaging 2 nm in diameter × 8 nm in length, (6) Cr and/or Mo dissolved in coherent clusters in martensite, (7) Co dissolved in martensite, perhaps with short-range order, (8) precipitated austenite, and (9) Ni dissolved in austenite. The amount of retained austenite is negligible due to refrigeration.[5] Precipitated austenite is present as a thin layer (~3 nm) at martensite lath interfaces, based on electron microscopy observations, but the volume fraction from X-ray diffraction measurements is uncertain, ranging from an average of 0.8 vol pct[5] to 4 vol pct[6] for the 482 °C temper. As-quenched samples were also made to yield a microstructure of large-undissolved carbides in dislocated martensite, but without M_2C precipitates. Throughout, AERMET 100 denotes the aged (or tempered) state, unless it is indicated to be "as-quenched."

B. Electrochemical H Charging

Hydrogen was charged into AERMET 100 samples that were maintained potentiostatically at a constant electrochemical potential in saturated $Ca(OH)_2$ at 60 ± 2 °C for 72 hours. The

Table I. Chemical Composition (Weight Percent) of AERMET 100

Fe	Co	Ni	Cr	Mo	C	Ti	P	S	H (wppm)
Bal.	13.43	11.08	3.00	1.18	0.23	0.009	0.003	0.0008	0.35

Table II. Mechanical Properties of AERMET 100

Hardness (Rockwell C)	σ_{YS} MPa (ksi)	σ_{UTS} MPa (ksi)	RA (Pct)	K_{IC} MPa$\sqrt{m}$ (ksi$\sqrt{in.}$)
54	1765 (256)	1985 (288)	61	139 (120)

σ_{YS} = yield strength, σ_{UTS} = tensile strength, RA = reduction of area, and K_{IC} = plane strain fracture toughness.

specimen used was a thin plate ($12.7 \times 6.4 \times 0.5$ mm) that was ground to a 600-grit finish and degreased ultrasonically. The solution was prepared with pre-electrolyzed, deionized (18.2 MΩ) water and exhibited a pH of 12.1. This exposure time was at least 30 pct longer than that required to achieve uniform H saturation throughout the specimen thickness, estimated based on a model of one-dimensional diffusion in a plane sheet and a conservative value of $D_{app} = 3 \times 10^{-8}$ cm^2/s at 60 °C.[39,41] The reversible H oxidation/reduction potential ($E_{R_{H^+/H}}$) for the Ca(OH)$_2$ charging solution was -1.33 V (with reference to Hg/Hg$_2$SO$_4$). For H charging, two electrochemical potentials ($E_{applied}$) were applied (-1.95 and -2.5 V), giving corresponding H overpotentials ($\eta_{chg} = E_{applied} - E_{R_{H^+/H}}$) of -0.62 and -1.17 V, respectively. These charging conditions produced diffusible H concentrations ($C_{H,diff}$) of 7.4 and 7.6 wppm, respectively,* and a total H

---

*The diffusible H concentration was observed to strongly depend on η_{chg} up to $\eta_{chg} = -0.6$ V, then become η_{chg}-independent.[39]

---

concentration of 31.5 wppm for the lower overpotential, each in peak-aged AERMET 100.[39] As-charged specimens were stored in liquid nitrogen prior to TDS experimentation.

C. TDS Measurements

The experimental method for characterizing H trapping and evolution was temperature-ramp-programmed TDS.[35] The gas analyzer was computer interfaced using MOTF* software

---

*MOTF is a trademark of Ametek, Paoli, PA.

---

for data acquisition. The background hydrogen pressure (P_{H_2}) in the vacuum chamber was eliminated by performing TDS experiments on uncharged specimens to provide a "zero-H" spectra, which was subtracted from each spectra for H-charged specimens to yield background-corrected P_{H_2} vs time (t) data for subsequent analysis. Corrected P_{H_2} vs t data were transformed to values for the desorbed H concentration (C_H) and its rate of variation (dC_H/dt) vs time or temperature for constant-rate heating. The latter were further used to calculate the parameters for H diffusion and trapping/detrapping.

For each TDS test, the specimen was first held at room temperature for 20 to 30 minutes in an upper vacuum chamber to restore the primary-chamber vacuum upset by specimen installation, then dropped into the lower chamber for immediate analysis by the quadrupole gas analyzer. This hold time was small compared to the 72 hour charging time, and H loss was minimal given the low H diffusivity for AERMET 100 at room temperature. A temperature-programmed desorption mode was used for characterizing H desorption/detrapping behavior by quantifying the variation of desorption maxima with heating rate. The PEAKFIT* software package

---

*PEAKFIT is a trademark of Systat Software Inc., Richmond, CA.

---

established the temperature (T_m) at which a desorption peak occurs, since overlapped and partially hidden peaks are typical of H trapping at multiple states in a complex microstructure. A peak was recognized only if reproduced in multiple-sample tests. The TDS specimen was heated from room temperature to 550 °C at a constant rate (dT/dt) between 1 °C and 10 °C/min immediately upon loading into the lower chamber.

An isothermal TDS testing mode was used for measuring H diffusivity. Tests were conducted at constant temperatures, such that either trap-affected diffusivity (in the range of 60 °C to 200 °C) or lattice diffusivity (D_L, at 450 °C, 500 °C, and 550 °C) could be determined. The desired test temperature was stabilized prior to specimen loading into the lower chamber. A detailed description of diffusivity measurements is given elsewhere.[39]

The experimental method to establish $D_L(T)$ for H in AERMET 100 was based on isothermal determination of $D_{app}(T)$ coupled with the assumption that $D_{app}(T)$ approaches ideal lattice diffusivity at high temperatures where trapping is minimized. The temperature dependence of lattice H diffusivity is described by[42]

$$D_L(T) = D_0 \exp\left(-\frac{E_m}{RT}\right) \qquad [1]$$

where D_0 is the pre-exponential diffusion coefficient and E_m is the activation energy for lattice diffusion of H in the absence of trapping. For clarity, E_m^{app} denotes trap-affected activation energy in the heat-treated alloy, corresponding to $D_{app}(T)$. The key experimental issue is whether rapid heating to the temperature for TDS analysis is achieved without significant H loss. This capability was verified by measuring D_L for high-purity Ni over a high temperature range, using TDS, and the results were compared to results established by other methods.[43]

D. Determination of Apparent Activation Energy for H Desorption

Thermal desorption from a homogeneously charged specimen is described by[44]

$$\frac{dX_d}{dt} = v_x(1 - X_d)^n \exp\left(\frac{-E_d}{RT}\right) \qquad [2]$$

where X_d is the fraction of integrated quantity of H desorbed, v_x is a constant, E_d is the activation energy for H desorption, R is the gas constant (8.31 J/mol K), and T is the absolute temperature. An E_d value can be calculated using TDS data obtained at different heating rates. The T_m value increases with dT/dt, as demonstrated in TDS[45] and differential thermal analysis,[46] and E_d depends on T_m and dT/dt according to[46]

$$\frac{d\left(\ln\left(\dfrac{dT/dt}{T_m^2}\right)\right)}{d\left(\dfrac{1}{T_m}\right)} = -\frac{E_d}{R} \qquad [3]$$

where E_d was calculated from the linear-regression slope of $\ln\left((dT/dt)/T_m^2\right)$ vs $1/T_m$ data, obtained from desorption maxima as a function of dT/dt. This analysis was applied to each trap peak observed during a temperature-programmed TDS experiment.

The E_d values provide the basis for estimating the binding energy for H trapping associated with each of the observed states, provided that the relationship between E_d and E_b is known. In this article, E_d is assumed to equal $E_m + E_b$, where E_m is the activation energy for H diffusion by an

interstitial-jump mechanism in the trap-free steel lattice containing the alloy elements in the solid solution of AERMET 100. This sum is a valid description of the energetics of desorption, provided that detrapping and lattice diffusion are the dominant processes during H desorption (e.g., H release is not surface controlled). Moreover, this sum is valid as long as the activation-energy barrier for trapping equals E_m, while detrapping from the trap to interstitial site equals $E_m + E_b$. The former assumption was confirmed in previous work, where H egress during desorption was shown to be a first-order process.[39] The latter is a common assumption in trap theory in the case of nonsaturable physical traps such as interfaces and boundaries.[20,47] Both experimental and analytical procedures have been employed to determine E_m for trap-free H diffusion in AERMET 100.

E. Determination of Overall H-Trap Binding Energy

Trap-affected H diffusivity is used to determine an overall trap binding energy relevant to a specific temperature range. Oriani proposed an equation relating D_{app} to the density of trap sites and trap binding energies,[23] which has been successfully applied to steels.[39] Assuming a low-reversible trap-site coverage and low lattice solubility of H, $D_{app}(T)$ is related to the number of reversible trap sites of each type per unit volume (N_r) and E_b, according to a modification to Oriani's expression:[23]

$$D_{app}(T) = \frac{D_L(T)}{1 + \sum_i \frac{N_r^i}{N_L} \exp\left(\frac{E_b^i}{RT}\right)(1 - \Theta_T^i)} \quad [4]$$

where $D_L(T)$ is the diffusivity for lattice migration of H, N_L is the number of ordinary interstitial sites available for H in the perfect lattice, Θ_T is fractional trap-site coverage of H, and i is the index that identifies each trap state.

As site coverage is generally far less than unity ($\Theta_T \ll 1$) and assuming a single dominant trap state that affects $D_{app}(T)$, Eq. [4] is simplified to

$$D_{app}(T) = \frac{D_L(T)}{1 + \frac{N_r}{N_L} \exp\left(\frac{E_b}{RT}\right)} \quad [5a]$$

$$\ln\left(\frac{D_L(T)}{D_{app}(T)} - 1\right) = \ln\left(\frac{N_r}{N_L}\right) + \frac{E_b}{RT} \quad [5b]$$

By obtaining $D_{app}(T)$ at various temperatures, an overall trap binding energy and overall trap fraction (N_r/N_L) can be determined from the slope and intercept, respectively, defined by linear regression of $\ln ((D_L(T)/D_{app}(T)) - 1)$ vs $1/T$ data. Experimental data giving $D_{app}(T)$ in the range of 60 °C to 200 °C were obtained previously[39] and used in the present study to determine E_b by Eq. [5b]. In order to use Eq. [5b] to determine E_b and N_r/N_L, $D_L(T)$ must be known for the same range of T values where $D_{app}(T)$ data are collected. Since it is not known a priori if a single trap state controls D_{app} for AERMET 100 over a given temperature range, an overall E_b value is determined by this method.

F. Confirmation of Ideal Lattice Diffusivity

The TDS-measured ideal lattice diffusivity vs temperature relationship was confirmed by ensuring that choices for D_0, E_m, and N_r/N_L obeyed Eq. [5b]. A procedure to estimate D_L (i.e., D_0 and E_m in Eq. [1]) was conducted using Eq. [5a] or [5b], as described in Appendix A.

III. RESULTS

A. Determination of Temperature-Dependent Apparent and Lattice Diffusivities of H in AERMET 100

Experimental values of trap-sensitive D_{app} values were obtained by isothermal TDS experiments over the temperature range of 23 °C to 200 °C with AERMET 100 specimens H charged at $\eta_{chg} = -0.62$ and -1.17 V.[39] These results are plotted in Figure 1 for the lower H overpotential and are represented by least-squares analyses:

$D_{app}(cm^2/s)$

$$= \begin{cases} 3.71 \times 10^{-5} \exp\left(\frac{-17.7(kJ/mol)}{RT}\right) & (\eta_{chg} = -1.17 \text{ V}) \\ 1.59 \times 10^{-5} \exp\left(\frac{-18.0(kJ/mol)}{RT}\right) & (\eta_{chg} = -0.62 \text{ V}) \end{cases}$$

$$[6]$$

Hydrogen diffusivity in aged AERMET 100 was measured by isothermal TDS at temperatures ranging from 450 °C to 550 °C for direct experimental determination of D_L. The data are presented in Figure 1 and are well described by

$$D_{app}(cm^2/s) = 7.1 \times 10^{-6} \exp\left(\frac{-10.8(kJ/mol)}{RT}\right) \quad [7]$$
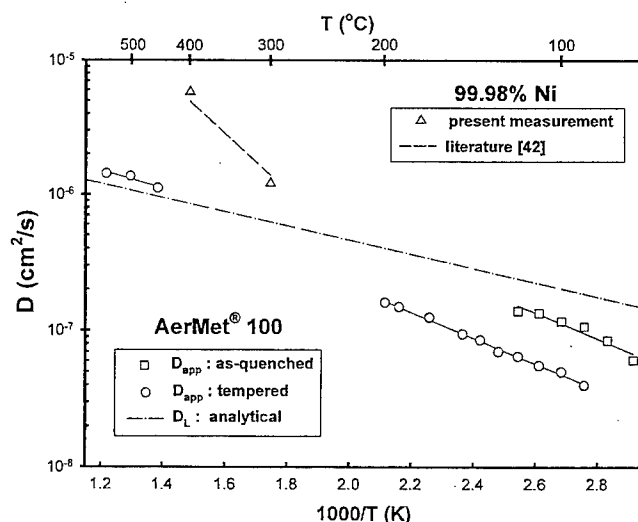

Fig. 1—Temperature-dependent experimental data on D_{app} for AERMET 100, determined by isothermal TDS experiments at elevated temperatures and compared to trap theory estimated D_L in AERMET 100 solid solution. D_{app} data for lower temperatures are included from Ref. 39 for aged AERMET 100 and from TDS experiments for as-quenched AERMET 100. Hydrogen diffusivity data for pure Ni confirm the validity of the TDS experimental method and rapid heating procedure. All data were obtained for specimens H-charged at $\eta_{chg} = -0.62$ V.

The assumption is that $D_{app} \approx D_L$ at these high temperatures, since H trapping is minimal. The results in Figure 1 show that the high-temperature $D_{app}(T)$ trend line for aged AERMET 100 (Eq. [7]) is substantially higher upon extrapolation to low temperatures compared to measured low-temperature D_{app} values (Eq. [6]). This result supports the speculation that the high-temperature diffusivities are typical of lattice H diffusion, with substantially less trapping than encountered at lower temperatures.

The short time (<1 hour) for isothermal TDS measurement did not apparently cause appreciable γ precipitation that could slow H transport due to the low H mobility in this fcc phase. This precipitation is only likely to be substantial above 510 °C.[5] The D_{app} value at 510 °C is not expected to be affected by changes in M_2C coherency and trapping or formation of new trap states during heating, because the thermal energy of the lattice far exceeds typical trap binding energies. The satisfactory agreement between experimental and literature H diffusivity data (trap-free D_L) for pure Ni, indicated in Figure 1, confirms the validity of the experimental method applied at higher temperatures, where high values of the diffusivity introduce the potential for H loss during the TDS specimen insertion and heating to the isothermal exposure condition.

Considering the extensive diffusion data for H in relatively pure α-iron,[43] the majority of D_L vs T data points are located in a narrow band defined by an E_m value of $\sim$10 kJ/mole. This

lattice migration energy, rather than the value of 10.8 kJ/mol from the limited data in Figure 1, was used to determine trap binding energies for AERMET 100. The finding that E_m^{app} of 17 to 18 kJ/mol in Eq. [6] exceeds the E_m value of 10 to 11 kJ/mol for lattice diffusion of H is consistent with trap theory.[47]

B. Apparent (Total) Activation Energy for H Desorption

Figure 2 shows representative H desorption results (dC_H/dt vs temperature) measured during temperature-programmed TDS. For the temperature range from 23 °C to 500 °C, at least three desorption peaks are identified and marked as peaks 1b, 2, and 3 in the order of increasing T_m values. For the low temperatures preceding peak 1b, a "shoulder" exists on the dC_H/dt vs temperature curve, especially for the high dT/dt values.

Figure 2 shows that T_m associated with each peak shifts to a higher temperature as dT/dt increases. The TDS data were processed to generate $\ln((dT/dt)/T_m^2)$ plotted against the reciprocal absolute temperature ($1/T_m$), as shown in Figure 3, for the H detrapping associated with desorption-rate peak 1b. Using Eq. [3], E_d for H detrapping associated with this peak was determined by linear-regression analysis for the two dissolved H concentrations produced by $\eta_{chg} = -0.62$ and -1.17 V. Similar results are shown for peaks 2 and 3 in Figures 4 and 5, respectively. The E_d values with 95 pct–confidence-interval estimates of uncertainty from the regression are listed in Table III for all test conditions. The desorption activation energy for each peak is essentially statistically equal at the 95 pct confidence level for the two charging conditions, and
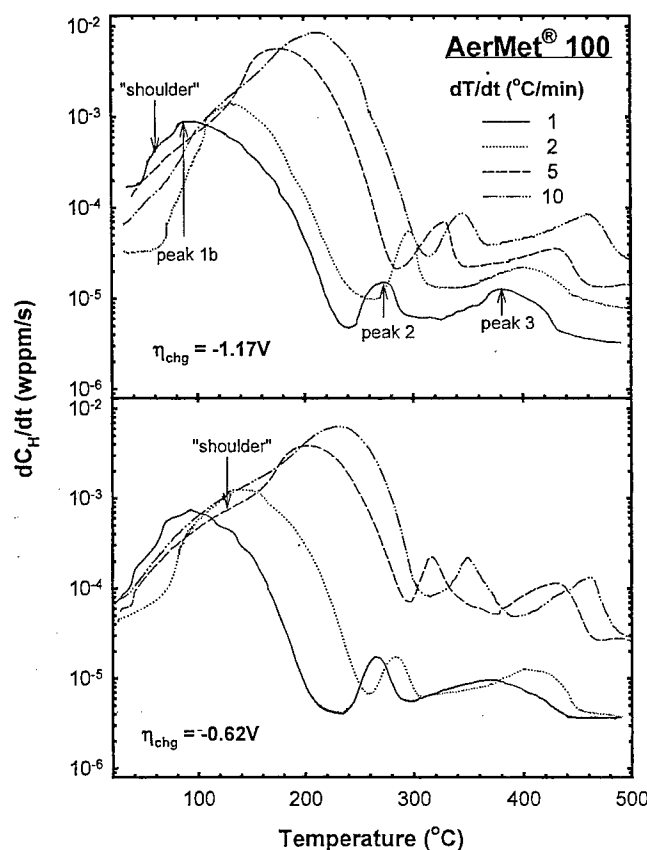

Fig. 2—H desorption rate (dC_H/dt) as a function of temperature obtained from TDS experiments at various ramp rates (dT/dt = 1 °C/min to 10 °C/min) for AERMET 100 steel charged at 60 °C and two overpotentials (η_{chg} = −0.62 and −1.17 V), showing increasing desorption maximum temperature with increasing dT/dt.
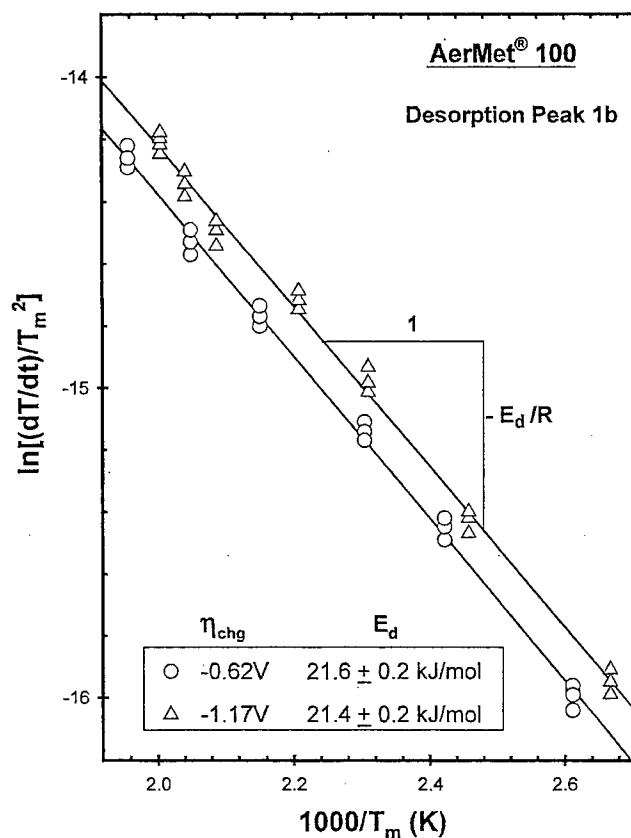

Fig. 3—Experimental determination of the apparent activation energy for H desorption, E_d, associated with detrapping-peak 1b from the H desorption curves in Fig. 2, using Eq. [3].
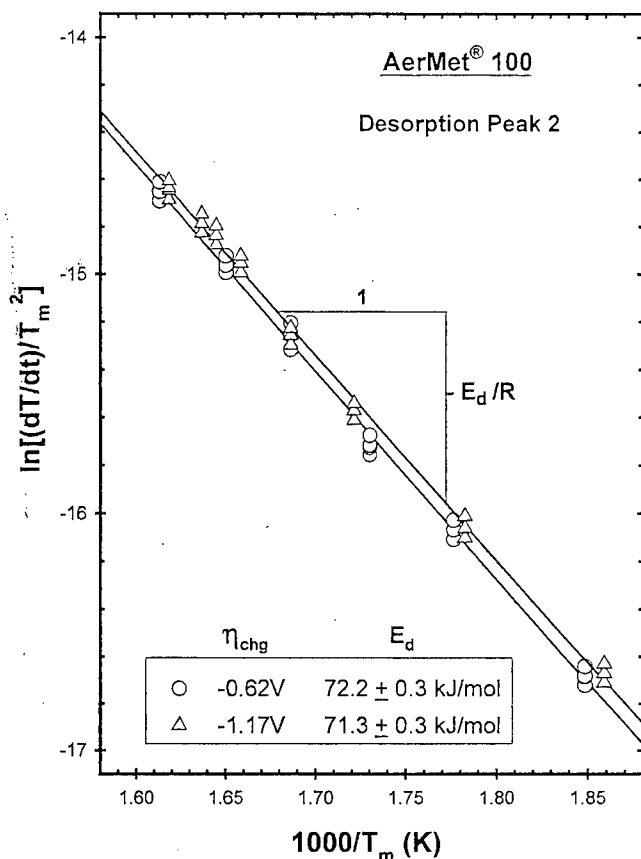
Fig. 4—Experimental determination of the apparent activation energy for H desorption, E_d, associated with detrapping-peak 2 from the H desorption curves in Fig. 2, using Eq. [3].
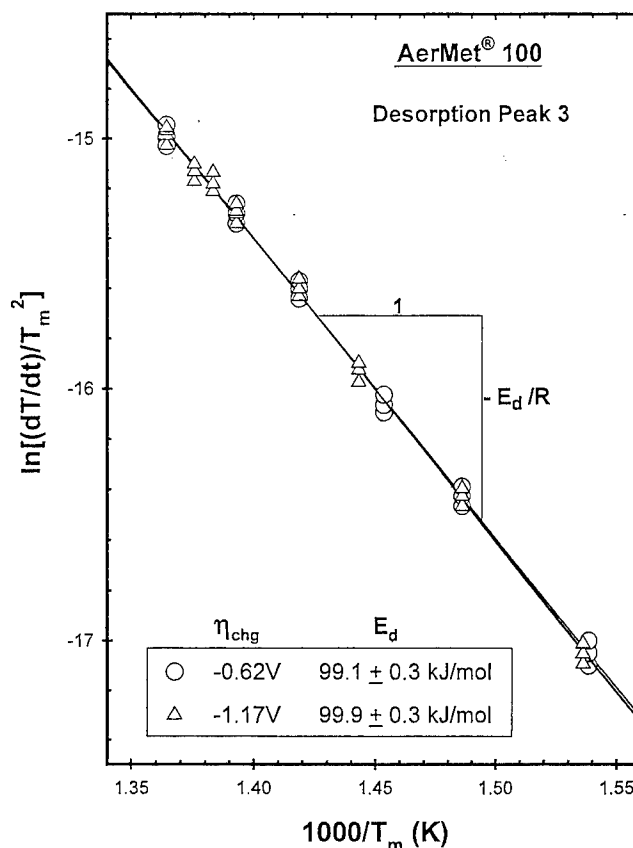
Fig. 5—Experimental determination of the apparent activation energy for H desorption, E_d, associated with detrapping-peak 3 from the H desorption curves in Fig. 2, using Eq. [3].

Table III. Activation Energies for Thermal Desorption of Hydrogen, E_d [kJ/mol (eV/atom)], for AERMET 100

η_{chg}	Peak 1a*	Peak 1b**	Peak 2	Peak 3
−0.62 V	18.9 ± 0.2 (0.196 ± 0.002)	21.6 ± 0.2 (0.224 ± 0.002)	72.2 ± 0.3 (0.748 ± 0.003)	99.1 ± 0.3 (1.027 ± 0.003)
−1.17 V	—	21.4 ± 0.2 (0.222 ± 0.002)	71.3 ± 0.3 (0.739 ± 0.003)	99.9 ± 0.3 (1.035 ± 0.003)

*For as-quenched alloy.
**For aged alloy.

no new trap state is created by microstructural damage (e.g., vacancy formation) at the more negative overpotential.[30] This is consistent with the small effect of applied overpotential on the amount of diffusible H produced in AERMET 100 in the more negative overpotential regime (7.4 and 7.6 wppm produced by η_{chg} = −0.62 and −1.17 V, respectively[39]). Each E_d value is linked to a specific trap state and associated microstructural feature, as represented by each peak in Figure 2.

To clarify the connection between M_2C precipitates and the trap states shown in Figure 2, temperature-programmed TDS tests were performed for specimens with the as-quenched microstructure heated at various dT/dt levels. Figure 6 shows the H desorption rate (dC_H/dt) vs temperature data for as-quenched martensitic AERMET 100, charged at η_{chg} = −0.62 V and analyzed by TDS at dT/dt = 5 °C/min, compared with the aged alloy under the same charging and heating conditions. The area for peak 1b in the as-quenched alloy is substantially decreased compared with aged AERMET 100, and a new small peak (denoted as peak 1a) is apparent in the vicinity of peak 1b and at a temperature higher than the shoul-

der observed for the aged steel. The TDS tests at other dT/dt levels produced similar results. Based on the area under the dC_H/dt vs time curve, the amount of H desorbed over the temperature range where peak 1b appeared for the aged alloy decreases by 98 pct for the as-quenched case (note: logarithmic scale). It is certain that the as-quenched martensitic microstructure does not contain M_2C precipitates that are predominant in the aged alloy.[5] Therefore, the results in Figure 6 strongly suggest that M_2C plays a dominant role in trapping H in the aged alloy, with an energy state associated with peak 1b.

The desorption maximum temperature for peak 1a uncovered in the as-quenched alloy occurs at a lower temperature than peak 1b in the aged alloy (Figure 6), while the changes of T_m for peaks 2 and 3 are negligible. This behavior was observed for each dT/dt level investigated. Values of T_m for peak 1a were obtained at various dT/dt levels and were processed to generate ln $((dT/dt)/T_m^2)$ vs $1/T_m$ and E_d, according to Eq. [3]. The value of E_d for the as-quenched alloy is 18.9 ± 0.2 kJ/mol for peak 1a, which is about 87 pct of the corresponding E_d value for the aged alloy (Table III).
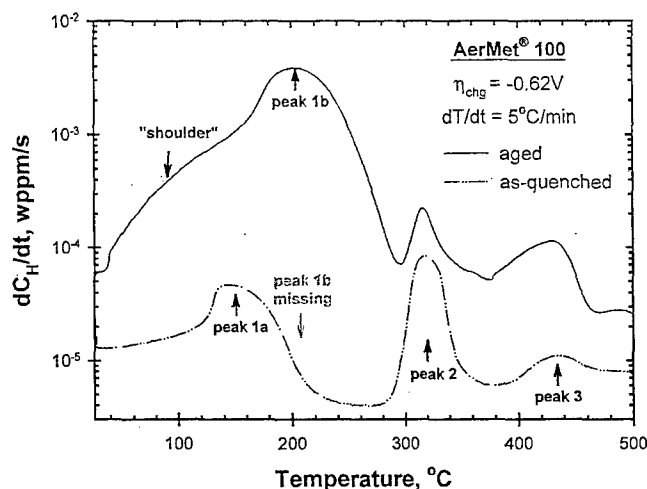
Fig. 6—H desorption rate (dC_H/dt) vs temperature for as-quenched (dashed line) and aged (solid line) AERMET 100, H charged at $\eta_{chg} = -0.62$ V and TDS tested at a heating rate (dT/dt) of 5 °C/min.

Fig. 7—Variation of apparent desorption energy (E_d), trap fraction (N_r/N_L), and lattice-H diffusivity at room temperature ($D_{L,RT}$) vs pre-exponential constant D_0, using a migration energy (E_m) of 10 kJ/mol for AERMET 100 charged with $\eta_{chg} = -0.62$ V. This plot illustrates allocation of the qualified range of these parameters consistent with trap theory in Eq. [5a].

Modeling established that the activation energy for desorption of lattice hydrogen in the absence of traps produces an apparent E_d value equal to E_m, based on the temperature-ramp approach.[34] As considered in Section IV, E_m is 10 to 11 kJ/mol for H in the solid solution of AERMET 100. This comparison suggests that a weak trap of lower binding energy exists between the E_d values of 21.4 to 21.6 kJ/mol for peak 1b in the aged alloy and the E_m value of 10 kJ/mol. This weak trap is not detected by TDS in the aged alloy because of the dominance of the M_2C trap peak. The as-quenched alloy does not display the shoulder seen below the temperature range over which peak 1b (Figure 2) is detected in the aged alloy. The peak temperature associated with peak 1a in the as-quenched alloy is above that of the low shoulder seen at lower temperatures near peak 1b in the aged alloy (Figure 2). This suggests that peak 1a and the shoulder are not the same features as discussed subsequently.

The magnitudes of peaks 2 and 3 for the as-quenched alloy are less than those for the aged alloy, but the extent of change between the as-quenched and tempered conditions is much less than the changes seen in the vicinity of peak 1b. The stronger trap states indicated by peaks 2 and 3 possess identical peak temperatures in the as-quenched and the aged alloys. Quantitative analysis of $\ln((dT/dt)/T_m^2)$ vs $1/T_m$ yielded identical E_d values for peaks 2 and 3 in the as-quenched and aged forms of AERMET 100. The microstructural features that cause peaks 2 and 3 do not change during tempering.

C. *Confirmation of* D_L, E_m, *and* N_r/N_L *Using an Analytical Approach*

Based on measured D_{app} data at temperatures of 60 °C to 200 °C[39] and E_d values measured previously, the TDS-measured values of D_0 and E_m for lattice diffusion of H in AERMET 100 were validated using the selection criteria described in Appendix A and assuming applicability of Eqs. [4] and [5]. This check verifies whether high- and low-temperature data, deemed representative of perfect lattice and trap-affected H diffusivity, respectively, are consistent with trap theory used in this study. It also provides a method
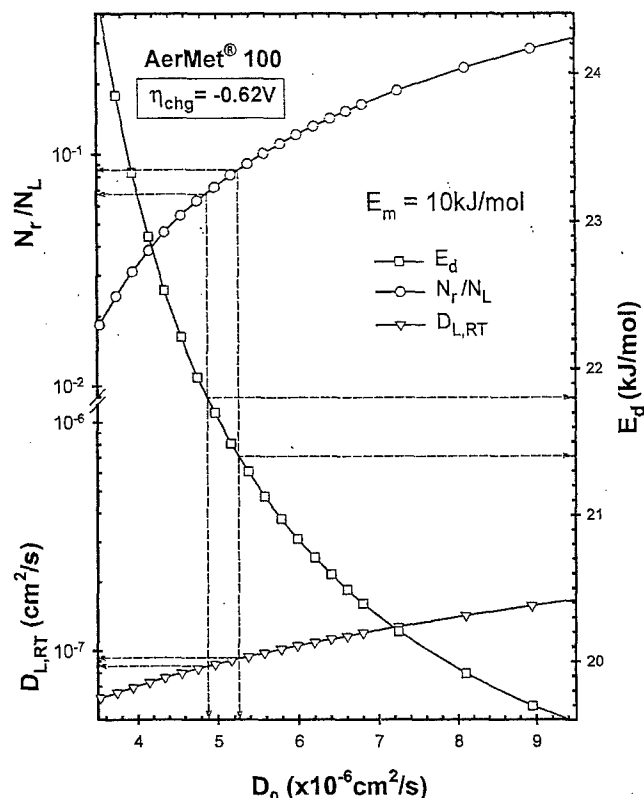
for verifying whether the value of N_r/N_L determined using Oriani trap theory (Eq. [5b]) is reasonable and compatible with the other parameters determined in this study. Model results for a single value of E_m (10 kJ/mol, determined from high-temperature $D_{app} \sim D_L$ measurements for AERMET 100 in Figure 1, as well as broad literature results for iron) are illustrated in Figure 7 as an example of the range of parameters consistent with the guidelines in Appendix A.

From calculations of the type shown in Figure 7, all sets of the D_0, E_m, $D_{L,RT}$, and N_r/N_L values that meet the criterion $E_b + E_m = E_d$ and satisfy Eq. [5b] are plotted in Figure 8. From Figure 8, when the trap-free lattice E_m value approaches the upper-bound activation energy (i.e., E_m^{app} of $\sim$18 kJ/mol for aged AERMET 100), either $D_{L,RT}$ approaches $D_{app,RT}$ for aged AERMET 100 ($\sim 10^{-8}$ cm^2/s), or the sum of E_m and a reasonable E_b exceeds the E_d found by experiment for peak 1b (21.5 kJ/mol in Table III). In contrast, selection of lower values of E_m results in a higher value of $D_{L,RT}$ and a lower value of N_r/N_L that is much less than 1. It is expected that $N_r/N_L \ll 1$, because the number of trap sites per unit volume for a specific trap state are often a small fraction of the density of interstitial sites in the bcc lattice.[48] As such, the parameters compatible with Eq. [5b] justify selecting an E_m value that approaches the energy (7 to 10 kJ/mol) reported for pure iron.[43]

The combination of this analysis based on trap theory, with limited high-temperature TDS measurements of D_L, validate the migration energy of 10 kJ/mol for AERMET 100. The

temperature dependence of D_L for AERMET 100 is plotted in Figure 1 for $E_m = 10$ kJ/mol. Table IV compares lattice diffusion parameters determined both experimentally and estimated analytically for AERMET 100, as well as summarized literature data for pure iron.[43] The results in Figure 1 and Table IV demonstrate good agreement between the experimental determination of D_L and the consistency analysis using trap theory. These results show that D_0, and, hence, D_L, for the solid-solution composition of this steel, are reduced by two orders of magnitude compared to the lattice diffusivity of H in pure iron, while the activation energy for lattice diffusion is unchanged by alloy addition. These results follow the expected effects of solid-solution alloying elements on D_L for interstitial H transport in bcc Fe,[49,50,51] as discussed later.

D. Determination of Trap Binding Energies

1. Overall or effective E_b determined from D_{app} data

Experimental data for $D_{app}(T)$ from TDS, over the range of 23 °C to 200 °C where M_2C trapping is dominant,[39] were

Fig. 8—Analytical results showing the range of and the correlation among $D_{L,RT}$, N_r/N_L, E_m, and D_0 that meet the criterion of $E_d = E_m + E_b$ and obey Eq. [5a].

used in Eq. [5b] to determine an effective or overall E_b and N_r/N_L, given the analytical results of $D_L(T)$. Figure 9 shows the results. Although experimentally determined D_{app} values at various temperatures differ in the case of the two different H-charging overpotentials, the resultant values of overall E_b are statistically equal at a 95 pct confidence level, 11.6 ± 0.4 vs 11.4 ± 0.4 kJ/mol, regardless of charging overpotential. The values of N_r/N_L range from 0.03 to 0.07.

2. Trap-site-specific E_b values determined for trap states 1a, 1b, 2, and 3

Assuming that E_m is constant and equal to 10 kJ/mol over a wide temperature range, the values of E_b for all trap sites identified by the three major peaks were calculated from TDS data assuming physical traps (e.g., the validity of $E_b = E_d - E_m$). Table V lists the E_b values determined for H in the three unique trap states in AERMET 100, charged to two different albeit similar diffusible H concentrations. At the 95 pct confidence level, the overall E_b of 11.4 to 11.6 (±0.4) kJ/mol, determined from D_{app} data over the temperature range of 23 °C to 190 °C using Eq. [5b], equals the E_b of 11.4 to 11.6 (±0.2) kJ/mol obtained from ramp TDS results for peak 1b. The agreement is noteworthy for two reasons, even though physical traps were assumed in both approaches. First, the TDS method does not rely on the choice of Oriani trap theory, as did the method based on D_{app} data used in Figure 9. Second, D_{app} data over the range of 23 °C to 200 °C are apparently dominated by the trap state associated with peak 1b and do not reflect less-significant traps such as the peak 1a trap resolved for as-quenched AERMET 100.

The E_d value of 18.9 ± 0.2 kJ/mol for peak 1a, uncovered at low temperatures in the as-quenched alloy, yields an E_b value of 8.9 ± 0.2 kJ/mol. This value is lower than that determined for peak 1b in the aged alloy (11.6 ± 0.2 kJ/mol, Table V), suggesting that it represents a different low-energy trap state in the carbide-free microstructure.

IV. DISCUSSION

A. Alloying Effects on Interstitial Hydrogen Diffusion

Determination of the migration energy for H diffusion in iron and iron alloys has been controversial. Considering extensive diffusion data for H in relatively pure α-iron, the majority of D_L vs T data are located in a narrow band defined by E_m of ~10 kJ/mol.[43] Occasional studies reported lower E_m values of ~5 kJ/mol, while others report higher migration energies that are likely trap compromised.[43,52] The present results confirm that the E_m value of 10 kJ/mol describes the temperature dependence of lattice H diffusion in AERMET 100, similar to that of trap-free pure iron, but the substantial alloying in this UHSS does decrease D_0 considerably. This finding is in good accordance with the literature. Hagi[49] con-
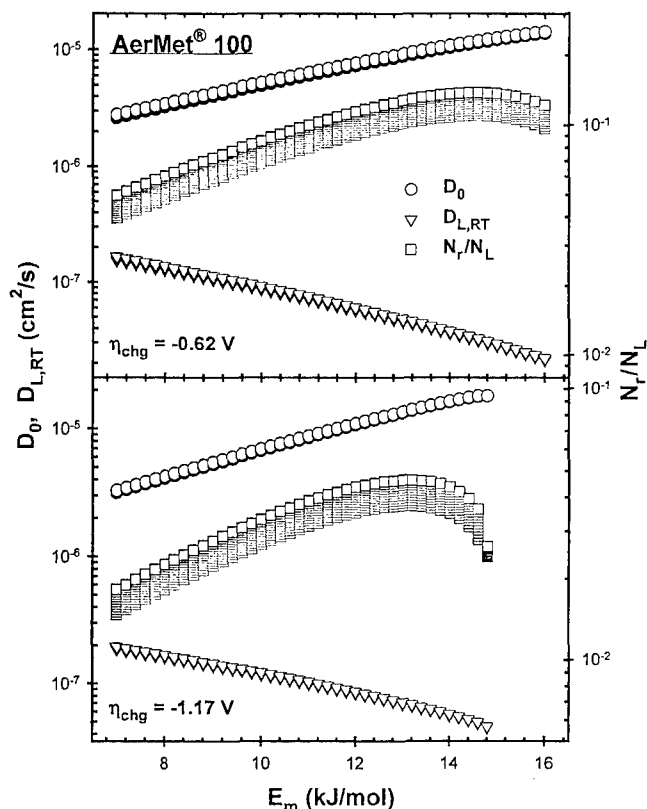
Table IV.   Experimental and Analytical Diffusivity Data for H in Aged AERMET 100 and Iron

Material	D_0 [cm²/s]	D_L (25 °C) [cm²/s]	E_m [kJ/mol]
Aged AERMET 100—analytical	5.1 to 6.7 × 10⁻⁶*	8.9 to 1.2 × 10⁻⁷*	10
Aged AERMET 100—experimental	7.1 × 10⁻⁶**	1.3 × 10⁻⁷**	10.8
Pure iron[43]	7.4 × 10⁻⁴	1.2 × 10⁻⁵	10

*Data range for $\eta_{chg} = -0.62$ to -1.17 V.
**Data for $\eta_{chg} = -0.62$ V.

ducted a systematic investigation of alloying effects on the diffusivity of H in α-Fe, in which elements (M) including Co, Cr, Mo, and Ni were individually added at varying amounts to iron. Heat treatments ensured the single bcc phase without other trap states. The lattice D_0 decreased continuously with increasing amount of these alloying elements, expressed as the summed atomic percentage of M. The log D_L vs $1/T$ relationships for varying atomic percentages of M were linear and parallel to that for pure iron, but shifted to lower rates,[49] showing that solid-solution alloying decreases D_0 while E_m is unchanged. Similar trends of alloying effects were found by other investigators in 1Cr-0.5 pct Mo and 2.25Cr-1 pct Mo steels[50] and a Fe-2.25Cr-1 wt pct Mo alloy.[51]

The aforementioned literature data[49,50,51] were used to estimate the dependence of D_0 on atomic percentage of M for alloying with Co, Cr, Mo, and Ni in AERMET 100. The total effect of alloying on D_0 was estimated simply by summing the atomic concentration of each element, without weighting.
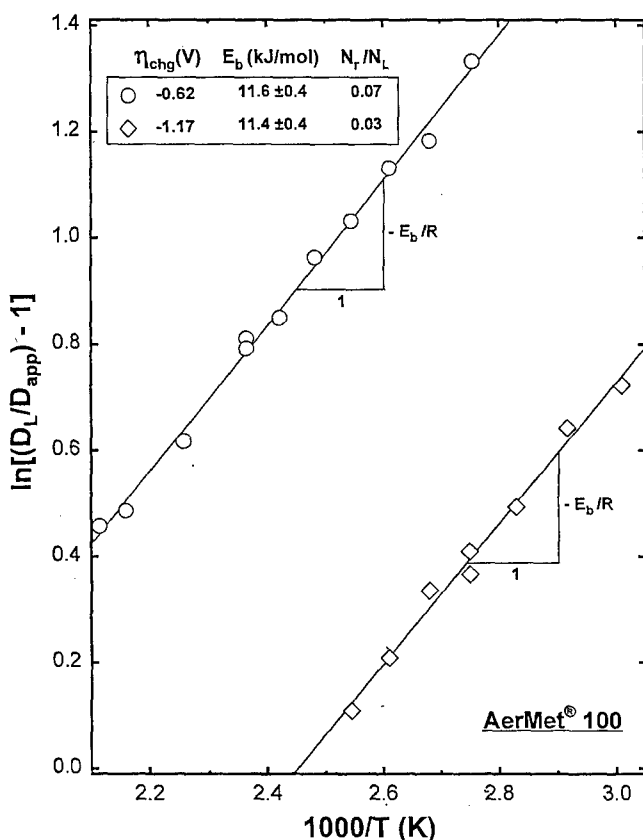
This approach is justified since these substitutional solutes have similar atomic radii and, presumably, chemical bonding characteristics. Formation of M_2C should take no more than 2 pct of the Cr and Mo, while Ni and Co should not be involved in precipitation. Elemental partitioning to other carbide phases and austenite was assumed to be inconsequential, since the volume fractions of these phases are less than 1 pct. The calculated results are plotted in Figure 10 and show a consistent alloying-element effect on D_0 for H in bcc steel, expressed as

$$D_0(\text{cm}^2/\text{s}) = -2.675 \times 10^{-5} \, M(\text{at. pct}) + 7.390 \times 10^{-4}$$
[8]

When extrapolated to a total value of 27.4 at. pct M (Co + Cr + Mo + Ni) in AERMET 100, $D_0 \approx 6 \times 10^{-6}$ cm^2/s. This reduced D_0 value is in excellent agreement with the analytical and experimental values of D_0 (5 to 7 $\times$ 10^{-6} cm^2/s) in Table IV. Therefore, the analytical and experimental parameters associated with D_L and used to establish the important E_m and, thus, E_b values are validated by these literature results.

B. Desorption of Lattice H

Figures 2 and 6 reveal a peak associated with the low-temperature shoulder preceding peak 1b in the desorption rate vs temperature curve for aged AERMET 100. The magnitude of the shoulder is lowered upon a 72-hour exposure (baking) of the as-charged specimen at room temperature.[39] The peak causing this shoulder could be associated with H located in interstitial lattice positions. This speculation was verified using two independent analytical approaches, i.e., (1) a finite-difference solution to Eq. [3] and (2) the Ono–Meshii desorption model,[53] as detailed in Appendix B. The results are shown in Figure 11. Both analyses confirm that egress of interstitial lattice hydrogen (e.g., E_b = 0 kJ/mol) with an associated desorption energy of E_d = $E_m \sim$ 10 kJ/mol would produce a peak desorption temperature at 93 °C to 98 °C for the ramp rate and specimen dimensions used in the TDS experiments.

C. H Trap Sites in AERMET 100

Through the temperature-programmed TDS experiments, at least three and possibly four distinct trap states have been identified in the present investigation, as exemplified by the multiple H desorption peaks in Figure 2 for aged AERMET 100 and in Figure 6 for the as-quenched alloy. Table VI compares the values of E_b obtained in the present study with similar ranges of values reported for various steels.[26,31,48,54–63]

Table VII lists the total available atomic H in aged AERMET 100 and its distribution in the three peaks resolved by TDS. In calculating the results in Table VII, the total H concentration in weight parts per million for charged AERMET 100[39] was converted to the number of H atoms per unit volume.

Fig. 9—Data plot demonstrating the determination of the overall H binding energy with the dominant trap state by Eq. [5a]. D_{app} is from isothermal TDS test data on diffusivity[39] and D_L is calculated according to Eq. [1] using E_m and D_0 listed in Table IV.

Table V. Calculated Values of E_b, kJ/mol (eV/atom) in AERMET 100 Using E_m = 10 kJ/mol

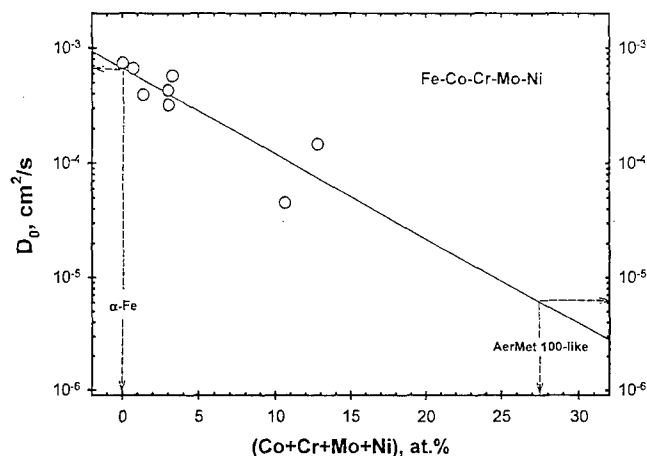| η_{chg}	Peak 1a*	Peak 1b**	Peak 2	Peak 3
-0.62 V	8.9 ± 0.2 (0.092 ± 0.002)	11.6 ± 0.2 (0.120 ± 0.002)	62.2 ± 0.3 (0.644 ± 0.003)	89.1 ± 0.3 (0.924 ± 0.003)
-1.17 V	—	11.4 ± 0.2 (0.118 ± 0.002)	61.3 ± 0.3 (0.635 ± 0.003)	89.9 ± 0.3 (0.932 ± 0.003)

*For as-quenched alloy.
**For aged alloy.

Fig. 10—Influence of equivalent substitutional alloy concentration (Co, Cr, Mo, or Ni) on the pre-exponential coefficient, D_0, in Eq. [1]. Data for individual alloying elements are obtained from Refs. 49 through 51.
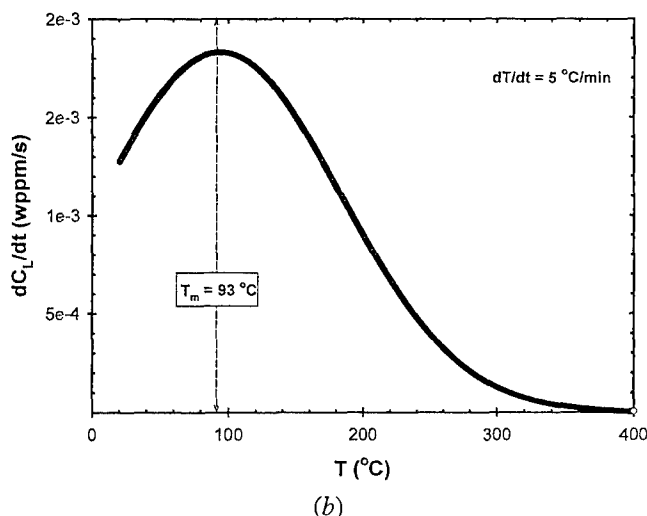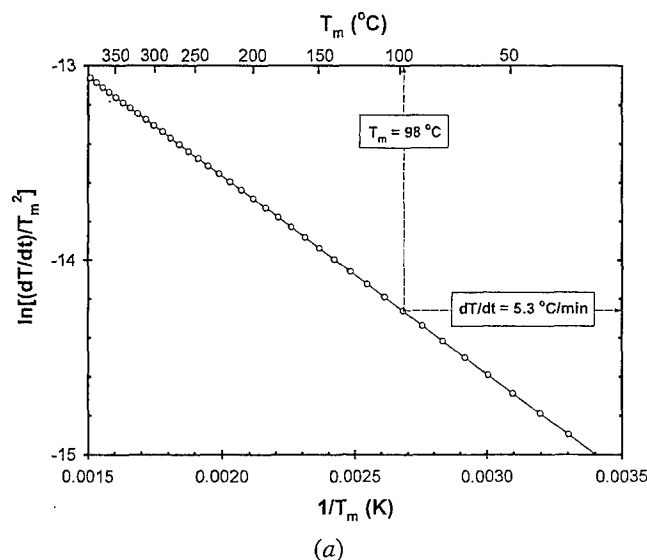

(a)

(b)

Fig. 11—(a) Relationship between peak temperature (T_m) and dT/dt for egress of lattice H from AERMET 100 at fixed $E_d = 10$ kJ/mol obtained from Eq. [3] and (b) Ono-Meshii model results for H egress depicting dC_L/dt vs T at a fixed $E_d = 10$ kJ/mol according to Eq. [B1] (Appendix B). $T_m = 93$ °C as seen from the peak position.

Then, from the temperature-programmed TDS test results (similar to Figure 2, but presented as dC_H/dt vs time), the area under each desorption peak was calculated to give the fraction of this total H that egressed during the evolution of each peak. The calculated results show that the ratio of H among the three types of trap sites is 95 to 98, 1 to 2, and 1 to 3 pct of the total, corresponding to peaks 1, 2, and 3, respectively. This distribution is basically constant for specimens H charged at two different overpotentials (−1.17 and −0.62 V) and TDS tested at different dT/dt levels from 1 °C to 10 °C/min.

1. Trap state 1: Peak 1a in as-quenched alloy

Substitutional solute atoms introduce a strain field and produce electronic interactions that serve as relatively low-energy H traps. The binding energy of H to Ni atoms in Fe was reported to be 7.7 kJ/mol and that of H to Cr in Fe was 9.7 kJ/mol.[54] These values are similar to the E_b value of 8.9 kJ/mol determined for peak 1a in as-quenched AER-MET 100. Using $E_b = 8.9$ kJ/mol as input to Ono–Meshii's trap desorption model[53] (Appendix B), the simulated desorption curve (similar to Figure 11(b)) for a 8.9 kJ/mol trap state results in a T_m value of ~120 °C, similar to the observed T_m value of ~140 °C for peak 1a in Figure 6.

Considering AERMET 100, solutes of potential importance to trapping are Cr, Mo, Ni, and Co. Information on E_b for H trapped to Co and Mo is not available. Co would likely assume a short-range ordered structure in the iron lattice. While not confirmed for AERMET 100, ordering was established for other types of UHHS.[8] For Cr ($E_b = 9.7$ kJ/mol[54]), Table VIII summarizes the atomic availability of this species, as well as Mo, in aged AERMET 100. (This calculation is based on the weight percentage of each element (Table I), typical composition of M_2C. (i.e., $(0.75Cr-0.13Fe-0.12Mo)_2C$),[5] and volume and number fractions of M_2C.[64,65]) The M_2C precipitation consumes only a small portion of the total Cr and Mo atoms available in AERMET 100. The site density for these alloying elements in the bcc lattice of AERMET 100 is 3.3×10^{21}, a level likely sufficient to trap the relatively small amount of H associated with peak 1a in the quenched microstructure. Ayer and Machmeier reported that solute clustering, particularly of Cr and Mo, preceded M_2C precipitation in AERMET 100 and did not dissolve or evolve into precipitates until the aging temperature exceeded 500 °C.[5,66] Such clusters were not imaged for the as-quenched condition, but this does not prove that such features are absent. Solute-atom clusters may provide a trap state with a low binding energy, similar to a coherent precipitate, but higher than that for the single atom. The number of atoms that cluster likely reduces the trap-site density from the value calculated for individual Cr + Mo atoms.

Ni atoms are likely an important reversible H trap state, since this element is not in M_2C. While some of the 11 wt pct Ni in AERMET 100 could partition to austenite, this phase is not present in the quenched microstructure,[5] suggesting a significant Ni content in the martensite. As such, Ni is a likely low-energy trap state ($E_b = 7.7$ kJ/mol[54]) and may contribute to peak 1a in the as-quenched alloy. It is unclear whether trap state 1a is absent in the aged alloy or cannot be detected due to the large size of trap state 1b. Since the volume fraction of precipitated austenite is low (~0.8 to 4 vol pct) in aged (482 °C) AERMET 100, the Ni-solute trap state should not be eliminated by aging.

Table VI. Selected Trap Binding Energy Values for H in Steel

Trap Site (This Work)	E_b (kJ/mol) (This Work)	E_b (kJ/mol) (Literature Data)				Trap Site Description
Peak 1a*	8.9 ± 0.2		7.7	9.7		substitutional Ni, Cr in Fe[54]
Peak 1b**	11.4 to 11.6 ± 0.2	8.4	9.2	10.9	13.4	ferrite-cementite interface[55–58]
			~52			austenite-ferrite interface[59]
Peak 2	61.3 to 62.2 ± 0.3		~58			mixed dislocation cores[60]
			~59			grain boundaries[31,61,62]
			~68			Cr carbides in Fe-Cr steel[62]
			67.5 to 96.5			various incoherent particles in Fe[54]
Peak 3	89.1 to 89.9 ± 0.3		~95			TiC in Fe-Ti-C alloy[26]
			up to 97			incoherent carbides[26,31,48,62,63]

*For as-quenched alloy.
**For aged alloy.

Table VII. Availability and Distribution of H in AERMET 100 (atoms/cm³)

Total (100 Pct)	Peak 1b (95 to 98 Pct)	Peak 2 (1 to 2 Pct)	Peak 3 (1 to 3 Pct)
1.52×10^{20}	1.44 to 1.49×10^{20}	1.52 to 3.03×10^{18}	1.52 to 4.55×10^{18}

Note: H concentration data for $\eta_{chg} = -0.62$ V.

Table VIII. Availability and Distribution of Cr and Mo (atoms/cm³) in AerMet® 100

Element	Total Available	In M_2C	In sites other than M_2C
Cr	2.8×10^{21}	5.6×10^{19}	2.7×10^{21}
Mo	6.1×10^{20}	9.0×10^{18}	6.0×10^{20}

Substructure from the martensite phase transformation could provide a low-energy trap state (peak 1a) in AERMET 100, but evidence is lacking. Dislocations and twins are present in quenched AERMET 100 and are retained during aging at 482 °C, since Co retards recovery and recrystallization.[67] For a high dislocation density of 10^{12} cm/cm³,* the N_r value of

*The dislocation density from martensitic transformation in AERMET 100 is not known,[5] but a value of 10^{12} cm/cm³ was estimated for low-carbon lath martensite.[68]

10^{20} trap sites per cm³ (10^{12} cm/cm³ × 10^{8} sites/cm) is similar to the total H (1.4 to 1.5×10^{20} atoms/cm³, Table VII) associated with peak 1b, and much less H is evolved for peak 1a. The measured E_b for peak 1a (8.9 kJ/mol) in as-quenched AERMET 100 (Figure 6) is less than the lowest E_b reported for H trapping in the strain field of a dislocation (20 to 40 kJ/mol).[61] However, this binding energy decreases with distance from the dislocation core,[48] and internal-friction experiments with bainitic and martensitic Cr-Mo steels yielded E_b for H-dislocation interaction to be as low as 11 kJ/mol and up to 20 kJ/mol.[36,69] Such experimental results are specific to a high migration energy (E_m = 30 to 40 kJ/mol) that is at odds with the low (10 kJ/mol) E_m value indicated by the present study and substantial literature.[43,49,52] Hydrogen trapping at twin interfaces has not been studied,[48] but it is reasonable to speculate that the crystallographic correspondence of a twin interface results in a low binding energy similar to H trapped at coherent interfaces in iron. Additional work is required to resolve the role of the martensite substructure in the peak 1a trap state. The ensuing discussion establishes that such a substructure is not the cause of the peak 1b trap state,

since this feature is not seen for the quenched microstructure with a large amount of martensite substructure.

2. Trap state 1: Peak 1b in aged alloy

The trap state marked by peak 1b in the aged UHSS represents a reversible H trap with E_b = 11.4 to 11.6 kJ/mol and an incredibly high value of N_r/N_L = 0.03 to 0.07. The amount of H desorption associated with peak 1a (Figure 6) for the as-quenched alloy lacking any carbide precipitates is ~2 pct of that of peak 1b, seen in the aged alloy. This proves that the coherent M_2C precipitates in the aged martensite of AERMET 100 are the responsible trapping sites for formation of the dominant peak 1b.*

*Clusters of Cr and Mo may coexist with this precipitate for the 482 °C age and contribute to peak 1b trapping.[5,66] Developed clusters may not be present in the as-quenched microstructure of AERMET 100.

The M_2C in peak-hardened AERMET 100 maintains considerable coherency with the matrix, as suggested by coherency strains inferred from contrast patterns in transmission electron microscopy images.[66] This coherent interface explains the low binding energy associated with peak 1b, as binding energy decreases with increasing interface coherency.[70] Analysis of the availability of H trap sites about the M_2C precipitates in aged AERMET 100 supports this conclusion. The amount of H necessary for single-layer full coverage on all M_2C cylindrical surfaces of the size and volume fraction expected for peak-aged AERMET 100[64,65] is estimated to be ~1.5×10^{20} atoms/cm³.* This value agrees with the total amount of atomic

*M_2C is needle-shaped, 2 nm in diameter and 8 nm long, from aging at 482 °C for 5 hours,[64] corresponding to a cylindrical surface area of 5.0 × 10^{-17} m² per needle. As the number density of M_2C precipitates is 1.5 × 10^{23}/m³,[65] the total area per unit volume of cylindrical surfaces of M_2C is 7.54 × 10^{6} (m²/m³). For simplicity, it is assumed that H is trapped only on the cylindrical surface of the M_2C/alloy interface; then, the maximum coverage ratio of carbide surfaces by H atoms is 0.91. The radius of the H atom is 0.12 nm. Thus, the number of trapped H atoms per unit volume is 1.5 × 10^{20} atoms/cm³.

H desorbed in peak 1b (1.4 to 1.5×10^{20} atoms/cm³ (Table VII)), consistent with the conclusion that M_2C precipitates are the dominant H trap site revealed by desorption peak 1b.

The N_r/N_L value in Oriani's analysis of trap-affected diffusion in Eqs. [4], [5a], and [5b][23] can be compared to experimental results for AERMET 100 to shed light on the identification of trap states. N_L is the total interstitial sites in the alloy. For bcc Fe and its alloys, $N_L = 2.6 \times 10^{23}$ sites/cm³ (octahedral sites). In the present analytical work, the values of N_r/N_L are determined (using Eq. [5b]) to be 0.03 to 0.07 for the trap state identified by peak 1b (Figure 9). An $N_L = 2.6 \times 10^{23}$ sites/cm³ yields $N_r = 0.8$ to 1.8×10^{22} sites/cm³. This site density is higher than the site density for single-layer atom coverage on interfaces of M_2C (~1.5×10^{20} atoms/cm). For carbide traps only, this discrepancy is reduced if a multiple-layer coverage of H on M_2C is considered and/or when the coherency of M_2C[66] is considered, so that H may also be trapped at lattice sites at a distance from the carbide rod surface. Furthermore, a considerable quantity of dislocations at M_2C interfaces might be justified for additional trap sources in a zone around M_2C carbides. Given the high value of N_r/N_L and the low E_b value, M_2C carbides provide an enormous capacity to store reversibly trapped H.

Finally, the cementite/ferrite interface was reported to trap H with E_b values of 8.4 to 13.4 kJ/mol in a series of steels.[55–58] This binding-energy range is on the order of the E_b determined for peak 1b in the present work (Table VI). However, this feature is excluded from consideration for potential trap sites, since cementite is not present in AERMET 100 aged at 482 °C.[5]

3. Trap state 2 (peak 2)
Peak 2 indicates traps with measured E_b values of 61.3 to 62.2 kJ/mol. There are quite a few potential trap states with high E_b values close to the presently determined range for peak 2. Several studies established a consistent E_b value of ~59 kJ/mol for trapping at grain boundaries,[31,61,62] very close to the 61.3 to 62.2 kJ/mol value for peak 2. For the fine microstructure of AERMET 100, there is a substantial area covered by various forms of incoherent interface and grain boundaries.[5] Therefore, there is no doubt that these can serve as H trap sites. It is not, however, possible to determine the relative importance of the various boundaries present, including martensite/martensite lath interfaces, martensite packet boundaries, martensite/precipitated austenite interfaces (if present), and prior-austenite grain boundaries.

Mixed dislocation cores have been identified to trap H in steels with an E_b value as high as ~58 kJ/mol,[60] which is close to the present E_b set for peak 2 (Table VI). In AERMET 100, the density of dislocations is high and a large portion may be configured as mixed dislocation cores. Thus, mixed dislocation cores are possibly another type of trap that contributes to peak 2. Incoherent chromium carbides in an Fe-9Cr alloy have been detected to trap H with a binding energy of about 68 kJ/mol,[60] larger than but still close to the 61.3 to 62.2 kJ/mol range set for peak 2. In addition, the lower bound of E_b for H trapping with incoherent particles is about 67.5 kJ/mol.[54] Hence, it is probable that at least part of the incoherent particles in AERMET 100 (($MoCr)_7C_3$, $(FeCr)_xC_y$, TiC, and (TiCrMo)C[7]), are potential H traps with E_b values approaching the range determined for peak 2.

4. Trap state 3 (peak 3)
The trap sites associated with peak 3 are representative of a state with E_b values as high as 89.1 to 89.9 kJ/mol. Solutionizing AERMET 100 at 885 °C dissolves almost all of the metal carbides such as $(MoCr)_7C_3$, $(FeCr)_xC_y$, TiC, and

(TiCrMo)C.[7] However, a fraction remains in the alloy for grain refinement. Binding energies of 67.5 to 96.5 kJ/mol were determined for various incoherent particles in Fe.[54] Incoherent carbides were identified to trap H with very high binding energies of up to 97 kJ/mol.[26,31,48,62,63] Some interfaces can also trap H at this high level of E_b.[26] Allowing for experimental errors and differences in individual analyses, these reported E_b values are considered to be at the same level as the presently determined values for peak 3. Therefore, trap sites responsible for peak 3 may include undissolved metal carbides and highly misoriented boundaries in AERMET 100.

D. Implications to H-Assisted Cracking

Hydrogen interactions with trap sites, including quantitative results on D_{app}, E_b, N_r/N_L, and trap identity in the microstructure, are critically important to understanding IHE in an UHSS such as AERMET 100.[9] The plateau or stage II rate of H-enhanced subcritical crack propagation (da/dt_{II}) in high-strength alloys containing dissolved hydrogen is limited by diffusion of H to the crack-tip process zone from the surrounding microstructure. Reduced mobility of diffusible H results in decreased crack growth rate, with data and modeling establishing that da/dt_{II} is directly proportional to D_{app}.[71] From this kinetic perspective, the IHE resistance of peak-aged AERMET 100 is improved relative to older steels such as AISI 4340, due to the substantial reduction in apparent H diffusivity. The present work shows that this reduction in D_{app} is caused by reduced lattice diffusivity due to alloy addition(s) in solid solution, as well as the high site density of reversible trap sites at M_2C interfaces.

In sharp contrast, the quasi equilibrium aspect of IHE in high-strength alloys can be exacerbated by a high density of sites for reversible trapping of H, as well as stronger trapping at sites that constitute a connected crack path through the microstructure. Such behavior is demonstrated by the low threshold-stress intensity (K_{TH}) for transgranular IHE in peak-aged AERMET 100 containing a bulk-dissolved diffusible H concentration in excess of 0.5 to 10 wppm.[15] This behavior was explained by the hypothesis that, upon stressing, H repartitions from low- to moderate-strength reversible trap sites and is attracted to the crack-tip stress field in an amount that depends on the relative values of E_b and the stress field–H interaction energy. The TEM observations show that the M_2C spacing is 20 to 50 nm.[5,66] The plastic-zone size for the threshold of IHE in AERMET 100 is of the order of 50 μm at $K = 30$ MPa$\sqrt{m}$ and contains a substantial amount of M_2C trap sites as the H source. This H is attracted to process-zone traps with higher binding energies in the range of 30 to 60 kJ/mol and interconnected to yield a transgranular crack path. Such features could include interfaces associated with the martensitic microstructure and vacancy clusters from H-deformation interaction.[30] Identification of the high density of M_2C sites for reversible trapping of H in AERMET 100 in the present work, as well as the three H-trap binding energies summarized in Table VI, further establish this explanation.

From thermodynamic consideration, the lattice H concentration is enhanced from an unstressed level of C_L to a stress-affected $C_{H\sigma}$, depending on the magnitude of the crack-tip hydrostatic stress, σ_H:[72]

$$C_{H\sigma} = C_L \exp\left(\frac{\sigma_H V_H}{RT}\right) \qquad [9]$$

assuming a dilute H concentration, negligible effect of dissolved H on elastic constants of the material, and no negative deviation from the logarithmic proportionality between $C_{H\sigma}$ and σ_H.[48,73] The H concentration at trap sites in the crack-tip process zone is further enhanced to $C_{H\sigma T}$, according to[18]

$$C_{H\sigma T} = C_{H\sigma} \exp\left(\frac{E_b}{RT}\right) = C_L \exp\left(\frac{E_b + \sigma_H V_H}{RT}\right) \quad [10]$$

Hydrogen repartitions from a reversible trap state to the crack tip if the stress-field interaction energy ($\sigma_H V_H$) exceeds the $E_{b\text{-source}}$ value for the supplying trap near the tensile hydrostatic stress field, following Eq. [10]. The amount of crack-tip H is governed by the sum of $\sigma_H V_H$ and $E_{b\text{-fracturesites}}$, where this binding energy is for the highest-energy trap state in the stress field that provides the interconnected crack path.

The results in Figure 12 establish that the M_2C trap state is a likely H supply source to enable low K_{TH} values for IHE in AERMET 100. The three measured E_b values for AERMET 100 are shown by the horizontal dashed lines, with the lowest-energy state (11.4 to 11.6 kJ/mol in Table VI) corresponding to M_2C interface traps and the intermediate energy (61.3 to 62.2 kJ/mol in Table VI) for disordered interfaces, including martensite packet and lath surfaces. The binding energy for H trapped at vacancies and vacancy clusters is between 40 and 70 kJ/mol,[30] also well above E_b for trapping at M_2C. The plotted values (Δ) of crack-tip interaction energy are given by $\sigma_H V_H$; however, the crack-tip stress state is controversial for low-stress-intensity cracking typical of IHE, and the ordinate covers a range of hydrostatic stress levels normalized to the tensile yield strength of AERMET 100.[9] Classical continuum fracture mechanics suggests that σ_H is 2.5 σ_{YS} for a low-strain-hardening UHSS.[74,75] Analyses based on either a crack-tip dislocation perspective[76,77,78] or strain-gradient plasticity hardening included in the flow curve[79,80] suggest that σ_H may be as high as $8\sigma_{YS}$. The former lower-stress estimate of interaction energy (9 kJ/mol) is less than the M_2C binding energy of 11.5 kJ/mol, while the high-stress

estimate corresponds to a higher interaction energy of 27 kJ/mol in Figure 12.

The extent of H repartitioning from reversible M_2C traps to the crack tip is given by[81,82]

$$P_\sigma = \frac{\exp\left(\sigma_H V_H / RT\right)}{\exp\left(\sigma_H V_H / RT\right) + \exp\left(E_b / RT\right)} \quad [11]$$

where P_σ is the probability that H occupies a lattice site under the influence of the crack-tip hydrostatic stress field vs occupation of trap sites at M_2C interfaces. With the measured E_b of 11.5 kJ/mol, this probability is 0.22 for the low estimate of σ_H (2.5σ_{YS}) and is 0.998 for the higher bound of $8\sigma_{YS}$. For each case, and particularly for the higher crack-tip stresses, there is a significant driving force for H repartitioning from this dominant low-energy trap state to the crack tip.

This source of H from M_2C traps, as well as the high level of $C_{H\sigma T}$ that can accumulate at martensite interfaces in the crack-tip process zone ($10^{14} C_L$ from Eq. [10], assuming that $\sigma_H = 5 \sigma_{YS}$, and actually exceeding 100 wt pct, assuming that C_L is of the order of 10^{-4} wppm), explain the severe IHE produced in AERMET 100 at low $K_{TH} \sim 0.1 K_{IC}$.[15] Notably, this hydrogen embrittlement was eliminated by baking the H-charged specimen at 190 °C for 24 hours, which effectively removed H from the low-temperature shoulder and trap state 1b based on TDS characterization of the H-charged and baked microstructure.[83] Heating at 190 °C did not eliminate H from trap states 2 and 3. However, this strongly trapped H did not produce embrittlement, since the comparison in Figure 12 shows that the probability for H repartitioning to the crack tip is very low when H is present only in traps with $E_b \sim$ 60 kJ/mol; from Eq. [11], P_σ is 10^{-6} even for $\sigma_H = 8 \sigma_{YS}$.

This analysis suggests an approach to improve the IHE resistance of aged AERMET 100. The coherence of M_2C decreases and Cr/Mo clusters are eliminated by aging at temperatures above about 500 °C.[5] The resulting precipitates should have a higher H-binding energy typical of incoherent interfaces, and alloy yield strength will be reduced. From Figure 12, it follows that these changes will tend to reduce H partitioning from the reversible trap sites at M_2C to the crack-tip hydrostatic stress field. If the reduction is sufficiently large, then H damage will be reduced.[15] Experiments are required to test this speculation and establish the balance between the tensile strength, fracture toughness, and IHE resistance of AERMET 100. A similar approach could be based on reductions in M_2C coherence by alloy additions.[64]

V. CONCLUSIONS

1. Solid-solution alloy elements in AERMET 100 substantially reduce the lattice mobility of H, as established by desorption measurements of H diffusivity and confirmed by both an analytical estimation from trapping theory as well as literature diffusivity and activation energies. The activation energy for lattice migration (E_m) is 10 to 11 kJ/mol, similar to that of pure iron.
2. There are three resolvable H trap states in peak-aged AERMET 100, with TDS yielding desorption energies of 21.4
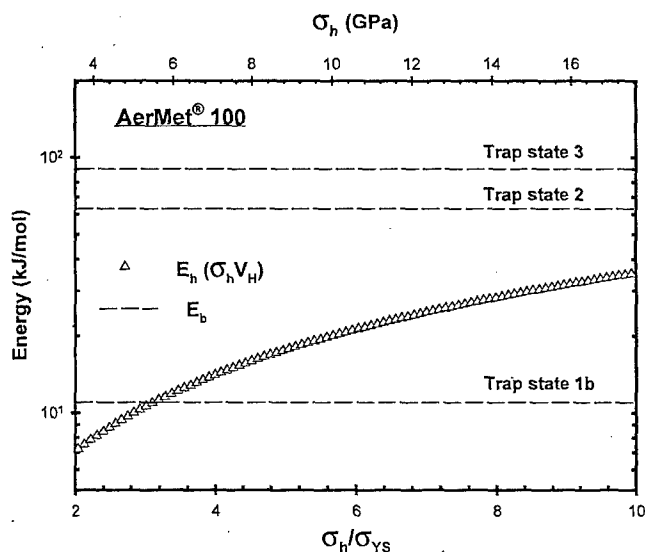

Fig. 12—The interaction energy E_h ($=\sigma_h V_H$) associated with a given hydrostatic tensile stress, σ_h, ahead of the crack tip compared with E_b for major trap states in aged AERMET 100, where V_H, the partial molar volume of H in Fe, is 2.0 cm³/mol.[48]

to 21.6, 71.2 to 71.3, and 99.1 to 99.9 kJ/mol. A fourth trap state exists for as-quenched steel, with a desorption activation energy of 18.9 kJ/mol. From the measured and estimated migration energy, these four trap states are defined by H binding energies of 8.9, 11.4 to 11.6, 61.3 to 62.2, and 89.1 to 89.9 kJ/mol.

3. The coherent M_2C precipitates are the dominant-reversible H trap sites in aged AERMET 100, corresponding to H desorption associated with a H binding energy of 11.4 to 11.6 kJ/mol and a N_r/N_L value of 0.03 to 0.07. The latter is consistent with the fine-scale microstructure of AERMET 100, and this trap state was eliminated for the as-quenched precipitate-free microstructure. This reversible trap is responsible for part of the reduced-apparent H diffusivity in AERMET 100.

4. A strong trap state with E_b of 61.3 to 62.2 kJ/mol is likely associated with martensite interfaces, austenite grain boundaries, and mixed dislocation cores. Undissolved metal carbides and highly misoriented grain boundaries trap H with the highest binding energy determined ($E_b = 89.1$ to 89.9 kJ/mol).

5. Severe-transgranular internal hydrogen embrittlement in peak-aged AERMET 100 at a low threshold-stress intensity is due to H repartitioning from reversible traps on the M_2C interface to the crack tip under the influence of hydrostatic tensile stress. This process is exacerbated by high stresses, traced to high yield strength and restricted crack-tip plasticity, as well as the large number density of homogeneously dispersed M_2C traps. Increased binding energy for H trapping at M_2C should reduce the IHE susceptibility of an UHHS such as AERMET 100.

ACKNOWLEDGMENTS

APPENDIX A

An iterative procedure was used to confirm the TDS-measured lattice diffusivity *vs* temperature relationship for AERMET 100 by requiring that that Eq. [5b] be obeyed. Specifics of the procedure are as follows.

1. An E_m value is selected to be smaller than the trap-affected E_m^{app} value for heat-treated AERMET 100 in the 60 °C to 200 °C range (17 to 18 kJ/mol[39]), but not less than E_m for pure iron (7 to 10 kJ/mol[43]).

2. With this E_m value, a selected D_0 value must yield a lattice diffusivity at room temperature ($D_{L,RT}$) that is significantly larger than $D_{app,RT}$ for heat-treated AERMET 100 ($\sim 10^{-8}$ cm²/s[39]).

3. This $D_L(T)$ is combined with a known $D_{app}(T)$ and plotted *vs* $1/T$ to yield E_b and N_r/N_L to satisfy Eq. [5b], using linear-regression analysis.

4. N_r/N_L must be significantly less than unity.

5. A specific D_L value, and associated E_b and N_r/N_L values, are valid if $E_m + E_b = E_d$, assuming H diffusion and detrapping are the rate-limiting processes during desorption.

6. If these conditions are not upheld, then steps 1 through 3 are repeated. If these conditions are upheld, then D_L is determined using all reasonable combinations of E_m and D_0. From this a D_L value is determined that results in the most reasonable values of lattice H diffusivity as expected from literature and experiment.

APPENDIX B

Two independent analytical methods can verify that the shoulder appearing on the H desorption curve in the low-temperature range in Figures 2 and 6 is associated with desorption of lattice H. In the first, E_d is selected to represent the lattice diffusion of H, *i.e.*, $E_d = E_m = 10$ kJ/mol ($E_b = 0$ kJ/mol), and Eq. [3] is numerically solved using a finite-difference method with its boundary condition set based on the results of Figures 3 through 5. The result is shown in Figure 11(a) and suggests that the maximum egress rate of H from interstitial sites in AERMET 100 occurs at about 98 °C for a heating rate of 5.3 °C/min. This compares favorably to the experimental finding using the PEAKFIT software to establish that $T_m = 98$ °C for the peak associated with the shoulder in AERMET 100.

Alternatively, assuming that H desorption is dominated by diffusion and detrapping processes, Ono and Meshii[53] proposed a numerical solution for hydrogen desorption from a specimen in the presence of a single trap state with N_r sites and a binding energy of E_b. According to this model, the desorption (or evolution) rate, expressed in the variation of H concentration in normal interstitial sites (C_L) in response to detrapping over an incremental time ($\partial C_L/\partial t$), is described by

$$\frac{\partial C_L}{\partial t} = C_H \left(\frac{\pi}{2d}\right)^2 D_0 \exp\left(\frac{-E_m}{RT}\right)\left(1 + \gamma \frac{N_r}{N_L}\exp\left(\frac{E_b}{RT}\right)\right)^{-1} \quad [B1]$$

where C_H is the current total H concentration (lattice H + trapped H), $2d$ is the thickness of a semi-infinite plate specimen, and

$$\gamma = \frac{Z_t V_t \exp\left(\dfrac{S_t}{k}\right)}{Z_d V_d \exp\left(\dfrac{S_d}{k}\right)} \quad [B2]$$

in which E_m is the lattice migration energy, k is Boltzmann's constant, Z_d and Z_t are the coordination numbers for H in interstitial and trap sites, V_d and V_t are the vibrational frequencies, and S_d and S_t are the entropies of detrapping and trapping, respectively.[53]

Equation [B1] was used to simulate the H desorption rate *vs* time spectrum, from which T_m was estimated from the desorption-rate maximum. The analytical simulation was performed for the case of H desorption at a constant thermal ramp rate (dT/dt) for a specimen in the as-charged state. Since C_H is time dependent during desorption, a recursive procedure was adopted to update C_H using the instantaneous values of $\Delta C_L/\Delta t$ and Δt in order to continue the simulation. For this purpose, a computer program coded with the programming

language C^{++} was used to simulate the H desorption process. For data input, $D_0 = 5 \times 10^{-6}$, $E_b = 0$ kJ/mol, and $E_m = 10$ kJ/mol were used to reflect egress of lattice hydrogen as speculated for the low-temperature shoulder (Table IV). The value of $N_r/N_L = 10^{-6}$ was assigned. Selection of γ was guided by the valid range suggested by Ono and Meshii[53] and the best desorption curve fitting, giving $\gamma = 1.1$. Other input values were from the present experimental conditions.

The simulation results for $dT/dt = 5$ °C/min are shown in Figure 11(b). From this simulated desorption curve for the egress of lattice hydrogen with $E_b = 0$ kJ/mol, $T_m \approx 93$ °C, in good agreement with the value of $T_m = 98$ °C obtained experimentally.

REFERENCES

1. M.G.H. Wells: *Key Eng. Mater.,* 1993, vols. 77–78, pp. 71-80.
2. G.B. Olson: *Adv. Mater. Processes,* 1997, July, pp. 72-79.
3. R.M. Hemphill and D.E. Wert: U.S. Patent Number 5,087,415, Carpenter Technology Corporation, Reading, PA, Feb. 11, 1992.
4. W.M. Garrison, Jr.: *J. Met.,* 1990, vol. 46, pp. 20-24.
5. R. Ayer and P.M. Machmeier: *Metall. Trans. A,* 1993, vol. 24A, pp. 1943-55.
6. C.H. Yoo, H.M. Lee, J.W. Chan, and J.W. Morris: *Metall. Mater. Trans. A,* 1996, vol. 27A, pp. 3466-72.
7. C.J. Kuehmann: Ph.D. Dissertation, Northwestern University, Evanston, IL, 1994.
8. G.B. Olson: *Innovations in Ultra-High Strength Steel Technology,* 34th Sagamore Army Materials Conf., United States Army Laboratory Command, Watertown, MA, 1987, pp. 3-65.
9. R.P. Gangloff: in *Comprehensive Structural Integrity,* I. Milne, R.O. Ritchie, and B. Karihaloo, eds., Elsevier Science, New York, NY, 2003, vol. 6, 2003, pp. 31-101.
10. E.U. Lee, H. Sanders, and B. Sarkar: in *Proc. Tri-Service Conf. on Corrosion,* J.V. Kelley and B. Placzankis, eds., Army Research Laboratory, Aberdeen, MD, 2000, CD file S08p2a.pdf.
11. P. Buckley, B. Placzankis, J. Beatty, and R. Brown: *Corrosion/94,* NACE, Houston, TX, 1994, paper no. 547.
12. P.F. Buckley, R. Brown, G.H. Graves, E.U. Lee, C.E. Neu, and J. Kozol: *Metallic Materials for Lightweight Applications,* 40th Sagamore Army Materials Research Conf., M.G.H. Wells, E.B. Kula, and J.H. Beatty, eds., United States Army Laboratory Command, Watertown, MA, 1993, pp. 377-88.
13. J.B. Boody and V.S. Agarwala: *Corrosion/87,* NACE, Houston, TX, 1987, paper no. 224.
14. D.A. Berman: *Mater. Performance,* 1985, vol. 24, pp. 36-41.
15. R.L.S. Thomas, J.R. Scully, and R.P. Gangloff: *Metall. Mater. Trans. A,* 2003, vol. 34A, pp. 327-44.
16. G.N. Vigilante, J.H. Underwood, and D. Crayton: in *Fatigue and Fracture Mechanics,* Proc. 30th Nat. Symp., ASTM STP 1360, ASTM International, West Conshohocken, PA, 2000, pp. 377-87.
17. E.U. Lee: *Metall. Trans. A,* 1995, vol. 26A, pp. 1313-16.
18. W.W. Gerberich, T. Livne, X.-F. Chen, and M. Kaczorowski: *Metall. Trans. A,* 1988, vol. 19A, pp. 1319-34.
19. C.D. Kim and A.W. Loginow: *Corrosion,* 1968, vol. 24, pp. 313-18.
20. H.H. Johnson and R.W. Lin: in *Hydrogen Effects in Metals,* I.M. Bernstein and A.W. Thompson, eds., TMS, Warrendale, PA, 1980, pp. 3-25.
21. G.M. Evans and E.C. Rollason: *J. Iron Steel Inst.,* 1969, vol. 207, pp. 1591-98.
22. M. Wang and P.G. Shewmon: in *Hydrogen Embrittlement: Prevention and Control,* ASTM STP 962, L. Raymond, ed., ASTM, Philadelphia, PA, 1988, pp. 117-24.
23. R.A. Oriani: *Acta Metall.,* 1970, vol. 18, pp. 147-57.
24. L.S. Darken and R.P. Smith: *Corrosion,* 1949, vol. 5, pp. 1-16.
25. G.M. Pressouyre and F.M. Faure: in *Hydrogen Embrittlement: Prevention and Control,* ASTM STP 962, L. Raymond, ed., ASTM, Philadelphia, PA, 1988, pp. 353-71.
26. G.M. Pressouyre and I.M. Bernstein: *Metall. Trans. A,* 1978, vol. 9A, pp. 1571-80.
27. G.M. Pressouyre: in *Hydrogen Effects in Metals,* I.M. Bernstein and A.W. Thompson, eds., TMS, Warrendale, PA, 1981, pp. 27-36.
28. K. Yamakawa, S. Yonezawa, and S. Yoshizawa: in *International Congress on Metallic Corrosion,* National Research Council, Toronto, 1984, pp. 254-61.
29. R.P. Gangloff: in *Corrosion Prevention and Control,* M. Levy and S. Isserow, eds., United States Army Materials Technology Laboratory, Watertown, MA, 1986, pp. 64-111.
30. M. Nagumo, M. Nakamura, and K. Takai: *Metall. Mater. Trans. A,* 2001, vol. 32A, pp. 339-47.
31. G.M. Pressouyre and I.M. Bernstein: *Acta Metall.,* 1979, vol. 27, pp. 89-100.
32. M.F. Stevens and I.M. Bernstein: *Metall. Trans. A,* 1985, vol. 16A, pp. 1879-86.
33. J.R. Scully, J.A. Van Den Avyle, M.J. Cieslak, A.D. Romig, and C.R. Hills: *Metall. Trans. A,* 1991, vol. 22A, pp. 2429-43.
34. A. Turnbull, R.B. Hutchings, and D.H. Ferriss: *Mater. Sci. Eng.,* 1997, vol. A238, pp. 317-28.
35. S.W. Smith and J.R. Scully: *Metall. Mater. Trans. A,* 2000, vol. 31A, pp. 179-93.
36. Yu. Jagodzinski, A. Tarasenko, S. Smuk, S. Tähtinen, and H. Hänninen: *J. Nucl. Mater.,* 1999, vol. 275, pp. 47-55.
37. B.G. Pound: *Acta Metall.,* 1998, vol. 46, pp. 5733-43.
38. A. McNabb and P.K. Foster: *Trans. AIME,* 1963, vol. 227, 618-27.
39. R.L.S. Thomas, D. Li, R.P. Gangloff, and J.R. Scully: *Metall. Mater. Trans. A,* 2002, vol. 33A, pp. 1991-2003.
40. *Alloy Data-AERMET 100 Alloy,* Carpenter Steel Division, Carpenter Technology Corporation, reading, PA, 1992.
41. J. Crank: *The Mathematics of Diffusion,* Oxford University Press, Inc., New York, NY, 1975, p. 414.
42. P. Shewmon: *Diffusion in Solids,* TMS, Warrendale, PA, 1989, pp. 9-51.
43. J. Völkl and G. Alefeld: in *Hydrogen in Metals 1—Basic Properties,* G. Alefeld and J. Völkl, eds., Springer-Verlag, New York, NY, 1978, pp. 26-29.
44. D.P. Woodruff and T.A. Delchar: *Modern Techniques of Surface Science,* Cambridge University Press, Cambridge, United Kingdom, 1986, p. 284.
45. J.Y. Lee, J.L. Lee, and W.Y. Choo: in *Current Solutions to Hydrogen Problems in Steels,* ASM, Metals Park, OH, 1982, pp. 423-27.
46. H.E. Kissinger: *Analytical Chemistry,* 1957, vol. 29, pp. 1702-06.
47. G.M. Pressouyre: *Metall. Trans. A,* 1979, vol. 10A, pp. 1571-73.
48. J.P. Hirth: *Metall. Trans. A,* 1980, vol. 11A, pp. 861-90.
49. H. Hagi: *J. Jpn. Inst. Met.,* 1991, vol. 55 (12), pp. 1283-90.
50. O.F. Angeles, R.J. Stueber, and G.H. Geiger: *Corrosion,* 1976, vol. 32 (5), pp. 179-83.
51. T.P. Perng and C.J. Altstetter: *Metall. Trans. A,* 1986, vol. 17, pp. 2086-90.
52. D.J. Fisher: in *Hydrogen Diffusion in Metals, A 30-Year Retrospective,* SCITEC Publications Ltd., Zuerich-Uetikon, Switzerland, 1999, pp. 59-126.
53. K. Ono and M. Meshii: *Acta Metall.,* 1992, vol. 40, pp. 1357-64.
54. I.M. Bernstein and G.M. Pressouyre: in *Hydrogen Degradation of Ferrous Alloys,* R.A. Oriani, J.P. Hirth, and M. Smialowski, eds., Noyes Publications, Park Ridge, NJ, 1985, pp. 641-711.
55. G.W. Hong and J.Y. Lee: *Scripta Metall.,* 1983, vol. 17, pp. 823-26.
56. G.W. Hong and J.Y. Lee: *Metall. Trans. A,* 1983, vol. 14A, pp. 156-62.
57. G.W. Hong and J.Y. Lee: *J. Mater. Sci.,* 1983, vol. 18, pp. 271-77.
58. B.D. Craig: *Acta Metall.,* 1979, vol. 25, pp. 1027-35.
59. A. Turnbull and R.B. Hutchings: *Mater. Sci. Eng.,* 1994, vol. A177, pp. 161-71.
60. R. Gibala and A.J. Kumnick: in *Hydrogen Embrittlement and Stress Corrosion Cracking,* R. Gibala and R.F. Hehemann, eds., ASM International, Materials Park, OH, 1984, pp. 61-77.
61. E. Serra, A. Perujo, and G. Benamatti: *J. Nucl. Mater.,* 1997, vol. 245, pp. 108-15.
62. C. Paes de Oliveira, M. Aucouturier, and L. Lacombe: *Corrosion,* 1980, vol. 36, pp. 53-59.
63. G.M. Pressouyre: in *Current Solutions to Hydrogen Problems in Steels,* C.G. Interrante and G.M. Pressouyre, eds., ASM International, Materials Park, OH, 1982, pp. 18-34.
64. R. Ayer and P.M. Machmeier: *Metall. Trans.,* 1996, vol. 27A, pp. 2510-21.
65. J.S. Montgomery and G.B. Oslon: in *Gilbert R. Speich Symp. on the Fundamentals of Aging and Tempering in Bainitic and Martensitic Steel Products,* Proc. 34th MSWP Conf., ISS-AIME, Warrendale, PA, 1992, pp. 177-214.

66. R. Ayer and P.M. Machmeier: *Metall. Mater. Trans. A,* 1998, vol. 29A, p. 903-05.
67. G.R. Speich, D.S. Dabkowski, and L.F. Porter: *Metall. Trans.,* 1973, vol. 4, pp. 303-15.
68. G. Krauss: *Steels, Heat Treatment and Processing Principles,* ASM INTERNATIONAL, Materials Park, OH, 1990, p. 75.
69. H. Hänninen, Y. Yagodzinskyy, O. Tarasenko, P. Castelio, and J.-P. Schosger: in *Hydrogen Effects in Materials,* N.R. Moody and A.W. Thompson, eds., TMS, Warrendale, PA, 2003, in press.
70. D.L. Johnson, G. Krauss, J.K. Wu, and K.P. Tang: *Metall. Trans. A,* 1987, vol. 18A, pp. 717-21.
71. R.P. Gangloff: in *Hydrogen Effects in Materials,* N.R. Moody and A.W. Thompson, eds., TMS, Warrendale, PA, 2003, in press.
72. R.A. Oriani: in *Fundamental Aspects of Stress Corrosion Cracking,* NACE, Houston, TX, 1969, pp. 32-50.
73. W.C. Johnson and J.Y. Huh: *Metall. Mater. Trans.,* 2003, in press.
74. K.N. Akhurst and T.J. Baker: *Metall. Trans. A,* 1981, vol. 12A, pp. 1059-70.
75. T.L. Anderson: *Fracture Mechanics: Fundamentals and Applications,* 2nd ed., CRC Press, Boca Raton, FL, 1995, pp. 117-81.
76. W.W. Gerberich, R.A. Oriani, M.-J. Li, X. Chen, and T. Foecke: *Phil. Mag. A,* 1991, vol. 63, pp. 363-76.
77. Y. Katz, N. Tymiak, and W.W. Gerberich: *Eng. Fract. Mech.,* 2001, vol. 68, pp. 619-46.
78. X. Chen and W.W. Gerberich: *Metall. Trans. A,* 1991, vol. 22A, pp. 59-70.
79. Y. Wei and J.W. Hutchinson: *J. Mech. Phys. Solids,* 1997, vol. 45, pp. 1253-73.
80. H. Jiang, Y. Huang, Z. Zhuang, and K.C. Hwang: *J. Mech. Phys. Solids,* 2001, vol. 49, pp. 979-93.
81. T.Y. Zhang and J.E. Hack: *Metall. Mater. Trans. A,* 1999, vol. 30A, pp. 155-59.
82. T.Y. Zhang, H. Sheu, and J.E. Hack: *Scripta Metall. Mater.,* 1992, vol. 27, pp. 1605-10.
83. D. Li, R.P. Gangloff, and J.R. Scully: *Hydrogen Diffusion and Trapping Behavior in Ultrahigh Strength AERMET 100 Steel,* University of Virginia, Charlottesville, VA, 2002.

Controlling Hydrogen Embrittlement in Ultra-High Strength Steels

John R. Scully, Hakan Dogan, Daoming Li and Richard Gangloff

CONTROLLING HYDROGEN EMBRITTLEMENT IN ULTRA-HIGH STRENGTH STEELS

John R. Scully, Hakan Dogan, Daoming Li, and Richard P. Gangloff
Center for Electrochemical Science and Engineering
Department of Materials Science and Engineering
University of Virginia
Charlottesville, VA 22904-4745
USA

ABSTRACT

A Fe-13Co-11Ni-3Cr-1Mo-0.2C steel alloy, processed for ultra-high strength and fracture toughness, exhibits three distinct hydrogen trap states in a complex precipitation hardened martensitic microstructure and is susceptible to severe hydrogen embrittlement (HE) at threshold stress intensity levels as low as 20 MPa$\sqrt{m}$. The causes of HE susceptibility include very high crack-tip tensile stresses and a reservoir of diffusible hydrogen that is trapped reversibly with a binding energy, E_b, of 11.5 ± 0.5 kJ/mol at $(Fe,Cr,Mo)_2C$ precipitates. This reversibly trapped hydrogen repartitions to interstitial sites proximate to the highly stressed crack tip and, subsequently, may retrap at martensitic lath interfaces to produce substantial local hydrogen concentrations and transgranular embrittlement. These results are pertinent to the control of HE in this modern ultra-high strength steel with a cadmium-plated coating and co-deposited hydrogen (H). Thermal Desorption Spectroscopy demonstrates that 190°C baking removes the detrimental hydrogen associated with $(Fe,Cr,Mo)_2C$ traps in both precharged but unplated steel as well as in thin porous, cadmium-plated steel. Restoration of a high fracture toughness and a ductile fracture mode correlates directly with the removal of hydrogen from $(Fe,Cr,Mo)_2C$ traps as well as other low energy trap states. However, the internal H concentration at such traps is at first intensified upon baking of cadmium-plated steel. Later H egress is retarded by the slow H diffusivity in steel and the barrier action of the cadmium plating. Hydrogen trapped at higher trap binding energy sites is not removed by 190°C baking, but cannot redistribute to the crack tip fracture process zone and does not participate in subcritical hydrogen cracking. Strategies for controlling hydrogen embrittlement are proposed based on the information generated.

Keywords: ultra-high strength steel, hydrogen embrittlement, hydrogen trapping, thermal baking, cadmium plating.

INTRODUCTION

Ultrahigh-strength steel (UHSS) enables high performance aerospace structures that require high tensile strength and fracture toughness.[1,2] A secondary hardening UHSS, Fe-13Co-11Ni-3Cr-1Mo-0.2C (AerMet® 100,[(1)]), was developed to provide plane strain fracture toughness (K_{IC}) in excess of 120 MPa$\sqrt{m}$, doubling that of

---

(1) AerMet 100 is a trademark of Carpenter Technology Corp., Reading, PA 19612-4662

older steels such as AISI 4340 and 300M, each at constant yield strength (σ_{YS}) of 1750 MPa.[3,4] This strength is produced by a homogeneous distribution of nanoscale coherent $(Fe,Cr,Mo)_2C$ alloy carbides in Fe-Ni martensite laths that are highly dislocated due to Co retardation of recovery.[5,6] The high K_{IC} is achieved by advanced melting to minimize S + P and inclusion contents, austenitization to control undissolved carbides and grain size, and aging to optimize austenite precipitates along martensite lath interfaces.[2,4,7,8]

Ultra-high strength steels are susceptible to severe internal hydrogen embrittlement (IHE) as well as hydrogen environment embrittlement (HEE), and Fe-13Co-11Ni-3Cr-1Mo-0.2C steel is no exception.[9] Several studies demonstrated subcritical HEE at apparent threshold stress intensity (K_{TH}) levels as low as 20-30 MPa√m when the microstructure, optimized for high K_{IC} (~ 130 MPa√m), was stressed in neutral chloride near the free corrosion potential.[10-12] UHSS is often electroplated for corrosion resistance, introducing the potential for IHE.[13,14] Thomas and coworkers demonstrated that optimally aged Fe-13Co-11Ni-3Cr-1Mo-0.2C steel is susceptible to severe IHE at K_{TH} levels as low as 20 MPa√m and produced by diffusible H contents as low as 1 part-per-million by weight (wppm).[15] Both IHE and HEE in Fe-13Co-11Ni-3Cr-1Mo-0.2C steel are predominantly transgranular (TG), associated with cracking of interfaces in the martensitic microstructure.[10-12,15-17] The TG H-cracking mode is traced to the low concentration of metalloid impurities segregated to austenite grain boundaries, to minimize intergranular cracking, coupled with substantial H accumulation by trapping at transgranular sites in the crack tip process zone.[9,15]

Cadmium electroplating produces a protective coating on steel surfaces that improves corrosion resistance, but atomic hydrogen (H) can be co-deposited during plating and may enter the steel substrate.[13,14] A post-plating baking process is frequently required to remove this residual H,[13,14,18-20] however, effectiveness has been questioned for UHSS such as AISI 4340.[13,14,21] A coating can further complicate H egress/desorption during baking exposure by acting as a diffusion barrier and H source. For electroplated Cd, H is co-deposited in both the Cd coating and steel substrate.[13,14,21] The H concentration in the steel increases during the early stage of baking with the electroplated Cd layer serving as a H source, since H solubility in Cd is higher than that in Fe.[13,14,21] The Cd layer also acts as a diffusion barrier during baking, due to a much slower H diffusivity in Cd than in steel.[21] Hence, considerable-diffusible H may remain in a baked steel, even after heating for 100 h.[13] The 1-5 wppm level of residual-dissolved H, typical of Cd plating and subsequent baking, embrittles high strength AISI 4340 steel.[22] Similar problems were reported for Cd-plated steel fasteners.[23]

The influences of H trapping on IHE and HEE are important and complex.[24-27] The amount of residual trapped hydrogen depends on the time-temperature conditions during baking. The chance that trapped hydrogen redistributes to the crack tip or resides along a connected crack path depends on the details of trapping, baking, microstructure, and local stress. Therefore, the outcome of baking is complicated. A typical example was evidenced for a high carbon steel where baking at 200°C dramatically increased embrittlement susceptibility.[20] Reversible trap sites with low binding energy provide a reservoir of mobile H that diffuses to areas of lower H chemical potential, such as the dilated region associated with triaxial tensile stress ahead of a crack tip. Such traps exacerbate IHE, as illustrated by decreasing threshold stress intensity with increasing diffusible H concentration reported for AISI 4340-type steels,[28-30] as well as Fe-13Co-11Ni-3Cr-1Mo-0.2C steel.[15] In contrast, a homogeneous distribution of irreversible or strong-reversible traps, that do not constitute a connected path of fracture initiation sites and resist H repartitioning to the hydrostatic tensile stress field of a crack tip, may not play a role in IHE or may shield the material from brittle H cracking.[31-33]

There is limited information on which trap states govern IHE compared to those that release H when baked at specified temperatures. Previous work demonstrated that weak or reversible trap sites provide a reservoir of mobile H that is capable of diffusing to the crack tip process zone and exacerbating IHE.[29-31] There may be considerable residual H in higher energy (reversible) trap sites after conventional baking treatment.[8] Whether such H repartitions to the hydrostatically stressed region ahead of a crack tip and facilitates embrittlement depends on the energetics of trapping at microstructural features compared to the energetics of stress field occlusion. For a microstructure containing plentiful trap sites, it is necessary to consider the effectiveness of baking in removing hydrogen from various trap states.[34,35] It is important to compare the trap binding energies of states that liberate hydrogen at conventional baking temperatures to the trap states that are important in IHE.

In a recent study on H trapping states in Fe-13Co-11Ni-3Cr-1Mo-0.2C steel, various H traps with different binding energies were identified and assigned to fine-scale microstructural features.[36] A H desorption shoulder at low temperatures (<100°C) was likely associated with lattice H, whereas at least three distinct desorption peaks were ascribed to different reversible and irreversible trap states. The first and dominant trap state is attributed to predominant H trapping at $(Fe,Cr,Mo)_2C$ precipitates (peak 1b), in addition to possible alloying solute and martensitic substructure (peak 1a). This trap state possesses a very high H trap occupancy (N_r/N_L of 0.03-0.07, where N_r is the number of reversible trap sites per unit volume and N_L is the number of ordinary interstitial sites available for H in the perfect lattice). Energy analysis established H repartition from this trap state to the crack tip in UHSS under the influence of high-hydrostatic stress.[36] In contrast the second and third trap states (peaks 2 and 3) are associated with H trapping at strong trap sites such as martensite interfaces, austenite grain boundaries, mixed dislocation cores, and undissolved metal carbides. It seems unlikely that H repartitions to the crack tip from these high-energy trap states for a practically attainable hydrostatic stress.[36] Information on release of hydrogen and residual hydrogen at trap states capable of supplying hydrogen to the crack tip is, therefore, necessary to control hydrogen embrittlement either through baking practice or microstructural optimization.

The objective of this research is to establish the effect of baking on H detrapping and egress from electroplated UHSS. Specifically, the influence of thermal baking on H desorption is characterized for electrochemically charged bare, thin and thick cadmium plated Fe-13Co-11Ni-3Cr-1Mo-0.2C steel. The focus is on H egress as a function of H trap state, as established systematically by varying baking time at fixed baking temperature. The baking temperature for embrittlement relief is specified as 190-220°C for steels having tensile strength of 1000 MPa and higher (Table 1);[19] thus, 190°C was selected for study. The amount of H desorbed during baking from each trap state was quantified by both electrochemical extraction and thermal desorption methods, and correlated with restoration of fracture toughness. The results of these experiments provide basic understanding that better enables control of IHE in Fe-13Co-11Ni-3Cr-1Mo-0.2C steel.

EXPERIMENTAL PROCEDURES

Material

The material selected for the present investigation was Fe-13Co-11Ni-3Cr-1Mo-0.2C steel. This alloy, of composition shown in Table 2, was received as annealed bar (15.2 cm in diameter and 30.5 cm long). To achieve an optimal strength and toughness combination, specimens were vacuum heat-treated as follows: solution treat at 885°C for 1 h, air cool to room temperature in 2 h, chill at -73°C for 1 h, and temper at 482°C for 5 h.[37,38] Major mechanical properties resulting from this treatment are given in Table 3.[15] While the microstructure is detailed elsewhere,[5-7] the main features relevant to this study are: (1) less than 0.1 μm diameter incoherent carbides (i.e., $(MoCr)_7C_3$, $(FeCr)_XC_Y$, TiC, (TiCrMo)C) that provide grain refinement, (2) prior austenite grain boundaries, (3) martensite laths on the order of 0.15 μm thick, both twinned and un-twinned, with interfaces that are high-angle and arrayed in packets, (4) dislocations in martensite and not recovered at this tempering temperature, (5) finely distributed, partly coherent M_2C (where M = 75 at.% Cr, 13 Fe and 12 Mo) in martensite, averaging 2 nm diameter x 8 nm length, (6) Cr and/or Mo dissolved in coherent clusters in martensite, (7) Co dissolved in martensite, perhaps with short range order, (8) precipitated austenite, and (9) Ni dissolved in austenite. Retained austenite is negligible due to refrigeration.[5] Precipitated austenite is present as a thin layer (~ 3 nm) at martensite lath interfaces based on electron microscopy, but the volume fraction from X-ray diffraction measurements is uncertain, ranging from an average volume pct of 0.8 [3] to 4 [6] for the 482°C temper.

Electrochemical hydrogen charging

Planar steel coupons were ground to 600-grit surface finish, degreased with methanol and H charged in saturated $Ca(OH)_2$ (pH ~ 12.1), prepared with pre-electrolyzed 18.2 MΩ deionized water. Hydrogen charging was performed at various constant H overpotentials ($\eta_{chg} = E_{Applied} - E_{RH^+/H}$) under potentiostatic control at either 23°C or 60°C. The calculated reversible H oxidation/reduction potential, $E_{RH^+/H}$, in this solution was −1.330 V (vs

Hg/Hg$_2$SO$_4$). Charging time necessary to develop a uniform hydrogen concentration was calculated from a saturation curve given by a solution for Fick's second law for one-dimensional diffusion in a planar sheet with conservative estimates of the trap-affected apparent hydrogen diffusivity (D_H) of 8 x 10^{-9} cm^2/s at 23°C and 3 x 10^{-8} cm^2/s at 60°C.[39] As-charged specimens were stored in liquid nitrogen for testing as needed.

Cadmium plating, baking and stripping

Cadmium plating was according to the QQ-P-416F standard as Type I (As-Plated) CLASS 3.[40] Two different batches were plated, with Cd thickness of 18 μm (Batch I) and 10 μm (Batch II).[41] Prior to plating, specimens were ground to 600-grit surface finish, cleaned with methanol, rinsed with distilled water, and air-dried. Cadmium plating parameters were: sodium cyanide (NaCN) bath with a cyanide concentration of 128.5 g/L and pH of 11.7, cathodic current density of 0.15 to 0.20 A/cm^2 and cadmium metal concentration of 31 g/L. Plating was conducted at ambient temperature for 30 minutes. Following plating, specimens were rinsed with water, dried and immediately stored in liquid nitrogen. Specimens were baked in a laboratory furnace and moist air environment, at a temperature of 190°C ($\pm$ 2°C) unless stated otherwise and over the range from 1 minute to 500 h. For uncoated specimens, exposure time was normalized by a characteristic time ($\tau = L^2/D_H$, where L is the half of sample thickness) to account for thickness variation. Cadmium plate was stripped by immersion in 300g/L NH$_4$NO$_3$ for 2 minutes.[42] Experiments indicated that this procedure did not introduce detectable levels of hydrogen into specimens that would bias the results presented here.

Determination of diffusible hydrogen concentration

The Barnacle Electrode method was used to measure diffusible hydrogen concentration, $C_{H,Diff}$ from charged and plated samples.[43] The flat cell consisted of a hydrogen-containing specimen as the working electrode (anode), a platinized-niobium mesh as counter electrode, and a Hg/Hg$_2$SO$_4$ reference electrode. Saturated Ca(OH)$_2$ solution (pH ~ 12.1) was used as the H extraction solution in the Barnacle cell. One hour prior to and during extraction, Ca(OH)$_2$ solution was deaerated continuously using N$_2$. During measurement, an extraction potential of -1.00 V (*vs.* Hg/Hg$_2$SO$_4$) (330 mV anodic to $E_{H/H}{}^+$) was maintained potentiostatically. Temperature was maintained at room temperature. Diffusible H concentrations were calculated using the formula:[43]

$$C_{H\,Diff} = \frac{J_t}{zF}\left[\frac{D_H}{\pi t}\right]^{-1/2} \tag{1}$$

where J_t is the H oxidation current density recorded at time t, z is the number of electrons involved in the oxidation (1 equivalent/mol), and F is the Faraday constant (96,500 coulombs/equivalent). Eq. 1 assumes $C_{H,Diff} = 0$ at the steel surface where H is oxidized at t > 0 and a uniform $C_{H,Diff}$ in the steel sample at t = 0. Equation 1 is the first-term approximation of a complex expression and requires that $L^2/D_H t_{max} \geq 4$, where L is thickness.[43] The t_{max} is the time up to which $C_{H,Diff}$ may be calculated from the experimental value of J_t using the first term solution shown in Eq. 1. This condition was ensured for all experiments. $C_{H,Diff}$ was determined using Eq. 1 applied to the H oxidation current density at t = 300, 600 and 1200 s. Conversion to weight parts per million was done by multiplying the experimental results from Eq. 1 (as mol H/cm^3) by 1.27×10^5 based on the density of Fe-13Co-11Ni-3Cr-1Mo-0.2C steel. Hydrogen diffusion is concentration dependent and the specific H diffusivities used in Eq. 1 for each H charging overpotential were determined from prior work.[44]

Determination of fracture toughness

Compact tension (CT) specimens were machined in the C-R orientation with a width (W) of 38.1 mm and thickness (B) of 2.8 mm. Specimens were heat-treated, ground to a 600-grit surface finish and fatigue precracked using decreasing maximum stress intensity from 24.5 MPa√m to 10 MPa√m at a final crack length-to-width of

0.50. Fatigue precracking was performed on a closed loop servohydraulic test machine operated in load control at a frequency of 10 Hz. After precracking, each specimen was H charged for 20 days in 60°C saturated $Ca(OH)_2$ at an overpotential of -0.30 V in order to achieve a 4.6 wppm diffusible H concentration.[22] One of the H-charged specimens was baked at 190°C for 24 h according to the QQ-P-416F Standard to eliminate dissolved H. Each H-charged CT specimen was stressed under rising-crack mouth opening displacement, δ, to determine the plane strain threshold stress intensity for initiation of subcritical H induced cracking at room temperature. Testing was done with a closed-loop servoelectric tensile loading machine operated under δ-feedback control with a dK/dt=3.33 x 10^{-2} MPa√m/s for as-charged specimens and 4.85 x 10^{-2} MPa√m/s for charged and baked specimens. Crack mouth opening displacement was measured using a clip gauge mounted across the notch mouth. Crack length was monitored continuously with the direct current potential difference technique. Load was plotted vs. δ for data analysis.

Determination of trap states and H occupancy by thermal desorption spectroscopy

Thermal Desorption Spectroscopy (TDS) was used to characterize H desorption and detrapping during heating processes. A detailed description of TDS is provided by Smith and Scully.[45] For cadmium plated specimens, the plated layer was stripped. Specimens were then cleaned in methanol, rinsed with distilled water, and stored in LN_2 prior to TDS tests. After background subtraction, the corrected P_{H2} - t data were transformed to data sets of H-concentration (C_H) and its rate of variation (dC_H/dt, or desorption rate) versus time or temperature (T). Specimens were tested under a temperature programmed ramp mode to characterize the H in defined trap states by locating the temperature for the desorption maximum for each trap state (i.e. peaks on dC_H/dt vs. T curves) and comparing with those observed for as-charged samples. Unambiguous peak identification in the case of overlapping peaks was enabled using PeakFit™ [(2)] software. A H desorption energy, E_d, was calculated using TDS data obtained at different heating rates. The peak desorption temperature, T_m, increases with heating rate, dT/dt as demonstrated for both TDS[46] and differential thermal analysis.[47] The E_d depends on T_m and dT/dt according to:[47]

$$\frac{d\left[\ln\left(\frac{dT/dt}{T_m^2}\right)\right]}{d\left[\frac{1}{T_m}\right]} = -\frac{E_d}{R} \tag{2}$$

E_d was calculated from linear regression slope of $\ln[(dT/dt)/T_m^2]$ vs $1/T_m$ data, obtained from desorption maximum as a function of dT/dt. This analysis was applied to each peak observed during a temperature programmed TDS experiment. The E_d values provide the basis for estimating the binding energy, E_b, for H trapping in each of the observed states, provided that the relationship between E_d and E_b is known. In this paper E_d is assumed to equal $E_m + E_b$, where E_m is the activation energy for H diffusion by an interstitial jump mechanism in the trap-free steel lattice containing the alloy elements in the solid solution.

RESULTS

Effect of predissolved H on K_{TH} in Fe-13Co-11Ni-3Cr-1Mo-0.2C steel

Predissolved H degrades the subcritical crack growth resistance of Fe-13Co-11Ni-3Cr-1Mo-0.2C steel and the amount of degradation increases dramatically with increasing H content. The results of slow-rising δ (dK/dt = 2.2 x 10^{-4} MPa√m/s) experiments in Fig. 1 show the threshold stress intensity for the onset of stable-

---

[(2)] PeakFit is a product of AISN Software Inc., Mapleton, OR 97453

subcritical crack growth (K_{TH}) as a function of diffusible dissolved-H concentration.[15] The K_{TH} decreased strongly, from K_{JIC} of 132-143 MPa√m with essentially no dissolved-mobile H, to a K_{TH} less than 30 MPa√m for $C_{H,Diff}$ between 0 and 1 wppm. The level of K_{TH} decreased to less than 15 MPa√m as $C_{H,Diff}$ increased to 7.6 wppm. Testing with replicate specimens containing $C_{H,Diff}$ = of 0, 0.5, 3.9 to 4.0, 5.9, and 7.6 wppm confirmed experimental reproducibility. The dissolved H in steel caused a microscopic fracture mode transition that correlated with decreasing K_{TH}.[15] Fracture in H-free steel at high K_{JIC} occurred by microvoid coalescence (MVC). In contrast the reduction in crack growth resistance due to a $C_{H,Diff}$ of 4.6 wppm correlated with a completely brittle transgranular crack path, as shown in Fig. 2. The brittle TG character of the crack in steel intensified with increasing hydrogen content, correlating with decreasing K_{TH}.

Effect of post-H-charging baking on K_{TH} in Fe-13Co-11Ni-3Cr-1Mo-0.2C steel

Figure 3 shows load vs. δ data for Fe-13Co-11Ni-3Cr-1Mo-0.2C steel CT specimens that were tested after either H-precharging only or H-precharging then baking. The H charged specimen ($C_{H,Diff}$ = 4.6 wppm) exhibited severe hydrogen embrittlement as expected given the measured K_{TH} of 15.9 MPa√m. Baking the identically precharged specimen at 190°C for 24 h eliminated all diffusible H from bare steel without a cadmium plate, as verified by electrochemical extraction (Barnacle Electrode) and TDS experiments, as discussed in an ensuing section. Hydrogen elimination correlated with a complete reversal in IHE and restored fracture resistance to K_{JIC} = 123 MPa√m, which essentially equals the fracture resistance of as-received Fe-13Co-11Ni-3Cr-1Mo-0.2C steel without precharged H. An SEM image of the fracture surface of the H-charged and baked specimen revealed that the brittle TG fracture mode was restored to MVC typical of this steel with $C_{H,Diff}$ = 0 wppm, Fig. 4.

Hydrogen trapping states in Fe-13Co-11Ni-3Cr-1Mo-0.2C steel

Fig. 5 shows representative H desorption results (dC_H/dt versus temperature) measured during temperature-programmed TDS. For the temperature range from 23 to 500°C, at least three desorption peaks are identified and marked as peak 1b, 2 and 3 in the order of increasing peak temperature T_m. For low temperatures preceding peak 1b, a "shoulder" exists on the dC_H/dt versus temperature curve; this peak was particularly apparent for heating at the higher dT/dt values. The analysis procedure described above and Eq. 2 were used to determine E_d for trap state 1b. This analysis is shown in Fig. 6. Table 4 lists the E_b values determined for H in the four unique trap states in Fe-13Co-11Ni-3Cr-1Mo-0.2C steel, charged to two different albeit similar diffusible H concentrations and using a lattice-migration energy of E_m = 10 kJ/mol.[36]

To clarify the connection between (Fe,Cr,Mo)$_2$C precipitates and the trap states shown in Fig. 5, temperature-programmed TDS tests were performed for specimens with the as-quenched microstructure heated at various dT/dt.[36] The area for peak 1b in the as-quenched alloy was substantially decreased compared with aged alloy, and a new small peak (1a) was apparent in the vicinity of peak 1b but at a temperature higher than the shoulder observed for the aged steel. TDS tests at other dT/dt produced similar results. Based on the area under the dC_H/dt vs. time curve, the amount of H, desorbed over the temperature range where peak 1b appeared for the aged alloy, decreased by 98% for the as-quenched case.[36] The amount of H desorption associated with peak 1a for the as-quenched alloy was only ~2% of that of peak 1b seen only in the aged alloy. The as-quenched martensitic microstructure does not contain (Fe,Cr,Mo)$_2$C precipitates that are predominant in the aged alloy.[5] This proves that the coherent (Fe,Cr,Mo)$_2$C precipitates in the aged martensite alloy are the trapping sites responsible for formation of the dominant peak 1b. This trap state is reversible, characterized by an E_b of 11.4 – 11.6 kJ/mol, and represented by an incredibly high ratio of trap sites to lattice sites of 0.03 – 0.07.[36] The (Fe,Cr,Mo)$_2$C in peak hardened alloy maintains considerable coherency with the matrix, as suggested by strains inferred from contrast patterns in transmission electron microscopy images.[48] This coherent interface explains the low E_b associated with peak 1b, as binding energy decreases with increasing interface coherency.[49] Quantitative analysis yielded identical-high E_b values for peaks 2 and 3 in the as-quenched and aged forms of Fe-13Co-11Ni-3Cr-1Mo-0.2C steel. The strong trap state with E_b of 61.3-62.2 kJ/mol is likely associated with martensite interfaces, austenite grain boundaries, and mixed dislocation cores. Undissolved metal carbides and highly misoriented grain boundaries likely trap H with the highest binding energy determined (E_b = 89.1-89.9 kJ/mol). The microstructural features that cause peaks 2 and 3 do not change during tempering.

Residual trapped hydrogen in charged and baked uncoated Fe-13Co-11Ni-3Cr-1Mo-0.2C steel

Concerning precharged steel without a coating, the amount of H egressed increases significantly with increasing time at the baking temperature, and the amount of residual hydrogen decreases continually, as shown in Figs. 7 and 8. The diffusible hydrogen concentration measured by the Barnacle Electrode method (Fig. 7) decreases at all baking times. Diffusible hydrogen was essentially removed after $t/\tau \geq 1$. Regarding TDS data (Fig. 8), there is an obvious decrease in the height and area coverage of the dC_H/dt vs. T curves, particularly for peak 1b after each baking time at 190°C. The "shoulder" associated with peak 1 disappears after 5 minutes of baking. Within 30 minutes, peak 1b on desorption rate curve disappears as a result of substantial H egress. Based on trap state identification, this suggests that hydrogen trapped at $(Fe,Cr,Mo)_2C$ carbides is removed after sufficient baking time at 190°C.[36] However, hydrogen trapped at peaks 2 and 3 remains.[(3)]

For each peak in Fig. 8, the H concentration was calculated by integrating the dC_H/dt versus time curve for the range of time corresponding to the peak coverage. Fig. 9 shows the variation of H concentration for baked specimens, $C_{H(baked)}$, relative to that of the as-charged specimen, $C_{H(as-charged)}$, expressed as percentage for each peak. For the shoulder, there was a dramatic change in the relative H concentration in the initial 5 minutes of baking ($t/\tau \leq 0.6$). $C_{H(baked)}/C_{H(as-charged)}$ dropped to ~20% after baking for $t/\tau = 0.12$ and to near zero after baking for $t/\tau = 0.6$. Concerning peak 1b, the change was less dramatic. $C_{H(baked)}/C_{H(as-charged)}$ was reduced to ~60% after baking for $t/\tau = 0.12$. Peak 1b was eliminated after baking for $t/\tau = 3.6$. For peaks 2 and 3, $C_{H(baked)}/C_{H(as-charged)}$ increased to more than 160% after baking for $t/\tau = 0.12$. Following this increase, $C_{H(baked)}/C_{H(as-charged)}$ decreased for both peak 2 and 3 but was never eliminated after baking for t/τ at least up to 3.6. This decrease was not definitive because of the relatively low levels of dC_H/dt and the variability associated with the data recorded from these peaks.

All diffusible hydrogen (measured by the Barnacle Electrode method), as well as the H trapped at $(Fe,Cr,Mo)_2C$ carbides associated with peak 1b, is readily removed by baking at 190°C given a sufficient and relatively short baking time. The detrapping of such H corresponded with complete restoration of fracture toughness and the corresponding ductile fracture mode (Figs. 3 and 4). Therefore, removal of H from trap state 1b is crucial to recovery of fracture toughness. It is technologically important to determine whether such detrapping can be achieved in Cd-plated and baked Fe-13Co-11Ni-3Cr-1Mo-0.2C steel after baking at the same temperature.

Residual trapped and diffusible hydrogen in cadmium plated and baked Fe-13Co-11Ni-3Cr-1Mo-0.2C steel

The coating thickness and porosity of two different batches of dull-Cd plated Fe-13Co-11Ni-3Cr-1Mo-0.2C steel are indicated in Figs. 10-13. The thicknesses of these layers of Cd are 18 μm and 10 μm, and the thin layer appears to be more porous. This is a qualitative judgment since porosity was not quantified. Figure 14 illustrates the change in residual diffusible hydrogen concentration after baking with a thick Cd layer. The relative diffusible hydrogen concentration first increases with baking time, reflecting additional H entry into the steel from the Cd layer that contains codeposited hydrogen. At very long baking times relative to uncoated and H-precharged steel (Fig. 7), the diffusible hydrogen concentration is lowered. This process is hindered by the Cd layer, which serves as a permeation barrier,[13] and the slow H diffusivity in Fe-13Co-11Ni-3Cr-1Mo-0.2C steel.[22,44] Diffusible H content data are not available for the thin, more porous cadmium plate shown in Figs. 12 and 13.

TDS data are shown in Figs. 15 and 16 for the thin and thick Cd coatings, respectively. In addition to trap states 1b, 2 and 3, an additional unidentified state is also seen. This peak 1a is uncovered due to the low overall hydrogen content of the Cd-plated specimens relative to the specimens precharged in $Ca(OH)_2$ solution, especially the absence of the large shoulder adjacent to peak 1b in Fig. 5. There are distinct differences between the TDS data taken after various baking times for thin vs. thick cadmium plated steel. For the thin coating, the residual hydrogen associated with peak 1a decreases at short baking times, while that associated with state 1b first rises

---

(3) Note that dC_H/dt is plotted logarithmically in Fig. 5, but on a linear axis in Fig. 8; only the former clearly reflects the H egress that constitutes peaks 2 and 3.

then decreases as a function of time (Fig. 17). However, over 100 h of baking are required to reduce the residual hydrogen associated with peak 1b. Concerning the thicker Cd layer, both peaks 1a and 1b increase as a function of baking time (Fig. 18). After long baking times, residual H associated with peak 1a is eliminated. However, the status of H associated with peak 1b is unclear, but it does not appear to have been reduced significantly. For both thin and thick Cd layers, H associated with trap states 2 and 3 may be decreased, but only by a modest percentage, and this conclusion is confounded by low peak heights and measurement variability. Based on these results, short baking times could promote IHE, and very long baking times are required to remove damaging-diffusible H, even for the thin-porous Cd plated layer and certainly for thick Cd with low porosity.

DISCUSSION

Correlation between detrapping of hydrogen and restoration of fracture toughness

All diffusible hydrogen (Barnacle Electrode measurements) as well as H trapped at $(Fe,Cr,Mo)_2C$ carbides (peak 1b) is removed by baking at 190°C in both uncoated and porous-cadmium coated Fe-13Co-11Ni-3Cr-1Mo-0.2C steel given sufficient baking time. The detrapping of such hydrogen corresponded with complete restoration of fracture toughness and transition from a brittle TG to ductile MVC fracture mode (Fig. 3 and 4). Trap state 1b has a binding energy of 11.4-11.6 kJ/mol and a desorption energy of 21.4-21.6 kJ/mol. The results of these TDS experiments demonstrate that 190°C baking readily removes the detrimental hydrogen from $(Fe,Cr,Mo)_2C$ traps, as expected theoretically because the thermal energy of baking at 190°C is similar to this trap binding energy and overall trap desorption energy so as to enable a high probability of hydrogen release from trap sites (e.g., $kT_{190C} = 3.85$ kJ/mol $\approx 11.5\pm0.5$ kJ/mol). However, H egress is unfortunately retarded by both the slow H diffusivity in this steel[15,22] and by the cadmium plated coating that functions as a permeation barrier.[13] Specifically, thick and thin cadmium plated coatings both intensify the H levels retained in the steel upon short to intermediate term 190°C baking, up to about 50 h, as seen in Figs. 15-18. Longer term baking removes hydrogen associated with interstitial lattice sites and unidentified weaker traps (peak 1a), as well as at $(Fe,Cr,Mo)_2C$ trap sites (peak 1b), when cadmium plated coatings are thin and porous as shown in Figs. 15 and 17. However, thicker cadmium coatings with lower porosity are a more permanent barrier to H egress. In this case, hydrogen associated with $(Fe,Cr,Mo)_2C$ traps (peak 1b) is not removed by long term baking at 190°C, as seen in Figs. 16 and 18. The absolute values of these times are correct for the Cd-plated thin specimens that were characterized, but are not directly relevant to plated components. Rather, the time for H egress must be determined by a diffusion analysis that includes the Cd barrier thickness, H content, and H diffusivity, as well as geometry of the UHSS component in question.

These results suggest that H may be retained in trap state 1b, the finely dispersed strengthening precipitates, when dull cadmium layers are thick and less porous. Such residual trapped hydrogen is thus available to affect the fracture resistance of Fe-13Co-11Ni-3Cr-1Mo-0.2C steel, at least near the surface of thick sections even after long baking times. In contrast, hydrogen associated with trap states 2 and 3 was not removed by 190°C baking in bare or Cd plated steel. These hydrogen trap states do not govern subcritical H-enhanced cracking, but may alter fracture toughness at faster loading rates that is governed by microvoid fracture.[15] It is worth reviewing the fundamental reason why the removal of hydrogen associated with trap state 1b, in particular, is crucial to control and mitigation of time-dependent subcritical IHE in this UHSS.

The role of traps in time-dependent subcritical IHE

IHE in high strength alloys can be exacerbated by a high density of sites for reversible trapping of H, as well as stronger trapping at sites that constitute a connected crack path through the microstructure. Such behavior is demonstrated by the low threshold stress intensity (K_{TH}) for transgranular IHE in peak aged Fe-13Co-11Ni-3Cr-1Mo-0.2C steel containing bulk-dissolved diffusible H concentration in excess of 0.5 to 10 wppm.[15] This behavior was explained by the hypothesis that, upon stressing, H repartitions from low to moderate strength reversible trap sites and is attracted to the crack tip stress field in an amount that depends on the relative values of E_b and the stress field-H interaction energy. TEM observations show that the $(Fe,Cr,Mo)_2C$ spacing is 20–50 nm.[5,48] The plastic zone size for the threshold of IHE in Fe-13Co-11Ni-3Cr-1Mo-0.2C steel is of order 50 μm at

K = 30 MPa√m and contains a substantial amount of (Fe,Cr,Mo)$_2$C trap sites as the H source. This H is attracted to process zone traps with higher binding energies in the range of 30-60 kJ/mol and interconnected to yield a TG crack path. Such features could include interfaces associated with the martensitic microstructure and vacancy clusters from H-deformation interaction.[30] Identification of the high density of (Fe,Cr,Mo)$_2$C sites for reversible trapping of H in this steel, as well as the four H-trap binding energies summarized in Table 4 further establish this explanation.

From thermodynamic consideration, lattice H concentration is enhanced from an unstressed lattice-soluble level of C_L to a stress-affected $C_{H\sigma}$ depending on the magnitude of the crack tip hydrostatic stress, σ_H:[50]

$$C_{H\sigma} = C_L \exp\left(\frac{\sigma_H V_H}{RT}\right) \tag{3}$$

assuming dilute H concentration, negligible effect of dissolved H on elastic constants of the material, and no negative deviation from the logarithmic proportionality between $C_{H\sigma}$ and σ_H.[51,52] The H concentration at trap sites in the crack tip process zone is related to the local lattice H solubility, provided that local equilibrium exists, and is thus enhanced by dilatational stress to $C_{H\sigma T}$, according to:[24]

$$C_{H\sigma T} = C_{H\sigma} \exp\left(\frac{E_b}{RT}\right) = C_L \exp\left(\frac{E_b + \sigma_H V_H}{RT}\right) \tag{4}$$

Hydrogen repartitions from a reversible trap state to the crack tip if the stress field interaction energy, $\sigma_H V_H$, exceeds the $E_{b\text{-Source}}$ for the supplying trap near the tensile hydrostatic stress field, following Eq. 4. The amount of accumulated crack tip H is governed by the sum of $\sigma_H V_H$ and $E_{b\text{-Fracture Sites}}$, where this binding energy is for the highest energy trap state in the stress field and that provides the interconnected crack path.

The results in Fig. 19 establish that the (Fe,Cr,Mo)$_2$C trap state is a likely H-supply source to enable low K_{TH} for IHE in Fe-13Co-11Ni-3Cr-1Mo-0.2C steel. The three measured E_b for this steel are shown by the horizontal-dashed lines, with the lowest energy state (11.4 to 11.6 kJ/mol in Table 4) corresponding to (Fe,Cr,Mo)$_2$C interface traps and the intermediate energy (61.3-62.2 kJ/mol in Table 4) for disordered interfaces including martensite packet and lath surfaces. The binding energy for H trapped at vacancies and vacancy clusters is between 40 and 70 kJ/mol,[30] also well above E_b for trapping at (Fe,Cr,Mo)$_2$C. The plotted values (Δ) of crack tip interaction energy are given by $\sigma_H V_H$. However, the crack tip stress state is controversial for low stress intensity cracking typical of IHE, and to account for this uncertainty, the ordinate covers a range of hydrostatic stress levels normalized to the tensile yield strength of Fe-13Co-11Ni-3Cr-1Mo-0.2C steel.[9] Classical continuum fracture mechanics suggests that σ_H is 2.5 σ_{YS} for a low strain hardening UHSS.[53,54] Analysis based on either a crack tip dislocation perspective,[24,55,56] or strain gradient plasticity hardening included in the flow curve,[57,58] suggest that σ_H may be as high as 8σ_{YS}. The former lower stress estimate of interaction energy (9 kJ/mol) is less than the (Fe,Cr,Mo)$_2$C binding energy of 11.5 kJ/mol, while the high stress estimate corresponds to higher interaction energy of 27 kJ/mol in Fig. 19.

The extent of H repartition from reversible (Fe,Cr,Mo)$_2$C traps to the crack tip is given by:[59,60]

$$P_\sigma = \frac{\exp\left[\sigma_H V_H / RT\right]}{\exp\left[\sigma_H V_H / RT\right] + \exp\left[E_b / RT\right]} \tag{5}$$

where P_σ is the probability given in infinite time that H occupies a lattice site in the fracture process zone under the influence of the crack tip hydrostatic stress field *vs.* occupation of trap sites near the crack tip at $(Fe,Cr,Mo)_2C$ interfaces. With the measured E_b of 11.5 kJ/mol, this probability is 0.22 for the low estimate of σ_H ($2.5\sigma_{YS}$) and 0.998 for the higher bound of $8\sigma_{YS}$. For each case, and particularly for the higher crack tip stresses, there is a significant probability for H repartition from this dominant low energy trap state to the crack tip.

This source of internal H from $(Fe,Cr,Mo)_2C$ traps, as well as the high level of $C_{H\sigma T}$ that can accumulate at martensite interfaces in the crack tip process zone (10^{14} C_L from Eq. 4, assuming that $\sigma_H = 5$ σ_{YS}, and exceeding 100 wt pct assuming that C_L is of order 10^{-4} wppm), explain the severe IHE produced in precharged steel at low $K_{TH} \sim 0.1$ K_{IC} in the absence of baking.[15] Notably, this hydrogen embrittlement was eliminated by baking the H-charged specimen at 190°C for 24 h, which effectively removed H from the low temperature shoulder and trap state 1b [($Fe,Cr,Mo)_2C$ interfaces] based on TDS characterization of the H charged and baked microstructure.[61] Heating at 190°C did not eliminate H from trap states 2 and 3. However, this strongly trapped H did not produce embrittlement since the comparison in Fig. 19 shows that the probability for H repartition to the crack tip is very low when residual H is only present in traps with $E_b \sim 60$ kJ/mol; from Eq. 5, P_σ is 10^{-6} even for $\sigma_H = 8$ σ_{YS}. However, such strongly trapped residual H may enhance microvoid fracture. This potential problem has not been investigated.

Control of IHE by microstructural manipulation

Analysis of the energetics of H partitioning in a FPZ suggests a metallurgical approach to improve the IHE resistance of aged Fe-13Co-11Ni-3Cr-1Mo-0.2C steel. The coherence of $(Fe,Cr,Mo)_2C$ decreases and Cr/Mo clusters are eliminated by aging at temperatures above about 500°C.[5] The resulting precipitates should have higher H-binding energies than 11.5 kJ/mol, typical of incoherent interfaces, and alloy yield strength will be reduced modestly. These changes will tend to reduce H repartitioning from the reversible trap sites at $(Fe,Cr,Mo)_2C$ to the crack tip hydrostatic tensile stress field, as illustrated by the argument summarized in Fig. 19. If the reduction is sufficiently large and if aging does not introduce another reversible trap state, then H damage will be reduced.[15] Experiments are required to test this speculation and establish the balance between the tensile strength, fracture toughness and IHE resistance of Fe-13Co-11Ni-3Cr-1Mo-0.2C steel. A similar approach could be based on reductions in $(Fe,Cr,Mo)_2C$ coherence by alloying element addition.[62]

Either approach to reducing TG hydrogen embrittlement could augment the important–prior development of IG hydrogen cracking resistance derived from reduced metalloid segregation through impurity control to produce IHE resistant UHSS.[9] This broad development would represent a breakthrough in high performance structural materials. Since H supply is uniquely different for IHE and HEE, understanding of the interaction of crack tip trap sites and H must be extended to the hydrogen environment case where the damaging H is delivered to FPZ damage sites from the electrochemically active crack tip surface and over a sub-micrometer distance.[63] This H transport situation is fundamentally different from that which governs IHE in UHSS.

Control of IHE in cadmium plated Fe-13Co-11Ni-3Cr-1Mo-0.2C steel

We have established the technical basis for controlling IHE through understanding of hydrogen-microstructure interactions that play a strong role in IHE, with emphasis on crack tip process zone damage. This is a more scientific approach than the established methodology based on trial and error analysis of the effects of various thermal baking treatments on fracture toughness of plated steels. The results presented here provide a scientific understanding of which hydrogen trap states exist in Fe-13Co-11Ni-3Cr-1Mo-0.2C steel, and which control internal hydrogen embrittlement. If this information is coupled with knowledge of the trap states that release hydrogen for egress during remedial baking procedures, then strategies for controlling IHE emerge. Control of IHE in cadmium plated UHSS such as Fe-13Co-11Ni-3Cr-1Mo-0.2C steel requires that the following considerations be adhered to; Note that these comments only apply to IHE with a finite quantity of internal hydrogen.

1. The damaging source of hydrogen during IHE is from those trap sites as well as interstitial lattice sites that are the source for repartitioning of H to the tensile stress field of a crack tip where it retraps. By definition, these damaging traps that supply hydrogen must have low enough binding energies such that $E_b < \sigma_H v_H$. Therefore, thermal baking must be performed to remove diffusible hydrogen from such trap states that energetically allow hydrogen repartitioning to the crack tip fracture process zone. In the case of Fe-13Co-11Ni-3Cr-1Mo-0.2C steel, this requires that the thermal energy imparted by baking approaches the desorption energy (e.g., $kT_{baking} \approx E_d = E_m + E_b$) of $(Fe,Cr,Mo)_2C$ traps or others that supply damaging hydrogen to the crack tip. This concept also requires that thermal energy imparted during baking approach the desorption energy of diffusible H from the crack tip stress field in an UHSS; that is $kT_{baking} \approx \sigma_H v_H + E_m$. If this is the case, then H will be eliminated from reversible trap sites that can supply embrittling H during IHE as summarized in Fig. 19.

2. Sufficiently long baking times are required to avoid short term intensification of hydrogen levels in cadmium-plated ultra-high strength steels including Fe-13Co-11Ni-3Cr-1Mo-0.2C steel. This phenomenon results from hydrogen ingress supplied from electrochemically co-deposited H existing in cadmium layers. This occurs during early baking periods at 190°C.

3. Control of dull cadmium plated layer thickness and porosity is necessary so that thermal egress of hydrogen from weak trap states such as $(Fe,Cr,Mo)_2C$ precipitates in Fe-13Co-11Ni-3Cr-1Mo-0.2C steel is not hindered by the H-barrier action of the coating.

4. Microstructural control of trapping states must be optimized such that strong traps, that do not release hydrogen upon 190°C baking, cannot themselves serve as crack initiation sites or be interconnected to provide a continuous crack propagation path. Trap states 2 and 3 in Fe-13Co-11Ni-3Cr-1Mo-0.2C steel do not form such a propagation paths, but may affect microvoid fracture.

Moreover, microstructural control is necessary to avoid a high density of intermediate binding energy trap states that resist thermal egress of hydrogen (e.g., $kT_{baking} \ll E_d$), but allow repartitioning of hydrogen to the stress field of extremely sharp crack tips (e.g., $E_b < \sigma_H v_H$) with associated high hydrostatic stress levels. It appears fortuitous that $(Fe,Cr,Mo)_2C$ traps do not fall into this category and instead satisfy the criteria listed in (1) above. However, this is not assured for all ultra-high strength steels in all applications under all H producing conditions, including IHE and HEE.

CONCLUSIONS

(1) Fe-13Co-11Ni-3Cr-1Mo-0.2C steel, processed for ultra-high strength and fracture toughness, exhibits at least three distinct hydrogen trap states in a complex precipitation hardened martensitic microstructure and is susceptible to severe internal hydrogen embrittlement (IHE) at threshold stress intensity levels as low as 20 MPa√m.

(2) The causes of IHE susceptibility include very high crack-tip tensile stresses and a reservoir of diffusible hydrogen that is trapped reversibly with a binding energy, E_b, of 11.5±0.5 kJ/mol at $(Fe,Cr,Mo)_2C$ precipitates. This reversibly trapped hydrogen repartitions to interstitial sites proximate to the highly stressed crack tip and, subsequently, may retrap at martensitic lath interfaces to produce substantial local hydrogen concentrations and transgranular embrittlement.

(3) 190°C baking readily removes the detrimental diffusible hydrogen associated with $(Fe,Cr,Mo)_2C$ traps and other low energy sites in electrochemically precharged but unplated Fe-13Co-11Ni-3Cr-1Mo-0.2C steel. Such hydrogen detrapping and egress correlates directly with a restoration in ultra-high fracture toughness and a ductile fracture mode. Hydrogen trapped at higher trap binding energy sites is not removed by 190°C baking, but cannot redistribute to the crack tip fracture process zone and does not participate in subcritical hydrogen cracking.

(4) 190°C baking eventually removes the detrimental hydrogen associated with $(Fe,Cr,Mo)_2C$ traps in cadmium-plated steel as long as the cadmium-plated layer is thin and porous. However, the internal H

concentration in Fe-13Co-11Ni-3Cr-1Mo-0.2C steel at such traps is at first intensified upon baking of cadmium-plated steel for short time periods as a consequence of H supply from as-deposited cadmium-plated layers. H egress occurs at long baking times but is retarded by the slow H diffusivity in steel and the barrier action of the cadmium plating.

ACKNOWLEDGEMENTS

REFERENCES

1. M.G.H. Wells, *Key Engineering Materials*, Vol. 77-78, pp. 71-80, 1993.

2. G.B. Olson, *Advanced Materials and Processes*, pp. 72-9, July 1997.

3. R.M. Hemphill and D.E. Wert, *U. S. Patent Number 5,087,415*, Carpenter Technology Corporation, Reading, PA, February 11, 1992.

4. W.M. Garrison Jr., *Journal of Metals*, Vol. 46, pp. 20-4, 1990.

5. R. Ayer and P.M. Machmeier, *Metallurgical Transactions A*, Vol. 24A, pp. 1943-55, 1993.

6. C.H. Yoo, H.M. Lee, J.W. Chan and J.W. Morris, *Metallurgical and Materials Transactions A*, Vol. 27A, pp. 3466-72, 1996.

7. C.J. Kuehmann, *Thermal Processing Optimization of Nickel-Cobalt Ultrahigh-Strength Steels*, Ph.D. Dissertation, Northwestern University, Evanston, IL, 1994.

8. G.B. Olson, in *Innovations in Ultra-High Strength Steel Technology, 34th Sagamore Army Materials Conference*, US Army Laboratory Command, Watertown, MA, pp. 3-65, 1987.

9. R.P. Gangloff, in *Comprehensive Structural Integrity*, I. Milne, R.O. Ritchie and B. Karihaloo, editors-in-Chief, Vol. 6, Elsevier Science, New York, NY, pp. 31-101, 2003.

10. E.U. Lee, H. Sanders, and B. Sarkar, *Proc. Tri-Service Conf. On Corrosion*, J.V. Kelley and B. Placzankis, editors, Army Research Laboratory, Aberdeen, MD, CD file S08p2a.pdf, 2000.

11. P. Buckley, B. Placzankis, J. Beatty, and R. Brown, *Corrosion/94*, paper no. 547, NACE, Houston, TX, 1994.

12. P.F. Buckley, R. Brown, G.H. Graves, E.U. Lee, C.E. Neu, and J. Kozol, in *Metallic Materials for Lightweight Applications, 40th Sagamore Army Materials Research Conf.*, M.G.H. Wells, E.B. Kula, and J.H. Beatty, editors, United States Army Laboratory Command, Watertown, MA, pp. 377-88, 1993.

13. J.B. Boody and V.S. Agarwala, *Corrosion /87*, paper no. 224, NACE, Houston, TX, 1987.

14. D.A. Berman, *Materials Performance*, Vol. 24, pp. 36-41, 1985.

15. R.L.S. Thomas, J.R. Scully, and R.P. Gangloff, *Metallurgical and Materials Transactions A*, Vol. 34A, pp. 327-44, 2003.

16. G.N. Vigilante, J.H. Underwood, and D. Crayton, in *Fatigue and Fracture Mechanics, Proc. 30th Nat. Symp.*, ASTM STP 1360, ASTM International, West Conshohocken, PA, pp. 377-87, 2000.

17. E.U. Lee: *Metallurgical Transactions A*, Vol. 26A, pp. 1313-6, 1995.

18. H.E.Townsend, *Corrosion*, Vol. 37, no. 2, pp. 115-20, 1981.

19. B850-98: Standard Guide for Post-Coating Treatment of Steel for Reducing Risk of Hydrogen Embrittlement, *Annual Book of ASTM Standards Vol. 02.05*, ASTM International, West Conshohocken, PA, pp. 613-5, 2001.

20. M.J. Robinson and R.M. Sharp, *Corrosion*, Vol. 41, no. 10, pp. 582-86, 1985.

21. T. Zhong-Zhuo, H. Chi-Mei, L. Rong-Bong, F. Yi-Feng, and C. Xiang-Rong, in *Current Solutions to Hydrogen Problems in Steels*, C.G. Interrante and G.M. Pressouyre, editors, ASM International, Materials Park, OH, p. 98-103, 1982.

22. R.L.S. Thomas, *Internal Hydrogen Embrittlement of a Trap-Rich Ultra-High Strength Steel AerMet® 100*, MS Thesis, University of Virginia, Charlottesville, VA, 2000.

23. E.L. Williams and D.M. Anderson, *Materials Performance*, Vol. 24, no. 12, pp. 9-12, 1985.

24. W.W. Gerberich, T. Livne, X.-F. Chen, and M. Kaczorowski, *Metallurgical Transactions A*, Vol. 19A, pp. 1319-34, 1988.

25. G.M. Pressouyre and F.M. Faure, in *Hydrogen Embrittlement: Prevention and Control, ASTM STP 962*, L. Raymond, editor, ASTM, Philadelphia, PA, pp. 353-71, 1988.

26. G.M. Pressouyre and I.M. Bernstein, *Metallurgical Transactions A*, Vol. 9A, pp. 1571-80, 1978.

27. G.M. Pressouyre, in *Hydrogen Effects in Metals*, I.M. Bernstein and A.W. Thompson, editors, The Minerals, Metals, and Materials Society, Warrendale, PA, pp. 27-36, 1981.

28. K.Yamakawa, S. Yonezawa and S. Yoshizawa, in *International Congress on Metallic Corrosion*, National Research Council, Toronto, Canada, pp. 254-61, 1984.

29. R.P. Gangloff, in *Corrosion Prevention and Control*, M. Levy and S. Isserow, editors, U.S. Army Materials Technology Laboratory, Watertown, MA, pp. 64-111, 1986.

30. M. Nagumo, M. Nakamura and K. Takai, *Metallurgical and Materials Transactions A*, Vol. 32A, pp. 339-47, 2001.

31. G.M. Pressouyre and I.M. Bernstein, *Acta Metallurgica*, Vol. 27, pp. 89-100, 1979.

32. M.F. Stevens and I.M. Bernstein, *Metallurgical Transactions A*, Vol. 16A, pp. 1879-86, 1985.

33. J.R. Scully, J.A. Van Den Avyle, M.J. Cieslak, A.D. Romig and C.R. Hills, *Metallurgical Transactions A*, Vol. 22A, pp. 2429-43, 1991.

34. G.M. Pressouyre, *Acta Metallurgica*, Vol. 28, pp. 895-911, 1980.

35. N. Suzuki, N. Ishii and T. Miyagawa, *Tetsu-to-Hagane (Journal of the Iron and Steel Institute of Japan)*, Vol. 82, no. 2, pp. 170-5, 1996.

36. D. Li, R.P. Gangloff and J.R. Scully, "Hydrogen Trap States in Ultrahigh-Strength AerMet® 100 Steel", submitted to *Metallurgical and Materials Transactions A*, in press, 2003.

37. *Alloy Data-AerMet® 100 Alloy*, Carpenter Technology Corporation Carpenter Steel Division, Reading, PA, 1992.

38. J.M. Dahl, "Ferrous-Base Aerospace Alloys", *Advanced Materials and Processes*, pp. 33-6, 2000.

39. J.F. Shackelford, *Introduction to Materials Science for Engineers*, Fifth Edition, Prentice Hall, Upper Saddle River, New Jersey, pp. 164-8, 2000.

40. QQ-P-416F, *Plating, Cadmium (Electrodeposited)*, Federal Specification, Naval Air Engineering Center, Systems Emgineering and standardization Department, Lakehurst, NJ April 1986.

41. B487-85 *Standard Test Method for Measurement of Metal and Oxide Coating Thickness by Microscopical Examination of a Cross Section*, Annual Book of ASTM Standards, Vol. 02.05, ASTM, Philadelphia, PA, pp. 237-240, 1991.

42. B767-88 *Standard Guide for Determining Mass Per Unit Area of Electrodeposited and Related Coatings by Gravimetric and Other Chemical Analysis Procedures,* Annual Book of ASTM Standards, Vol. 02.05, ASTM, Philadelphia, PA, pp. 555-560, 1991.

43. J.J. DeLucia and D.A. Berman, *An Elecrochemical Tecnique to Measure Diffusible Hydrogen in Metals (Barnacle Electrode),* In Electrochemical Corrosion Testing, ASTM STP 727, F. Mansfeld and U. Bertocci, editors, ASTM, Philadelphia, PA, pp. 256-273, 1981.

44. R.L.S. Thomas, D. Li, R.P. Gangloff and J.R. Scully, *Metallurgical and Materials Transactions - A,* Vol. 33A, pp. 1991-2003, 2002.

45. S.W. Smith and J.R. Scully, *Metallurgical and Materials Transactions-A,* Vol. 31A, pp. 179-93, 2000.

46. J.Y. Lee, J.L. Lee and W.Y. Choo, *Current Solutions to Hydrogen Problems in Steels,* ASM, Metals Park, OH, pp. 423-7, 1982.

47. H.E. Kissinger, *Analytical Chemistry,* Vol.29, pp. 1702-6, 1957.

48. R. Ayer and P.M. Machmeier, *Metallurgical and Materials Transactions A,* Vol. 29A, p. 903-5, 1998.

49. D.L. Johnson, G. Krauss, J.K. Wu and K.P. Tang, *Metallurgical Transactions A,* Vol. 18A, pp. 717-21, 1987.

50. R.A. Oriani, in *Fundamental Aspects of Stress Corrosion Cracking,* NACE, Houston, TX, pp. 32-50, 1969.

51. J.P. Hirth, *Metallurgical Transactions A,* Vol. 11A, pp. 861-90, 1980.

52. W.C. Johnson and J.Y. Huh, "Thermodynamics of Stress-induced Interstitial Redistribution in BCC Metals", *Metallurgical and Materials Transactions A,* in press, 2003.

53. K.N. Akhurst and T.J. Baker, *Metall. Trans. A,* Vol. 12A, pp. 1059-70, 1981.

54. T.L. Anderson, *Fracture Mechanics: Fundamentals and Applications,* 2nd Ed., CRC Press, Boca Raton, FL, pp. 117-81, 1995.

55. Y. Katz, N. Tymiak and W.W. Gerberich, *Engineering Fracture Mechanics,* Vol. 68, pp.619-46, 2001.

56. X. Chen and W.W. Gerberich, *Metallurgical Transactions A,* Vol. 22A, pp. 59-70, 1991.

57. Y. Wei and J.W. Hutchinson, *Journal of Mechanics and Physics of Solids,* Vol. 45, pp. 1253-73, 1997.

58. H. Jiang, Y. Huang, Z. Zhuang and K.C. Hwang, *Journal of Mechanics and Physics of Solids,* Vol. 49, pp. 979-93, 2001.

59. T.Y. Zhang and J.E. Hack: *Metallurgical and Materials Transactions A,* Vol. 30A, pp. 155-9, 1999.

60. T.Y. Zhang, H. Sheu and J.E. Hack, *Scripta Metallurgica et Materialia,* Vol. 27, pp. 1605-1610, 1992.

61. D. Li, R.P. Gangloff and J.R. Scully, *Hydrogen Diffusion and Trapping Behavior in Ultrahigh Strength AerMet® 100 Steel,* Technical Report, University of Virginia, Charlottesville, VA, 2002.

62. R. Ayer and P.M. Machmeier, *Metallurgical Transactions,* 27A, pp.2510-21, 1996.

63. R.P. Gangloff, in *Hydrogen Effects on Material Behavior and Corrosion Deformation Interactions,* N.R. Moody, A.W. Thompson, R.E. Ricker, G.S. Was and R.H. Jones, eds., The Minerals, Metals & Materials Society, Warrendale, PA, pp. E03:1-21, 2003.

TABLE 1
EXAMPLES OF CURRENT BAKING PRACTICE FOR SOME HIGH STRENGTH STEELS

Steel Type	Temperature (°C)	Time (h)	Reference
Tensile strength of 1201-1800 MPa	190-220	min. 12 - 22	[19]
Engineering Cr-plated items	440-480	min. 1	[19]
Surface-hardened parts	130-160	min. 8-16	[19]
Cd-coated parts	190	5 - 24	[13]
AISI 1080	191	3	[18]
Cd-coated AISI 4340 and 300M	190	>100	[14]
High carbon steel	200	2	[20]

TABLE 2
CHEMICAL COMPOSITION OF Fe-13Co-11Ni-3Cr-1Mo-0.2C STEEL (wt%) [15]

Fe	Co	Ni	Cr	Mo	C	P	S	H (wppm)
Bal.	13.40	11.10	3.10	1.20	0.23	0.003	0.0008	0.35

TABLE 3
MECHANICAL PROPERTIES OF HEAT-TREATED Fe-13Co-11Ni-3Cr-1Mo-0.2C STEEL [15, 37]

Orientation	Yield Strength		Ultimate Tensile Strength		Elongation	Charpy V-Notch Impact Energy		Fracture Toughness K_{IC}	
	Ksi	MPa	Ksi	MPa	%	Ft-lbs	J	Ksi√in	MPa√m
L	250	1724	285	1965	14	30	41	115	126
T	250	1724	285	1965	13	25	34	100	110

L: Longitudinal, T: Transverse

TABLE 4
CALCULATED VALUES OF TRAP BINDING ENERGIES, E_b, kJ/mol (eV/atom)
IN Fe-13Co-11Ni-3Cr-1Mo-0.2C STEEL USING E_m = 10 kJ/mol [36]

η_{chg}	Peak 1a *	Peak 1b **	Peak 2	Peak 3
-0.62V	8.9±0.2 (0.092±0.002)	11.6±0.2 (0.120±0.002)	62.2±0.3 (0.644±0.003)	89.1±0.3 (0.924±0.003)
-1.17V	-------	11.4±0.2 (0.118±0.002)	61.3±0.3 (0.635±0.003)	89.9±0.3 (0.932±0.003)

* for as-quenched alloy   ** for aged alloy
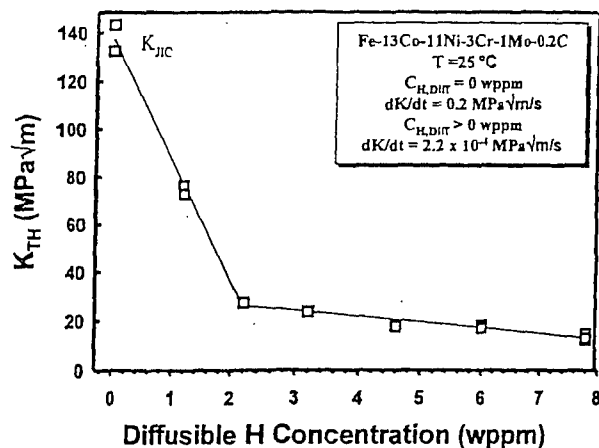
FIGURE 1. Threshold stress intensity for hydrogen embrittlement, K_{TH}, of Fe-13Co-11Ni-3Cr-1Mo-0.2C steel at various diffusible H concentrations obtained during pre-charging.[15]
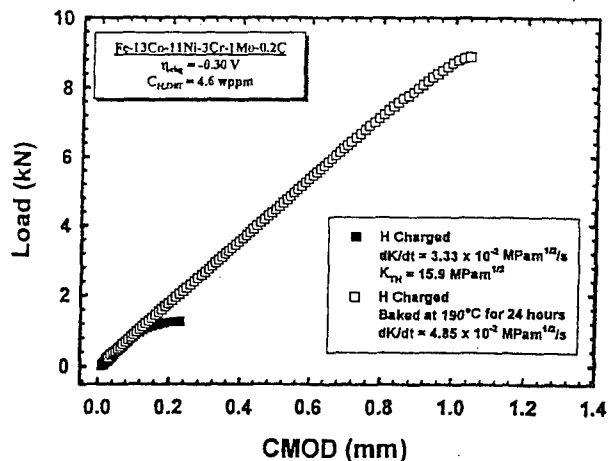
FIGURE 3. Load versus CMOD data for H precharged ($C_{H,Diff}$ = 4.6 wppm) and precharged/baked Fe-13Co-11Ni-3Cr-1Mo-0.2C steel. Charging was conducted in saturated Ca(OH)₂ at overpotential of –0.30 V at 60°C for 20 days. Baking was performed at 190 °C for 24 hours.[15]
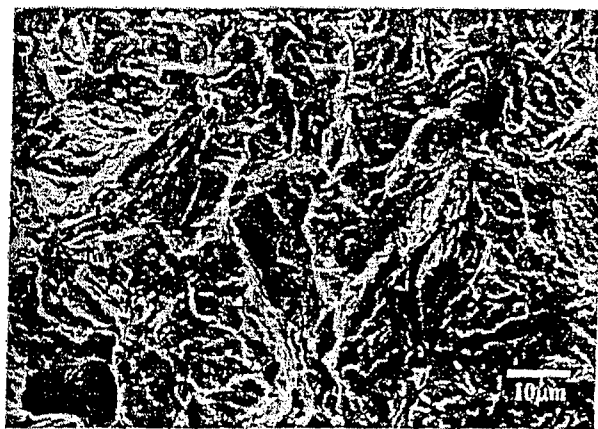
FIGURE 2. Scanning electron image of the fracture surface of Fe-13Co-11Ni-3Cr-1Mo-0.2C steel with diffusible H concentration of 4.6 wppm. Fracture occurred completely by a brittle transgranular mode. Crack growth was from top to bottom.[15]
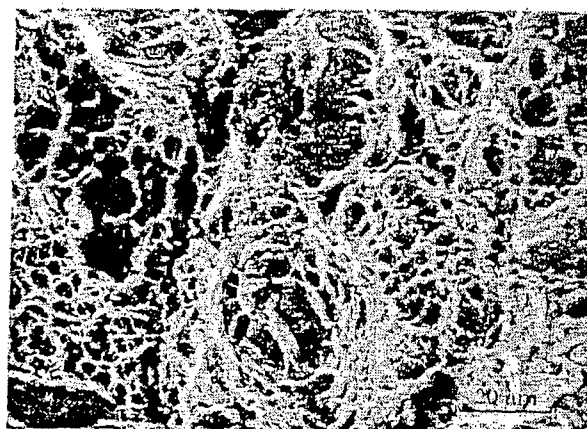
FIGURE 4. Scanning electron image of the fracture surface of hydrogen-charged Fe-13Co-11Ni-3Cr-1Mo-0.2C steel after baking at 190 °C for 24 hours. The specimen was previously charged to a diffusible H concentration of 4.6 wppm.
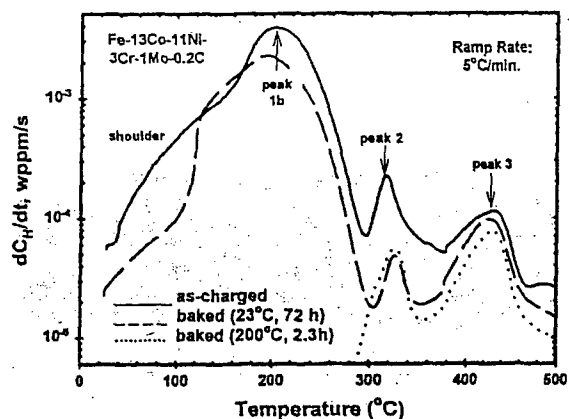
FIGURE 5. H desorption rate as a function of temperature for peakaged Fe-13Co-11Ni-3Cr-1Mo-0.2C steel, measured by TDS at a ramp heating rate of 5°C/min, showing the effect of baking compared with the as-charged condition (charged at overpotential of –0.62 V at 60°C).[36]
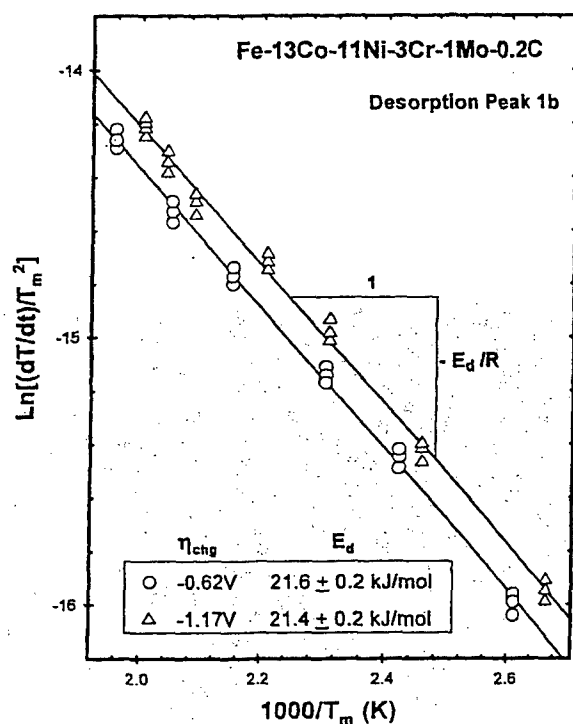
FIGURE 6. Experimental determination of the apparent activation energy for H desorption, E_d, associated with detrapping-peak 1b from the H desorption curves for peakaged Fe-13Co-11Ni-3Cr-1Mo-0.2C steel.[36]
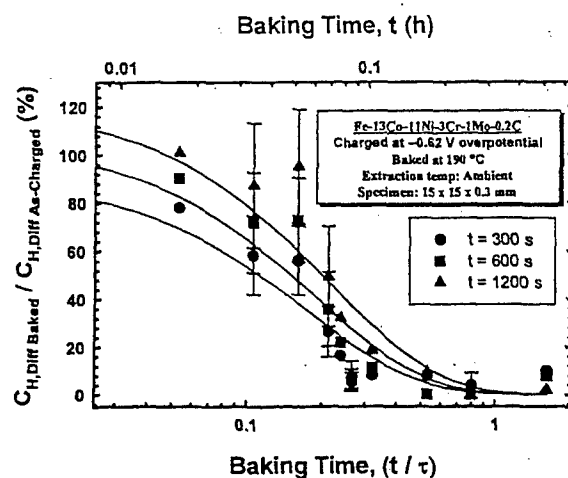
FIGURE 7. Residual diffusible H concentrations in hydrogen charged and baked peakaged Fe-13Co-11Ni-3Cr-1Mo-0.2C steel (without cadmium coating) after the indicated baking times expressed as t/τ ($\tau = L^2/D$, L = 0.015 cm and $D_{eff} = 2 \times 10^{-7}$ cm^2/sec). Results are shown for the various times (t) used to calculate $C_{H,Diff}$ values from Equation 1 and are normalized to as-charged values. Measurements were performed using the Barnacle Electrode method and background was subtracted. (Standard deviation given, when three or more tests were conducted)
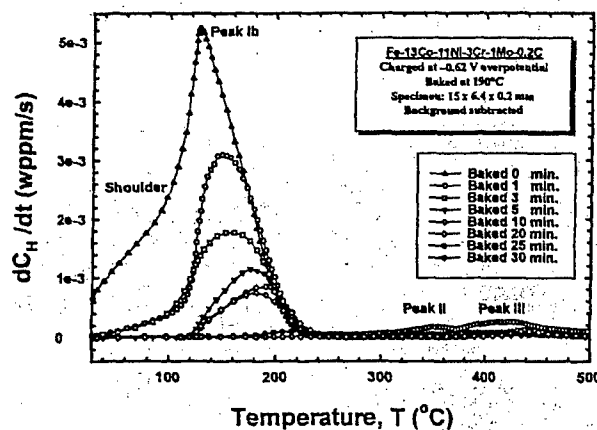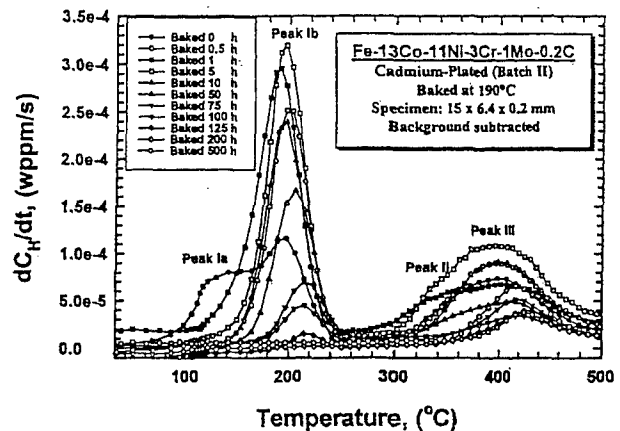

FIGURE 8. Hydrogen desorption rates versus TDS ramp temperature for H precharged and baked uncoated Fe-13Co-11Ni-3Cr-1Mo-0.2C steel specimens after the indicated baking times at 190 °C. TDS tested at dT/dt = 5 °C. Charging was performed in saturated Ca(OH)$_2$.
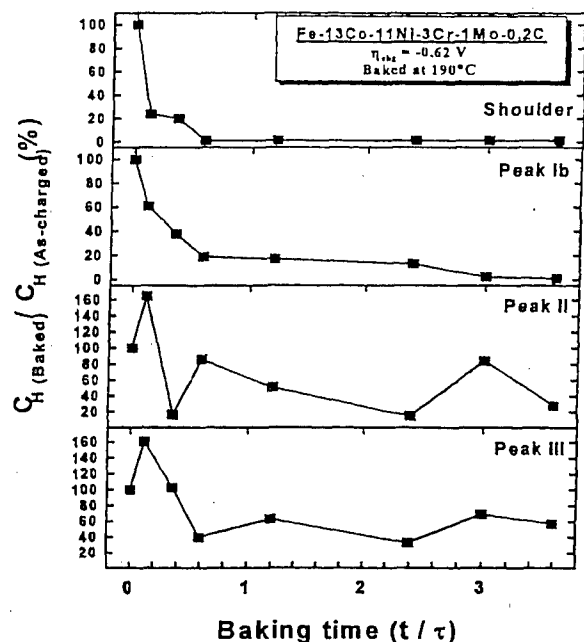
FIGURE 9. Percentage of the H concentration egressed from each peak of $Ca(OH)_2$ precharged and baked uncoated Fe-13Co-11Ni-3Cr-1Mo-0.2C steel specimens, $C_{H\ Baked}$, relative to the corresponding concentration for the as-charged specimen, $C_{H\ As-charged}$. Results were reported versus t/τ where t is baking time (sec.) and τ is the time constant ($\tau = L^2/D$, L = 0.01 cm and $D_{eff} = 2 \times 10^{-7}$ cm^2/sec).

FIGURE 11. Cross section of thick cadmium plated Fe-13Co-11Ni-3Cr-1Mo-0.2C steel examined using optical microscopy.

FIGURE 10. SEM micrograph of the as-plated surface of a thick cadmium deposit on Fe-13Co-11Ni-3Cr-1Mo-0.2C steel.
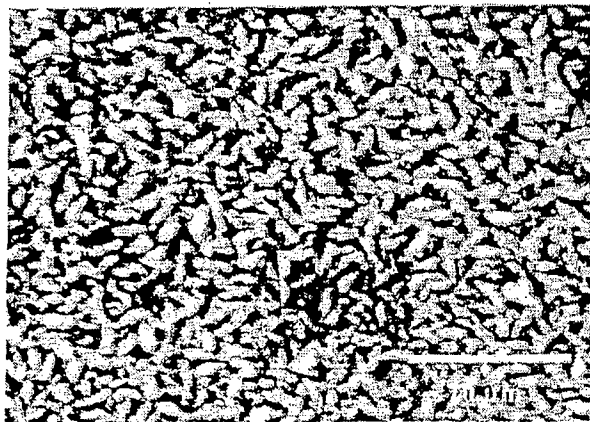
FIGURE 12. SEM micrograph of the as-plated surface of a thin cadmium deposit on Fe-13Co-11Ni-3Cr-1Mo-0.2C steel.
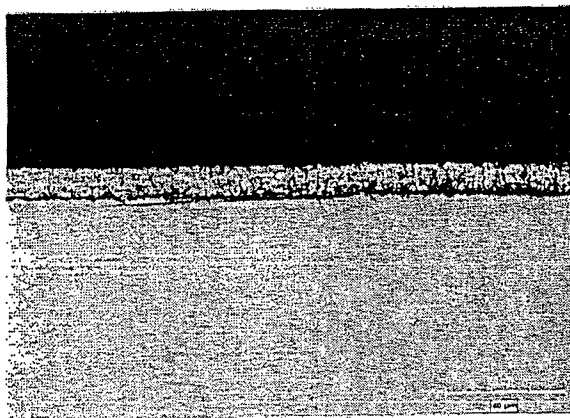
FIGURE 13. Cross section of thin cadmium plated Fe-13Co-11Ni-3Cr-1Mo-0.2C steel examined using optical microscopy at 400X magnification.

FIGURE 15. Hydrogen desorption rate versus TDS ramp temperature for thin cadmium plated and baked Fe-13Co-11Ni-3Cr-1Mo-0.2C steel specimens after the indicated baking time at 190 °C. TDS tested at dT/dt = 5 °C.
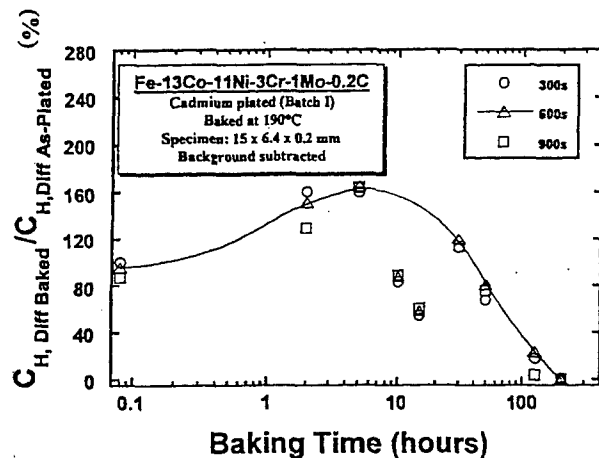
FIGURE 14. Residual diffusible H concentration from thick cadmium plated Fe-13Co-11Ni-3Cr-1Mo-0.2C steel after the indicated baking time. Concentrations were calculated for three different t values, where t is the extraction time used in Equation 1. Results are normalized to the as-plated value.
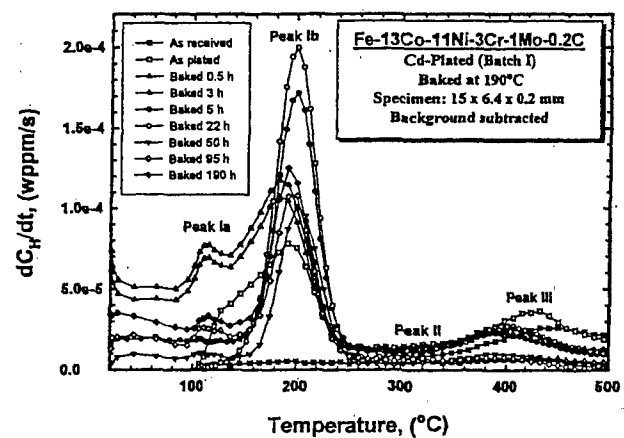
FIGURE 16. Hydrogen desorption rate versus TDS ramp temperature for thick cadmium plated and baked Fe-13Co-11Ni-3Cr-1Mo-0.2C steel specimens after the indicated baking time at 190 °C. TDS tested at dT/dt = 5 °C.
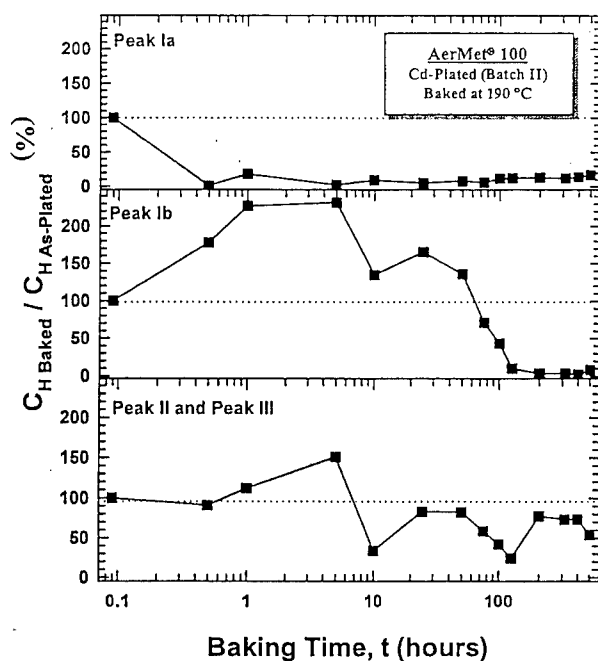
Figure 17. Residual H concentration associated with each peak identified from the H desorption curves of thin cadmium plated and baked AerMet® 100 steel specimens as a function of baking time. Results are normalized to the as-plated value and expressed as % of initial H concentration. Background was subtracted. Coating thickness ~ 10μm.

Figure 19. The interaction energy E_h (= $\sigma_h V_H$) associated with a given hydrostatic tensile stress, σ_h, ahead of the crack tip compared with E_b for major trap states in aged AerMet® 100, where V_H, the partial molar volume of H in Fe, is 2.0 cm³/mol.
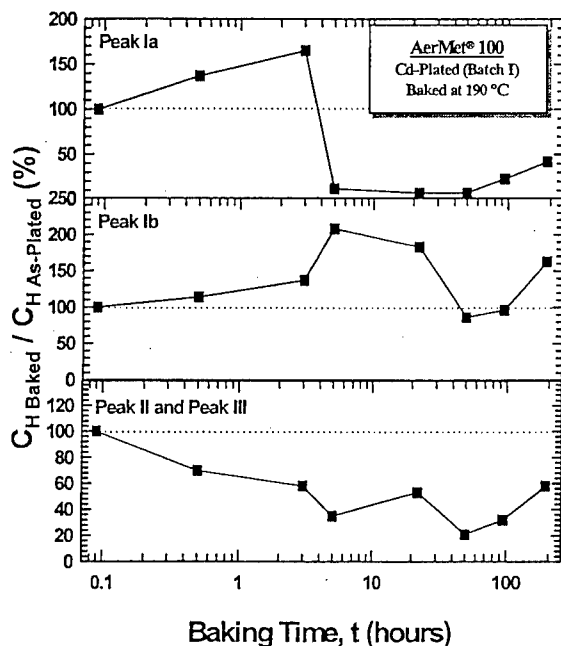
Figure 18. Residual H concentration associated with each peak identified from the H desorption curves of thick cadmium plated and baked AerMet® 100 steel specimens expressed as a function of baking time. Results are normalized to the as-plated values and expressed as % of initial H concentration. Background was subtracted. Coating thickness ~ 18μm.

Investigation of Local Hydrogen Uptake in Rescaled Model Occluded Sites using Crevice Scaling Laws

John R. Scully and Michael Switzer

Investigation of Local Hydrogen Uptake in Rescaled Model Occluded Sites using Crevice Scaling Laws

John R. Scully, Michael A. Switzer

Center for Electrochemical Science and Engineering

Department of Materials Science and Engineering,

The University of Virginia

Charlottesville, VA 22904, USA

Abstract

The effects of occluded site geometry and applied potential on hydrogen production and uptake in a martensitic stainless steel (Fe-13Cr-8Ni-2Mo-1Al) were explored. On planar electrode surfaces, the total hydrogen concentration was found to increase exponentially with hydrogen overpotential. The x^2/gap scaling law, where x is the pit/crevice depth and "gap" is the pit/crevice width, was utilized to rescale model pits from micrometer to millimeter dimensions. Such rescaling enabled local hydrogen measurements as a function of pit depth in rescaled pits. Two values of x_{crit} were identified. Significant local hydrogen (H) uptake was observed at $x > x_{crit}$ under conditions where external surfaces were in a passive state and above the hydrogen electrode potential ($E_{H/H+}$). The local potential drops below $E_{H/H+}$ at a depth, $x_{crit1} = x_{HER}$ and reaches the primary passivation potential (E_{Pass}) of the stainless steel at a depth, $x_{crit2} = x_{Pass}$. Thus, at $x > x_{crit1}$, the stainless steel experiences H production and uptake but remains passivated. At $x > x_{crit2}$, the material absorbs hydrogen on an actively dissolving pit surfaces since the local potential drops below E_{Pass}. Nuclear reaction analysis revealed that concurrent metal dissolution

and hydrogen uptake lead to significant amounts of local hydrogen absorption just beneath simulated pit surfaces.

1. INTRODUCTION

Pits and other occluded sites serve several roles that promote stress corrosion cracking and hydrogen environment-assisted cracking (HEAC) of engineering alloys in aqueous environments.[1,2,3] Pits can act as stress concentrators that facilitate crack initiation, expose susceptible grain boundaries and interfaces not available on machined surfaces, and provide an occluded site enabling locally aggressive environment formation. For instance, the acidic environment of freely corroding and anodically polarized pits or crevices with actively corroding surfaces can promote accelerated corrosion as well as H production and entry. The latter occurs as a consequence of hydrolytic acidification of dissolved metal cations and ohmic potential drop such that the pit bottom potential is near or below the reversible hydrogen electrode potential, $E_{H/H+}$. Hydrolysis of metal cations can drastically lower the pH of the occluded site such as a pit or crack so that it is much more acidic than the bulk solution.[4] This may enhance the proton reduction reaction depending on reaction order with respect to proton activity and also affect the exchange current density for proton reduction. Moreover, acidification may lead to depassivation and activation of the occluded site surfaces by chemical dissolution of any pre-existing oxide film that limits H production and uptake. In addition, ohmic potential drop, as a function of the pit geometry and the solution resistance of the pit electrolyte, may promote activation of a passive metal when the local potential falls below the Flade potential or the primary passive potential, E_{Pass}, even though the external surface of the metal is held at a potential where it is passive. Moreover, the local potential may drop below $E_{H/H+}$ enabling generation of H that can readily diffuse into the metal. Furthermore, metal oxidation or selective dissolution of on element in a solid solution alloy can inject vacancies into the metal [5] that forms clusters, [6] alter other aspects its near-surface metallurgical condition such as changing the near surface composition or causing void formation [7] as well as possibly triggering dynamic trap state

creation when vacancies function as H traps. [8]   The amount of H generation within the pit coupled with slow effective H diffusivity within a trap-rich high-strength steel could result in large local H concentrations at such pits or crevices sites, despite the large chemical driving force for H diffusion into the metal.   These factors may lead to an underestimation of subsurface diffusible and trapped H concentrations in H uptake experiments that sample global H concentrations averaged over large areas and volumes.

A critical unresolved issue in HEAC is the local crack tip H concentration. This information may not be accessible by conventional analysis and may differ from global hydrogen concentrations over large sampling area as discussed above. Quantifying H uptake and local H concentrations in pits, crevices and cracks is difficult due to the size scale of the damage process zone particular at environmental crack tips where crack surface opening displacements underestimate continuum predictions.[9]   The solution chemistry within HEAC sites has been determined by freezing and isolating the solution present in the crack tip, and using indicator papers to identify the solution pH and the presence of metal ions.[10] Recently, capillary electrophoresis has been used.[11]   While these procedures determine the presence of certain ions within the crack tip solution, few methods for measuring local H concentrations have been employed. A crevice chamber has been added to the charging side of a Devanthan permeation cell in order to simulate an occluded site.[12,13]   However, precise crevice scaling in order to duplicate the electrochemical conditions of a smaller sized crack or pit was not considered. Secondary ion mass spectroscopy and tritium detection methods show large increases in hydrogen concentrations near actual crack tips but often lack spatial resolution to probe sharp crack tips.[14,15] Experiments utilizing thermal emission methods for determining total H concentrations require a large sample mass.   Therefore, such techniques generally yield globally averaged concentrations, which cannot capture the presence of severe H concentration gradients such as might exists at the tip of a crack or in a pit.   Large scale H permeation measurements using a charging solution that mimics the composition of acid pits may not reproduce the exact chemistry, surface state, metallurgy or electrochemistry of the metal within occluded sites. Furthermore, high pit dissolution rates may alter the near surface metallurgy of pits and thickness changes during permeation confound accurate measurements.   Micron-scale potential changes and chemical gradients in real pits, crevices and cracks are difficult to quantify and reproduce with large commercial microelectrodes given the micro-liter solution volumes present at real

occluded sites. The bulk solutions used in permeation experiments are approximations of the solutions in real pits. Consequently, it is difficult to accurately quantify H uptake in pits. It is possible that poorly understood local factors at real cracks, pits and crevices conspire to produce high local H concentrations that would be absent in planar electrode experiments with simulated occluded sites chemistries. Knowledge of the relevant crack tip concentration is a critical unresolved issue in HEAC. This information is required to forecast HEAC susceptibility as a function of electrochemical conditions such as potential and possible mitigation strategies. This is especially important when the damage mechanism involves crack initiation when the local hydrogen concentration exceeds a critical concentration over a critical depth at a sharp crack tip.[16]

Precipitation-aged hardened martensitic stainless steels (i.e., Fe-Cr-Ni-Mo alloys) that release hydrolysable Cr and Fe cations during electrodissolution are ideal candidates for intensified local H uptake at anodically polarized pits, crevices or cracks not otherwise seen in global measurements of H absorption. These alloys, at high strength levels, also have known to be susceptible to internal hydrogen embrittlement and HEAC, and are extremely sensitive to crack tip H concentration.[17] Cathodic polarization to introduce global uniform hydrogen levels show clear evidence of environmental hydrogen embrittlement.[18] Such steels are quite susceptible to acid pitting, resulting in sufficient ohmic voltage drop and local acidification to promote H production and uptake in pits and crevices.[19] Under such conditions, external surfaces remain passive and at electrochemical potentials above EH/H+, while H production and absorption occurs inside pits.[20] Slow effective diffusion rates restrict rapid transport of high levels of diffusible H away from hot spots such as pits where local H uptake may be severe[25] For instance, K_{Th} differs significantly for open-circuit potential (OCP) exposure in 3.5% NaCl versus 20% NaCl, which likely establishes a different set of electrochemical conditions such as OCP, resulting in a different local crack tip chemistry and level of H uptake.[21]. The K_{th} vs yield strength data for PH 13-8 Mo suggest an extreme sensitivity to electrochemical conditions that enable such local H uptake.

There is a need to develop a better understanding of the conditions under which pits and recesses might promote local H production and uptake when H production and uptake is not expected such as at open circuit and under anodic polarization, and to quantify local H concentrations. One approach is to exploit pit scaling laws.[20],[22] This paper characterizes local

H concentrations over small length scales in model pits in a precipitation-hardened martensitic stainless steel, utilizing appropriate geometric crevice scaling laws to design and manufacture model pits of millimeter dimensions that are analogous to actual pits of micrometer scale dimensions. These pits were then used to examine H uptake at various locations within the pits under selected electrochemical conditions. Quantification of the absorbed hydrogen was facilitated by the use of thermal desorption spectroscopy (TDS) and nuclear reaction analysis (NRA). Both have the ability to analyze small-scale samples. NRA has extremely good depth resolution with a millimeter lateral scale resolution, This paper demonstrates the concept of occluded site rescaling for the purposes of local hydrogen measurement.

2. APPROACH

2.0 Materials

The focus for investigation of local H uptake was a precipitation-hardened stainless steel, PH 13-8 Mo stainless steel, (H1050 condition, σ_{YS} = 1241 MPa, K_{IC} = 96-165 MPa$\sqrt{m}$). The alloy composition indicated in Table 1 was selected for investigation. In preliminary experiments, constant temperature TDS experiments were performed to determine the effective diffusion behavior (D_{eff}). D_{eff} was found to follow an Arrhenius text expression with an effective activation energy of 21.1 kJ/mole.

$$D_{eff}(T) = (9.25 \times 10^{-5} \text{ cm}^2/\text{sec}) \ \exp[-\frac{21.1 kJ/mole}{RT(K)}]$$

[Eq. 1]

This expression yields a diffusion coefficient at 25 °C of 1.9 x10^{-8} cm^2/sec consistent with a temper martensitic microstructure containing secondary hardening precipitates.[21] Both planar electrodes and model rescaled localized corrosion sites were studied under conditions mimicking those encountered during acid pitting.

Table 1. Composition of PH 13-8 Mo Stainless Steel

	Cr	Ni	Mo	Al	Mn	C	Si	P	S	N	Fe
Wt. %	12.5	8.14	2.12	1.1	0.09	0.03	0.04	0.006	0.0004	0.005	75.97
At. %	13.3	7.66	1.22	2.3	0.09	0.14	0.08	0.011	0.001	0.020	75.24

2.1 Hydrogen Analysis

TDS was utilized to quantify absorbed H concentrations in model-occluded sites. The TDS system utilizes a quadrupole mass spectrometer to measure the change in H_2 partial pressure via monitoring of selected mass/charge ratios in a high vacuum chamber containing a H charged sample that is the source of the outgassing.[23] H analysis was measured from specimens cut from rescaled pits less than one gram in mass and less than 0.1 cm^3. The amount of H outgassed is dependent on the programmed temperature of the furnace surrounding the analysis chamber since the total H released at a given temperature includes both diffusible and trapped H.[24] H trapping sites within PH 13-8 Mo include grain and lath boundaries, dislocations and strengthening precipitates. Each trapping site has an associated binding energy.[25] A programmed ramp rate of 3°C/min from room temperature to a maximum temperature of 330°C was confirmed to release H from lattice and major trap states. The integrated amount of hydrogen released was used to quantify the global diffusible and trap-affected hydrogen concentrations in specimens removed from LN_2 storage after potentiostatic polarization. This was conducted after subtraction of the background hydrogen level detected before hydrogen charging. Nuclear reaction analysis was performed on hydrogen charged planar electrodes of PH 13-8 Mo at the ion beam facility at the University of Albany of New York. Hydrogen was detected using $^1H(^{15}N,\gamma\alpha)^{12}C$ nuclear reaction (6.385+/- 0.005 MeV resonant energy) using a beam of high-energy $^{15}N^+$ ions to bombard a sample over a lateral area of square millimeters. The gamma ray output results from the nuclear reaction of the N^{15} ions with atomic hydrogen and is proportional to the hydrogen concentration over a finite depth range. Depth profiling is achieved by varying the kinetic energy of the ionized nitrogen beam above the threshold resonant energy. In this way the beam of N^{15} ions penetrated the material, energy loss occurred, and the resonant energy was achieved at a given sample depth. Thus the gamma ray output was proportional to hydrogen concentration at that depth. In this way, energy loss was exploited to sample hydrogen concentration over precise ranges of depth perpendicular to planar electrode surfaces. A depth resolution of a few nanometers is achieved due to the four order of magnitude difference in cross-section and hence gamma-ray yields at the resonance energy compared to off-resonance energies.

2.2 Planar Electrode Experiments to Measure Hydrogen Uptake

Studies were conducted on planar electrodes exposed to room temperature deaerated solutions of 0.1 M HCl (simulating an acidic solution associated with occluded sites) and 5 M H_2SO_4 solution (pH = -0.57) plus dissolved iron, chromium, and nickel ions (simulating a acid pit environment in a stainless steel after metal dissolution). A Hg/Hg_2SO_4/sat. K_2SO_4 reference electrode was used in H_2SO_4 (+640 mV vs. SHE at 25°C). A saturated calomel electrode was used in HCl solutions (+241 mV vs. SHE at 25°C). Cathodic E-Log(i) data were analyzed over a range of pH levels to provide reaction kinetics for the H evolution reaction (HER) as a function of pH and cathodic H overpotential. The volume of hydrogen gas generated during potentiostatic polarization was collected and determined volumetrically with an inverted funnel/burret system. H uptake was subsequently studied by TDS at selected potentials. TDS was used to characterize steady state total hydrogen concentrations, C_H, under conditions where bulk H charging occurs at cathodic potentials, under local pitting conditions, as well as under conditions promoting pit depassivation and surface activation simultaneous with H production. TDS was performed on planar electrodes charged for time periods enabling homogeneous distributions in H concentration. TDS and NRA were performed on exposed materials that were charged for time periods enabling homogeneous distributions in H concentration. Two separate cleaning procedures were used (methanol rinse and nitric acid cleaning) and specimens were immediately stored in LN_2. TDS analysis of the hydrogen charged samples was used to produce relationships between absorbed hydrogen concentration and charging potential.

2.3 Rescaling Methods to Enable Spatially Resolved H Analysis in Pits

Local corrosion scaling laws were implemented to duplicate occluded site conditions representative of a small pit or crevice in larger sized "rescaled" model pits more accessible to H measurements but able to reproduce equivalent mass transport, ohmic potential and electrochemical properties over larger scaled dimensions. The precise scaling laws that apply to PH 13-8 Mo were identified using the *CREVICERv2.0* computer program.[26] Various pit geometries were modeled using actual experimental electrochemical parameters obtained from PH 13-8 Mo such as critical current density, passive current density and E_{Pass}. The modeled pit geometry contained a square crevice opening and depth to produce a pit cavity shaped as a right angle prism. The pit mouth dimension is analogous to a crevice gap (G) and represents the edge

length of the square pit mouth The potential distribution was determined as a function of the pit depth dimension (x) for various pit mouth dimensions. Relationships between two critical depths -- the depth for depassivation and activation of the stainless steel in an acid, $x_{crit1} = x_{Pass}$, as well as the depth for the local potential to drop below the reversible H potential, $x_{crit2} = x_{HER}$ -- were developed for a given pit gap. Relationships between x_{crit}^2 vs. gap were then developed over a range of G. Complexity was reduced by conducting experiments and modeling in 5M H_2SO_4 containing metal salts that minimized pit chemistry variations as a function of pit depth so that a single electrochemical boundary condition could be utilized at all positions in the pit. After constructing plots of local potential versus depth, x, for various applied potentials at the pit mouth and dimensions G, x_{crit1} and x_{crit2} were plotted versus G.[27,28] The nearly linear x^2/G relationships obtained served as scaling laws that guided development of rescaled pits for experimental study by enabling specification and fabrication of larger dimension pits with a cylindrical occluded sites capable of allowing spatially resolved H measurements. These pits were electrochemically equivalent to small-scale versions of occluded sites with the exception that H_2 bubble, corrosion-salt film formation and dynamic straining were not incorporated. Bubbles restrict ionic transport in crevices and pits, and are expected to induce greater IR drop. However, recesses subjected to H evolution were previously found to follow the x^2/G relationship when equivalence of Tafel kinetics was considered.

Experimentally, rescaled pit specimens were potentiostatically charged under conditions where the pit mouth resided in the passive region and H uptake was possible given sufficient IR drop at a certain pit depth. Specimens were held under these conditions until uniformly charged from interior surfaces of the rescaled pit according to the H diffusivity in PH 13-8 Mo. Micro-reference electrode measurements (World Precision Instruments Driref-450 Micro-ref. Electrode) recorded local pit potential as a function of pit depth, x, using a micrometer resolution positioning system. Thus, the depth at which the local potential dropped below E_{Pass} and $E_{H/H+}$ could be determined by comparison of E-log(i) and $E_{H/H+}$ to potential distributions. C_H versus rescaled pit depth profiles were constructed by two methods. Cylindrical pits were stored in LN_2, cold sectioned at various depths from the exposed pit mouth and analyzed by TDS to measure global H concentration, C_H, in slices cut perpendicular to the x direction at various pit depths. Secondly, the previously established relationships between C_H versus IR corrected electrochemical charging potential obtained from planar electrodes were used. Local potential

distributions within pits were compared to planar electrode data at precise potentials to predict the potential dependent C_H, anodic, i_{an}, as well as cathodic, i_{ca}, half-cell reaction rates.

3. RESULTS

3.1 Electrochemistry Associated with Passive-to-Active Transitions and HER

E-Log(i) polarization data for PH 13-8 Mo exposed to various concentrations of sulfuric acid containing dissolved metal ions can be seen in Figure 1. PH 13-8 Mo exhibits an active-passive transition in each of these solutions. A passive region is seen above approximately –0.5 $V_{Hg/Hg2SO4}$. The alloy exposed to 5 M H_2SO_4 plus dissolved metal ions shows a large critical current density of approximately 3×10^{-3} A/cm^2. A 5M H_2SO_4 solution was chosen to examine H uptake in the model pits. The reversible H potential for this solution is -0.59 $V_{Hg/Hg2SO4}$. It is possible that a rescaled pit or crevice held in the passive range would undergo a passive-to-active transition and the OCP of the crevice could fall below –0.75 $V_{Hg/Hg2SO4}$. A the simplified version of Fig. 1 was used as the E-log(i) boundary condition in CREVICERv2 using i_{pass}, i_{crit}, and E_{pass} from 5M H_2SO_4.

Figure 2 shows the E-logi behavior for PH 13-8 Mo in deaerated 0.1M NaCl. A passive region is observed with characteristic current increases upon pitting. In 0.5 and 1 M HCl, active polarization behavior is observed. The alloy exposed to 0.1 M HCl solution exhibits a several hundred mV passive range above reversible hydrogen where minimal hydrogen production and uptake would be expected. This solution was chosen for focus of remaining experiments.

Concerning the HER deaerated sulfuric acid plus 0.1 M Fe^{+2}, 0.018 M Cr^{+3} and 0.01 M Ni^{+2} solutions at 25 °C., IR correction of the cathodic E-Log(i) data was used to generate an expression for cathodic HER current density as a function of H overpotential and pH:

$$i_{H_2} = (1.31 \times 10^{-4})[H^+]^{0.525} \exp(-14.45\eta_c) \qquad \text{[Eq. 2]}$$

where i_{H2} is the cathodic HER current density (A/cm^2), [H$^+$] is the hydronium ion concentration (mole/L) and η_c is the H overpotential (V). The Tafel slope was ~160 mV/decade. For a given solution pH, Equation 2 can be used to predict the cathodic current density at various hydrogen overpotentials as illustrated in Figure 3.

The cathodic E-Log(i) data were IR corrected and an expression for cathodic current density as a function of pH and overpotential was also developed for 0.1 M HCl:

$$i_{H_2} = (5.45 \times 10^{-5})[H^+]^{0.185} \exp(-12.74\eta_c)$$ [Eq. 3]

where i_{H2} is the HER current density (A/cm^2), $[H^+]$ is the hydronium ion concentration (mole/L), and η_c is the hydrogen overpotential (V). This expression is consistent with an HER Tafel slope of 181 mV/decade. This expression, again, enables determination of hydrogen evolution half-cell reaction rates over a broad potential range including prediction of i_{H2} where the applied current density is net anodic.

3.2 Global Hydrogen Uptake on Planar Electrodes as a Function of IR-Corrected Potential

Planar samples of PH 13-8 Mo anodically and cathodically polarized in 0.1 M HCl and in 5 M sulfuric acid plus dissolved metal ions were analyzed to determine C_H, adsorbed after charging to achieve a homogeneous global H distribution considering the effective diffusion coefficient of 1.8x 10^{-8} cm^2/sec. An example of the change in thermal desorption spectra versus cathodic overpotential with respect to reversible hydrogen in shown in Fig. 4. The area under the thermal desorption peak is proportional to the diffusible and trapped hydrogen absorbed under each charging condition. Such analysis was performed across a broad range of potentials.

Regarding global hydrogen ingress in 5 M sulfuric acid plus dissolved metal ions, C_H is greatest at potentials cathodic to the reversible H potential as expected (Figure 5). Hydrogen concentration is seen to increase exponentially with hydrogen overpotential (Figure 5). For instance; uptake at a charging potential of -1.10 $V_{Hg/Hg2SO4}$ is 40 times greater than uncharged levels (uncharged levels were a fraction of a wppm). It is interesting to note that H absorption is observed above the reversible H potential. Fig. 5 also illustrates that considerable H uptake could occur in pits or crevices when ohmic voltage drop places the pit surface at a potential of, for instance, -0.75 V even if the pit mouth were polarized to a more positive potential. The scatter bars in the TDS results shown in Figure 5 were determined by analyzing multiple samples charged in the same bulk solution under the same electrochemical conditions. The hydrogen concentration measured reflects the global hydrogen concentration and is not surface sensitive. The global hydrogen concentration data as a function of potential (Figure 5) were fit with an

exponential expression to relate normalized hydrogen concentration ($C_H/C_{H,unch}$) to true charging potential and was valid over the experimental range of -0.15 to -1.2 V_{Hg/Hg_2SO_4}:

$$(C_H/C_{H,unch}) = (0.35)exp(-3.95 \times E_{true}) \qquad [Eq. 4]$$

where C_H and $C_{H,unch}$ are the hydrogen concentrations for charged and uncharged specimens, respectively, with units of g H/g alloy, and E_{true} is in Volts. Using this equation, a sample held at a potential of -0.35 V_{Hg/Hg_2SO_4} would have a normalized hydrogen concentration of 1.4 ± 0.2, i.e., the sample would contain 1.4 ± 0.2 times the amount of hydrogen of an uncharged sample. A sample held at a potential of -1.2 V_{Hg/Hg_2SO_4} would have a normalized hydrogen concentration of 40.1 ± 5.2 times an uncharged specimen.

Figure 5 also reports the charge associated with hydrogen production (e.g., H_2 charge) as a function of potential. Good agreement is seen between the three methods used to asses the charge for a time period equal to the "saturation time" required to obtain a uniform hydrogen concentration within the steel assuming Fickian diffusion and D_{eff} of 1.9 x10^{-8} cm^2/sec at 25°C. A semi-logarithmic relationship is observed between accumulated H_2 charge and H_2 overpotential. It can be seen that H_2 is produced at both overpotentials and underpotentials as expected.

Hydrogen concentration as a function of charging potential for the PH 13-8 Mo exposed to 0.1 M HCl is shown in Figure 6. These data show a similar trend to that seen for 5 M sulfuric acid plus dissolved metal salts. Specifically, hydrogen uptake on an IR-free planar electrode is low near and above the reversible hydrogen potential in the passive region. Uptake occurs globally under cathodic polarization and locally after anodic polarization above pitting thresholds when acid pits are formed. Hydrogen uptake under cathodic polarization in 0.1 M HCl is significantly greater than seen in 5 M H_2SO_4 with metal salts. For instance, C_H reaches 300 times the as-received levels at -1.0V_{SCE}. A fit of the data containing the cathodically polarized samples produced the following relationship over the range of potentials -0.15 to -1.0 V_{SCE}:

$$(C_H/C_{H,unch}) = (0.93)exp(-5.9 \times E_{true}) \qquad [Eq. 5]$$

where C_H and $C_{H,unch}$ are again in g H/ g alloy and E_{true} is in volts versus SCE. According to Equation 5, a sample held at a potential of -0.50 V_{SCE} would have a hydrogen concentration 17.8 $\pm$ 2 times that of an uncharged specimen. A specimen held at -1.2 V_{SCE} would have a hydrogen concentration 1105 $\pm$ 144 times the hydrogen concentration of an uncharged sample. This is markedly greater than for samples charged in sulfuric acid plus dissolved metal ions. From Equation 5, a sample charged at -1.599 V_{Hg/Hg_2SO_4} (equivalent to -1.2 V_{SCE}) would only have a hydrogen concentration of 194 $\pm$ 25 times an uncharged specimen.

The fact that absorbed hydrogen concentration also is elevated for samples charged above the pitting potential (E_{pit} = 0.05 V_{SCE}), as shown in Figure 7, confirms that hydrogen production and entry occurs in acid pits. A sample charged at an applied potential 150 mV above the pitting potential exhibited a relative hydrogen concentration slightly higher than that of a sample charged at a true potential of 150 mV below the reversible hydrogen potential.[1]

3.3 Near Surface Hydrogen Uptake on Planar Electrodes as a Function of IR-Corrected Potential

Results of nuclear reaction analysis (NRA) of planar electrodes charged at open circuit potential ($\sim -.790$ $V_{Hg/Hg2SO4}$), -0.35 $V_{Hg/Hg2SO4}$ and -1.2 $V_{Hg/Hg2SO4}$ (cathodically polarized) for 10 hours in 5 M sulfuric acid plus dissolved metal ions can be seen in Figure 8. From inspection of Figure 8, low, intermediate and high global C_H values are expected, respectively. In this charging period, hydrogen penetrates to at depth of at least 270 μm assuming Fickian diffusion with a D_{eff}^H =1.9x10^{-8} cm^2/s. H/total atom ratio was calculated from γ-ray yield as a function of specimen depth. For both samples, the hydrogen concentration measured by NRA for an uncharged, cleaned specimen was subtracted from the data presented in Figure 8 so that only hydrogen due to charging at the three potentials is represented. The results after cathodic polarization show a negligible H concentration profile as expected because the global hydrogen concentration obtained from TDS for -1.2 $V_{Hg/Hg2SO4}$ polarization is far below the detection limit of NRA (ca. $<10^{-3}$ H atoms/total atoms).[29] However, Figure 8 illustrates a local near-surface H/total atom ratio of >0.04 that remains above 0.01 until a depth of approximately 0.25 μm for

---

[1] Anodically polarized samples which pitted experienced local hydrogen uptake which was normalized in a conventional manner to the entire specimen mass. Normalization by a small area surrounding each pit was not attempted but clearly would result in a 10-100 fold increase in the local hydrogen concentration.

samples charged at open circuit potential as compared to samples charged for the same time period at -1.2 $V_{Hg/Hg2SO4}$. Recall that the sample charged at open circuit exhibited much more extensive metal dissolution compared to the cathodically polarized sample yet was polarized below the reversible hydrogen potential (Figure 5). In contrast, the sample polarized at -0.35 V was above the reversible hydrogen potential and within the passive range. All samples show a high surface hydrogen concentration at analysis depths less than 0.02 μm (20 nm) that could be associated with surface hydrogen contamination, as often seen in NRA. This near surface peak was observed on both nitric acid and methanol cleaned samples never exposed to hydrogen at high fugacity. However, the hydrogen concentration for the sample charged at -1.2 $V_{Hg/Hg2SO4}$ rapidly decreased towards the lower detection limit at a depth between 0.02-0.05 μm below the exposed sample surface suggestive of surface hydrogen, possibly in the form of an hydroxide layer. In contrast, the hydrogen concentration for the sample charged at OCP remained significantly higher through 0.30 μm of depth. This is inconsistent with surface contamination. A H/metal atom ratio of 0.01 corresponds to about 216 wppm of H. Hence, near surface hydrogen concentrations with concurrent dissolution and hydrogen production may exceed 1000 wppm with 0.35 um of the planar surface that was exposed to high hydrogen fugacity and simultaneous metal dissolution.

3.4 Pit Scaling Relations and H Uptake in Rescaled Model Pits

Pit rescaling was undertaken for PH 13-8 Mo in 5 M sulfuric acid plus dissolved metal ions to facilitate manufacture of rescaled occluded site that enabled spatially resolved hydrogen measurements. Figure 9 shows the E-logi data used as derived from 5 M H_2SO_4. An example of local potential profiles calculated using the crevice modeling program (*CREVICERv2*) is shown in Fig. 10 at an applied potential (E_{app}) of -0.475 $V_{Hg/Hg2SO4}$. The electrochemical parameters used in the model are shown in Fig. 9. Fig. 10 shows that the locally computed potential, E, is equivalent to the applied potential, E_{app}, at the crevice mouth. However, ohmic potential drop decreases the locally computed potential towards the deaerated OCP with increasing depth within the crevice. This occurs over shallower depths as the crevice mouth dimension (gap) decreases. The local potential drops below $E_{H/H+}$ at $x_{crit1} = x_{HER}$ and reaches the primary passivation potential, E_{pass}, at a further depth $x_{crit2} = x_{Pass}$. The applied potential at the mouth of a crevice is also an important factor (Figure 11). When E_{app} is raised to higher levels, the position

of x_{crit1} associated with potential drop below $E_{H/H+}$ is shifted towards deeper positions in the crevice assuming fixed chemistry which is likely in the case of the concentrated metal salt solution. Similarly, $x_{crit2} = x_{Pass}$ is shifted towards deeper depths when E_{app} is raised. The opposite effect is seen when E_{app} is lowered. Thus, beyond a critical depth given by $x > x_{crit1}$, a passive stainless steel is subjected to net H production, but remains in the passive state. When the local potential drops far enough, the material undergoes a passive-active transition and net H production is thermodynamically favorable on the actively dissolving surface (e.g., $x > x_{crit2}$). From these results, relationships for two critical distances from the mouth of the crevice were developed that apply to the selected potentials. The first critical distance is the distance from the crevice mouth at which the pit potential equals $E_{H/H+}$, $x_{crit1}(E_{H/H+}) = x_{HER}$. The second critical distance, $x_{crit2}(E_{pass})$, was designated as the distance from the mouth of the crevice where the local crevice potential drops to E_{pass}.

Figs. 12 and 13 show the corresponding anodic and cathodic half-cell reaction rates versus depth x. The anodic reaction rate peaks due to the active polarization nose (Figure 1 and 9) while the HER rate increases with potential decrease (Figure 3), and levels at the OCP of the pit bottom. However, i_{an} can decrease with pit depth, as the active polarization curve indicates, when potentials reach the OCP of the pit. The relationship between x_{crit1}, x_{crit2} and G for PH 13-8 Mo in 5 M H_2SO_4 plus metal salts are shown in Fig. 14. The square of each critical distance is, indeed, a linear function of G to very good approximation. A plot of x versus G (not shown) is not linear, confirming that x^2/G is the correct geometrical scaling relationship for both the case of H the passive-to-active transition modeled here. The x-G relation is critical to translating actual pits of micron scale to manufactured pits of millimeter scale.[20,26] Guided by Fig. 14, model pits/crevices of millimeter scale (e.g., 1500 μm inside cylindrical diameter (G) and 40 mm length, x) were produced using PH 13-8 Mo. Fig. 14 shows that this is equivalent to a 60 μm diameter crevice with x > 3 mm, etc. It can be seen that rescaled model pits possess x_{crit1} and x_{crit2} over macroscopic lengths from 5-10 mm. Hence, different potential dependent corrosion and H uptake behavior would occur over lengths of millimeters instead of depths of micrometers typical of actual pits. These samples were held in 5 M H_2SO_4 plus dissolved metal ion under potentiostatic control. Local potential was measured versus depth x in rescaled crevices. Potentials were held at potentials ranging from -0.4 to -0.60 $V_{Hg/Hg2SO4}$. IR drop was insufficient at high passive potentials such as -0.40 $V_{Hg/Hg2SO4}$ to produce significant potential drop inside

one-dimensional pits because pits walls exhibited low anodic passive current densities (Figures 1 and 9) near these potentials that did not produce enough ohmic voltage drop to drop the potential below E_{Pass} in order to activate stainless steel surfaces. However, when E_{app} was decreased to -0.60 $V_{Hg/Hg2SO4}$, significant potential drop was seen versus x such that the bottom of the pit approached the limiting or open circuit potential near –0.76 V (Fig. 1-2). Rescaled pit specimens were exposed, removed, rinsed, stored in LN_2 and sectioned radially for H analysis versus depth x. Fig. 15 shows one potential profile experimentally measured using the micro-reference electrode for a sample held in 5M H_2SO_4 plus dissolved metal ions at -0.60 $V_{Hg/Hg2SO4}$ (applied potential) with a 1500 μm inside diameter and 40 mm length. The pit exhibits a 150 mV potential drop from its mouth to its bottom. Most of the potential drop occurs in the first 10 mm of depth, consistent with the modeling results (Fig. 10 and 11). An indication of anodic dissolution as a function of x, is recorded by examining the increase in inside diameter of the pit. This increase in pit diameter indicates increased anodic dissolution as a function of x due to loss of passivity and high dissolution rates in the active E-i region. The decrease in diameter back towards the original value at the pit bottom is consistent with a decrease in i_{an} at the OCP near the bottom of the crevice (Fig. 15).

The decrease in E and increase in i_{ca} produce an increase in C_H with depth in the crevice when the applied potential at the mouth is held at -0.60 $V_{Hg/Hg2SO4}$ (Fig. 15). The local level of C_H within pits increases even when uptake is minimal on external passive surfaces. Independent corroboration is obtained when C_H predicted from the planar electrode studies using an identical solution is plotted at each interfacial potential recorded using the microelectrode (Fig. 15). The predicted values from a combination of bulk electrode studies and local potential measurements are consistent with TDS measured values. The local C_H within the model pit increases nearly 100% from approximately 4 times an uncharged specimen near the pit mouth to almost 7 times that of an uncharged specimen at x greater than 10 mm within the pit where potential is lowest and cathodic current density is at its highest value. Therefore, a planar electrode held just in the passive region at –0.6 V would be expected to produce and concentrate H in pits or crevices at depths greater than $x > x_{HER}$.

The analysis described can be repeated at various E_{app} to provide indication of the potential and depth, x, dependency of C_H as a function of x for occluded sites of selected geometries. In limited testing, other anodic and cathodic potentials were applied to rescaled pits. Microelectrode measurements were performed in conjunction with hydrogen analysis. At an externally applied potential of -0.20 V $_{Hg/Hg_2SO_4}$ in the passive range, very little H was measured. However, a few high measurements were recorded in sections which contained pit sites. Figure 16 shows the results for the same model pit geometry as Figure 15, with an externally cathodic applied potential of -1.2 V $_{Hg/Hg_2SO_4}$ (cathodic). The local potential measured within the rescaled pit increases to the open circuit potential beyond a critical depth and the measured hydrogen profile is in agreement with the calculated hydrogen profile using data obtained using the data base from the bulk electrode experiments (Figure 5). Higher hydrogen concentrations were measured at more negative (more cathodic) local potentials as expected from the bulk electrode experiments. Under cathodic polarization, higher levels of cathodic polarization are achieved near the pit mouth and the level of polarization decreases with pit depth. In this case, C_H is greatest at smaller x. Examination of the cathodic current density as a function of measured potential within the pit shows a decrease in current density with increasing x to a final value of approximately 3 x 10^{-3} A/cm^2 in the first 5 mm of crevice depth.

4. DISCUSSION

Global and Local Surface Hydrogen Uptake on Planar Electrodes

_____Steady state global hydrogen concentrations in a Fe-13Cr-8Ni-2Mo-1Al alloy (i.e., potential dependent effective solubilities) were enhanced as an exponential function of hydrogen overpotential in both 0.1 M HCl and H$_2$SO$_4$ plus concentrated metal ions (Figures 5 and 6). Hydrogen uptake was also seen in pitted samples in 0.1 M HCl (Figure 7). However, pits deviate from IR free planar electrodes and rescaled pits enabled quantification. Such a exponential dependency may be predicted between the interfacial potential at a pit bottom and steady state effective hydrogen solubility using the theory of electrochemical hydrogen absorption and solubility in metals. The operative HER mechanism for steels with comparable Tafel slopes is coupled discharge-chemical recombination.[21] This reaction mechanism occurs in two steps[30]:

$$1) \quad H^+ + e^- + M \xrightarrow{\quad k_1 \quad} M - H_{ads} \qquad\qquad \text{[Eq. 6]}$$

$$(2) \quad M - H_{ads} + M - H_{ads} \xrightarrow{k_2} 2M + H_2 \qquad \text{[Eq. 7]}$$
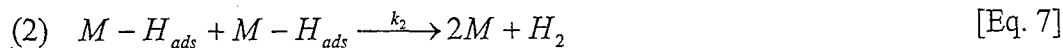
The hydrogen fugacity experienced at the metal/electrolyte interface for this mechanism is related to cathodic overpotential according to[30]

$$f_{H_2} = 10^{1.5} \exp\left(\frac{-\eta F}{2RT}\right) \qquad \text{[Eq. 8]}$$

Hydrogen dissolves in metals according to the following additional step which occurs in competition with the second step shown in Eq. 7 above:[30]

$$(3) \quad 2H = 2M\text{-}H_{ads} = 2M\text{-}H_{diss} \qquad \text{[Eq. 9]}$$

Where H_{ads} is atomic hydrogen adsorbed on the surface of the metal and H_{diss} is atomic hydrogen that has dissolved into the metal either interstitially or through atomic vacancies. The expression describing the equilibrium perfect lattice interstitial concentration in equilibrium with a give hydrogen pressure can be represented by:[30,31]

$$C_o = K_{eq} \, p^{1/2} = 0.00185 p^{1/2} \exp(-28.6 kJ / mole / RT) \qquad \text{[Eq. 10]}$$

where K_{eq} is the equilibrium constant for the nearly perfect lattice hydrogen solubility in iron; $K_{eq} = 0.00185\exp(-28.6 \text{ kJ/mole/RT})$, C_o is the concentration of lattice-dissolved atomic hydrogen, p is the sensible pressure of H_2 gas such as in gas phase charging, R is the ideal gas constant and T is the temperature. The sensible pressure of hydrogen gas is related to electrochemical hydrogen fugacity.[2],32 Assuming that fugacity is directly proportional to pressure at low overpotentials, then the lattice dissolved atomic hydrogen concentration for the coupled discharge-chemical recombination reaction mechanism can be described as:

$$C_o \propto K_{eq}\left(10^{0.75}\right)\exp\left(\frac{-\eta F}{4RT}\right) \qquad \text{[Eq. 11]}$$

where K_{eq} is described above, F is Faraday's constant and R and T have been defined above. Since η is negative, increasing the hydrogen overpotential must therefore increase the amount of dissolved hydrogen in the material exponentially. However, the quantity of hydrogen, C_H, actually measured in the TDS method and reported in Figures 5, 6 and 7 reflects the total hydrogen concentration, C_{Htot}, (e.g., includes the sum of lattice, c_o, and trapped $C_{H,trap}$,

---

[2] The assumption that fugacity is directly proportional to pressure is only valid at low pressures or for ideal gases.

hydrogen). Assuming that the trapped hydrogen concentration is proportional to the lattice hydrogen concentration as well as the trap strength through a Boltzmann type expression and that $C_{H,trap} \gg C_o$, the following relationship describes the relationship between C_o, the concentration of lattice-dissolved atomic hydrogen and C_{H}trap.

Recall that C_o is an exponential function of hydrogen overpotential as indicated in Eq. 11:

$$C_{Htrap} = \frac{C_O \exp\left(\dfrac{E_B}{RT}\right)}{1 + C_O \exp\left(\dfrac{E}{RT}\right)} \qquad \text{[Eq. 12]}$$

In this expression, E_B is the trap binding energy: in this case the binding energy associated with the dominating broad TDS peak indicating a trap state in the TDS data around 450 K (Figure 4). An exponential relationship between $C_H/C_{H,unch}$ and E_{true} is seen in Figures 5 and 6. Equation 12 produces an relationship that is quite consistent with these experimental findings when potential dependent values of C_o from Eq. 11 are inserted into Eq. 12. For instance, Eq 12 predicts a 450 fold increase in $C_{Htrap} \sim C_{Htot}$ at 25°C assuming $E_B = 12$ kJ/mol when the hydrogen overpotential is increased on the steel from 0 to about 480 mV (e.g., -780 mV $_{SCE}$) in 0.1 M HCl. Such an increase is in reasonable agreement with Figure 6 and suggests that Eq. 12 is a valid expression describing the relationship between $C_{H,trap}$ and C_o and, therefore, $C_{H,trap}$ and η taking into consideration Eq. 11. The results in experimental $C_{H,trap}$ versus η for H_2SO_4 and metal salts are significantly less than seen in HCl solution despite similar H_2 production rates indicating that the salt film and possible Ni replating limit hydrogen ingress. For example, Ni^{+2}, which has the most noble standard reduction potential of Ni^{2+}, Cr^{3+} and Fe^{2+}, would plate out first at approximately -0.949 V_{Hg/Hg_2SO_4} [43]. Below this potential, reduced nickel on the surface of the alloy may inhibit hydrogen ingress because fcc nickel could serve as a permeation barrier.

Local Hydrogen Uptake

The NRA results of Figure 8 indicate a high local total hydrogen concentration at the surface of the specimen exposed at the open circuit potential in 5 M H_2SO_4 plus dissolved metal ions. This concentration profile extended to a depth of almost 0.35 μm (350 nm). This depth

exceeds likely oxide film[33] and selectively dissolved metallic film thicknesses[3] but does not extend to the full depth to which diffusible hydrogen might penetrate by Fickian diffusion processes (i.e., ~300 μm) during the 10 h charging period. It is likely that a lower concentration of diffusible hydrogen penetrates well beyond a 0.35 μm depth but that such a global concentration of hydrogen is below the detection limit of the NRA method. On the other hand, TDS measurements conducted on mm thick specimens under the same conditions as NRA studies would have difficulty detecting the locally high hydrogen concentrations detected by NRA owing to the fact that specimen thicknesses used in planar electrode tests exceed the thin layer detected by NRA by many orders of magnitude. Thus NRA results detect high near surface hydrogen concentrations within tens of microns of the charging surface that are not detected by TDS. In contrast, TDS is not a surface sensitive technique that would sense high local hydrogen levels within hundreds of nm of the sample surface, it would report the average of such high local surface concentrations over the entire sample thickness. In combination, rescaled crevices would enable TDS measurements over mm length scales that represent micrometers in real crevices and enables NRA measurements which have great depth sensitivity but poor lateral resolution limiting its use in real pits and cracks.

The near surface H concentration profile produced from NRA is not consistent with Fickian transport of diffusible hydrogen. In summary, two possibilities exist: that high detected levels of local near-surface hydrogen reside in both lattice and trapped sites in the alloy or that high levels of detected near-surface hydrogen are present in some other state (i.e., such as OH⁻ present in oxide films or dealloyed layers) that is not actually hydrogen within the bulk metal. The latter is not supported by layer thickness estimates in the literature associated with selective dissolution (dealloying) below the parting limit[34]. High hydrogen concentrations within the bulk metallic phase would be hard to attribute to lattice solubility alone because the electrochemical fugacity within active pits, albeit high, does not necessarily support such equilibrium concentrations assuming that the perfect lattice solubility of hydrogen in PH 13-8 Mo is similar to that in iron[35] and the normal density of trap sites in such steels.[25] This is especially true near OCP where the hydrogen overpotential is less than 100 mV.

---

[3] One explanation is that the high hydrogen concentration detected by NRA is hydrogen associated with OH⁻ in a passive or dealloyed layer instead of atomic hydrogen in solid solution at lattice or in clustered trap sites. In order for this to be possible the oxide film on the corroded surface and /or the dealloyed layer would have to reach thicknesses of 0.35 um which appears unlikely given that typical oxide and dealloyed layer thicknesses (below the parting limit) are often restricted to less than 100 nm (0.1 μm).

One other explanation is that high concentration hydrogen-vacancy or divacany trap-like complexes are formed at corroding surfaces and that these account for a very high near-surface hydrogen concentration not seen at equilibrium or normal quenched in vacancy concentrations. This process would be speculated to occur via vacancy injection via incongruent or selective alloying element dissolution concurrent with hydrogen production. This scenario would produce abnormally high hydrogen concentrations restricted to limited surface regions. Such non-Fickian hydrogen concentration profiles would not be altered by hydrogen diffusion into the specimen bulk because of the relative immobility of the vacancy clusters. Few prior experiments have reported direct evidence of such a result, possibly because techniques with high spatial resolution have only recently become available and applied to H uptake in electrochemical charging at occluded sites.[36] However, high room temperature hydrogen concentrations recently have been observed in electrochemically charged Al[37,38] and at Al crack tips.[36] Little evidence of this phenomenon has been reported in bcc stainless steel prior to this publication.

Hydrogen Uptake in Occluded Sites

PH 13-8 Mo exhibits an active-passive transition in a simulated pit/crevice solution. Moreover, this alloy exhibits a deaerated OCP below $E_{H/H+}$ (Figure. 1). Given this behavior, there are a variety of ways that an anodically polarized pit, crevice or crack that experiences IR drop, acidification and O_2 depletion could lead to H uptake under conditions where boldly exposed planar PH 13-8 Mo surfaces would be expected to remain passive and above $E_{H/H+}$. H uptake was observed in 5 M H_2SO_4 + dissolved metal salts at the deaerated OCP (Fig. 5) as well as when a rescaled pit was held in at −0.6 V in the passive region (Figure 15). Here, ohmic voltage drop decreased the local potential below $E_{H/H+}$ at $x > x_{HER}$ even though the applied potential at the mouth of the occluded site was above the passivation potential. These data help to explain the finding that PH stainless steels are susceptible to H embrittlement at OCP or under anodic polarization in chloride solutions, especially when pitting or crevice corrosion occurs leading to acidification.[39,40] H production has also been observed in model pits in iron,[41] carbon steel[41] and a duplex stainless steel[42] when $x > x_{HER}$ despite external polarization to noble potentials in the passive region. H uptake has also been reported in the literature during permeation experiments on anodically polarized planar electrodes[43] under pitting conditions,[44] as well as during intergranular corrosion.[45] At issue here is accurate quantification of local H

concentrations in such corrosion sites. The use of rescaled occluded sites in conjunction with NRA and TDS measurement of hydrogen concentration provides the opportunity for greater quantification of H levels over a range of applied potentials.

Ultimately, C_H values determined in this manner could be compared to C_{Hcrit} values that produce a large drop in K_{Ic}. This would enable determination of the potential dependency of HEAC susceptibility. In this alloy, and similar Cr-containing high strength precipitation age hardened stainless steels, both external anodic and cathodic polarization cause a decrease in K_{th} (Figure 17). The result is interpreted through increases in hydrogen uptake upon cathodic polarization as well as both IR drop and crack tip acidification in the case of anodic polarization. Moreover, the potential, chemical and x^2/G combinations that produce HEAC could be predicted from identification of the combinations of conditions where $C_H > C_{Hcrit}$. Hence, such a potential dependency could be predicted. The rescaled crevice data above supports this notion. Embrittlement is expected upon cathodic polarization but also would be expected upon anodic polarization depending on acidification and IR drop that lowers $E < E_{H/H+}$ at $x > x_{crit1}$. Moreover, it could be predicted whether electrochemically long or short cracks might be more prone to HEAC in the case where local hydrogen uptake at the occluded site dominates over bulk specimen charging. Note that local hydrogen uptake is likely more important for complex high strength materials with low D_{eff} such as the PH 13-8 Mo steel discussed here because rapid diffusion away from a local site of locally high hydrogen concentration is not possible given slow long range Fickian diffusion. These preliminary results suggest that electrochemically short cracks might be of greater concern than electrochemically long cracks when external cathodic polarization is extensive because the crack tip would be located at a position near the surface where C_H is greater. However, long cracks might lead to higher levels of C_H when anodic polarization prevails because the ohmic potential drop lowers the interfacial potential below $E_{H/H+}$ when $x > x_{crit1}$ which is possible in deep cracks. Evidence is being collected to support or refute this assertion using long and short crack data.

Utilization of crevice scaling laws to rescale occluded sites when considering various critical potentials

Modeling shows that IR drop in a crevice can produce local crevice potentials that enable activation of an anodically polarized metal surface within the crevice concurrent with H

production and uptake (Figures 10 and 11). The relationship $x^2/G = constant$ applies for E_{pass} and E_{H/H^+} albeit with different constants (Figure 14). Thus, the notion of a critical potential can be applied to hydrogen embrittlement as well as crevice corrosion. Such scaling relationships have been seen before;[22,26,26,27] the exact values of the constant in this paper are specific to PH 13-8 Mo under the conditions studied. The $x^2/G = constant$ relationship has been previously used to describe depassivation and activation phenomena of concern in crevice corrosion (i.e., IR* model of Pickering).[22,28,41,42] In this study both x_{crit1} and x_{crit2} have been specified, although such relations should hold at any potential of interest. Different regimes have been identified for crevices or pits in PH 13-8 Mo. Under anodic polarization, there is a combination of x and G in a crevice or crack where the stainless steel would be passive and remain above E_{H/H^+}, a region where H production could occur but not activation, and a deep crevice depth (x_{crit2}) beyond which both activation and net H production occur. Here, H absorption was greatest (Fig. 5), charging efficiency was greatest and nuclear reaction analysis indicated very high local hydrogen concentrations within fractions of micrometer depths from a corroding surface undergoing concurrent hydrogen production. A variety of alloys could exhibit such generic behavior albeit with different details. The requirements include pit susceptibility, a passive-to-active transition in a solution analogous to the pit solution, an OCP in the active deaerated state that is below the E_{H/H^+} and $x>x_{HER}$ at appropriate G. The relationship described can provide guidance for construction of model pits of a large enough scale to measure local potentials and C_H electrochemically identical to an actual crevice of micrometer scale. Such a real crevice would be too small for interrogation to obtain C_H values. The model pit results in Figures 10-15 show that H uptake can occur under conditions where the rescaled pit mouth is held in the passive range when $x>x_{crit}$. The local C_H values (with mm scale spatial resolution) increase to 7 times the value in an uncharged specimen exposed to humid air and the behavior versus x could not be predicted from global H measurements alone on planar specimens containing pits or crevices (Figure 15).

5. CONCLUSIONS

The effects of occluded site (e.g., pit or crevice) geometry and electrochemical conditions on local hydrogen production and uptake in a precipitation age-hardened Fe-13Cr-8Ni-2Mo-1Al stainless steel (PH 13-8 Mo) were explored. On planar electrode surfaces that did not contain

intentional occluded sites, the total hydrogen concentration was found to increase exponentially with increasingly negative true interfacial potential. This finding was shown to be consistent with electrochemical theory of hydrogen absorption using the coupled discharge-chemical recombination hydrogen evolution reaction mechanism. The effective hydrogen solubility at each hydrogen overpotential was greater in 0.1 M HCl solution compared to a simulated pit solution comprising of 5 M sulfuric acid plus dissolved metal ions. Anodic polarization and subsequent pitting created elevated hydrogen levels in the case of 0.1 M HCl solutions as the pit bottom was rationalize to fall below the reversible hydrogen potential. High levels of near-surface hydrogen uptake was observed under conditions where joint uptake and dissolution occurred.

Crevice scaling laws were used to rescale pits to sizes that enable spatially resolved quantification of local H concentrations as a function of both E_{app} and pit depth. Separate scaling relationships of the form x^2/G described the relation between the critical depth to achieve both passive-to-active potentials and $E_{H/H+}$ as a function of the gap (G) associated with the occluded site. Exposure of a PH stainless steel to a simulated pit chemistry confirms that H uptake occurs locally on anodically polarized planar electrodes whose surfaces are polarized in the passive range when containing an occluded site. Specifically uptake occurred at occluded site depths such that the condition $x > x_{HER}$ is met. Such occluded sites experience sufficient IR drop to shift local potentials below $E_{H/H+}$ even when external surfaces are polarized to passive potentials. The rescaling technique can be applied to study HEAC susceptibility versus applied potential for various occluded site geometries.

External anodic polarization resulted in hydrogen ingress which increased at depths in the occluded site where $x > x_{HER}$. In contrast, external cathodic polarization, such that the interfacial potential was more negative than $E_{H/H+}$ at the mouth of the occluded site, produced greater levels of hydrogen ingress at small values of x. These results suggest that electrochemically short cracks may experience a greater extent of hydrogen uptake when subjected to net cathodic polarization but that electrochemically long cracks would be more deleterious in the case of anodic polarization in situations where local hydrogen uptake at the occluded site is favored over bulk charging.
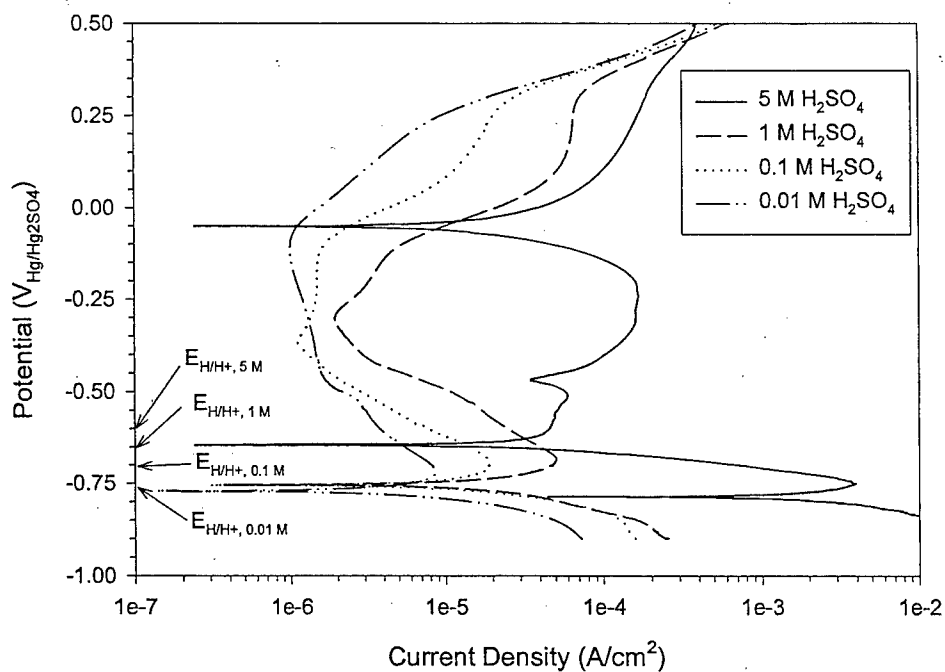
6. ACKNOWLEDGMENTS

LIST OF FIGURES

Figure 1. Anodic E-Log(i) data for PH 13-8 Mo stainless steel in the H1050 heat treated condition exposed to various deaerated sulfuric acid plus 0.1 M Fe^{+2}, 0.018 M Cr^{+3} and 0.01 M Ni^{+2} solutions at 25°C. Measurements taken versus a Hg/Hg_2SO_4 electrode.
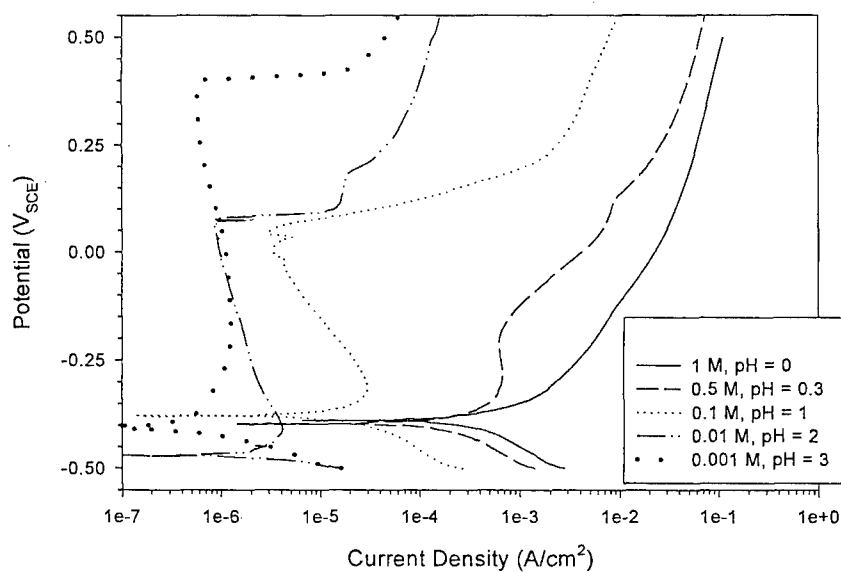
Figure 2. Anodic E-Log(i) data for PH 13-8 Mo stainless steel in the H1050 heat treated condition exposed to various deaerated hydrochloric acid solutions at 25 °C. Measurements taken versus a saturated calomel reference electrode.
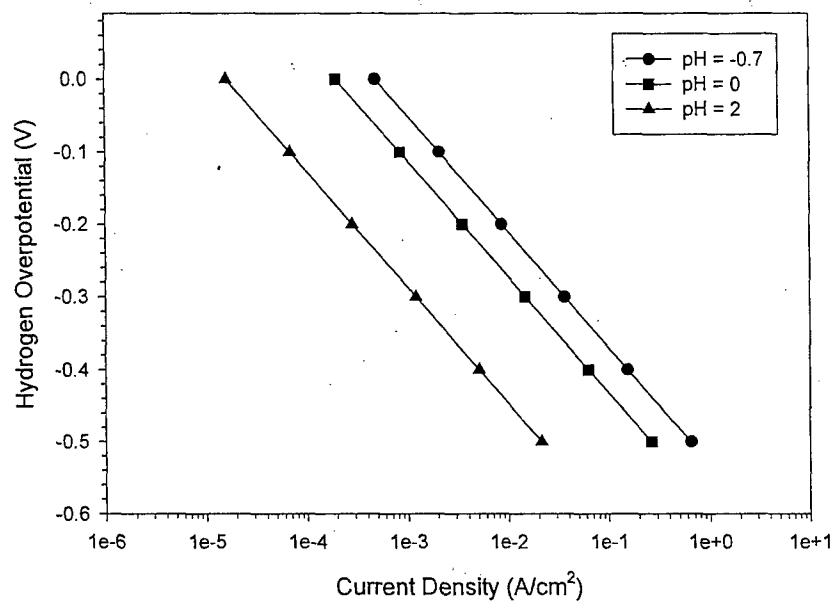
Figure 3. Calculated cathodic hydrogen overpotential versus true cathodic current density, i_{H2} ,(from relationship) for PH 13-8 Mo in the H1050 heat treated condition exposed to deaerated sulfuric acid plus 0.1 M Fe^{+2}, 0.018 M Cr^{+3} and 0.01 M Ni^{+2} solutions at 25 °C.

Figure 4. Hydrogen partial pressure versus time data from outgassing during programmed thermal desorption after exposure to various hydrogen charging overpotentials for PH 13-8 Mo in the H1050 heat treated condition. Samples charged for 1.5 days in 0.1M HCl. Temperature ramp rate is 3 °C/min.

Figure 5. $C_{H,tot}$ obtained from TDS and hydrogen charge densities versus interfacial potential for planar PH 13-8 Mo specimens in the H1050 heat treated condition after charging in deaerated 5 M H_2SO_4 plus dissolved metal ions at 25°C.

Figure 6. $C_{H,tot}$ obtained from TDS and hydrogen charge densities versus interfacial potential for planar PH 13-8 Mo specimens in the H1050 heat treated condition after charging in deaerated 0.1 M HCl at 25°C.

Figure 7. $C_{H,tot}$ obtained from TDS and hydrogen charge densities versus potential for planar PH 13-8 Mo specimens in the H1050 heat treated condition after charging in deaerated 0.1 M HCl at 25°C. Cathodic and anodic data are shown with C_H not normalized to local pit volume in case of data points A and B.

Figure 8. Local total H concentration from NRA versus perpendicular distance from sample surfaces for planar PH 13-8 Mo electrodes charged for 10 hours at OCP, -1.2 $V_{Hg/Hg2SO4}$, and -0.35 V $_{Hg/Hg2SO4}$ in deaerated 5 M H_2SO_4 plus dissolved metal salts at 25 °C. Measurement by nuclear reaction analysis.

Figure 9. Polarization data entered in CREVICERv2 program. Curved line represents actual polarization data from PH 13-8 Mo exposed to 0.1 M sulfuric acid solutions containing dissolved metal salts and adjusted so that i_{crit}, E_{pp}, and i_{pass} are representative of the 5 M sulfuric acid plus metal salts E-Log(i) data.. Straight-line segments represent linear fit of data entered into CREVICERv2.

Figure 10. Potential versus depth data using the Fig. 9 E-log(i) data for a square prism shaped crevice as determined by *CREVICERv2* for a square prism shaped crevice at the indicated square gap. Selected externally applied potential (E_{app}) was -0.475 $V_{Hg/Hg2SO4}$.

Figure 11. Potential versus depth data for various externally applied potentials at the mouth of a square prism shaped crevice as determined by *CREVICERv2* using the 0.1 M sulfuric acid plus dissolved metal ions E-Log(i) curve modified with the 5 M sulfuric acid plus dissolved metal ions E-Log(i) parameters. Gap size = 1000 μm. Solution conductivity = 0.46 mho/cm.

Figure 12. Current density versus depth modeling data for square prism shaped crevice showing (a) i_{anodic} and (b) the absolute value of $i_{cathodic}$. The externally applied potential, E_{app}, was -0.475 $V_{Hg/Hg2SO4}$.

Figure 13. Current density versus depth modeling data for square prism shaped crevice showing (a) i_{anodic} and (b) the absolute value of $i_{cathodic}$. The externally applied potential, E_{app}, was -0.475 $V_{Hg/Hg2SO4}$.

Figure 14. x_{crit2} versus gap data for PH 13-8 Mo. Two x_{crit} parameters are plotted for conditions: $i_{crit} = 10^{-2}$ A/cm^2, $E_{H/H+} = -0.59$ V Hg/Hg$_2$SO$_4$, $E_{pass} = -0.70$ V Hg/Hg$_2$SO$_4$, $E_{app} = -0.475$ V Hg/Hg$_2$SO$_4$.

Figure 15. Potential, C_H and pit diameter versus pit depth from a rescaled experimental pit for a 1500 μm diameter by 40 mm depth cylinder exposed to 5 M H$_2$SO$_4$ + dissolved metal ions. E_{app} = -0.60 V Hg/Hg$_2$SO$_4$

Figure 16. Model pit results for a 1500 um gap and 40 mm depth drilled cylinder in the upright position exposed to 5 M sulfuric acid plus dissolved metal ions. E_{app} = -1.2 $V_{Hg/Hg2SO4}$. $E_{H/H+}$ = -0.59 $V_{Hg/Hg2SO4}$. E_{pass} = -0.70 $V_{Hg/Hg2SO4}$. a) Measured potential, TDS measured C_H, and calculated C_H versus depth.

Figure 17. Normalized threshold stress intensity for hydrogen environment assisted crack initiation of pre-cracked precipitation age hardened martensitic stainless steels as a function of applied potential in 0.6 M NaCl solution. Data shown is for high strength (σ_{ys} = 1476 MPa) PH 13-8 (Fe-13Cr-8Ni-2Mo-1Al) [ref. 22], high strength (σ_{ys} =1220 MPa) PH 17-4 [ref. 17], and high strength (σ_{ys} = 1130 MPa) PH 17-7 (Fe-6%Ni-19%Cr-1%Al-03.%Cu)) [ref. 40].

Figure 1. Anodic E-Log(i) data for PH 13-8 Mo stainless steel in the H1050 heat treated condition exposed to various deaerated sulfuric acid plus 0.1 M Fe^{+2}, 0.018 M Cr^{+3} and 0.01 M Ni^{+2} solutions at 25°C. Measurements taken versus a Hg/Hg_2SO_4 electrode.
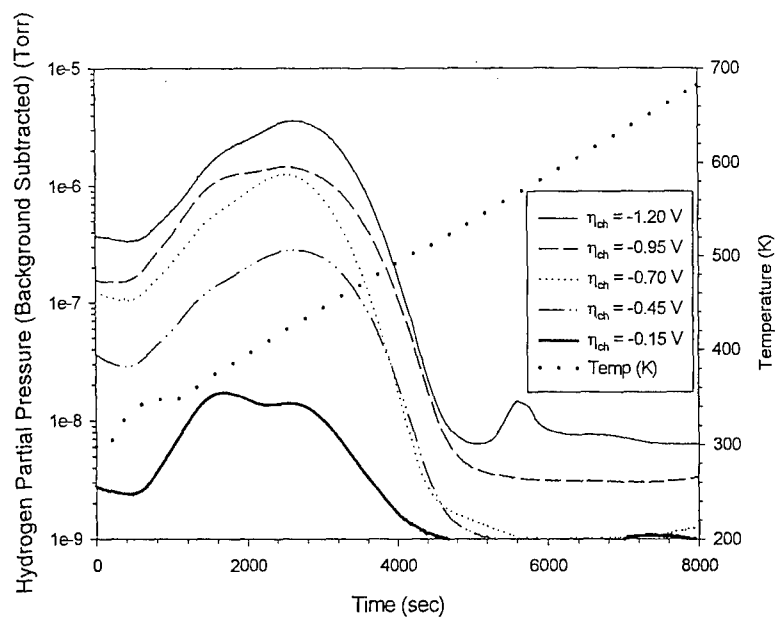
Figure 2. Anodic E-Log(i) data for PH 13-8 Mo stainless steel in the H1050 heat treated condition exposed to various deaerated hydrochloric acid solutions at 25 °C. Measurements taken versus a saturated calomel reference electrode.

Figure 3. Calculated cathodic hydrogen overpotential versus true cathodic current density, i_{H2}, (from relationship) for PH 13-8 Mo in the H1050 heat treated condition exposed to deaerated sulfuric acid plus 0.1 M Fe^{+2}, 0.018 M Cr^{+3} and 0.01 M Ni^{+2} solutions at 25 °C.

Figure 4. Hydrogen partial pressure versus time data from outgassing during programmed thermal desorption after exposure to various hydrogen charging overpotentials for PH 13-8 Mo in the H1050 heat treated condition. Samples charged for 1.5 days in 0.1M HCl. Temperature ramp rate is 3 °C/min.

Figure 5. $C_{H,tot}$ obtained from TDS and hydrogen charge densities versus interfacial potential for planar PH 13-8 Mo specimens in the H1050 heat treated condition after charging in deaerated 5 M H_2SO_4 plus dissolved metal ions at 25°C.

Figure 6. $C_{H,tot}$ obtained from TDS and hydrogen charge densities versus interfacial potential for planar PH 13-8 Mo specimens in the H1050 heat treated condition after charging in deaerated 0.1 M HCl at 25°C.

Figure 7. $C_{H,tot}$ obtained from TDS and hydrogen charge densities versus potential for planar PH 13-8 Mo specimens in the H1050 heat treated condition after charging in deaerated 0.1 M HCl at 25°C. Cathodic and anodic data are shown with C_H not normalized to local pit volume in case of data points A and B.

Figure 8. Local total H concentration from NRA versus perpendicular distance from sample surfaces for planar PH 13-8 Mo electrodes charged for 10 hours at OCP, -1.2 $V_{Hg/Hg2SO4}$, and -0.35 V $_{Hg/Hg2SO4}$ in deaerated 5 M H_2SO_4 plus dissolved metal salts at 25 °C. Measurement by nuclear reaction analysis.

Figure 9. Polarization data entered in CREVICERv2 program. Curved line represents actual polarization data from PH 13-8 Mo exposed to 0.1 M sulfuric acid solutions containing dissolved metal salts and adjusted so that i_{crit}, E_{pp}, and i_{pass} are representative of the 5 M sulfuric acid plus metal salts E-Log(i) data.. Straight-line segments represent linear fit of data entered into CREVICERv2.

Figure 10. Potential versus depth data using the Fig. 9 E-log(i) data for a square prism shaped crevice as determined by *CREVICERv2* for a square prism shaped crevice at the indicated square gap. Selected externally applied potential (E_{app}) was -0.475 $V_{Hg/Hg2SO4}$.

Figure 11. Potential versus depth data for various externally applied potentials at the mouth of a square prism shaped crevice as determined by *CREVICERv2* using the 0.1 M sulfuric acid plus dissolved metal ions E-Log(i) curve modified with the 5 M sulfuric acid plus dissolved metal ions E-Log(i) parameters. Gap size = 1000 μm. Solution conductivity = 0.46 mho/cm.

Figure 12. Current density versus depth modeling data for square prism shaped crevice showing (a) i_{anodic} and (b) the absolute value of $i_{cathodic}$. The externally applied potential, E_{app}, was -0.475 $V_{Hg/Hg2SO4}$.

Figure 13. Current density versus depth modeling data for square prism shaped crevice showing (a) i_{anodic} and (b) the absolute value of $i_{cathodic}$. The externally applied potential, E_{app}, was -0.475 $V_{Hg/Hg2SO4}$.

Figure 14. x_{crit2} versus gap data for PH 13-8 Mo. Two x_{crit} parameters are plotted for conditions: $i_{crit} = 10^{-2}$ A/cm^2, $E_{H/H+} = -0.59$ V Hg/Hg$_2$SO$_4$, $E_{pass} = -0.70$ V Hg/Hg$_2$SO$_4$, $E_{app} = -0.475$ V Hg/Hg$_2$SO$_4$.

Figure 15. Potential, C_H and pit diameter versus pit depth from a rescaled experimental pit for a 1500 μm diameter by 40 mm depth cylinder exposed to 5 M H_2SO_4 + dissolved metal ions. E_{app} = -0.60 V Hg/Hg_2SO_4

Figure 16. Model pit results for a 1500 um gap and 40 mm depth drilled cylinder in the upright position exposed to 5 M sulfuric acid plus dissolved metal ions. E_{app} = -1.2 $V_{Hg/Hg2SO4}$. $E_{H/H+}$ = -0.59 $V_{Hg/Hg2SO4}$. E_{pass} = -0.70 $V_{Hg/Hg2SO4}$. a) Measured potential, TDS measured C_H, and calculated C_H versus depth.

Figure 17. Normalized threshold stress intensity for hydrogen environment assisted crack initiation of pre-cracked precipitation age hardened martensitic stainless steels as a function of applied potential in 0.6 M NaCl solution. Data shown is for high strength (σ_{ys} = 1476 MPa) PH 13-8 (Fe-13Cr-8Ni-2Mo-1Al) [ref. 22], high strength (σ_{ys} =1220 MPa) PH 17-4 [ref. 17], and high strength (σ_{ys} = 1130 MPa) PH 17-7 (Fe-6%Ni-19%Cr-1%Al-03.%Cu)) [ref. 40].

7. REFERENCES

1. R.N. Parkins, *Materials Science and Engineering*, A103, p. 143, (1988).
2. G. Cragnolino, L.F. Lin, and Z. Szklarska-Smialowska, *Corrosion*, 37, 6, p. 312, (1981).
3. Y. Kondo, M. Bodai, M. Takei, Y. Sugita, and H. Inagaki, "Environmentally Assisted Cracking of 3.5NiCrMoV Low Alloy Steel Under Cyclic Straining," Effects of the Environment on the Initiation of Crack Growth: *ASTM STP 1298*, Philadelphia: ASTM, (1997).
4. C.F. Baes, Jr., R.E. Mesmer, The Hydrolysis of Metal Cations, Robert Krieger Publishing Co., Malabar FL, (1986).
5. H.W. Pickering, C. Wagner, *J. Electrochem. Soc.*, 114(7), pp. 698-706, (1967)
6. C.E. Birchenall, *J. Electrochem. Soc.*, 103, p. 618 (1956).
7. K. Muthukrishnan, K.R. Hebert, T. Makino, *J. Electrochem. Soc.*, 151(6), B340-B346 (2004).
8. G.A. Young, Jr., J.R. Scully, "The Effects of Test Temperature, Temper and Alloyed Copper on Hydrogen Controlled Crack Growth of an Al-Zn-Mg-(Cu) Alloy," *H-CDI Conference Proceedings*, Ed. N. Moody, A.W. Thompson, TMS, (2002).
9. B.P. Somerday, L.M. Youing, R.P. Gangloff, Fatigue and Fracture of Engr. Matl Struc., 23, pp. 39-58 (2000).
10. B.F. Brown, In "Stress Corrosion Cracking and Hydrogen Embrittlement of Iron Base Alloys, " Eds., J. Hockmann, J.E. Slater, R. W. Staehle, NACE-5, Houston, TX, pp. 747-750, (1977).
11. K. R. Cooper, R. G. Kelly, J. Chromtag. A 850, pp. 381-9, (1999).
12. H. Okada, In Stress Corrosion Cracking and Hydrogen Embrittlement of Iron Base Alloys, Eds., J. Hockmann J.E. Slater and R. W. Staehle, NACE-5, Houston, TX, pp. 747-750, (1977).
13. E.A. Taqi and R. A. Cottis. In Corrosion Chemistry Within Pits, Crevices and Cracks, National Physical Laboratory; Teddington, Middlesex; UK; 1-3 Oct. 1984. pp. 483-494 (1987).
14. A.M. Brass, J. Chene, A. Boutry-Forveille, Corrosion Sci., 38(4), pp. 569-585 (1996).
15. L.J. Qiao, J. L. Luo, X. Mao, Corrosion, 54(2), p115-120 (1998).
16. K.N. Akhurst and T.J. Baker, Metal and Matl. Trans A, 12A, pp. 1059-1070, (1981).
17. C.T. Fujii, In Stress Corrosion Cracking - New Approaches, ASTM STP 610, ASTM, Philadelphia, PA, pp. 213-225, (1976).
18. L.M. Young, M.R. Eggleston, H.D. Solomon, L.R. Kaisand, Mater. Sci. and Eng. J., A203, p. 377, (1995).
19. W.R. Cieslak, R.E. Semarge, F.S. Bovard, In Microbeam Analysis, editors: A.D. Romig, W.F. Chambers, pp. 303-306, (1986).
20. H.W. Pickering, In NACE 2001 Topical Research Symposium, CORROSION 2001, eds. G.S. Frankel, J.R. Scully, NACE, Houston, TX, (2001).
21. J.R. Scully, J.A. Van Den Avyle, M.J. Cieslak, A.D. Romig, Jr., C.R. Hills, Metall. and Mater. Trans. A, 22A, pp. 2429-2444, (1991).
22. P.S. Tyler, M. Levy, L. Raymond, Corrosion, 47, p. 82, (1991).
23. J.S. Lee, M.L. Reed, R.G. Kelly, J. Electrochem. Soc., 151(7), B423-B433 (2004).
24. S.W. Smith, Ph.D. Dissertation, The University of Virginia, (1995) and S.W. Smith, J.R. Scully, Metall. and Mat. Transactions A, 31A, pp. 179-193, (2000).

25. D. Li, R.P. Gangloff, J.R. Scully, Metall. and Mater. Trans. A, 22A, pp. 2429-2444, (2004).

26. R.G. Kelly, In NACE 2001 Topical Research Symposium, CORROSION 2001, eds. G.S. Frankel, J.R. Scully, NACE, Houston, TX, (2001).

27. Y. Xu and H.W. Pickering, J. Electrochem. Soc, 140, p. 658, (1993).

28. B.G. Ateya, H.W. Pickering, J. Electrochem. Soc., 122, p. 1025, (1975).

29. L.C. Feldman, J.W. Mayer, Fundamentals of Surface and Thin Film Analysis, North Holland, NY, p. 283, (1986).

30. Subramanyan, P.K., Comprehensive Treatise of Electrochemistry, Plenum Press, New York, 1981.

31. N.R. Quick, H.H. Johnson, Acta Met., 26 pp. 903-907, (1978).

32. Interrante, C.G., "Basic Aspects of the Problems of Hydrogen in Steels," *Current Solutions to Hydrogen Problems in Steels*, editors: C.G. Interrante and G.M. Pressouyre, ASM, Ohio, (1982).

33. C.R. Clayton, I. Olefjord, Passivity of Austenitic Stainless Steels, in Corrosion Mechanisms in Theory and Practice, ed. By P. Marcus, J. Oudar, pp. 175-199, (1995).

34. B.G. Ateya, G.Geh, A.H. Carim, H.W. Pickering, J. Electrochem. Soc., 149, pp. B27-33, (2002).

35. N. Lewis, S.A. Attanasio, D.S. Morton, G.A. Young, in "Chemistry and Electrochemistry of Corrosion and Stress Corrosion Cracking," Ed. R.H. Jones, TMS, pp. 421-445, (2001).

36. G.A. Young, Jr., J.R. Scully, "The Effects of Test Temperature, Temper and Alloyed Copper on Hydrogen Controlled Crack Growth of an Al-Zn-Mg-(Cu) Alloy," Metall. and Materials. Trans,

37. C.E. Buckley, H.K. Birnbaum, J. of Alloys and Compounds, 330-332, pp. 649-653 (2002).

38. C.E. Buckley, H.K. Birnbaum, J.S. Lin, S. Spooner, D. Bellmannn, P. Staron, T.J. Udovic, E. Hollar, J. of Applied Crystallography, 34, pp. 119-129, (2001).

39. C.S. Carter, D.G. Farwick, A.M. Ross, J.M. Uchida, Corros. J., 27, p.190, (1971).

40. G. Burnell, D. Hardie, R.N. Parkins, Br. Corros. J., p.229, Nov. (1987).

41. K. Cho, M.I. Abdulsalam, H.W. Pickering, J. Electrochem. Soc., 145, p. 1862, (1998).

42 J.N. Al-Khamis, H.W. Pickering, J. Electrochem. Soc., 148, pp. B314, (2001).

43. C.F. Barth, E.A. Steigerwald, and A.R. Troiano, Corrosion, 25, p. 353-358, (1969).

44. R.J. Gest, A.R. Troiano, Corrosion, 30, p. 274-279, (1974).

45. A. Sehgal, B.G. Ateya, H.W. Pickering, Acta Mater. 45, p. 3389 (1997).

Critical Issues in Hydrogen Assisted Cracking of Structural Alloys

Richard P. Gangloff

Critical Issues in Hydrogen Assisted Cracking of Structural Alloys

Richard P. Gangloff

Department of Materials Science and Engineering, University of Virginia, Charlottesville, VA 22903-2442, USA

Abstract

Both internal and hydrogen environment assisted cracking continue to seriously limit high performance structural alloys and confound quantitative component prognosis. While intergranular H cracking assisted by impurity segregation can be minimized, other mechanisms promote IG cracking and transgranular H cracking modes have emerged; new alloys suffer serious H cracking similar to old materials. Micromechanical models of crack tip H localization and damage by decohesion predict important trends in threshold and subcritical crack growth rate behaviour. H diffusion appears to limit rates of cracking for monotonic and cyclic loading; however, uncertain-adjustable parameters hinder model effectiveness. It is necessary to better define conditions within 0.1-5 μm of the crack tip, where dislocations and microstructure dominate continuum mechanics, and chemistry is localized. Nano-mechanics modeling and experimental results show very high levels of H accumulated in the crack tip fracture process zone, as necessary for interface decohesion. Contributing mechanisms include high crack tip stresses due to dislocation processes such as strain gradient plasticity, as well as powerful H production and trapping proximate to the electrochemically reacting crack tip surface. New sub-micrometer resolution probes of crack tip damage will better define features such as crack path crystallography (EBSD + Stereology) and surface morphology (high brightness, dual detector SEM), local H concentration (TDS and NRA), and validate crack tip mechanics modelling (micro-Laue x-ray diffraction and EBSD).

Keywords: (A) alloy, (B) modelling studies, (C) hydrogen embrittlement, (C) corrosion fatigue, (C) stress corrosion

1. Introduction

Both internal hydrogen assisted cracking (IHAC) and hydrogen environment assisted cracking (HEAC) limit the performance of most modern structural alloys, and confound prognosis of component safety, durability and capability. Figure 1 demonstrates that subcritical IHAC and HEAC occur at threshold stress intensity (K_{TH}) levels well below

plane strain fracture toughness, K_{IC}, for modern Ti alloys and ultra-high strength steels subjected to quasi-static loading. IHAC and HEAC occur at similarly low K_{TH} (shaded areas) and are governed by important variables of alloy composition and yield strength, heat treatment and microstructure, applied K level and application rate, temperature, and hydrogen concentration. IHAC and HEAC are severe in precipitation hardened Al and Ni alloys, and the damaging effect of atomic hydrogen (H) is exacerbated in most materials by cyclic loading.
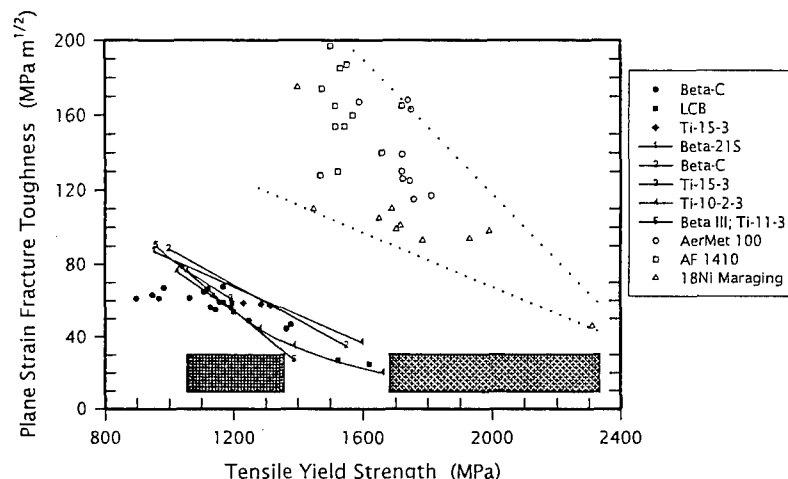
Figure 1. Yield strength dependence of K_{IC} for high strength α-precipitation hardened β-Ti alloys and ultra-high strength tempered martensitic alloy steels. Shaded areas represent lower bound K_{TH} regimes for IHAC and HEAC in these structural alloys.

In response a massive literature has developed; particularly a proceedings on hydrogen and stress corrosion cracking in iron alloys [1], the first International Conference on Environment-Induced Cracking of Metals [2], 6 conferences on hydrogen effects in metals [e.g., 3], a dedicated journal volume [4], and recent reviews of subcritical H-assisted crack growth under quasi-static loading [5] and fatigue deformation [6,7].

The objective of this review is to present recent results and suggest new approaches relevant to the persisting uncertainties that hinder: (a) understanding of hydrogen damage physics and the role of H in environment assisted cracking, (b) alloy development for H cracking control, and (c) mechanism-based models of material subcritical crack growth kinetics for use in component prognosis.

2. Hydrogen Damage Mechanisms

Two mechanistic issues dominated scientific discussion over the past several decades.

What is the basic mechanism for hydrogen damage leading to subcritical crack growth when brittle hydride does not precipitate?

Does the HEAC mechanism explain environment-assisted (stress corrosion) crack growth in high strength alloys stressed in moist environments?

Candidate damage mechanisms; Hydrogen Enhanced Bond Decohesion, Hydrogen Enhanced Localized Plasticity, and Adsorption Induced Dislocation Emission; are reviewed elsewhere [5,8-11]. Arguments supporting each are not definitive, but a consensus is emerging that H-reduced bond strength is the mechanism for cracking of Fe, Ti, Al and Ni alloys. This view is strong for interface cracking, while plasticity may play a role in slip band and crystallographic cracking. Decohesion is suggested by high magnification examination of intergranular surfaces (see Section 5), as well as modelling and experimental evidence of H enrichment in the crack tip fracture process zone (FPZ); Sections 4 and 5. Neither observations nor modeling establish a role for H-affected plasticity damage in complex microstructures. Slip about a crack tip has not been characterized to show H stimulated dislocation emission and crack extension. High strength alloys contain an array of finely spaced barriers to dislocations that should provide back-stress to stifle dislocation emission and act as preferred traps to strip H from dislocations. The argument that only dislocation-based processes explain rapid rates of subcritical crack growth is refuted by analysis of H diffusion about a crack tip (Section 4). Micromechanical modeling of K_{TH} and growth rate (da/dt) for subcritical IHAC and HEAC has focused on decohesion, while H-stimulated plasticity has not been incorporated into testable models of macroscopic cracking kinetics.

Controversy has centered on the extent to which H damage explains subcritical crack growth in alloys stressed in environments that support concurrent crack tip dissolution, passive film formation, and atomic hydrogen production. A consensus has emerged that H provides the dominant damage mechanism for high strength alloys stressed in moist environments [5]. A critical element of this conclusion is modeling and measurement to predict the amount of H produced on occluded crack surfaces. Figure 2 shows such a result, where K_{TH} declines systematically with increasing amount of H absorbed on the crack tip surface in precipitation hardened nickel based superalloys [12,13].[1] A single correlation describes cracking in H_2 and acidic chloride solution, and the crack path varied from transgranular (TG) slip-band based to intergranular (IG) with increasing H content for each environment. These results support HEAC. Additional support was provided by measurements and modeling that explained the effect of applied electrode potential on da/dt in aluminum alloys stressed in acidified chloride [14]. Increased da/dt, in response to anodic and cathodic polarization, correlated to increased crack uptake of H measured by thermal desorption spectroscopy. Crack electrochemistry, and the use of applied electrode potential as a probe of cracking mechanism, are detailed elsewhere [5,16].

Additional debate on these issues will undoubtedly occur at this meeting [9].

3. Alloy Development for H-Cracking Resistance

The question is: *Can metallurgical advances in high strength and fracture toughness be extended to develop structural alloys that resist H cracking?* Recent results show that this goal remains elusive. Intergranular H cracking is mitigated by reduced impurity segregation [10,17], but other grain boundary damage mechanisms exist, TG

---

[1] The calculation in Fig. 2 included H crack chemistry change for the acid, but not potential decrease from the boldly exposed surface to the crack tip; and included H trapping at microstructural sites, but not enhancement due to hydrostatic stress. These factors should not alter comparison between the gas and electrolyte environments, but affect absolute H content.

H cracking modes have emerged, and causal microscopic factors are not understood. As such, new alloys suffer severe H cracking similar to older materials; strength and toughness gains from decades of research are compromised by H cracking.
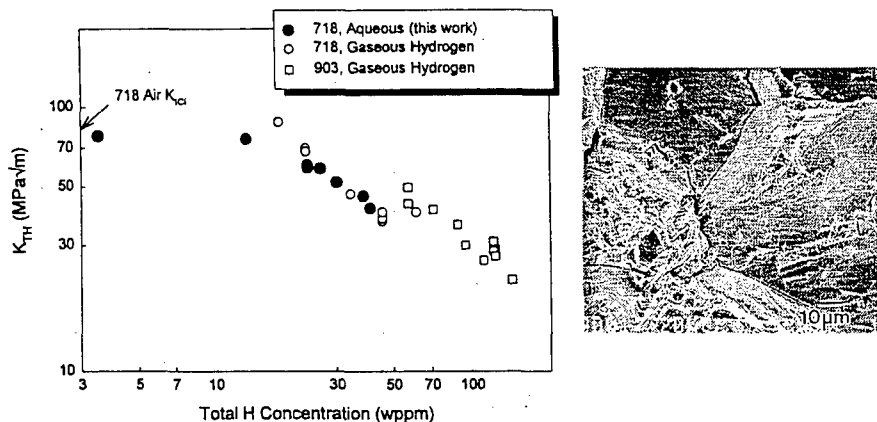

Figure 2. Threshold stress intensity for HEAC in peak aged IN718 and IN903, stressed in high pressure H_2 (9, O) or acidified chloride solution with cathodic polarization (•), vs. calculated H content produced at the crack tip. H-free superalloys cracked by microvoid processes at high K_{IC}, while HEAC in each environment produced mixed IG and TG slip-plane based cracking, as shown in the SEM fractograph (IN718 at K = 53 MPa√m) [12].

Severe HEAC and IHAC are produced in modern hcp-α precipitation hardened bcc β-Ti alloys, as shown in Figs. 3 [18,19] and 4 [20]. In each case H cracking depended on the rate of applied K (dK/dt) and required a critical amount of aging time and/or α precipitation. Experiments implicated grain boundary segregation for the IG HEAC in Fig. 3, rather than α precipitation [21]. However, no segregant was resolved by analytical electron microscopy and the fundamental cause of IG H cracking was not established. The TG IHAC in Fig. 4 is along α precipitate interfaces, formed in the Widmanstatten orientation on 4 variants of {111} in β. Hydrogen trapping at these interfaces likely explains this TG cracking and the aging dependence suggests a critical amount of α plate interface is required to form a connected path in β [20].

The IHAC in a modern tough and ultra-high strength steel (AerMet®100) is severe, Fig. 5, with K_{TH} as low as 10% of the H-free K_{IC} [22]. While dramatic at lower dK/dt, reduction in toughness persists to the highest loading rates studied (2000 MPa√m/s). This steel is not susceptible to IG H cracking, due to high purity that reduced elemental segregation to austenite grain boundaries [10,17]. Rather, cracking at low dK/dt is along interfaces in the lath martensite microstructure, while reduced toughness at higher loading rates correlates to microvoid-based cracking, with reduced void size due to predissolved H. Severe IHAC at the lower dK/dt was explained based on redistribution of H from a high density of low-binding energy trap sites at coherent M_2C carbides to martensite lath interfaces under high crack tip hydrostatic stresses [23]. As detailed in Section 5, this amount of trapped H can be estimated and model correlated to K_{TH} [23]. Metallurgical alteration to reduce M_2C coherence, and raise H-trap binding energy to
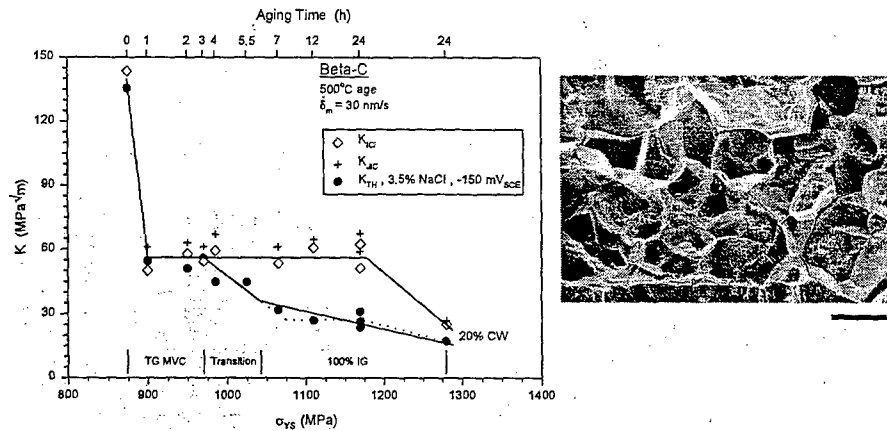
Figure 3. Strength and aging time dependencies of fracture toughness and K_{TH} for the onset of HEAC in solution treated Beta-C (Ti-3Al-8V-6Cr-4Mo-4Zr) stressed under slow-rising CMOD (δ_m) in moist air and aqueous-chloride solution at constant applied electrode potential of -150 mV$_{SCE}$ and 25°C. The highest strength and lowest cracking resistance were achieved by 20% cold work (CW) prior to aging. The SEM fractograph shows the morphology of 100% intergranular HEAC for the 6 to 24 h age cases (100 µm bar).
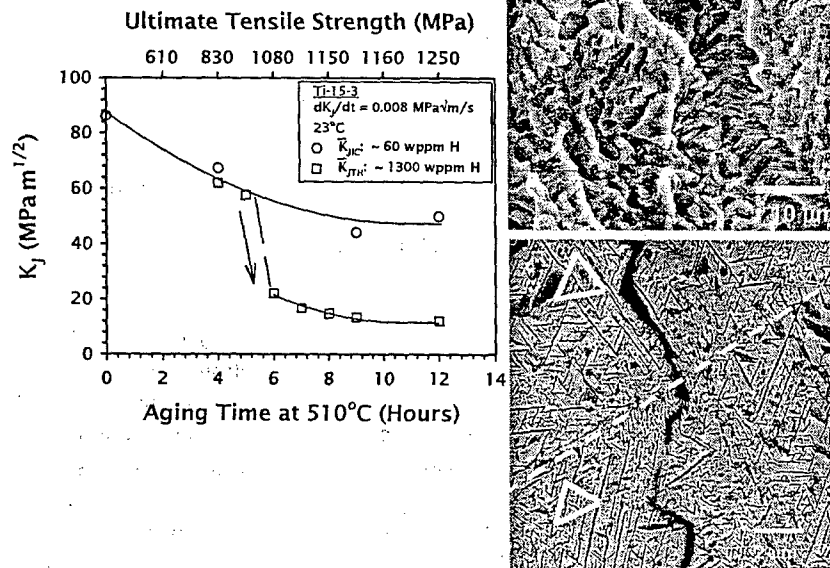
Figure 4. The aging time and yield strength dependencies of plane strain fracture toughness at the as-processed H content of 60 ppm and K_{TH} for IHAC in H-precharged (C_{H-TOT} = 1300 wppm) Ti-15V-3Al-3Sn stressed in moist air at 25°C. The SEM fractograph (top) shows TG IHAC for the 12 h age case and metallographic cross-section (Bottom) shows that H-cracking progresses along β/α interfaces, with the α needles (dark phase) present in three variants on {111} in β shown by the triangles on either side of a high angle grain boundary (dashed line). The subscript, J, denotes elastic K calculated from the elastic-plastic J-integral, and the bar indicates the average of 1st initiation and blunting-line offset definitions of crack growth [20].

retard crack tip H repartition, should reduce IHAC. This hypothesis has not been tested. This steel is susceptible to severe TG HEAC in chloride solution [5].
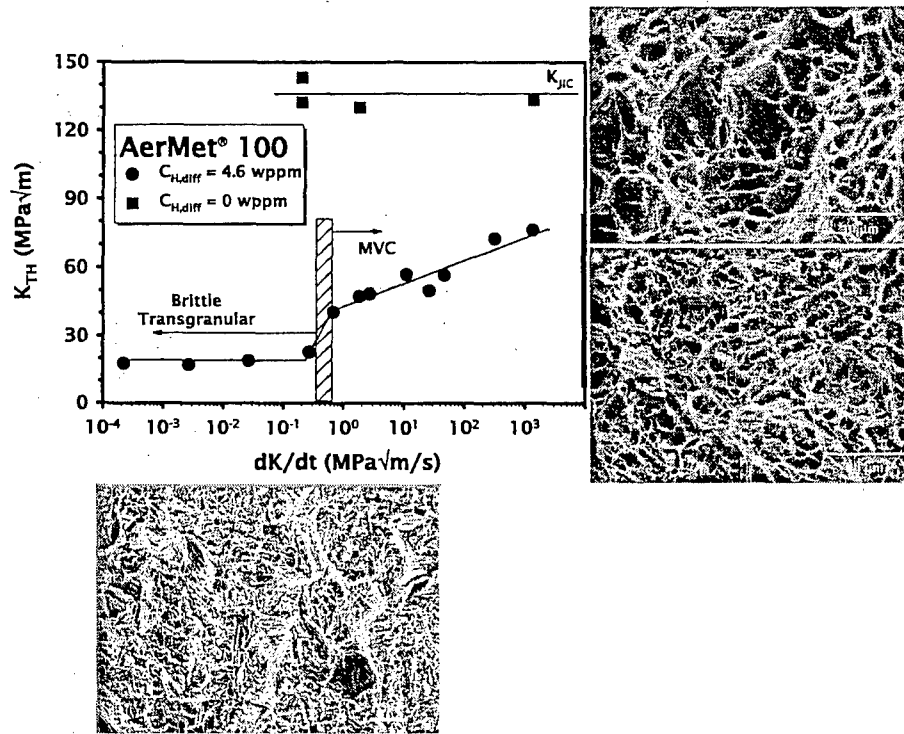

Figure 5. Rising CMOD K_{TH} vs. applied-initial dK/dt for AerMet$^®$100 steel precharged to a diffusible H content (C_{H-DIFF}) of 4.6 wppm. At dK/dt less than 0.3 MPa√ms, brittle-TG fracture occurs at K_{TH} < 20 MPa√m. At dK/dt greater than 0.7 MPa√m/s, fracture is by microvoid processes. The H-free K_{IC} of AerMet$^®$100 is ~135 MPa√m [22].

A modern α/β-Ti alloy and precipitation hardened 7000-series aluminum are susceptible to severe HEAC in H producing chloride solutions; Figs. 6 and 7 [24,25]. Both alloys were investigated for thermomechanical processing and aging developed for optimal yield strength and fracture toughness, not considering H cracking. The TG cracking in Ti-6-22-22 correlated with dislocation shearing of fine Ti_3Al (α_2) precipitates, analogous to the behavior of older α/β alloys [26,27]. The K_{TH} declined monotonically with increasing slip step height, as shown in Fig. 8 for the slip morphology in Fig. 6 [28]. Overaging for particle coarsening to block α_2 shearing and reduce HEAC was unsuccessful; 175 h aging at high temperature (593°C) produced severe slip band localization. Compositional modification can eliminate this phase, as known for decades, but novel metallurgical routes involving a second population of hard particles should be pursued to retain high strength.

While the beneficial effect of modest overaging in retarding IG HEAC in 7000-series aluminum alloys is well known and exploited in technology [29], Fig. 7, the
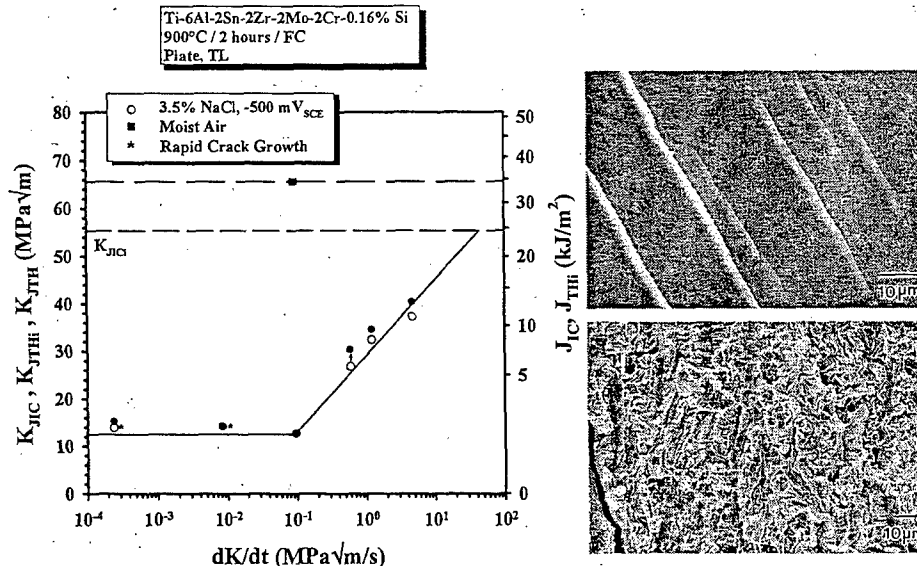
Figure 6. Loading rate dependence of K_{TH} for HEAC in Ti-6-22-22 plate stressed under rising K in aqueous NaCl solution. Cracking is TG as shown by the SEM image (lower right) and traced to highly localized planar slip from sheared Ti_3Al precipitates, as shown by the SEM image of a polished and deformed surface (top right) [24].

specific manifestation of aging that reduces H damage is not established [30]. Understanding is hindered because multiple microstructural variables change with aging time (e.g., boundary composition and precipitate size/spacing/composition, as well as intragranular precipitation, slip mode and PFZ characteristics). The causal factors are likely nano-scale and highly gradated in the vicinity of the crack tip along high angle grain boundaries, thus complicating structure and damage probes. The goal in this material class is to retain the strength of a peak aged microstructure and achieve immunity to HEAC. Better fundamental understanding of the aging effect is necessary.

4. Continuum Fracture Mechanics Modelling

The question is: *Can effective models of H-cracking kinetics be developed, based on fundamental decohesion or plasticity damage mechanisms, for use in next generation quantitative component life prediction and prognosis methods?*

The continuum fracture mechanics framework exists for macroscopic predictions of component subcritical crack growth in hydrogen service [31]. Major advances have been achieved in life prediction programs such as NASGRO (*http://www.nasgro.swri.org*), AFGROW (*http://afgrow.wpafb.af.mil*), and REACT (*http://www.srt-boulder.com*). For next generation prognosis, experimental cracking threshold and growth rate databases must be extended by models based on fundamental principles [32]. Micromechanical models of stress intensity thresholds and growth rates for IHAC and HEAC exist, but contain multiple-adjustable parameters due to persisting uncertainties, as reviewed in detail elsewhere [33-36].
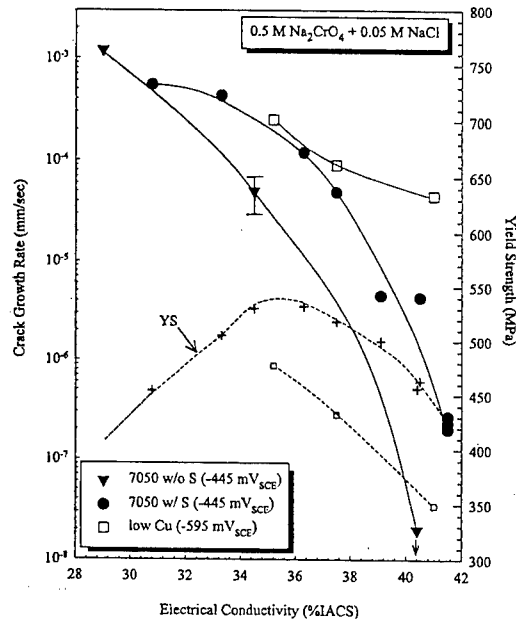
Figure 7. The effect of under age to overage (low to high conductivity) on HEAC da/dt at fixed CMOD and decreasing stress intensity (20 > K > 10 MPa√m) and electrochemical conditions for S-free (□) and S-bearing (●) AA7050, as well as low-Cu (□) AA7050. Yield strength is presented for S-bearing (+) AA7050 and low-Cu AA;7050 (□). The crack orientation is SL (stress parallel to the short transverse direction and crack growth in the rolling direction). The metallographic section shows IG cracking in the T6 temper (36% IACS) of AA7050 with S [25].
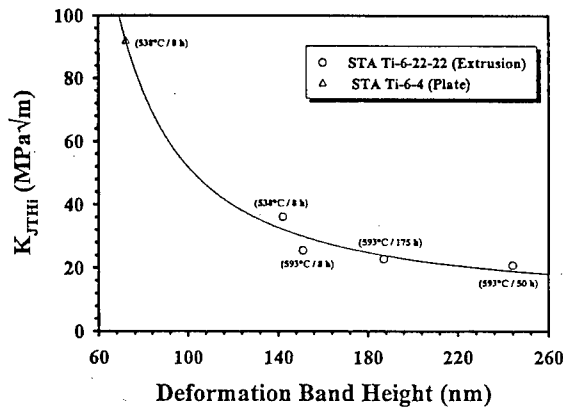

Figure 8. The effect of slip step height, from a polished-strained surface and varied by aging (temperature/time) to affect the size of Ti$_3$Al precipitates, on K$_{TH}$ for two α/β titanium alloys stressed under slow-rising K in NaCl solution; Fig. 6 [28].

Two recent examples are presented, based on the hypothesis that subcritical crack growth rate is limited by H diffusion from crack tip H uptake sites to a critical distance, χ_{CRIT}, within the FPZ where H damage forms. In a large body of literature, the K-independent Stage II crack growth rate, da/dt$_{II}$, is modeled as the ratio of χ_{CRIT} to the time for H diffusion over this distance to reach a critical level, C$_{CRIT}$, relative to a crack tip surface H content of C$_S$ [35]. Models are of varying complexity depending on whether the H-diffusion field is: (a) concentration and/or stress driven, (b) transient or

steady state, (c) ahead of a stationary or moving crack, (d) modeled in one or two dimensions, (e) emanating from environment-sensitive C_S, (f) microstructure-trap affected, (g) plastic strain-trap affected, and (h) coupled with a H-failure criterion. The results of this 1-dimensional modeling are of the form [35]:

$$\frac{da}{dt_{II}} = \frac{D_H}{\chi_{CRIT}}\left[\xi\left(\frac{C_s}{C_{CRIT}}, D_H, \chi_{CRIT}, \sigma_{YS}, t\right)\right] \tag{1}$$

where ξ is a function of the indicated variables and is 0.01-3.0 depending on the details in (a) through (h).

A large amount of experimental data on the relationship between da/dt_{II} and H-trap sensitive diffusivity, D_{H-eff}, is plotted in Fig. 9. Hydrogen diffusion control of HEAC is supported by the observed and predicted proportionality between da/dt_{II} and D_{H-eff}. The highest-reasonable value of ξ is 3 giving an χ_{CRIT} of 0.7 μm from the trend line in Fig. 9, independent of alloy. Smaller ξ result in smaller χ_{CRIT}. The results for gaseous-H producing environments are separate from those for electrolytes, as explained speculatively based on reduced D_{H-eff} due to vacancy trapping of H, where vacancies are produced at crack tip surfaces by dissolution during cathodic H production [35]. This trend suggests that the χ_{CRIT} is nm-scale, even for low da/dt_{II} situations. While this result suggests that H diffusion rate limits da/dt_{II} for a range of HEAC situations, uncertain-adjustable parameters limit model effectiveness.

Hydrogen diffusion from surface reaction sites to locations of damage in the crack tip FPZ was proposed to rate limit environment enhanced fatigue crack propagation by HEAC [36]. If H diffusion is rate limiting, rather than mass transport in the environment or crack surface (electro)chemical reaction [37], then a 1-dimensional model predicts that the fastest (or plateau) rate of HEAC (da/dN_{CRIT}) occurs for all cyclic loading frequencies (f) less than a critical value (f_{CRIT}) given by:

$$\frac{da}{dN_{CRIT}} = \Delta a^* f_{CRIT} = 2\sqrt{\frac{D_H}{f_{CRIT}}}erf^{-1}\left(1 - \frac{C_{CRIT}}{C_s}\right) \tag{2}$$

where the terms are as defined with regard to Eq. 1. In this model, a H-enhanced increment of crack growth occurs instantaneously at K_{MAX} in each fatigue cycle. Hydrogen production, diffusion, and discontinuous crack growth repeat between the present and next K_{MAX}, with the time between successive crack growth increments given by $1/f$. The maximum increment of crack growth, Δa^*, is determined by the location of maximum tensile stress ahead of the crack tip as controlled by K_{MAX}. In the plateau, loading time per cycle is sufficiently slow to enable H diffusion over the whole of Δa^*. Above f_{CRIT}, per-cycle time is insufficient to achieve C_{CRIT} over this distance and the amount of crack extension per cycle, or da/dN, is reduced. Extensive data for 7000-series alloys show that $da/dN_{CRIT} \propto 1/\sqrt{f}$, however, the values of D_{H-eff}, C_{CRIT} and C_S in Eq. 2 are uncertain and the model is not quantitatively predictive.

Hydrogen diffusion control of da/dN provides a unique description of HEAC for fatigue of aluminum alloys in pure water vapor and NaCl solution [36]. In Fig. 10, da/dN measured at a single stress intensity range, ΔK, is plotted as a function of an environmental exposure parameter. For fatigue in water vapor, this parameter is the
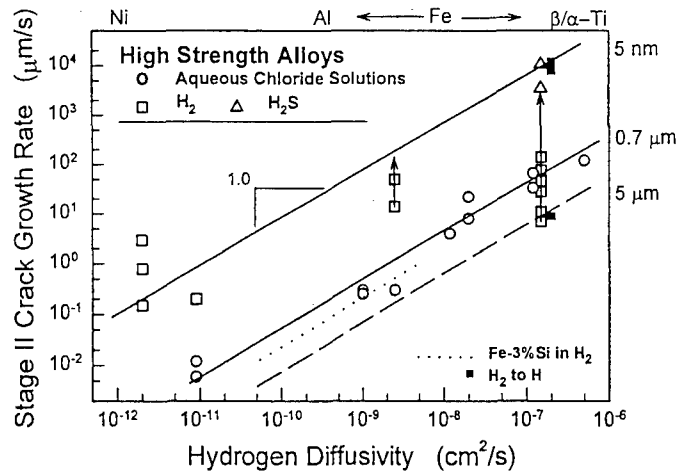
Figure 9. The dependence of da/dt$_{II}$ on trap sensitive D$_{H\text{-eff}}$ for high strength alloys that exhibit HEAC in gases and electrolytes at 25°C. High strength austenitic stainless steel and nickel superalloys were cracked in high pressure (100–200 MPa) H$_2$, while maraging and tempered-martensitic steels were cracked in low pressure (~100 kPa) H$_2$. The dotted line represents TG cracking of Fe-3%Si single crystal in 100 kPa H$_2$ at 0°C to 125°C. Filled symbols (□) represent the transition from molecular to atomic hydrogen gas [35].
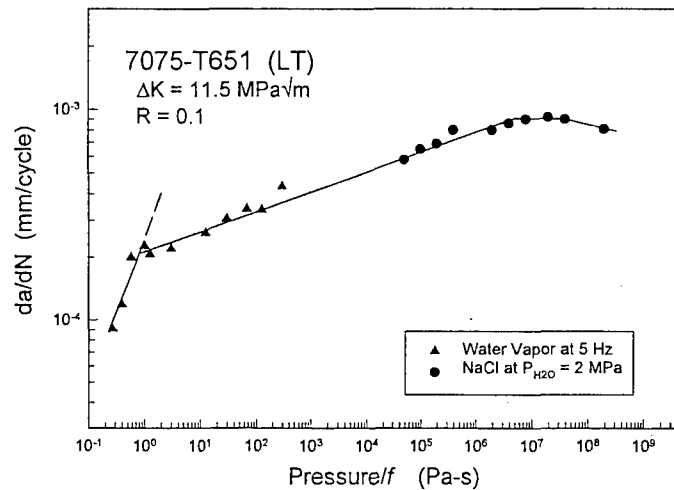

Figure 10. Fatigue crack growth rate for AA7075 in water vapor and NaCl solution *vs.* environmental exposure given by water vapor pressure/loading frequency. Results for NaCl (□) were positioned to provide a best fit with the water vapor data, assuming an effective H pressure of 2 MPa [36].

ratio of water vapor pressure to loading frequency [36,37]. The parameter for electrolytes is problematic due to uncertain crack H production. In Fig. 10, da/dN for NaCl are shifted along the exposure axis for a best fit with water vapor data using an

effective "pressure" of 2 MPa. This correlation suggests that da/dN is rate-limited by molecular transport at low P_{H2O}/f, surface reactions are rapid and produce increasing coverage of H through the oxidation of Al, and the da/dN vs exposure trend is represented by the steep-solid line [37]. The transition from this behavior is ascribed to da/dN limited by H diffusion in the FPZ [36]. A single line fits all data, suggesting that process zone H diffusion is rate-controlling for water vapor at intermediate to high pressures, as well as aqueous-chloride solution. The plateau at high environmental exposure is described by Eq. 2 and the subsequent falloff in da/dN is caused by corrosion-product induced crack closure promoted at very long per-cycle exposure times. While the correlation in Fig. 10 is interesting, a critical uncertainty remains; that is, the amount of H produced on crack tip surfaces during HEAC.

5. New Directions in Modelling and Measurement for H Cracking

The question is: *Can new solid mechanics and experimental developments be exploited to achieve breakthroughs in understanding and modeling hydrogen cracking?* Strong gradients in H concentration and stress about the crack tip govern crack growth in IHAC and HEAC, and challenge modeling and H-damage characterization necessary to develop next generation crack growth models and resistant alloys [5]. There is need for improved understanding of:

- Concentration of H absorbed on crack tip surfaces and dissolved in the crack tip FPZ, 0.05 to 5 μm ahead of the crack tip surface.

- Crack tip stresses within 0.05 to 5 μm of the crack tip, as affected by novel H-plasticity interaction and dislocation processes.

- High resolution determinations of crack morphology, crystallography, and FPZ hydrogen content.

- Effect of active monotonic and cyclic plastic strain on H cracking.

5.1 Crack Tip Hydrogen Enrichment

Hydrogen is enriched in the crack tip FPZ ($C_{H-FPZ\ trap}$) by 3 mechanisms: (a) crack surface accumulation at C_S by electrochemical processes, (b) high hydrostatic tension (σ_H) that dilates the lattice, and (c) segregation at trap sites with a binding energy, E_B. This enrichment is described approximately by:

$$\left(C_{H-FPZ\ trap}\right) = C_s \exp\left(\frac{E_B + \left(\sigma_H V_H\right)}{RT}\right) \tag{3}$$

where V_H is the partial molar volume of H in the host lattice [5]. Trap sites are typically interfaces and boundaries that constitute a connected path for brittle H-cracking. High values of C_S, σ_H and E_B promote H enrichment to exacerbate IHAC and HEAC. Emerging results support the notion that very high levels of crack tip H are accumulated, as likely necessary for the decohesion mechanism to be reasonable [38].

5.1.1 Stress and H Trapping Enrichment

The presence of very large stresses in the sub-micron crack tip FPZ is a requisite for hydrogen embrittlement, as recognized qualitatively by Oriani [38]. The reason is the need to raise low lattice and trapped concentrations of H at crack nucleation sites to justify lowering cohesive strength of the lattice or interface. It is critical to define the stress distribution about the H-affected crack tip, with emphasis on the mechanics over a sub-micrometer length scale. Classic continuum fracture mechanics formulations of blunt-crack tip stress and plastic strain distributions, J_2 in Fig. 11, predict that opening direction tensile (σ_{YY}) and hydrostatic stresses are (3-5)σ_{YS} dependent on alloy work hardening. These descriptions are inadequate for the next generation of material-behavior model building [39]. It is necessary to refine such predictions within 0.1 - 10 μm of the crack tip surface, considering dissolved H and for the length scale where dislocations and microstructure dominate continuum mechanics. Guidance is provided by important studies of H-free cleavage fracture in the presence of plastic deformation.

Each of several approaches show that stresses are larger than the blunted crack solution, using dislocation distributions that alter the near tip field. For an atomistically sharp IG crack tip, Thompson and then Kameda [40] invoked a dislocation-free zone between the crack tip and dislocation pile-up; σ_{YY} in this zone equaled (4-7)σ_{YS} at applied K typical of hydrogen cracking thresholds and joined the HRR field at the outer edge. Gerberich and coworkers modeled interaction of a distribution of dislocations that dominate very-near tip stresses and a superdislocation (removed from the tip) that defines global crack tip plasticity with work hardening [34,41]. The near-tip dislocations produce a constant sliding stress along the dislocation pile-up, canceling the crack tip singularity and producing a stress field with $\sigma_H \sim$ (30-50)σ_{YS}, maximized 20 nm ahead of a sharp crack tip [42]. Lipkin et al. note that if the rate of strain hardening exceeds the divergence of the stress field, material can no longer deform plastically. This is guaranteed by a large strain gradient that requires geometrically necessary dislocations (GND)and increased hardening [43]. The size of the resulting elastic core is determined by stress continuity with the HRR field. Calculations with material properties used for the J_2 curve in Fig. 11 place the size of the elastic core at ~250 nm (or 0.25l), and predict significant stress elevation over the J_2 results.
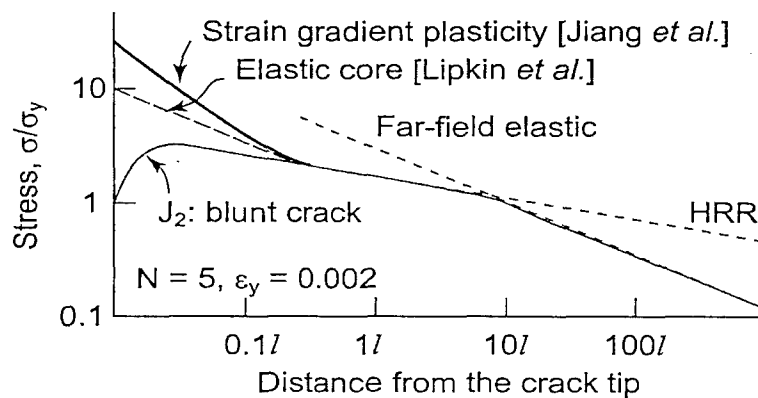

Figure 11. Crack tip stress distributions from various modeling approaches and normalized to a material-based length, l, that is of order 1 μm [44]. (σ_Y is flow stress, ~σ_{YS}, and σ is σ_{YY}.)

The GND concept provides a related explanation for enhanced crack tip stresses [45,46]. A finite density of GND accommodate a large strain gradient, implying that strain hardening is exacerbated at a crack tip where a gradient is implicit and broad-scale plasticity from blunting is limited. Hydrogen cracking at low K provides such a situation. An intrinsic material length scale controls the contribution of a strain gradient to Taylor-based strain hardening. This length scale is a phenomenological constant that relates to microstructure [46], or is connected analytically to specific dislocation interactions [47]. The curve in Fig. 11 depicts the σ_{YY} distribution derived from incorporating strain gradient terms into the material hardening description [47]. The length scale of the stress elevation is controlled by the material length scale, l; this parameter was inferred to be 0.5-5 μm from micro-indentation and wire torsion experiments applied to model single phase metals [46]. For comparison with dislocation-based models, it is convenient to assume $l = 1$ μm in Fig. 11. For this case, it is clear that the strain gradient is large enough to significantly alter the HRR field over ~ 300 nm. The location of the maximum stress in a gradient-affected fracture is not clear, since only asymptotically sharp cracks have been modeled.

Discrete dislocation dynamics simulations support these explicit treatments of near tip dislocations and enhanced hardening due to a strain gradient [48]. The near-tip fields resulting from simulation reveal many of the characteristics obtained via continuum models that invoke a priori assumptions of dislocation behavior: (i) crack tip openings remain sharp, (ii) near tip stresses are significantly higher than those predicted by plasticity models without reference to microstructure, (iii) a dislocation free zone can arise near the crack tip, and (iv) crack tip shielding is a function of the density of dislocation nucleation sources. Quantitative comparison of maximum stresses at the crack tip with the models in Fig. 11 is not feasible due to the inclusion of a cohesive zone fracture element at finite critical stress.

A recent investigation of IHAC in ultra-high strength AerMet®100 steel demonstrates the role of crack tip stress in promoting H accumulation and embrittlement. The cracking threshold data in Fig. 5 were determined for a constant diffusible H content ($C_{H\text{-diff}}$) of 4.6 wppm [22]. The low-dK/dt K_{TH} level decreased monotonically with rising $C_{H\text{-diff}}$ from 0.5 to 8 wppm. Cracking was along martensite lath-interface microstructure, as illustrated in Fig. 5. The explanation for the cause of this severe IHAC is provided by the comparison in Fig. 12. Hydrogen repartitions from a lower binding energy trap state, in this case nano-scale M_2C with a coherent interface and E_B ~12 kJ/mol, to the crack tip and martensitic interfaces when the stress-interaction energy ($\sigma_H V_H$) > E_B for the source trap. The calculation in Fig. 12 (left) shows that this happens for AerMet®100 (σ_{YS} = 1760 MPa) when the ratio of σ_H/σ_{YS} > 3.0. The probability that this repartition of H occurs rises as the difference between E_B and $\sigma_H V_H$ increases, demonstrating that IHAC is exacerbated by increased crack tip stresses. For example, the probability that H repartitions from M_2C interfaces to lattice sites acted on by σ_H is 0.22 when σ_H is $2.5\sigma_{YS}$, 0.92 when σ_H is $5.0\sigma_{YS}$ and 0.998 when σ_H is $8.0\sigma_{YS}$, each for an M_2C binding energy of E_B = 12 kJ/mol [23,49,50].

The combined effects of interface trapping and hydrostatic stress on enhancing the concentration of H in the FPZ are dramatic. For a martensite lath boundary, E_B is 40 kJ/mol and $\sigma_H V_H$ is 9–30 kJ/mol for σ_H ~ 4-15 GPa. From Eq. 3, the $C_{H\text{-}FPZ\ trap}$ is 6×10^6 C_l. The lattice solubility (C_l) of H in AerMet®100 is unknown, but is 3×10^{-4} wppm for pure Fe exposed to 100 kPa H_2 at 298K [23]. This environment produces a hydrogen
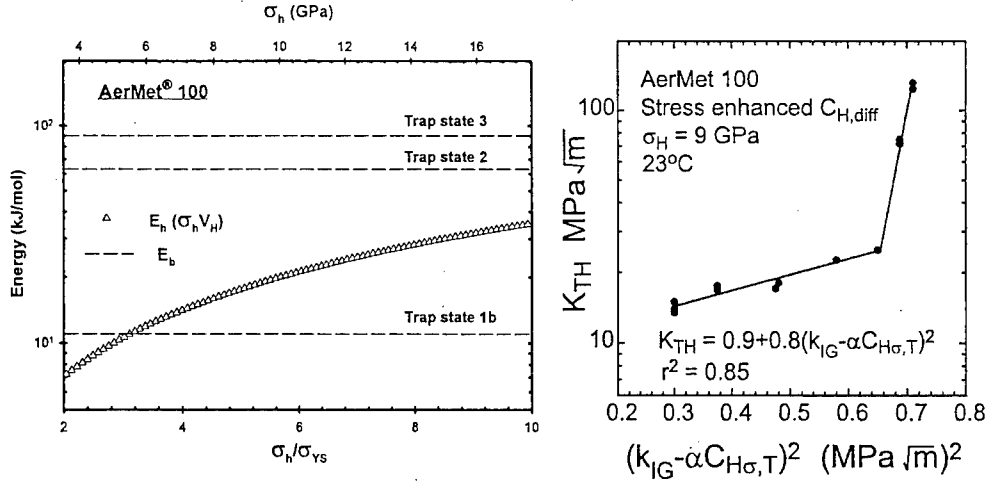
Figure 12. Left: The interaction energy $E_H = \sigma_h V_H$ vs. hydrostatic stress ahead of the crack tip compared with E_B for major trap states in aged ultra-high strength alloy steel [23]. Right: Measured and modeled effects of trapping + stress enhanced H concentration $C_{H\sigma,T}$ (or $C_{H\text{-Diff trap}}$ in Eq. 3) on the threshold for IHAC. $K_{TH} < 30$ MPa√m relates to brittle, transgranular cracking, while fracture at higher K_{TH} involved some microvoid fracture [22]. σ_h in this plot is denoted as σ_H in the text.

fugacity equivalent to electrochemical charging at $\eta_{chg} = 0.0$ V and hence equals the lattice solubility for Fe precharged in $Ca(OH)_2$ at zero overpotential [22]. Using this estimate of C_l, $C_{H\text{-}FPZ\,trap}$ is on the order of 1600 wppm (9 atom pct) at 23°C. The effect of increasing H concentration in reducing the threshold for IHAC is predicted by coupling this trap and stress enhanced crack tip H content with a cracking model first developed to predict the temperature dependence of the macroscopic fracture toughness for cleavage, then extended to predict the yield strength, temperature and H concentration dependencies of K_{TH} [33]. Crack tip fracture is governed by the intrinsic Griffith toughness, k_{IG}, for cleavage fracture without H ($G_C \sim \gamma_S \sim k_{IG}{}^2/E$), where E is elastic modulus and γ_S is the energy required to produce unit crack surface. The local toughness is assumed to be reduced by H, yielding a Griffith-type threshold stress intensity for hydrogen embrittlement, k_{IH}, that equals ($k_{IG} - \alpha\, C_{H\text{-Diff trap}}$) where α is a coefficient and $C_{H\text{-Diff trap}}$ is enhanced according to Eq. 3. Local k_{IG} and k_{IH} were connected to macroscopic K_{IC} and K_{TH} using the super dislocation model of the crack tip discussed in conjunction with Fig. 11. The model predicts:

$$K_{TH} = \frac{1}{\beta'_{IHE}} \exp\left[\frac{\left(k_{IG} - \alpha C_{H-FPZ\,trap}\right)^2}{\alpha'' \sigma_Y} \right] \qquad (4)$$

The parameters β'_{IHE} and α'' are constants determined by computer simulation of the dislocation structure about the crack tip. Comparison of theory and experiment is shown in Fig. 12 (right) [23]. Two parameters reported for Fe-Si ($k_{IG} = 0.85$ MPa√m and $\alpha = 0.5$ MPa√m/atom fraction H [33]) were used to calculate the concentration term in Eq. 4 and plotted in Fig. 12. The fit to these IHAC data yielded values of β'_{IHE}

(0.13 *vs.* 0.2 (MPa√m)$^{-1}$) and α'' (3x10^{-4} *vs.* 2x10^{-4} MPa·m) essentially equal to those that fit measured K$_{TH}$ *vs.* H$_2$ pressure and temperature for HEAC of a high strength steel [33]. These results suggest that modern formulations of high crack tip stresses are reasonable and necessary for next generation models of hydrogen embrittlement. Substantial crack tip H enhancement is supported quantitatively. There are, however, uncertainties in the details of such formulations, as well as in the additional amount of H produced by novel crack tip electrochemical reactions for HEAC compared to the more well defined total-dissolved H operative in IHAC.

5.1.2 *Electrochemical Production of Crack Surface H*

During HEAC, H may enrich by electrochemical and chemical reactions on crack tip surfaces. Experimental evidence is limited owing to the strong gradient of H penetration into the fracture process zone, localized over a 0.1-1 μm length scale as inferred from diffusion modeling discussed in Section 4. Several studies using secondary ion mass and quadrupole mass spectroscopies showed H uptake during stressed environmental exposure of Ni and Al alloys [51-53], however, these studies lacked spatial resolution and were not designed to measure crack tip H concentration.

Recent results demonstrate substantial H uptake and a new path to probe crack tip H enrichment. Thermal desorption spectroscopy (TDS) measurements of trapped H were performed on thinned specimens (~1 mm thick) machined inward from the wake surface of an HEAC crack in the aluminum alloy represented in Fig. 7. The measured amounts of H correlated with da/dt$_{II}$ that depended on applied electrode potential and aging variables [14,30]. Levels of TDS-measured H were unexpectedly high since the FPZ is of order 0.1% of TDS specimen thickness and dilution should reduce H concentration to below TDS resolution. The obvious explanation is that H was enriched intensely in immediate proximity to the crack surface. This speculation was proved by Nuclear Reaction Analysis (NRA) applied to aluminum alloy specimens frozen in liquid nitrogen immediately after removal from stressed exposure in acidified-chloride solution at 23°C [14] or water vapor saturated air at 50-90°C [54]. In each environment, a high concentration of H was localized within 1 μm of the crack wake surface. A typical NRA measurement is presented in Fig. 13 [14], showing high H enrichment (~0.5 atom pct H) within 1 μm of the crack surface for the chloride solution case with 3 separate specimens and crack wake locations. Similar measurements were obtained for specimens cracked in hot water vapor, with up to 50 atom pct H, and experiments, confirmed that such H enrichment was not an artifact of the NRA method [54]. The H profiles in Fig. 13 are only reasonable if H diffuses slowly in aluminum, with D$_{H-eff}$ ~ 10^{-13} to 10^{-14} cm^2/s, several orders of magnitude less than reported [54]. This behavior is consistent with H trapping at vacancies injected into the crack wake lattice during metal oxidation [55-57]. Intense H enrichment in a micrometer sized crack tip volume, and the role of vacancies, are consistent with the results of the diffusion analysis discussed in conjunction with Fig. 9.

5.2 *High Resolution Probes of Crack Tip Hydrogen Damage*

New nano and micro-scale characterization methods must be applied to understand mechanisms of IHAC and HEAC. Fracture surface observation by scanning electron microscopy (SEM) has been used for decades to distinguish features suggestive of decohesion and plasticity damage [5,8,9]. For example, the presence of small voids on
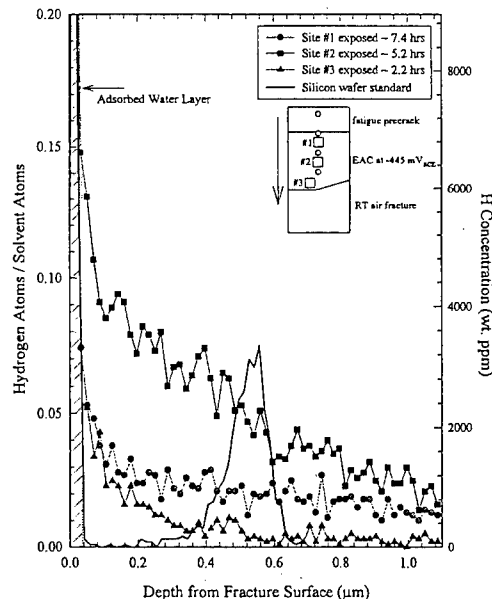
Figure 13. Nuclear reaction analysis of crack surface H accumulated during HEAC of 7075-T651 stressed quasi-statically in aqueous chloride solution at 23°C. Specimens were sectioned after testing, at 3 locations behind the crack tip and stored chilled. The solid line without data points measures H implanted precisely in a Si standard for calibration [14].

intergranular facets from HEAC suggests a strong role of H-enhanced plasticity and strain localization, but results are controversial. The argument that small-shallow voids are only resolved by careful transmission electron microscopy of shadowed replicas viewed at high tilt was reasonable [58], but modern SEM methods provide a means to test this concept. An example is summarized in Fig. 14, where an IG facet from HEAC in α hardened β-Ti (see Fig. 3) was examined with a high brightness electron source, multiple detectors to change surface topography, high magnification, and matching surface stereographic analysis [21,59]. Shallow microvoids as small as 0.02-0.04 μm in diameter should be resolved with this method; however, there was no evidence of an organized surface structure indicative of such voids. Rather, the features were undulations with occasional matching ridges and protrusion-cavity pairs, consistent with decohesion of β-Ti grain boundaries impacted by α precipitates in the underlying microstructure. Such a facet morphology does not prove decohesion, but provides evidence of the lack of structure manifest from H-sensitive slip band localization or microvoid formation during HEAC.

As a second example, transgranular cracking is prevalent in HEAC of aluminum alloys subjected to cyclic loading, and the crystallographic characteristics of fatigue crack surface features have important mechanistic implications [6,7]. Cracking is often along facet surfaces that are possibly parallel to {111} slip planes for inert environment plasticity driven damage, but shift to a {100} or {110} orientation when cyclic deformation occurs in the presence of crack tip H production from environmental reaction. It is important to characterize these features with sub-micrometer spatial

resolution to understand and model the physics of H damage. Ro reviewed methods employed to characterize crack facet surface crystallographic orientation [60]. He concluded that a combined Electron Back Scattered Diffraction (EBSD) analysis of grain orientation and stereological determination of vectors normal to facet surfaces in each oriented grain, provides the optimal approach to this problem [61]. This method is well suited to examine crack features in fine-grain size microstructures typical of commercial alloys. The method probes a large area of cracking, and sample preparation and alignment are relatively simple in comparison with other techniques. Modern scanning electron microscopes provide automated orientation determination by EBSD. The small probe size, combined with high resolution, provide the capability to analyze small elements of complex fatigue crack surfaces.

An example result from this method is presented in Fig. 15 for an Al-Li-Cu alloy stressed cyclically in ultra-high vacuum or two environments that produce H at the crack tip leading to fatigue by HEAC [60]. The SEM image (top) shows the fatigue crack surface morphology for water vapor and the intersecting metallographically
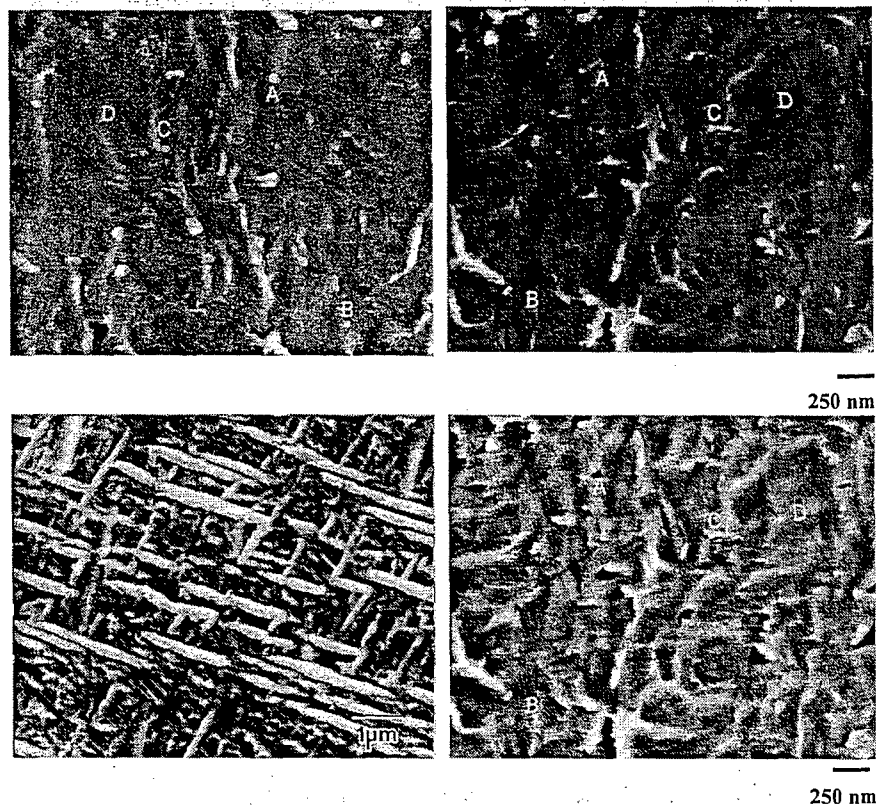

Figure 14. Matching field emission SEM images of an IG facet in α-hardened β-Ti cracked in aqueous NaCl following the conditions illustrated in Fig. 3. These high magnification images were formed with the signal accumulated from: (top left and right) the secondary electron detector immediately above the specimen, and (bottom right) dual secondary electron detectors and signal averaging. These top left-right two images were obtained from the matching-opposite areas of the fracture surface. Features A, B, and C are matching protrusion/cavity pairs; D shows subtle undulations on the fracture surface. The underlying microstructure is shown in the SEM back-scattered SEM image (bottom left) [21,59].

prepared plane with EBSD imaging of grain orientation. The stereographic triangles summarize the relationship between measured normals to crack facets and the orientation of the underlying grain structure. For vacuum, fatigue crack facets are essentially parallel to {111} slip planes, as expected given that this alloy is prone to slip band formation caused by shearable Al_3Li strengthening precipitates [61]. For fatigue in moist environments, the crack facet appearance is dramatically different from vacuum; the typical morphology is shown by the SEM fractograph. These facets were not predominantly parallel to low index planes, as simply hypothesized based on H-enhanced cleavage-like cracking for fatigue loading [7,61]. Rather, crack facets assume all orientations between {100} and {110}. This result was first reported for a different Al-Li-Cu-Zr alloy, based on manually determined and lower resolution EBSD/stereology [61].
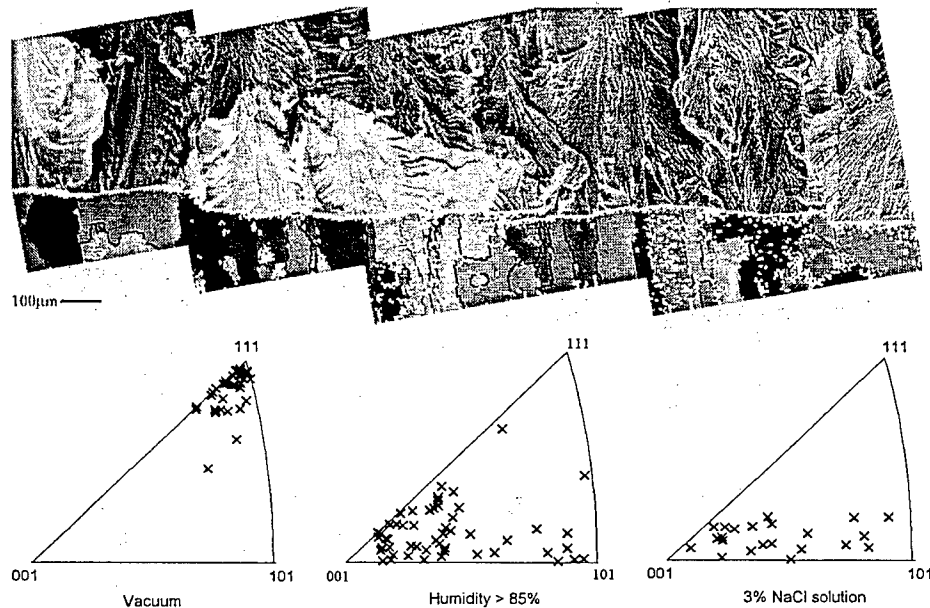

Figure 15. Crystallographic orientations of fatigue crack surface facets, determined by combined EBSD and stereological analyses, for an Al-2.5Cu-1.6Li-0.6Zn-0.08Zr alloy stressed cyclically in ultra-high vacuum and two environments that produce crack tip surface H that enhances fatigue crack propagation. The SEM fractograph and intersecting metallographic section, with superimposed orientation imaging map, are shown in the top image for fatigue cracking in moist air [60].

There are two mechanistic implications from the results in Fig. 15. For an alloy prone to slip band cracking in vacuum, H produces a sharp transition from slip based damage. If H-affected plasticity is critical to fatigue, then {111}-based cracking should be exacerbated, not eliminated. Second, facets observed for the moist environments assumed a wide range of possible orientations, but always consistent with planes subjected to high levels of crack tip normal and hydrostatic stresses [60]. This is consistent with decohesion, but the irrational character of crack facets suggests that the

physics of the H effect is not simple lattice cleavage. A working hypothesis is that cyclic plastic deformation evolves a dislocation cell structure that traps H and provides a path of connected damage for cracking that is not always crystallographic [60]. This notion has not been probed experimentally. Transmission electron microscope examination of a crack wake thin foil prepared by focused ion beam machining is a new technique that should be used to establish such mechanisms of H cracking [62].

It is critical to use new experimental methods to calibrate and validate crack tip stress and strain distributions (Section 5.1.1), with emphasis on the strong gradients over 0.05-10 μm. Geometrically necessary dislocations change lattice orientation and may be detected by diffraction-based techniques. EBSD was applied to investigate local plasticity associated with cracking [63] and this technique should be exploited. Micro-Laue diffraction using focused synchrotron x-rays probes a material in 3 dimensions with spatial resolution of ~0.5 x 0.5 x 1.0 μm [64]. For aluminum, the maximum probe depth is ~75 μm. Work is ongoing to measure fatigue crack tip plasticity in aluminum alloys cracked in ultra-high vacuum or moist N_2 [65]. The experiment involves depth resolved synchrotron line scans perpendicular to the cracking direction and on a polished surface. Figure 16 shows how crack wake plasticity is manifest in a micro-Laue diffraction pattern. Undeformed material away from the crack produces sharp-intense spots (left image), while the region near the crack exhibits asterism (right image) characteristic of plasticity. Such results are connected with non-local plasticity models and the notion that geometrically necessary dislocations are responsible for hardening [66]. This extra dislocation content can be assessed and its impact on local flow stress predicted for use in crack tip mechanics models. This method is suitable to investigate the effects of dissolved H, grain microstructure/anisotropy, and ΔK level on crack tip plasticity. A specific issue being studied is differences in GND content for crack growth in vacuum compared to moist N_2 that produces substantial H dissolved in the zone about the crack tip.
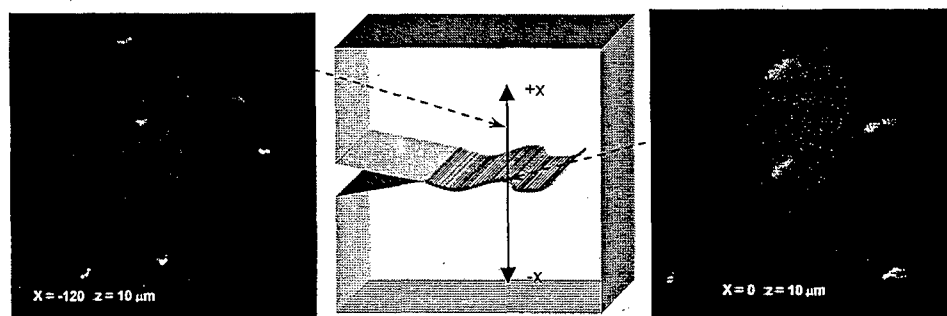

Figure 16. Micro-Laue diffraction patterns, obtained adjacent to (x = 0 μm, right image) and below (x = -120 μm, left image) the crack plane under (z = 10 μm) the surface, for a vacuum fatigue crack in a specimen of the Al-Li alloy represented in Fig. 15 [65].

5.3 Effect of Active Strain Rate on Hydrogen Embrittlement

It is well known that IHAC and HEAC are promoted by loading formats that produce active crack tip strain rates in excess of the level from quasi-static loading and slow

crack growth, with the effect particularly significant in lower strength alloys [5]. Considering HEAC, crack tip strain rate is a dominant factor for alloys that form a crack tip passive film concurrent with H production [19,24,28]. In this case H production and uptake are promoted if crack tip strain rate is sufficient to repeatedly fracture the passive film, perhaps at sites where active slip bands intersect the reacting crack tip surface [67]. Based on this mechanism, the rising-CMOD (crack mouth opening displacement) test provides an effective method to characterize alloy resistance to HEAC and can promote cracking that is not otherwise caused by quasi-static K loading [5]; typical results are shown in Figs. 3 and 6.

The effect of crack tip strain rate is strong for IHAC of low to moderate strength steels, as illustrated in Fig. 17 for a bainitic Cr-Mo steel, precharged with H by exposure to high temperature and pressure H_2 then loaded in moist air at 23°C [68,69]. The threshold stress intensity for crack arrest at fixed CMOD (and decreasing K) increases dramatically with declining steel yield strength for a constant-dissolved H content. This is well known behavior [5]. In sharp contrast, the threshold K for the onset of subcritical H cracking under rising CMOD (and rising K) is constant or declines mildly with decreasing σ_{YS}. Since crack tip strain rate depends much more strongly on dK/dt than da/dt [19], Fig. 17 suggests that IHAC is exacerbated greatly by higher crack tip strain rate but only for the lower strength regime.
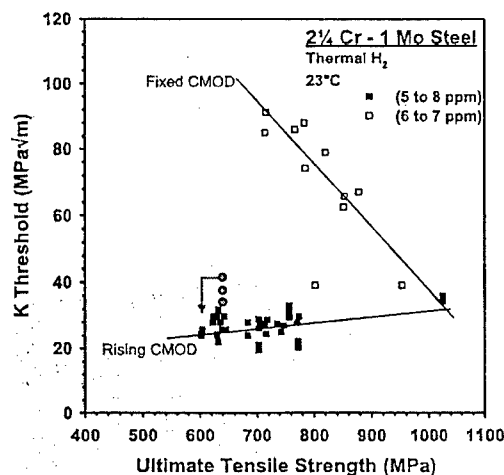

Figure 17. The effect of loading format, including fixed CMOD crack arrest (open) and rising CMOD causing crack growth initiation (filled), on IHAC of a tempered bainitic alloy steel containing H precharged from either bulk-H_2 exposure at elevated temperature (9, □) or active electrochemical charging on a slot surface remote from the crack tip (♦) [68-70].

The mechanism for the effect of crack tip strain rate on IHAC is not well defined. A first step is to demonstrate that this response is not an artifact of H loss from the precharged specimen and during the long testing time typical of crack arrest at fixed CMOD. A new method was developed to eliminate H loss using the slotted and fatigue precracked compact tension specimen shown in Fig. 18. Hydrogen is precharged from electrochemical reactions limited to the slot surfaces, before loading and continuously during rising CMOD loading, to provide a fixed H flux incoming to the crack tip without crack tip electrolyte exposure and complicating HEAC. The necessary elastic-plastic J integral, elastic stress intensity, and elastic compliance solutions, as well as 3-dimensional H diffusion modeling by finite elements, were developed to analyze the threshold and kinetics of IHAC in the slotted specimen [70]. Severe H cracking was

produced with this method applied to temper embrittled Cr-Mo weld metal, as indicated by (♦) in Fig. 17 [70]. The threshold is substantially lower than K_{IC} for this steel (~120 MPa√m), but somewhat higher than the standard specimen results in Fig. 17 because the high H content produced by H_2 exposure at elevated temperature (5-8 wppm) was not achieved by electrochemical charging that yielded 3 wppm H at best [70].

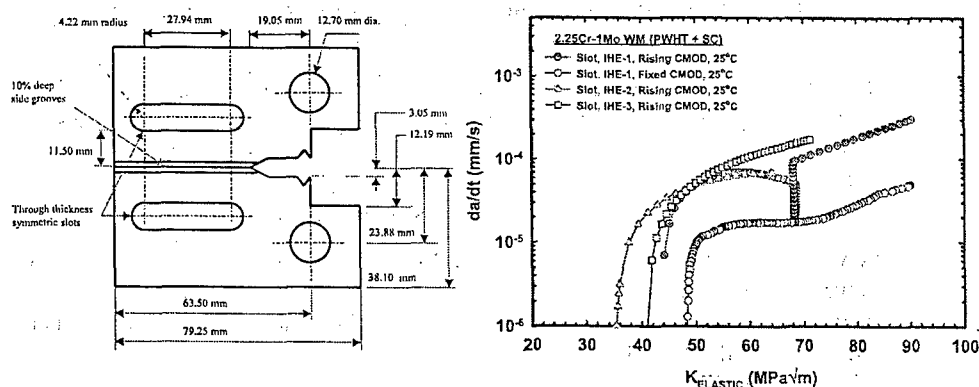The slotted specimen test method showed that applied CMOD exacerbated H

Figure 18. Left: The slot-modified compact tension specimen. Right: Crack growth rate *vs.* applied K for Cr-Mo steel weld metal loaded in moist air at 23°C, concurrent with H charging from a sulfuric acid-thiosulfate electrolyte and cathodic polarization in contact with the slot surfaces but isolated from the crack tip [70].

cracking. If loading was stopped after IHAC initiated, crack growth rate immediately declined. This behavior is shown in Fig. 18 where 3 replicate da/dt *vs.* K results for rising CMOD exceed the growth rates measured for fixed CMOD. For the former, K rises with subcritical crack growth, but K falls for the fixed CMOD crack arrest condition. Where CMOD was fixed during rising CMOD, crack growth slowed to the quasi-static fixed CMOD result. A single da/dt *vs.* K relationship was not observed for these different loading formats, attesting to the effect of crack tip strain rate for constant H flux to the crack tip. Additional experiments showed that da/dt is directly proportional to dK/dt, and furthermore, this severe IHAC is eliminated as test temperature increased above 50°C [70]. This temperature effect is well known for H cracking in high strength alloys [5], but this is the first demonstration of such behavior where H loss from bulk precharging is precluded.

The crack tip damage mechanism for the IHAC behavior indicated in Figs. 17 and 18 most likely involves interaction of H trapping and plasticity. The finite element calculated amount of H, delivered to the crack tip FPZ from H_2 or slot charging and including the enriching effects of microstructural trapping and crack tip hydrostatic stress (Eq. 3), correlates the effects of bulk H level and temperature on threshold [70].

6.0 Conclusions

❑ Modern strong-tough alloys suffer severe H cracking, similar to older materials and limiting structural applications. Transgranular cracking modes are

particularly important, but precise microstructural causes are not understood sufficiently to enable H-cracking resistant alloy development.

❑ H-cracking limits alloy performance for both monotonic and cyclic loading, and similar crack tip damage mechanism and modeling approaches are valid.

❑ Micromechanical models of crack tip conditions predict important trends in threshold and subcritical crack growth rate behaviour for IHAC and HEAC. H diffusion appears to rate limit da/dt and da/dN for monotonic and cyclic loading, however, uncertain-adjustable parameters limit model effectiveness.

❑ Nano-mechanics modeling and experimental results show high levels of H accumulated in the crack tip fracture process zone, as necessary for decohesion. Contributing mechanisms include high crack tip stresses due to localized dislocation-based processes such as gradient plasticity, as well as powerful H production and trapping proximate to electrochemically reacting crack surfaces.

❑ New sub-micrometer resolution probes of crack tip damage will better define features such as crack path crystallography (EBSD + Stereology) and surface morphology (high brightness, dual detector SEM), local H concentration (TDS and NRA), and will validate crack tip mechanics modelling (micro-Laue x-ray diffraction and EBSD).

❑ Active crack tip strain rate exacerbates H-cracking, particularly in low to moderate strength alloys. A new method shows that IHAC is governed by intrinsic H-plasticity interaction rather than H loss during loading.

7.0 Acknowledgements

8.0 References

[1] R.W. Staehle, et al. (Eds.) Stress Corrosion Cracking and Hydrogen Embrittlement of Iron Base Alloys, NACE, Houston, TX, 1977.

[2] R.P. Gangloff and M.B. Ives (Eds.) Environment Induced Cracking of Metals, NACE, Houston, TX, 1990.

[3] N.R. Moody et al. (Eds.) Hydrogen Effects on Material Behavior and Corrosion Deformation Interactions, Minerals, Metals & Materials Society, Warrendale, PA, 2003.

[4] P. Sofronis (Ed.) Engr. Frac. Mech. 68, 2001.

[5] R.P. Gangloff, in: I. Milne, R.O. Ritchie and B. Karihaloo (Eds.) Comprehensive Structural Integrity, Vol. 6, Elsevier Science, New York, NY, 2003, pp. 31-101.

[6] R.P. Gangloff, in: R.P. Gangloff and M.B. Ives (Eds.) Environment Induced Cracking of Metals, NACE, Houston, TX, 1990, pp. 55-109.

[7] R.P. Gangloff, in: Fatigue 02, Anders Blom (Ed.) Engineering Materials Advisory Services, West Midlands, UK, 2002, 3401-3433.

[8] S.P. Lynch, in: N.R. Moody et al. (Eds.) Hydrogen Effects on Material Behavior and Corrosion Deformation Interactions, Minerals, Metals & Materials Society, Warrendale, PA, 2003, 449-466.

[9] H.K. Birnbaum, I.M. Robertson, P. Sofronis and D. Teter, in: T. Magnin (Ed.) 2nd International Conference on Corrosion-Deformation Interactions, Institute of Materials, London, UK, 1997, pp. 172-195.

[10] C.J. McMahon, Jr., Engr. Frac. Mech. 68 (2001) 773-788.

[11] R.A. Oriani, in: R.P. Gangloff and M.B. Ives (Eds.) Environment Induced Cracking of Metals, NACE, Houston, TX, 1990, 439-448.

[12] J.A. Lillard, Environment Assisted Cracking of a Nickel-Based Superalloy in Hydrogen-Producing Solutions, PhD Dissertation, University of Virginia, Charlottesville, VA, 1998.

[13] N.R. Moody, M.W. Perra and S.L. Robinson, Scripta Metall. 22 (1988) 1261-1266.

[14] K.R. Cooper, L.M. Young, R.P. Gangloff, and R.G. Kelly, Matls. Sci. For. 331-337 (2000) 1625-1634.

[15] A. Turnbull, Corrosion, 57 (2001) 175-189.

[16] S.P. Lynch, in: This proceedings, 2004.

[17] G.B. Olson, Advanced Matls. Proc. July (1997) 72-79.

[18] B.P. Somerday and R.P. Gangloff, Matls. Sci. Engr. A254 (1998) 166-178.

[19] B.P. Somerday, L.M. Young and R.P. Gangloff, Fatg. Fract. Engr. Matls. Struct. 23 (2000) 39-58.

[20] S.P. Hayes, Internal Hydrogen Embrittlement of High Strength Beta-Alpha Titanium Alloys, PhD Dissertation, University of Virginia, Charlottesville, VA, 2000.

[21] B.P. Somerday, A.W. Wilson, J.M. Howe, and R.P. Gangloff, Microstructural Cause of Intergranular Hydrogen Environment Embrittlement of Aged Beta-titanium Alloys. Unpublished research, University of Virginia, Charlottesville, VA, 2004.

[22] R.L.S. Thomas, J.R. Scully and R.P. Gangloff, Metall. Mater. Trans., A 34A (2003) 327-344.

[23] D. Li, R.P. Gangloff, and J.R. Scully, Metall. Mater. Trans., A 35A (2004) 849-864.

[24] E. Richey, III and R.P. Gangloff, in R.D. Kane (Ed.) Environmentally Assisted Cracking, STP 1401, ASTM International, West Conshohocken, PA, 2000, 104-127.

[25] L.M. Young and R.P. Gangloff, in: M. Tiryakioglu (Ed.) Advances in the Metallurgy of Aluminum Alloys, ASM International, Materials Park, OH, 2001, 135-140.

[26] M.F Blackburn and J.C. Williams, Trans. ASM 62 (1969) 398-409.

[27] H.G. Nelson, in: I.M. Bernstein and A.W. Thompson (Eds.) Hydrogen in Metals, ASM International, Materials Park, OH, 1974, 445-464.

[28] E. Richey, III, Microstructure and Strain Rate Effects on the Environment Assisted Cracking of α/β-Ti Alloys in Aqueous Chloride, PhD Dissertation, University of Virginia, Charlottesville, VA, 2000.

[29] N.J.H. Holroyd, in: R.P. Gangloff and M.B. Ives (Eds.) Environment-Induced Cracking of Metals, NACE, Houston, TX, 1990, 311-345.

[30] L.M. Young, Microstructural Dependence of Aqueous-Environment Assisted Crack Growth and Hydrogen Uptake in AA7050, PhD Dissertation, University of Virginia, Charlottesville, VA, 1999.

[31] J.M. Barsom and S.T. Rolfe, Fracture and Fatigue Control in Structures, 2nd Ed., Prentice-Hall, Englewood Cliffs, NJ, 1987.

[32] R.P. Wei and D.G. Harlow, in: This proceedings, 2004.

[33] W.W. Gerberich, P.G. Marsh and J.W. Hoehn, in: A.W. Thompson and N.R. Moody (Eds.) Hydrogen Effects in Materials, Minerals, Metals & Materials Society, Warrendale, PA, 1996, 539-553.

[34] Y. Katz, N. Tymiak and W.W. Gerberich, Engr. Frac. Mech. 68 (2001) 619-646.

[35] R.P. Gangloff, in: N.R. Moody et al. (Eds.) Hydrogen Effects on Material Behavior and Corrosion Deformation Interactions, Minerals, Metals & Materials Society, Warrendale, PA, 2003, 477-497.

[36] Z. Gasem and R.P. Gangloff, in: R.H. Jones (Ed.) Chemistry and Electrochemistry of Corrosion and Stress Corrosion Cracking, Minerals, Metals & Materials Society, Warrendale, PA, 2001, 501-521.

[37] R.P. Wei and R.P. Gangloff, in: R.P. Wei and R.P. Gangloff (Eds.) Fracture Mechanics: Perspectives and Directions, STP 1020, ASTM International, West Conshohocken, PA, 1989, 233-264.

[38] R.A. Oriani, Annual Reviews in Materials Science, 8 (1978) 327-357.

[39] R.P. Gangloff, Matls. Sci. Engr. A103 (1988) 157-166.

[40] J. Kameda, Acta Metall., 34 (1986) 867-882.

[41] W.W. Gerberich, R.A. Oriani, M.J. Lii, X. Chen, and T. Foecke, Phil. Mag. A 63 (1991) 363-376.

[42] X. Chen and W.W. Gerberich, Metall. Trans. A 22A (1991) 59-70.

[43] D.M. Lipkin, D.L. Clarke, and B. Beltz, Acta Mater., 44 (1996) 4051-4058.

[44] M.R. Begley, S.R. Agnew, U. Komaragiri, and R.P. Gangloff, "Hydrogen Damage in the Crack Tip Environment", in: A. Carpinteri et al. (Eds.) Proceedings, International Congress on Fracture-11, Elsevier Science, Oxford, UK, (2004).

[45] A. Needleman and J.G. Sevillano, Scripta Mater, 48 (2003) 109-111.

[46] N.A. Fleck and J.W. Hutchinson, in: J.W. Hutchinson and T.Y. Wu (Eds.) Advances in Applied Mechanics, Vol. 33, Academic Press, NY, 1992, 295-361.

[47] H. Jiang, Y. Huang, Z. Zhuang and K.C. Hwang, J. Mech. Phys. Solids., 49 (2001) 979-993.

[48] H.M.M. Cleveringa, E. Van der Giessen, and A. Needleman, J. Mech. Phys. Solids 48 (2000) 1133-1157.

[49] T.Y. Zhang and J.E. Hack, Metall. Mater. Trans. A 30A (1999) 155-159.

[50] T.Y. Zhang, H. Sheu, and J.E. Hack, Scripta Metall. Mater 27 (1992) 1605-1610.

[51] J. Okahana, S. Kuramoto and M. Kanno, in: N.R. Moody et al. (Eds.) Hydrogen Effects on Material Behavior and Corrosion Deformation Interactions, Minerals, Metals & Materials Society, Warrendale, PA, 2003, 909-917.

[52] P. Rozenak, E. Siros, I.M. Robertson, and H.K. Birnbaum, Isr. J. Technol. 24 (1988) 183-189.

[53] B. Ladna and H.K. Birnbaum, Acta Metall. 35 (1987) 2537-2542.

[54] G.A. Young and J.R. Scully, in: N.R. Moody et al. (Eds.) Hydrogen Effects on Material Behavior and Corrosion Deformation Interactions, Minerals, Metals & Materials Society, Warrendale, PA, 2003, 893-907.

[55] C.E. Buckley and H.K. Birnbaum, Physica B 241-243 (1997) 344-346.

[56] H.K. Birnbaum, C. Buckley, F. Zeides, E. Sirois, P. Rozenak, S. Spooner, and J.S. Lin, J. Alloys and Compounds 253-254 (1997) 260-264.

[57] R.B. McLellan and D. Zang, Acta Mater. 49 (2001) 377-387.

[58] S.P. Lynch, in: P.R. Swann, F.P. Ford, and A.R.C. Westwood (Eds.) Mechanisms of Environment Sensitive Fracture of Materials, Metals Society, London, UK, 1977, 201-212.

[59] B.P. Somerday, Metallurgical and Crack-Tip Mechanics Effects on Environment-Assisted Cracking of Beta-Titanium Alloys in Aqueous Chloride, PhD Dissertation, University of Virginia, Charlottesville, VA, 1998.

[60] Yunjo Ro, Fatigue Crack Surface Crystallography of Precipitation Hardened Aluminum Alloys, MS Thesis, University of Virginia, Charlottesville, VA, 2004.

[61] D.C. Slavik and R.P. Gangloff, Acta Metall. Mater. 44 (1996) 3515-3534.

[62] S.M. Kazanjian, Fatigue Deformation in Beta Titanium Ti-15V-3Al-3Sn-3Cr, Ph.D. Dissertation, University of Virginia, Charlottesville, VA, 2004.

[63] L.N. Brewer, M.A. Othon, L.M. Young, and T.M. Angeliu, Microscopy and Microanalysis 8 (2002) 684CD ~ 685CD.

[64] B.C. Larson, W. Yang, G.E. Ice, J.D. Budai, and J.Z. Tischler, Nature. 415 (2002) 887-890

[65] S.R. Agnew, Y.J. Ro, M.R. Begley, and R.P. Gangloff, "Fatigue Crack Tip Damage-Based Models in Structural Prognosis", in: A. Carpinteri et al. (Eds.) Proceedings, International Congress on Fracture-11, Elsevier Science, Oxford, UK, 2004.

[66] C.S. Hartley, TMS Lett. 1 (2004) 11-12.

[67] D.G. Kolman and J.R. Scully, Phil. Mag. A 79 (1999) 2313-2338.

[68] R.P. Gangloff, in: M. Levy and S. Isserow (Eds.) Corrosion Prevention and Control, US Army Laboratory Command, Watertown, MA, 1986, 64-111.

[69] R.P. Gangloff, B.P. Somerday and D.L. Cooke, in: P.L. Andresen and R.N. Parkins (Eds.) Life Prediction of Structures Subject to Environmental Degradation, NACE, Houston, TX, 1996, 161-175.

[70] A.M. Al-Rumaih, Measurement and Modeling of Temperature Dependent Hydrogen Embrittlement of Cr-Mo Steel to Enable Fitness-for-Service Modeling, PhD Dissertation, University of Virginia, Charlottesville, VA, 2004.

Strategies for Mitigation of Hydrogen Environment Assisted Cracking of High Strength Steels

John R. Scully, Beth A. Kehler, Yongwon Lee and Richard P. Gangloff

STRATEGIES FOR MITIGATION OF HYDROGEN ENVIRONMENT ASSISTED CRACKING OF HIGH STRENGTH STEELS

ABSTRACT

Modern ultra high strength alloy steels (UHSS) have been developed with outstanding combinations of strength and fracture toughness. Such steels are characterized by high purity and nanoscale strengthening clusters/coherent precipitates in a complex precipitation hardened, martensitic microstructure. However, the performance of such steels is degraded dramatically by internal hydrogen embrittlement (IHE) and hydrogen environment embrittlement (HEE). Thus, the development of an UHSS that is immune to hydrogen embrittlement is of seminal importance. The issues that hinder understanding of IHE/HEE center on the capability to first understand fracture process zone damage mechanisms, and second to quantify and ultimately predict crack tip hydrogen concentrations relative to critical concentrations that trigger fracture. Mitigation of the hydrogen-cracking resistance of modern UHSS requires reduction in hydrogen uptake and/or modification of critical hydrogen concentrations for a given material by improving the intrinsic tolerance to dissolved and trapped hydrogen. Strategies for controlling and/or mitigating HEE and IHE of UHSS include control of intrinsic intergranular susceptibility governed by hydrogen-segregated impurity interactions and metallurgical alteration of H trap states. Another strategy is to exploit the strong electrochemical potential dependency of HEE cracking by using tailored cathodic protection schemes. Lastly, coatings can be designed to release ions that reduce H production and/or block H uptake at crack tips. A combination of a responsive coating that provides a tailored-low level of cathodic protection and active corrosion inhibition, as well as control of metallurgical purity and H trap states, provides a necessary-couple strategy to mitigate HEE of modern high strength steels.

INTRODUCTION

Ultrahigh-strength steel (UHSS) is susceptible to severe internal hydrogen embrittlement (IHE), as well as hydrogen-environment embrittlement (HEE) [1-24]. In martensitic steels such as AISI 4340, this time-dependent subcritical cracking is typically intergranular (IG) along prior-

austenite grain boundaries, at apparent threshold stress-intensity (K_{TH}) levels approaching 10 MPa√m, and crack growth rates (da/dt) up to 10^4 μm/s [10,11,16]. K_{TH} for IG IHE and HEE decreases, and da/dt increases, with increasing σ_{YS} [2,10,13,14], dissolved-H concentration [2,6,10,19,23,24], and impurity content [1,3,4,18]. The da/dt value is directly proportional to the trap-sensitive effective diffusivity of H (D_H) for IHE and HEE in a wide range of high-strength alloys, but the critical distance ahead of the crack tip where H damage nucleates differs for IHE versus HEE due to different crack tip H distributions. Hydrogen diffusion about the crack tip limits the rate of such cracking, however, surface reaction kinetics can dominate rates of HEE for weak H-producing environments and high H-diffusivity alloys [11].

The mechanism for IG hydrogen cracking likely involves reduced grain boundary cohesion due to segregated H and impurities such as S, P, Sb, or Sn [3,18-20]. Thus, modern UHSS may resist IG hydrogen embrittlement through composition control. For example, UHSS AerMet 100 is produced by double-vacuum melting to yield ultra-low S and P levels, and neither Mn nor Si is added. This processing leads to a material that is prone to only limited IG HEE in acids and near-neutral chloride solutions with cathodic polarization, certainly much less so than less-pure UHSS [25-33]. The susceptibility of AERMET 100 to IG IHE is not established. Olson speculated that IG hydrogen cracking is eliminated by rare-earth element additions that reduce grain-boundary impurity segregation in UHSS [34,35]. However, micromechanical models of grain boundary decohesion suggest that H trapping and high stress at a crack tip are sufficient to promote hydrogen embrittlement without a dominant impurity contribution [2,11,13,14,19,36]. For example, 18Ni maraging steels contain only trace levels of P, S, Si, and Mn, but are susceptible to severe IG IHE and HEE [6-8].

Time-dependent IHE and HEE can also occur along transgranular (TG) paths in high strength steels [7,12,14,22], including martensite interfaces [3,9,37,38] and cleavage planes [39-41]. Interface cracking may be governed by decohesion, and cleavage cracking may occur due to a reduction in the work of fracture, both traced to dissolved H [39]. Changing environmental variables and the predissolved-H content affect an IG to TG crack-path change, as illustrated by the effect of temperature on HEE of 18Ni Maraging steel [9] and H-partitioning modeling [42]. For moderate strength, high purity steels, it has been found that subcritical TG cracking occurs at K_{TH} levels higher than those for IG H cracking [3,4]. Substantial TG HEE was reported for peak-aged AERMET 100 at low K_{TH} levels [25-33]. This TG H-cracking mode is traced to the low

concentration of metalloid impurities segregated to prior austenite grain boundaries, to minimize intergranular cracking, coupled with substantial H accumulation by trapping at transgranular sites in the crack tip process zone [43,44]. Thomas and coworkers demonstrated that optimally aged AERMET 100 is susceptible to severe IHE at threshold stress intensity levels as low as 20 MPa√m and produced by diffusible H contents as low as 1 part-per-million by weight (wppm) [44]. Lee and coworkers found that K_{TH} can be reduced to less than 20 MPa√m by HEE in 0.6 M NaCl at both anodic and cathodic potentials [45]. Both IHE and HEE in AERMET 100 are transgranular, associated with cracking of the various interfaces associated with the martensitic microstructure [25,26,30-32,44].

The IHE situation involves a fixed total amount of internal hydrogen introduced by H precharging. The cause of the time-dependent TG IHE susceptibility of AERMET 100 is the high concentration of diffusible H ($C_{H,diff}$) provided by easily repartitioned reversible trapping at strengthening precipitates and other sites in the martensite, high crack-tip stresses, and a connected path for TG cracking. Such reversibly trapped hydrogen may repartition to the tensile hydrostatic stress field of sharp cracks [46,47]. IHE resistance of UHSS may be improved by controlling these factors. For example, alloy additions that may enhance cohesion (B, C, or N) could displace elements than enhance decohesion (P, S, or Sn) and consequently raise the critical H level required to induce interfacial decohesion [48,49]. Metallurgical alteration of H trap states provides another means to eliminate IHE and possibly HEE in UHSS. For instance, reduction in M_2C carbide interface coherence by aging/Cr in a Co/C-hardened martensitic alloy steel (i.e., Fe-13Co-10Ni-3Cr-1Mo-0.25C) can raise the H trap binding energy of this benign site to reduce H repartitioning to martensite interfaces at stressed crack tips [50-53]. Metallurgical trap site modification forces a redistribution of hydrogen that is partitioned between lattice sites and trapping sites so that the critical hydrogen level required to induce interfacial decohesion is not readily obtained at the same hydrogen fugacity used in precharging [53,54]. However, overaging to affect this change in AERMET 100 will result in some strength loss and more precipitated austenite at martensite lath interfaces. The role of this austenite in IHE is uncertain. Alternately, carbides retained after solution treatment of AERMET 100 appear to be strong H traps [46]. The volume fraction of such carbides can be increased by changes in solution-treatment temperature or steel composition [55]. $C_{H,diff}$ would be reduced by strong and homogeneously distributed trap states, and time-dependent TG IHE resistance would be improved. However, these carbides

likely degrade K_{IC} by promoting void sheeting. Trapped H exacerbates this microvoid damage. In addition, time-dependent IHE resistance may be improved if martensite interfaces could be altered to lower E_b associated with these fracture sites. This would lead to a reduction in the amount of H that is strongly trapped at these sites and available for embrittlement.

The cause of HEE is the establishment of a high $C_{H,diff}$ at the crack tip governed by chemical and electrochemical factors, as well as crack tip metallurgy. Unlike the IHE situation that involves a fixed amount of hydrogen in a closed system, a continuous supply of hydrogen at the crack tip presents a greater challenge to mitigation of TG HEE. Strategies for controlling and/or mitigating HEE include controlling the intrinsic intergranular susceptibility governed by hydrogen-segregated impurity interactions. It is also possible that lowering of the trap-sensitive effective hydrogen diffusion rate slows the transport of hydrogen from the crack tip to the fracture process zone so as to severely restrict HEE crack growth rates [56]. Another metallurgical feature that can be controlled in this class of steel is retained austenite [57], which may act to getter H or control H transport from the crack tip to the fracture process zone. An additional strategy is to understand and possibly exploit the strong electrochemical potential dependency of HEE cracking [7,25,30,45,58-62]. Degradation of fracture toughness is a strong function of applied electrochemical potential in marine environments. Tailored coating compositions can be utilized to produce a galvanic couple potential at an optimal level to retard H production and uptake at near-surface crack tips. Exploitation of the potential dependency can lead to lower rates of hydrogen production and ingress, thereby lowering the dissolved and segregated hydrogen concentration in the lattice [53,63,64]. Lastly, coating design to release ions that reduce H production and/or block H uptake at crack tips is a possibility. A recently synthesized amorphous Al-Co-Ce-Mo coating could possibly serve in this function [65,66]. Co, Mo, Ce dissolve from a homogeneous amorphous coating or from phases in a heat treated alloy. Mo dissolves as Mo^{6+} (MoO_4^{2-}) that passivates (as does Cr^{6+}) an acidic crack. Co^{2+} and Ce^{3+} ions that are insoluble in alkaline solution can be precipitated to reduce cathodic H reaction kinetics and H uptake. Distributed storage of ions proximate to random cracks, release on demand, and transport to critical-occluded sites are feasible.

In summary, the combination of a responsive coating that provides a tailored low level of cathodic protection and active corrosion inhibition as well as control of metallurgical purity and H trap states offers the opportunity to mitigate HEE of modern high strength steels. The

theoretical implications of each of these strategies are discussed below in the context of the potential dependency of AERMET 100 HEE in 0.6 M NaCl. Confirmatory experiments are in progress.

MATERIAL

A forged bar of AERMET 100 was austenitized at 885°C, quenched in liquid nitrogen and peak aged at 482°C for an optimal combination of toughness and strength [44,46,47]. The chemical composition and mechanical properties for the peak aged condition are summarized in Tables 1 and 2 and the details of the microstructure are well documented [57].

Table 1. Chemical Composition of AERMET 100 (Weight Percent)

Fe	Co	Ni	Cr	Mo	C	Ti	P	S	H
Bal	13.43	11.08	3.00	1.18	0.23	.009	.003	.0008	0.26

Table 2. Mechanical Properties of AERMET 100

HRC	σ_{YS} (MPa)	σ_{UTS} (MPa)	RA (pct)	Strain-Hardening Exponent (1/n)	E (GPa)	σ_0 (MPa)	K_{IC} (MPa$\sqrt{m}$)
54	1725	1965	65	0.03	194.4	1985	126(LR)

AERMET 100 was developed to provide plane strain fracture toughness (K_{IC}) in excess of 120 MPa$\sqrt{m}$, doubling that of older steels such as AISI 4340 and 300M, each at constant yield strength (σ_{YS}) of 1750 MPa [67,68]. This strength is produced by a homogeneous distribution of nanoscale coherent M_2C alloy carbides in a highly dislocated Fe-Ni lath martensite matrix [69,70]. The high K_{IC} of AERMET 100 is achieved by advanced melting to minimize S + P and inclusion contents, austenitization to control undissolved carbides and grain size, and aging to optimize austenite precipitates along martensite lath interfaces [34,35,55,67].

APPROACH

Single edge notch (SEN) specimens were machined with a width (W) of 10.2 mm and thickness (B) of 2.54 mm. All specimens were machined parallel lengthwise to the radial direction of the

bar. The notch was electrospark discharge machined to a notch depth of 110 ± 10 μm and width of 65 ± 15 μm. Specimens were fatigue precracked to a total crack depth of 200 μm in air at 10 Hz at constant maximum stress intensity of 11 MPa√m and constant stress ratio of 0.10. Each precracked specimen was loaded in a 340 mL cylindrical Plexiglas cell. Non-deaerated (i.e., natural aeration conditions) 0.6 M NaCl (pH 6.4) was circulated from a 10 L reservoir at 24 mL/min. Only the gauge length of the specimen was exposed in the solution. Experiments were run in potentiostatic mode with applied potentials ranging from -1.1 to -0.5 V_{SCE} at a constant actuator displacement rate of 0.046 mm/hr, producing an initially constant rising stress intensity at a rate of 2.5 MPa-m$^{1/2}$/hr. Throughout the test duration, specimen load, actuator displacement, time, and direct current potential drop (dcPD) values were recorded with an automated data acquisition system [45]. The crack length (a) was calculated from the dcPD using an established calibration for the SEN specimen [71] and was corrected based on post-test measurements. The threshold stress intensity (K_{TH}) above which the environment induces resolvable subcritical crack growth was calculated form a plot of load (P) and dcPD (V) vs actuator displacement (δ). This procedure is described in previous work by Thomas, et al. [44].

RESULTS AND DISCUSSION

Potential Dependency of K_{TH}

Results presented in Figure 1 show that there is a narrow window of applied potentials that dramatically reduces the otherwise severe susceptibility of AERMET 100 to HEE. The severe drop in K_{TH} at applied potentials outside the narrow window can be attributed to high levels of hydrogen production and entry at crack tips. Scanning electron micrographs of the fracture surfaces at cathodic and anodic applied potentials reveal that the low levels of K_{TH} are associated with transgranular cracking (Figure 1b, left side of micrograph and Figure 1c) that is unique compared to the normal microvoid fracture mode (Figure 1b, right side of micrograph) and equivalent to the morphology of IHE in this steel [44]. The very high K_{TH} in Figure 1a, approaching K_{IC}, reflects a major improvement in resistance to HEE. However, a limited amount (~30 μm) of very slow H-enhanced TG crack growth was produced for this applied

potential of -625 mV$_{SCE}$, perhaps at $K < K_{TH}$. This residual amount of stable H cracking, as well as the occurrence of similar slow H cracking at -700 mV$_{SCE}$ is under investigation.

Micromechanical Modeling

IHE has been modeled micromechanically to predict K_{TH}, which decreases with increasing H concentration in the FPZ [36]. A recent model of brittle cracking in the presence of crack tip plasticity in the form of specific dislocation–crack-tip interactions, predicts K_{TH} for H-decohesion-based fracture relative to the crack-tip Griffith toughness for H-free cracking [72].

$$K_{TH} = \frac{1}{\beta'_{IHE}} \exp\left[\frac{\left(k_{IG} - \alpha C_{H\sigma,T}\right)^2}{\alpha'' \sigma_{YS}}\right] \qquad (1)$$

In this formulation, the Griffith threshold stress intensity for hydrogen embrittlement (k_{IH}) equals (k_{IG} - $\alpha C_{H\sigma,T}$) where α is a coefficient in units of MPa$\sqrt{m}$/atom fraction H and $C_{H\sigma,T}$ is the concentration of H localized by both trapping and stress field occlusion at the embrittlement site. The term k_{IG} is the critical Griffith stress-intensity factor for cleavage fracture without H ($G_C \sim \gamma_S \sim k_{IG}^2/E$), E is the elastic modulus, and γ_S is the energy required to produce a unit crack surface. For the Fe-Si system, k_{IG} = 0.85 MPa$\sqrt{m}$ and α = 0.5 MPa$\sqrt{m}$/atom fraction H [72]. The β' and α'' terms are constants determined by computer simulation of the dislocation structure about the crack tip. Gerberich reported good correlation between modeled and experimental measurements of K_{TH} vs H$_2$ pressure and temperature for HEE of UHSS using α'' = 2x10^{-4} MPa·m and β'_{IHE} = 0.2 (MPa$\sqrt{m}$)$^{-1}$ [72]. This model has been applied to AERMET 100 and yields reasonable agreement with experimental results as shown in Figure 2 [44]. However, it is important to note that K_{TH} is defined as the threshold stress intensity (K_{TH}) above which the environment induces a defined level of resolvable subcritical crack growth. For HEE, this value is affected by loading rate and crack growth can occur at $K<K_{TH}$. However, the Gerberich model provides a means a predicting the effects of metallurgy and electrochemistry on HEE.

Effect of Cohesion Promoters/Decohesion Inhibitors That Alter Work of Fracture

Approaches to produce H-cracking resistant UHSS by improving the purity of prior-austenite grain boundaries are important in mitigating intergranular HEE but may not be sufficient [18,34,35,37,38,73]. McMahon argued that segregants such as P, S, Sn, and Sb are a requisite for IG cracking, because H alone cannot localize sufficiently in the FPZ to enable low-K_{TH} IHE or HEE [3,18]. A correlation showed that HEE is eliminated if a bulk-composition parameter Ψ (Ψ = Mn + Si/2 + P + S + 10^4 C_H in at.%) is less than about 0.5 at.% for moderate-strength steels of 800 MPa < σ_{YS} < 1400 MPa and tempered martensitic microstructures heated through the temper-embrittlement regime [3,18]. Severe IG IHE seen in AISI 4340 and 300M steels is consistent with a high value of Ψ. However, Ψ is essentially 0 for AERMET 100 and 18Ni maraging steels, but hydrogen cracking along TG sites is severe as indicated in Figure 1. Thus, one mitigation strategy would be to add cohesion promoters or remove decohesion promoters in order to effectively increase k_{IG} and/or alter α. However, modeling of k_{IG} shown in Figure 3 for AERMET 100 over a range of applied potentials suggests that either a cohesion promoter or removal of a decohesion impurity is beneficial but insufficient in mitigating HE in AERMET 100. Figure 3 shows that decreasing k_{IG} from 1.31 to 0.85 MPa-m$^{1/2}$ has the effect of reducing the maximum K_{TH}, $K_{TH,MAX}$. However, while $K_{TH,MAX}$ increases with increasing k_{IG}, predicted K_{TH} values remain low at elevated hydrogen concentrations such as achieved at highly positive and negative potentials. That is, increasing k_{IG} has little effect on increasing the potential range over which susceptibility to HEE is reduced.

Effect of Raising E_b of Source Trap Sites that supply H to the Crack Tip via Stress Activated Repartitioning

For the case of IHE, a fixed total amount of internal H may be partitioned between various trap states and the lattice. From thermodynamic consideration, lattice H concentration is enhanced from an unstressed level of C_L to a stress-affected $C_{H\sigma}$ depending on the magnitude of the crack tip hydrostatic stress, σ_H [74]. The following equation applies assuming dilute H concentration, negligible effect of dissolved H on elastic constants of the material, and no negative deviation

from the logarithmic proportionality between $C_{H\sigma}$ and σ_H [50,75].

$$C_{H\sigma} = C_L \exp\left(\frac{\sigma_H V_H}{RT}\right)$$ (2)

The H concentration at trap sites in the crack tip process zone is further enhanced to $C_{H\sigma,T}$, according to Equation (3) where $E_{b\text{-site}}$ represents the binding energy of the trap at the fracture site [14]:

$$C_{H\sigma,T} = C_{H\sigma} \exp\left(\frac{E_{b\text{-site}}}{RT}\right) = C_L \exp\left(\frac{E_{b\text{-site}} + \sigma_H V_H}{RT}\right)$$ (3)

Hydrogen repartitions from a reversible trap state ($E_{b\text{-source}}$) to the trap at the crack tip ($E_{b\text{-site}}$) if the stress field interaction energy, $\sigma_H V_H$, exceeds $E_{b\text{-Source}}$ for the supplying trap near the tensile hydrostatic stress field. The amount of crack tip H at the crack tip fracture site is governed by the sum of $\sigma_H V_H$ and $E_{b\text{-site}}$ where this binding energy is for the highest energy trap state in the stress field that provides the interconnected crack path. The extent of H repartitioning from reversible traps to the stress field at the crack tip is given by [76,77]:

$$P_\sigma = \frac{\exp\left[\sigma_H V_H / RT\right]}{\exp\left[\sigma_H V_H / RT\right] + \exp\left[E_{b\text{-source}} / RT\right]}$$ (4)

where P_σ is the probability that H occupies a lattice site under the influence of the crack tip hydrostatic stress field *vs* occupation of reversible trap sites surrounding the crack tip. Figure 4 shows the probability that hydrogen will repartition from a reversible trap state to the crack tip for several values of σ_H. Classical continuum fracture mechanics suggests that σ_H is 2.5 σ_{YS} for a low strain hardening UHSS [2,78]. Analyses based on either a crack tip dislocation perspective [40,79,80], or strain gradient plasticity hardening included in the flow curve [80,81] suggest that σ_H may be as high as 8σ_{YS}. For each case, and particularly for the higher crack tip stresses, there

is a significant driving force for H to repartition from a dominant low energy trap state ($E_{b\text{-source}}$) to the crack tip.

This source of H from reversible traps contributes to the high level of $C_{H\sigma}$ that can accumulate at martensite interfaces in the crack tip process zone (10^{14} C_L from Equation (3), assuming that $\sigma_H = 5$ σ_{YS}, and actually exceeding 100 wt pct assuming that C_L is of order 10^{-4} wppm), thus explaining the severe IHE produced in AERMET 100 at low $K_{TH} \sim 0.1$ K_{IC} [44]. Notably, this hydrogen embrittlement was eliminated by baking the H-charged specimen at 190°C for 24 hours, which effectively removed diffusible and weakly trapped hydrogen [47]. Heating at 190°C did not eliminate H from higher energy trap states. However, this strongly trapped H did not produce embrittlement because it did not repartition to the crack tip. The probability for H repartitioning to the crack tip is very low when H is present only in higher energy traps (see Figure 4).

This analysis suggests an approach to improve the IHE resistance of aged AERMET 100. The coherence of M_2C decreases and Cr/Mo clusters are eliminated by aging at temperatures above about 500°C [57]. The resulting precipitates should have higher H-binding energy typical of incoherent interfaces. The idea would be to raise E_b above 30 kJ/mol as suggested by Figure 4 to suppress repartitioning of trapped hydrogen from source traps to the crack tip. A similar approach could be based on reductions in M_2C coherence by alloy additions [69]. Alloy yield strength will also be somewhat reduced. These changes will tend to reduce H partitioning from the reversible trap sites at M_2C to the crack tip hydrostatic stress field. If the reduction is sufficiently large, then H damage will be reduced, especially in a closed system such as pre-charged steel [44]. Experiments are required to test this speculation and establish the balance between the tensile strength, fracture toughness and IHE resistance of AERMET 100. However, this strategy may be more effective for IHE where a finite amount of hydrogen is available, assuming the traps are saturable, than for HEE where the crack tip can provide a constant H source.

Effect of Reducing E_b of Trap Sites involved in Fracture

Small palladium alloying additions reduce the susceptibility to hydrogen-assisted cracking in certain steels (e.g., quenched and tempered AISI 4130 steel) [82-87]. K_{ISCC} in sustained load

tests is significantly improved [54,84]. The fracture surface is modified such that intergranular cracking is replaced by transgranular tearing and ductile microvoid formation [54,84,85] when 1 wt pct Pd is added to the martensitic alloy at both 745 MPa (110 ksi) [54,84] and 1170 MPa (170 ksi) [85] yield strength levels. Explanations for this benefit of Pd addition are summarized below. Submonolayer coverages of Pd were found at lath boundaries and MnS-ferrite interfaces [84,88]. Tritium autoradiography indicated the absence of tritium at MnS inclusions when complexed by segregated Pd [89]. The reported explanation was that interfacial segregation of Pd to lath boundaries and interphase interfaces, such as sulfide inclusions, promoted rejection of hydrogen from these otherwise strong trapping sites for hydrogen [63,84,85,88,89]. The explanation for the role of Pd at such a site is based upon theoretical calculations of the Pd-hydrogen binding energies for Pd when present as individual substitutional atoms in an iron host lattice [90,91]. The calculated interaction energy for such diatomic complexes, which is the sum of a physical interaction and an electronic interaction, is dominated by the electronic interaction for Pd in an Fe host lattice [90]. This interaction energy is positive (repulsive), meaning that hydrogen should be repelled from such an impurity site in a host lattice. The argument made to support this concept is that elements to the right of iron in the periodic table tend toward filled valence electron shells and are less likely to accept additional electrons from a screened interstitial proton in the lattice [90-93]. This implies that Pd repels hydrogen when present as a single atom in an iron lattice. Therefore, it was postulated that hydrogen was either repelled from Pd-rich solid-solid interfaces or the binding energy was lowered [85,88]. Alternatively, elements such as Ti, which are to the left of iron in the periodic table, have more valence band electron vacancies than Fe and tend to trap hydrogen reversibly (negative electronic interaction) when present as sole atoms in an Fe host lattice [90-93].

The predicted effect of a reduced binding energy on K_{TH} is shown in Figure 5. The model assumes that E_b of the site controlling fracture was 30 kJ/mol, which may be associated with dislocations in the martensitic microstructure [46]. This value was used to compute $C_{H\sigma,T}$ (and thus $C_{lattice}$) values for experimental K_{TH} values using Equation (1) and assuming $k_{IG} = 1.31$ MPa-m$^{1/2}$, $\alpha = 1$ MPa-m$^{1/2}$, $\beta' = 0.2$ (MPa-m$^{1/2}$)$^{-1}$, and $\alpha'' = 3\times10^{-4}$ MPa-m (as per Figure 3). Then reduced $C_{H\sigma,T}$ values for trap sites with $E_b < 30$ kJ/mol were computed using Equation (3) enabling the prediction of K_{TH} using Equation (1). Note that a reduced trap site binding energy

leads to a greater range of potentials over which there is reduced susceptibility to hydrogen embrittlement.

Possible benefits of electrochemical potential control

The threshold for HEE is substantially increased and growth rates decreased in a narrow window of applied electrode potential for UHSS susceptible to severe transgranular HEE as shown in Figure 1. Figure 6 replots the effect of applied potential on K_{TH} for AERMET 100 in 3.5% NaCl revealing the window of reduced susceptibility to HEE in comparison to the open circuit potentials of various coatings [65,94,95]. Such coatings could control the galvanic couple potential and thus, K_{TH} (see Figure 6).

Thus, this window can be exploited by manipulating the galvanic couple potential between the coating and the exposed area of UHSS. In the case of the Al-Co-Ce coating, a range of OCPs can be preselected based on alloy composition and metallurgy [65]. Additionally, the width of this window of reduced susceptibility can be manipulated through the other strategies discussed above. For example, Figure 5 shows the effect of applied potential on K_{TH} for $E_{b\text{-site}}$ ranging from 20 to 30 kJ/mol. A reduced trap site binding energy leads to a greater range of potentials over which there is reduced susceptibility to hydrogen embrittlement. Using both alloy modification to lower $E_{b\text{-site}}$ plus a coating for polarization into the regime of increased resistance to HEE offers a viable strategy to mitigate hydrogen embrittlement.
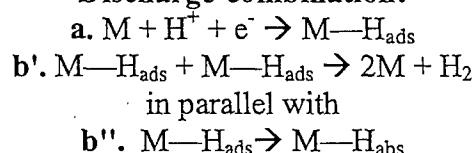
Effect of Inhibitors that Retard H uptake at Crack Tips

Galvanic coupling between a coating and an UHSS is unlikely to independently reduce the severity of HEE when potential windows of good HEE resistance are small. This is inferred from the severe IHE produced in AERMET 100 over a wide range of low to moderate diffusible hydrogen concentrations [44]. Results showed that there exists a critical diffusible hydrogen concentration of approximately 1 wppm above which K_{TH} is greatly reduced from K_{IC}. Thus, in order to mitigate HEE, the rate of hydrogen production and/or absorption must be reduced such that $C_{H,diff}$ remains below 1 wppm. Therefore, a coating must be multi-functional to act as a
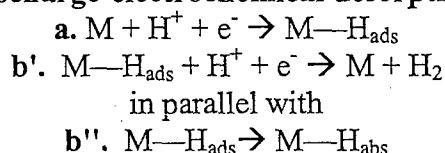
permeation barrier, to provide low levels of cathodic protection, and to act as a source for a supply of inhibiting ions in the vicinity of the crack tip.

Inhibitors function through several mechanisms including cathodic inhibition, anodic inhibition, H absorption inhibition, and enhanced H_2 recombinative desorption [96]. Indirect methods of inhibition include Cl^- absorption, pH buffers, and passivators. Two basic mechanisms for the hydrogen evolution reaction follow [97]:

<div align="center">

Discharge-combination:
a. $M + H^+ + e^- \rightarrow M\!-\!H_{ads}$
b'. $M\!-\!H_{ads} + M\!-\!H_{ads} \rightarrow 2M + H_2$
in parallel with
b''. $M\!-\!H_{ads} \rightarrow M\!-\!H_{abs}$

Discharge-electrochemical desorption:
a. $M + H^+ + e^- \rightarrow M\!-\!H_{ads}$
b'. $M\!-\!H_{ads} + H^+ + e^- \rightarrow M + H_2$
in parallel with
b''. $M\!-\!H_{ads} \rightarrow M\!-\!H_{abs}$

</div>

Cathodic inhibitors act to reduce the overall rate of the hydrogen evolution reaction. Additionally, the recombination promoters work by increasing the rate of b', thereby reducing the rate of $H_{ads} \rightarrow H_{abs}$ via reaction b'' for a given overall reaction rate. Thus, cathodic inhibition and recombination promoters likely lead to a reduction in the amount of hydrogen absorbed into the metal [98]. Anodic inhibitors affect hydrogen absorption by inhibiting corrosion and thus inhibiting the hydrolysis reactions that create H^+ in an occluded solution, which can subsequently be reduced and absorbed at the crack tip [99]. Absorption inhibitors affect reaction kinetics by blocking absorption sites and thus reducing the effective surface area (i.e., inhibiting b'' above) or by promoting recombination of H atoms to produce H_2 (i.e., promoting b' above) [100]. Table 3 shows the traditional classes of H uptake inhibitors and examples.

Table 3. Inhibitor functions and examples [96,101,102].

Inhibitor function	Example compounds or species
Cathodic inhibitor	Polyphosphate, zinc, silicate
Anodic inhibitor	Chromate, nitrate, molybdate, cerate, orthophosphate, ferrocyanide
Chloride absorbers	Not determined
Acid Buffers	Borax, Sodium bicarbonate, etc.
Hydrogen entry inhibitors (not including passivators)	Bi, Pb, Zn, Noble metals, Various organic film formers
Recombination promoters	Ir, Pd, Pt

Thus, in the context of the Gerberich model, where K_{TH} decreases with increasing crack tip H concentration ($C_{\sigma H,T}$), inhibitors act by reducing the lattice H concentration, C_L, through direct or indirect reduction in reaction rates or absorption rates (see Figure 7), and subsequently, reducing $C_{\sigma H,T}$ (see Figure 3). It can be seen from Figure 7 that a 10-fold reduction in $C_{lattice}$ may be necessary to raise K_{TH} sufficiently at high anodic and cathodic potentials assuming $E_{b-site} = 30$ kJ/mol.

CLOSING STATEMENTS

Several strategies are possible for controlling and/or mitigating HEE and IHE of UHSS. These include controlling the intrinsic intergranular and transgranular susceptibility governed by hydrogen-segregated impurity interactions and metallurgical alteration of H trap states. Application of the Gerberich model to HEE of AERMET 100 showed that adding cohesion promoters or removing decohesion promoters (i.e., increasing k_{IG}) acts to increase $K_{TH,MAX}$, but does not substantially increase the potential range over which HEE susceptibility is reduced. Thus, this strategy may be more effective for IHE than for HEE. Application of the Gerberich model to alteration of H trap states (i.e., decreasing E_b of the trap site involved in fracture) shows an increased window of reduced susceptibility to HEE with decreasing E_{b-site}. Conversely, an increasing $E_{b-source}$ for sites that act as hydrogen sources was found to be beneficial as the probability of repartitioning to the FPZ decreases with increasing $E_{b-source}$. However, this strategy of increasing $E_{b-source}$ of the hydrogen sources may be more effective for IHE, assuming the source traps are saturable, than for HEE where there is a continuous supply of hydrogen. Lastly, coating design to release ions that reduce H production and/or block H uptake at crack tips is a possibility. Application of the Gerberich model shows that decreasing $C_{lattice}$ through inhibitor function leads to an increased window of reduced susceptibility to HEE for $E_{b-site} = 30$ kJ/mol. Thus, there are several strategies for controlling and/or mitigating HEE, but it is likely that a single strategy is not sufficient. Therefore, in order to exploit the outstanding combination of strength and fracture toughness in modern UHSS, a multi-pronged approach is recommended. A combination of a smart coating that provides a tailored-low level of cathodic protection and active corrosion inhibition as well as control of metallurgical purity and H trap states offers the opportunity to suppress HEE susceptibility of modern high strength steels.

REFERENCES

[1.] K. YOSHINO AND J. C.J. MCMAHON, METALL. TRANS. A, 1974. 5A: P. 363.

[2.] K.N. AKHURST AND T.J. BAKER, METALL. TRANS. A, 1981. 12A: P. 1059.

[3.] N. BANDYOPADHYAY, J. KAMEDA, AND J. C.J. MCMAHON, METALL. TRANS. A, 1983. 14A: P. 881.

[4.] S.K. BANERJI, H.C. FENG, AND J. C.J. MCMAHON, METALL. TRANS. A, 1978. 9A: P. 237.

[5.] C.F. BARTH AND E.A. STEIGERWALD, METALL. TRANS., 1970. 1: P. 3451.

[6.] D.P. DAUTOVICH AND S. FLOREEN, METALL. TRANS., 1973. 4: P. 2627.

[7.] D.P. DAUTOVICH AND S. FLOREEN, IN *STRESS CORROSION CRACKING AND HYDROGEN EMBRITTLEMENT OF IRON ALLOYS*, R.W.S.E. AL., EDITOR. 1977, NACE: HOUSTON, TX. P. 798.

[8.] R.P. GANGLOFF AND R.P. WEI, METALL. TRANS. A, 1977. 8A: P. 1043.

[9.] R.P. GANGLOFF AND R.P. WEI, IN *FRACTOGRAPHY IN FAILURE ANALYSIS, ASTM STP 645*, B.M. STRAUSS AND J. W.H. CULLEN, EDITORS. 1978, ASTM: WEST CONSHOHOCKEN, PA. P. 87.

[10.] R.P. GANGLOFF, IN *CORROSION PREVENTION AND CONTROL*, M. LEVY AND S. ISSEROW, EDITORS. 1986, UNISTED STATES ARMY MATERIALS TECHNOLOGY LABORATORY: WATERTOWN, MA. P. 64.

[11.] R.P. GANGLOFF, IN *HYDROGEN EFFECTS IN MATERIALS*, N.R. MOODY, ET AL., EDITORS. 2002, TMS: WARRENDALE, PA. P. 477.

[12.] M. GAO, M. LU, AND R.P. WEI, METALL. TRANS. A, 1984. 15A: P. 735.

[13.] W.W. GERBERICH, T. LIVNE, AND X. CHEN, IN *MODELING ENVIRONMENTAL EFFECTS ON CRACK GROWTH PROCESSES*, R.H. JONES AND W.W. GERBERICH, EDITORS. 1986, TMS: WARRENDALE, PA. P. 243.

[14.] W.W. GERBERICH, T. LIVNE, X.-F. CHEN, AND M. KACZOROWSKI, METALL. TRANS. A, 1988. 19A: P. 1319.

[15.] H.H. JOHNSON, J.G. MORELET, AND A.R. TROIANO, TRANS. TMS-AIME, 1958. 216: P. 528.

[16.] G.E. KERNS, M.T. WANG, AND R.W. STAEHLE, IN *STRESS CORROSION CRACKING AND HYDROGEN EMBRITTLEMENT OF IRON ALLOYS*, E.A. R.W. STAEHLE, EDITOR. 1977, NACE: HOUSTON, TX. P. 700.

[17.] P. MCINTYRE, IN *HYDROGEN DEGRADATION OF FERROUS ALLOYS*, R.A. ORIANI, J.P. HIRTH, AND M. SMIALOWSKI, EDITORS. 1985, NOYES PUBLICATIONS: PARK RIDGE, NJ. P. 763.

[18.] C.J. MCMAHON(JR.), ENG. FRACT. MECH., 2001. 68: P. 773.

[19.] R.A. ORIANI AND P.H. JOSEPHIC, ACTA METALL., 1974. 22: P. 1065.

[20.] R.A. ORIANI, CORROSION, 1987. 43: P. 390.

[21.] E.A. STEIGERWALD, F.W. SCHALLER, AND A.R. TROIANO, TRANS. TMS-AIME, 1960. 218: P. 832.

[22.] R.P. WEI AND M. GAO, IN *HYDROGEN DEGRADATION OF FERROUS ALLOYS*, R.P. ORIANI, J.P. HIRTH, AND M. SMIALOWSKI, EDITORS. 1985, NOYES PUBLICATIONS: PARK RIDGE, NJ. P. 579.

[23.] Y. YAMAGUCHI, H. NONAKA, AND K. YAMAKAWA, CORROSION, 1997. 53: P. 147.

[24.] K. YAMAKAWA, S. YONEZAWA, AND S. YOSHIZAWA. IN *INT. CONGR. ON METALLIC CORROSION*. 1984. TORONTO: NATIONAL RESEARCH COUNCIL.

[25.] E.U. LEE, H. SANDERS, AND B. SARKAR. IN *PROC. TRI-SERVICE CONF. ON CORROSION*. 2000. ABERDEEN, MD: ARMY RESEARCH LABORATORY.

[26.] G.N. VIGILANTE, J.H. UNDERWOOD, AND D. CRAYTON. IN *FATIGUE AND FRACTURE MECHANICS, PROC. 30TH NAT. SYMP.* 2000. WEST CONSHOHOCKEN, PA: ASTM INTERNATIONAL.

[27.] J. KOZOL AND C.E. NEU. 1992, NAVAL AIR WARFARE CENTER: WARMINSTER, PA.

[28.] A. OEHLERT AND A. ATRENS, MATER. FORUM, 1993. 17: P. 415.

[29.] A. OEHLERT AND A. ATRENS, J. MATER. SCI., 1998. 33: P. 775.

[30.] P.F. BUCKLEY, R. BROWN, G.H. GRAVES, E.U. LEE, C.E. NEU, AND J. KOZOL, IN *METALLIC MATERIALS FOR LIGHTWEIGHT APPLICATIONS, 40TH SAGAMORE ARMY MATERIALS RESEARCH CONF.*, M.G.H. WELLS, E.B. KULA, AND J.H. BEATTY, EDITORS. 1993, UNITED STATES ARMY LABORATORY COMMAND: WATERTOWN, MA. P. 377.

[31.] P. BUCKLEY, B. PLACZANKIS, J. BEATTY, AND R. BROWN. IN *CORROSION/94*. 1994. HOUSTON, TX: NACE.

[32.] E.U. LEE, METALL. TRANS. A, 1995. 26A: P. 1313.

[33.] D.S. MCDARMAID, BR. CORR. J., 1980. 15: P. 172.

[34.] G.B. OLSON, IN *INNOVATIONS IN ULTRAHIGH STRENGTH STEEL TECHNOLOGY, 34TH SAGAMORE ARMY MATERIALS RESERACH CONF.*, G.B. OLSON, M. ARZIN, AND E.S. WRIGHT, EDITORS. 1987, UNITED STATES ARMY LABORATORY COMMAND: WATERTOWN, MA. P. 549.

[35.] G.B. OLSON, ADV. MATER. PROCESSES, 1997. JULY: P. 72.

[36.] R.P. GANGLOFF, MATER. SCI. ENG., 1988. A103: P. 157.

[37.] J. KAMEDA AND J. C.J. MCMAHON, METALL. TRANS. A, 1983. 14A: P. 903.

[38.] Y. TAKEDA AND J. C.J. MCMAHON, METALL. TRANS. A, 1981. 12A: P. 1255.

[39.] J.F. KNOTT, IN *HYDROGEN EFFECTS IN MATERIALS*, A.W. THOMPSON AND N.R. MOODY, EDITORS. 1996, TMS: WARRENDALE, PA. P. 287.

[40.] X. CHEN AND W.W. GERBERICH, METALL. TRANS. A, 1991. 22A: P. 59.

[41.] M. GAO AND R.P. WEI, ACTA METALL., 1984. 32: P. 2115.

[42.] M. GAO AND R.P. WEI, METALL. TRANS. A, 1985. 16A: P. 2039.

[43.] R.P. GANGLOFF, IN *COMPREHENSIVE STRUCTURAL INTEGRITY*, I. MILNE, R.O. RITCHIE, AND B. KARIHALOO, EDITORS. 2003, ELSEVIER SCIENCE: NEW YORK, NY. P. 31.

[44.] R.L.S. THOMAS, J.R. SCULLY, AND R.P. GANGLOFF, METALL. MATER. TRANS. A, 2003. 34A: P. 327.

[45.] Y. LEE, B.A. KEHLER, R.P. GANGLOFF, AND J.R. SCULLY, *HYDROGEN ENVIRONMENT EMBRITTLEMENT OF AERMET 100.* 2005: CHARLOTTESVILLE, VA.

[46.] R.L.S. THOMAS, D. LI, R.P. GANGLOFF, AND J.R. SCULLY, METALL. MATER. TRANS. A, 2002. 33A: P. 1991.

[47.] D. LI, R.P. GANGLOFF, AND J.R. SCULLY, *HYDROGEN DIFFUSION AND TRAPPING BEHAVIOR IN ULTRAHIGH STRENGTH AERMET 100 STEEL.* 2002, UNIVERSITY OF VIRGINIA: CHARLOTTESVILLE, VA.

[48.] H.J. GRABKE, *CHEMISTRY AND PHYSICS OF FRACTURE.* 1987, BOSTON, MA: MARTINUS NIJHOFF PUBLISHERS/NATO SCIENTIFIC AFFAIRS. 388.

[49.] J.R. RICE AND J.S. WANG, MATER. SCI. ENG. A., 1989. A107: P. 23.

[50.] J.P. HIRTH, METALL. TRANS. A, 1980. 11A: P. 861.

[51.] I.M. BERNSTEIN AND G.M. PRESSOUYRE, IN *HYDROGEN DEGREDATION OF FERROUS ALLOYS*, R.A. ORIANI, J.P. HIRTH, AND M. SMIALOWSKI, EDITORS. 1985, NOYES PUBLICATIONS: PARK RIDGE, NJ. P. 641.

[52.] G.M. PRESSOUYRE AND I.M. BERNSTEIN, METALL. TRANS. A, 1978. 9A: P. 1571.

[53.] G.M. PRESSOUYRE, IN *CURRENT SOLUTIONS TO HYDROGEN PROBLEMS IN STEELS, PROC. 1ST INT. CONF.*, C.G. INTERRANTE AND G.M. PRESSOUYRE, EDITORS. 1982, ASM: METALS PARK, OH. P. 18.

[54.] B.E. WILDE, C.D. KIM, AND J. J.C. TURN, CORROSION, 1982. 38: P. 515.

[55.] C.J. KUEHMANN. 1994, NORTHWESTERN UNIVERSITY: EVANSTON, IL.

[56.] R.P. GANGLOFF. *DIFFUSION CONTROL OF HYDROGEN ENVIRONMENT EMBRITTLEMENT IN HIGH STRENGTH ALLOYS*. IN *HYDROGEN EFFECTS ON MATERIAL BEHAVIOR AND CORROSION DEFORMATION INTERACTIONS*. 2003. MORAN, WYOMING: TMS (THE MINERALS, METALS & MATERIALS SOCIETY).

[57.] R. AYER AND P.M. MACHMEIER, METALL. TRANS. A, 1993. 24A: P. 1943.

[58.] B.F. BROWN, *STRESS CORROSION CRACKING OF HIGH STRENGTH STEEL ALLOYS*, IN *THEORY OF SCC IN ALLOYS*, J.C. SCULLY, EDITOR. 1971, NATO SCIENTIFIC AFFARIS DIVISION: BRUSSELS. P. 186.

[59.] B.F. BROWN. IN *STRESS CORROSION CRACKING AND HYDROGEN EMBRITTLEMENT OF IRON ALLOYS*. 1977: NACE.

[60.] B.F. BROWN, C.T. FUJII, AND E.P. DALBERG, J. ELECTROCHEM. SOC., 1969. 116: P. 218.

[61.] G. SANDOZ, *HIGH STRENGTH STEELS*, IN *STRESS CORROSION CRACKING IN HIGH STRENGTH STEELS AND IN TITANIUM AND ALUMINUM ALLOYS*, B.F. BROWN, EDITOR. 1972, NAVAL RESEARCH LABORATORY: WASHINGTON, DC.

[62.] P.S. TYLER, M. LEVY, AND L. RAYMOND, CORROSION, 1991. 47: P. 82.

[63.] M. ZAMANZADEH, A. ALLAM, AND H.W. PICKERING, J. ELECTROCHEM. SOC., 1980. 127: P. 1688.

[64.] M. IINO, N. NOMURA, AND H. TAKEZAWA, IN *CURRENT SOLUTIONS TO HYDROGEN PROBLEMS IN STEELS, PROC. 1ST INT. CONF.*, C.G. INTERRANTE AND G.M. PRESSOUYRE, EDITORS. 1982, ASM: METALS PARK, OH. P. 159.

[65.] M.E. GOLDMAN, N. UNLU, G.J. SHIFLET, AND J.R. SCULLY, ELECTROCHEMICAL AND SOLID-STATE LETTERS, 2005. 8(2): P. B1.

[66.] M. JAKAB AND J.R. SCULLY, NATURE MATERIALS, 2005(4): P. 1.

[67.] W.M. GARRISON(JR.), J. MET., 1990. 46: P. 20.

[68.] R.M. HEMPHILL AND D.E. WERT, 5087415, CARPENTER TECHNOLOGY CORPORATION, READING, PA, 1992.

[69.] R. AYER AND P.M. MACHMEIER, METALL. TRANS. A, 1996. 27A: P. 2510.

[70.] C.H. YOO, H.M. LEE, J.W. CHAN, AND J.W. MORRIS, METALL. MATER. TRANS. A, 1996. 27A: P. 3466.

[71.] H.H. JOHNSON, MATERIALS RESEARCH & STANDARDS, 1965. 5(9): P. 442.

[72.] W.W. GERBERICH, P.G. MARSH, AND J.W. HOEHN, IN *HYDROGEN EFFECTS IN METALS*. 1996, TMS: WARRENDALE, PA. P. 539.

[73.] J.F. WATTON, G.B. OLSON, AND M. COHEN, IN *INNOVATIONS IN ULTRAHIGH STRENGTH STEEL TECHNOLOGY, 34TH SAGAMORE ARMY MATERIALS RESERACH CONF.*, G.B. OLSON, M. AZRIN, AND E.S. WRIGTH, EDITORS. 1987, UNITED STATES ARMY LABORATORY COMMAND: WATERTOWN, MA. P. 549.

[74.] R.A. ORIANI, IN *FUNDAMENTAL ASPECTS OF STRESS CORROSION CRACKING*. 1969, NACE: HOUSTON, TX. P. 32.

[75.] W.C. JOHNSON AND J.Y. HUH, METALL. MATER. TRANS. A, 2003. 34A(12): P. 2819.

[76.] T.Y. ZHANG, H. SHEU, AND J.E. HACK, SCRIPTA METALL. MATER., 1992. 27: P. 1605.

[77.] T.Y. ZHANG AND J.E. HACK, METALL. MATER. TRANS. A, 1999. 30A: P. 155.

[78.] T.L. ANDERSON, *FRACTURE MECHANICS: FUNDAMENTALS AND APPLICATIONS*. 2ND ED. 1995, BOCA RATON, FL: CRC PRESS. 117.

[79.] W.W. GERBERICH, R.A. ORIANI, M.-J. LI, X. CHEN, AND T. FOECKE, PHIL. MAG. A, 1991. 63: P. 363.

[80.] Y. WEI AND J.W. HUTCHINSON, J. MECH. PHYS. SOLIDS, 1997. 45: P. 1253.

[81.] H. JIANG, Y. HUANG, Z. ZHUANG, AND K.C. HWANG, J. MECH. PHYS. SOLIDS, 2001. 49(979-93).

[82.] U.P. LEVENKO, CERNAJI METALL., 1975. 10: P. 116.

[83.] V.I. ARKHAROV, T.T. MOROZ, I.A. NOVOKHATSKII, S.I. KHOKHLOVA, AND M.I. EREMIA, SOV. MATER. SCI., 1976. 12: P. 38.

[84.] J.B. LUMSDEN, B.E. WILDE, AND P.J. STOCKER, SCRIPTA METALL., 1983. 17: P. 971.

[85.] B.E. WILDE, I. CHATTORAJ, AND T.A. MOZHI, SCRIPTA METALL., 1987. 21: P. 1369.

[86.] J.R. SCULLY, M.J. CIESLAK, AND J.A.V.D. AVYLE, SCRIPTA METALL., 1994. 31(2): P. 125.

[87.] J.R. SCULLY, J.A.V.D. AVYLE, M.J. CIESLAK, J. A.D. ROMIG, AND C.R. HILLS, METALL. MATER. TRANS. A, 1991. 22A: P. 2429.

[88.] M.K. MILLER, S.S. BRENNER, AND M.G. BURKE, METALL. TRANS. A, 1987. 18A: P. 519.

[89.] T.D. LE AND B.E. WILDE. IN *CURRENT SOLUTIONS TO HYDROGEN PROBLEMS IN STEELS, PROC. 1ST INT. CONF.* 1982. METALS PRAK, OH: ASM.

[90.] A.I. SHIRLEY AND C.K. HALL, SCRIPTA METALL., 1983. 17: P. 1003.

[91.] H. KRONMULLER, B. HOHLER, H. SCHREYER, AND K. VETTER, PHIL. MAG. B, 1978. 37(5): P. 569.

[92.] G.M. PRESSOUYRE, METALL. TRANS. A, 1983. 14A: P. 2189.

[93.] G.M. PRESSOUYRE, METALL. TRANS. A, 1979. 10A: P. 1571.

[94.] H.P. HACK, *METALS HANDBOOK*. 1987, ASM: METALS PARK, OH. P. 234.

[95.] B.N. POPOV. 2005.

[96.] V.S. AGARWALA. *MODIFICATION OF CRACK-TIP CHEMISTRY TO INHIBIT CORROSION AND STRESS CORROSION CRACKING IN HIGH-STRENGTH ALLOY. IN EMBRITTLEMENT BY THE LOCALIZED CRACK ENVIRONMENT.* 1983. PHILADELPHIA, PA: THE METALLURGICAL SOCIETY/AIME.

[97.] P.K. SUBRAMANYAN, *ELECTROCHEMICAL ASPECTS OF HYDROGEN IN METALS*, IN *COMPREHENSIVE TREATISE ON ELECTROCHEMISTRY*, J.O.M. BOCKRIS, B.E. CONWAY, AND E. YEAGER, EDITORS. 1981, PLENUM: NY, NY. P. 411.

[98.] L. MAKSAEVA, A. MARSHAKOV, Y. MIKHAILOVSKY, AND V. POPOVA. IN *CORROS. CONTROL LOW-COST RELIAB., PROC. - 12TH INT. CORROS. CONGR.* 1993: NACE.

[99.] C.C. JUANG AND J.K. WU, CORROSION SCIENCE, 1994. 36(10): P. 1727.

[100.] L. VRACAR AND D.M. DRAZIC, J. ELECTROANAL. CHEM., 1992. 339: P. 269.

[101.] C.T. LYNCH, K.J. BHANASALI, AND P.A. PARRISH, *INHIBITION OF CRACK PROPAGATION OF HIGH STRENGTH STEELS THROUGH SINGLE AND MULTI-FUNCTIONAL INHIBITORS*, W. PATTERSON, EDITOR. 1976.

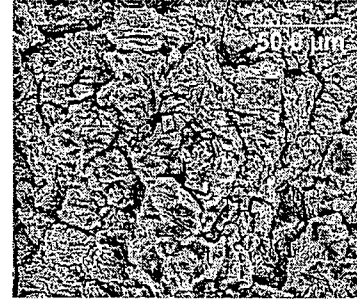[102.] B.N. POPOV, G. ZHENG, AND R.E. WHITE, CORROSION, 1995. 51(6): P. 429.

a.
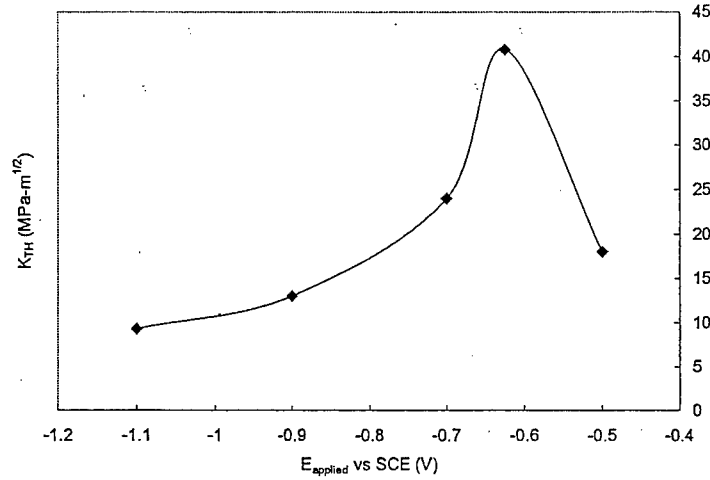
b.
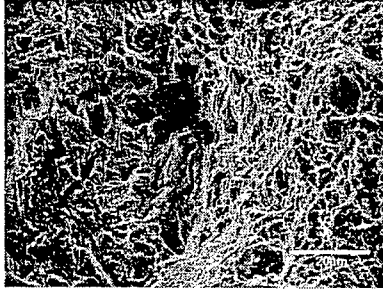
c.

Figure 1. a) K_{TH} versus applied potential for AERMET 100 in 0.6 M NaCl. b) and c) show scanning electron images of the fracture surfaces for applied potentials of -1.1 V_{SCE} and -0.5 V_{SCE}, respectively.
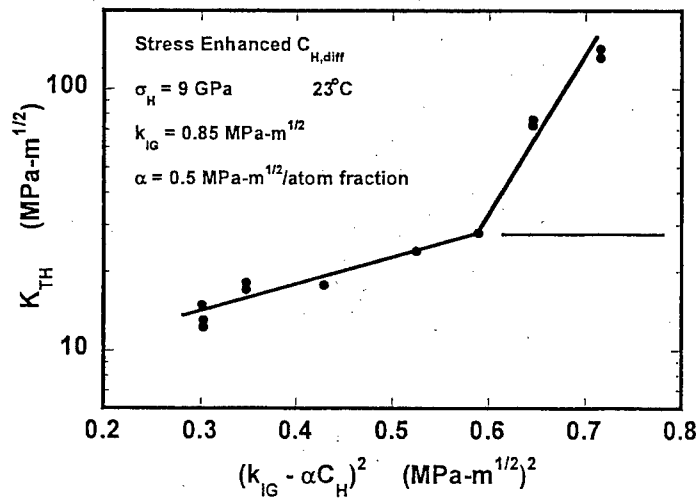

Figure 2. The measured (●) and model-predicted (—) effects of hydrostatic-stress enhanced H concentration on K_{TH} for IHE of AERMET 100. All measured K_{TH} values less than 30 MPa-$m^{1/2}$ relate to brittle-transgranular IHE and the associated regression line is $\log(K_{TH}) = 0.83 + 1.05 \ (k_{IG} - \alpha C_H)^2$ with $R^2 = 0.89$. Cracking at higher K_{TH} involved some MVC [44].
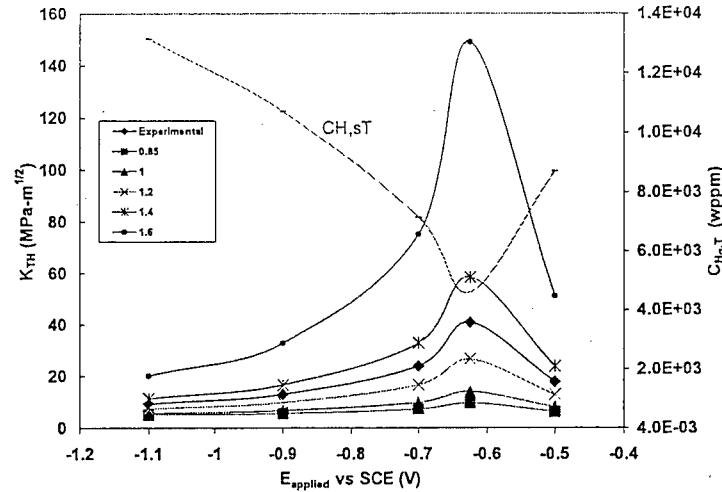
Figure 3. Predicted (dotted lines) and experimental (◆) K_{TH} versus $E_{applied}$ for values of k_{IG} ranging from 0.85 to 1.6 MPa-m$^{1/2}$. $C_{H\sigma,T}$ values were calculated through Equation (1) using experimental K_{TH} values for AERMET 100 in 0.6 M NaCl and a k_{IG} of 1.31 MPa-m$^{1/2}$. This value of k_{IG} was chosen to correspond to approximately 0 wppm hydrogen at K_{IC}. A value of α = 1 MPa-m$^{1/2}$/ atom fraction H was chosen corresponding with $\beta' = 0.2$ (MPa-m$^{1/2}$)$^{-1}$ and $\alpha'' = 3 \times 10^{-4}$ MPa-m.
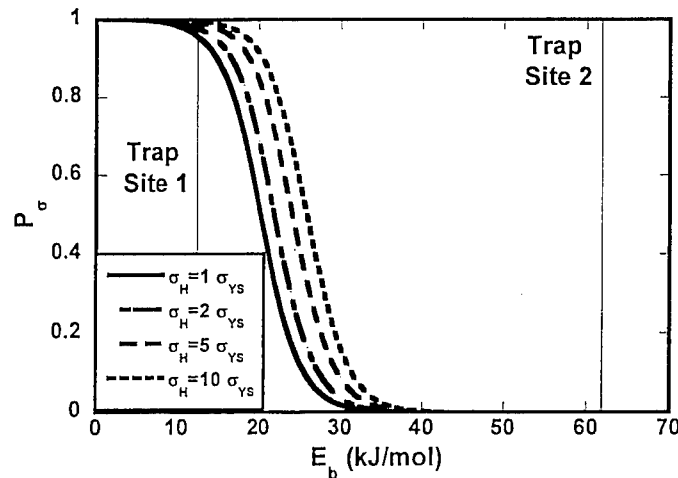
Figure 4. Probability of repartitioning to the FPZ given by Equation (4) at hydrostatic stresses ranging from σ_{YS} to 10 σ_{YS} for metallurgical trap sites with $E_b \leq 70$ kJ/mol. Also, shown are lines indicating AERMET 100 trap site 1, which is associated with coherent M_2C precipitates and trap site 2, which is associated with martensite interfaces, austenite grain boundaries, and mixed dislocation cores [47].
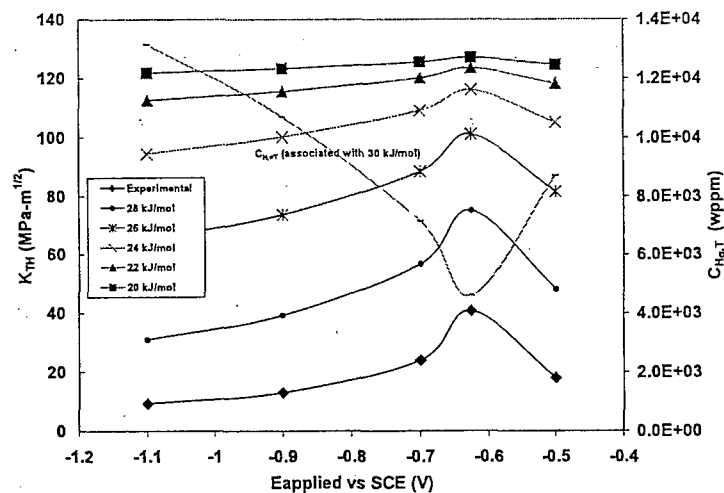
Figure 5. Predicted (dotted lines) and experimental (◆) K_{TH} versus $E_{applied}$ for trap site binding energies at the critical fracture site ($E_{b\text{-site}}$) ranging from 20 to 30 kJ/mol. A hydrostatic stress field, σ_H, of $5\sigma_{ys}$ is assumed.
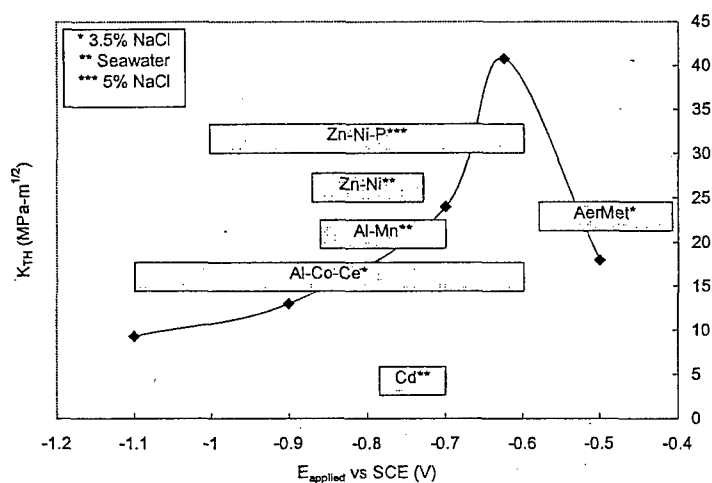

Figure 6. K_{TH} versus $E_{applied}$ for AERMET 100 in 3.5% NaCl. Open circuit potential ranges are also shown for various candidate coatings in NaCl electrolytes.
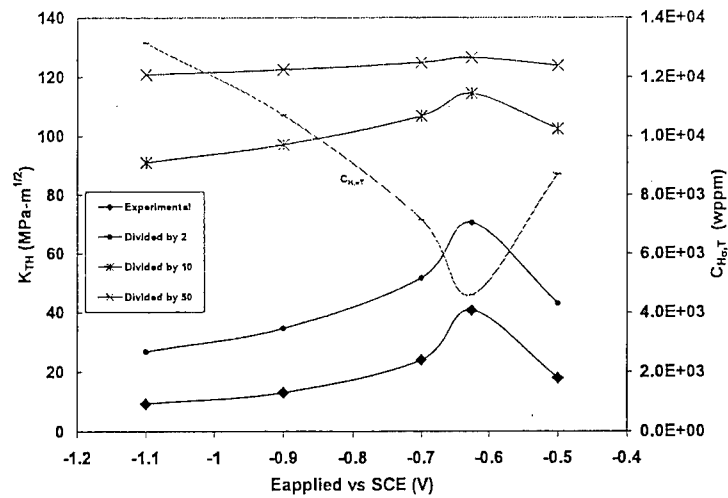
Figure 7. Predicted (dotted lines) and experimental (◆) K_{TH} versus $E_{applied}$ for varying values of $C_{lattice}$. The plotted $C_{lattice}$ values were calculated from experimental K_{TH} data. Predicted values of K_{TH} were determined using calculated $C_{lattice}$ values divided by 2, 10, and 50. A hydrostatic stress field, σ_H, of $5\sigma_{ys}$ is assumed.

Hydrogen Environment Assisted Cracking of Ultra-high Strength AetMet[TM] 100 Steel

Yongwon Lee and Richard. P. Gangloff

Hydrogen Environment Assisted Cracking of Ultra-high Strength AetMet™ 100 Steel

Yongwon Lee and Richard. P. Gangloff

Abstract

Precipitation hardened martensitic AetMet™ 100 is a high purity ultra-high strength steel with exceptional plain strain fracture toughness (K_{IC} ~ 130 MPa√m) and high yield strength (σ_{YS} ~ 1725 MPa). The hydrogen environment assisted cracking (HEAC) behavior of this modern steel is not well understood, and was characterized in neutral 3.5% NaCl solution at various applied potentials (E_{App}) relevant to coated applications in marine environments. A novel short crack specimen was stressed under constant displacement-rate, and monitored using a high resolution electrical potential crack monitoring technique to determine the Stage II crack growth rate (da/dt_{II}) and threshold stress intensity (K_{TH}) typically of the chemically short crack regime (250 to 1000 μm). AerMet™ 100 is susceptible to severe transgranular (TG) HEAC when stressed in neutral 3.5% NaCl and at near free corrosion potentials, as quantified by reduced K_{TH}, to as low as 10% of K_{IC}, and da/dt_{II} as high as 0.5 μm/s. Applied electrode potential (E_{App}) is a critical variable. As E_{App} increases from -1.1 volts vs. saturated calomel electrode (V_{SCE}) to -0.625 V_{SCE}, operationally defined K_{TH} increases from the very low level of 9 MPa√m to a maximum of 40 MPa√m, and da/dt_{II} decreases monotonically from 500 nm/s to 1 nm/s. Additional polarization to -0.5 V_{SCE}, typical of free corrosion in aerated solution, produces a decrease in K_{TH} to 16 MPa√m and increase in da/dt_{II} to 100 nm/s. The mechanism for this behavior is crack tip hydrogen embrittlement. The effect of electrode potential is understood based on occluded crack acidification at the anodic conditions and cathodic polarization at lower potentials, each favoring H production and uptake. Scanning electron fractography revealed predominantly transgranular cracking at martensite lath and/or packet interfaces for all applied potentials, caused by enhanced hydrogen localization due to high crack tip stresses and preferential hydrogen trapping. These results are compared to semi-quantitative models for H-enhanced subcritical crack propagation kinetics to identify the rate limiting step, which is likely H diffusion in the crack tip process zone. These results provide the foundation for mitigating HEAC based on electrochemical control of H production/uptake and microstructural control of H trapping/damage. This persisting challenge is to formulate predictive models of this behavior that are useful for engineering design of cracking resistant steels and coatings.

I. Introduction

Ultrahigh-strength steels (UHSS) with tempered martensitic microstructures are susceptible to internal hydrogen assisted cracking (IHAC)[1-4], as well as hydrogen environment assisted cracking (HEAC)[5-9]. Susceptibility is characterized effectively by the fracture mechanics threshold stress intensity, K_{TH}, below which hydrogen assisted cracking (HAC) is not observed, and rate of subcritical crack growth, da/dt, at stress intensity (K) levels above K_{TH}. The Stage II plateau rate, da/dt_{II}, is approximately independent of K and is characteristic of the rate limiting step in the sequence of time dependent elemental processes that delivers atomic hydrogen (H) to the crack tip fracture process zone (FPZ)[7]. The mechanism of hydrogen damage is debated between bond-strength reduction and H-plasticity interaction[5,6,8,10-15].

The severity of HAC is affected by numerous variables that complicate characterization and understanding of steel susceptibility[7]. A unifying variable is the amount of hydrogen accumulated in the FPZ. This H concentration and damage site location are governed by H trapping at microstructural features, crack tip hydrostatic stress distribution, and source of mobile H[7]. The FPZ appears to be about 1 μm ahead of the crack tip surface for HEAC in high strength alloys[17] and at the region of maximum crack tip hydrostatic tension for IHAC[87]. Traditional UHSS such as AISI 4340 and 300M are particularly susceptible to intergranular (IG) IHAC and HEAC, where impurity segregation at grain boundaries interacts with H to lower boundary cohesion and the associated K_{TH} to a small fraction of the hydrogen-free plane strain fracture toughness, K_{IC}[8,13,15]. As a third-important variable, K_{TH} generally decreases and da/dt_{II} increases with increasing tensile yield strength (σ_{YS})[7,8].

Modern UHSSs such as AerMet™ 100 (UNS K92580) are double-vacuum melted to reduce impurities at prior austenite grain boundaries, and heat treated to produce very high K_{IC} and σ_{YS}[19,20]. When cryogenically quenched and optimally aged, AerMet™ 100 is strengthened and toughened by the presence of nano-scale secondary hardening M_2C carbides in unrecrystallized martensite, absence of cementite particles, and formation of a very small amount of thin-film reverted austenite (γ'), resulting in K_{IC} of 130 MPa√m and σ_{YS} of 1725 MPa[21-24]. Despite these advances, AerMet™ 100 is susceptible to HAC comparable to older UHSS[18,25-30]. For example, IHAC of AerMet™ 100 occurs at a diffusible H concentration, $C_{H,diff}$, as low as 0.5-1 wppm and K_{TH} below 30 MPa√m. K_{TH} drops to 15 MPa√m as $C_{H,diff}$ increases to 8 wppm[18]. IHAC in AerMet™ 100 is transgranular (TG), attributed to improved austenite

boundary purity, but enabled by H trapping that promotes decohesion of martensite lath and packet interfaces[18,31,32]. AerMet™ 100 is also susceptible to SCC (that is, HEAC), with K_{TH} varying from 14 to 36 MPa√m for precracked specimens stressed in near-neutral 3.5% NaCl at the freely corroding condition[26-30]. Fractographic results for HEAC of AerMet™ 100 also vary: one experiment showed a bifurcated IG crack path[27,28], while others reported predominantly TG cracking[26,29,30]. Consequently, the hydrogen damage mechanism remains unidentified for AerMet™ 100, particularly the basis for the transgranular crack path.

I.A.   Hydrogen Trapping

Hydrogen trapping at microstructural features in UHSS; including carbides of varying coherency, martensite laths and packet interfaces, γ grain boundaries and precipitates, and dislocations[14,39-42]; can play a dominant role in HAC due to strong influences on the local solubility, C_H, and diffusivity, D_H, of hydrogen. Previous studies of AerMet™ 100 established that nano-scale, coherent and homogeneously dispersed M_2C carbide traps have low Hp-trap binding energies ($E_B \sim 11$ kJ/mol) and are reversible upon stress application, while martensite boundaries have higher binding energies ($E_B \sim 62$ kJ/mol) and are irreversible traps; these features interact to dominate IHAC[31,32]. Alternatively, Pound argued that irreversible traps dominate HAC and are large, incoherent carbides[43,44]. These differences in interpretation must be reconciled in order to understand susceptibility to HAC. Moreover, the role of hydrogen trapping depends on the H source and distribution conditions[45]. Considering IHAC of AerMet™ 100, crack tip stress causes H to repartition from uniformly distributed M_2C carbide traps to stronger trap sites at interconnected martensite interfaces within the FPZ to cause severe TG cracking[18,31,32]. In HEAC homogeneously dispersed precipitates may provide a shielding effect by trapping H within the FPZ but away from the crack path. Additionally, trapping will reduce D_H, which is predicted to reduce da/dt_{II}[17]. To test this prediction, precise measurements of crack growth and da/dt_{II} are needed.

I.B.   Effect of Applied Electrode Potential on HEAC of AerMet™ 100

Applied electrode potential, E_{App}, is a particularly important variable for aqueous HEAC because E_{App} controls crack tip overpotential that governs H production and uptake to establish C_H in the FPZ[7,46,47]. For steels, optimal resistance to HEAC is typically at E_{App} slightly cathodic to the freely corroding range, and resistance decreases for increasing cathodic as well as anodic

polarizations[47,48]. Steels are typically coated with Zn, Cd or Al to control general corrosion; coating damage will galvanically polarize the exposed steel and potentially degrade HEAC resistance[49]. On the other hand, galvanic coupling could be tailored by coating composition control to apply a potential that can reduce hydrogen production and thus subcritical cracking. The coating may also dissolve ions that inhibit crack growth by blocking hydrogen uptake at the occluded crack tip[50,51]. For AerMet™ 100, HEAC behavior in the potential range of -1.100 to -0.400 volts (saturated calomel electrode, V_{SCE}) must be understood to optimize coating design. Dependence of K_{TH} on E_{App} was investigated for AerMet™ 100[26,30], but results are limited and adversely affected by uncertainties in measured K_{TH} and limited measurements of the effect of applied potential on da/dt_{II}. This potential dependence of HEAC must be better characterized.

I.C. Time Dependence of HEAC and Loading Method

Since H production, uptake and diffusion in the FPZ are time-dependent, K_{TH} and da/dt_{II} are loading rate-dependent, given by dK/dt, and a correct protocol is necessary for accurate characterization of susceptibility[33,34]. Variances in reported K_{TH} for HEAC likely exist because determination of threshold is challenging despite efforts to standardize the method[35,36]. Reliable determination of K_{TH} with fixed load or displacement testing may require extremely long test duration (over 10,000 h) since HAC evolves very slowly in steels with low H diffusivity[17]. Characterizing HAC behavior with shorter duration testing requires a precise crack length monitoring method capable of sub-micrometer resolution, as well as consideration of time dependence. For steels with σ_{YS} above 1000 MPa√m, there is no expected difference between rising K ($dK/dt > 0$) and falling ($dK/dt < 0$) K loading protocols, and either method can be used if executed properly[7]. However, if the rate of loading exceeds the capability of the rate-limiting step to sustain HEAC, then hydrogen damage will be obscured giving false indication of increased resistance. The commonly used constant displacement protocol[35] overestimates K_{TH} if the test is terminated before crack arrest occurs or if crack length monitoring is unable to distinguish a slow moving from stationary crack.

A constant load-point displacement rate (rising K) protocol has been used successfully in studies of HEAC of UHSS[37] and IHAC of AerMet™ 100 in particular[18], as well as HEAC of high strength Al, Ni and Ti alloys[7,89]. An applied loading rate of $dK/dt \sim 0.002$ MPa√m/s enables a relatively short (~1 day) HEAC experiment. This test method produced severe IHAC in AerMet™ 100; K_{TH} was low and constant until increasing sharply with rising dK/dt only

above 0.3 MPa√m/s[18]. For HEAC of high strength 4340 steel in purified H_2, applied-rising dK/dt of 0.001-0.002 MPa√m/s yielded K_{TH} similar to that from long term constant displacement experiments[36-38]. The effect of dK/dt on K_{TH} for rising load HEAC of AerMet[TM] 100 has not been established for gaseous or aqueous environments.

I.D. Occluded Crack Electrochemistry and HEAC Test Method Design

The electrochemical conditions at a crack tip in the UHSS-chloride solution system are different from the exposed surface because the crack is occluded[46,47,52,53]. Important parameters that govern H production and uptake; particularly local pH[46], potential[53] and composition of the occluded crack solution[47]; depend on crack geometry. For example, at anodic potentials oxygen is rapidly depleted by reduction and metal dissolution causes acidification within the crack tip to increase H production and HEAC[46]. Cathodic potentials promote H production by increasing the hydrogen overpotential for alkaline crack solution and enhance the severity of HEAC[48]. These processes, and thus K_{TH} and da/dt, could depend on crack geometry[16].

Accurate electrochemical representation of service conditions requires replication of crack geometry in fracture mechanics specimens. Considering the relatively small critical crack size for an AerMet[TM] 100 landing gear on the F/A-18E/F fighter[54], the damage tolerant flaw size range of importance is a 100 μm to 3 mm deep surface defect. While a compact tension specimen with a 10 mm crack provides equivalent crack tip stress conditions, a long crack may not reproduce equivalent crack electrochemistry for a short crack[88]. Experiments established that HEAC for specimens with sub-mm cracks occurs at unexpectedly low K_{TH} values below 10 MPa√m, as reported for an older steel in chloride solution near free corrosion[16]. Specimens used in previous studies of HEAC in AerMet[TM] 100 employed fatigue precrack lengths above 1.7 mm[25-30]. This crack geometry effect must be characterized for modern UHSS. In order to monitor crack length at this scale, the direct current potential difference (dcPD) method was used to continuously measure crack length with 0.5 μm resolution[56].

I.E. Objectives

The objective of this research is to quantify the susceptibility of modern ultra-high strength steel, AerMet[TM] 100, to HEAC as a function of electrochemical polarization relevant to a coated component in the marine environment. The constant displacement rate method is employed to measure K_{TH} and da/dt_{II}, pertinent to subcritical growth of a chemically short crack.

A second objective is to understand the H-trapping and electrochemical factors that govern K_{TH} and da/dt_{II}. These results provide the basis for coating development as well as assessment of crack tip damage models necessary to predict and optimize the HEAC resistance of modern UHSS.

II. Procedure

II.A. Material and Specimen Design

Forged bar of AerMet™ 100—15 cm in diameter and 1.6 cm thick—was austenitized at 885°C for 1 h, quenched in liquid nitrogen and cold stabilized for 1 h, then aged at 482°C for 5 h and air cooled to obtain the optimal combination of plane strain fracture toughness and strength[18,21]. The chemical composition and mechanical properties are summarized in Table 1 and 2. The AerMet™ 100 microstructure was characterized by Ayer and Machmeier[21,24].

Table 1. Chemical Composition of AerMet™ 100 (Weight Percent)								
Fe	Co	Ni	Cr	Mo	C	Ti	P	S
Bal	13.43	11.08	3.00	1.18	0.23	.009	.003	.0008

Table 2. Mechanical Properties of AerMet™ 100						
HRC	σ_{YS} (MPa)	σ_{UTS} (MPa)	Reduction in Area (pct)	E (GPa)	σ_o (MPa)	K_{IC} (MPa√m)
54	1725	1965	65	194.4	1985	130

Single edge micronotch tensile (SENT) specimens were machined with a width, W, of 10.2 mm and thickness, B, of 2.54 mm. All specimens were machined with the Mode I load applied in the circumferential (C) direction and crack growth in the radial (R) or length (L) direction in the original round-forged bar. C-R and C-L were considered identical because the microstructure of AerMet™ 100 is nearly isotropic. The notch was electrospark discharge machined to a depth of 110±10 μm and mouth opening width of 65±15 μm. To measure crack growth, two platinum wires were spot welded 385±25 μm above and below the notch centerline, across the specimen thickness. The wires were soldered to shielded copper wires that were

affixed to the specimen surface using water resistant epoxy. This specimen and lead wire attachment is detailed elsewhere[56]. The wired SENT specimen was fatigue precracked to a total notch plus crack depth (a_o) of 200-950 μm in moist air at 10 Hz under constant maximum stress intensity of 11 MPa√m and constant stress ratio of 0.10.

II.B. Electrochemical Control and Loading Conditions

Each precracked specimen was loaded in a 340 ml cylindrical Plexiglas cell containing non-deaerated 0.6 M NaCl circulated from a 10 l reservoir at 24 ml/min and room temperature. Solution was not buffered, and periodic measurements of pH confirmed a constant bulk pH of 6.4 for the experiment duration. The gauge length of the specimen was exposed in the solution, precluding solution contact and galvanic coupling with the metal clevis grips. The specimen was configured as the working electrode grounded through the testing machine, while the potentiostat was operated in floating mode to avoid a ground loop. Experiments were run in potentiostatic control with applied potentials ranging from -1.1 to -0.5 V_{SCE}.

The precracked specimen was secured inside the environment chamber with flowing solution, and loaded in a servo-electric feedback controlled tensile machine under constant-slow actuator displacement rate ($d\delta/dt$). The clevis-based gripping configuration allowed free rotation about the loading pins. All specimens were preloaded quickly to 6 MPa√m, within 30 minutes of specimen polarization, then loaded at a slower test rate. Specimen load, actuator displacement, time, and dcPD data were recorded by automated acquisition.

II.C. Crack Length Measurements Using Direct Current Potential Difference

The dcPD method was used to measure crack length *in-situ*[55,56]. A constant 10.000 ± 0.005 A direct current source was attached to the specimen grips and voltage-probe wires were connected to a 10,000 gain amplifier. Voltage measurements were unaffected by electrochemical polarization because conflicting ground levels were avoided. The resolution in measured potential was 0.1 μV, which corresponded to a resolvable average crack extension, Δa, of 0.5 μm. A reference specimen was not used to compensate for spurious temperature-dependent dcPD changes because the test duration was relatively short, and additional error can be introduced due to local environmental differences between the active and reference specimens. The slowest reliably distinguishable crack growth rate was 0.2 nm/s.

For every dcPD data point recorded to file, 2,240 potential measurements were taken

over 8.6 s. Thermal voltage contribution to dcPD was eliminated through current reversal where the first 1,120 potentials were measured at an applied current of 10 A, and the latter 1,120 potentials were measured at -10.000 A with a 0.5 s delay to allow for voltage stabilization after current polarity change. The absolute values of these 2,240 voltages were averaged to calculate a single recorded dcPD value that reflected crack length only. This process was triggered every 30 s. The dcPD data were converted to crack lengths by Johnson's equation:[55]

$$a = \frac{W}{\pi}\cos^{-1}\frac{\cosh\left(\frac{\pi\,y}{W}\right)}{\cosh\left\{\frac{V}{V_0}\cosh^{-1}\left[\frac{\cosh\left(\frac{\pi\,y}{W}\right)}{\cos\left(\frac{\pi\,a_0}{W}\right)}\right]\right\}} \qquad [1]$$

where a is crack length, W is specimen width, 2y is the distance between lead wire attachments, V is measured potential, V_0 is the dcPD value at a_0 where a_0 is the initial notch depth plus crack length after fatigue precracking, as measured post-fracture. If the final crack length form dcPD did not match within 2% of the actual final crack length, then crack lengths from Eq. 1 were scaled using the following relationship:

$$a_{\text{corrected}} = a_0 + \left(a_{\text{dcPD}} - a_0\right)\frac{\left(a_{\text{final, actual}} - a_0\right)}{\left(a_{\text{final, dcPD}} - a_0\right)} \qquad [2]$$

where a_{dcPD} is the crack length calculated from Eq. 1 for a given dcPD value. $a_{\text{final,actual}}$ and $a_{\text{final,dcPD}}$ are measured and calculated values of the final crack length, respectively. Both a_0 and $a_{\text{final,actual}}$ were measured by scanning electron microscopy. A 5 point average of perpendicular distance from the notch front to final crack length was used as actual final crack length. If branching was observed, post-test correction was performed by equating $a_{\text{final,dcPD}}$ to $a_{\text{final,actual}}$, but data collected after the onset of branching were not presented.

II.D. Stress Intensity and Determination of K_{TH}

The following stress intensity solution was used for the SENT specimen with free rotation at the load points[59]:

$$K = \frac{P\sqrt{\pi a}}{BW} \sqrt{\left[\left(\frac{2W}{\pi a}\right)\tan\left(\frac{\pi a}{2W}\right)\right]} \frac{\left\{0.752 + 2.02\left(\frac{a}{W}\right) + 0.37\left[1 - \sin\left(\frac{\pi a}{2W}\right)^3\right]\right\}}{\cos\left(\frac{\pi a}{2W}\right)} \qquad [3]$$

where P is load, B is specimen thickness, W is specimen width and a is crack length.

To define K_{TH}, a plot of P and dcPD values *vs* load-point displacement, δ, was used (Figure 1)[58]. First, a probable crack growth initiation point, δ`, was chosen by visually estimating first deviation in the linear dcPD-$\delta$ data (Figure 1b). A baseline was fit by linear regression from 0.7 $\delta$` to 0.95 δ`, a range selected to eliminate artifacts such as precrack closure in the 0-0.7 $\delta$` range. A 0.2 µV vertical offset was constructed from this baseline. A crack growth line is conventionally fit by linear regression from 1.05 δ` to 1.3 $\delta$`. However, due to large variance in crack growth behavior among specimens, the growth line fit was based on an assumed initiation dcPD level (*dcPD*`); with linear regression from 1.01 *dcPD*` to 1.05 *dcPD*`. K_{TH} was defined operationally as K at the intersection of this growth line and the 0.2 µV initiation line offset. To calculate crack growth rate at a given time and K, a 2nd order polynomial was fit to a *vs* t data over $t \pm 25$ data points. The slope of the tangent at the mid-time point was *da/dt* and this process was repeated to obtain *da/dt* at every value of a. Loading rate (*dK/dt*) was defined in the same manner. The *da/dt*$_{II}$ is the average *da/dt* over the Stage-II regime, or reported as a range if growth rate depends mildly on K.

II.E. Fracture Surface Analysis

Fracture surfaces were cleaned ultrasonically in acetone then methanol for 10 minutes, dried, and stored in a desiccator. When necessary, specimens were polarized to -1.5 V_{SCE} in 0.5 M H_2SO_4 for 60 s or soaked in 10% HCl for 1 ~ 20 minutes to remove corrosion products. A specimen was examined using optical and scanning electron microscopes (SEM). All SEM images are secondary electron images obtained using either 10 kV or 20 kV accelerating voltage. The working distance was varied from 10 mm to 39 mm for optimal conditions. Unless noted, the crack advanced from bottom to top of an SEM or optical image.

III. Results

III.A. K_{TH} and Crack Growth Kinetics Near Free Corrosion

AerMet[TM] 100 is susceptible to severe HEAC in neutral 3.5% NaCl near the free corrosion potential. Figure 1 is a plot of P and dcPD *vs.* δ for an SENT specimen tested at -0.500 V_{SCE}, maintained constant near the measured open circuit potential of -0.51 $\pm$ 0.01 V_{SCE}. From Figure 1b, the operationally defined K_{TH} is 18 MPa√m, followed by accelerating dcPD and thus subcritical crack growth. Crack initiation is easily detected due to high resolution dcPD crack length monitoring and fast da/dt. The low K_{TH} of 18 MPa√m agrees with previously reported threshold values[26-29], validating the constant extension rate test method for evaluating K_{TH}. Figure 2 shows the stark contrast in crack growth resistance for AerMet[TM] 100 stressed in 3.5% NaCl compared to moist air[18], illustrating severe HEAC susceptibility.

Measured subcritical crack growth kinetics are typical of HEAC and reported in Figure 3. The apparent non-zero da/dt below K_{TH} (below 0.2 nm/s) is an experimental artifact related to crack tip blunting, dcPD signal variability, and crack opening effects on dcPD as discussed later. Stage I crack growth behavior is shown clearly; da/dt increases nearly 3 orders of magnitude as K increases from 13 MPa√m to 27 MPa√m. While dK/dt is initially constant with fixed dP/dt (0.0007 MPa√m/s), the onset of subcritical crack propagation leads to continuous increase in dK/dt to as high as 0.004 MPa√m/s. For this loading, a clear Stage-II region is shown with an average da/dt_{II} of 80 nm/s mildly dependent on K. Figure 3 shows that the operationally defined K_{TH} from Figure 1b is greater than the K level at the onset of Stage I growth, in this case 18 MPa√m *vs.* 13 MPa√m for loading at -0.5 V_{SCE}.

Optical micrographs (Figure 4a-b) show the macro morphology and extent of Mode I HEAC with severe crack branching. The crack branched at K of about 80 MPa√m after 1 mm of growth, similar to crack branching reported for a constant displacement, falling K test with AerMet[TM] 100[33]. SEM images at crack initiation were compromised due to corrosion, however, fractographs from near the end of the crack (location A in Figure 4a) reveal TG fracture mixed with some evidence of IG growth (Figure 4c and d). This TG crack path is very different from the microvoid-based morphology typical of ductile fracture in AerMet[TM]100 at K_{IC}[18].

III.B. Effect of Applied Electrode Potential on K_{TH} and Crack Growth Kinetics

Applied electrode potential has a pronounced effect on K_{TH}, as summarized in Figure 5. At the most negative potential of -1.100 V_{SCE}, K_{TH} is lowest at 9.3 MPa√m, which is only 7% of K_{IC}. As potential is raised, K_{TH} increases to a peak value of 41 MPa√m (32 % of K_{IC}) at -0.625 V_{SCE} and drops sharply to 18 MPa√m (14 % of K_{IC}) at -0.5 V_{SCE}. An operationally defined K_{TH} value could not be obtained for the -0.625 V_{SCE} polarization with a 242 µm precrack because dcPD signal variability obscured slow-crack growth detection and the maximum K level achievable without significant net-section plastic deformation was 50 MPa√m. Therefore a specimen with a 947 µm precrack was used to expand the linear-elastic loading range to 100 MPa√m, and a threshold value was obtained following the protocol illustrated in Figure 1. These results establish significant resistance to HEAC at E_{App} of -0.625 V_{SCE} and -0.700 V_{SCE}.

HEAC kinetics are highly dependent on applied electrode potential, with Stage-II growth rates varying over 3 orders of magnitude. Figure 6 shows that specimens polarized at E_{App} of -1.1 V_{SCE}, -0.9 V_{SCE} and -0.5 V_{SCE} exhibited clearly distinguishable Stage-I and II crack growth regimes. As specimens are loaded above K_{TH}, subcritical crack growth initiates and crack velocity increases rapidly. These crack velocities reached plateaus suggesting approximately K-independent Stage-II growth. Notably, da/dt_{II} decreased from about 500 nm/s to 8-20 nm/s as E_{App} changed from -1.1 V_{SCE} to -0.9 V_{SCE}, and to as low as 0.5-2 nm/s at E_{App} of –0.7 V_{SCE} and –0.625 V_{SCE}, before rising to 60-90 nm/s at -0.5 V_{SCE}. This trend is quantified in Figure 7 using average measured da/dt_{II} represented by the filled symbols. Subcritical cracking over mm-scale distances and severe susceptibility to HEAC are unmistakable for three potentials; -1.1 V_{SCE}, -0.9 V_{SCE}, and -0.5 V_{SCE}.

As shown in Figure 6 and 7, E_{App} of -0.625 V_{SCE} and -0.7 V_{SCE} produced unique behavior with substantially slower da/dt, suggesting high resistance to HEAC. Large increases in K caused only small increases in crack velocity, even when the specimens were loaded beyond the operationally defined level of K_{TH} plotted in Figure 5. For these cases, it is likely that Stage-I behavior exists, but the levels of da/dt are below the 0.2 nm/s noise level inherent in dcPD instrumentation. The behavior observed at -0.625 V_{SCE} and -0.7 V_{SCE} is not complete immunity because subcritical crack growth in fact occurred at these potentials, albeit at very slow growth rates. For example, the specimen polarized to -0.625 V_{SCE} with $a_0 = 242$ µm showed 28 µm of crack growth as it was loaded to $K = 50$ MPa√m over 20 h. The da/dt_{II} is two orders of

magnitude slower than the level at -0.5 V_{SCE}. The sharp increase in *da/dt* at *K* of 100 MPa√m for the specimen stressed at -0.625 V_{SCE} is likely due to hydrogen enhanced microvoid nucleation at *K* somewhat below the H-free K_{IC} level of 130 MPa√m[18].

III.C. Effect of Applied Potential on HEAC Morphology in AerMet™ 100

Fractographic analyses show that HEAC occurred at all electrode potentials examined, but such subcritical cracking was limited to very small increments of growth for E_{App} of -0.700 V_{SCE} and -0.625 V_{SCE}, and consistent with Figure 6 and 7. Post-fracture optical images in Figure 8 characterize the macroscopic HEAC front shape as a function of potential. In these low magnification images, specimen thickness is 2,550 μm and the notch plus fatigue precrack of about 250 μm is barely visible as a bright area at the bottom of each image. The post-test fracture surfaces are shaded and HEAC is darkened in tone from surface roughness and slight corrosion. Parts (a) and (b) show significant crack growth at *K* below 20 MPa√m for the two most negative potentials, while (c) and (d) show no optically resolvable crack growth at *K* = 50 MPa√m for E_{App} = -0.7 V_{SCE} and -0.625 V_{SCE}. The specimen in (e) contained a larger precrack (947 μm) and was loaded above *K* of 100 MPa√m, but crack growth is not visible. What appears to be a H crack is the fatigue precrack with surface staining. Figure 8f shows substantial HEAC, with the surface covered with black corrosion products produced by polarization at -0.5 V_{SCE}.

The effect of potential on HEAC susceptibility is apparent in Figure 8. Test duration for each specimen was approximately 20 h, with the exception at E_{App} of -1.1 V_{SCE}, which fractured after 7 h. With identical specimen geometry and loading, E_{App} of -0.7 V_{SCE} produced crack growth of 0.05 mm in 20 h, while the E_{App} of -1.1 V_{SCE} produced 5 mm of HEAC in 7 h. Cracking was similarly limited at -0.625 V_{SCE}, but extensive at -0.5 V_{SCE} and -0.9 V_{SCE}. Above E_{App} of -0.7 V_{SCE}, the final crack front is parallel to the fatigue precrack. However, at E_{App} below -0.9 V_{SCE} the crack front is V shaped (Figure 8a and b). Since all specimens were fatigue precracked to a flat initial crack front, with similar *K* levels and constraint, the final crack front shape must result from an electrochemical effect on H production and uptake.

High magnification scanning electron microscopy established that HEAC in AerMet™ 100 was predominantly transgranular at all potentials examined, with the exception of cracking near the open circuit potential. This cracking morphology is clearly unique compared to the microvoid fracture mode typical of H-free fracture in moist air[18], confirming HEAC at each

potential. There was only limited evidence of IG cracking at cathodic applied potentials. An example is shown in Figure 9; HEAC at -1.1 V_{SCE} was completely TG (Figure 9b) and very different from the microvoid morphology typical of fracture in moist air (Figure 9a). Evidence of martensite lath interface cracking is indicated by arrows in Figure 9b, and this path of HEAC is similar to the fractographs obtained for IHAC of this same steel and heat treatment[18]. This TG HEAC is more complex at other potentials, as illustrated in Figure 4 and 10. At E_{App} of -0.9 V_{SCE}, the fracture surface shows predominantly TG cracking (Figure 10a) with localized areas of rough morphology with IG character (triangular arrows in Figure 10a and b). Evidence of martensite lath interface or packet boundary cracking can be found (diamond tipped arrows in Figure 10a and b). Because IG fracture was only suggested on this specimen and not observed at other potentials, the behavior could be due to localized impurity segregation. Alternatively, small deviations in temperature and H concentration can are known to cause a change in the fracture mode for HEAC of UHSS[9,90]. Diffusible hydrogen concentration of 7.8 wppm caused limited IG cracking in IHAC of this steel[60].

Two fractographs for E_{App} of -0.7 V_{SCE} and -0.625 V_{SCE} (Figure 10c and e) represent the entire loading range from K of 10 MPa√m to 50 MPa√m. These figures prove that HEAC cracking occurred at both -0.7 V_{SCE} and -0.625 V_{SCE} at growth rates below 1 nm/s with Δa of 50 and 28 μm, respectably, during the 20 h exposure. The fracture surface at -0.7 V_{SCE} is rough (Figure 10d), but the larger features are TG with little resemblance to IG cracking. (Prior austenite grains in this steel are approximately 10~20 μm in diameter.) At -0.625 V_{SCE}, the crack path is completely TG, ending in a flat area seen in Figure 10e and that could be associated with the limited extent of rapid cracking at high K (Figure 6). For this E_{App}, there is no evidence of IG features (Figure 10e and f). Martensite lath interface cracking was observed at both potentials (diamonded tipped arrows in Figure 10c to f). In general, the likelihood of the limited IG-type features coincided with increasing K, crack branching and increased hydrogen production.

III.D. Alternative Method for Measuring K_{TH}

The operational definition of K_{TH} shown in Figure 1b characterizes the stress intensity required to cause the onset of a resolvable amount of HEAC in AerMet™ 100 under rising load-point displacement. At -1.1 V_{SCE} and -0.5 V_{SCE}, K_{TH} is easily established because rapid Stage I cracking is readily detected. However, the operational values exceed a true threshold by a significant amount due to the offset method of K_{TH} determination (Figure 1b) and rapid da/dt.

This is illustrated by the interval between 13 MPa√m and the operational K_{TH} of 18 MPa√m, Figure 3. A second error is evident for loading at -0.7 V_{SCE} and -0.625 V_{SCE}, where crack growth initiation is masked due to extremely slow Stage I crack growth and Stage II crack growth is below 1 nm/s. The combined SEM images and dcPD data suggest that real crack growth occurred below the operational threshold at these slow cracking potentials and that this operational K_{TH} not an accurate descriptor of a true threshold.

To improve estimation of a threshold for the onset of HEAC and exploit high resolution crack monitoring, an alternative K_{TH}^* was defined as the level of K required to produce measured da/dt of 1 nm/s. This growth rate was chosen because it is the lowest distinguishable rate from the baseline dcPD signal in Figure 6 that can be unambiguously confirmed by SEM images. K_{TH}^*, along with the key results of all experiments, are summarized in Table 3.

Table 3. Summary of HEAC Test Results

E_{App} (V_{SCE})	a_o (µm)	Initial dK/dt (MPa√m/s)[#]	K_{TH} (MPa√m) Figure 5	K_{TH}^* (MPa√m) Figure 6	da/dt_{II} (nm/s) Figure 7	Total Δa (mm)	Termination
-1.100	251	6.1 x 10⁻⁴	9.3	8.3	300-700	~5	Fracture
-0.900	234	7.1 x 10⁻⁴	13.0	10.7	8-20	~4	Branched
-0.700	212	5.5 x 10⁻⁴	24.0	20.1	0.9-2	0.050	Stop/Unload
-0.625	242	5.0 x 10⁻⁴	-	-	-	0.028	Stop/Unload
-0.625	947	11.0 x 10⁻⁴	40.8	22.3	~1	0.1	Stop/Unload
-0.500	250	6.8 x 10⁻⁴	18.0	15.8	60-90	~2	Branched

[#] Applied $d\delta/dt$ = 12.7 nm/s for all experiments

IV. Discussion

IV.A. HEAC of AerMet™ 100

The short precrack rising displacement results in Figure 3 and Table 3 establish that optimally aged AerMet™ 100 is susceptible to severe transgranular HEAC in neutral 3.5 % NaCl at free corrosion potentials (~ -0.5 V_{SCE}). The values of K_{TH}^* and K_{TH} are between 16 and 18 MPa√m compared to K_{IC} that is almost an order of magnitude higher. This HEAC behavior is consistent with severe TG IHAC of AerMet™ 100[18], as well as previous HEAC studies with

AerMet™ 100 using specimens with longer fatigue precracks and various loading methods[25-30]. Specifically, constant displacement testing showed crack arrest at K_{TH} of 14 MPa√m for 1,000 h total exposure time[26-28], and constant load testing for 10,000 h resulted in K_{TH} of 16-22 MPa√m[25,26]. Rising step load experiments yielded K_{TH} of 27 MPa√m[25,26,30] and a single short-term crack arrest result equated K_{TH} to 14 MPa√m for 20 h exposure[29]. These test results exhibit substantial variability that bracket the present results, as summarized for E_{App} of -0.5 V_{SCE} in Figure 11. Considering the electrode potential dependence of HEAC in AerMet™ 100, operationally defined K_{TH} values are consistent and perhaps lower compared to previous reports[25-30] (Figure 11). Compared to rising step-load test results[25,26,30], this K_{TH} is lower at E_{App} of -1.1 V_{SCE} and -0.9 V_{SCE}, essentially equal for -0.7 V_{SCE}, and higher for -0.625 V_{SCE}. For K_{TH}^*, Figure 11 shows a lower measured threshold compared to existing literature at all tested potentials. Either measure of threshold stress intensity demonstrates that HEAC in AerMet™ 100 is severe at both open circuit potential and below -0.9 V_{SCE}, while E_{App} from -0.625 V_{SCE} to -0.7 V_{SCE} provides optimal resistance to HEAC.

Results show that the present accelerated test method, coupled with high resolution crack growth measurement by dcPD, efficiently provides lower bound K_{TH} values (Figure 11) that are relevant to alloy and coating system design, as well as component performance prediction. While all specimens tested were relatively small, the maximum net section tensile stress was below the steel flow strength (1,845 MPa, Table 2), and the plastic zone diameter ($(K/\sigma_{YS})^2/(3\pi)$ = 160 μm at 70 MPa√m) was less than 10% of the remaining ligament, even at the highest K levels and longest crack lengths examined. As such, small scale yielding was guaranteed. Moreover, the small plastic zone diameter to thickness ratio (< 1-4%), lack of resolvable shear walls (Figure 8), and Mode I crack geometry strongly suggest that HEAC was under predominant plane strain deformation. As such, the results in Figure 11 are scalable to large components. The low values of threshold validate the selected dK/dt (~ 0.0007 MPa√m/s in Table 3) as producing K_{TH} that is independent of loading rate. This result is consistent with the loading rate independence of K_{TH} for IHAC in AerMet™ 100 for all dK/dt < 0.3 MPa√m/s[18] and results for gaseous environment HEAC in high strength 4340 steel[37]. A strong effect of precrack length on K_{TH} is not apparent in Figure 11, particularly given test method and crack resolution differences[16]. It is reasonable to conclude that these values represent lower bounds on HEAC resistance.

Experimental characterization establishes that improved steel composition and thermal-mechanical processing increased σ_{YS} and K_{IC} for AerMet™ 100, but did not provide immunity to HEAC at any tested E_{App}. This susceptibility of AerMet™ 100 to HAC typified by low K_{TH}* may limit application of this modern alloy. However, the dramatic decrease in HEAC susceptibility at optimal E_{App} illustrated by greatly reduced da/dt_{II} is established for the short crack case. This behavior is relevant to small surface cracks in coated UHSS components such as a landing gear.

IV.B.   Effect of Steel Composition on Intergranular HEAC

Instances of intergranular HEAC and IHAC in AerMet™ 100 were rarely observed in the present experiments and evidence for this failure mode is limited. Eun reported IG HEAC along interfaces speculated to contain impurities segregated during processing[28], but such an IG crack growth path was not observed in present experiments or other reports[26,29,30]. In sharp contrast, older UHSSs such as AISI 4340, 18Ni Maraging and 300M show severe IG HEAC for a wide range of composition, thermal treatment and environmental conditions[7,8,48]. Impurity segregation to prior austenite grain boundaries is reported to interact with H and cause IG cracking[8], as characterized by McMahon and coworkers using an impurity-weighted composition parameter (ψ = Mn + 0.5 Si + S + P in weight %)[8,13,15]. As ψ increases, K_{TH} decreases and the amount of IG cracking increases; immunity to IG HAC is expected for ψ below about 0.05 wt % for steel of σ_{YS} = 1450 MPa[15]. While ψ accurately predicts the lack of IG HAC in high purity AerMet™ 100, K_{TH} values measured for TG HEAC (Table 3) and TG IHAC[18] are far below the values predicted by ψ for this lower strength level of steel. To further investigate the impurity dependence of HEAC of UHSS, high purity 18Ni Maraging and Custom 465™ stainless steels with low Mn and Si were compared to AerMet™ 100). Despite low ψ values of 0.05 to 0.08 wt %, 18Ni Maraging steel and Custom 465™ are susceptible to severe IG HEAC for chloride solution at free corrosion potentials with K_{TH} below 15 MPa√m.

	σ_{YS} (MPa)	H-free ψ	Mn (wt %)	Si (wt %)	P (wt %)	S (wt %)	K_{TH} at free corrosion (MPa√m)	HEAC Mode
AerMet™ 100	1725	0.029	0.019	0.016	0.001	0.0008	~15	TG
18 Ni Maraging[48]	1700	0.045	0.025	0.015	0.008	0.005	~10	IG
Custom 465™ *	1600	0.079	0.05	0.04	0.001	0.008	~10	IG

Table 4. Comparison of HEAC and ψ for Commercial High Purity UHSS

Hydrogen uptake and steel yield strength affect this ψ correlation, as recognized by McMahon et al.[8,15]. For a high purity (Mn and Si free) steel, K_{TH} decreased from 95 MPa√m to 35 MPa√m with increasing yield strength from 1450 MPa to 1860 MPa and increasing H_2 pressure, presumably associated with increasing intergranular cracking. These additional effects were well described by a revised composition parameter that included an estimate of crack tip H content, $\psi = 10^4\ C_{H-S} + Mn + 0.5\ Si + S + P$, with immunity suggested for ψ below 0.7 atom %[8,15]. Here, C_{H-S} was calculated from Sievert's law for gaseous exposure, increased to account for crack tip stress but not considering trapping. The multiplier of 10^4 was necessary to fit the H concentration effect with that of the other elements. While the Maraging and Custom 465™ steels are relatively pure, the H concentration from NaCl may be sufficiently high to align K_{TH} results with this H-containing ψ correlation for IG cracking in H_2. Compared to AerMet™ 100, prominent IG cracking may be due to somewhat higher S, Mn and Si contents in the Maraging and Custom 465 steels, and hence slightly higher H-modified ψ (Table 4), but this is speculative since austenite grain boundary compositions were not measured. While it is uncertain whether lower purity AerMet™ 100 will display IG HEAC and IHAC, these comparisons show that grain boundary purity is not the single critical factor that governs HAC immunity in modern and relatively pure UHSS. As developed in an ensuing section, very high levels of H can be trapped at austenite and martensite boundaries in UHHS, enhanced by very high crack tip stress and high trap binding energy. K_{TH} is controlled by this localized H, coupled with the intrinsic boundary strength and reduction due to H decohesion. The H-modified ψ suggested by McMahon and

---

* In collaboration with Kehler and Scully, 2 cm diameter round bar of Custom 465™ was aged for 4 h at 482°C and air cooled to obtain σ_{YS} = 1600 MPa[91]. Specimens were machined and tested with identical loading and electrochemical conditions outlined for AerMet™ 100. HEAC of Custom 465™ was IG with K_{TH} below 12 MPa√m at all tested E_{App} of -1.100, -0.625, -0.575, and -0.500 V_{SCE} [91].

coworkers[8,15] is aligned with this explanation, but is not sufficiently quantitative.

IV.C. Effect of Applied Potential

Applied electrode potential strongly affects the kinetics of HEAC in AerMet[TM] 100, as shown by the results in Figures 6, 7 and 11. Pioneering work by Brown qualitatively demonstrated the effect of E_{App} on da/dt, with the slowest crack growth rates for older UHSSs in the applied potential range of -0.8 V_{SCE} to -0.9 V_{SCE} and increased cracking at more anodic and more cathodic potentials[47]. Similar effects were noted for HEAC of 18Ni Maraging steel, with optimal cracking resistance at an applied potential ~0.2 V cathodic of free corrosion[48]. AerMet[TM] 100 parallels this potential dependence (Figure 11), with the highest K_{TH} and lowest da/dt_{II} values when polarized to -0.7 V_{SCE} and -0.625 V_{SCE}, or slightly cathodic with regard to the open circuit potential of -0.51 V_{SCE}.

The potential dependence of HEAC is explained based on changes in the concentration of lattice-dissolved H (C_L), in equilibrium with crack tip pH and potential. The electrochemical principles that govern C_L vs. E_{App} are well established[7,47,52,61,62] and modeling approaches for idealized-quantitative prediction have been developed[16,46,63]. It is not, however, possible to accurately predict absolute values of C_L, $K_{TH}*$, and da/dt_{II} vs. E_{App}[7]. The trend in these properties is predicted based on a minimum in the overpotential for crack tip H production. Specifically, H overpotential and C_L are large, with associated low $K_{TH}*$ and high da/dt_{II} for two regimes of applied potential. When crack tip corrosion occurs near free corrosion, local pH is lowered relative to the bulk-neutral chloride solution via hydrolytic acidification of Fe and Cr, to increase overpotential at the crack tip relative to the boldly exposed surface. At the other extreme, substantial and increasing cathodic polarization promotes increasingly high H overpotential and thus increased C_L. The maximum in $K_{TH}*$ and minimum in da/dt_{II} are produced in the range of E_{App} where crack tip dissolution and acidification are reduced to near 0 and crack tip cathodic polarization is minimal, producing minimal overpotential and minimal C_L.[†] Quantitative coupling of this E_{App} dependence of C_L with $K_{TH}*$ and da/dt_{II} is considered in

---

[†] Crack front shape exhibited significant differences due to applied potential change, as shown in Figure 8. This behavior is consistent with the fact that crack tip cathodic polarization is somewhat less than that at bold surfaces due to crack potential difference and crack pH increase. At anodic potentials, the crack advances as a flat front without preferential propagation at the side surface because H overpotential is much larger within the crack compared to the boldly exposed surfaces.

the ensuing section on micromechanical modeling of FPZ H embrittlement.

IV.D. Stress and Trapping Enhanced H Localization

The severity of transgranular HEAC in a high purity UHSS such as AerMet[TM] 100 is understood based on significant crack tip microstructural trapping and stress enhancement of C_L. This enhanced H concentration, $C_{H\sigma,T}$, is approximated by:[7,84,93]

$$C_{H\sigma,T} = C_L \exp\left(\frac{E_B}{RT}\right) \cdot \exp\left(\frac{\sigma_H V_H}{RT}\right)$$ [4]

where V_H is the partial molar volume of H in the lattice (2.0 cm^3/mol), σ_H is crack tip hydrostatic stress, E_B is the binding energy of H to a specific trap site, R the universal gas constant and T is temperature. Equation 4 is accurate for the situation where $C_{H\sigma,T}$ << 100 atom percent. For a given value of C_L, the equilibrium concentration of hydrogen at interconnected microstructural sites that constitute the crack path is determined by the stress field interaction energy ($\sigma_H V_H$) plus E_B, assuming that σ_H does not affect E_B. While C_L is typically low, of order 0.0005 wppm for a H overpotential of 0[14,18,62], $C_{H\sigma,T}/C_L$ is high for a high purity UHSS and it is this enhancement that drives HEAC. Crack tip σ_H is 3 to 10 times σ_{YS} due to various crack tip shielding mechanisms as modeled by traditional plasticity considerations, dislocation mechanics or strain gradient continuum plasticity[7,64-66]. For a reasonable crack tip hydrostatic stress of 5σ_{YS}, $\sigma_H V_H$ is ~17.5 kJ/mol for AerMet[TM]100, yielding $C_{H\sigma,T}/C_L$ of 1,200 from Eq. 4. Fractographic results in Figure 9 and 10 show brittle TG features consistent with cracking along martensite lath interfaces and packet boundaries. A very large concentration of H accumulates along these incoherent interfaces due to preferential trapping. The binding energy for H to such trap sites is about 60 kJ/mol[31,32]; from Eq. 4, $C_{H\sigma,T}/C_L$ = 6 x 10^6 for a lower bound of this binding energy (40 kJ/mole) coupled with $\sigma_H V_H$ of ~17.5 kJ/mol. For the zero overpotential estimate of C_L, the maximum value of $C_{H\sigma,T}$ enriched along martensite interfaces is 1,600 wppm (9 atom pct). This hydrogen enrichment provides ample cause for interface weakening by the decohesion mechanism and thus the path for HEAC, consistent with results for IHAC of AerMet[TM] 100[18]. Crack tip electrochemical conditions that cause a finite H overpotential will increase this level of FPZ H to lower K_{TH}, while surface reaction rate and H diffusion rate limitations will reduce da/dt_{II}

The lack of prior austenite boundary cracking in HEAC or IHAC is not explained by increased grain boundary purity because the binding energy of H to incoherent grain boundaries typically exceeds 50 kJ/mol[32], and such interfaces should trap H analogous to the case for martensite lath and packet boundaries. Such a high $C_{H\sigma,T}$ should embrittle prior austenite grain boundaries in the absence of co-segregated impurities. The fact that IG cracking is observed in a wide range of UHSSs negates the argument that there is a small probability that large (10-20 μm) prior austenite grain boundaries intersect the sub-μm FPZ compared to martensite lath and packets sized from 0.5 μm to 5 μm. The alternate hypothesis is that the intrinsic fracture strength of segregation-free prior austenite boundaries exceeds that of certain martensite interfaces for equal or even greater concentrations of trapped H.

Thin-film austenite that precipitates between martensite laths could provide an explanation for a preferred martensite interface crack path crack path in both IHAC[18] and HEAC of AerMet™100. This phase, which forms during aging, likely enhances $C_{H\sigma,T}$ through trapping and solubility considerations. Moreover, elevated stresses in the FPZ could cause thin-flim γ` to transform to martensite of higher volume ahead of the crack tip[67,68]. If this fcc austenite is enriched with H, the martensite will be supersaturated causing a transient increase in interlath hydrogen concentration which will further enhance interface cracking. Conversely, Ritchie et al. showed that retained interlath austenite is mechanically stable when present as a continuous network, and enhances intergranular cracking resistance by attracting impurities and impeding H diffusion[69]. Olson argued that a thin austensite film is stabilized because the number of martensite nucleation sites is small and partitioned alloy content is high[70]. Nohara's composition correlation for stainless steels (which does not consider Co) shows that the deformation induced martensite transformation temperature (M_D) of γ` in AerMet™ 100 is far below 0 K ($M_D$ = -390 °C)[71]. This stability is countered by the fact that dissolved H promotes γ transformation to martensite[72,73]. The relative importance of these competing mechanisms is unclear for γ` in AerMet™100.

Hydrogen traps play a complex role in both IHAC and HEAC of high strength alloys[7,14,39,44,74]. In HEAC consideration of H diffusion suggests that H damage is localized to within 1 μm from the crack tip surface[7,17]. The dcPD measurements of HEAC in AerMet™ 100 stressed in NaCl did not evidence discontinuous crack advance at the 1μm resolution level, consistent with this small FPZ distance. For a prior austenite grain size of 10~20 μm, a 1μm

FPZ contains a small fraction of γ grain boundaries and coarse carbides, a somewhat higher density of martensite boundaries, but a very dense population of homogeneously distributed M_2C precipitates. M_2C traps within the FPZ could shield the FPZ from hydrogen damage by trapping H preferentially away from the martensite interfaces. A homogeneously dispersed fine carbide phase will only act as a beneficial shielding trap in HEAC if: (a) E_B is substantially higher than E_B for crack path trapping,[‡] and (b) trapping at fine particles is not saturated by the high level of C_L and finite number of carbides in the FPZ. These conditions were not realized for peak aged AerMet[TM] 100, and low K_{TH}* for TG HEAC were produced at both cathodic and anodic potentials. Speculatively, the M_2C phase could be coarsened to reduce coherence and increase E_B to induce H shielding, for example through higher temperature aging or Cr addition[21,23,24]. Such shielding may be particularly exploited at E_{App} between -0.625 and -0.700 V_{SCE} where the absorbed hydrogen concentration is reduced by lower crack tip driving force for H production. While K_{TH} is controlled by equilibrium C_L, da/dt_{II} may be limited by H diffusion or surface reaction rate control. When the latter is important, the likelihood of carbide trap saturation is reduced and the relative beneficial effect of such shielding should be enhanced. In the least, interaction with M_2C results in reduced H diffusivity and thus reduced da/dt_{II} as developed in the next section.

IV.E. HEAC Propagation Kinetics

HEAC propagation kinetics are understood based on the concept of a rate limiting step in the overall sequence of H production on the crack surface and delivery to the FPZ [7,9,92]. Surface reaction controls da/dt_{II} if the rates of H production, migration, adsorption or absorption are slower than the rate of H diffusion from the sub-surface to the FPZ. Weakly aggressive environments or coated surfaces which block H permeation are representative cases of surface reaction limited growth, in which trap enhanced H concentration under the exposed crack tip surface, C_S, changes with time. For more aggressive environments, C_S reaches an equilibrium level quickly and H diffusion controls da/dt_{II}[63]. A one dimension model, solved with a variety of boundary conditions, yields a prediction for da/dt_{II} of the form[17]:

[‡]   Based on relative trap binding energies, E_B = 11 kJ/mole for coherent M_2C and 40-60 kJ/mol for incoherent martensite interfaces[32], the probability that H partitions to the martensite from M_2C is near unity[75,76].

$$da/dt_{II} = \frac{D_H}{X_C}\left[\xi\left(\frac{C_S}{C_C}, D_H, X_C, \sigma_{YS}, t\right)\right] \qquad [5]$$

where t is time, X_C is a critical distance ahead of the crack tip surface, C_C is a critical H concentration necessary for damage, and ξ is a functional description of the driving force for H ingress that depends on the assumed boundary conditions[17,77,78,80-82,93]. The C_C depends on local stress. In this modeling, the crack is hypothesized to propagate when C_C is reached at X_C such that:

$$\frac{da}{dt_{II}} = \frac{X_C}{\Delta t} \qquad [6]$$

where Δt is the time required for the hydrogen concentration to reach C_C at locations on average X_C within the FPZ.

Figure 7 shows that E_{App} strongly affects da/dt_{II} for HEAC in AerMet™100, with a minimum produced by cathodic polarization from free corrosion through -0.7 V_{SCE}, followed by increasing da/dt_{II} to 0.7 µm/s at -1.1 V_{SCE}. The electrochemical driving force for H production is very high at this potential and HEAC can be presumed to be diffusion limited. This expectation is supported by an empirical correlation between upper bound plateau crack growth rates for a wide variety of high strength alloys, plotted in Figure 12 vs. trap sensitive H diffusivity, D_H[17]. The linear dependence of da/dt_{II} on D_H is confirmed for situations involving very severe environments, including AerMet™100 under severe cathodic polarization (-1.1 V_{SCE}) and presumably high levels of C_S that are established rapidly resulting in diffusion limited HEAC. For this upper bound correlation, and an assumed value of the ξ function equal to 3, the data in Figure 12 suggest that X_C = 0.7 µm. It is important to determine the extent to which the diffusion based modeling, Eqs. 5 and 6, can predict the electrode potential dependence of da/dt_{II} shown in Figure. 7. Kehler et al. used the measured E_{App} dependence of K_{TH} shown in Figure 5 with the constants shown in Table 5 to predict the E_{App} dependence of C_S for AerMet™ 100 in NaCl solution[50]. This is the local H concentration in the FPZ and in equilibrium with a given applied potential, and crack tip H overpotential. This crack surface concentration boundary condition is a critical element of crack growth rate analysis, and the use of reverse engineering from a threshold-based model is a valid starting point for da/dt_{II} modeling, as demonstrated by Symon and Hall for HEAC of nickel-based superalloys[82,93]. This kinetics modeling will be complicated by the likelihood that: (a) D_H depends on hydrogen concentration and trap density, (b) the

binding energies of trap states associated with the critically important martensite lath and packet interfaces are not sufficiently quantified[32], and (c) the critical distance developed from the correlation shown in Figure 12 may vary with E_{App} and thus C_S. Additionally, C_S may not be at equilibrium with the crack tip H overpotential in the time frame of crack advance; as such, da/dt_{II} would not be strictly H diffusion limited as required for Eq. 5 to be valid[63]. This detailed analysis of crack growth kinetics is the subject of proposed research in the next phase of this project[94].

The engineering significance of da/dt_{II} is especially pronounced when da/dt_{II} is slow, as it is at -0.625 V_{SCE} and -0.7 V_{SCE} in Figure 7. For example if a component is polarized to -0.625 V_{SCE}, it would take 70 days of continuous loading at 50 MPa√m in 3.5% NaCl to grow the critical crack size of 6 mm prescribed for an AerMet[TM]100 landing gear[54]. This is of critical importance, because the same loading conditions at -0.5 V_{SCE} would grow the same crack length in 20 h; at -1.1 V_{SCE} it would take less than 4 h. Although the experimental results in this work show that perfect immunity is not obtained at any potential, polarization at -0.7 V_{SCE} to -0.625 V_{SCE} can significantly prolong component lifetime and reduce inspection frequency. This regime of applied potential is ideally suited for coupling with H production or uptake inhibitors, or microstructural alteration of H trap states, as the foundation for mitigating HEAC of UHSS.

V. Conclusions

1. AerMet[TM] 100 is susceptible to severe transgranular hydrogen environment assisted cracking (HEAC) when stressed under slow-rising displacement in neutral 3.5% NaCl and at near free corrosion potentials, as quantified by two parameters: reduced threshold stress-intensity for HEAC, K_{TH}, to as low as 10% of K_{IC}, and subcritical crack growth rate, da/dt, as high as hydrogen diffusion rate limited values on the order of 0.5 μm/s.

2. The slow-rising load method with high-precision dcPD monitoring of crack growth provides an accurate and accelerated characterization of the operationally defined threshold-onset of HEAC for da/dt above 1-2 nm/s. The true threshold and Stage I growth kinetics are ambiguous for cases where da/dt is less than this level.

3. Short crack size does not dramatically promote HEAC of AerMet[TM] 100 in NaCl compared
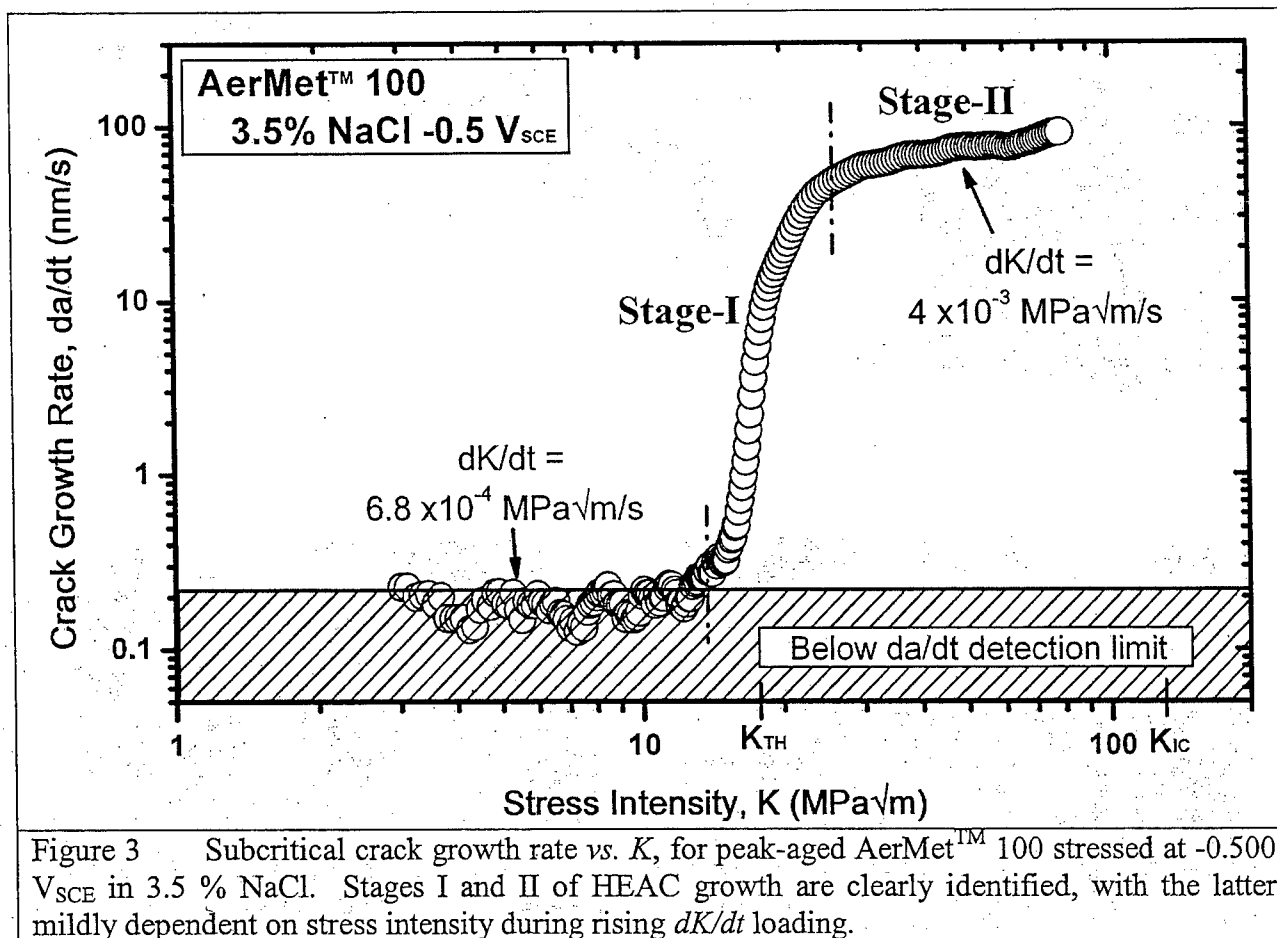
to more conventional measurements of K_{TH} and da/dt based on fracture mechanics specimens with long cracks.

4. High binding energy traps, in particular martensite lath/packet boundaries form the transgranular crack path of HEAC in AerMet^{TM} 100.

5. The improved purity of AerMet^{TM} 100, in particular reduced S and P as well as Mn and Si contents, does not provide immunity to HEAC or substantially increase K_{TH}. However, the increased purity may increase the inherent grain boundary strength leading to the absence of intergranular cracking.

6. The HEAC susceptibility of AerMet^{TM} 100 is strongly dependent on applied potential. Severe HEAC, with low K_{TH} and high da/dt_{II}, is produced at potentials that are substantially cathodic, as well as at or mildly anodic with regard to the free corrosion potential regime for aerated sodium chloride solution.

7. An electrode potential range exists at slightly cathodic potentials between -0.625 and –0.700 V_{SCE}, where HEAC susceptibility is greatly reduced, particularly as characterized by reduced crack growth rates. However, complete immunity to HEAC is not obtained at any applied potential.

8. The applied potential dependence of K_{TH} and the crack front shape agree with electrochemical considerations for an occluded crack tip in chloride solution, including increased H production from crack acidification at anodic potentials and crack polarization at cathodic potentials.

9. A semi-quantitative analysis of da/dt_{II} shows that HEAC is likely to be H-diffusion limited at potentials that are substantially cathodic, as well as at or mildly anodic, with regard to the free corrosion potential regime for aerated sodium chloride solution. Significant uncertainties exist and preclude mechanism based modeling of the electrode potential dependence of da/dt_{II}.

Figures

Figure 1   Load, P, and dcPD *vs.* actuator displacement, δ, for an AerMet[TM] 100 SENT specimen polarized to -0.500 V_{SCE} in 3.5 % NaCl. The dotted box in (a) is enlarged in (b) to show the method used to operationally define K_{TH} for the onset of crack growth. Note that (a) is a scatter plot, but the high density of data collection gives the appearance of a line graph.

Figure 2 Stress intensity, K, *vs.* crack extension ratio, $\Delta a/W$, for an AerMet™ 100 SENT specimen polarized at -0.500 V_{SCE} in 3.5 % NaCl. Baseline data from a CT specimen stressed to failure in moist air are superposed to show the severity of HEAC.

Figure 3   Subcritical crack growth rate *vs. K*, for peak-aged AerMet[TM] 100 stressed at -0.500 V$_{SCE}$ in 3.5 % NaCl. Stages I and II of HEAC growth are clearly identified, with the latter mildly dependent on stress intensity during rising *dK/dt* loading.

(a)

(b)

(c) -0.500 V_{SCE}

(d) -0.500 V_{SCE}

Figure 4   Optical and scanning electron images of an AerMet^{TM}100 specimen tested in 3.5% NaCl at -0.5 V_{SCE}.   (a) ① = notch and fatigue precrack, ② = HEAC and ③ = fracture in air. (b) The side profile shows the extent of branching, with HEAC occurring from right to left. At the location of branch; average crack length is about 1 mm and approximate stress intensity is 75 MPa√m. The SEM images (c) and (d) are taken from location (A), and shows TG fracture mixed with some IG fracture (arrow).
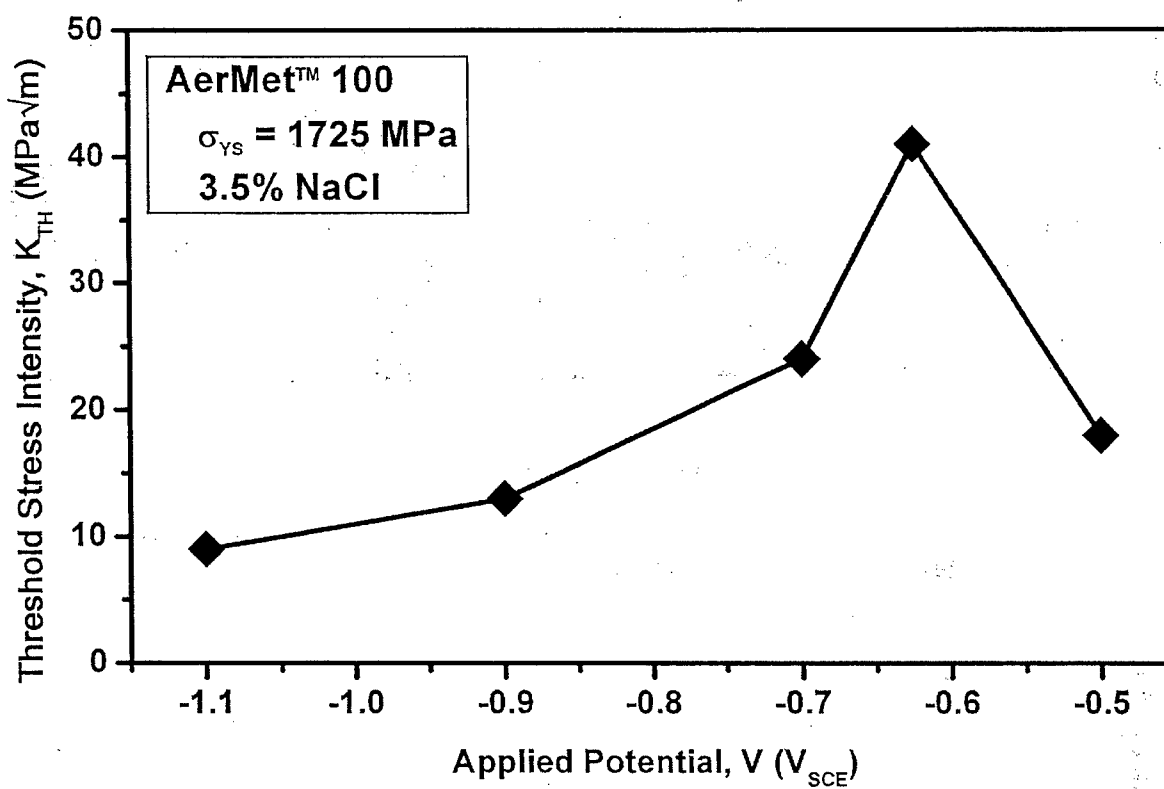
Figure 5   Threshold stress intensity, K_{TH}, vs. applied potential for peak-aged AerMet[TM]100 stressed at constant $dK/dt = 6 \times 10^{-4}$ MPa√m/s in 3.5 % NaCl.
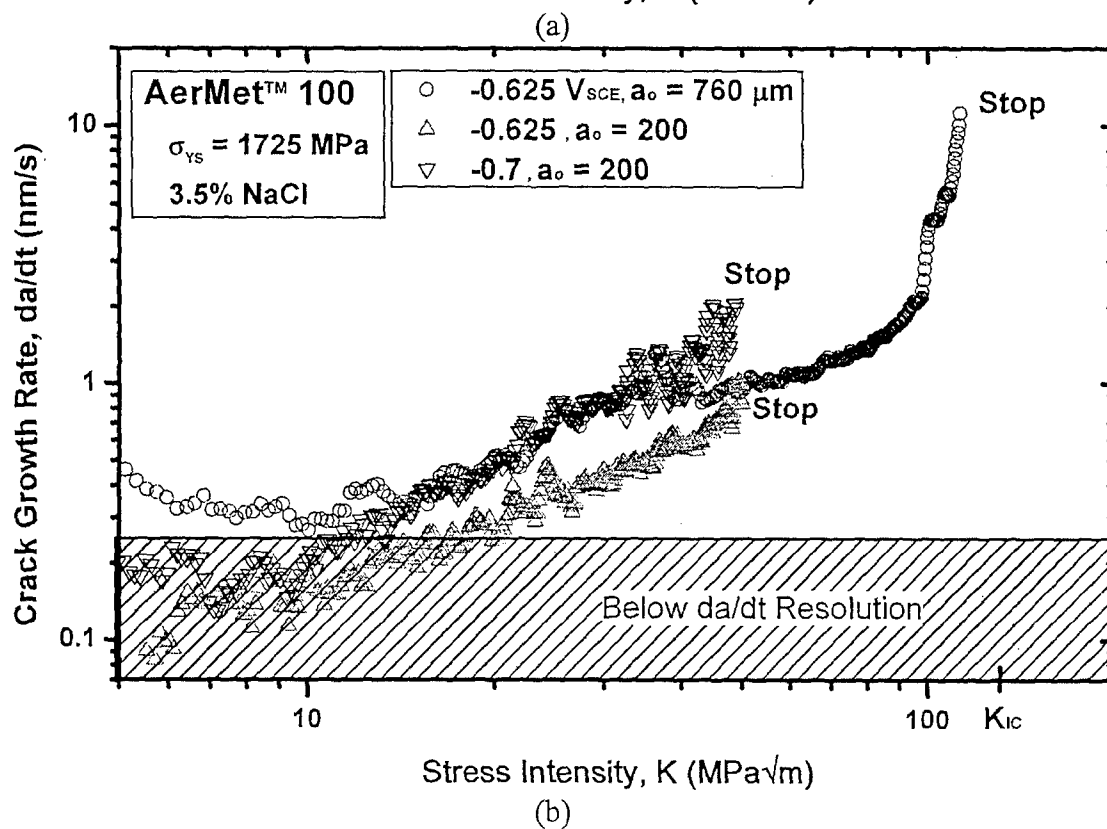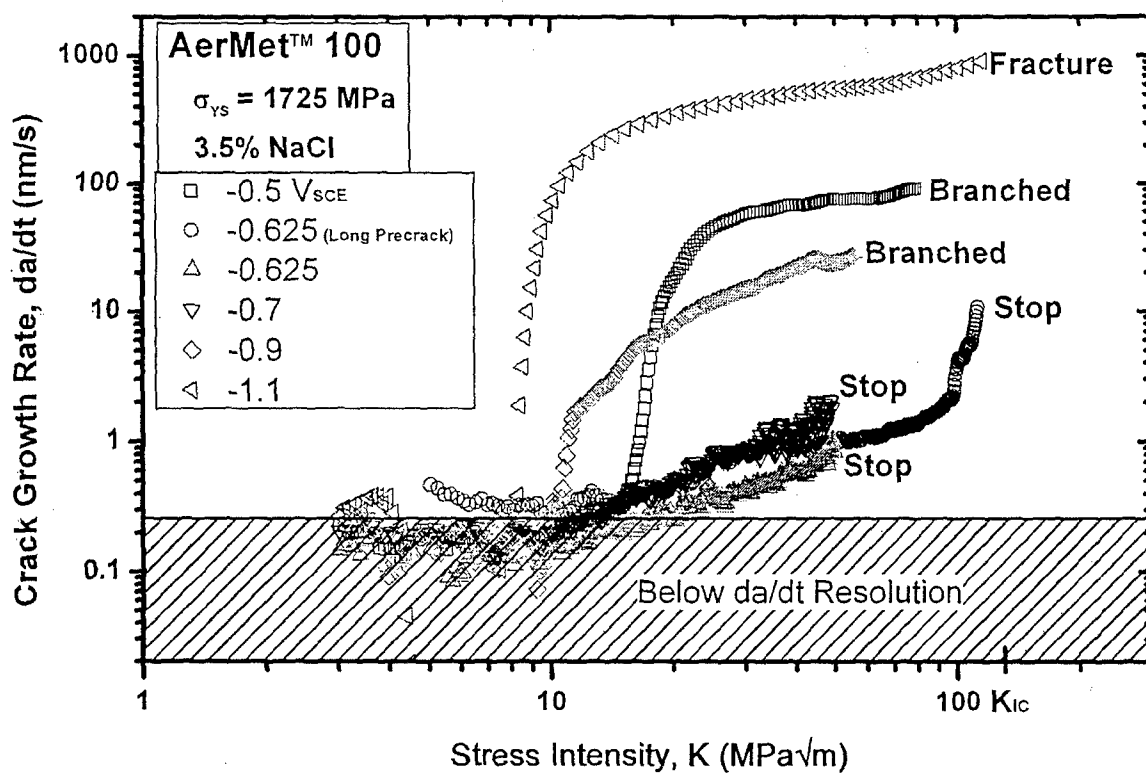
Figure 6   Crack growth rate *vs.* stress intensity for peak-aged AerMet[TM]100 in 3.5 % NaCl.
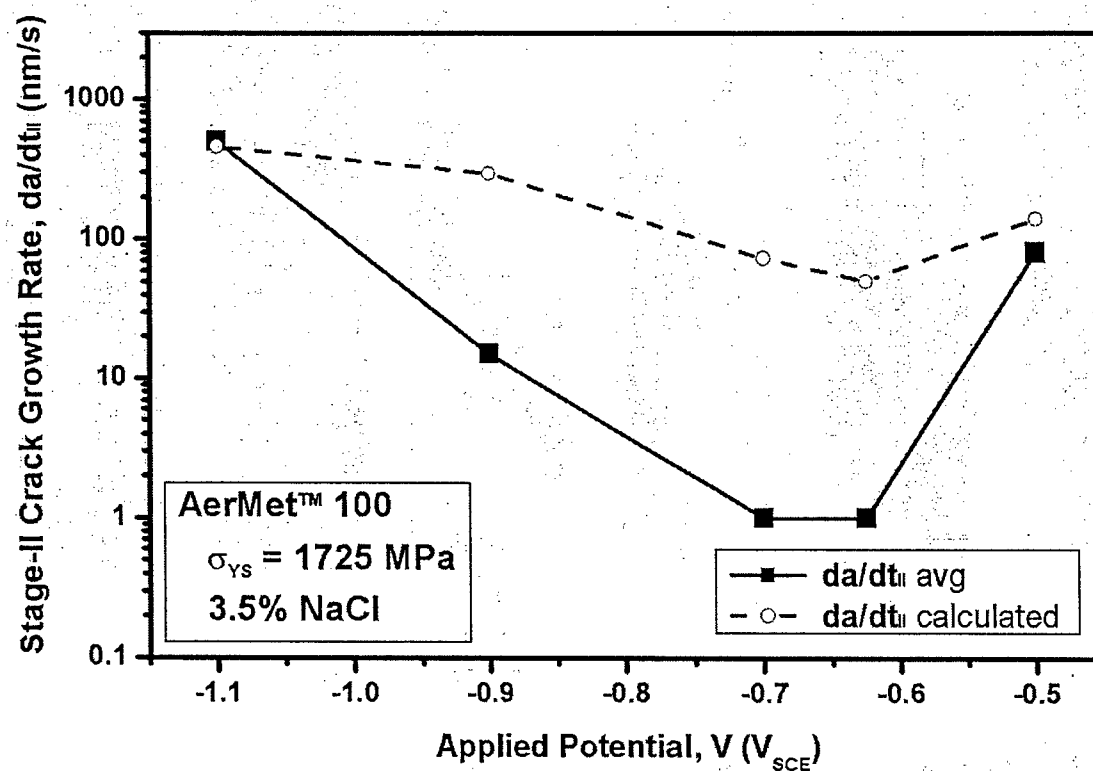
Figure 7   Stage-II crack growth rate, da/dt_{II}, vs. applied potential for peak-aged AerMet^{TM} 100 in 3.5 % NaCl. da/dt_{II} is an average value obtained from Table 3 and is substantially slower at -0.700 V_{SCE} and -0.625 V_{SCE}. The calculated da/dt_{II} for H diffusion limited controlled crack growth is based on simple application of Eq. 5 coupled with data on the applied potential dependence of C_S from Kehler et al.[50].

(a)-1.1 V$_{SCE}$ (b)-0.9 V$_{SCE}$ (c)-0.7 V$_{SCE}$ (d)-0.625 V$_{SCE}$ short precrack   (e)-0.625 V$_{SCE}$ long precrack   (f)-0.5 V$_{SCE}$
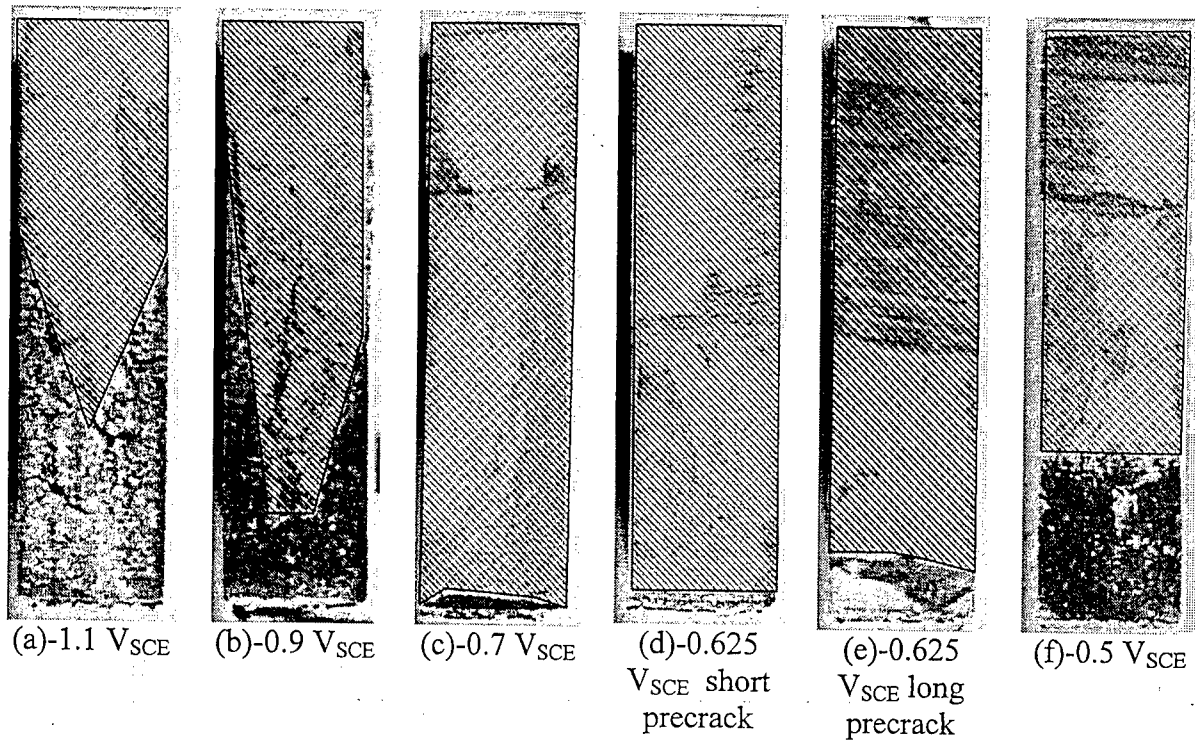
Figure 8   Low magnification optical images of the fracture surfaces for peak-aged AerMet^{TM} 100 stressed at varying applied potentials in 3.5 % NaCl solution. All specimens measure 10 mm vertically in this view, with crack growth from bottom to top on the page. Parts (a) and (b) show significant crack growth at K below 20 MPa$\sqrt{m}$. (c) and (d) show no optically visible crack growth at $K = 50$ MPa$\sqrt{m}$. Specimen (e) with a larger precrack (0.76 mm) was loaded above $K = 100$ MPa$\sqrt{m}$, and still shows no visible crack. (f) Shows the fracture surface covered with black corrosion products.

(a) Microvoid fracture in 3.5% NaCl, $K > 110$ MPa$\sqrt{m}$

(b) HEAC TG fracture, $K \sim 10$ MPa$\sqrt{m}$
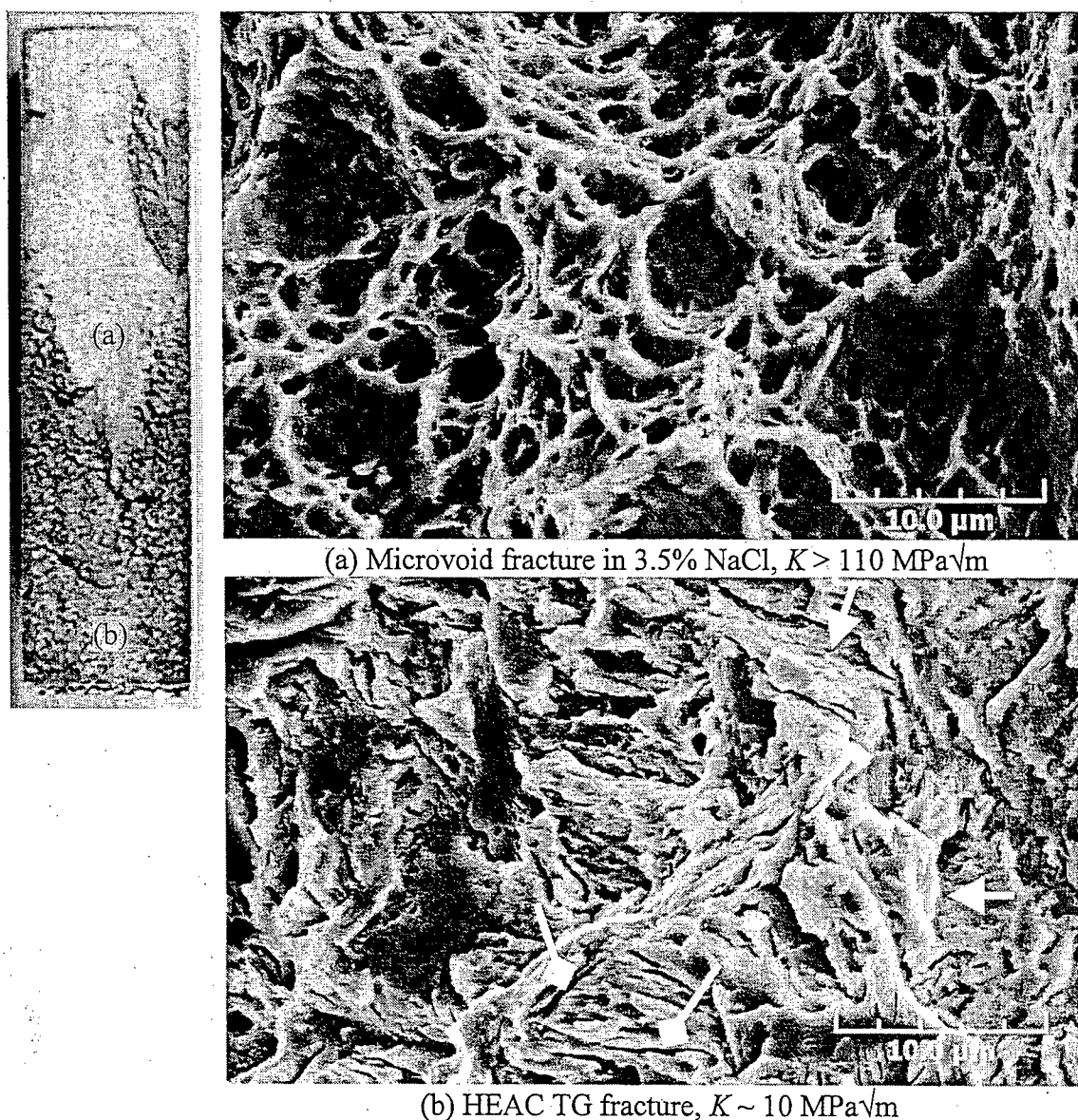
Figure 9   Scanning electron fractographs at two locations on the fracture surface of an AerMet^{TM} 100 specimen fractured in 3.5 % NaCl polarized to -1.100 V_{SCE}. The optical image locates the SEM images. (a) inside ductile fracture at $K > 110$ MPa$\sqrt{m}$ showing microvoid fracture. (b) at crack initiation, triangular arrows showing possible martensite lath packet boundaries, and diamond tipped arrows showing possible martensite lath interface cracking.

(a) -0.900 V$_{SCE}$

(b) -0.900 V$_{SCE}$

(c) -0.700 V$_{SCE}$

(d) -0.7 V$_{SCE}$

(e) -0.625 V$_{SCE}$, a$_0$ = 242 μm

(f) -0.625 V$_{SCE}$, a$_0$ = 947 μm
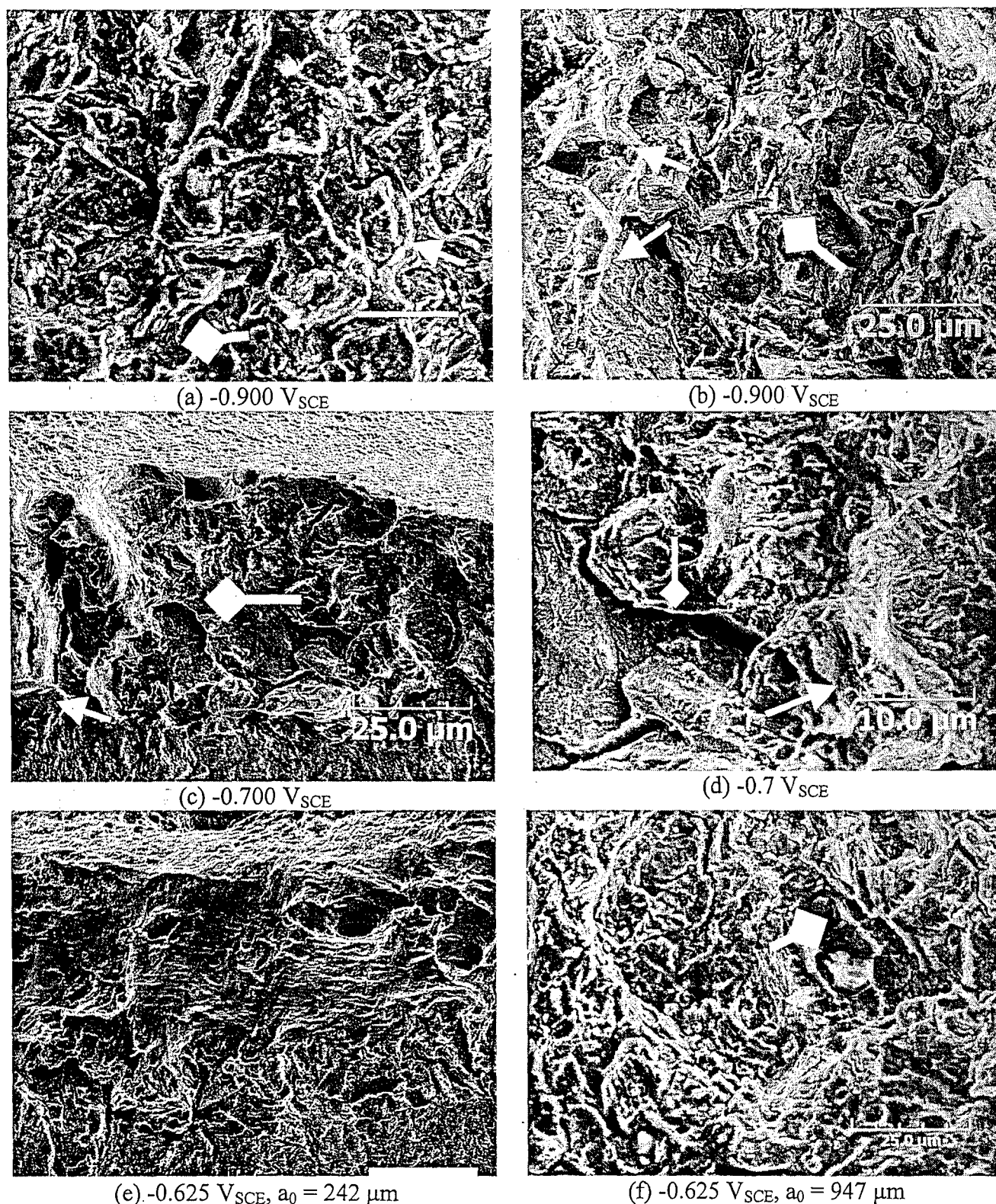
Figure 10   High resolution scanning electron images of fracture surfaces in peak-aged AerMet[TM] 100 in 3.5 % NaCl, showing the dependence of fracture mode on applied potential. All surfaces show predominantly transgranular fracture. (a) and (b) were both taken from the same specimen near the crack initiation adjacent to the fatigue precrack, but (b) shows limited IG fracture features. Triangular arrows show possible cracking at prior austenite grain boundaries or martensite lath packet boundaries, and diamond tipped arrows show possible martensite lath interface cracking. (d) shows some areas of an atypical flat fracture surface beyond TG HEAC, generally interpreted as stretch zones. All markers represent 25 μm except (d).
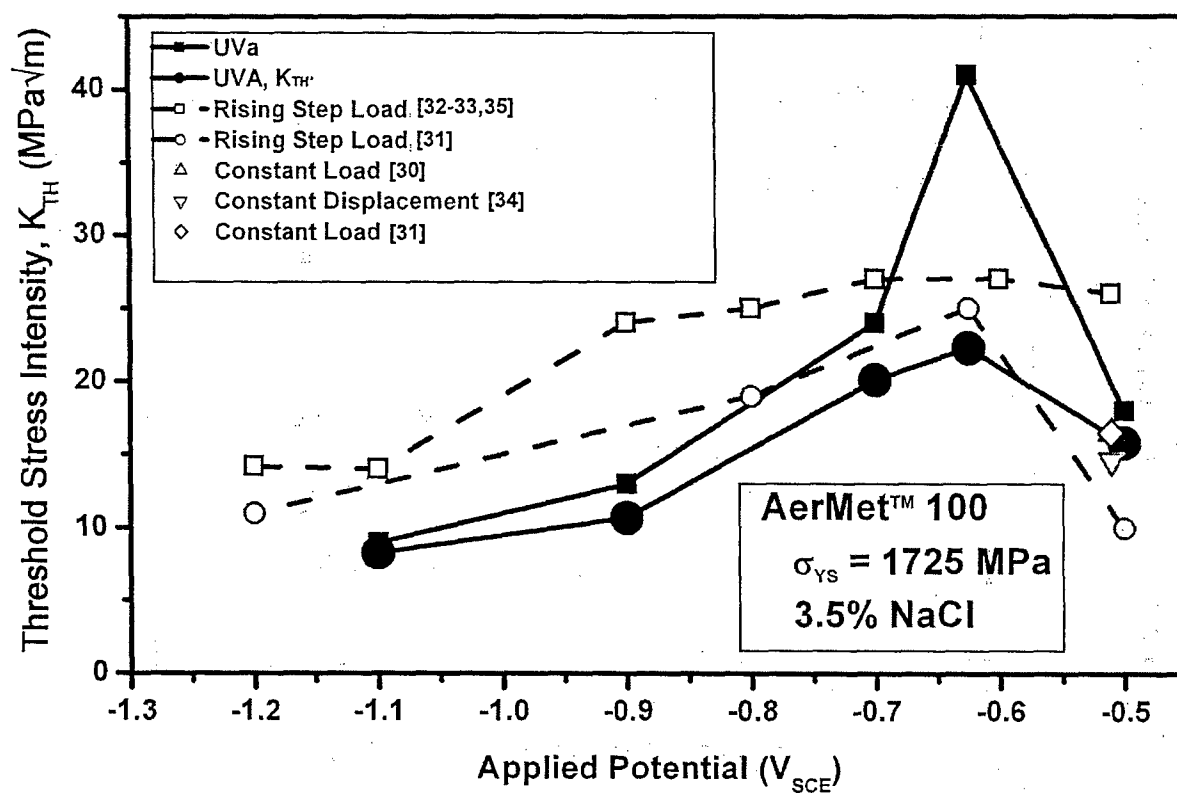
Figure 11   Threshold stress intensity *vs.* applied potential for peak-aged AerMet^{TM}100 in neutral 3.5% NaCl from various literature reports. K_{TH*}, the level of K required to produce crack growth at *da/dt* of 1 nm/s, is also shown. The constant load-point displacement rate testing method can accurately replicate K_{TH} obtained from 10,000 h constant load tests.
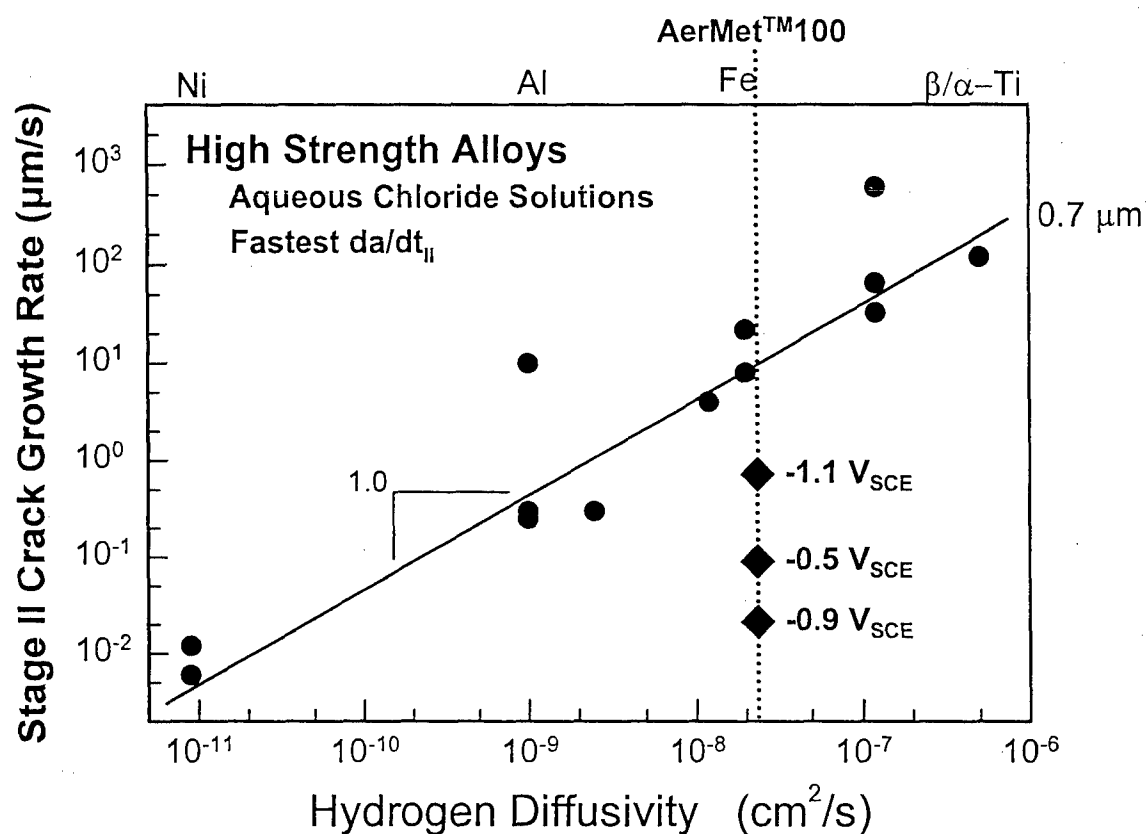
Figure 12   The dependence of the fastest-measured da/dt_{II} on D_H from permeation measurements for a variety of high strength alloys that exhibit HEAC in aqueous chloride solutions at 25°C.[17]

References

1. N.V. Parthasaradhy: *Metal Finishing*, 1974, vol. May, pp. 88-94.

2. M.M. Markhlouf and Jr. Sisson, R.D.: *Hydrogen Effects on Material Behavior*, The Minerals, Metals & Materials Society, Worcester, MA, 1990, pp. 211-21,

3. T. Casanova, F. Soto, M. Eyraud and J. Crosier: *Corrosion Science*, 1997, vol. 39, pp. 529-37.

4. E.M.K. Hillier and M.J. Johnson: *Corrosion Science*, 2004, vol. 46, pp. 715-27.

5. R.A. Oriani and P.H. Josephic: *Acta Metallurgica*, 1977, vol. 25, pp. 979-88.

6. R.A. Oriani and P.H. Josephic: *Acta Metallurgica*, 1974, vol. 22, pp. 1065-74.

7. Richard P. Gangloff: *Environmentally Assisted Failure*, Elsevier Ltd., 2003, pp. 31-101,

8. C.J. McMahon Jr.: *Engineering Fracture Mechanics*, 2001, vol. 68, pp. 773-88.

9. M. Gao and R.P. Wei: *Met. Trans. A*, 1985, vol. 16A, pp. 2039-50.

10. S.P. Lynch: *Hydrogen Effects on Materials Behavior and Corrosion Deformation Interactions*, TMS, 2003, pp. 449-66,

11. C. D. Beachem: *Metallurgical Transactions*, 1972, vol. 3, pp. 437-51.

12. G.F. Li, R.G. Wu and T.C. Lei: *Metallurgical and Materials Transactions A*, 1992, vol. 23A, pp. 2879-85.

13. Y. Takeda and C.J. McMahon Jr.: *Met. Trans. A*, 1981, vol. 12A, pp. 1255-66.

14. J.P. Hirth: *Met. Trans. A*, 1980, vol. 11A, pp. 861-90.

15. N. Bandyopadhyay, J. Kameda and C.J. McMahon Jr.: *Met. Trans. A*, 1983, vol. 14A, pp. 881-8.

16. R.P. Gangloff and A. Turnbull: *Modeling Environmental Effects on Crack Initiation and Propagation*, TMS AIME, Warrendale, PA, 1986, pp. 55-81,

17. R. P. Gangloff: *Hydrogen Effects on Material Behavior and Corrosion Deformation Interactions*, The Minerals, Metals & Materials Society, Warrendale, PA, 2003, pp. 477-97,

18. Richard L.S. Thomas, John R. Scully and Richard P. Gangloff: *Met. Trans. A*, 2003, vol. 34A, pp. 327-44.

19. M.G.H. Wells: *Key Engineering Materials*, 1993, vol. 77-78, pp. 71-80.

20. G.B. Olson: *Advanced Materials and Processes*, 1997, vol. pp. 72-9.

21. R. Ayer and P.M. Machmeier: *Met. Trans. A*, 1993, vol. 24A, pp. 1943-55.

22. R. Ayer and P. M. Machmeier: *Metallurgical and Materials Transactions A*, 1996, vol. 27A, pp. 2510-17.

23. Choong Hwa Yoo, Hyuck Mo Lee, Jin W. Chan and J. W. Morris Jr.: *Metallurgical and Materials Transactions A*, 1996, vol. 27A, pp. 3466-72.

24. R. Ayer and P. M. Machmeier: *Metallurgical and Materials Transactions A*, 1998, vol. 29A, pp. 903-05.

25. J. Kozol and C. E. Neu: Report No. NAWCADWAR-92018-60, Naval Air Warfare Center, Warminster, PA, Jan 10, 1992 1992

26. P.F. Buckley, R. Brown, G.H. Graces, E.U. Lee, C.E. Neu and J. Kozol: *Metallic Materials for Lightweight Applications-Proceedings of the 40th Sagamore Army Materials Research Conference*, United States Army Laboratory Command, Watertown, MA, 1993, pp.

27. E.U. Lee: Report No. NAWCADWAR-94001-60, Naval Air Warfare Center, Warminster, PA, Oct. 23, 1993 1993

28. E.U. Lee: *Metallurgical and Materials Transactions A*, 1995, vol. 26A, pp. 1313-16.

29. A. Oehlert and A. Atrens: *Journal of Materials Science*, 1998, vol. 33, pp. 775-81.

30. E.U. Lee, H. Sanders and B. Sarkar: *Tri-Service Conference on Corrosion*, US Army Research Laboratory, 1999, pp.

31. Richard L.S. Thomas, Daoming Li, Richard P. Gangloff and John Scully: *Met. Trans. A*, 2002, vol. 33A, pp. 1991-2004.

32. Daoming Li, Richard P. Gangloff and John R. Scully: *Metallurgical and Materials Transactions A*, 2004, vol. 35A, pp. 849-64.

33. Joanne McLaughlin, John Douglas Weir and J. B. Boodey: *AEMR Conference*, 1998, pp.

34. R.W.J. Koers, A.H.M. Krom and A. Bakker: *Environmentally Assisted Cracking: Predictive Methods for Risk Assessment and Evaluation of Materials, Equipment, and Structures*, American Society for Testing and Materials, West Conshohocken, PA, 2000, pp. 303-16,

35. *2005 Annual Book of Astm Standards Vol. 3.01*, ASTM, West Conshohocken, PA, 2003, pp. 1004-15,

36. Wolfgang Dietzel: *Environmentally Assisted Cracking: Predictive Methods for Risk Assessment and Evaluation of Materials, Equipment, and Structures*, American Society for Testing and Materials, West Conshohocken, PA, 2000, pp. 317-26,

37. W. G. Clark and J.D. Landes: *Stress Corrosion-New Approaches, Astm Stp 610*, American Society for Testing and Materials, West Conshohocken, PA, 1976, pp. 108-27,

38. R.A. Oriani: *Fundamental Aspects of Stress Corrosion Cracking*, NACE, Houston, TX, 1969, pp. 32-50,

39. R.A. Oriani: *Acta Metallurgica*, 1970, vol. 18, pp. 147-57.

40. G.M. Pressouyre and I.M. Bernstein: *Met. Trans. A*, 1978, vol. 9A, pp. 1571-80.

41. S. Hinotani, Y. Ohmori and F. Terasaki: *Materials Science and Engineering*, 1985, vol. 76, pp. 57-69.

42. A. Turnbull, M.W. Carroll and D.H. Ferriss: *Acta Metallurgica*, 1989, vol. 37, pp. 2039-46.

43. B.G. Pound: *Hydrogen Effects on Material Behavior and Corrosion Deformation Interactions*, TMS, Warrandale, PA, 2003, pp. 93-103,

44. B.G. Pound: *Acta Metallurgica*, 1998, vol. 46, pp. 5733-43.

45. G. M. Pressouyre: *Acta Metallurgica*, 1980, vol. 28, pp. 895-911.

46. A. Turnbull: *Corrosion*, 2001, vol. 57, pp. 175-89.

47. B.F. Brown: *Stress Corrosion Cracking and Hydrogen Embrittlement of Iron Base Alloys*, National Association of Corrosion Engineers, Houston, TX, 1977, pp. 747-50,

48. D.P. Dautovich and S. Floreen: *Stress Corrosion Cracking and Hydrogen Embrittlement of Iron Base Alloys*, National Association of Corrosion Engineers, Houston, TX, 1977, pp. 798-815,

49. Brian E. Placzakis and J. H. Beatty: *Tri-Service Conference on Corrosion*, US Army Research Laboratory, Weapons and Materials Research Directorate, 1997, pp. 7.18-7.32,

50. J.R. Scully, Beth. A. Kehler, Yongwon Lee and R.P. Gangloff: *Tri-Service Corrosion Conference*, NACE, Orlando, Florida, 2005, pp.

51. M.A. Jakab and J.R. Scully: *Nature Materials*, 2005, vol. 4, pp. 667-70.

52. B.G. Ateya and H.W. Pickering: *Journal of the Electrochemical Society*, 1975, vol. 122, pp. 1018-26.

53. H.W. Pickering: *Corrosion Science*, 1989, vol. 29, pp. 325-41.

54. James M. Dahl: *Advanced Materials & Processes*, 2000, vol. May, pp. 33-.

55. H.H. Johnson: *Materials Research & Standards*, 1965, vol. 5, pp. 442-45.

56. Richard P. Gangloff, Donald C. Slavik, Robert S. Piascik and Robert H. Van Stone: *Small-Crack Test Methods, Astm Stp 1149*, American Society for Testing and Materials, Philadelphia, 1992, pp. 116-68,

57. Robert S. Piascik and Richard P. Gangloff: *Met. Trans. A*, 1991, vol. 22A, pp. 2415-28.

58. M.J. Haynes and R.P. Gangloff: *Journal of Testing and Evaluation*, 1997, vol. 25, pp. 82-98.

59. H. Tada, P. C. Paris and G. R. Irwin: *The Stress Analysis of Cracks Handbook*, Paris Productions Incorporated, St. Louis, Missouri, 1985, pp.

60. R.L.S. Thomas: University of Virginia, unpublished research, 1999

61. B. Force and H.W. Pickering: *Journal of Materials*, 1995, vol. 47, pp. 22-27.

62. P.K. Subramanyan: *Comprehensive Treatise of Electrochemistry Volume 4: Electrochemical Materials Science*, Plenum Press, New York, NY, 1981, pp. 411-62.

63. A. Turnbull, D. H. Ferriss and H. Anzai: *Mater. Sci. Engr. A*, 1996, vol. 206, pp. 1-13.

64. K.N. Akhurst and T.J. Baker: *Met. Trans. A*, 1981, vol. 12A, pp. 1059-70.

65. Yueguang Wei and J.W. Hutchinson: *Journal of Mechanics and Physics of Solids*, 1997, vol. 45, pp. 1253-73.

66. H. Jiang, Y. Huang, Z. Zhuang and K.C. Hwawng: *Journal of Mechanics and Physics of Solids*, 2001, vol. 49, pp. 979-93.

67. Z. Gao and J. W. Morris Jr.: *Scripta Metallurgica*, 2005, vol. 53, pp. 933-36.

68. Y. H. Kim, H. J. Kim and J. W. Morris Jr.: *Metallurgical and Materials Transactions A*, 1986, vol. 17A, pp. 1157-64.

69. R.O. Ritchie, V.F. Castro Cedeno, V.F. Zackay and E.R. Parker: *Met. Trans. A*, 1978, vol. 9A, pp. 35-40.

70. G.B. Olson: *Innovations in Ultrahigh Strength Steel Technology, 34th Sagamore Army Materials Research Conference*, US Army Laboratory Command, Watertown, MA, 1987, pp. 3-66,

71. J. I. Kim and J. W. Morris Jr.: *Metallurgical and Materials Transactions A*, 1980, vol. 12A, pp. 1957-63.

72. A. Szummer: *Hydrogen Degradation of Ferrous Alloys*, Noyes Publications, Park Ridge, NJ, 1985, pp.

73. M. L. Holzworth and M. R. Louthan Jr.: *Corrosion*, 1968, vol. 24, pp. 110-24.

74. G.M. Pressouyre: *Hydrogen Effects in Metals*, The Minerals, Metals, and Materials Society, Warrendale, PA, 1981, pp. 27-36,

75. T.Y. Zhang, H. Sheu and J.E. Hack: *Scripta metall. Mater.*, 1992, vol. 27, pp. 1605.

76. T.Y. Zhang and J.E. Hack: *Metallurgical and Materials Transactions A*, 1999, vol. 30A, pp. 155.

77. W.W. Gerberich, T. Livne and X. Chen: *Modeling Environmental Effects on Crack Growth Processes*, The Metallurgical Society, Warrandale, PA, 1985, pp.

78. J. Toribio and V. Kharin: *International Journal of Fracture*, 1997, vol. 88, pp. 233-45.

79. P. Shewmon: The Minerals, Metals, & Materials Society, Warrendale, PA, 1989, pp. 9-51,

80. P. Doig and G. T. Jones: *Metallurgical and Materials Transactions A*, 1977, vol. 8A, pp. 1993-98.

81. W.W. Gerberich, T. Livne, X.-F. Chen and M. Kaczorowski: *Met. Trans. A*, 1988, vol. 19A, pp. 1319-34.

82. M.M. Hall and D.M. Symons: *Chemistry and Electrochemistry of Stress Corrosion Cracking*, The Minerals, Metals, & Materials Society, Warrandale, PA, 2001, pp. 447-66,

83. Y. Katz, N. Tymiak and W. W. Gerberich: *Engineering Fracture Mechanics*, 2001, vol. 68, pp. 619-46.

84. W. W. Gerberich, P.G. Marsh and J.W. Hoehn: *Hydrogen Effects in Metals*, TMS, Warrendale, PA, 1996, pp. 539-,

85. A.J. Kumnick and H.H. Johnson: *Metallurgical Transactions*, 1974, vol. 5, pp. 1199-206.

86. I.W. Kang, S.I. Pyun and K.T. Kim: *Scripta Metallurgica*, 1989, vol. 23, pp. 223-6.

87. R.A. Page and W.W. Gerberich, The effect of hydrogen source on crack initiation in 4340 steel. *Metall. Trans. A*, **13A**, 1982, 305-311.

88. R.P. Gangloff and R.P. Wei: *Small Fatigue Cracks*, R.O. Ritchie and J. Lankford, eds., TMS-AIME, Warrendale, PA., 1986, pp. 239-264.

89. B.P. Somerday, L.M. Young and R.P. Gangloff: *Fatigue and Fracture of Engineering Materials and Structures*, 2000, Vol. 23, pp. 39-58.

90. R.P. Gangloff and R.P. Wei: *Fractography in Failure Analysis, ASTM STP 645*, ASTM, Philadelphia, PA, 1978, pp. 87-106.

91. B.A. Kehler, Yongwon Lee, J.R. Scully and R.P. Gangloff: University of Virginia, unpublished research, 2004.

92. R.P. Wei and R.P. Gangloff: *Fracture Mechanics: Perspectives and Directions, ASTM STP 1020*, R.P. Wei and R.P. Gangloff, eds., ASTM, Philadelphia, PA, 1989, pp. 233-264.

93. D.M. Symons: *Engineering Fracture Mechanics*, 2001, vol. 68, pp. 751-71.

94. J.R. Scully and R.P. Gangloff, "Mechanism-Based Modeling of Hydrogen Assisted Cracking in High Strength Alloys for Marine Applications", SEAS Proposal No. MSE-DOD/ONR-2792-06, University of Virginia, Charlottesville, VA (2006).

Microstructural Mitigation of Hydrogen Environment Embrittlement of Ultra-high Strength AerMet™ 100

Yongwon Lee and Richard P. Gangloff

Mitigation of Hydrogen Environment Embrittlement in AerMet™ 100 by Microstructural Modification

Yongwon Lee and Richard P. Gangloff

ABSTRACT

AerMet™ 100, a secondary precipitation hardened martensitic steel, has excellent strength (σ_{YS} = 1725 MPa) and toughness (K_{IC} = 130 MP√am) when optimally tempered at 482°C. However, it is susceptible to severe hydrogen environment assisted cracking (HEAC) in near-neutral 3.5% NaCl at very low threshold stress intensities (K_{TH}) and with rapid Stage II plateau rates for subcritical crack propagation (da/dt_{II}). Interaction between environmental hydrogen and the complex microstructure influences the HEAC response, and modifications to heat treatment could improve HEAC resistance, particularly considering H-trap interactions. The effect of aging condition on HEAC of AerMet™ 100 was examined. Specimens were aged for 5 h at 482°C, 510°C and 538°C or studied in the as-quenched condition; then stressed at slow constant displacement rate in 3.5% NaCl at two polarization levels. When polarized to -0.9 V_{SCE}, all aged specimens showed substantial HEAC with low K_{TH} (10~20% of K_{IC}) and high da/dt_{II} (up to 30nm/s); but the as-quenched condition had substantially higher K_{TH} (70% of K_{IC}) and slow da/dt_{II} (1 nm/s). The HEAC path was mostly transgranular for all conditions, but predominantly intergranular when aged at 538°C. The aging independence of HEAC at -0.9 V_{SCE} may be consistent with a mechanistic explanation based on H diffusion control of crack growth rate, but material dependent terms in the model for da/dt_{II} and the detail of the model are uncertain. It is not possible to design alloy composition and processing conditions based on such existing models. Qualitatively, increasing incoherence of M_2C precipitates does not result in reduced da/dt_{II}, perhaps due to the counterbalancing effects of increased trapping causing reduced H diffusivity but increased H solubility. Relatively low H-trap binding energy of these precipitates for all tempers examined prevents beneficial shielding of H partition to martensite lath/packet boundary interfaces where such segregation enables decohesion. The absence of uniformly distributed carbide H traps in the non-aged condition increases the HEAC crack growth rate, following this analysis, but lack of thin-film austenite may reduce martensite boundary cracking compared to that provided by aging at 482°C and 510°C. The presence of greatly increased intra-lath austenite appears to protect the martensite boundary to allow IG HEAC for the 538°C temper. These experiments build on IHAC and HEAC results for peak strength/toughness AerMet™ 100 and provide further understanding of the role of microstructure in HEAC necessary to predict and optimize the HEAC resistance of modern UHSS. However, this work does not provide strong improvement in cracking resistance, demonstrating the overriding importance of HEAC to this class of steels and the challenge in microstructural design.

I. Introduction

When aged at 482°C to achieve peak toughness, AerMet™ 100 is susceptible to internal hydrogen assisted cracking (IHAC)[1], as well as hydrogen environment assisted cracking (HEAC) in near-neutral 3.5% NaCl[2] at very low threshold stress intensities (K_{TH}) and rapid Stage II plateau rates for subcritical crack propagation (da/dt_{II}) comparable to older UHSS[3]. Contrary to the IG HEAC fracture path of older UHSS, hydrogen assisted cracking is predominantly transgranular in AerMet™ 100. This change is attributed to improved austenite boundary purity, and significant H trapping that promotes decohesion of martensite lath and packet interfaces[1,4,5]. Accordingly, it is hypothesized that changes in microstructure caused by varying heat treatments may alter the fracture path of HEAC. The kinetics of HEAC in ultra-high strength alloys are likely governed by atomic hydrogen (H) diffusion from the reacting crack tip surface to damage sites located within the fracture process zone (FPZ), of order 1 μm from the surface[3]. Accordingly, the trap-sensitive diffusivity of H (D_H) and local reversibly-trapped H concentration (C_H) are critical factors that influence threshold and crack growth rate properties. Each of these parameters is sensitive to microstructure, as understood by the binding energy (E_B) between H and the trap site[5]. Although the microstructural evolution of AerMet™ 100 for various heat treatments is well documented[6-10], precise consequences for HEAC have not been studied. Modifications to microstructure can be critical in HEAC mitigation, and the results from this research provide an initial basis to reduce cracking susceptibility.

I.A. Hydrogen Trapping and Microstructure in AerMet™ 100

Hydrogen is trapped at multiple microstructural features in AerMet™ 100, including nanoscale carbides (M_2C = $(Cr,Mo)_2C$), cementite, undissolved alloy carbides, martensite laths and packet interfaces, prior austenite grain boundaries, and dislocations[4-9]. These traps play a dominant role in hydrogen assisted cracking (HAC) due to strong influences on the local solubility (C_H) and diffusivity (D_H) of hydrogen; and the exact properties of each trap is determined by the heat treatment once the bulk composition is fixed. According to previous studies of AerMet™ 100[1,2,4,5], the most critical H traps relevant to IHAC and HEAC in the peak toughness temper (482°C) are those associated with M_2C carbides and martensite lath and packet boundaries. Those studies concluded that nano-scale, coherent and homogeneously dispersed M_2C carbide traps have low H-trap binding energies (E_B ~ 11 kJ/mol) and are reversible upon

stress application, while martensite boundaries have higher binding energies ($E_B \sim 61$ kJ/mol) and are more akin to irreversible traps. In IHAC of AerMet[TM] 100, crack tip stress causes H repartitioning from precharged M_2C carbide traps to interconnected martensite interfaces within the fracture process zone (FPZ) to cause severe TG cracking[1,4,5]. In HEAC, H diffuses to the same martensite interfaces and causes similar TG fracture[2]. It was speculated that uniformly distributed M_2C carbide traps may beneficially impede H accumulation at (or diffusion to) the higher energy martensite traps, but this effect was not evident in the peak-toughness condition[2].

When aged at higher temperatures or extended duration, the M_2C carbides increase in size and lose coherency with the matrix[6,9], likely increasing H-trap binding energy[5]. As long as particle coarsening does not change distribution uniformity, such an increase in E_B may allow the carbides to act as H diffusion barriers and also trap H away from susceptible boundaries and increase resistance to HEAC. This effect will be better achieved though higher temperature tempering rather than extended duration aging because studies suggest that extended isothermal aging causes sudden deterioration in the yield strength and alters M_2C distribution in a manner less predictable than those caused by temperature adjustment[7,8]. Therefore, aging time was fixed at 5 h, and aging temperature was varied. The exact value of E_B for each trap site in each tempering condition has not been investigated. Such detailed work is only justified if initial characterization suggests substantially improved resistance to HEAC.

I.B. Microstructure Design

Four conditions were chosen to control the critical microstructural features in AerMet[TM] 100, selected based on detailed existing studies of microstructure[6-9]. These heat treatments retain the high strength ($\sigma_{YS} > 1300$ MPa) and toughness ($K_{IC} > 100$ MPa$\sqrt{m}$) of this alloy steel. At the aging temperature of 482°C, the predominant rod-shaped M_2C carbides are approximately 9 nm long and 3 nm in diameter and uniformly distributed in the matrix. These carbides are coherent with the matrix and coexist with solute zones at this temperature[6-9]. A small amount of thin-film reverted austenite (γ`) forms between the martensite plates, 0.5%[6] or 4%[9,10] in volume fraction based on measurements reported by two separate groups.

At 510°C, the volume fraction of γ` increases to 1%[6] or 7%[9,10] and remains in the thin film inter-plate morphology. The M_2C carbides increase in size to ~17 nm x 6 nm, and begin to lose coherency by both reported accounts[6,9]. The Cr content of the carbide reduces slightly to 70%, while the Fe and Mo concentrations increase. At 538°C, the volume fraction of γ`

increases to 5.5%[6] or perhaps higher[9,10] and begins forming intra-plate. The M_2C carbides increase in size to approximately 28 nm x 10 nm, and further lose coherency with the matrix[6]. The Cr content of the carbide further reduces to 65%. In the quenched and cryogenically stabilized condition that precedes aging, the matrix is predominantly unrecovered martensite with 0[6] to 3[10] vol.% of retained austenite. M_2C carbides have not formed and there are only undissolved 100-500 nm scale $MC/M_{23}C_6$ carbides[6]. This condition provides the reference for studying the effect of M_2C and thin-film reverted austenite, due to their absence. Moreover, the martensite is unrecovered and the undissolved carbides do not coarsen during the ages employed. Although large, incoherent carbides are irreversible traps which are reported to dominate HAC in certain steels[11,12], the importance of such particles is challenged and are viewed by the present authors to be unimportant to IHAC and HEAC[2,3]. Cementite is absent from AerMet[TM] 100 in both the as-quenched condition and at aging temperatures above 482°C.

I.C.   Effect of Applied Electrode Potential on HEAC of AerMet[TM] 100

The effect of applied electrode potential, E_{App}, on HEAC of AerMet[TM] 100 was accurately established by various loading methods including slow strain rate[2] and step rising load[13-15]. Although there is variability in the exact values of K_{TH}, it is clear that optimal resistance to HEAC in near-neutral 3.5% NaCl exists near -0.6 with respect to the saturated calomel reference (V_{SCE}), and severe HEAC occurs at both anodic (-0.5 V_{SCE}) and cathodic (-0.9 V_{SCE}) potentials. Two potentials were chosen to probe the interaction of microstructure and electrochemical approaches to mitigate HEAC. The effect of aging on HEAC of AerMet[TM] 100 is isolated by experiments at a single E_{App} of -0.9 V_{SCE} where cracking is severe for the high strength-toughness microstructure. These experiments are augmented by testing at -0.625 V_{SCE} to establish the effect of aging for the applied potential regime where HEAC in the susceptible peak aged microstructure is substantially mitigated by reduced electrochemical production of H.

I.D.   Objectives

The objective of this research is to quantify the effect of aging condition on the susceptibility of AerMet[TM] 100 to HEAC. Four aging conditions that give good strength and fracture toughness are examined. The K_{TH} for the onset of HEAC under rising stress intensity and da/dt_{II} are determined at two constant electrochemical conditions representing the extremes of crack tip H production and uptake. The HEAC path and morphology are examined compared

to the microstructure produced by different tempering temperatures. These experiments build on IHAC and HEAC results for peak strength/toughness AerMet™ 100 and provide further understanding of the role of microstructure in HEAC necessary to predict and optimize the HEAC resistance of modern UHSS.

II. Procedure

II.A. Material and Specimen Design

Specimen design was identical to that used in the peak-age HEAC study[2], as outlined in the previous chapter of this report, with the following exceptions. Eight discs of forged bar of AerMet™ 100, each 15 cm in diameter and 1.6 cm thick, were austenitized at 885°C for 1 h, quenched in liquid nitrogen and cold stabilized for 5 h. Six discs were tempered in vacuum for 5 h and air cooled to obtain two discs per aging temperature: 482°C, 510°C, 538°C. The remaining two pieces were not aged and studied in the as-quenched (AQ) condition. Steel composition was identical to that examined in the HEAC study of peak aged AerMet™ 100 [2]. The heat treatments and key mechanical properties reported by previous investigators[6-9] are summarized in Tables 1 and 2.

Table 1.   Mechanical Properties of Peak-Aged AerMet™ 100

HRC	σ_{YS} (MPa)	σ_{UTS} (MPa)	Reduction in Area (pct)	E (GPa)	σ_o (MPa)	K_{IC} (MPa√m)
54	1725	1965	65	194.4	1985	130

Table 2.   Properties of Aged AerMet™ 100

Age	HRC	σ_{YS} (MPa)	K_{IC} (MPa√m)	Carbide morphology	γ' volume fraction (%)
As Quenched	52	1350	123	Undissolved MC/$M_{23}C_6$ carbides	-
482°C 5 h	56	1725	130	Solute zones and coherent M_2C [6] 9 x 3 nm[6]	Plate boundary 0.5[6], 4[9]
510°C 5 h	52	1580	130	Coherent M_2C [6,9] 17 x 6 nm[6]	Plate boundary 1[6], 7[9]
538°C 5 h	48	1380	118	Incoherent M_2C [6,9] 27 x 10 nm[6]	Intra-plate 5.5[6]

Single edge micronotch tensile (SENT) specimens were machined with identical methods and dimensions as previously used[2]. The Mode I load was applied in the circumferential (C) direction and crack growth occurred in the length (L) direction in the original round-forged bar. To obtain a sharp precrack, a wired SENT specimen was fatigue precracked to a total notch plus crack depth (a_o) of 200-2500 μm in moist air at 20 Hz with decreasing maximum stress intensity from 15 MPa√m to 5 MPa√m and constant stress ratio of 0.10. The longer precracks were required to retain small scale yielding for the stress intensity (K) levels of interest in the somewhat lower strength microstructures. Due to the differences in a_o, some variances were introduced into the loading rate. These experimental variables and possible complicating effects are discussed later.

II.B.   Experimental Setup

The HEAC test setup was identical to previous experiments[2] with the following exceptions. The SENT specimen was immersed fully in 3.5% NaCl solution and configured as the working electrode grounded through a wire connected from the specimen to building ground. The potentiostat was operated in floating mode to avoid a ground loop. Experiments were conducted in potentiostatic control with two applied-constant potentials, E_{App} of -0.900 or -0.625 V_{SCE}. All specimens were preloaded quickly to 3 MPa√m, within 1 h of specimen polarization, then loaded at a slower-constant rate of grip displacement. The direct current electrical potential difference (dcPD) method was used to measure crack length in-situ[16-18] in identical fashion to the previous HEAC experiments[2]. The applied stress intensity, K, and threshold stress intensity, K_{TH}, were defined as in the previous report[2]. K_{TH}* was defined as the K required to exceed crack growth rate of 1 nm/s. Fracture surfaces were cleaned ultrasonically in acetone then methanol for 10 minutes, dried, and stored in a desiccator. When necessary, specimens were polarized to -1.5 V_{SCE} in 0.5 M H_2SO_4 for 60 s or soaked in 10% HCl for 30 s to remove corrosion products. Scanning electron microscope (SEM) fractographs were obtained using identical conditions as before[2], and the crack advanced from bottom to top of an SEM image.

III. Results

III.A. K_{TH} and Crack Growth Kinetics at E_{App} = -0.900 V$_{SCE}$

When aged at the selected temperatures between 482°C and 538 °C, AerMet™ 100 was susceptible to severe HEAC in neutral 3.5% NaCl for constant applied potential of -0.900 V$_{SCE}$. Figure 1 shows measured and operationally defined K_{TH} as a function of aging temperature, with the reference K_{IC} from Table 2 plotted for each condition. These data show that aging at 482°C and 510°C produced similar HEAC susceptibility at K_{TH} of 13 MPa√m (11% of K_{IC} from Table 2) and 13.5 MPa√m (12% of K_{IC}), respectively. Tempering at higher temperature (538°C) improved K_{TH} to 23 MPa√m, 20% of the K_{IC} for this condition. Remarkably, substantial recovery of cracking resistance was observed for the AQ condition with K_{TH} of 87 MPa√m (71% of K_{IC}). The initial crack length of the AQ specimen was substantially longer (2.5 mm) than other specimens (0.25 ~ 0.76 mm). The K_{TH}* followed the same general trend, and the values are listed in Table 3. This form of threshold represents the stress intensity level required to produce a crack growth rate of 1 nm/s, as justified in the preceding chapter of this final report[2].

Table 3. Summary of HEAC results for E_{App} = -0.900 V$_{SCE}$

Heat Treatment	a_o (mm)	Initial dK/dt (MPa√m/h)	K_{TH} (MPa√m) [Figure 1]	K_{TH}* (MPa√m)	da/dt_{II} (nm/s) [Figure 2]	Fracture Mode [Figures 3-4]
AQ	2.8	1.7×10^{-3}	87	77	1	TG + Branching
482°C	0.24	6.1×10^{-4}	13	10.7	10	TG + Branching
510°C	0.30	5.6×10^{-4}	13.5	11.6	10	TG + Branching
538°C	0.79	1.7×10^{-3}	23	21.7	10	IG

Measured subcritical crack growth kinetics for the various aged microstructures of AerMet™ 100 are similar to previous HEAC experiments[2] and reported in Figure 2. Due to the differences in initial crack length, the constant loading rate (dK/dt) prior to the onset of subcritical crack growth varied as noted in Figure 2 and Table 2. The Stage I and II regimes of growth behavior are not distinguishable for all specimens in Figure 2, so closer examination is required. For the AQ condition, what appears to be Stage-I growth at high K is actually H-induced crack branching and tearing at K below the H-free K_{IC}, also called Stage-III growth.

Therefore, the flat region below K of 70 MPa√m represents Stage-II growth at da/dt_{II} far below that of the other aging temperatures at the same electrochemical condition, and Stage-I growth is not shown in Figure 2 for this specimen. For this AQ condition, load and dcPD data were not collected for stress intensity levels below K of 30 MPa√m. Clearly subcritical HEAC occurred, but the two measures of threshold are uncertain due to this loss of data. The value of K_{TH} (87 MPa√m) plotted in Figure 1 for the AQ condition is particularly suspect. This interpretation is confirmed by fractographic observations presented in Section III.B. The specimen aged at 538°C displays somewhat erratic behavior and limited data collection, which was due to a machine malfunction that caused premature truncation of the data at $K \sim 30$ MPa√m. None-the-less, the sharply increasing da/dt around K of 20 MPa√m for this aging temperature correctly represents Stage-I HEAC growth. The crack kinetics response for the 510°C age is nearly identical to that of the peak-aged condition with the Stage-II behavior somewhat dependent on K. The da/dt values for the 538°C age show modestly delayed Stage-I to Stage-II transition at a higher K level. The Stage-II crack growth rate, da/dt_{II}, was approximately the same at 10nm/s for the 482°C, 510°C and 538°C tempers. However, da/dt_{II} for the AQ condition was significantly slower at 1 nm/s, a result not compromised by the missing data for the lower K regime.

III.B. Effect of Aging Temperature on HEAC Morphology at E_{App} = -0.900 V$_{SCE}$

Fractographic analyses show that HEAC occurred at E_{App} -0.9 V$_{SCE}$ for all aging conditions of AerMet™ 100, but such subcritical cracking was limited to a very small region (< 100 μm) for the AQ condition. The results of this SEM analysis are shown in Figure 3. For the AQ condition, the entire loading range from 5 to 80 MPa√m produced only 70 μm of HEAC calculated from dcPD measurements, and the crack branched with further loading. The fracture surface was oxidized, prohibiting a precise correlation of actual crack length to dcPD calculations. However, the location of the onset of crack branches shown in Figure 3 accurately coincides with the dcPD-measured extent of slow cracking prior to the onset of the Stage III behavior (Figure 2). The tearing above 80 MPa√m produced a unique fracture surface, shown in Figure 2b, unlike the ductile microvoids typical of fracture in air for this steel; however, this is not definitive since the surfaces were damaged from corrosion that occurred post-fracture.

AerMet[TM] 100 specimens aged at 482°C and 510°C showed transgranular HEAC, as well as some macroscopic crack branching, when stressed in NaCl solution at E_{App} of -0.9 V_{SCE}. Fractographs are presented in Figure 4. These two temperatures showed essentially identical fracture surface features. Evidence of martensite lath interface cracking is prominent when aged at 510°C (Figure 3b), and is virtually identical to the fractographs obtained for severe IHAC[1] and HEAC[2] of this steel aged at 482°C.

HEAC was predominantly intergranular for the specimen aged at 538°C (Figures 4c and d). Such prominent IG cracking has not been observed previously in IHAC or HEAC of AerMet[TM] 100, although partial-minority features of IG HEAC have been noted[2,13,19]. Previous reports of IG HEAC of AerMet[TM] 100 always coincided with crack branching[2,13,19], while such branching was not observed for this specimen aged at 538°C. Both TG and IG HEAC of this steel at various aging conditions (Figures 3 and 4) were very different from the microvoid morphology typical of fracture in moist air. Key experimental results for each aging condition stressed under this electrochemical condition are summarized in Table 3.

III.C.   Effect of Aging on HEAC at E_{App} = -0.625 V_{SCE}

A second set of experiments were conducted at E_{App} of -0.625 V_{SCE}, a potential which previously gave the highest HEAC resistance for the 482°C temper explained based on electrochemically limited H production and uptake at the crack tip[2]. Experimental findings are summarized in Figure 5 and Table 4. The initial crack size for each specimen was essentially identical, however the loading rate was slower for the 510°C age. When aged at 510°C, the operationally defined K_{TH} decreased to 30.6 MPa√m (24% of K_{IC}), compared to higher K_{TH} of 40.8 MPa√m for the microstructure aged at 482°C. Unexpectedly, the AQ condition produced the lowest K_{TH} at 20 MPa√m (16% of K_{IC}), although this specimen showed the highest K_{TH} for E_{App} of -0.9 V_{SCE} (Figure 1). This reversal of HEAC resistance is possibly due to the shorter precrack used for the experiment at -0.625 V_{SCE}, and will be discussed later. Additionally, the exact value of K at initiation of HEAC may be masked due to slow crack growth in the vicinity of the dcPD resolution limit, and the operationally defined K_{TH} values reported here do not necessarily represent the true threshold[2]. If the alternate measurement of susceptibility, K_{TH}*, is used, the AQ condition still has the lowest K_{TH}*, although the trend reverses for the 482°C and 510°C aging temperatures, as shown in Figure 5.

Rates of HEAC measured at -0.625 V_{SCE} are low and to a first approximation comparable for all aging conditions, as shown in Figure 6. These crack growth rate results are generally similar in that da/dt values are low compared to HEAC at -0.900 V_{SCE}. In Figure 6 the Stage-I growth regime is obscured by the resolution limit of the dcPD system and is not observable for any heat treatment with the possible exception of the AQ condition. Reasonably constant da/dt with increasing K (da/dt_{II}) is not strongly apparent, again with the possible exception of the AQ condition. Approximate da/dt_{II} values for K of about 35 MPa√m are shown in Figure 5 and Table 4. Differentiation of true microstructurally based differences in slow crack growth rates, typical of this regime of low-electrochemical H uptake and in the range below about 2 nm/s, is challenging. Insufficient experiments were conducted to achieve definitive results. The rapidly increasing da/dt at high K (above 50 to 80 MPa√m) may represent Stage-III growth and perhaps H interaction with microvoid fracture processes.

III.D. Effect of Aging Temperature on HEAC Morphology at E_{App} = -0.625 V_{SCE}

Subcritical HEAC was confirmed by SEM analysis for each aging condition of AerMet™ 100 stressed at this near-free corrosion potential; the HEAC fracture mode was TG for all tested heat treatments as shown in Figure 7. The TG features were similar in the 482°C and 510°C temper (Figures 7c and d), where the crevices in the latter image was caused by removing the corrosion damage. However, the fracture in the AQ condition (Figures 7a-b and 8) was dissimilar, showing a flatter, rounder variation of transgranular cracking. Some martensite plate cracking is observed (arrow in Figure 7b), but not as dominant nor common as those found in the 482°C age. Some dimples are visible even at low magnification, possibly showing cracking at the larger carbide. Overall, the cracking does not appear to be restricted to martensite plate and packet boundaries as it did in the other two aged specimens, and there are larger areas of completely flat fracture (Figure 7a and b).

The low magnification SEM image for the AQ specimen, Figure 8, shows that HEAC occurred, but the extent was limited. This particular specimen was fatigued to fracture after HEAC testing, thus clearly indicating the exact extent of HEAC. Of the 240 μm total crack growth, the crack only advanced 35~50 μm upon loading to K of 40 MPa√m, based on dcPD measurements. The dcPD calculated crack growth was approximately 15% higher than measurements from the SEM image (Figure 8); most of the error is likely due to high K loading

(above 130 MPa$\sqrt{m}$) which caused some plastic deformation induced dcPD signals. The rest of the crack growth is related to the Stage-III behavior shown in Figure 6. Comparing the AQ and 510°C conditions, the reduction in da/dt_{II} with increased aging temperature was barely an order of magnitude, as shown in Figure 6 and Table 4. A factor-of-three difference is confirmed based on fractographic measurements; a 140 h test produced only 240 μm of total-SEM measured crack growth for 510°C, compared to the same amount of SEM observed cracking (Figure 8) in the AQ condition stressed for 44 h.

Heat Treatment	a_o (mm)	Initial dK/dt (MPa$\sqrt{m}$/h)	K_{TH} (MPa$\sqrt{m}$) [Figure 5]	K_{TH}^* (MPa$\sqrt{m}$) [Figure 5]	da/dt_{II} (nm/s) [Figure 6]	Fracture Mode [Figures 7 and 8]
AQ	0.81	1.8×10^{-3}	40.8	19.3	~1.5	TG
482°C	0.95	1.9×10^{-3}	20	22.3	~0.9	TG
510°C	0.78	8.3×10^{-5}	30.6	67	~0.4	TG

Table 4. Summary of HEAC results for E_{App} = -0.625 V_{SCE}

IV. Discussion

IV.A. Effect of Aging Temperature on HEAC of AerMet™ 100

Over the aging temperature range of 482°C to 538°C, AerMet™ 100 is susceptible to severe transgranular HEAC when stressed in neutral 3.5% NaCl at E_{App} of -0.9 V_{SCE}. The K_{TH} values are between 13 to 23 MPa$\sqrt{m}$, which is only a small fraction of K_{IC}. The severe reduction in cracking resistance remains significant for AerMet™ 100 aged to retain K_{IC} above 110 MPa$\sqrt{m}$ and σ_{YS} above 1300 MPa. As shown in Table 2, the highest strength/toughness combination is obtained when optimally aged at 482°C. However, this temper showed exceptionally severe IHAC and HEAC susceptibility, and it was speculated that modifications to heat treatment could reduce the severity by M_2C coarsening[2]. Tempering at 510°C provides only a small reduction in yield strength while retaining the fracture toughness, while the microstructure offers a higher volume fraction of M_2C with less coherent interfaces that presumably yield a higher H-trap binding energy[6]. This increased binding energy was

anticipated to increase HEAC resistance by preferentially trapping H away from the fracture site. Unfortunately, Figure 9 shows virtually no difference in HEAC response stressed at E_{App} of -0.9 V_{SCE} (and only a modest reduction in crack growth rates at -0.625 V_{SCE}). However, substantial resistance to HEAC was found in the as-quenched condition, with K_{TH} above 80 MPa√m, for the severe hydrogen environment condition of -0.9 V_{SCE}. The improvement in K_{TH} is partially attributed to the decreased σ_{YS} (Figure 5), which is known to improve HEAC resistance in many steels[3,20]. However, 400 MPa reduction in σ_{YS} alone cannot account for the 4-fold increase in K_{TH} or $K_{TH}*$. Moreover, σ_{YS} is approximately equal for the 538°C age and AQ condition; the measured differences in K_{TH} and da/dt_{II} are undoubtedly due to the microstructure-H interactions that govern HEAC.

Polarization to -0.625 V_{SCE} resulted in improved resistance to HEAC of AerMet™ 100, paralleling the behavior of the optimally aged (482°C) microstructure[2]. A typical example is presented in Figure 9. For E_{App} of -0.625 V_{SCE}, K_{TH} and da/dt_{II} varied less significantly across the tempering conditions than at -0.9 V_{SCE}. The general dependence was reversed, with lowest values of K_{TH} at the AQ condition and highest K_{TH} aged at 482°C. This is unexpected from the yield strength correlation, which predicts better HEAC resistance with decreasing strength[3]. However, when da/dt_{II} or $K_{TH}*$ is used as the benchmark, the highest resistance is found when aged at 510°C. Speculatively, crack tip H production for E_{App} of -0.625 V_{SCE} is already very low, which obscured the effect of microstructure on HEAC behavior as measured by K_{TH} or $K_{TH}*$. The fact that the AQ condition has the lowest K_{TH} or $K_{TH}*$ at this applied potential is significant considering the best resistance it displayed at E_{App} of -0.9 V_{SCE}. The exact values of K_{TH} and $K_{TH}*$ shown in Figure 5 and Table 4 may not accurately describe the true threshold and it is possible that cracking will occur below the operationally defined thresholds. Problems were also encountered in carrying out these complex HEAC experiments and additional work is required to define the behavior of the AQ condition. Such work is significant to mechanism interpretation, but not alloy development since secondary hardening carbides are critical to strength/toughness combinations required for steels such as AerMet™ 100.

In terms of da/dt_{II}, HEAC resistance measured for E_{App} = -0.9 V_{SCE} was virtually identical in all three aged conditions. This is particularly evident between the 482°C and 510°C conditions as shown in Figure 2. Since the intergranular crack path was dissimilar for the 538°C case, it is probably coincidental that da/dt_{II} for that temper matches those of the other two that

exhibited transgranular cracking. These results suggest that M_2C coarsening by aging at 510°C has not sufficiently increased the H binding energy to the precipitates (E_B = 11 kJ/mol at 482°C) to equal or exceed the binding energy characteristic of martensite interfaces (61 kJ/mol)[5]. As such, H diffusing from the crack tip surface to the high stress region within the fracture process zone will preferentially partition from the carbides to martensite interfaces due to the large binding energy difference for both aging conditions; a dramatic improvement in HEAC resistance is thus not achieved. Considering the possibility of more modest changes in cracking resistance with aging, diffusion limited da/dt_{II} is related to the effective H diffusivity, $D_{H,Eff}$, a characteristic distance, X_C, and surface hydrogen concentration in equilibrium with crack tip overpotential, C_S, in the following form[21]:

$$da/dt_{II} = \frac{D_{H,Eff}}{X_C} f(C_S, C_{Crit})$$

[1]

where $f(C_S, C_{Crit})$ is a functional description of the boundary conditions for H-diffusion and C_{Crit} is the critical amount of H required at the crack nucleation site for H damage to form. As a first approximation, it is reasonable to assume based on the form of Equation 1 that da/dt_{II} is proportional to the product of D_{H-Eff} and C_S^2 [21]. The hypothesis is that D_{H-Eff} decreases and C_S increases as the M_2C carbides loose coherence with increasing aging temperature from 482 to 510°C. This behavior is due to increasing H-trap binding energy as the coherence of M_2C interfaces decreases. The implication from the data is that constant da/dt_{II} with aging means that the trap-induced changes in the magnitude of decreasing $D_{H,Eff}$ and increasing C_S^2 are essentially offsetting.

Other terms in Equation 1 must be considered. The critical distance X_C is closely related to the stress distribution in the crack tip process zone which in turn is governed by alloy flow strength and work hardening[3,21]. It is reasonable to assume that these factors are affected to a secondary extent by aging between 482°C and 510°C. It is possible that C_{Crit} changes with aging. This critical concentration depends on the local normal stress acting on this H-laden site as well as the atomic details of the interface or lattice. For HAC in AerMet[TM] 100, results suggest that martensite lath and/or packet boundaries constitute this damage site and crack path[1,2] There is no documented reason to believe that the local stress, trapped H content, and atomic environment of these martensite interfaces change with aging between 482 and 510°C. Of course, subtle

differences may exist but have not been elucidated. Finally, it is possible that Equation 1 does not fully describe da/dt_{II} if the C_S crack surface boundary condition is surface reaction rate limited[3].

Considering the AQ condition, da/dt_{II} was substantially slower at -0.9 V_{SCE} (Figure 2) and the microscopic mode of HEAC was different from transgranular martensite interface cracking due to trapped H (Figures 3 and 4). Following the logic associated with H diffusion limited da/dt_{II}, in the absence of M_2C carbides and precipitated austenite, $D_{H,Eff}$ is expected to be substantially higher compared to the aged conditions. However, C_S will be proportionately lower and the change in the terms $D_{H,Eff}$ and C_H^2 is unknown but may be reasonably similar for AQ and the aged microstructures. The martensite should be of similar morphology and have unrecovered dislocation structure for both the as-quenched and aged conditions; thus the strong difference in HEAC resistance is not easily understood. Perhaps short range segregation is enabled by aging near 500°C to promote martensite interface decohesion in concert with trapped H. It is also possible that HEAC was promoted by increased crack tip stresses from the strength increase during aging, compared to the lower strength AQ condition, although severe HEAC produced for the 538°C age of AerMet™ 100 somewhat weakens this explanation. Also, it is likely that crack tip stresses are not substantially different for the different microstructures examined due to the fact that increased work hardening preferentially elevates crack tip stresses for the AQ (and 538°C) microstructures to offset reduced σ_{YS}.

These complications aside, the present results show that the as-quenched martensitic microstructure is not, per se, uniquely embrittled by H. Some aspect of aging must promote HEAC based on the results shown in Figures 2 through 4. Thermal desorption spectroscopy (TDS) results show dramatic differences in the trapping situation, for AQ vs. the 482°C age of AerMet™ 100, but only for the H outgassing peak characteristic of the lack of M_2C[5] and consistent with the above discussion. Subtle differences in H trapping were suggested by the desorption peak structure generally associated with martensite and undissolved TiC interface traps states. However, this behavior was not investigated in detail and additional experiments are required.

While H diffusion limitation of da/dt_{II}, coupled with H decohesion and trapping, provides a reasonable framework to examine the results of the present experiments, it is not possible to explain the observed microstructural effects. It is reasonable to speculate that da/dt_{II} values are

diffusion rate limited, as described by Equation 1, and the aging independence is traced to offsetting effects of trapping on H solubility and diffusivity. The magnitude of these effects are not known at present, but can be assessed based on the results of TDS experiments[5]. Such measurements, coupled with improved modeling of the threshold and kinetics of HEAC, are required to provide a fundamentally grounded basis for alloy and process development to mitigate IHAC and HEAC.

IV.B. Loading Rate and Crack Size Effects

Because changes in heat treatment affect yield strength, precrack length was increased to maintain small-scale yielding at high applied K for each condition. The loading rate was accordingly modified to maintain an approximately constant dK/dt and the test conditions are listed in Tables 3 and 4. In one specimen (E_{App} = -0.625 V_{SCE}, 510°C age), the loading rate was purposefully lowered to observe any possible effects on HEAC response. The slower loading rate resulted in higher K_{TH}* and slower da/dt_{II} when comparing 482°C and 510°C at E_{App} of -0.625 V_{SCE}, whereas the opposite trend is expected for loading-rate affected results[1-3,22]. The variations in loading rate presumably did not affect the results.

Due to occluded crack geometry, different crack lengths may produce different HEAC behavior[23,24]. In the range of crack sizes examined (0.3 ~ 3 mm), there is some evidence of adverse effects for cracks shorter than 1 mm[24]. Given the small differences between the 240 µm and 950 µm precracks in the 482°C temper, K_{TH} and da/dt_{II} are not likely affected. Additionally, previous findings suggest that long precracks (1 ~ 3 mm) show no variances in observed K_{TH}[24]. Overall, loading rate and crack size effects were not evident in the results.

IV.C. Intergranular HEAC Aged at 538 °C

Instances of intergranular fracture were rare in HEAC[2] and IHAC[1] of peak-toughness AerMet™ 100. However, aging at 538°C produced predominantly IG HEAC at E_{App} of -0.9 V_{SCE}. Since the specimens used for the IHAC[1], HEAC[2] and current experiments were cut from the same small forging of AerMet™ 100, the composition should be virtually identical across all the experiments. Assuming no significant segregation during forging, the onset of IG fracture mode must be attributed to changes in microstructure due to aging at 538°C. This assumption is substantiated since IG fracture on this specimen was not localized but prevalent across the entire fracture surface (Figure 4d). Uniform IG fracture was not observed on any

other experiments[1,2] or by any other observers[13-15,19,25] who focused on AerMet™ 100 aged at 482°C. It is unlikely that *localized* segregation can be responsible for such IG cracking.

Large-scale impurity segregation to prior austenite grain boundaries is a commonly cited reason for IG HAC in less pure and lower alloy content high strength steels[3,26]. For high strength tempered martensitic microstructures in general, H-free toughness is degraded by tempering in the range from 250°C to 450°C, traced to impurity (P in particularly) segregation to prior austenite boundaries coupled with cementite precipitation at martensite interfaces[26]. Susceptibility to HEAC due to H-impurity interaction has been characterized by an impurity-weighted composition parameter (ψ = Mn + 0.5 Si + S + P in weight %)[20]. While cementite precipitation in the range of 400°C degrades the toughness of AerMet™ 100[6,7], IG fracture with or without H is not expected for AerMet™ 100 given its very low ψ (0.029 wt%)[2]. Impurity segregation is thermally activated and exhibits classic "C-curve" time-temperature kinetics[26]. If the critical temperature range for optimal segregation lies above 510°C, it is possible that the low bulk concentration of impurities could sufficiently segregate at higher aging temperatures such as 538°C to enable IG HEAC, while not doing so at 482°C. This application of the classic impurity-H interaction mechanism requires confirmation of segregation by Auger spectroscopy and such results have not been reported for high purity ultra-high strength steels[26].

Given the high H-binding energy at both martensite boundaries and prior austenite grain boundaries, H will accumulate to very high concentrations at both trap sites. Previously, it was speculated that the H-degraded strength of the grain boundary of this steel was higher than the equivalently H-reduced martensite boundary strength[2]. Otherwise, IG cracking is expected at the peak-toughness age. In this view, the fracture mode transition from TG to IG can be due to weakened grain boundaries, strengthened martensite boundaries, or both, upon aging at the higher temperature. The fact that K_{TH} was higher than the 482°C and 510°C values but still low (23 MPa√m) suggests increased martensite boundary strength. However, K_{TH} was much higher in the AQ condition and cracking was not IG, which suggests weakened grain boundary strength at 538°C.

Aging at 538°C produces three significant changes to microstructure from the 482°C and 510°C ages; M_2C coarsening and loss of coherency with the matrix, increased γ` precipitation and intra-martensite plate γ` precipitation. There was no evidence of preferred M_2C precipitation on martensite boundaries or prior austenite grain boundaries at any aging temperature, so the

changes in M_2C characteristics are unlikely to directly cause grain boundary weakening or martensite boundary strengthening. Conversely, $\gamma`$ was reported to precipitate on martensite plate boundaries. Increased $\gamma`$ precipitation can increase the H-degraded fracture strength of the martensite plate interface by one of two hypothetical mechanisms: prohibiting the martensite transformation of $\gamma`$ or restricting a connected martensite lath crack path.

In the presence of H it was speculated that thin-film $\gamma`$ transforms to martensite by H-stress interactions to promote HEAC along martensite boundaries[2,27,28]. Given the composition of $\gamma`$ (30 wt. % Ni) in AerMet[TM] 100, it is unlikely to transform to martensite in its bulk form even with elevated stresses near the crack tip; thus a thin-film-specific mechanism was hypothesized[27,28]. Within their framework, discontinuous distribution of thin-film $\gamma`$ is necessary for such transformation, and networked distribution of thicker $\gamma`$ prohibits that transformation. If this mechanism actually facilitates TG HEAC at the peak toughness temper, then IG cracking in the 538°C age can be attributed to increased $\gamma`$ precipitation which is less likely to transform to martensite. That assumes that the HEAC fracture site for the 482°C and 510°C to be the interface between martensite and $\gamma`$. On the other hand, if the martensite-martensite interfaces are responsible for low K_{TH} HEAC, then the presence of intra-lath γ and increased γ precipitation would reduce the percentage of such boundaries by precluding direct contact between two martensite plates. Furthermore, with sufficient precipitation, $\gamma`$ may prevent "clean" martensite plate crack paths from connecting. Aging for 5 h at 538°C produces at least 5.5% $\gamma$ and partially interconnected $\gamma`$ (Figure 10)[6].

M_2C coarsening can indirectly increase the martensite boundary strength by the previously proposed mechanism of preferential H trapping[2]. If the binding energy of M_2C carbides is increased by particle coarsening and the distribution remains relatively uniform throughout the microstructure, then M_2C carbides can act as preferential traps to keep H away from potential fracture sites such as martensite plate boundaries. Since tempering at 538°C produces incoherent and presumably increased E_B of these carbides, this mechanism may be responsible for the lack of martensite lath cracking. M_2C coarsening does not increase the H-reduced fracture strength of the martensite laths; instead it reduces the amount of H accumulation at those sites. However, this is speculative since IG HEAC occurs at this temper at relatively low K_{TH}, and the only reasonable explanation is arbitrary: that low concentrations of H, after partitioning to incoherent M_2C, weakens the austenite grain boundaries more than the martensite

boundaries.

Alternatively, the increased aging temperature may change the grain boundary composition to lower the H-reduced fracture strength of the grain boundary. As mentioned previously, the changes in microstructure from 482°C to 538°C are limited to M_2C and γ'. The composition of those features change, but the differences are mild (less than 10%) and only involve elements (Cr, Mo, Fe, Co and Ni) that are not traditionally considered to be grain boundary embrittlers[20]. However, the grain boundary composition has not been measured and the possibility remains for low temperature diffusion of S and P[3,26].

IV.D. K_{TH} and da/dt_{II} in the As-Quenched Condition

The HEAC mode of non-aged AerMet[TM] 100 is unique from the aged specimens, as shown in Figures 3, 7a-b and 8. There are no IG features, and martensite lath/packet interface cracking found in peak-aged IHAC[1] and HEAC[2] are not prevalent. These features support the γ'-martensite transformation induced HEAC mechanism for aged conditions, as the non-aged specimen (0% γ'^1) produced substantially higher K_{TH} and lacked widespread indications of martensite boundary cracking when stressed at E_{App} of -0.9 V_{SCE}. Regardless of the exact mechanism, the experimental results show that thin film interlath reverted austenite, while increasing the H-free fracture toughness of AerMet[TM] 100, substantially reduces its HEAC resistance. Alternatively, the M_2C carbides that were anticipated to increase HEAC resistance may actually increase the susceptibility by somehow enhancing the fracture site H concentration. This alternative theory has not been developed.

When stressed at E_{App} of -0.625 V_{SCE}, the AQ condition actually shows the lowest K_{TH} and K_{TH}*. It seems particularly strange that the K_{TH} is lower at E_{App} = -0.625 V_{SCE} compared to -0.9 V_{SCE}. Close examination of the fractographs (Figures 3, 7 and 8) and crack growth curves (Figures 2 and 6) shows the onset of Stage III growth around 40 MPa$\sqrt{m}$ for E_{App} = -0.625 V_{SCE} and 100 MPa$\sqrt{m}$ for E_{App} = -0.9 V_{SCE}. Stage-III behavior depends on loading rate, and it is possible that the differences in operational threshold are affected by the early onset of atypical Stage III crack growth behavior. As it was shown previously[2], very slow crack kinetics could hinder the determination of exact values for K_{TH}. Presumably, the actual threshold lies

---

1   Although there is some evidence of retained austenite in the non-aged condition[10], reverted austenite does not exist in the AQ condition. Furthermore, retained austenite does not have thin-film interlath morphology.

somewhere in the range of 20 to 87 MPa$\sqrt{m}$.

Uncertainties in the exact value of K_{TH} and K_{TH}^* are not critical to the interpretation of aging effects on HEAC as long as the trend is accurate. It is clear from the fractographic results that HEAC cracking in the AQ condition is limited when compared to aged specimens. Moreover, the interpretations of microstructural effects on the HEAC response at E_{App} of -0.9 V_{SCE} are valid for the AQ condition. The da/dt_{II} is under 2 nm/s for the AQ microstructure at both potentials. Since both γ` and M_2C are suspected to slow H diffusion, their absence is expected to increase the crack growth rate, as observed in Figure 6.

Lastly, aging duration is a critical variable that has not been investigated in these experiments. Aging time has a pronounced effect on microstructure, particularly affecting the size and coherence of M_2C carbides and volume fraction of γ`[9]. For example, up to 23 vol. % of $\gamma$` was formed when aged at 482°C for 100 h compared to a near-0 volume fraction for 5 h[9]. Small differences in aging time can easily alter these properties, especially at the early stages (below 10 h). If the HEAC response to microstructural differences are as sensitive results show, additional studies for isothermal aging effects on HEAC are required.

V. Conclusions

1. When aged to obtain high strength (σ_{YS} > 1300 MPa) and plane strain fracture toughness (K_{IC} > 100 MPa$\sqrt{m}$), at several different aging temperatures, AerMet[TM] 100 is similarly susceptible to severe hydrogen environment assisted cracking in neutral 3.5% NaCl and at an applied potential of -0.9 V_{SCE}. This is quantified by two parameters: reduced threshold stress-intensity for HEAC, K_{TH}, to as low as 10% of K_{IC}, and subcritical Stage-II crack growth rate, da/dt_{II}, as high as 30 nm/s.

2. The aging independence of HEAC at -0.9 V_{SCE} may be consistent with a mechanistic explanation based on H diffusion control of crack growth rate, but material dependent terms in the model for da/dt_{II} and the very detail of the model remain uncertain. It is not possible to design alloy composition and processing conditions based on such existing models.

3. Qualitatively, increasing incoherence of M_2C precipitates does not result in reduced da/dt_{II}, perhaps due to the counterbalancing effects of increased trapping; causing reduced H diffusivity but increased H solubility; as suggested by the diffusion model. Relatively low H-trap binding energy of these precipitates for the tempers examined prevents beneficial shielding of H partition to martensite lath/packet boundary interfaces where such segregation enables decohesion.

4. When aged at 538°C for 5 h, the HEAC fracture mode is predominantly intergranular at an applied potential of -0.9 V_{SCE}. Hydrogen cracking was transgranular at all other aging conditions for E_{App} = -0.9 V_{SCE}, similar to the behavior of optimally aged (482°C) AerMet^{TM} 100. It is suggested that precipitation of intra-plate austenite at 538°C impedes fracture along martensite boundaries, promoting the less favorable intergranular crack path at higher K_{TH}.

5. In the as-quenched condition, susceptibility to HEAC at -0.9 V_{SCE} is substantially reduced, with K_{TH} of up to 70% of K_{IC} and slow da/dt_{II} of 1 nm/s. The fracture path is transgranular, but not limited to martensite plate boundary cracking as observed in IHAC and HEAC of the peak-aged condition. Speculatively, the lack of thin-film reverted austenite increases the K_{TH} as it otherwise aids martensite plate boundary cracking; but the lack of uniformly distributed M_2C carbides slightly increases da/dt_{II} due to increased effective H diffusivity not offset by reduced H solubility.

6. K_{TH} and da/dt_{II} levels for HEAC at an applied potential of -0.625 V_{SCE} are similar for the as-quenched and 482°C and 510°C aging temperatures. Notably, each aging condition shows a greatly reduced HEAC susceptibility, as established previously for optimally aged AerMet^{TM} 100. The combination of alternate aging temperatures and optimal electrochemical polarization did not produce immunity to HEAC.

7. The improved purity of AerMet^{TM} 100 does not provide immunity to IG HEAC. However, the increased purity may raise the K_{TH} required for IG fracture, causing TG fracture to be favored for optimally aged AerMet^{TM} 100.
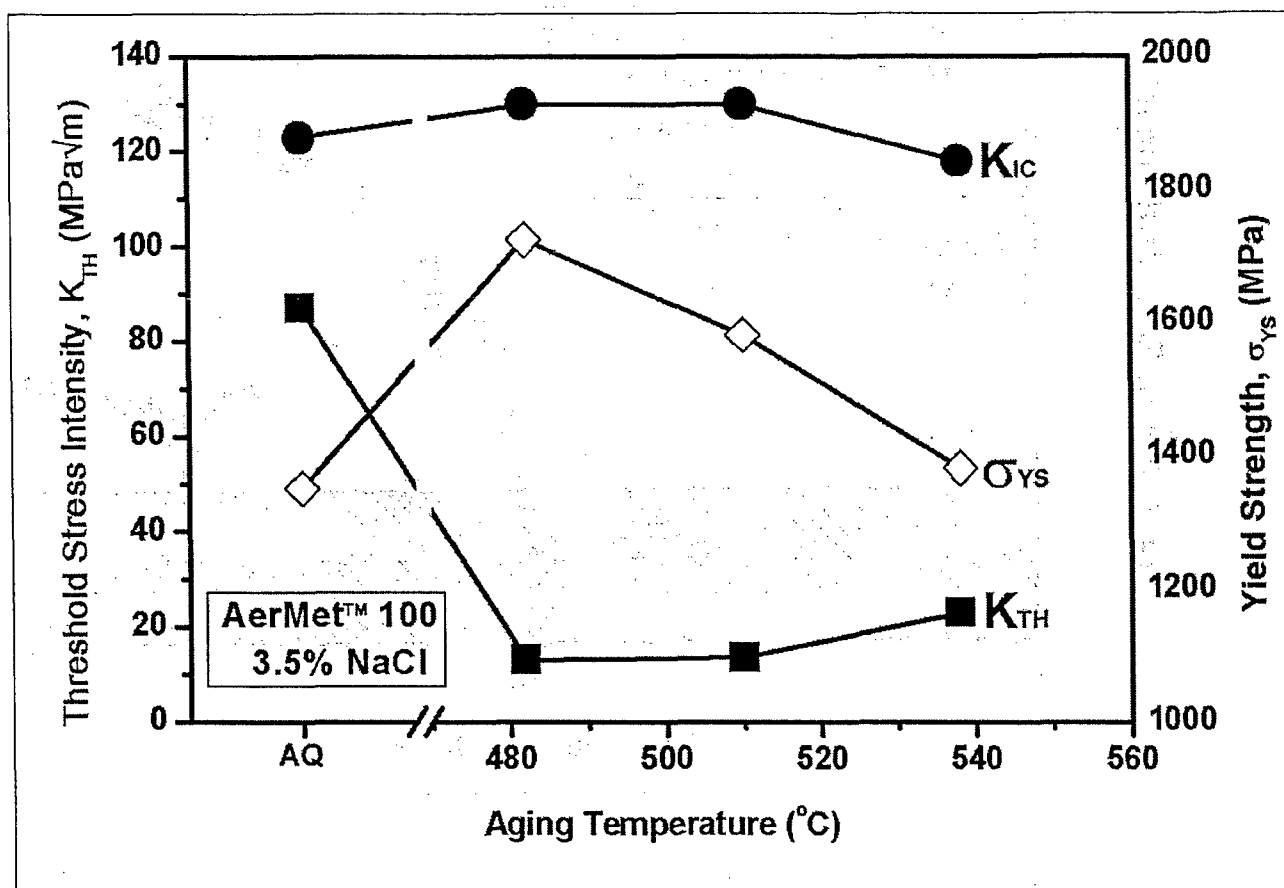
Figures

Figure 1   Threshold stress intensity, K_{TH}, *vs.* aging temperature for AerMet^{TM}100 stressed under slow-rising crack mouth opening displacement at E_{App} of -0.9 V_{SCE} in neutral 3.5 % NaCl. Literature reported K_{IC} and σ_{YS} values for each tempering condition in Table 2 are displayed for reference.
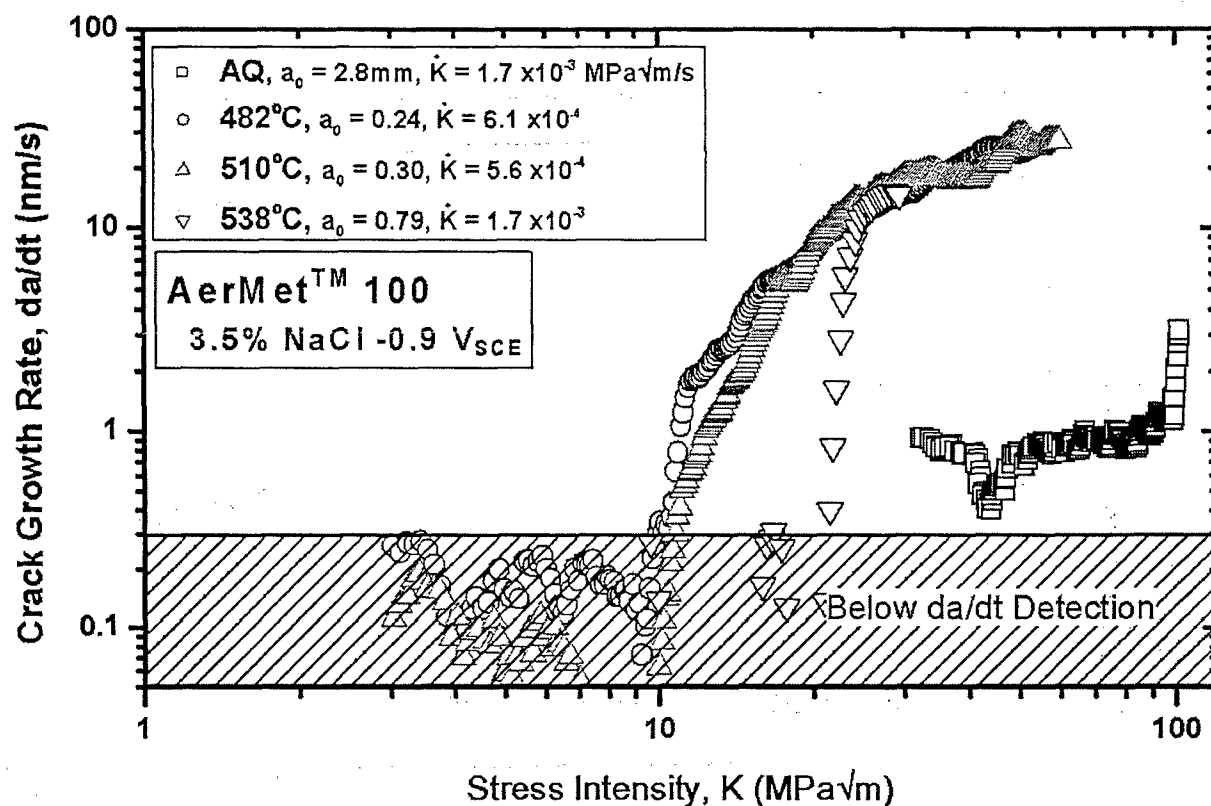
Figure 2   Subcritical crack growth rate *vs. K*, for various aging temperatures of AerMet[TM] 100 stressed under constant grip displacement rate in 3.5 % NaCl at E_{App} of -0.625 V_{SCE}. The initial loading rate, *dK/dt*, and fatigue precrack length for each condition are noted.   Load and dcPD data were not collected for the AQ condition at *K* less than 30 MPa√m.

(a) Fracture in 3.5% NaCl, $K = 3$ MPa√m (bottom of image) to $K > 80$ MPa√m (top of image)

(b) Higher magnification of location (b)
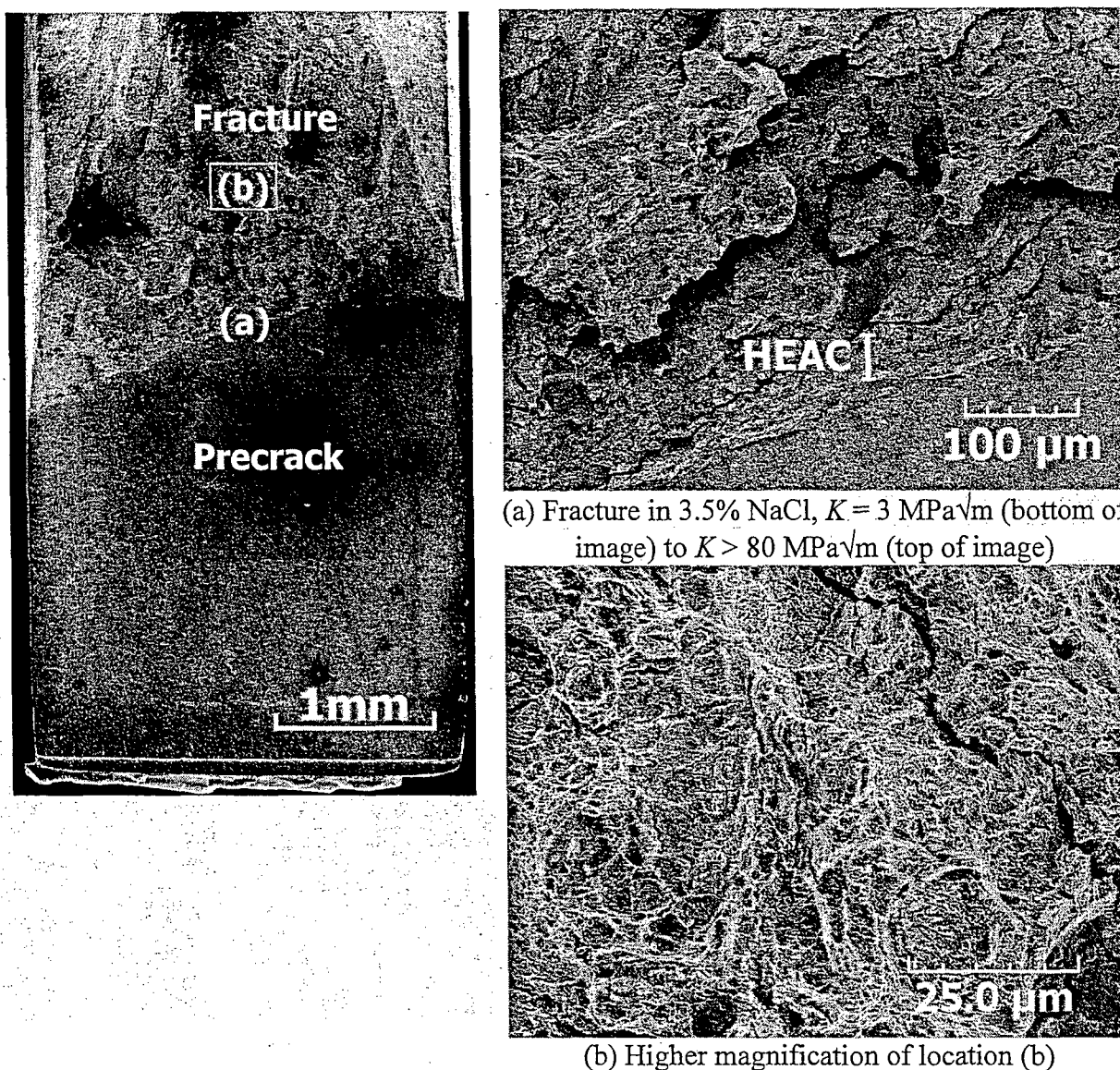
Figure 3 Scanning electron fractographs of the fracture surface of an as-quenched (AQ) AerMet™ 100 specimen fractured in 3.5% NaCl (-0.900 V_{SCE}). The SEM image on the left shows the macroscopic appearance. The black spots on the left image are due to oxidation. (a) shows a small region marked "HEAC" that represents HEAC crack growth of 70 μm over the loading range from K of 3 to 80 MPa√m. Above 80 MPa√m, extensive crack branching is evidenced and presumably H assisted since K_{IC} equals 123 MPa√m from Table 2. (b) shows the typical appearance of high K (above 80 MPa√m) cracking in this condition.

(a) 482 °C[2]

(b) 510 °C

(c) 538 °C

(d) 538 °C, Low Magnification
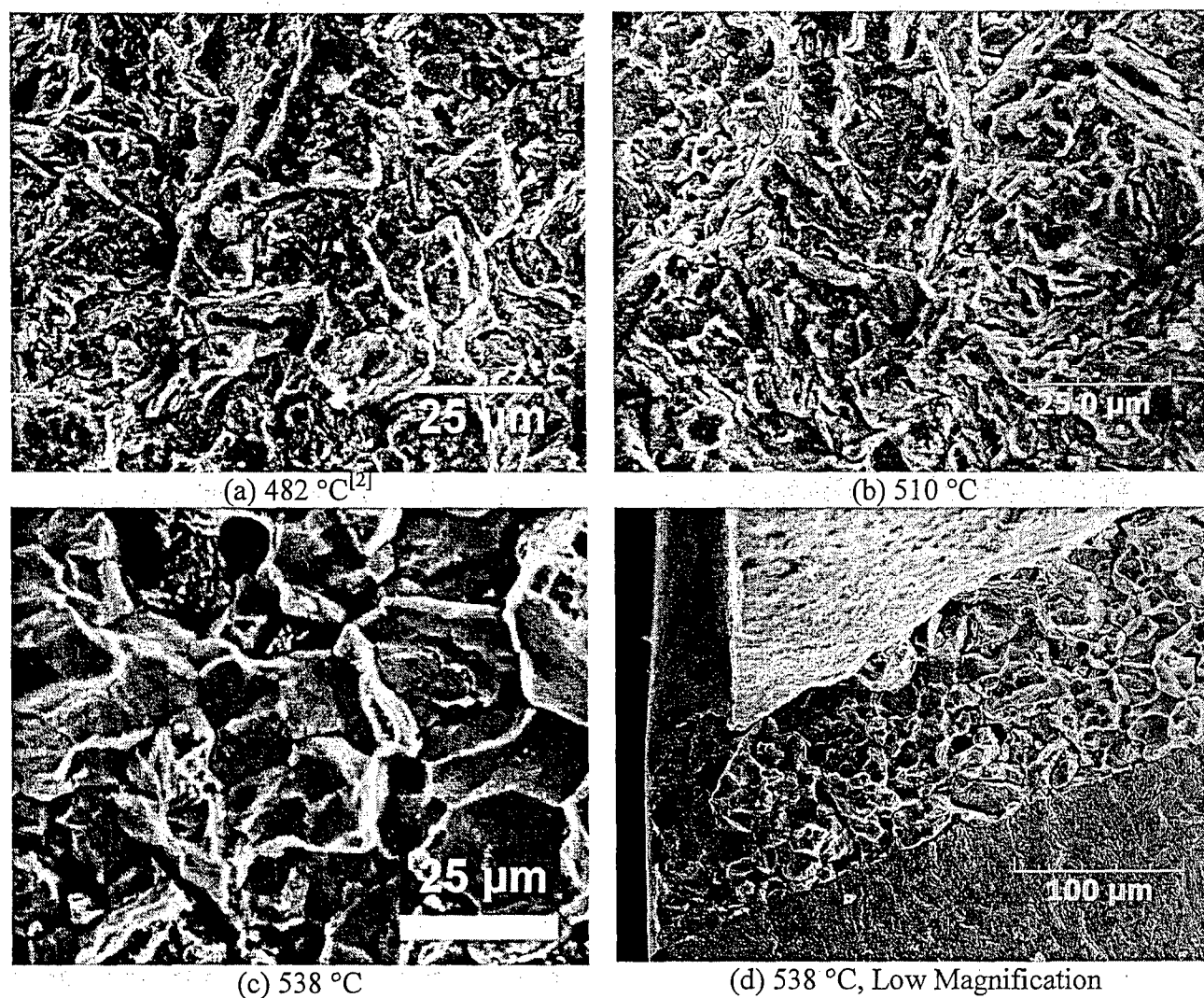
Figure 4 SEM images of hydrogen affected fracture surfaces for various aging temperatures of AerMet[TM] 100 stressed in 3.5% NaCl at an applied potential of -0.9 V_{SCE}. (a) and (b) show predominantly transgranular fracture, while (c) and (d) shows predominantly intergranular fracture.
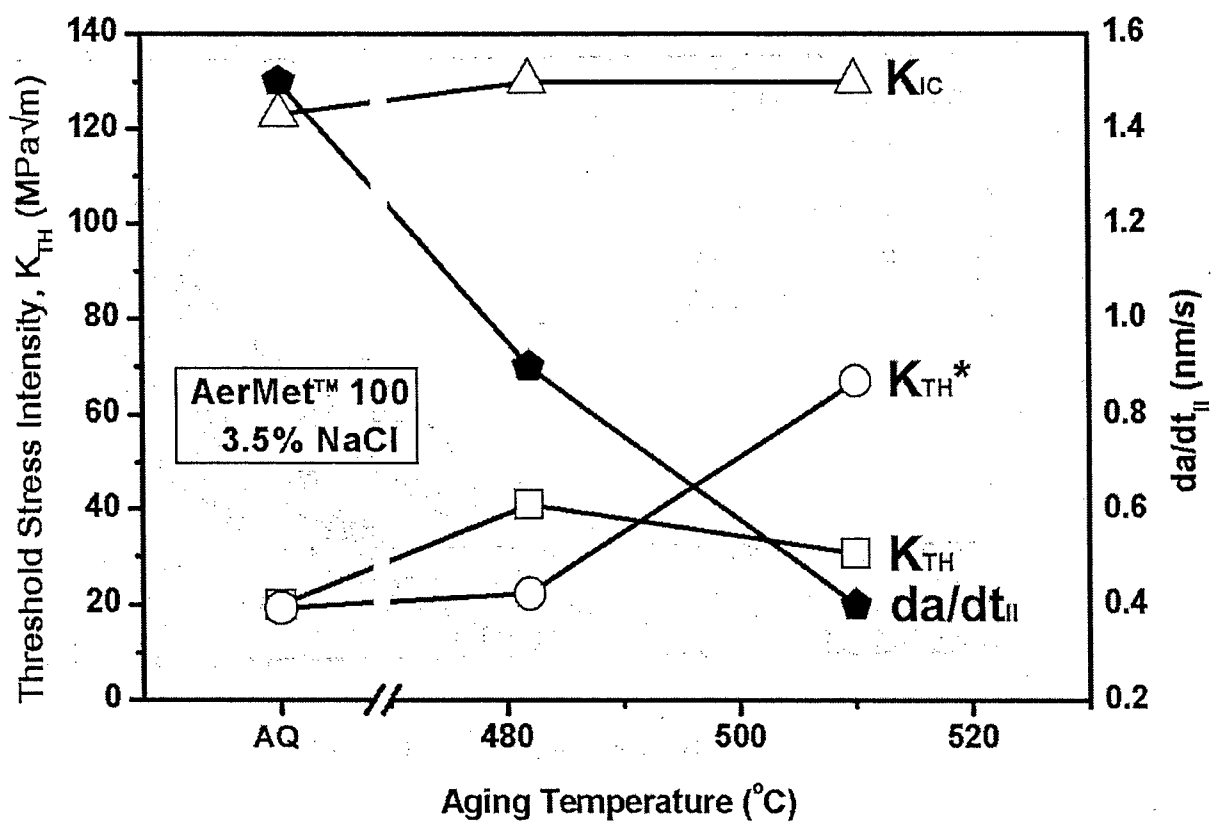
Figure 5 Threshold stress intensity, K_{TH}, and da/dt_{II} vs. applied potential for various ages of AerMet^{TM}100 stressed in 3.5 % NaCl at applied potential of -0.625 V$_{SCE}$. The K_{IC} for each tempering condition is displayed for reference.
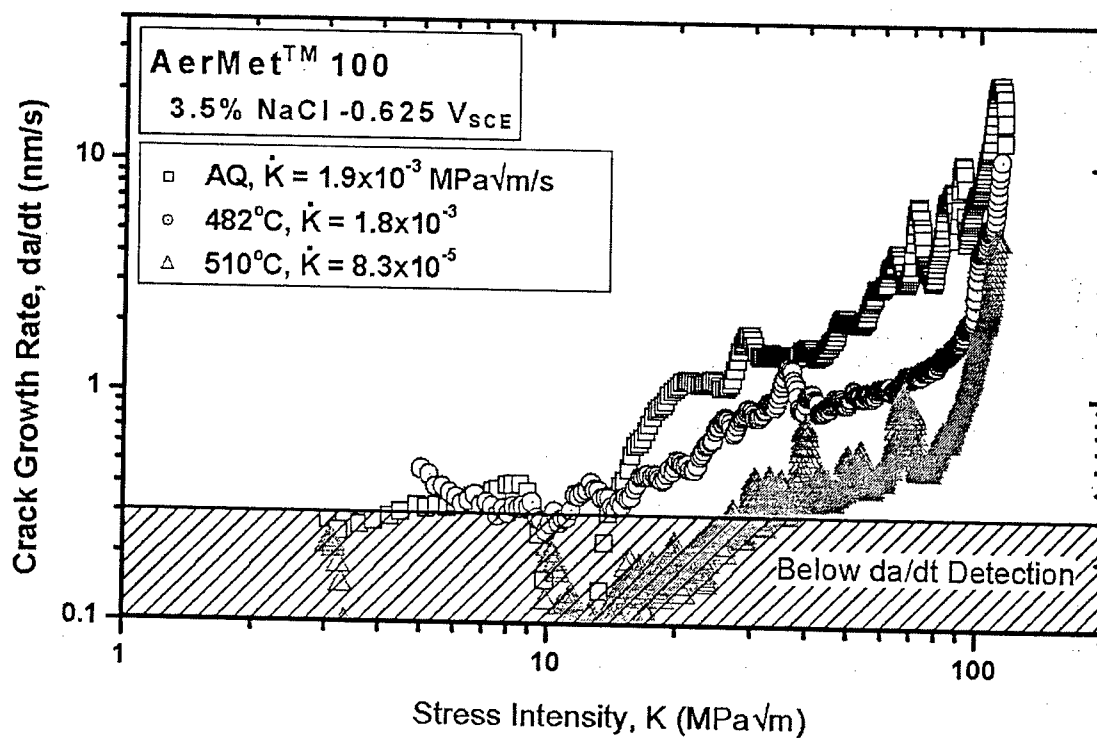
Figure 6 Subcritical crack growth rate *vs. K*, for various aging temperatures of AerMet^TM 100 stressed in 3.5 % NaCl at E_{App} of -0.625 V_{SCE}. The initial loading rate, *dK/dt*, is noted.

(a) AQ

(b) AQ

(c) 482 °C[2]

(d) 510 °C
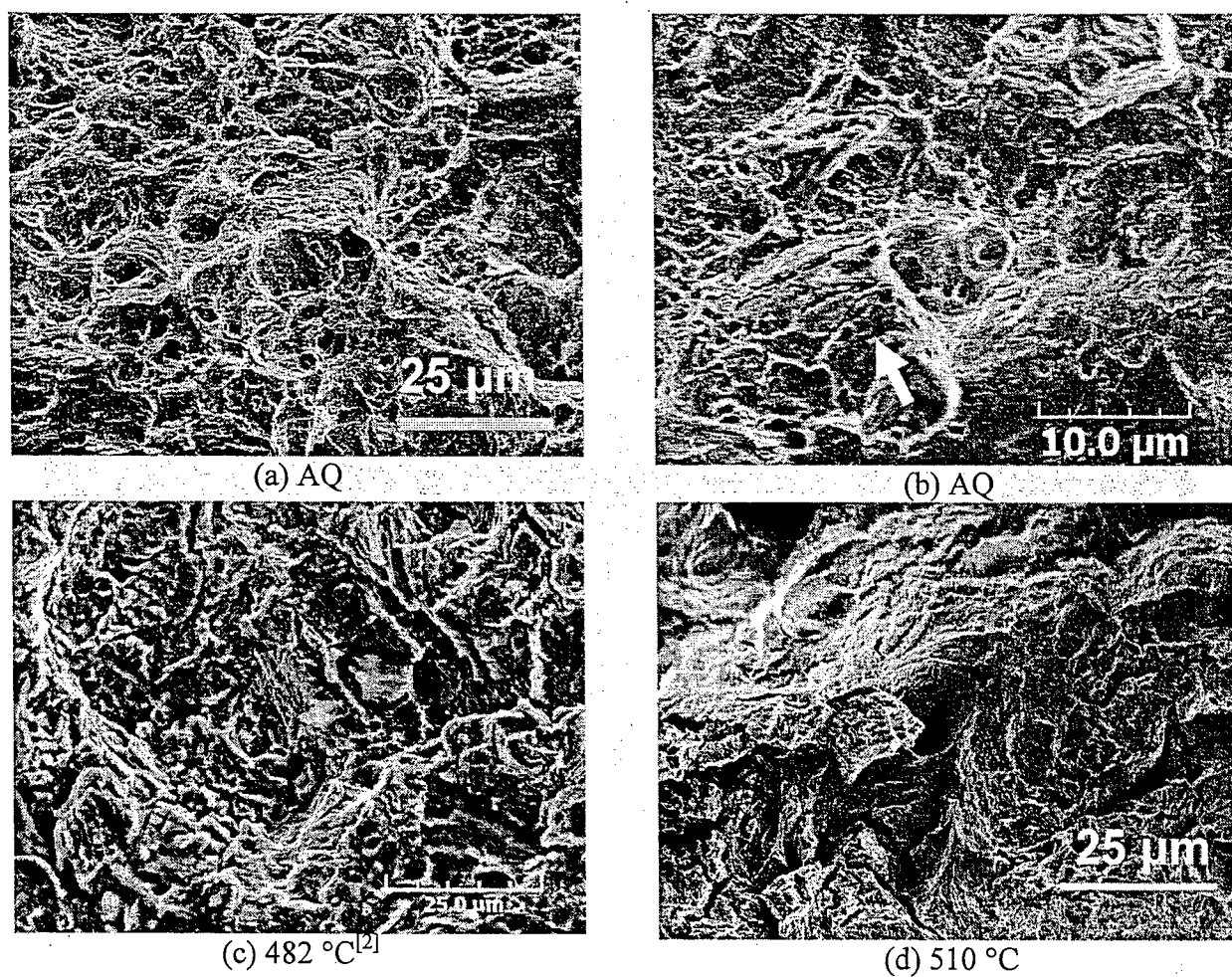
Figure 7   SEM images of HEAC surfaces for various aging conditions of AerMet[TM] 100 stressed in 3.5 % NaCl at an applied potential of -0.625 V_{SCE}.   All images show predominantly transgranular fracture.
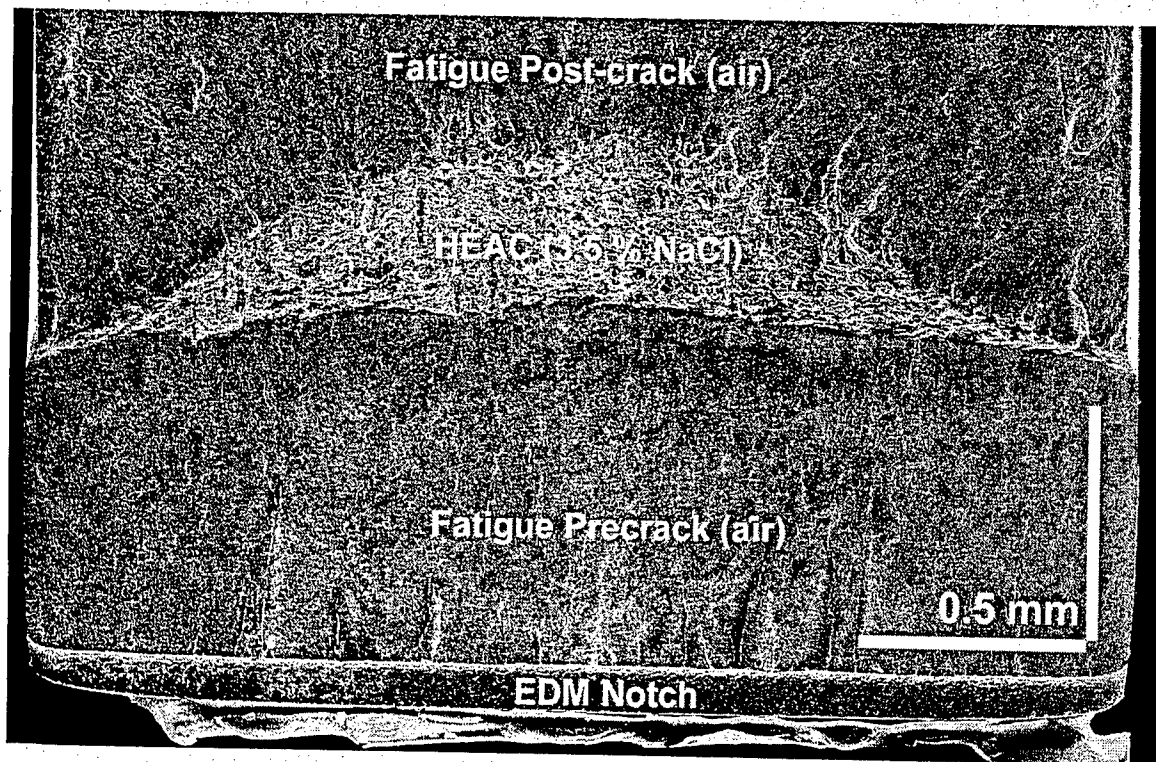
Figure 8 Low magnification scanning electron fractograph of the fracture surface of an as-quenched (AQ) AerMet[TM] 100 specimen cracked in 3.5% NaCl polarized to -0.625 V_{SCE}. The thumbnail region marked "HEAC" represents subcritical HEAC extending over an average of 240 μm for the loading range from K of 5 to 80 MPa√m. The post-test fatigue crack clearly marks the extent of HEAC.
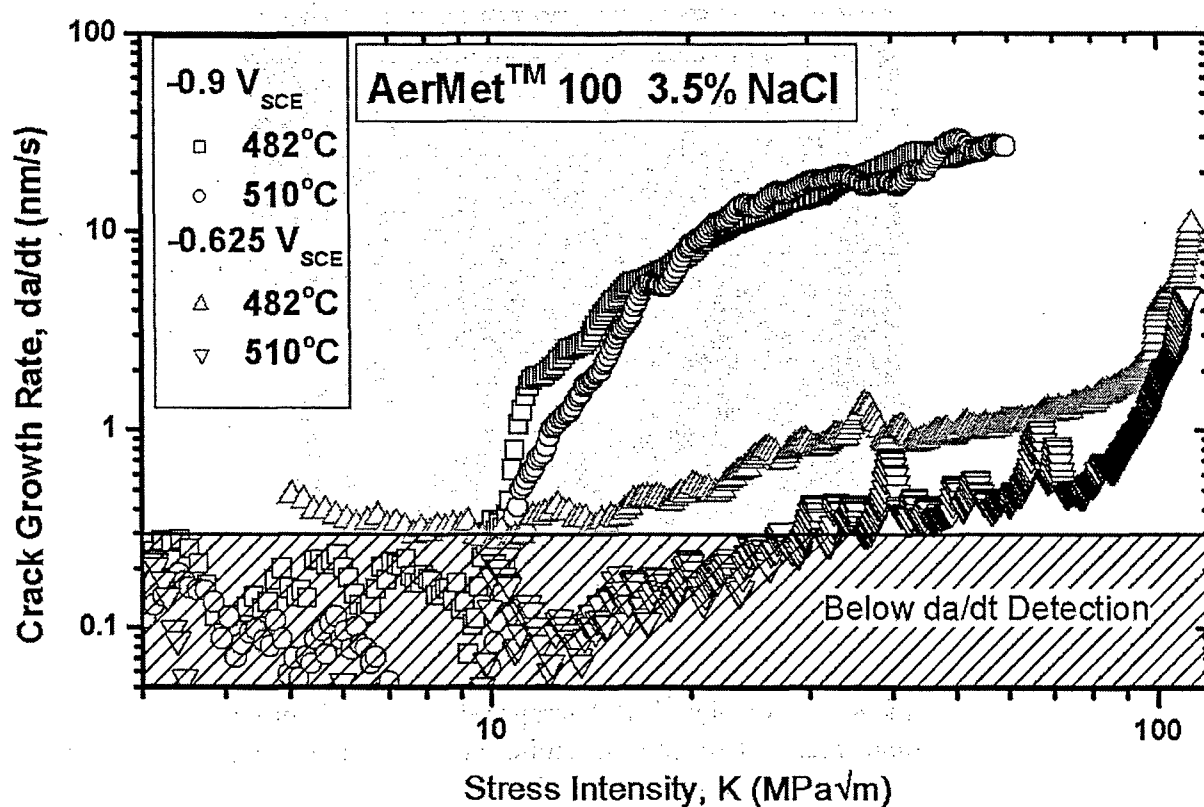
Figure 9 Subcritical crack growth rate *vs.* *K* for two aging temperatures of AerMet[TM] 100 stressed in 3.5 % NaCl. These two aging temperatures produce the highest toughness and strength in this steel.
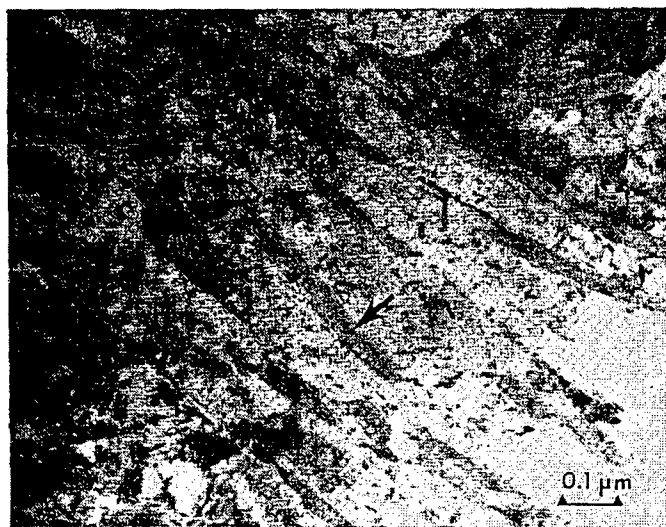
Figure 10 Transmission electron microscope image of AerMet^{TM} 100 tempered at 538°C; bright field image of revered austenite (arrow). Image and caption taken from Ayer and Machmeier[6]

References

1. Richard L.S. Thomas, John R. Scully and Richard P. Gangloff: *Metallurgical Transactions A*, 2003, vol. 34A, pp. 327-44.

2. Yongwon Lee and R. P. Gangloff: University of Virginia, unpublished research, 2005.

3. Richard P. Gangloff: *Environmentally Assisted Failure*, Elsevier Ltd., 2003, pp. 31-101.

4. Richard L.S. Thomas, Daoming Li, Richard P. Gangloff and John Scully: *Metallurgical Transactions A*, 2002, vol. 33A, pp. 1991-2004.

5. Daoming Li, Richard P. Gangloff and John R. Scully: *Metallurgical and Materials Transactions A*, 2004, vol. 35A, pp. 849-64.

6. R. Ayer and P.M. Machmeier: *Metallurgical Transactions A*, 1993, vol. 24A, pp. 1943-55.

7. R. Ayer and P. M. Machmeier: *Metallurgical and Materials Transactions A*, 1998, vol. 29A, pp. 903-05.

8. Hyuck Mo Lee, Hyunchul Sohn and Choong Hwa Yoo: *Scripta Materialia*, 1997, vol. 37, pp. 1931-37.

9. Choong Hwa Yoo, Hyuck Mo Lee, Jin W. Chan and J. W. Morris Jr.: *Metallurgical and Materials Transactions A*, 1996, vol. 27A, pp. 3466-72.

10. P. M. Novotny: *Gilbert R. Speich Symposium-Fundamentals of Aging and Tempering in Bainitic and Martensitic Steel Products*, Iron and Steel Society, Warrendale, PA, 1992, pp. 215-36.

11. B.G. Pound: *Hydrogen Effects on Material Behavior and Corrosion Deformation Interactions*, The Minerals, Metals & Materials Society, Warrendale, PA, 2003, pp. 93-103.

12. B.G. Pound: *Acta Metallurgica*, 1998, vol. 46, pp. 5733-43.

13. E. U. Lee, H. Sanders and B. Sarkar: *Tri-Service Conference on Corrosion*, US Army Research Laboratory, 1999.

14. P.F. Buckley, R. Brown, G.H. Graces, E.U. Lee, C.E. Neu and J. Kozol: *Metallic Materials for Lightweight Applications-Proceedings of the 40th Sagamore Army Materials Research Conference*, United States Army Laboratory Command, Watertown, MA, 1993.

15. J. Kozol and C. E. Neu: Report No. NAWCADWAR-92018-60, Naval Air Warfare Center, Warminster, PA, Jan 10, 1992.

16. H.H. Johnson: *Materials Research & Standards*, 1965, vol. 5, pp. 442-45.

17. R.P. Gangloff, D.C. Slavik, R.S. Piascik and R.H. Van Stone: *Small Crack Test Methods, ASTM STP 1149*, J.M. Larsen and J.E. Allison, eds., ASTM International, West Conshohocken, PA, 1992, pp. 116-168.

18. M.J. Haynes and R.P. Gangloff: *Journal of Testing and Evaluation*, 1997, vol. 25, pp. 82-98.

19. E. U. Lee: *Metallurgical and Materials Transactions A*, 1995, vol. 26A, pp. 1313-16.

20. C.J. McMahon Jr.: *Engineering Fracture Mechanics*, 2001, vol. 68, pp. 773-88.

21. R. P. Gangloff: *Hydrogen Effects on Material Behavior and Corrosion Deformation Interactions*, The Minerals, Metals & Materials Society, Warrendale, PA, 2003, pp. 477-97.

22. R. W. J. Koers, A. H. M. Krom and A. Bakker: *Environmentally Assisted Cracking: Predictive Methods for Risk Assessment and Evaluation of Materials, Equipment, and Structures*, ASTM International, West Conshohocken, PA, 2000, pp. 303-16.

23. R. P. Gangloff: *Metallurgical Transactions A*, 1985, vol. 16A, pp. 953-69.

24. R.P. Gangloff and A. Turnbull: *Modeling Environmental Effects on Crack Initiation and Propagation*, The Minerals, Metals & Materials Society, Warrendale, PA, 1986, pp. 55-81.

25. E. U. Lee: Report No. NAWCADWAR-94001-60, Naval Air Warfare Center, Warminster, PA, Oct. 23, 1993.

26. C.L. Briant and S.K. Banerji: *Treatise on Materials Science and Technology, Embrittlement of Engineering Alloys,* Vol. 25, Academic Press, New York, NY, 1983, pp. 21-58.

27. Y. H. Kim, H. J. Kim and J. W. Morris Jr.: *Metallurgical and Materials Transactions A*, 1986, vol. 17A, pp. 1157-64.

28. M. L. Holzworth and M. R. Louthan Jr.: *Corrosion*, 1968, vol. 24, pp. 110-24.

Electrochemical Mitigation of Hydrogen Environment Embrittlement of Ultra-high Strength AerMet[TM] 100

Sami Al-Ghamdi and John R. Scully

EFFECT OF SELECTED INHIBITORS ON HYDROGEN PRODUCTION, ABSORPTION AND ENVIRONMENTAL EMBRITTLEMENT OF AN ULTRA HIGH STRENGTH STEEL

Sami Al-Ghamdi and John R. Scully

ABSTRACT

The goal of this research is to extend the potential region of high toughness in an ultra-high strength steel (UHSS) to anodic and cathodic potentials where hydrogen environment embrittlement (HEE) is normally observed due to hydrogen uptake in the absence of inhibitors. This is being explored through the investigation of several selected chemical inhibitors (anodic inhibitors and cathodic blocking agents). The research is conducted in three stages. The effect of inhibition on lowering hydrogen production and ingress (absorption) is determined using planar coupons under conditions representative of crack tips. Studies are then extended to rescaled crevices that model occluded sites of much smaller dimensions (will not be discussed in this paper). Finally, verification of chemical inhibition of HEE susceptibility, in fracture experiments, is exhibited by a restoration in toughness and/or a reduction in crack growth rate on fatigue pre-cracked specimen. Fracture experiments are performed at various applied potentials in a marine environment. This research is part of an overall scheme to combine the study of inhibition with the control of metallurgical purity and hydrogen trap states, as well as tailored cathodic protection to optimize the fracture toughness of UHSS in marine environments. The long term goal is to provide a coupled strategy to mitigate HEE of modern high strength steels.

BACKGROUND

Ultra-high strength material

UNS K92580 is a secondary hardened martensitic steel. The alloy is initially austenitized @ 885°C, air-cooled for 2 hours, further quenched to -73°C, and then peak aged @ 482°C to

achieve optimal strength and fracture toughness as shown in Table 1. The chemical composition and mechanical properties for the peak aged condition are given in Tables 2 and 3.

The alloy was developed to provide high fracture toughness, $K_{IC} \approx 130$ MPa√m, compared to older generation UHSS steels. This was achieved by advanced melting in vacuum to minimize contaminant inclusions, mainly sulfur and phosphorous compounds [6,15]. The high fracture toughness is mainly attributed to the presence of fine (3 nm) reverted austenite uniformly dispersed coherent particles. The austenite was shown to be rich in C, Ni, and Co. These elements reduce martensite deformation temperature (M_d) and lead to the increase in austenite stability when straining specimen in fracture experiments. On the other hand, high strength, $\sigma_{YS} \approx 1765$, was due to the presence of the fine-cohesive M_2C carbides, which are the source of the secondary strengthening. Also, high strength was achieved due to the presence of extensive dislocation structures stabilized by the high concentration of Co in UNS K92580, around 13%wt. The microstructure is rich in hydrogen traps; prior-austenite grain boundaries, martensite laths, high dislocation density, coherent M_2C carbides and solute zones, and the thin film of precipitated reverted austenite on lath/plate boundaries as shown in Fig. 1 [10]. Each trap state possess it own hydrogen binding energy [2].

Table 1 – Heat treatment of UNS K92580

Process	Temperature (°C)	Duration (hours)
Austenitize (vacuum)	885	1
Air Cool	-	2
Cold Stabilize	-73	1
Age (air)	482	5

Table 2 – Chemical composition of UNS K92580 (weight percent)

Fe	C	Co	Ni	Cr	Mo	Ti	Si	S	P	H (ppmw)
bal.	0.23	12.80	10.89	2.78	1.21	0.010	0.016	0.0008	0.001	0.35

Table 3 – Mechanical properties of UNS K92580

HRC	σ_{UTS} (MPa)	σ_{YS} (MPa)	E (GPa)	K_{IC} (MPa√m)
54	1985	1765	194	130

Hydrogen embrittlement is a prime factor hindering the performance of UHSS alloy in naval service. UNS K92580 suffers an order of magnitude degradation in fracture toughness due to HEE caused by an increase in diffusible hydrogen concentration ($C_{H,diff}$), especially above 2 ppmw as shown in Fig. 2. Such hydrogen concentrations may be achieved by a combination of electrochemical polarization and occluded crack geometry in seawater.

Potential dependency of K_{TH} and C_H

HEE susceptibility is minimized if pre-cracked UHSS specimens are held close to theirs open circuit potential (OCP) which is near -0.7 to -0.6 V_{SCE}. The $C_{H,diff}$ in the fracture process zone (FPZ), implied from these experiments assuming a fracture model developed by Gerberich and adapted is minimal approaching zero near the OCP [8]. Therefore, the HEE and subsequent hydrogen environment-assisted cracking (HEAC) susceptibility of UNS K92580 are strongly potential dependant at both cathodic as well as anodic potentials as shown in Fig. 3. Hydrogen production can be severe at anodic potentials due to ohmic voltage drop and acidification at the crack tip, brought about principally by the hydrolysis of chromium ions into solutions [16]. Also, the slow hydrogen diffusion rate favors local uptake and accumulation at the crack tip. While, in cathodic conditions, there is a large hydrogen overpotential at external surfaces (η) and bulk charging occur. Increasing the applied potential even more cathodic results in an increasingly negative crack tip overpotentials for the same applied potential (E_{app}) [1].

Hydrogen production and absorption at occluded sites

Electrochemical conditions lead to hydrogen production within the crack. This production rate is dependent upon local potential and pH. Production of H^+ and its absorption into metal under crack cathodic conditions is due to dissolution of sacrificial coating and cathodic polarization of the crack tip, as per the following reactions (Fig. 4a):

- *Anodic reaction (sacrificial coating):*

  $M \rightarrow M^+ + e^-$

- *Cathodic reaction (crack tip and on bulk surfaces):*

  $H^+ + e^- \rightarrow H$ (acidic environment)

  $H_2O + e^- \rightarrow H + OH^-$ (basic environment)
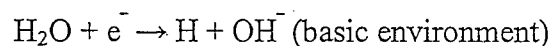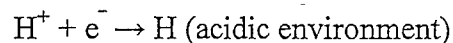
$\rightarrow$ Cations migrate to crack tip

While, under <u>crack anodic conditions</u>, production of H^+ and absorption into the metal, at the crack tip, occurs with the presence of an oxide film or a noble coating (Fig. 4b).

- *Anodic reaction (crack tip):*

$M \rightarrow M^+ + e^-$

$M^+ + H_2O \rightarrow MOH + H^+$
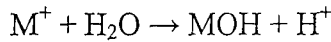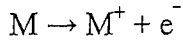
- *Cathodic reaction (bulk surfaces):*

$H^+ + e^- \rightarrow H$ (acidic), $H_2O + e^- \rightarrow H + OH^-$ (basic)

$O_2 + 4H^+ + 4e^- \rightarrow 2H_2O$ (acidic), $O_2 + 2H_2O + 4e^- \rightarrow 4OH^-$ (basic)
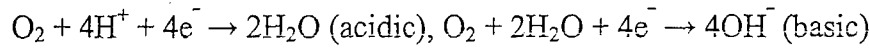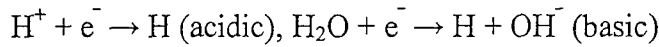
$\rightarrow$ Anions migrate to crack tip

Hydrogen concentration at the crack tip is enhanced by local stresses. The stress-enhanced hydrogen concentration ($C_{H,\sigma}$) depends on the lattice hydrogen concentration ($C_{H,lattice}$) and is enhanced by the hydrostatic stress (σ_H) at the crack tip, as follow [15]:

$$C_{H,lattice} = C_{H,diff} \left(\frac{D_H}{D_l} \right)$$

- Eq. 1

$$C_{H\sigma} = C_{H,lattice} \exp \left(\frac{\sigma_H V_H}{RT} \right)$$

- Eq. 2

where D_H is the hydrogen diffusivity, D_l is the lattice diffusivity, V_H is the partial molar volume of hydrogen, R is the gas constant, and T is the temperature.

Previous work has shown that the crack tip stress field can lead to a 35 to 2×10^5 – fold increase in hydrogen concentration over $C_{H,lattice}$ [5]. The dissolved hydrogen, as well as hydrogen trapped in weak trap sites with binding energies less than $\sigma_H V_H$, diffuses towards the crack tip stress field. Martensite lath interfaces are possible sites within the FPZ where hydrogen can segregate [4]. The total amount that segregates to these interfaces within the FPZ depends on the interaction between the crack tip stress field and the trap binding energy (E_b) of the lath interfaces, the concentration is further enhanced to $C_{H\sigma,T}$, as follow:

- 4 -

$$C_{H\sigma,T} = C_{H,lattice} \, \exp\left(\frac{E_b + \sigma_H V_H}{RT}\right)$$

- Eq. 3

The threshold stress intensity (K_{TH}) is then related to $C_{H\sigma,T}$ through the following [8]:

$$K_{TH} = \frac{1}{\beta'} \exp\left(\frac{(K_{IG} - \alpha \, C_{H\sigma,T})^2}{\alpha'' \sigma_{YS}}\right)$$

- Eq. 4

where K_{IG} is the critical Griffith stress-intensity factor for cleavage fracture without hydrogen, σ_{YS} is the yield strength, β' and α'' are constants related to analysis of dislocation structure about the crack tip, and α is a constant. Environmental hydrogen embrittlement thresholds (K_{TH}) are governed by the $C_{H,diff}$ at the crack tip FPZ.

Mitigation by Inhibition

Inhibitors function through different mechanisms to mitigate HEE of UHSS as seen in Table 4. Anodic inhibitors act to mitigate metal dissolution inhibiting hydrolysis that creates H^+ in an occluded site that could be reduced and absorbed into the UHSS. Cathodic inhibitors act to reduce the hydrogen uptake rate. This could be achieved by reducing the overall reaction rate (J_c), mitigating hydrogen absorption rate (k_{abs}), enhancing desorption rate (k_{des}) and/or recombination rate (k_r) leading to a reduction in the concentration of diffusible hydrogen in the UHSS. Inhibition could also be achieved by Cl^- absorption, pH buffering, and surface passivation [3,11,14].

A separate screening method was developed for selected anodic and cathodic inhibitors. The sought-after end result is test samples of UNS K92580 in simulated marine environment, with preferred inhibitor(s), in a fracture experiment to determine and characterize mitigation of HEE.

Table 4 – Inhibitor types with examples

Inhibitor function	Example compounds or species
Cathodic inhibitor	Polyphosphate, zinc, silicate
Anodic inhibitor	Chromate, nitrate, molybdate, cerate, orthophosphate, ferrocyanide
Chloride absorbers	Not determined
Acid Buffers	Borax, Sodium bicarbonate, etc.
Hydrogen entry inhibitors (not including passivators)	Bi, Pb, Zn, Noble metals, Various organic film formers
Recombination promoters	Ir, Pd, Pt

A combination of traditional and new types of inhibitors was chosen for evaluation as seen in Table 5. While chromate and molybdate are traditionally favored inhibitors, new rare earth metal (REM) organic inhibitors were also chosen to compare the performance of each set of experimental results [3,11,14,17].

Table 5 – List of selected chemical inhibitors [17]

No.	Inhibitor	Inhibitor Name	Proposed Action	Source
1	Ce(acetate)$_3$	Cerium acetate	Cathodic reaction inhibitor, physical barrier	Various
2	Zn(acetate)$_3$	Zinc acetate	Cathodic reaction inhibitor	Various
3	Ce(dbp)$_3$	Cerium dibutyl phosphate	Cathodic reaction inhibitor, physical barrier	University of Monash
4	REM Organic	Rare Earth Metal Organic	Cathodic reaction inhibitor, physical barrier	University of Monash
5	Na$_2$MoO$_4$	Sodium molybdate	Anodic inhibitor, passive film	Lynch, Parrish, Agarwala, others
6	Na$_2$CrO$_4$	Sodium chromate	Anodic inhibitor, passive film	Lynch, Parrish, Agarwala, others
7	Mn Molyblue	Manganese Molybdenum Blue	Anodic inhibitor, passive film	Rockwell Scientific (Kendig)
8	Y Molyblue	Yttrium Molybdenum Blue	Anodic inhibitor, passive film	Rockwell Scientific (Kendig)

Therefore, one challenge is to develop chemical inhibitors that operate to reduce HEAC during polarization. The goal of this research is to extend the potential region of high fracture toughness to anodic and cathodic potentials where HEE is normally observed in the absence of inhibitors (Fig. 3).

EXPERIMENTAL METHODS

Electrochemical Polarization (Potentiodynamic) in Selected Inhibitors

Initially, a small sample of UNS K92580 was cut (2mm wide x 10mm long x 0.2mm thick), tack-welded to a nickel wire and mounted into epoxy for ease of handling and testing. After curing, the specimen was polished to a 600-grit surface finish. The specimen was then clamped into a flat cell arrangement, and connected to a Potentiostat (Model 273A). For each

polarization scan, the specimens were left to stabilize at open circuit for 2 hours. Three scans were attempted in each solution to insure consistency of data. All scans were run at a rate of 1.67×10^{-2} mV/s.

Anodic polarizations were run in sulfuric acid solutions. Acid concentration was varied (0.01M, 0.05M and 0.1M H_2SO_4) so was the molybdate concentration ($10^{-2} - 10^{-5}$M Na_2MoO_4) to investigate the effect on anodic polarization behavior. Initially, tests were run in the lowest concentration acid solution, 0.01M H_2SO_4, and varying inhibitor concentration from lowest to highest to view the effect on the anodic scan profile. Addition of molybdate was chosen in low concentrations to limit the effect on raising solution pH. Any large shift in pH would include an additional complication to the evaluation of the inhibitor and its effective concentration. It would be difficult to single out the cause of the reduction in electrolyte corrosivity.

For cathodic polarizations, inhibited borate buffer solutions were initially used to measure the effectiveness of Na_2MoO_4 and Na_2CrO_4 against uninhibited borate buffer control. Ce(acetate)$_3$ and Zn(acetate)$_2$ were used, with equivalent acetate concentrations, based on their reduction of HER rate and/or hydrogen absorption. Na(acetate) was used as a control solution to view the inhibiting effect of Ce^{3+} and Zn^{2+}. REM inhibitors were also utilized to investigate their effect on the HER.

Electrochemical Hydrogen Charging and Extraction (Potentiostatic) – Barnacle Electrode Method

To further screen inhibitor types, results from the previous cathodic polarization scans were used to determine critical inhibitor concentrations. Potentiostatic testing, "barnacle electrode method," was used to determine $C_{H,diff}$ at different inhibitor concentrations and η in UNS K92580. The barnacle electrode method consisted of using a thin sample of the material (1cm^2 exposed surface x 0.10mm thick) in the flat cell arrangement [12]. The sample was then connected to a Potentiostat and a cathodic potentiostatic hold was applied, below $E_{H/H+}$, for a period of 48 hours to fully charge the sample with absorbed hydrogen. The overpotentials were varied to view the effect of inhibition in different conditions. After charging the samples with hydrogen, the samples were then removed from the inhibited electrolyte, cleaned with methanol and then inserted in a cell filled with borate buffer solution (pH 8.4). Another potentiostatic hold was applied just above $E_{H/H+}$, $\eta = 330$ mV, to oxidize and extract hydrogen from the

samples. The measured hydrogen oxidation current density was used to calculate $C_{H,diff}$ by fitting the profile to the following expression [5,12]:

$$C_{H,diff} = \frac{J_H}{zF}\left(\frac{D_H}{\pi t}\right)^{-\frac{1}{2}}$$
- Eq. 5

where J_H is the hydrogen oxidation current density, z is the hydrogen atomic number (+1), t is the hydrogen extraction time, and F is Faraday's constant. A complexity is that D_H values depend on $C_{H,diff}$ diffused in the UHSS. This was previously analyzed and a correlating was used to determine $C_{H,diff}$ with greater accuracy [5]:

$$\log D_H = -0.416\eta - 08.14\,(at\ room\ temp.)$$
- Eq. 6

Fracture Testing in Simulated Seawater Environments

A single edge notch specimen of UNS K92580 was machined, 10.2mm wide x 2.54mm thick. The notch was electrospark-machined to 0.065mm wide x 0.11mm deep. The specimen was fatigue precracked to 0.030mm deep in air. Finally, the specimen was fitted into a plexiglass cell and mounted into a fracture machine [1].

For anodic inhibition testing, the cell was initially filled with 0.6M NaCl (pH = 6.9) and tested then another run was run in 0.6M NaCl + 0.01M Na_2MoO_4 (pH = 7.1. Both solutions were aerated and had air bubbling into the cell to eliminate any solute precipitation in the stagnant solution. A Potentiostat was connected to the specimen to apply a constant η (slightly anodic) at a constant actuator displacement rate. For cathodic inhibition testing, the cell was first filled with 0.6M NaCl (pH = 6.9) then with 0.6M NaCl + 0.05M Ce(acetate)$_3$ (pH = 6.9). As before, both solutions were aerated and had air bubbling into the cell. The Potentiostat was used to apply a constant cathodic η at a constant actuator displacement rate.

During all the experiments' run, the load (P), actuator displacement (δ), time (t), and direct current potential drop (dcPD) values were recorded. The crack length (a) was calculated using the dcPD method [4].

RESULTS

Anodic Polarization (Potentiodynamic) in Selected Anodic Inhibitors

As expected, the addition of inhibitor, even in low concentrations, enhanced corrosion resistance and passivity as seen in Fig. 5. Tests were continued with higher H_2SO_4 concentrations and similar results were achieved. The critical current density (J_{crit}) was measured in H_2SO_4 solutions first with no Na_2MoO_4 then with the gradual addition of the inhibitor. Figure 6 shows that the values trend with the concentration of both H_2SO_4 and Na_2MoO_4 in the solutions. The lowest acidity solution had the lowest values for the same molybdate concentration. Also, the specimens tend to passivate quicker with the addition of more inhibitor, as indicated by the decrease in the passivation potential (E_{pp}) in each H_2SO_4 solution concentration with increasing inhibitor concentration. Finally, the values for the corrosion current density (J_{corr}) were estimated based on a Tafel fit. The estimated values of J_{corr} decrease with the decrease of H_2SO_4 concentration and the increase in Na_2MoO_4 concentration. Further mass loss tests are planned to accurately quantify corrosion rates.

Figure 7 shows anodic scans that were attempted in aerated 0.6M NaCl solutions to simulate sea water environments. A major reduction in J_{corr} was noticed when adding 0.01M and 0.05M Na_2MoO_4 into the solution compared to uninhibited test solution. The pitting potential (E_{pit}) tends to increase with the addition of the molybdate inhibitor leading to the increase in the passive region as seen in Fig. 8.

Another set of tests are currently being conducted to view the benefit of the addition of $Ce(acetate)_3$ to solutions containing Na_2MoO_4.

Cathodic Polarization (Potentiodynamic) in Selected Cathodic Inhibitors

Initially, test scans were run in borate buffer as the control solution. Then in 0.1M of the inhibitor (Na_2MoO_4 or Na_2CrO_4) was added to view effect on lowering HER rate. Figure 9 shows that, with the addition of chemicals, a decrease in the specimen OCP and the HER rate, down to η between -0.2 and -0.3V. Overpotentials below this limit show an increase in the reaction rate, which was evident from the enhancement in H_2 bubbling off of the sample surface with more cathodic potentials. This was further shown in proceeding charging experiments as seen in Figures 13 and 14, further discussion is provided in the following

section. The addition of both chemicals resulted in an insignificant increase in pH. This was resolved by plotting the cathodic current densities (J_c) vs. η instead of E_{app} (Fig. 9).

Another set of experiments were performed in acetate-based solutions to test the effectiveness of Ce and Zn to inhibit HER rate. Initial analysis of the results show that Ce(acetate)$_3$ slightly raises HER rate compared to Na(acetate), with similar acetate concentration. However, Figures 16 and 17 show that at higher η data indicate current decay in the 0.05M Ce(acetate)$_3$ solution producing less cathodic current densities (J_c) and HER charge (q_c) compared to 0.15M Na(acetate). During polarization, a hydroxide film forms in the presence of Ce(acetate)$_3$ on the exposed specimen surface due to the increase in local pH to levels where Ce^{3+} is no more soluble in solution.

Zn(acetate)$_2$ was also used, with similar acetate concentration, to view affect on HER rate. Although, Zn^{2+} is known to drastically reduce HER in acidic solutions [18], it had minimal effect on it in the solutions with neutral acidity. Figure 15 shows that Zn(acetate)$_2$ shifts the HER current density less cathodic compared to the control. Also, Zn(acetate)$_2$ has a drastic effect on HER charge (q_c) as it indicate very low values in Fig. 17. Unfortunately, its use is limited to overpotentials above $\eta = -0.5V$, below which Zn deposits from solution. Again, the overpotentials were used instead of the applied potential to compensate for the difference in pH amongst the different solutions.

Hydrogen Charging and Extraction (Potentiostatic) – Barnacle Electrode Method

Hydrogen charging was performed by applying a potentiostatic hold below $E_{H/H+}$ to promote HER, as below discharge-recombination and/or absorption reactions:

$$1.\ H_2O + e^- + M \rightarrow H_{ads}\text{-}M + OH^-$$
$$2.\ H_{ads} + H_{ads} \rightarrow H_2(g)\uparrow$$
$$\text{or}\ \ 3.\ H_{ads} \rightarrow H_{abs}$$
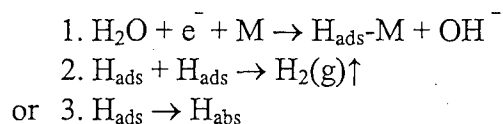
Figure 11 shows that as the overpotential (η) is decreased (more cathodic), the observed cathodic current density (J_c) decreases accordingly. The hydrogen oxidation current density (J_H) from extraction follows the overpotential values applied when charging the samples as seen for 0.15M Na(acetate) in Fig. 12. The J_H profile correlates well with the square root of time.

Initially, hydrogen charging of UNS K92580 was performed in borate buffer (pH = 8.4) as a control solution. Scans were then attempted in borate buffer with added chemical inhibitors
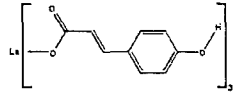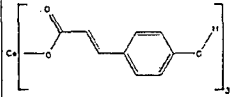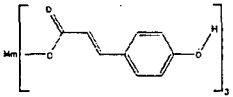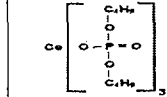
(Na$_2$MoO$_4$ and Na$_2$CrO$_4$) to test their effectiveness in reducing C$_{H,diff}$. Figure 13 shows that the hydrogen charging profiles decrease (more cathodic) with the addition of the chemicals. The HER charge density values for the inhibited solutions were significantly more cathodic than that of the uninhibited borate buffer solution as seen in Fig. 14. They correlate nicely with the applied η. Figure 18 indicates that the addition of both MoO$_4^{2-}$ and CrO$_4^{2-}$ did not decrease C$_{H,diff}$ compared to uninhibited borate buffer.

Again, acetate-based solutions were used to test the effectiveness of Ce and Zn compounds for inhibiting HER. Data at high overpotentials (less cathodic) suggest that Ce(acetate)$_3$ exhibits more cathodic J$_c$ (Fig. 15), while shifting the overpotential further cathodic shows much higher J$_c$ (Fig. 16). While Figure 17 shows its effect on lowering q$_c$ compared to Na(acetate) indicating its mitigation to HER. This reduction in q$_c$ of the HER results in Ce(acetate)$_3$ provided best inhibition and reduction of C$_{H,diff}$ for a wide range of applied η as seen in Fig. 18. During charging, an white film is noticed on the specimen surface indicating the deposition of Ce(OH)$_3$ due to the shift in local pH at the sample/electrolyte interface. Ce^{3+} is not soluble in alkaline conditions, above pH = 9 [18].

On the other hand, Zn(acetate)$_2$ showed limited reduction in C$_{H,diff}$ (Fig. 18), although analysis of the charging profiles indicates a major reduction in HER charge density (Figures 15 and 16). The profile from Fig. 16 shows a sloping profile with charging time. The associated charge density for this scan is 275 coulomb/cm^2. This includes Zn deposition in addition to the HER. Once the amount of Zn is weighed and the charge associated with the deposition (q$_{ZN}$ = 257 coulomb/cm^2) is subtracted from the total current, the resulting q$_c$ for Zn(acetate)$_2$ at η = - 0.5V is still lowest, compared to both Ce and Na acetates as indicated in Fig. 17.

As a continuation to screening new inhibitors, rare earth metal (REM) organic inhibitors were chosen, refer to Table 6 [3]. In the cathodic conditions, a thin film is deposited on the surface of the hydrogen charged specimen, similar to the behavior in Ce(acetate)3. But without the analysis of the film this could not be verified.

Table 6 – Properties of the rare earth metal organic inhibitors [17]

No.	1	2	3	4
REM Organic Inhibitor	Lanthanum 4-hydroxy cinnamate	Cerium 4-hydroxy cinnamate	Lanthanoides* hydroxy cinnamate	Cerium dibutyl phosphate
Chemical Formula	$La(C_9H_8O_3)_3.5H_2O$	$Ce(C_9H_8O_3)_3.5H_2O$	$Mm(C_9H_8O_3)_3.5H_2O$	$Ce(C_8H_{18}O_4P)_3$
Molecular Formula	*(structure)*	*(structure)*	*(structure)*	*(structure)*
MW (g/mol) - anhydrous	627.90	629.10	629.96	767.1
MW (g/mol) - hydrated	717.98	719.18	720.04	NA
Solubility Limit**	960 ppm (sugg. 400 - 800 ppm)	800 ppm (sugg. 300 - 600 ppm)	800 ppm (sugg. 300 - 700 ppm)	not determined

* Mm Elements	Sc	La	Ce	Pr	Nd	Gd	Tb	Dy	Er	Yb
Weight %	0.001	24.251	52.698	5.492	14.684	2.24	0.093	0.318	0.114	0.001

Cerium dibutyl phosphate, $Ce(dbp)_3$, showed similar q_c and $C_{H,diff}$ when compared to the control solution Na(dbp), at similar dibutyl phosphate concentrations. On the other hand, La(4-OHcinnamate)$_3$ and Mm(4-OHcinnamate)$_3$ showed very good protection at very low concentrations, 50-200 ppm, with similar solution conductivity as Na(dbp). Tests in control solutions are being conducted to verify inhibition.

Finally, the diffusible hydrogen concentration ($C_{H,diff}$) values for all inhibitors, except REM inhibitors, are reported vs. the square root of cathodic current density (J_c) as seen in Figures 19 and 20, because of the theoretical connection, refer to the discussion section. Again, the figures show that $Ce(acetate)_3$ is most effective in reducing $C_{H,diff}$ in a wide range of η (Fig. 18). $Zn(acetate)_2$ does not reduce $C_{H,diff}$ compared to control, but it reduces tremendously the HER current density (Fig. 17). Further analysis is made in the discussion section.

Fracture Testing in Inhibited Sea-water Solutions

UNS K92580 was tested in 0.6M NaCl + 0.01M Na_2MoO_4 (pH ~ 7.1) with a pre-crack length of 0.76 mm. The load was increased to a K of 100 MPa√m. The crack growth was inhibited, compared to the uninhibited case. The potential was held at a cathodic potential (-0.5V_{SCE}) to the bulk surface in the inhibited solution but not in uninhibited 0.6M NaCl. There was very little crack growth as seen in Figure 21. The potential was then increased above OCP to -0.4 V_{SCE}. Initially, no crack growth was observed since the net current was still cathodic. After 20 hours, dissolution of the metal commenced with an increase in anodic current resulting in significant acidification (Fig. 22) leading to substantial growth of the crack, 2.5mm in ~ 7 hours as seen in Fig. 21. The threshold stress intensity was restored to highest value at -0.5V_{SCE} but not at -0.4V_{SCE} as seen in Fig. 25.

Further analysis of a rescaled crack with a gap of 1.5 mm showed that Na_2MoO_4 inhibited the anodic reaction rate and prevented crack tip acidification at anodic potentials as seen in Fig 22. This effect was minimal in a rescaled crack with a gap of 5mm over the time period examined due to the effect of the oxygen reduction reaction in the rescaled crack. Results from applied cathodic potentials verified barnacle cell results showing that molybdate does not directly inhibit the cathodic reaction rate, but would limit cathodic current at open circuit through anodic inhibition. At highly cathodic or anodic potentials, the local E and pH at the crack tip can lead to H^+ reduction and subsequently H absorption [16].

In another test, 0.05M $Ce(acetate)_3$ was used in 0.6M NaCl to investigate its effectiveness in blocking hydrogen uptake. A specimen was used with a fatigue pre-crack of 2.5 mm. Results indicate no protection of sample resulting in fracture data resembling that of uninhibited environment at similar conditions as seen in Fig. 23. This could be attributed to not alloying enough time for $Ce(OH)_3$ to form onto the crack surface, although SEM micrographs show some patchy formation of the film on the pre-crack region of the specimen, but not full coverage (Fig. 24). This could be due to the dislodging of the film when cleaning the specimen with methanol/acetone before inserting it into the SEM chamber. The color of the film resembles that formed when charging specimen in the barnacle electrode method. Also, this film did not appear in the uninhibited NaCl solution concluding it being the hydroxide film.

DISCUSSION

Anodic Inhibition

Under crack anodic conditions, at high local potentials, metal dissolution occurs and hydrolysis follows releasing H^+, as shown in the below reactions. The released H^+ could then be reduced on the material's bulk surfaces and either recombine and bubble off as H_2 gas or become absorbed into the material causing its embrittlement and cracking. To eliminate HEE and HEAC from occurring, anodic inhibitors are utilized to mitigate metal oxidation.

$$1. M \rightarrow M^+ + e^- \text{ (metal oxidation)}$$
$$2. M^+ + H_2O \rightarrow MOH + H^+ \text{ (hydrolysis)}$$

In general, the anodic polarization scans in H_2SO_4 develop more stable passive films as the amount of inhibitor is increased and the active dissolution rates are lowered. The critical current density (J_{crit}) showed a decrease when increasing inhibitor concentration leading to

quicker passivation. In 0.1M H_2SO_4, J_{crit} was reduced from 2.3×10^{-2} to 2.7×10^{-3} A/cm^2. As previously mentioned, the inhibitor concentrations were limited to very low concentrations to limit the increase in solution pH value.

Fracture testing in 0.6M NaCl + 0.01M Na_2MoO_4 (pH ~ 7.1) showed that crack growth was inhibited at an applied potential of $-0.5V_{SCE}$. Also, no net cracking was initially observed after raising the potential above OCP to -0.4 V_{SCE}. This was due to the inhibition of the anodic reaction rate and the prevention of crack tip acidification at anodic potentials. After 20 hours, dissolution of the metal commenced with an increase in anodic current and the crack grew 2.5mm in 7 hours.

Cathodic Inhibition

In crack cathodic conditions, the production of H^+ and its absorption into metal occurs by the coupled discharge-recombination hydrogen evolution reaction (HER), as follow, where reactions 1 and 2 occur at the same rates [13]:

1. $H_2O + e^- + M \rightarrow H_{ads}\text{-}M + OH^-$
2. $H_{ads} + H_{ads} \rightarrow H_2(g)\uparrow$
   or 3. $H_{ads} \rightarrow H_{abs}$
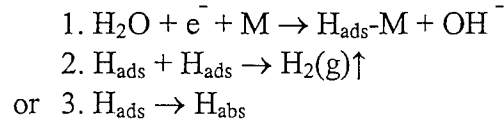
As such, the cathodic current density is defined as:

$$J_c = J_0 \exp\left(\frac{-\alpha\eta F}{2RT}\right) = k_r\theta^2$$

- Eq. 8

where J_0 is the exchange current density on for HER on Fe surface, α is the transfer coefficient, k_r is the recombination rate constant for adsorbed hydrogen on the surface, and θ is the surface coverage of adsorbed hydrogen on the surface.

The steady state lattice hydrogen concentration (C_H) is also a function of hydrogen surface coverage and is defined as following at equilibrium:

$$C_H = \frac{k_{abs}}{k_{des}}\theta$$

- Eq. 9

where k_{abs} is the absorption rate constant for hydrogen and k_{des} is the desorption rate constant for hydrogen at the surface.

Finally, an expression can be written to relate the lattice hydrogen concentration and the water reduction reaction rate at the surface by combining equations 8 and 9:

$$C_H = \left(\frac{k_{abs}}{k_{des}}\right)\left(\frac{J_c}{k_r}\right)^{1/2} = \left(\frac{k_{abs}}{k_{des}}\right)\left(\frac{J_0}{k_r}\right)^{1/2} \exp\left(\frac{-\alpha\eta F}{2RT}\right) \quad \text{- Eq. 10}$$

The data associated with Na_2MoO_4 and Na_2CrO_4 showed that both had little or no effect on $C_{H,diff}$ when compared to the control solution and at similar η. Although the hydrogen production charge associated with both inhibitors showed an increase, this may have been offset by an increase in recombination or desorption rates or a decrease in absorption rate since C_H remained unchanged (Eq. 10). These anodic inhibitors have no cathodic inhibition abilities.

On the other hand, Ce(acetate)$_3$ showed best inhibition of $C_{H,diff}$ in a wide range of η. Ce(acetate)$_3$ showed lower q_c (hence J_c) compared to Na(acetate) for the same applied η, especially at potentials more negative than -0.4V. In a fracture experiment, 0.05M Ce(acetate)$_3$ was used in 0.6M NaCl to investigate its effectiveness in blocking hydrogen uptake. Results indicate no protection of sample resulting in fracture data resembling that of uninhibited environment at similar conditions. This could be attributed to not alloying enough time for Ce(OH)$_3$ to form onto the crack surface, although SEM micrographs show some patchy formation of the film on the pre-crack region of the specimen, but not full coverage.

The use of Zn(acetate)$_2$ further lowered q_c, when compared to Na(acetate) and Ce(acetate)$_3$, but with no significant effect on $C_{H,diff}$. Further analysis shows that indeed Zn(acetate)$_2$ lowers J_c to values lower than that of the control solution. But the sharp decrease in J_c might have been offset by an increase in hydrogen absorption rate into the materials and/or a decrease in hydrogen desorption and recombination rates. Either of these factors could explain the limited effect of the lower values for J_c on the diffusible hydrogen concentration.

Analysis of the REM organic inhibitors show that they exhibit lowest current densities (J_c) compared to all other inhibitors. This might be promising, but could be attributed to the high resistivity of the solution altering the true potential applied, so tests in a control solution is

being conducted. But this could also be due to a decrease in HER rate. The values for $C_{H,diff}$ using these inhibitors are equal or better than in $Ce(acetate)_3$, at similar J_c.

CONCLUSIONS

- An active-passive transition developed when anodically polarizing UNS K92580 in inhibited acid solutions. The inhibition also led to a reduction in the corrosion current density in the active range.
- Fracture testing in 0.6M NaCl + 0.01M Na_2MoO_4 showed that environmental crack growth was inhibited when initially raising the potential above OCP to $-0.4V_{SCE}$. Na_2MoO_4 inhibited the anodic reaction rate and prevented crack tip acidification. Cracking only occurred after 20 hours, after general dissolution of the metal commenced with an increase in anodic current.
- There was no apparent advantage from the use of Na_2MoO_4 or Na_2CrO_4 as cathodic inhibitors, since they did not lower $C_{H,diff}$ at any cathodic potential.
- $Ce(acetate)_3$ showed best cathodic inhibition of $C_{H,diff}$ in a wide range of η. It lowered J_c, especially at potentials more negative than $-0.4V$.
- The addition of 0.05M $Ce(acetate)_3$ to 0.6M NaCl did not protect against hydrogen uptake and cracking in a fracture experiment. This could be attributed to not alloying enough time for $Ce(OH)_3$ to form onto the crack surface.
- The use of $Zn(acetate)_2$ resulted in lowest q_c values, but with no significant decrease in $C_{H,diff}$. This might have been offset by an increase in k_{abs} and/or a decrease in k_{des} and k_r.
- The use of the REM organic inhibitors result in lowest J_c and $C_{H,diff}$ values compared to all other inhibitors. Additional testing is being conducted to verify the results. This might be promising, but could be attributed to the high resistivity of the solution. This could also be due to a decrease in HER rate at a given η.

REFERENCES

[1] J.R. Scully, B.A. Kehler, Y. Lee, and R.P. Gangloff, Tri-Service Corrosion, No. 06T019, Orlando, FL, (2005)

[2] D. Li, R.P. Gangloff, J.R. Scully, Met. and Materials Trans. A, 35A, pp. 849-864 (2004)

[3] F. Blin, S.G. Leary, K. Wilson, G.B. Deacon, P.C. Junk, M. Forsyth, J. Appl. Electrochem., 34, pp. 591-599 (2003)

[4] R.L.S. Thomas, J.R. Scully, R.P. Gangloff, Met. and Materials Trans. A, 34A, pp. 327-344, (2003)

[5] R.L.S. Thomas, D. Li, J.R. Scully, R.P. Gangloff, Met. and Materials Trans. A, 33A, pp. 1991-2004 (2002)

[6] C.J. McMahon, Jr., Eng. Fract. Mech., 68, pp. 773-788 (2001)

[7] D.G. Enos, A.J. Williams, Jr., G.G. Clemena, and J.R. Scully, CORROSION/98, 54, No. 5, pp. 389-402, NACE Int'l., Houston, TX, (1998)

[8] W.W. Gerberich, P.G. Marsh, J.W. Hoehn, *Hydrogen Effects in Metals,* TMS, Warrendale, PA, (1996).

[9] P. Buckley, B. Placzankis, J. Beatty, R. Brown, Corrosion/94, No. 547, NACE Int'l, Houston, TX, (1994).

[10] R. Ayer and P.M. Machmeier, Met. and Materials Trans. A, 24A, pp. 1943-1955, (1993).

[11] V.S. Agarwala, *Modification of Crack Tip Chemistry to Inhibit Corrosion and SCC of High Str. Alloys In Embrittlement by the Local Crack Tip Environment,* Met. Soc. Of AIME, R.P. Gangloff, (1983).

[12] J.J. Deluccia, D.A. Berman, Electrochemical Corrosion Testing, ASTM STP 727, pp. 256-273, (1981)

[13] P.K Subramanyan., *Comprehensive Treatise of Electrochemistry,* Plenum Press, New York, (1981).

[14] C.T. Lynch, K.J. Bhanasali, P.A. Parrish, *Inhibition of Crack Propagation of High Strength Steels through Single and Multi-functional Inhibitors,* ARML-TR-76-120, Wright Patterson (1976).

[15] R. A. Oriani, Hydrogen in metals, Conf. Proc.: Fund. Aspects of Stress Corr. Cracking in 1967, 32-50. NACE Int'l, Houston, TX (1969)

[16] B.A. Kehler, S.M. Al-Ghamdi, Tri-Service Corrosion Conf. Poster, Orlando, FL, (2005)

[17] S.M. Al-Ghamdi, CORROSION/06, Student Poster, San Diego, CA, (2006)

[18] M. Pourbaix, *Atlas of Electrochemical Equilibria in Aqueous Solutions,* NACE Int'l, Houston, TX, (1974).
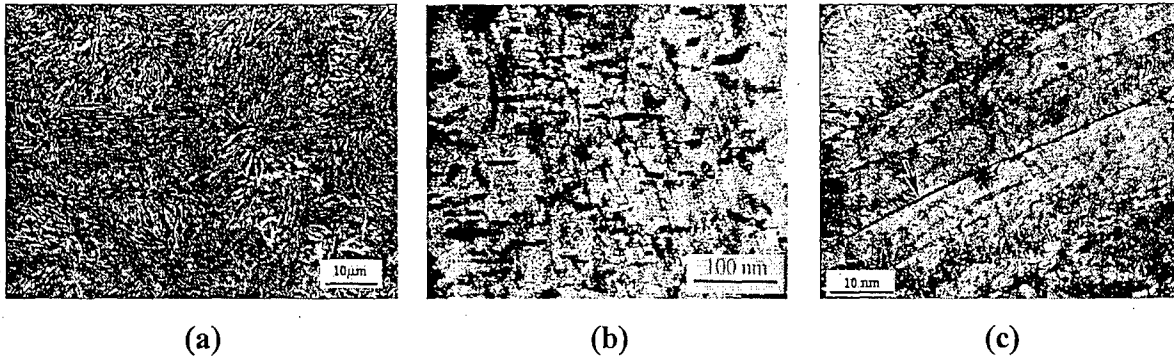
Fig. 1 – Microstructural features in UNS K92580: **(a)** the martensite packets, **(b)** fine dispersed M_2C carbides, and **(c)** reverted austenite on the martensite lath boundaries [10]
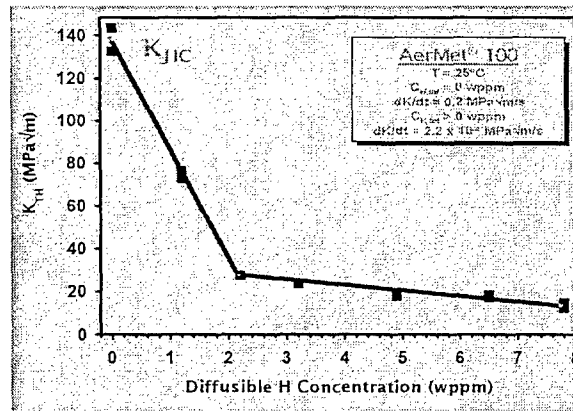
Fig. 2 – Dependence of K_{TH} on $C_{H,diff}$ in UNS K92580 [4]
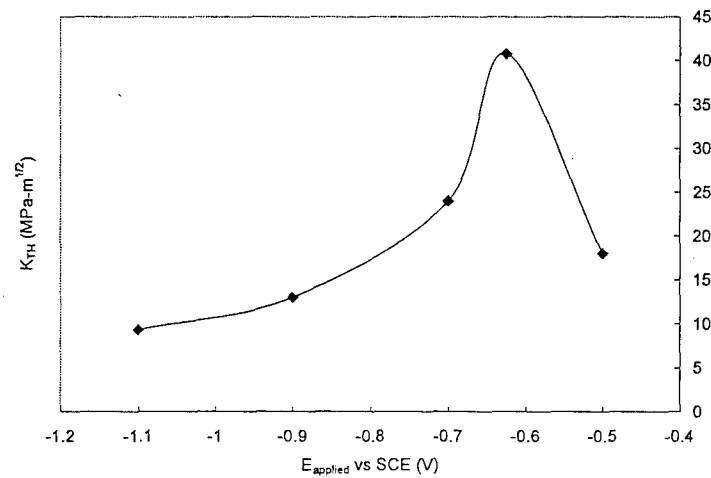
Fig. 3 – K_{TH} values vs. E_{app} for UNS K92580 in 0.6M NaCl. [1]
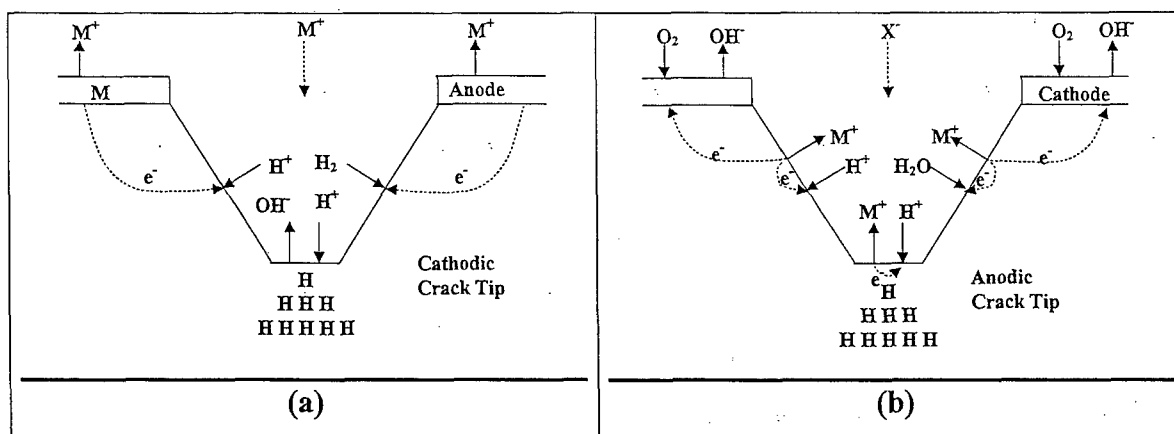
Fig. 4 – Schematic view of crack tip under: **(a)** cathodic conditions and **(b)** anodic conditions [16]
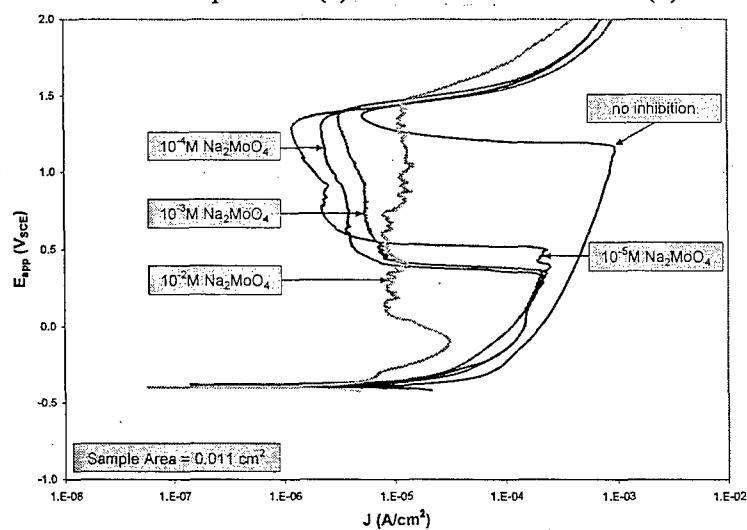
Fig. 5 – Anodic polarization profiles in 0.01M H_2SO_4 (deaerated, pH = 1.7, T = 23°C) [17]
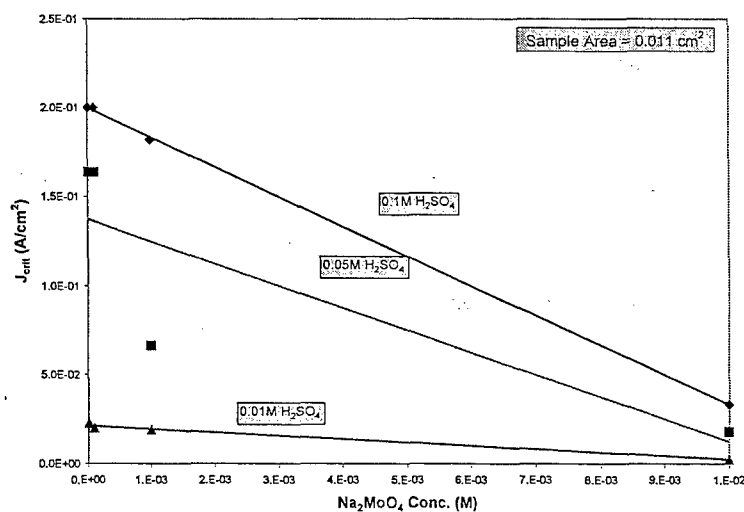
Fig. 6 – Evolution of the critical current density with Na_2MoO_4 conc. in H_2SO_4 solutions (deaerated, T = 23°C) [17]
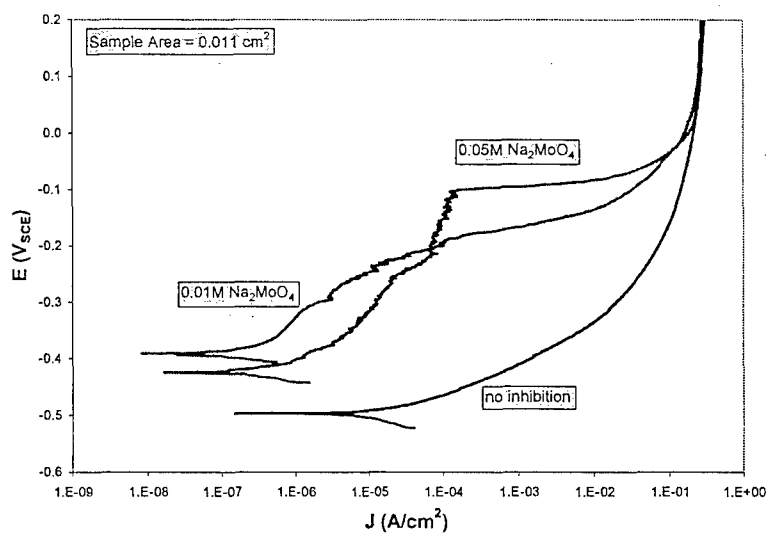
Fig. 7 – Anodic polarization profiles in 0.6M NaCl solutions (deaerated, pH = 7.1, T = 23°C) [17]
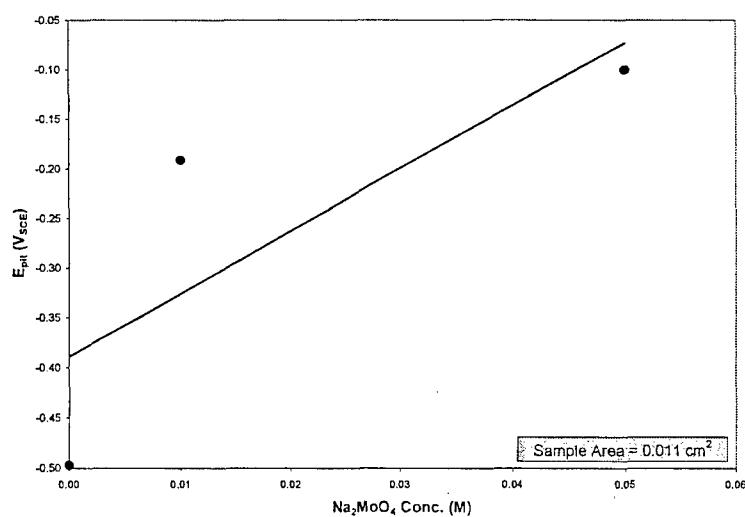
Fig. 8 – Evolution of the pitting potential with Na_2MoO_4 concentration in 0.6M NaCl solutions (deaerated, pH = 7.1, T = 23°C)
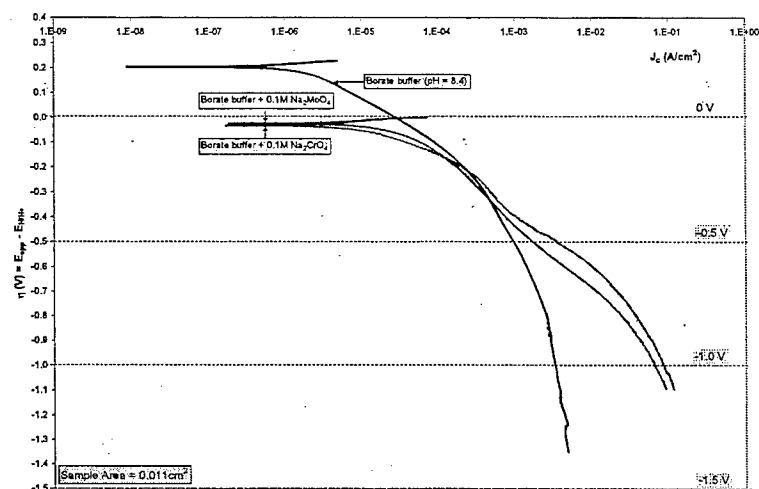
Fig. 9 – Cathodic polarization profiles in borate buffer solutions (deaerated, pH = 8.4, T = 23°C)
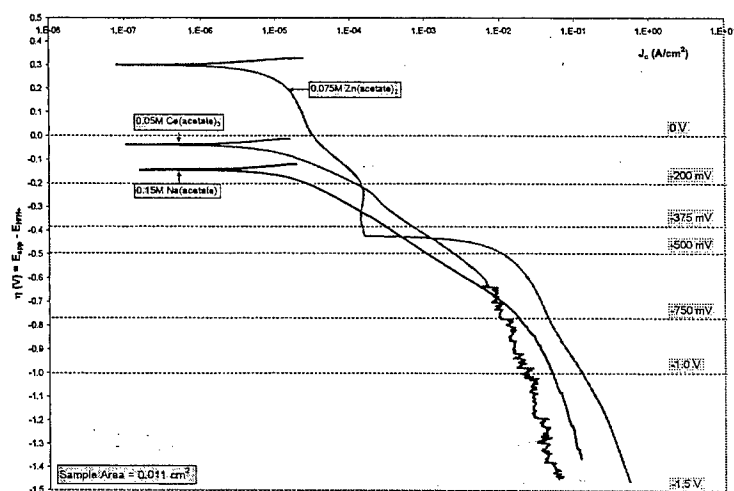
Fig. 10 – Cathodic polarization profiles in acetate-based solutions (deaerated, T = 23°C)
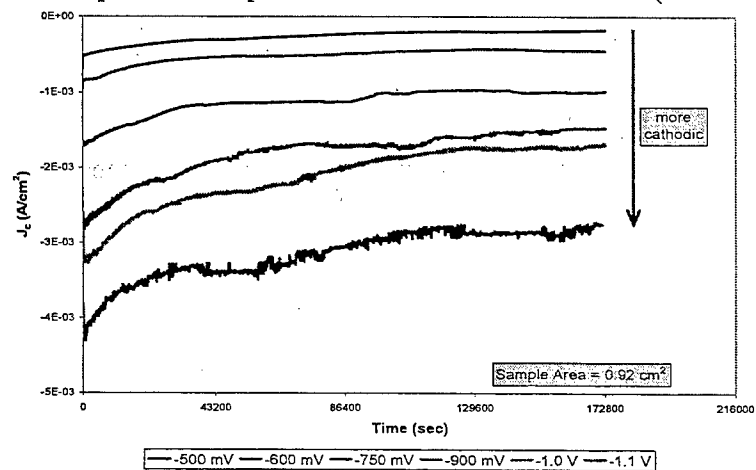
Fig. 11 – Effect of η on the hydrogen charging profiles in 0.05M Na(acetate) (deaerated, pH = 7.9, T = 23°C) [17]
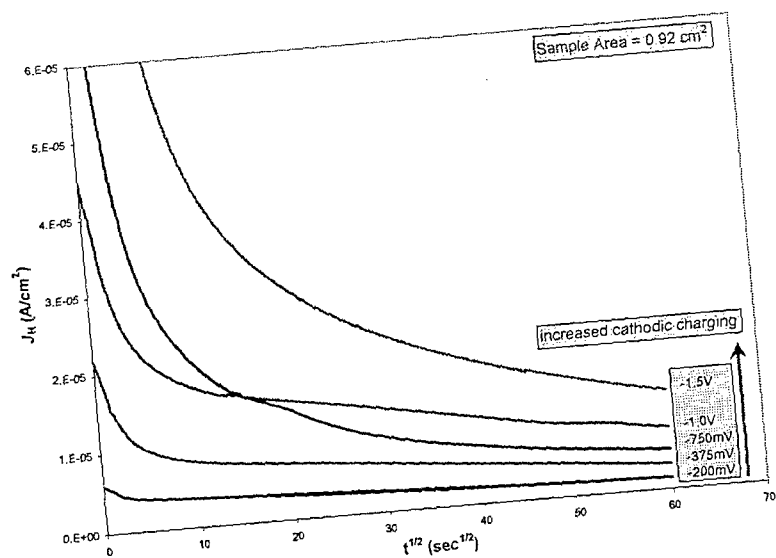
Fig. 12 – Hydrogen extraction profiles in borate buffer correlation with previous hydrogen charging η in 0.15M Na(acetate), (deaerated, pH = 8.4,T = 23°C).
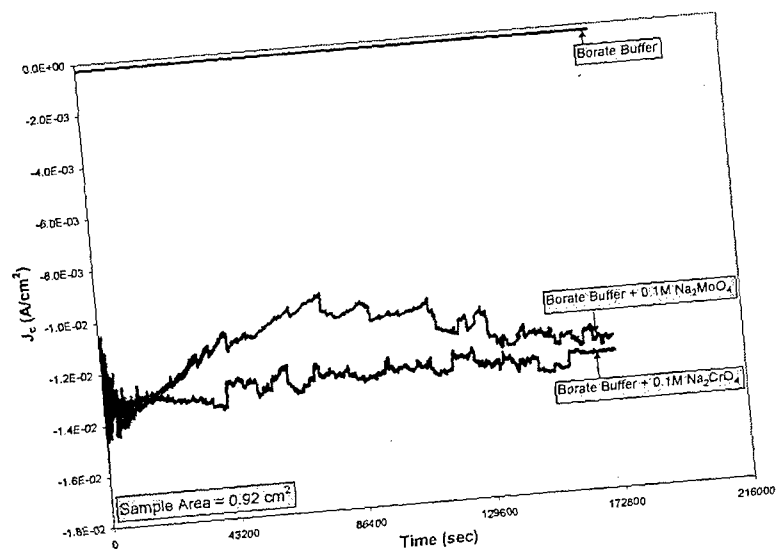
Fig. 13 – Hydrogen charging profiles in borate buffer solutions (deaerated, η = -1.0V, pH = 8.4, T = 23°C).
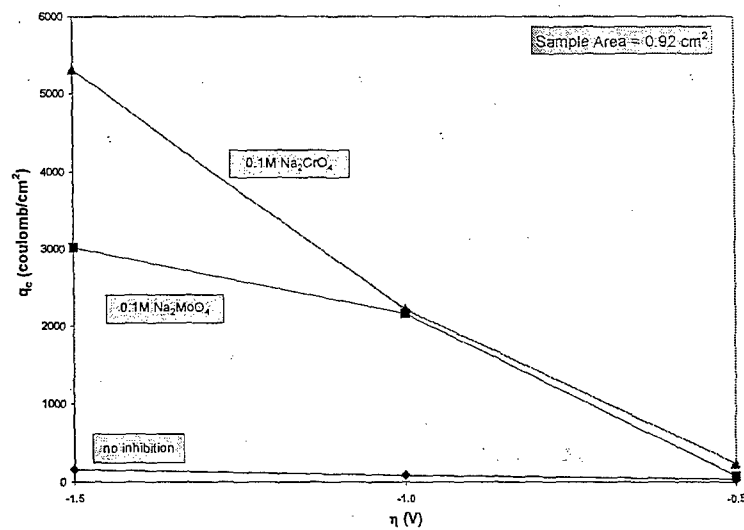
Fig. 14 – Hydrogen evolutions reaction charge density measured against applied η in borate buffer solutions (deaerated, pH = 8.4, T = 23°C)
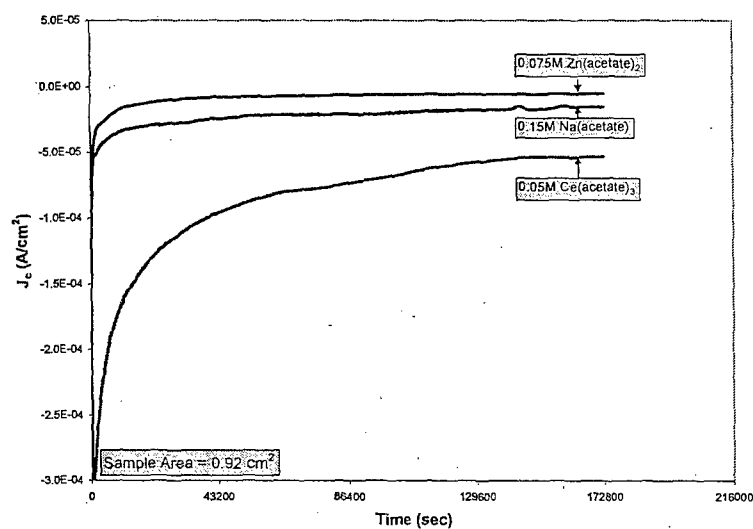
Fig. 15 – Hydrogen charging profiles in acetate-based solutions (deaerated, η = -0.375V pH = 8.2 for Na(ac), pH = 6.9 for Ce(ac)$_3$, pH = 6.8 for Zn(ac)$_2$, T = 23°C)
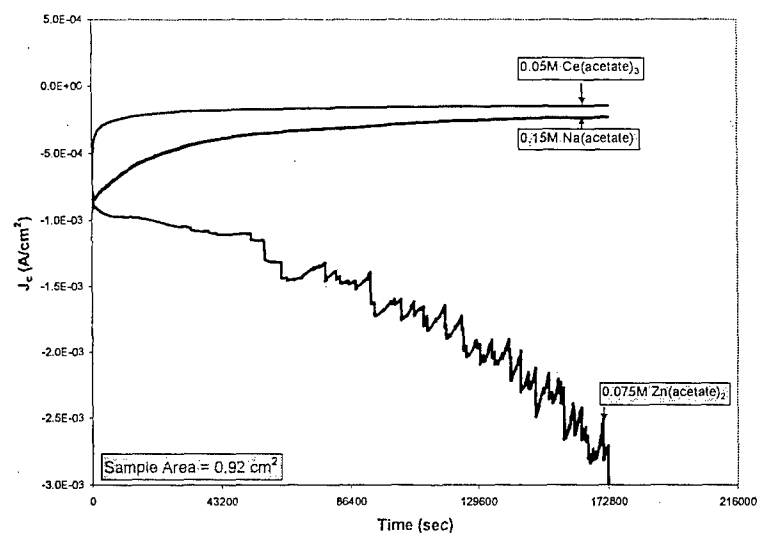
Fig. 16 – Hydrogen charging profiles in acetate-based solutions (deaerated, $\eta = -0.5V$ pH = 8.2 for Na(ac), pH = 6.9 for Ce(ac)$_3$, pH = 6.8 for Zn(ac)$_2$, T = 23°C)
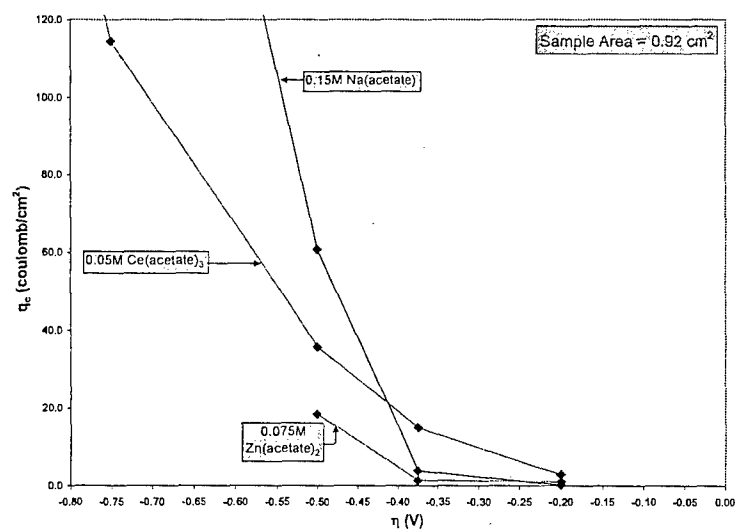
Fig. 17 – Hydrogen evolutions reaction charge measured against applied η in acetate-based solutions (deaerated, pH = 8.2 for Na(ac), pH = 6.9 for Ce(ac)$_3$, pH = 6.8 for Zn(ac)$_2$, T = 23°C) [17]
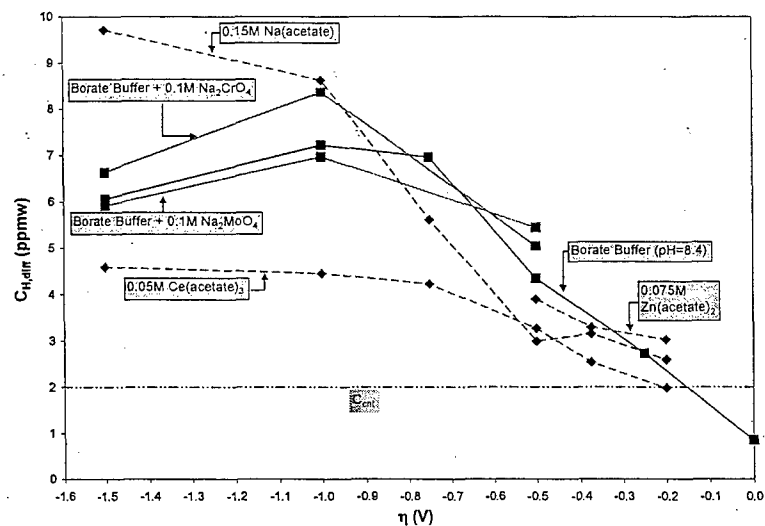
Fig. 18 – Diffusible hydrogen concentration vs. applied η for diff. inhibitor solutions (deaerated, pH = 8.4 for borates, pH = 8.2 for Na(ac), pH = 6.9 for Ce(ac)$_3$, pH = 6.8 for Zn(ac)$_2$, T = 23°C) [17]
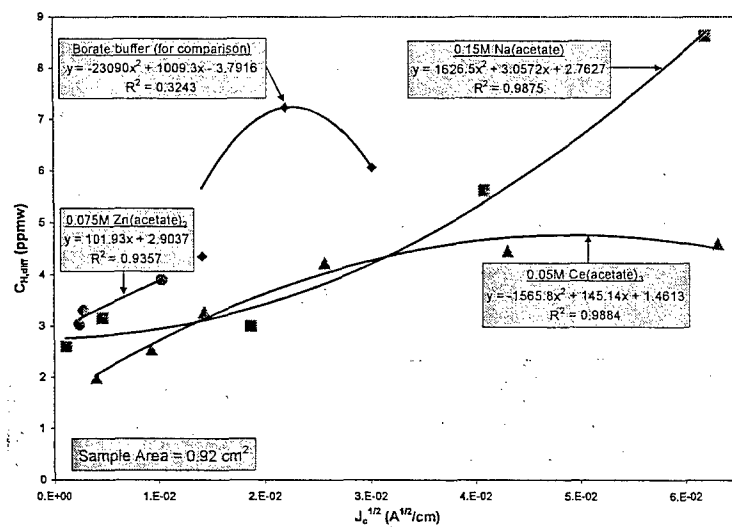
Fig. 19 – Diff. H conc. measured against the square root of cathodic current in acetate solutions (deaerated, pH= 8.4 for borate, pH= 8.2 for Na(ac), pH= 6.9 for Ce(ac)$_3$, pH= 6.8 for Zn(ac)$_2$, T= 23°C)
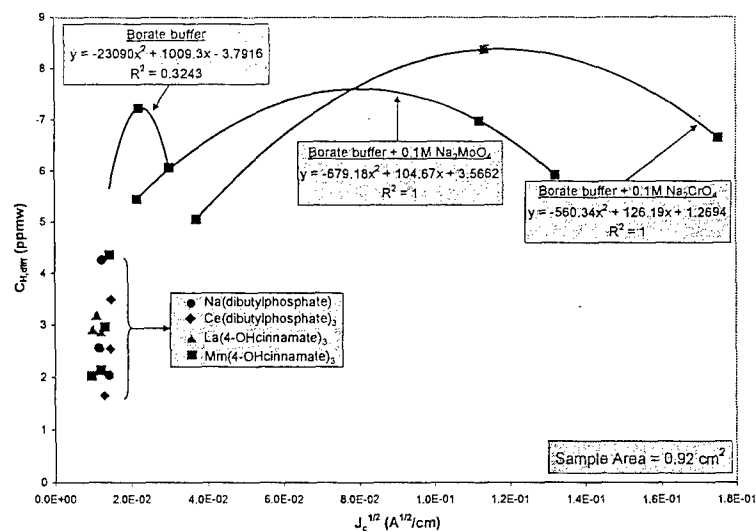
Fig. 20 – Diff. H conc. measured against the square root of cathodic current density in inhibitor solutions (deaerated, pH = 8.4 for borates, pH = 5.4 for dbp, pH = 6.0 for cinnamates, T = 23°C)
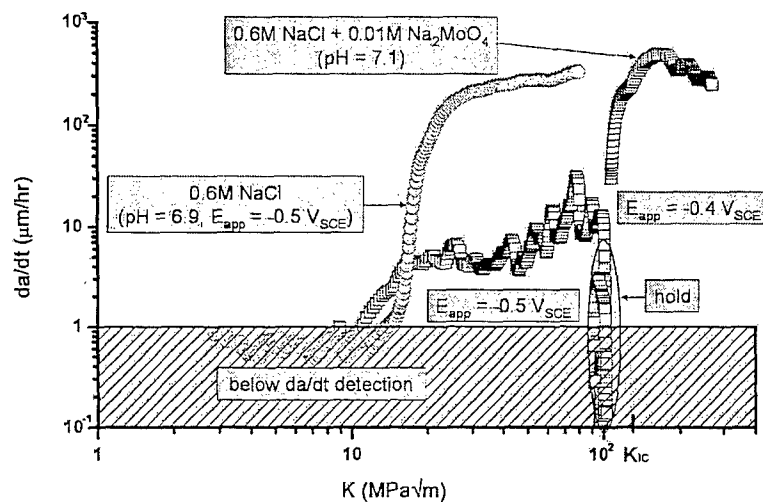
Fig. 21 – Effect of Na_2MoO_4 on da/dt in 0.6M NaCl (aerated, pH = 7.1, E_{app} = -0.5V_{SCE}, T = 23°C) [16,17]
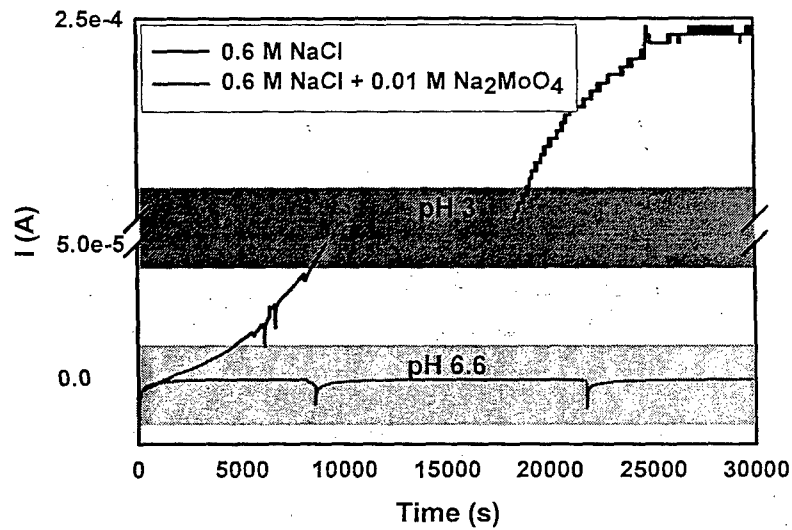
Fig. 22 – Current profile with time a rescaled crack in 0.6 M NaCl + 0.01 M Na$_2$MoO$_4$ (aerated, crevice gap = 1.5 mm, E$_{app}$ = -0.4V$_{SCE}$) [16]
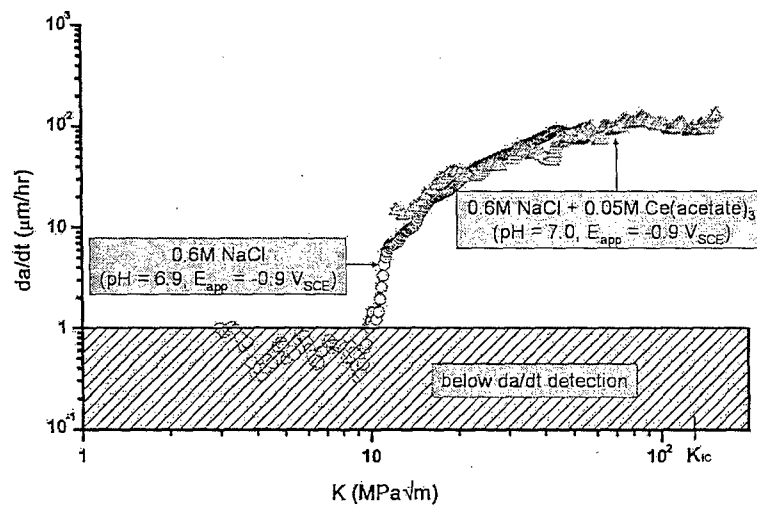

Fig. 23 – Effect of Ce(acetate)$_3$ on da/dt in 0.6M NaCl (aerated,pH= 7.0,E$_{app}$= -0.9 V$_{SCE}$, T = 23°C) [16,17]
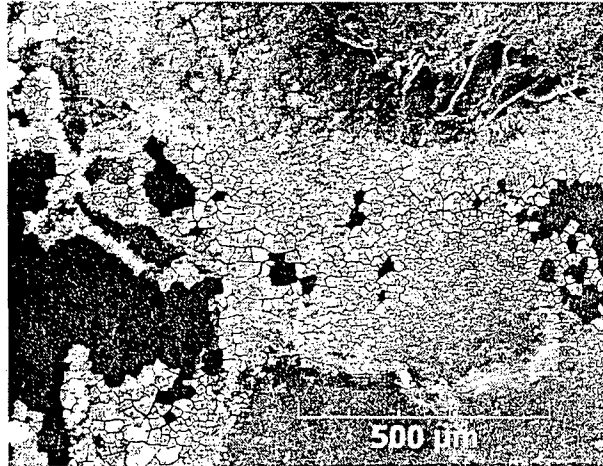
27

Fig. 24 - SEM micrograph of UNS K92580 pre-crack surface partially covered with Ce(OH)$_3$
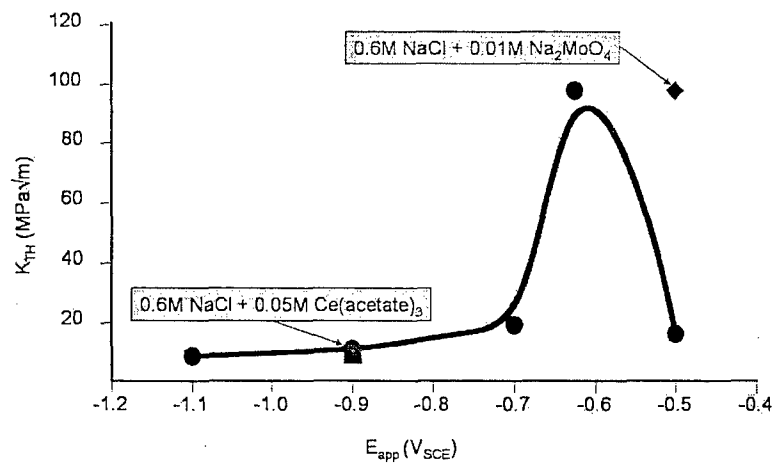[Y. Lee, 2005]

Fig. 25 – K$_{TH}$ profile vs. E$_{app}$ for UNS K92580 in 0.6M NaCl (Aerated, pH ~ 6.9 - 7.1, T = 23°C) [16,17]